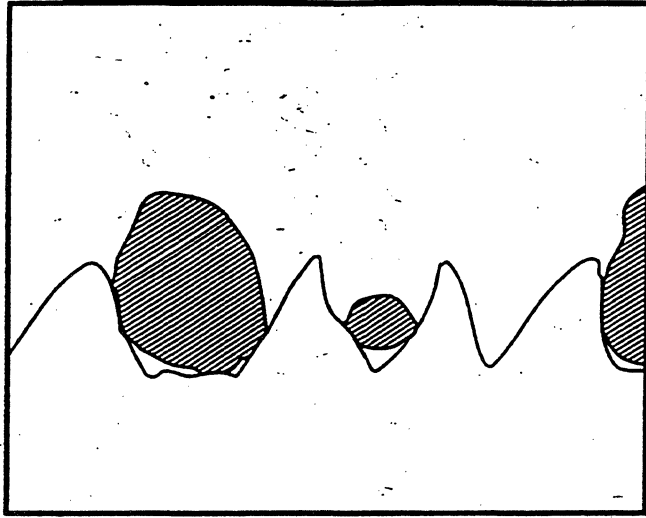


Instructor

Dr. Andrew M. Homola, Research Staff Member, Almaden Research Center, IBM Corporation, San Jose, Calif.

Tribology

in Hard Disk Drive



-
- 2.0 CEUs
 - Measuring Techniques
 - Properties of Interfaces
 - Surface Properties
 - Friction and Wear
 - Lubrication and Lubricants
-

**A 10-Week Continuing
Education Course**

**School of Engineering
Santa Clara University**

Course Schedule

LECTURE

1 Measuring techniques: mechanical profilometry, optical interference, electron microscopy, sectioning, electrical resistance, surface tunneling microscopy (STM), and atomic force microscopy (AFM).

LECTURE

2 Real and apparent contact area; effect of load and shear; factors affecting real area of contact, elasticity, plasticity, and creep.

LECTURE

3 Properties of interfaces: volumetric properties, plastic and elastic yield strength, penetration hardness, and stored elastic energy.

LECTURE

4 Surface properties: chemical reactivity, absorbed surface layers, and surface energy.

LECTURE

5 Interfacial forces: origin and magnitude of surface forces; van der Waals; electrostatic, steric, and meniscus forces; and role of surface forces in adhesion and friction.

LECTURE

6 Adhesion: basic concept of adhesion, factors affecting adhesion surface forces (dispersive, meniscus, and viscous), and effects of time and environment.

LECTURE

7 Friction: origin and magnitude of the friction force, quantitative laws of frictions, simple adhesion theory, and various contributions to the friction force.

LECTURE

8 Friction of metals and nonmetals, irregular friction (stick-slip), and experimental measurements of friction.

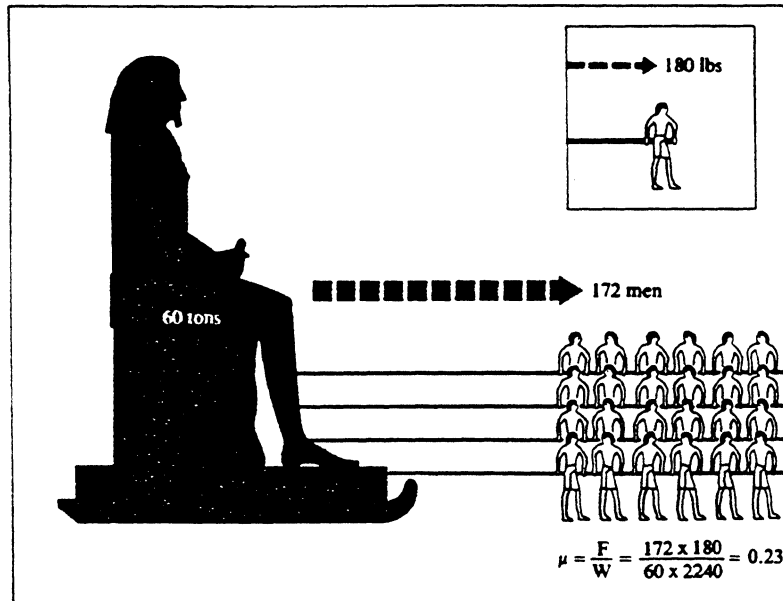
LECTURE

9 Wear: types of wear; adhesive, abrasive, corrosive, and surface fatigue; and measurements of wear.

LECTURE

10 Lubrication: properties of lubricants; boundary of lubrication; general requirements, mechanism, and role of lubricant attachment; solid film lubrication; shear properties of molecular thin films; and model of molecular friction.

Fig. 4.18
Tribology in Ancient Egypt –
calculation of the coefficient of
friction in the transport of an
Egyptian colossus.



as 180 lbf (800 N) per man for the present calculation. On this basis the total effort, which must at least equal the friction force (F), becomes, 172×180 lbf (172×800 N).

Thus, the coefficient of friction (μ) is given by

$$\mu = \frac{F}{W} = \frac{172 \times 800}{600 \times 10^3} = 0.23.$$

The basis of this calculation is summarized in Fig. 4.18. It is interesting to note that Bowden and Tabor (1950) quote coefficients of friction for wood-on-wood as follows:

wet 0.2 clean (and dry) 0.25–0.5

A comparison of the calculated coefficient of friction for the Egyptian sledge with the values quoted by Bowden and Tabor suggests that the sledge was indeed sliding over lubricated planks of wood.

This survey of the remarkable tribological achievements in connection with the drill, the potter's wheel, wheeled vehicles, the use of lubricants and the transport of heavy stone statues completes our study of the early civilizations in Mesopotamia and Egypt. Brief mention will now be made of a few similarities, and differences, in the developments in later civilizations in other parts of the world.



Fig. 4.16
Transporting the statue of
Ti—from a tomb at Saqqara,
Egypt (c. 2400 B.C.). (Steindorff,
1913).



Fig. 4.17
The first recorded tribologist—
pouring lubricant (water) in front
of the sledge in the transport of
the statue of Ti (c. 2400 B.C.).
(Steindorff, 1913)

References

- ^{Bbb} *"Tribology and Mechanics of Magnetic Storage Devices"*, by Bhushan B., Spring-Verlag New York Inc., 1990.
- *"Friction and Wear of Materials"*, by Rabinowicz E., John Wiley and Sons, Inc., New York, 1965.
- *"The Friction and Lubrication of Solids"* by Bowden, F.P. and Tabor, D., Oxford at the Clarendon Press, Part I (1950) and Part II (1964).
- *"Tribology"* by Czichos, H., Elsevier Scientific Publ. Co., New York, 1978.
- *"Surface Effects in Adhesion, Friction, Wear, and Lubrication"* by Buckley, D.H., Elsevier Sci. Publ. Co., New York, 1981
- *"Introduction to Tribology"*, by Halling, J., Springer-Verlag New York Inc., 1976.
- *"Handbook of Tribology"* by Bhushan B. and Gupta, B.K., McGraw-Hill, Inc., 1991.

60 tons → 172 people

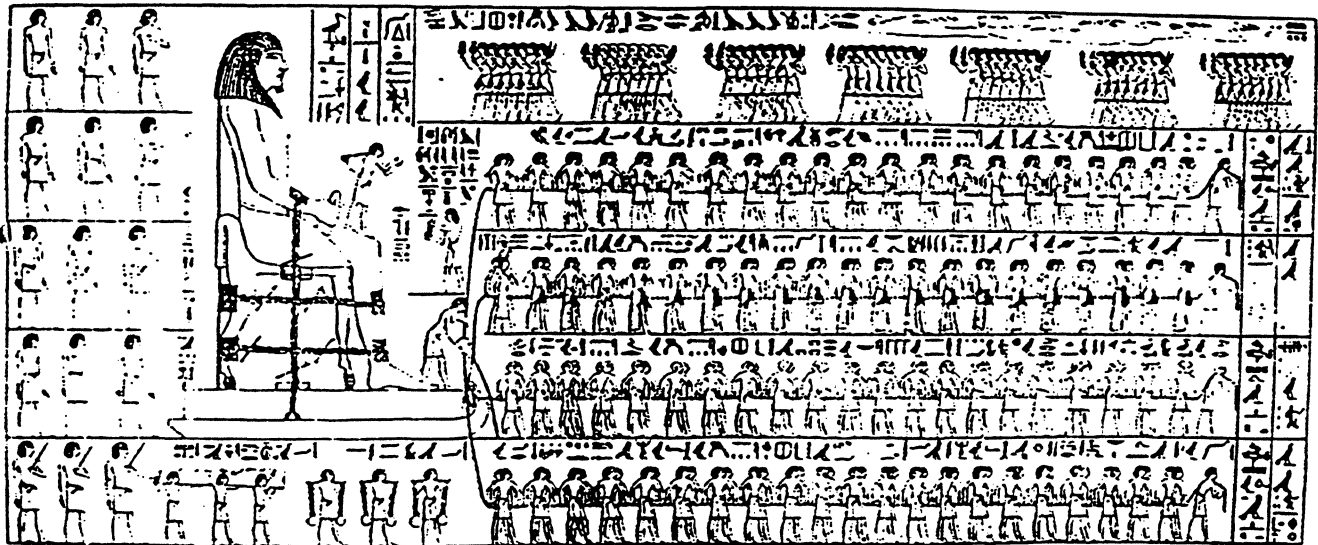


Fig. 1.3. Transporting an Egyptian colossus ca 1880 B.C. From a drawing in a grotto at El Bersheh. (Reproduced from Sir A. H. Layard, *Discoveries in Nineveh and Babylon.*)

TRIBOLOGY OF HEAD-TO-MEDIA INTERFACE

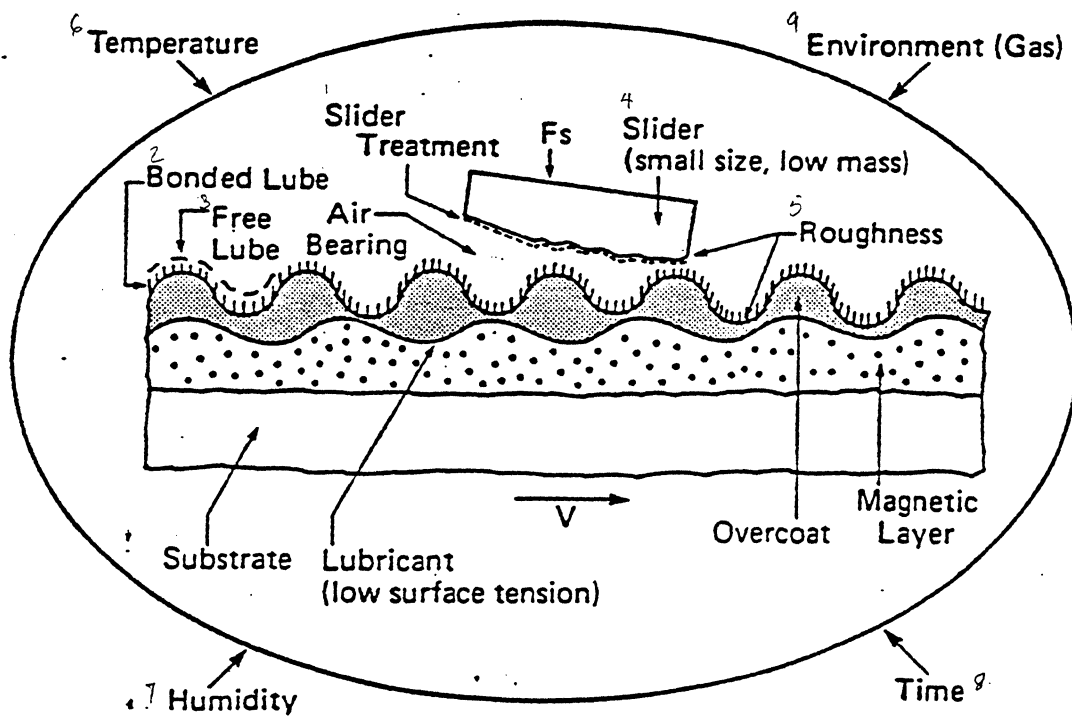
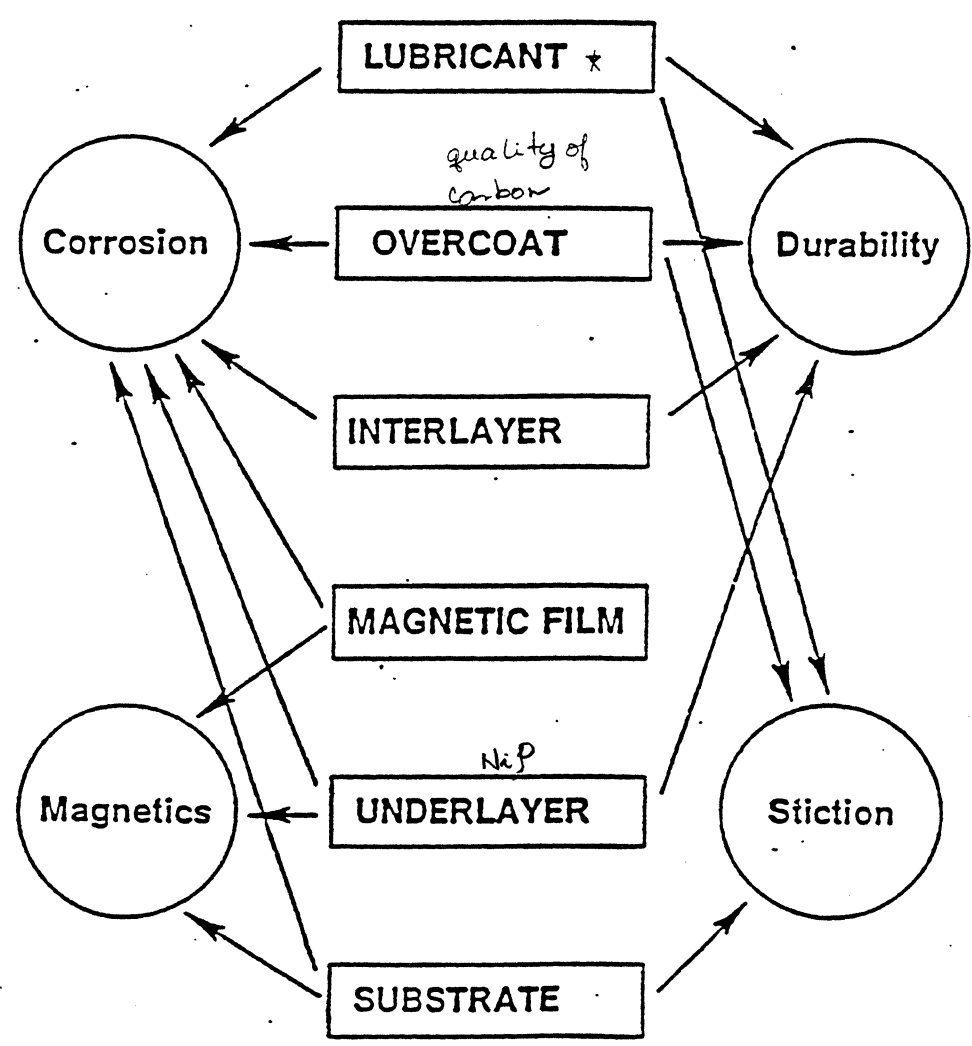


Figure 6. Schematic representation of various factors affecting reliability of the head/disk interface according to Mitsuya.¹⁵ (IEEE Trans. Magn. MAG-23, p. 2674, 1987)

FILM DISK: TECHNOLOGY ISSUES



TRIBOLOGICAL REGIMES

1. Stiction Regime *

when the power is switched on in a disk drive, enough force has to be applied to the slider to overcome the static friction or stiction force on the slider.

2. Dragging Regime *

during the relative low speeds, $\leq 10\text{m/ sec}$, encountered during takeoff and landing, the slider maintains almost constant contact with the disk. In this regime, dynamic frictional forces and wear dominate.

3. Flying Regime

during flying, the slider contacts the medium only infrequently, but at high speeds (10-40 m/sec) most contacts are caused by collision with media asperities, third bodies such as corrosion products, or other contaminants.

impact is so high

RECORDING MEDIA

- Historical

First came metal wires (remember Poulsen!), then metal tapes, next we went to oxide particles held in organic binder on polymer substrate (audio tapes).

For digital storage, plated metal films on drums were used, followed by particulate (oxide) media on disks. Today, we have returned to metal films for rigid disks for future applications.

- Particulate Media

- γ -ferric oxide particles, accicular, $M_s \approx 350 \text{ emu/cm}^3$, $H_c \sim 300\text{-}400 \text{ Oe}$.
- Advanced particulate media Co-modified γ - Fe_2O_3 (higher H_c), CrO_2 and metal particles.
- In general, oxides are stable, both thermally and chemically.

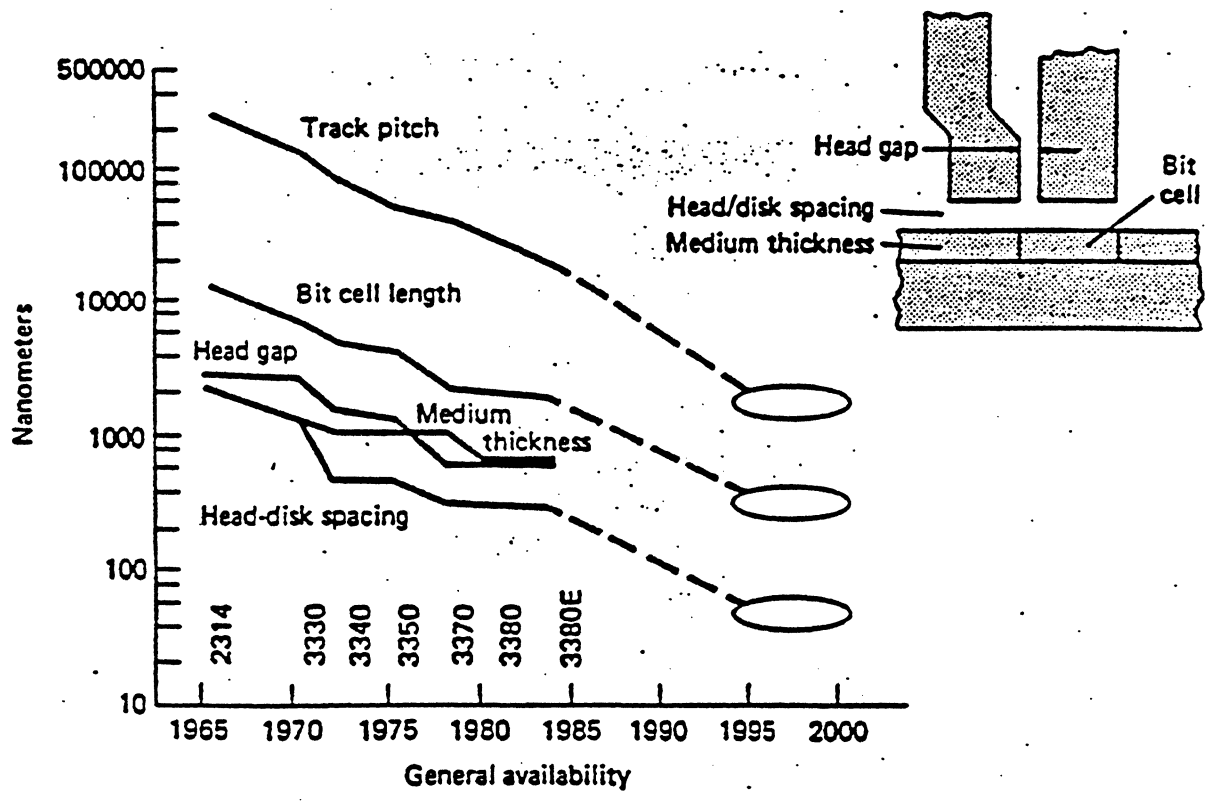
- Film Media

- Usually Co-based alloys (sputtered γ - Fe_2O_3 is the primary exception) with hexagonal crystal structure.
- Plated, evaporated or sputtered.
- Thickness 100\AA to $\sim 2000\text{\AA}$.
- M_s can be as high as 1000 emu/cm^3 and H_c can be in range $400\text{-}2000 \text{ Oe}$.

magnet = >
properties

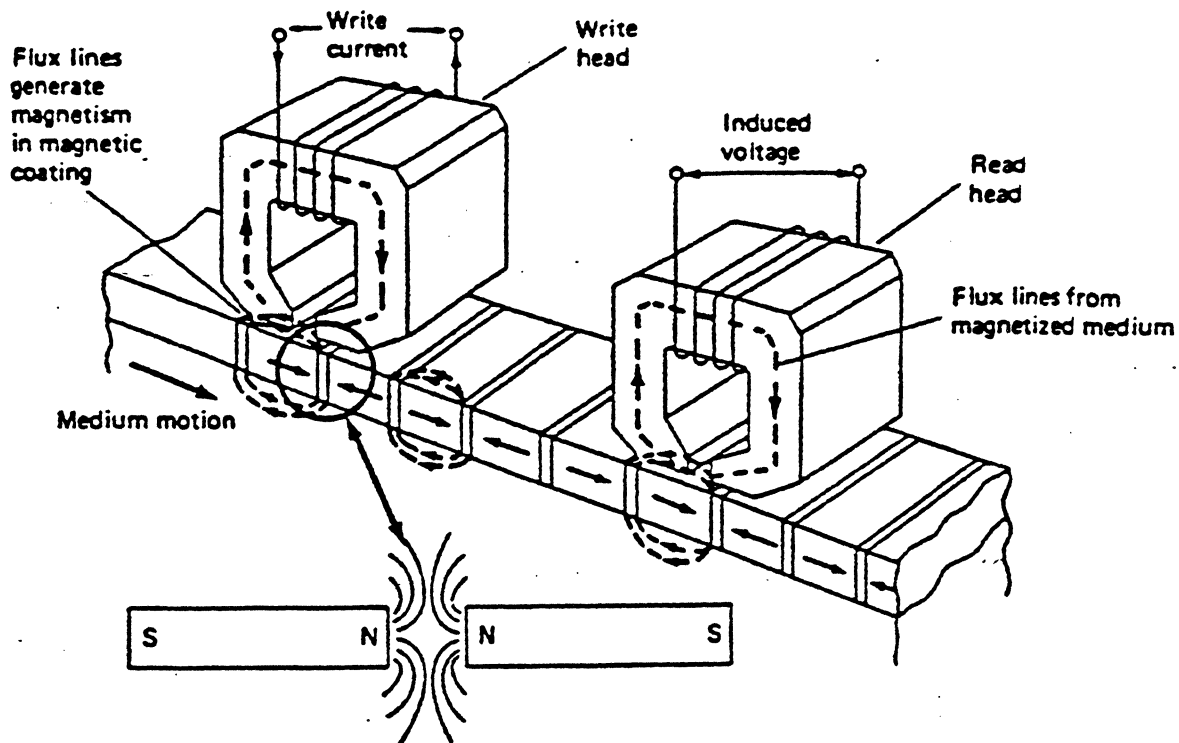
Adv:

Herein lies the advantage of film media - high moment, thinner layers - better resolution, high ^{force} coercivity and ability to tailor magnetics by the deposition process.

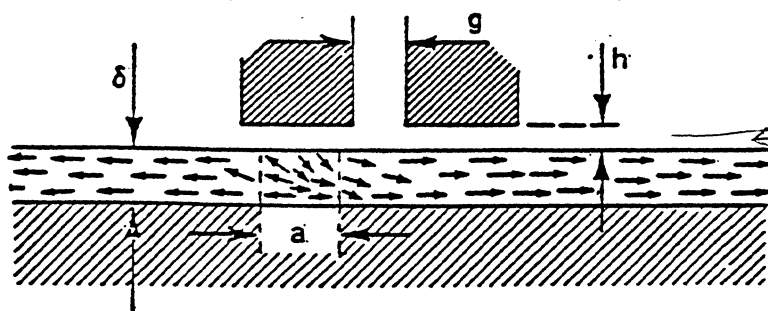


Evolution and future projections of head and disk parameters for IBM rigid disk drive products.

Principle of horizontal magnetic recording and playback.

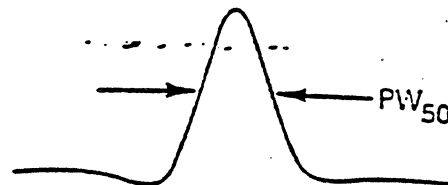


Recording Parameters



decrease the
← Covercoat

$$PW_{50} = \sqrt{g^2 + 4(a+h)(a+h+\delta)}$$



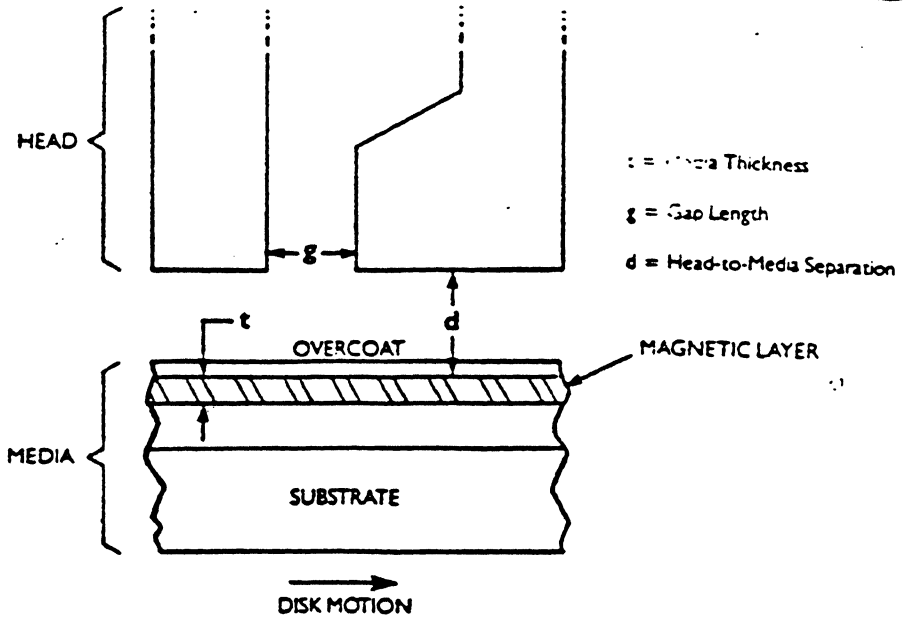
no arrow no
to...

- g = Head Gap
- h = Flying Height
- delta = Media Thickness

$$a = \text{Transition Width} = \frac{2M_R \delta}{H_C}$$

HEAD/MEDIA GEOMETRY.

KEY VARIABLES



Readback voltage

$$e(t) = 4\pi \times 10^{-8} \alpha N W \frac{\mu_r}{\mu_r + 1} M_r U (2\pi\delta/\lambda) T(\lambda) S(\lambda) G(\lambda) \cos(2\pi x_0/\lambda)$$

where

M_r = remanent magnetization (remanence or residual flux density) of the medium (emu/cc, G, or Wb/m²; 1 emu/cc = 4π G = 4π × 10⁻⁴ Wb/m²)

= Spσ_rρ,

$T(\lambda)$ = thickness loss

$$= \frac{1 - \exp(-2\pi\delta/\lambda)}{2\pi\delta/\lambda}$$

$S(\lambda)$ = separation loss

= exp(-2πd/λ),

or $S(\lambda) = -54.6d/\lambda$
(in dB form)

$G(\lambda)$ = read gap length loss

$$= \frac{\sin(\pi g/\lambda)}{(\pi g/\lambda)}$$

α = head efficiency factor,

N = number of turns in the head,

W = width of the head (mm),

μ_r = relative permeability of the core = flux density in the core / flux density in air.

U = sliding speed (m·s),

$x_0 = U t$, the longitudinal position of the head with respect to an arbitrary reference in the medium (mm),

t = time (s),

λ = recorded wavelength (μm),

δ = thickness of the medium (μm),

d = effective magnetic spacing between the head and the surface of the medium (μm) (which can be higher than the mechanical spacing),

g = gap length of the head measured from one pole face to another (μm),

S = remanence squareness (reduced saturation remanence) of the hysteresis loop of the medium = M_r/M_s ,

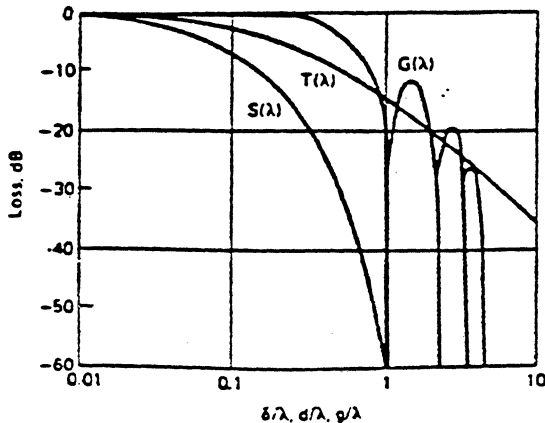
M_s = saturation magnetization of the medium (emu cc, G, Wb m⁻²),

ρ = packing fraction of particles in the coating (0-1.0),

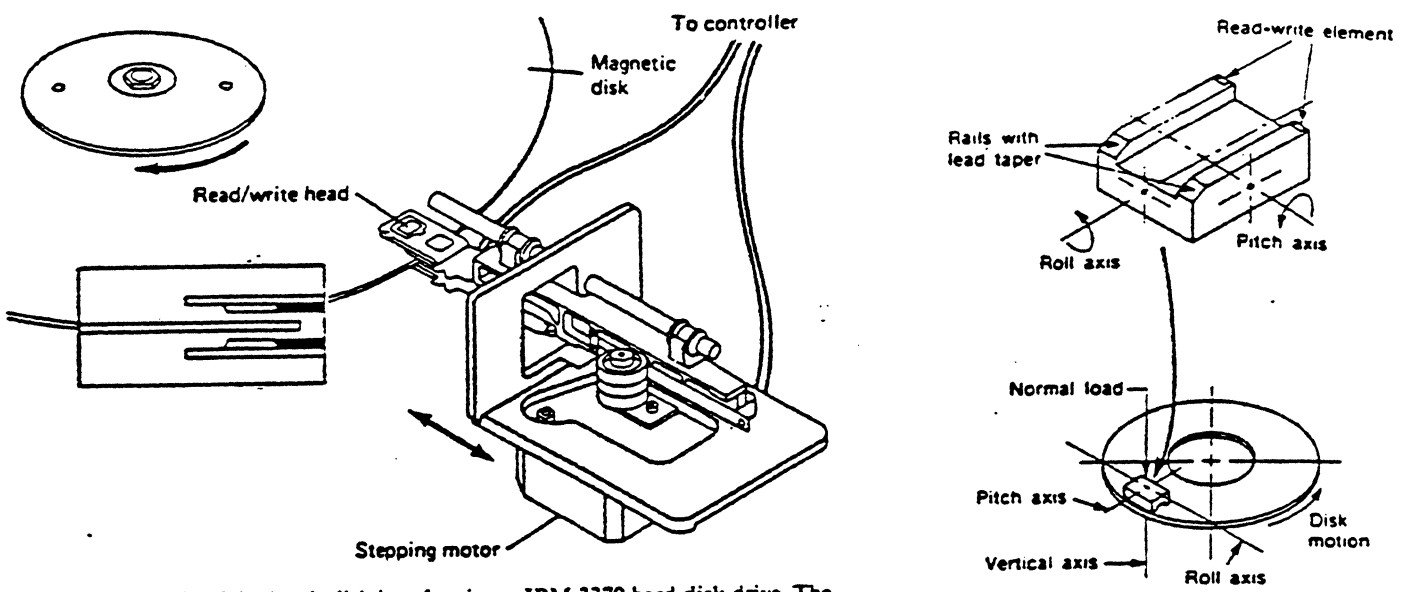
σ_r = specific saturation magnetization of particles (emu g) and

ρ = density of particles (g·cc).

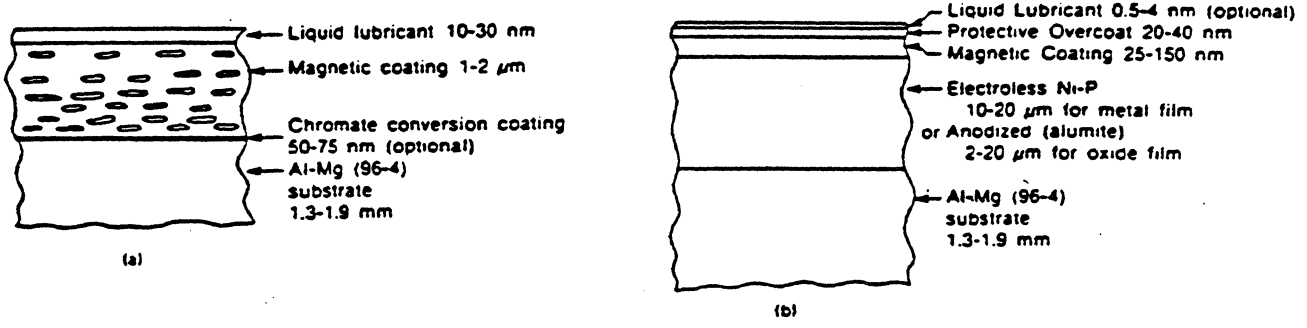
10°C - 65°C - no effect.



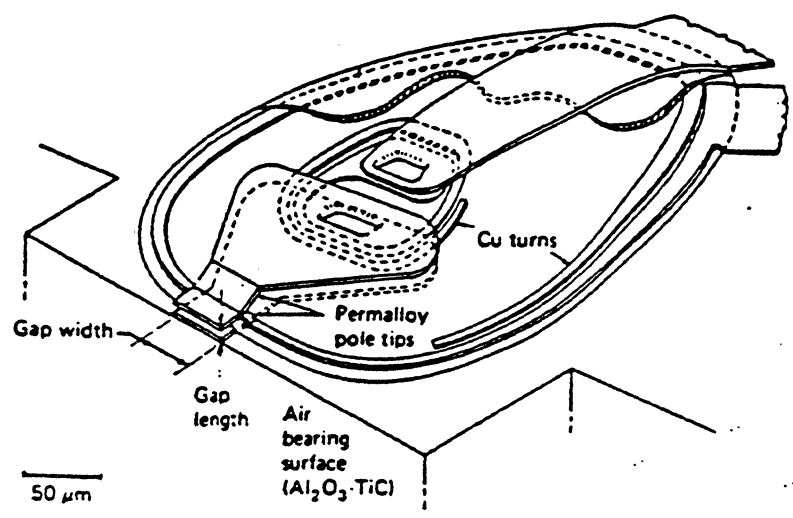
Wallace, R.L. J. Bell System Techn. 30, 1145 (1951).



Schematic of the head-disk interface in an IBM 3370 hard disk drive. The inset shows the profile of the head and disk and the spacing between them.

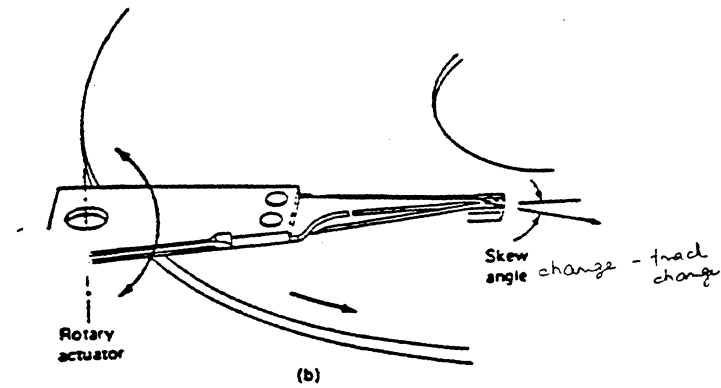
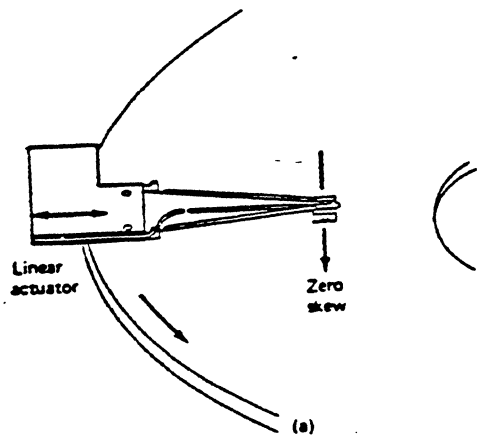


Sectional view of a rigid disk: (a) particulate and (b) thin film.

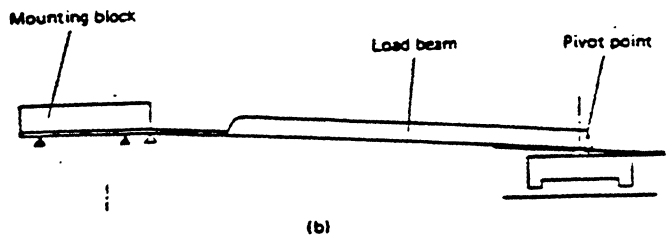
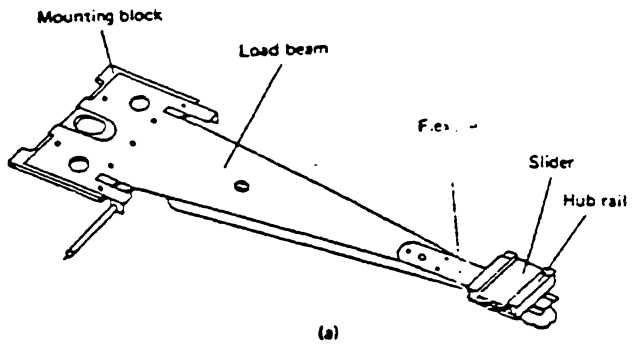


Schematic of an inductive-type thin-film read-write element in an IBM 3370 disk head slider (located at the trailing edge of each rail) (Jones, 1980).

Disk Storage Technology



Schematic of (a) linear and (b) rotary actuators with mini-Winchester heads.



Schematic of 3370-type suspension-head slider assembly.

5-62

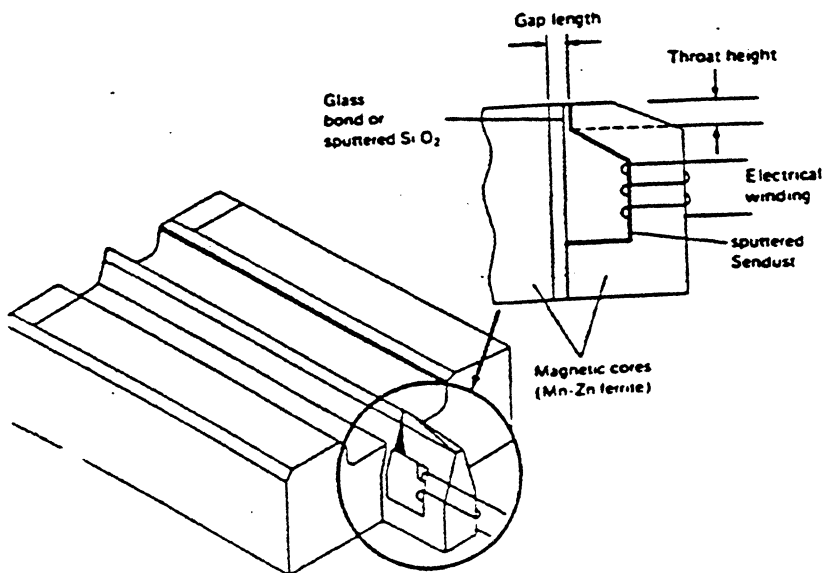
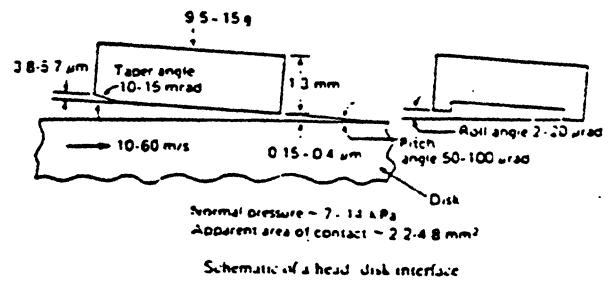
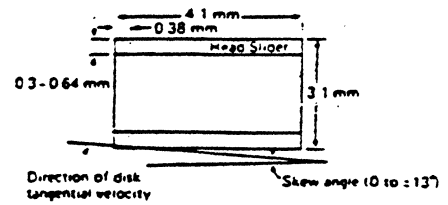


Table 1.8(b). Selected physical properties of various thin-film rigid disk substrates

Substrate material	Density, kg/m ³	Young's modulus, GPa	Knoop hardness of surface, GPa (kg/mm ²)	Flexural strength, MPa	* Thermal conductivity, W/m K	Specific heat, J/kg. K	Coefficient of thermal expansion, × 10 ⁻⁶ C	Elec resis, μohm · cm
Al-Mg (5086) with Ni-P	2680	70	5.9-7.8 (600-800)	115 ^{a,c} 250 ^{a,d}	127	900	23.8	5.6
Chemically strengthened (~ 15 μm) Soda-lime silica float glass (Nippon sheet glass)	2500	73	5.4 (550)	275 ^b	0.75 ✓	750	8.5-9.0	10 ¹⁸ ✓
Chemically strengthened (~ 125 μm) alkali-aluminosilicate glass (not break) (Corning U313)	2460	73	5.8 (590)	345 ^b			8.8	10 ²³ ✓
Lithium silicate glass ceramic (Corning)	2410	87	4.9 (500)	175 ^b	2.5 ✓	880	10.3	5 × 10 ²⁰ ✓
Cordierite (2MgO · Al ₂ O ₃ · 5SiO ₂) glass ceramic (Pyroceram-Corning 9606)	2600	120	6.9 (700)	225 ^b	3.1 ✓	970	5.7	
Stainless steel 440C (for reference)	7720	200	2.4 (240) ^e 6.4 (650) ^e	450 ^{a,c}	25	480	9.8	20

* Yield strength.
^a Maximum design stress is about 1/6 of flexural strength.
^c Annealed.
^d Strain hardened.
^e Heat treated.
smooth, light, mechanically strong.

Table 1.6. Selected physical properties of hard head materials

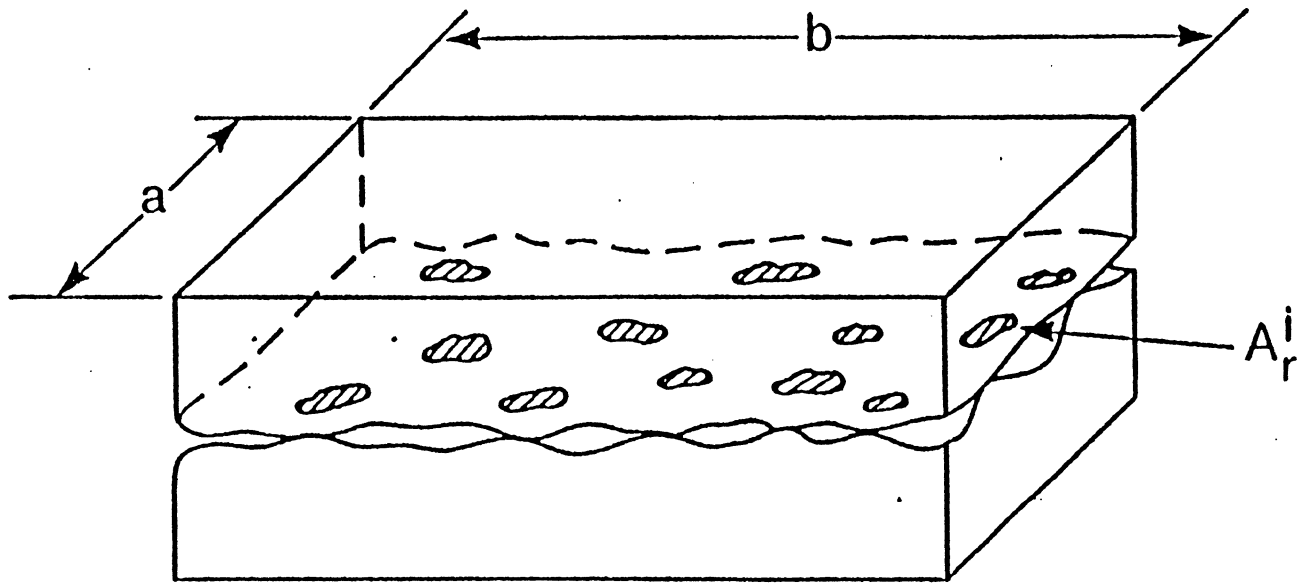
Material	Density, kg/m ³	Young's modulus, GPa	Knoop microhardness, GPa (kg/mm ²)	Flexural strength, MPa	Electrical resistivity, ohm · cm
Ni-Zn ferrite	4570	122	6.9 (700)	150	10 ⁴ -10 ⁷
* Mn-Zn ferrite	4570	122	5.9 (600)	120	5 × 10 ⁻² -5 × 10 ⁻¹
Al ₂ O ₃ -TiC (70-30) <i>ceramic</i>	4220	450*	× 22.6 (2300)	880	2 × 10 ⁻² -3 × 10 ⁻³
ZrO ₂ -Y ₂ O ₃ (94-6)	6360	210	12.8 (1300)	500-700	10 ¹⁰
CuTiO ₃	3950	110	9.3 (950)		
BaTiO ₃ (for reference)	4320	110	10.3 (1050)		
Pyroceram (Glass Ceramic)	2410	87	4.9 (500)	200	5 × 10 ¹⁴

Two surfaces should be same hardness for rubbing each other.

Table 1.10(b). Environmental requirements of a metal-film rigid disk with a 130-mm diameter for low-end applications

Disk operating environment	
Temperature:	5 to 60 C
Relative humidity:	8 to 80%..
Maximum wet bulb temperature:	30 C
Disk storage environment	
Temperature:	0 to 65 C
Relative humidity:	8 to 80%..
Maximum wet bulb temperature:	30 C
Disk shipping environment	
Temperature:	-40 to 65 C
Relative humidity:	8 to 80%..
Maximum wet bulb temperature:	30 C

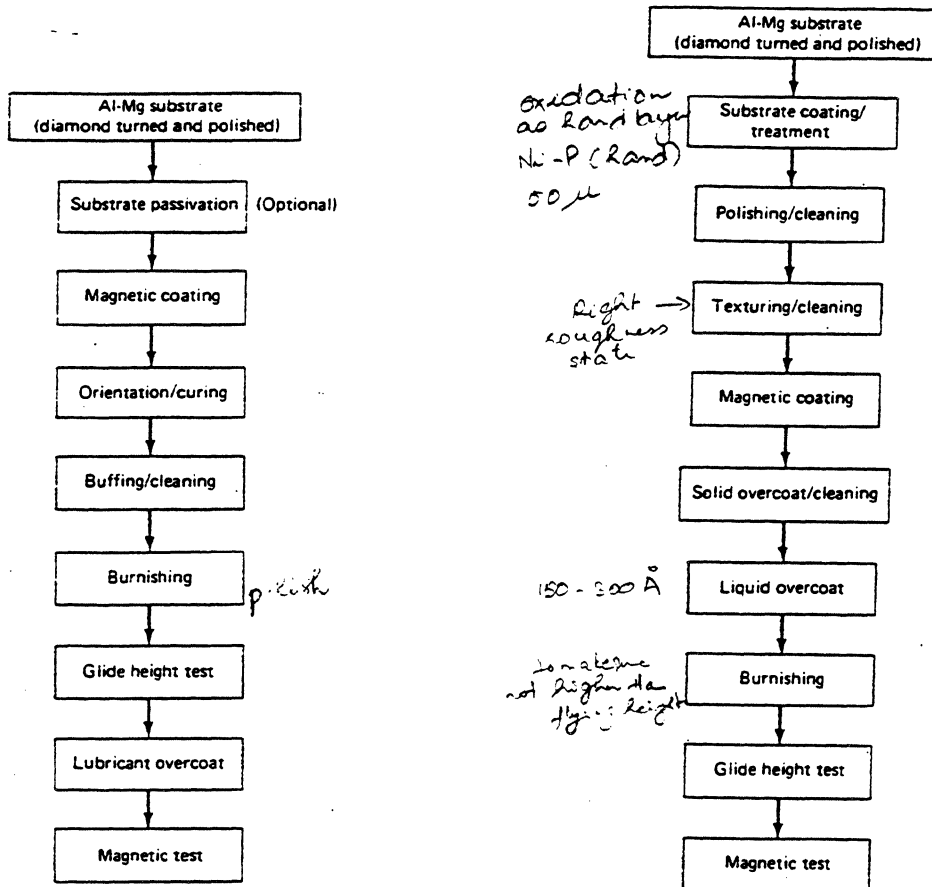
from B.B.



$$A_0 = a \cdot b \gg A_r = \sum_{i=1}^n A_r^i \quad (n: \text{number of contacts})$$

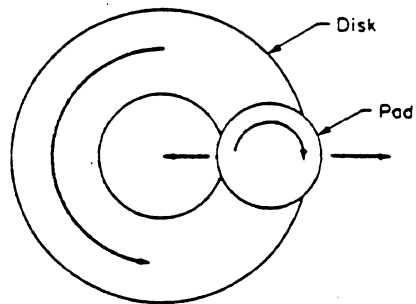
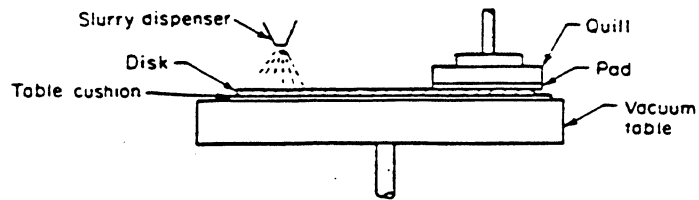
FIGURE 1.

Manufacturing Process of Rigid Disks

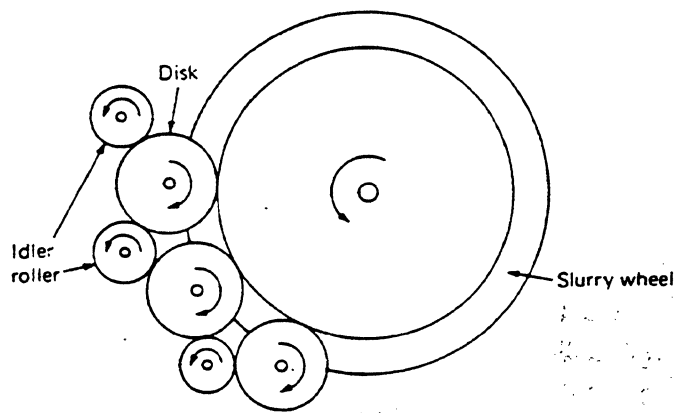


(a)
particulate media

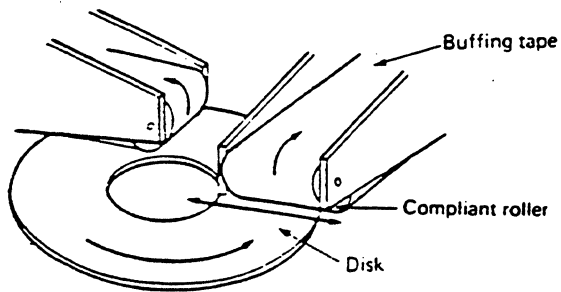
(b)
thin film media
not covalent bond.
physical strong bond



(a)



(b)



(c)

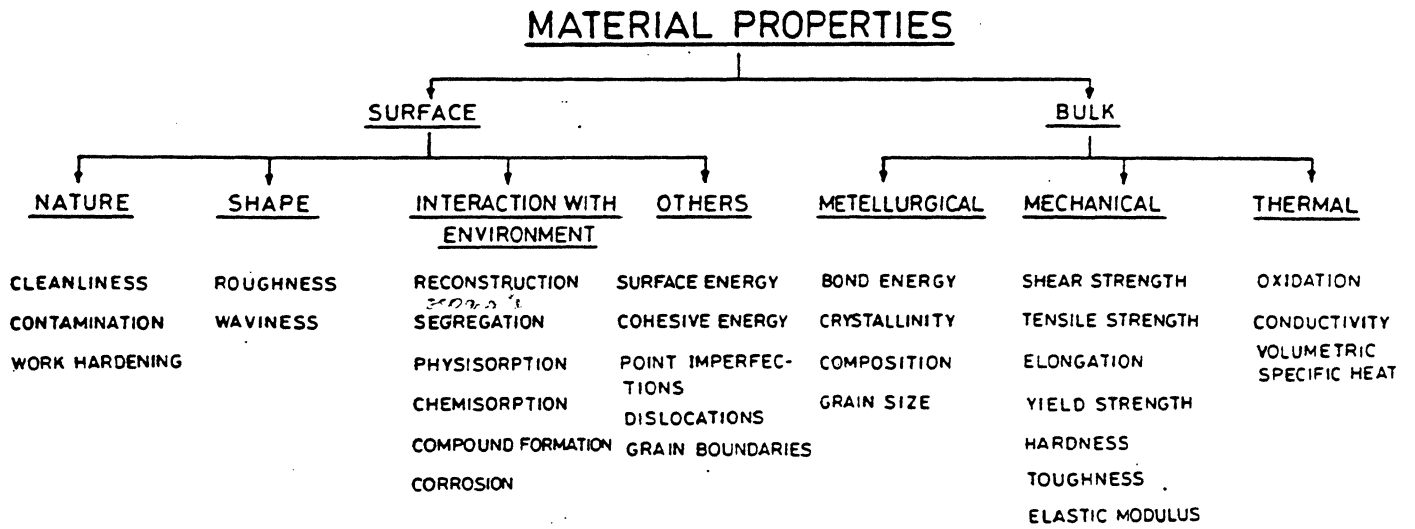
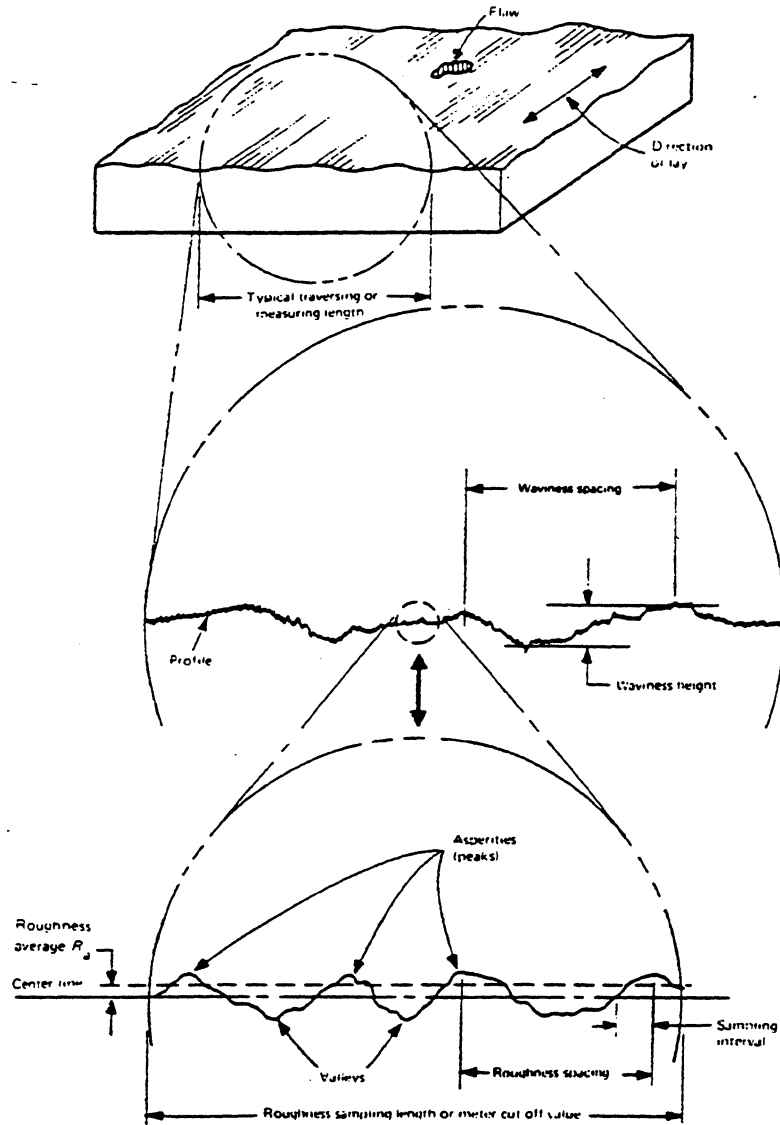


FIGURE 3.1 Various surface and bulk properties that are relevant to tribological behavior of materials.

from B.B.

Pictorial Display of Surface Texture



the geometric characteristics fall into three categories:

- **Roughness (or microroughness):** Surface irregularities of short wavelength, characterized by hills (or asperities) and valleys of varying amplitude and spacings that are larger than molecular dimensions. These create the predominant surface pattern, which exhibits those surface features intrinsic to the manufacturing process.
- **Waviness (or macroroughness):** Surface irregularities having much longer wavelength than microroughness. They often result from heat treatment, machine or workpiece deflections, vibration, or warping strains.
- **Errors of form:** Gross deviations from nominal shape. In general these deviations are not considered a part of the surface texture.

Average Roughness Parameters

Surface roughness most commonly refers to the variations in the height of the surface relative to a reference plane.

The departure of the profile from the reference plane may be identified by the parameters rms (root-mean-square) and cla (center-line-average).

$$rms = \left[\frac{1}{n} \sum_{i=1}^n (z_i)^2 \right]^{1/2} = \delta$$

It is statistically identical with the standard deviation .

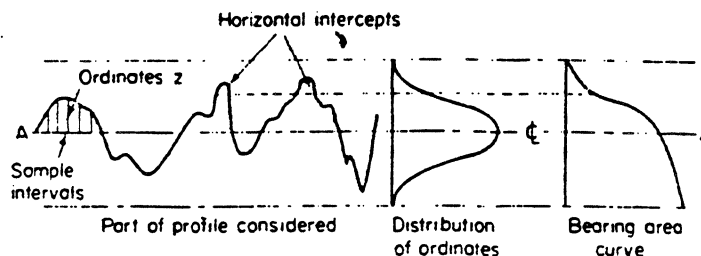
and

$$cla = \frac{1}{n} \sum |z_i|$$

It is often referred to as the arithmetic average or roughness height rating

for most engineering surfaces the rms and cla values are very similar and the rms is simply the standard deviation, δ , of the ordinate distribution curve.

$$\delta \sim \sqrt{\pi/2} cla \sim 1.25 cla$$



The conversion of a surface profile to an ordinate distribution and a bearing area curve.

other heights descriptors are also used

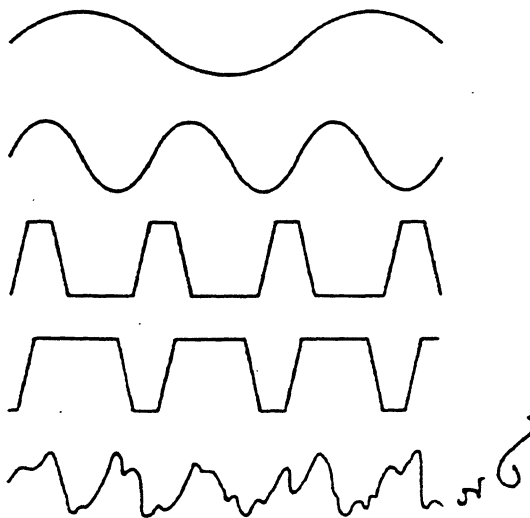
R_t (P-V) is the distance between the highest asperity (peak) and the lowest valley;

R_p is the distance between the highest asperity and the mean line;

R_z is the distance between the average of five highest asperities and the five lowest valleys. *density more ductility*

for complete characterization of a surface, any of these parameters are not sufficient.

They do not provide any information about the slopes, shapes, and sizes of the asperities or about the frequency and regularity of their occurrence.



Geometric profiles having the same c.l.a. value

They are mainly used for classification of the surfaces of the same type that are produced by the same method.

Surface Height Distribution Function

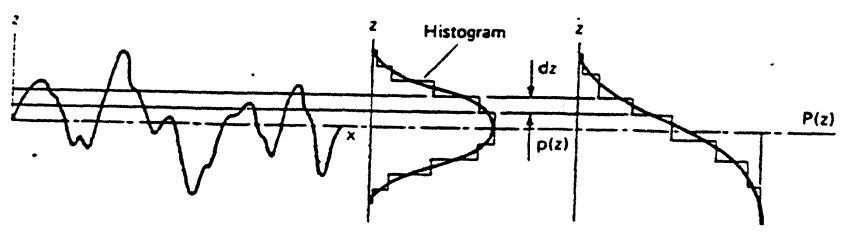
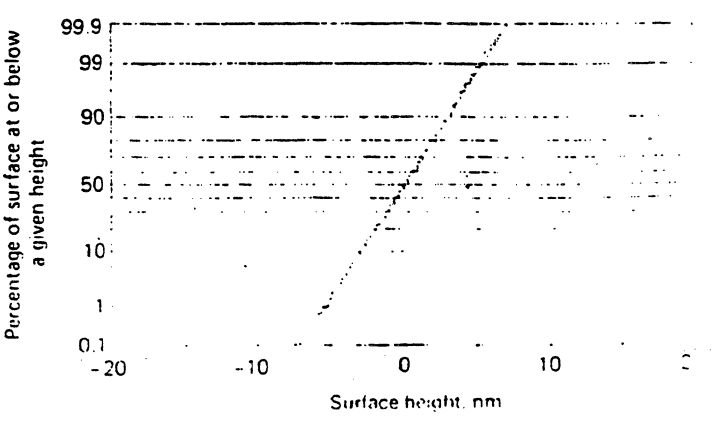
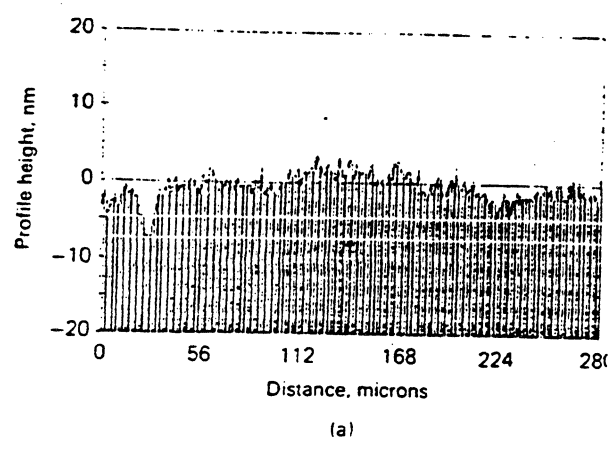
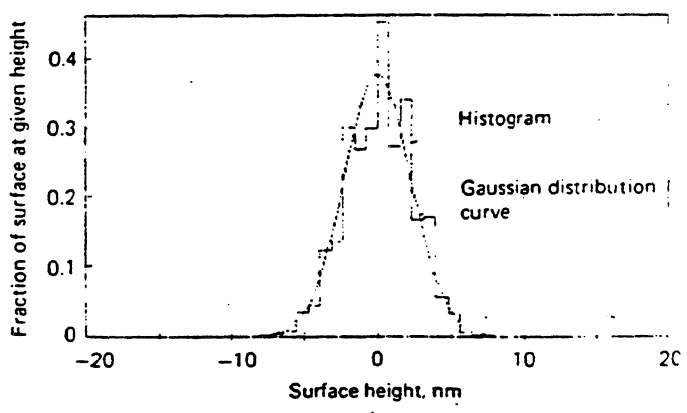


Fig. 2.7. Method of deriving the histogram and cumulative distribution function from a surface height distribution.

Surface profile can be represented statistically in terms of the probability density function P_z also known as a histogram. From the surface height distribution the cumulative distribution function can be derived. It is also known as the Bearing Area Curve.

Example of lapped nickel-zinc ferrite surface

rms = 2.2 nm
P-V = 34.6 nm



Gaussian or Normal Probability Density Function

The data representing a wide collection of random physical phenomena tend in practice to have a Gaussian function and in such cases the shape of the distribution curves is completely defined by the standard deviation σ (rms value), since the expression for the Gaussian distribution is:

$$P_z = \left[\frac{1}{\sigma \sqrt{2\pi}} \right] \exp \left[-\frac{z^2}{2\sigma^2} \right]$$

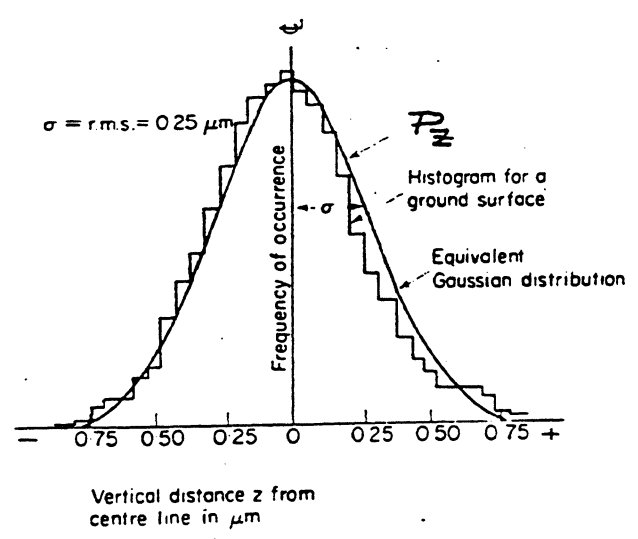


Fig. 2.13. A typical ordinate distribution curve for a ground surface.

68.3% of the results will differ from the average by less than one std. deviation ($\pm \sigma$),

95.5% by less than ($\pm 2\sigma$),

and

99.7% by less than ($\pm 3\sigma$).

9/21/94

recognizing the deficiency of one-parameter characterization, several authors proposed three and even five parameter modeling of surface roughness

SINGLE-PARAMETER MODELING OF SURFACE TEXTURE	
1. Nikuradse (1933)	Roughness factor (pipe flow)
2. —	Root-mean-square of profile (U.S.A.)
3. —	Centre-line-average of profile
4. Kreisle (1957)	Predominant peak roughness
5. Ocvirk and Du Bois (1958)	Predominant peak roughness
	RMS roughness
6. Myers (1962)	RMS of 1st derivative, or RMS of 2nd derivative, or directional parameter
7. Schultz and Beckmann (1962)	Mean void spacing
8. Horne and Dreher (1963), Sabey (1968)	Texture depth
9. Scrivner and Hudson (1964)	Length of profile
10. Peklenik (1965)	Autocorrelation function

THREE-PARAMETER MODELING OF SURFACE TEXTURE	
1. Posey (1946)	Histograms of profile, of 1st derivative (slope) and of 2nd derivative (curvature)
2. Rouse (1961)	Height, shape and spacing of asperities
3. Moore (1963)	Size, spacing and shape factors
4. Williamson and Hunt (1968)	Surface density, height distribution, and mean radius of asperities

according to Moore, D.F., in "The Friction and Lubrication of Elastomers", Pergamon Press, 1972.

- 1. Size
 - 2. Spacing
 - 3. Shape
- } Factors for typical average asperities (macro-roughness)
- 4. Micro-roughness at asperity peaks
 - 5. Height distribution of asperities

the parameters of interest in microcontacts of two rough surfaces are the surface density of the summits (n), the std. deviation of the probability distribution of summit heights (σ_p), and the mean radius (R_p) of the summit cups (G^{EW})

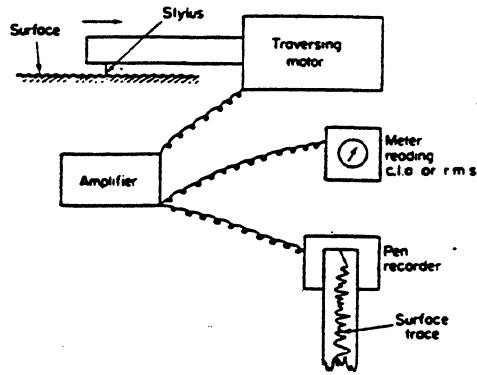
~~-----~~

Measurement of Surface Roughness

- ✓ **Mechanical Stylus Method** (requires contact)
 - ✓ **Optical Methods**
 - specular reflection
 - diffuse reflection
 - interference
 - ✓ **Electron Microscopy Methods** SEM
 - ✓ **Scanning Tunnelling Microscopy (STM)** atomic level
 - ✓ **Atomic Force Microscopy (AFM)**
- μ scale level* } non contact methods below μ level

Note:
STM and AFM are used for ultramicroscopic + measurements of surface roughness.

Mechanical Profilometer



(a)



(b)

Fig. 2.7. The basis of a profilometer and a typical profilometer trace.

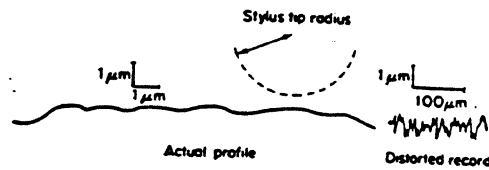
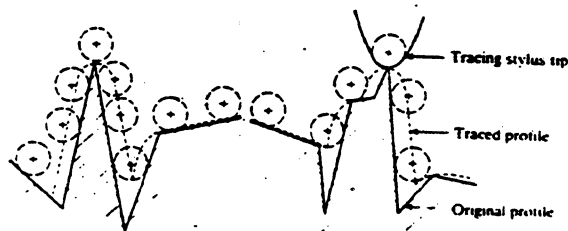


Fig. 2.8. The actual profile of a surface compared with the surface record obtained from a profilometer.

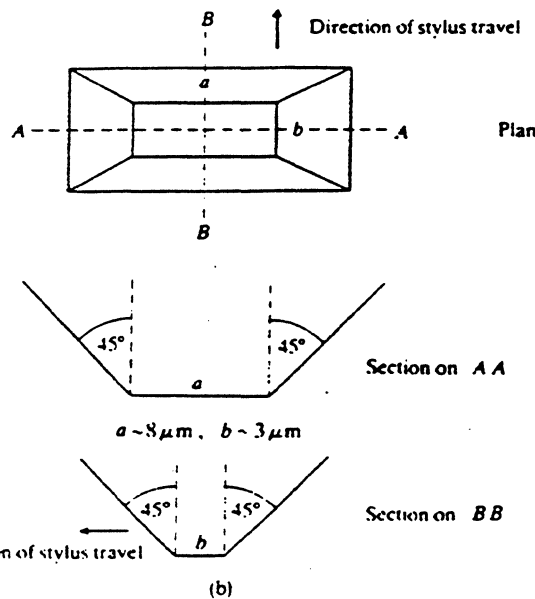
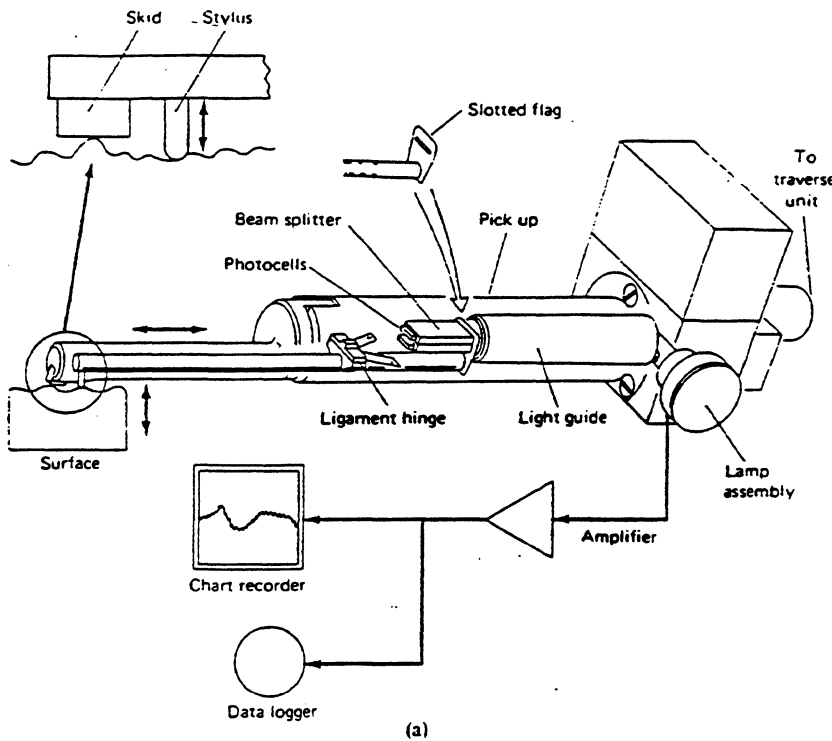
Sources of error



*distortion of profile
due to finite
dimensions of stylus
tip*

Talysurf..

one of the most popular stylus instruments



wavelength
resolution > 6 um

load 25-100 mg

max. vertical
resolution ~ 50 K

max. horizontal
resolution ~ 100

traversing

length 2-50 mm

vertical resolution
ca. 2 nm

surface mapping
possible with
a scanning
technique

Fig. 2.17. (a) Schematic of a modern stylus instrument (Talysurf 10, Rank Taylor Hobson, England). (b) Plan and section of a commercial diamond stylus showing typical dimensions (Reprinted with permission from: Groupement pour l'avancement de la mecanique industrielle; Mecanique-Materiaux-Electricité No 337, 1978).

TRACK BURNISHING

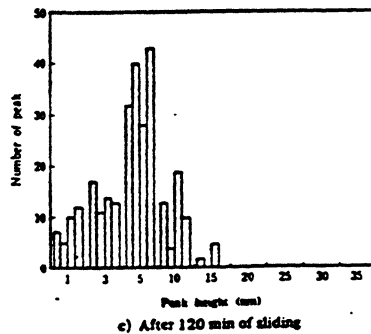
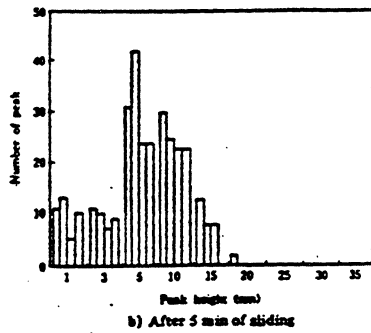
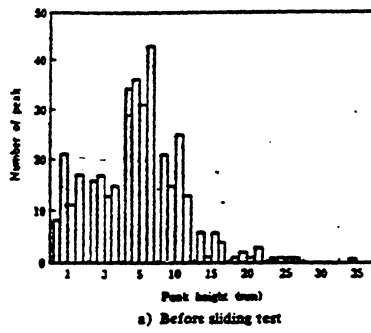


Fig. 17—Distribution of peak height before and after sliding test.

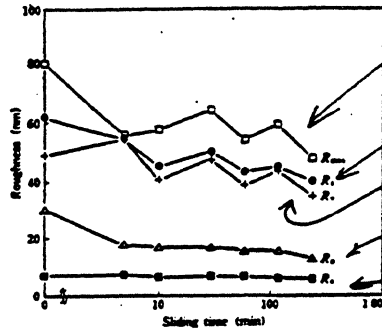


Fig. 18—Changes in roughness with increasing sliding time..

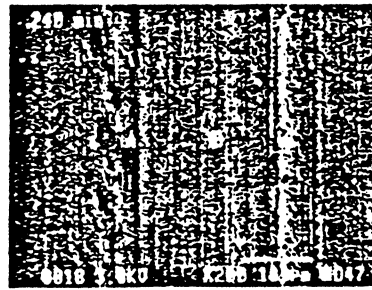


Fig. 16—SEM photograph of worn surface.

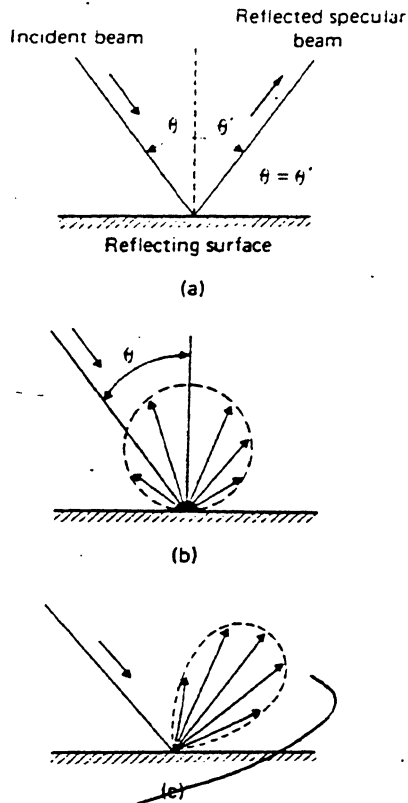
Figure 18 shows the relationship between various roughness parameters and the sliding time.

The parameters are as follows:

- R_{max} : Distance between the highest peak and lowest valley
- R_z : Distance between the averages of five highest peaks and five lowest valleys
- R_v : Distance between the lowest valley and the center line
- R_p : Distance between the highest peak and the center line
- R_a : Average roughness at the center line.

from Yamamoto et al.,
 "Head-Disk Interface"
 Fujitsu Sci. Tech. J.,
 26, 4 (1991)

Optical Methods



Modes of reflection of electromagnetic radiation from a solid surface

- a) specular only
- b) diffuse only, and
- c) combined specular and diffuse

Fig. 2.19. Modes of reflection of electromagnetic radiation from a solid surface: (a) specular only, (b) diffuse only, and (c) combined specular and diffuse.

Specular Reflection Method

$$R/R_0 = \exp[-(4\pi\sigma \cos\theta_i/\lambda)^2] \sim 1 - (4\pi\sigma \cos\theta_i/\lambda)^2$$

rms

Gloss or specular reflection depends on the surface property of the material, namely, the refractive index and surface roughness.

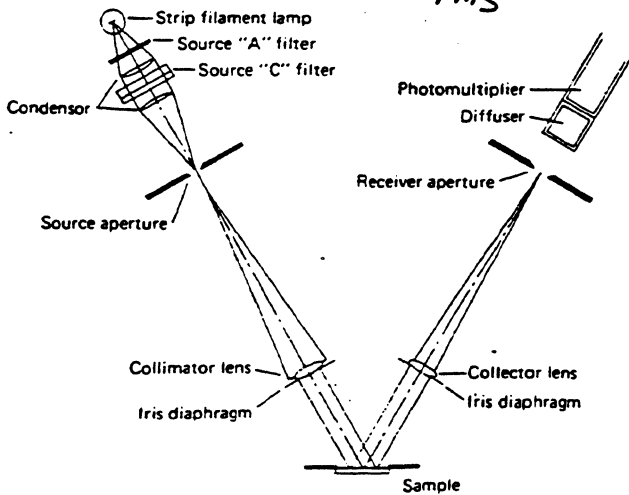


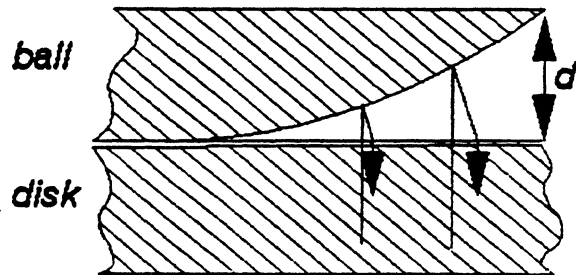
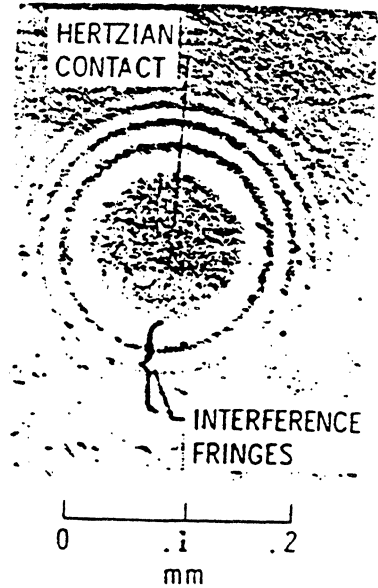
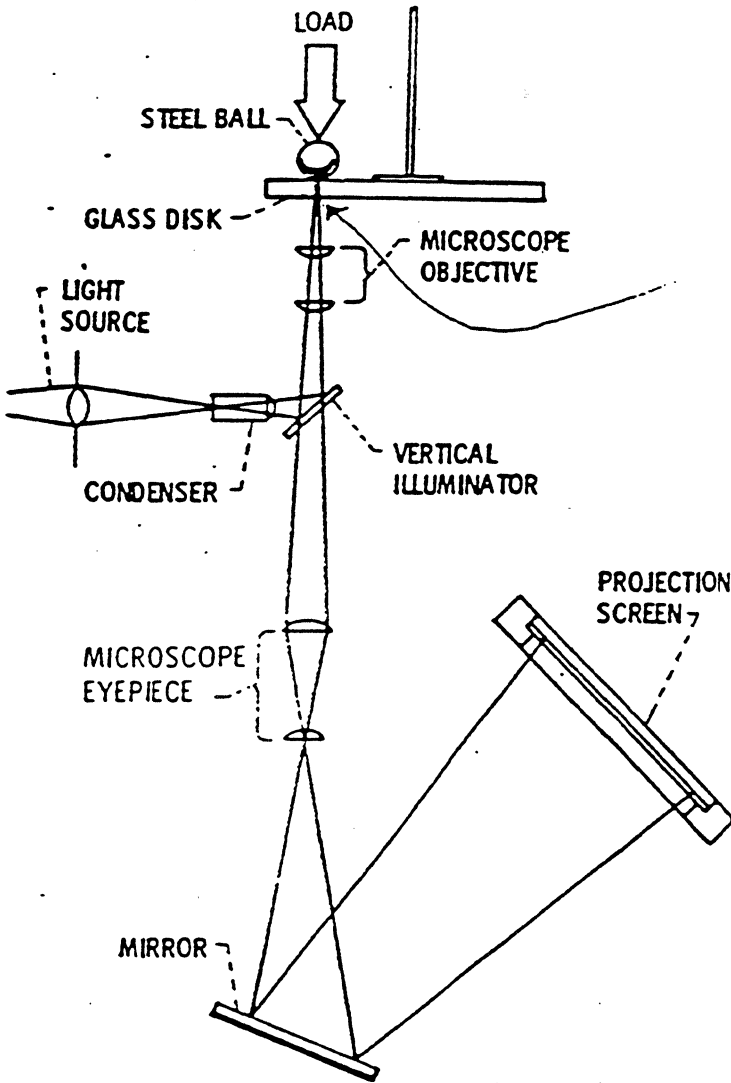
Fig. 2.21. Schematic of a glossmeter (Budde, 1980).

Appl. Optics 18, 2252 (1980)

Gloss meter operates from 380 to 760 nm wavelength and angles of incident of 20, 45, 60, 75 and 85 degrees. Higher angles for rougher surfaces required.

less light - better
bright - scatter all over

Interference Microscopy



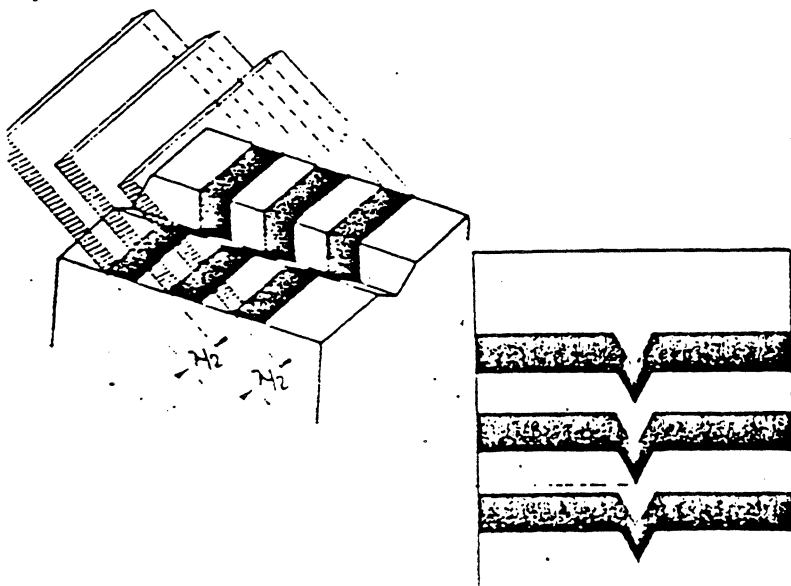
Black ring
constructive interference
 $2d = (m + 1/2)\lambda$

destructive interference
 $2d = m\lambda$

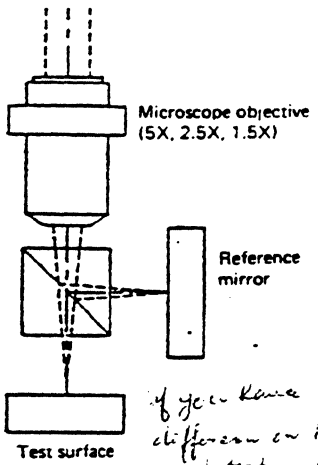
where $m = 0, 1, 2, 3..etc.$
 is interference order

image of a defect (scratch)
using the optical
interference microscope

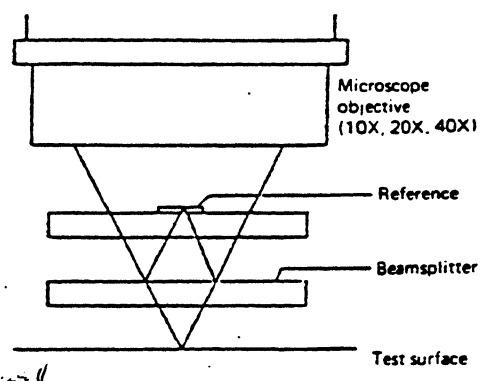
every $1/2$ of the wavelength
 you have constructive
 interference



Digital Optical Profiler

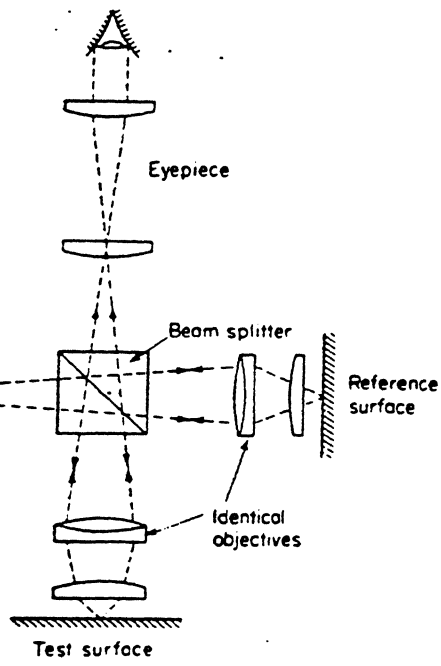
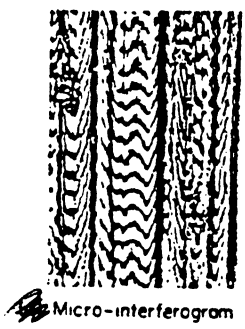


if you have difference on Ref. and test, you will measure roughness

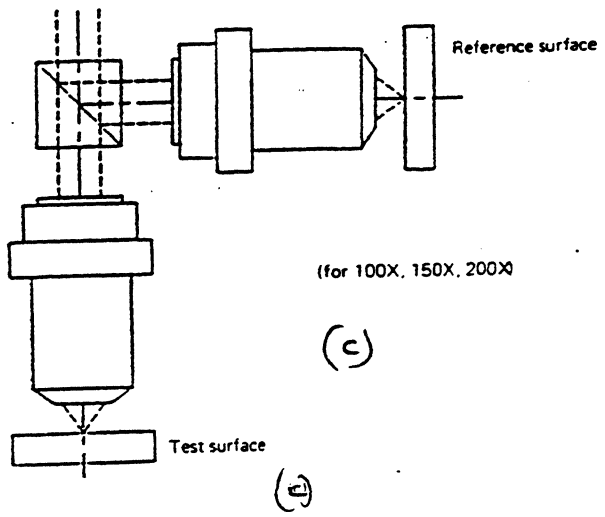


Optical schematics:

- a) **Michelson interferometer**
- b) **Miraou interferometer**
- c) **Linnik interferometer**



Schematic layout of a surface interferometer



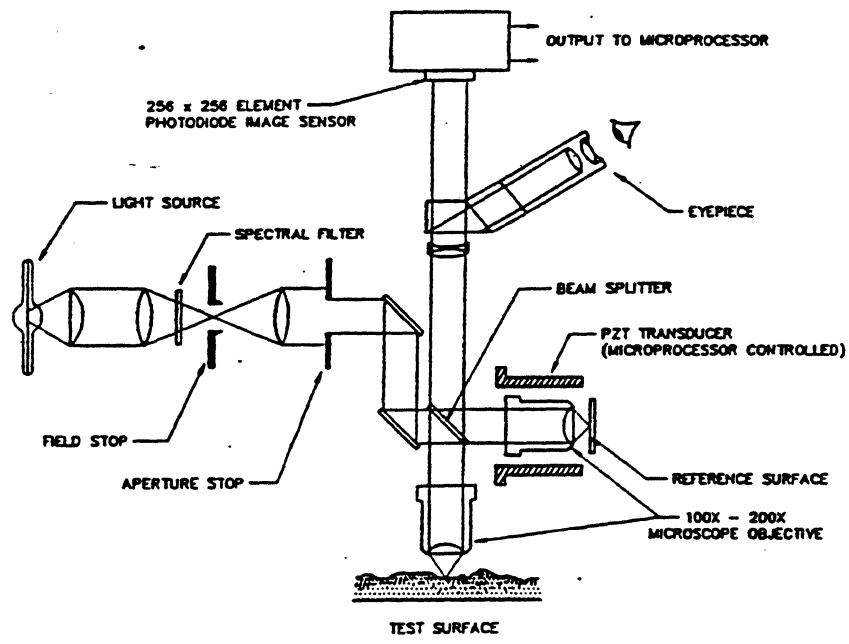


Fig. 2.29. Optical schematic of the three-dimensional digital optical profiler with Linnik interferometer (Bhushan et al. 1988).

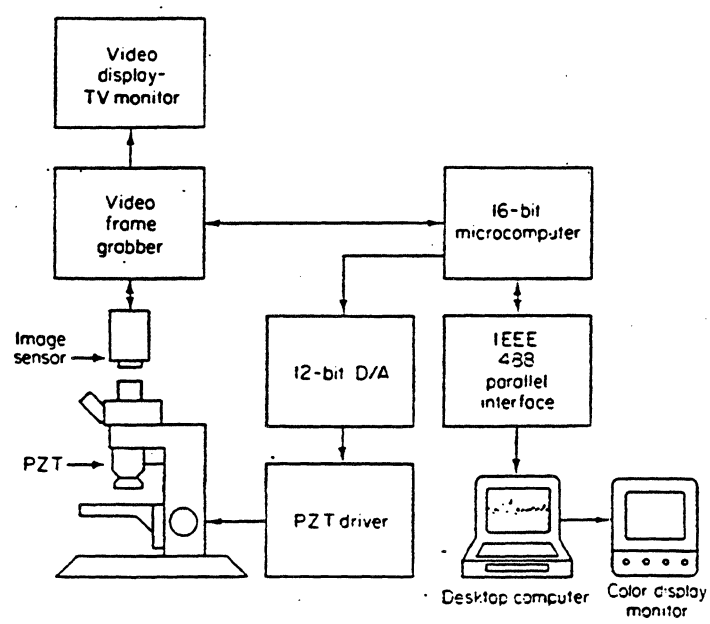


Fig. 2.30. Block diagram of the instrumentation and processing system of the digital optical profiler (Wyant et al., 1984).

Vertical resolution ~ 0.1nm
 Lateral resolution ~ 0.5um
 for high mag.
 Linnik interf.
 can measure
 stochastic and
 quantitative.

Table 2.2. Optical profiler options

Features	CID array	Objective magnification*								
		1.5x	2.5x	5x	10x	20x	40x	100x	150x	200x
Interferometer type		Michelson	Michelson	Michelson	Mirau	Mirau	Mirau	Linnik	Linnik	Linnik
Profile length (mm) ^b	2D	8.87	5.32	2.66	1.33	0.666	0.333	0.133	0.089	0.067
	3D	6.8 x 6.8	4.1 x 4.1	2.0 x 2.0	1.0 x 1.0	0.5 x 0.5	0.25 x 0.25	0.1 x 0.1	0.068 x 0.068	0.05 x 0.05
Spatial sampling interval (μm)	2D	8.67	5.20	2.60	1.31	0.650	0.325	0.130	0.087	0.065
	3D	26.67	16.00	8.00	4.00	2.00	1.00	0.40	0.267	0.200
Working distance (mm)		11.5	1.5	1.5	4.5	2.5	4.0	1.0	0.2	0.2
Maximum surface heights (μm)		7.92	7.92	7.92	7.80	3.05	1.95	0.60	0.54	0.54
Maximum surface slopes (deg)	2D	0.81	1.34	2.69	5.37	10.74	21.49	48.12	53.85	53.85
	3D	0.26	0.44	0.87	1.75	3.49	6.98	17.46	26.19	34.91
Numerical aperture		0.0366	0.075	0.1	0.25	0.4	0.5	0.9	0.95	0.95
Optical resolution (μm)		10.83	5.29	3.97	1.59	0.99	0.79	0.44	0.42	0.42

* Vertical resolution (0.1 nm) is unchanged for different magnification.
*** Profile length can be extended to several centimeters using a computer controlled X-Y stage.**

Handwritten notes:
 i-FeO₂/c
 Co-Al-Ni spin coated/c
 Co-Ni spin coated/sio₂
 Co-PP plated/c
 B.B., p. 11c

Table 2.5. Surface topography statistics of various rigid disks and slider from optical profiler at objective magnification of 40x

Roughness parameter ^a	Particulate disk	Thin-film disk	Thin-film disk	Thin-film disk	3570-type slider
	A	B1	C	D	
Rms surface height, nm	9.39	7.33	2.11	4.62	1.63
Rms profile slope x, mrad	3.73	4.15	0.50	2.40	0.99
Rms profile slope y, mrad	1.56	0.55	0.50	0.60	0.61
Rms surface slope, mrad	4.03	4.17	0.70	2.47	1.16
Rms profile curvature x, 1/mm	3.96	5.27	0.70	2.61	1.43
Rms profile curvature y, 1/mm	1.57	0.67	0.69	0.52	0.79
Rms surface curvature, 1/mm	2.16	2.67	0.35	1.35	0.84
Summit height, nm					
Mean	6	5	1	9	2
Standard deviation	9	7	2	4	2
Summit slope , mrad					
Mean	2.02	2.13	0.16	1.06	0.43
Standard deviation	0.96	1.17	0.32	0.53	0.32
Summit curvature, 1/mm					
Mean	4.79	4.90	2.24	3.30	0.53
Standard deviation	1.92	2.34	0.32	0.32	0.32
Summit-to-valley distance, nm	74.0	48.5	16.3	37.4	17.2
* Number of summits/mm ²	5935 * than this	732	911*	33 * much better	2406
Profile zero crossings x, 1/mm	73	125	52	117	97
Profile zero crossings y, 1/mm	25	4	38	38	113
Average autocorrelation distance, μm	19	4	36	3	20
Anisotropy ratio	∞	∞	2	∞	4
	(circumference) ^b	(circumference) ^c	(random) ^b	(circumference) ^c	

^a Here, x is along the radial axis for disks and along the slider length for sliders.
^b Polishing orientation.
^c Texturing orientation.

B.B., p. 124

17:17 03/27/87

20.0x

RMS: 10.6nm

SURFACE

WVLEN: 436.0nm

RA: 8.46nm

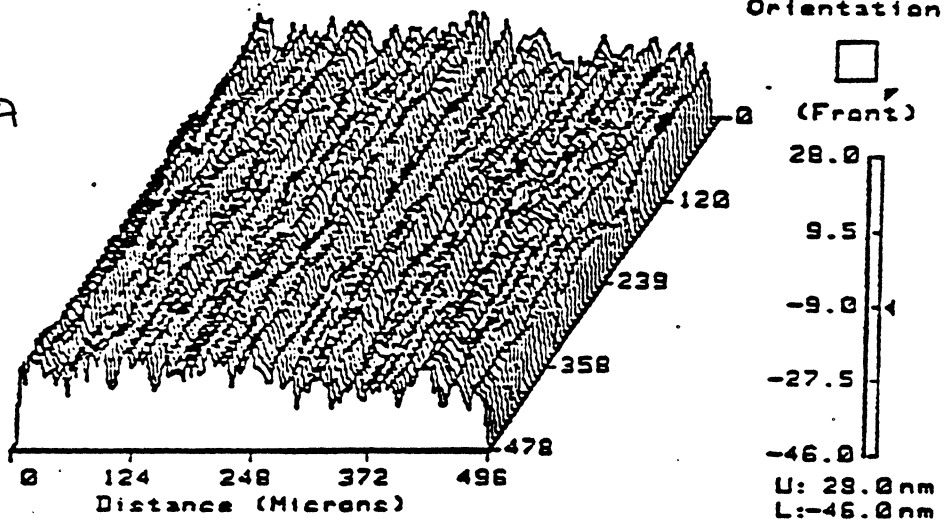
Tilt Removed

P-V: 73.8nm

*Amplitude of roughness
of surface*

$\sigma = 1.25 \text{ Ra}$

$\text{RMS} = 1.25 \text{ RA}$



rough surface
smooth surface
rough surface
smooth surface

17:21 03/27/87

20.0x

RMS: 2.13nm

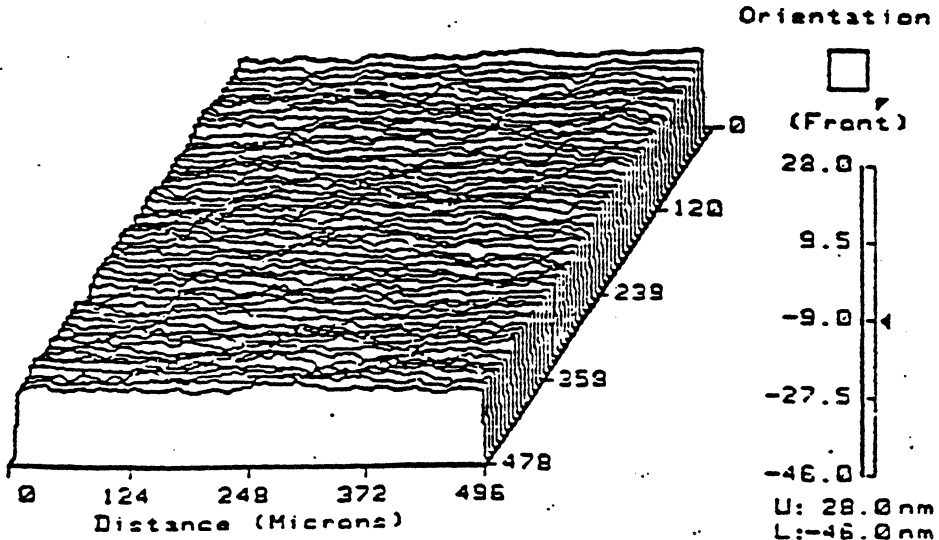
SURFACE

WVLEN: 436.0nm

RA: 1.71nm

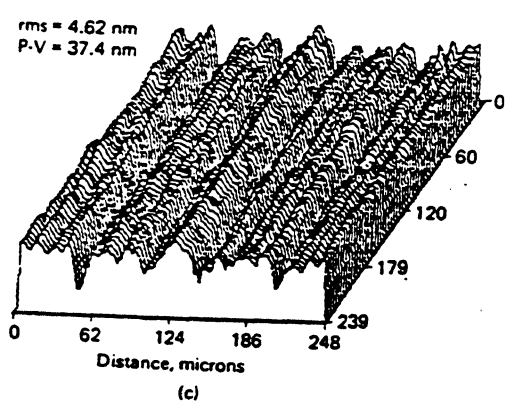
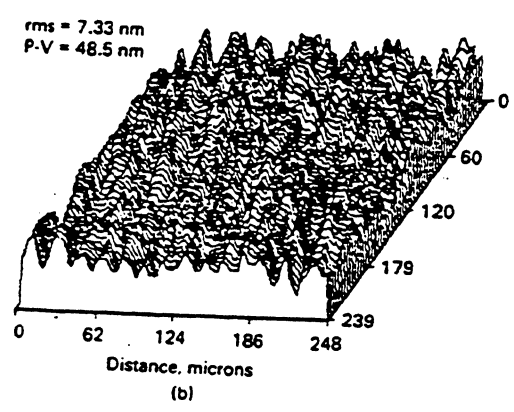
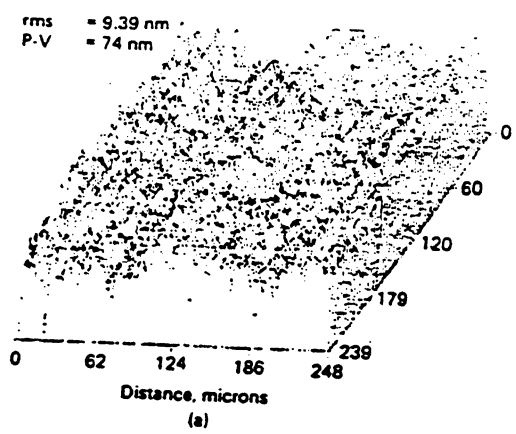
Tilt Removed

P-V: 17.8nm



if surface is not homogeneous you will get false roughness
homogeneous right

TYPICAL 3-D PLOTS FOR VARIOUS DISKS AND A HEAD SLIDER



Ni-P

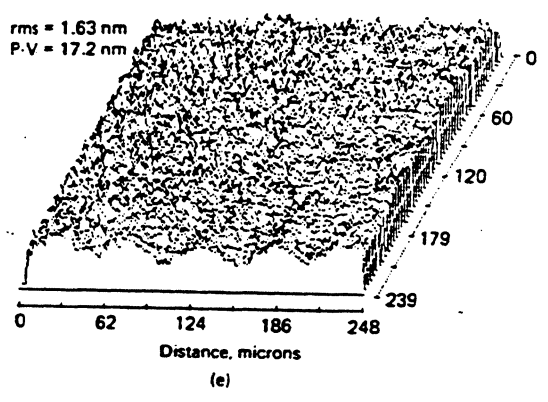
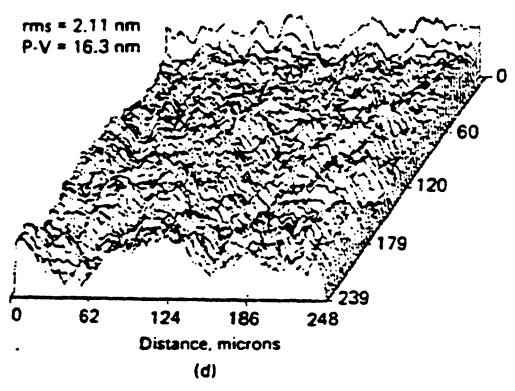
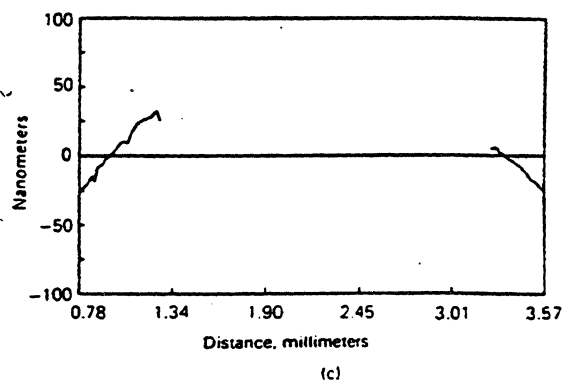
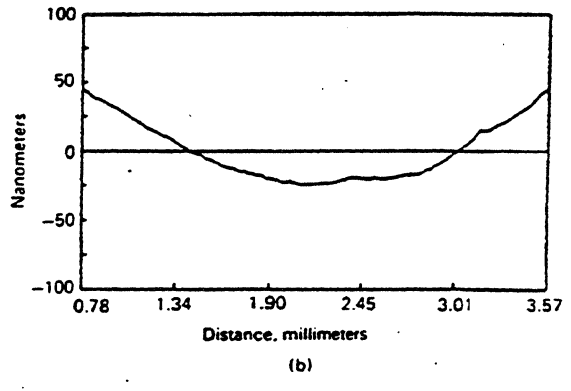
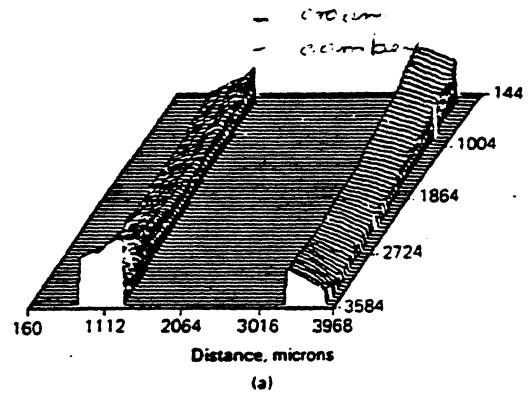
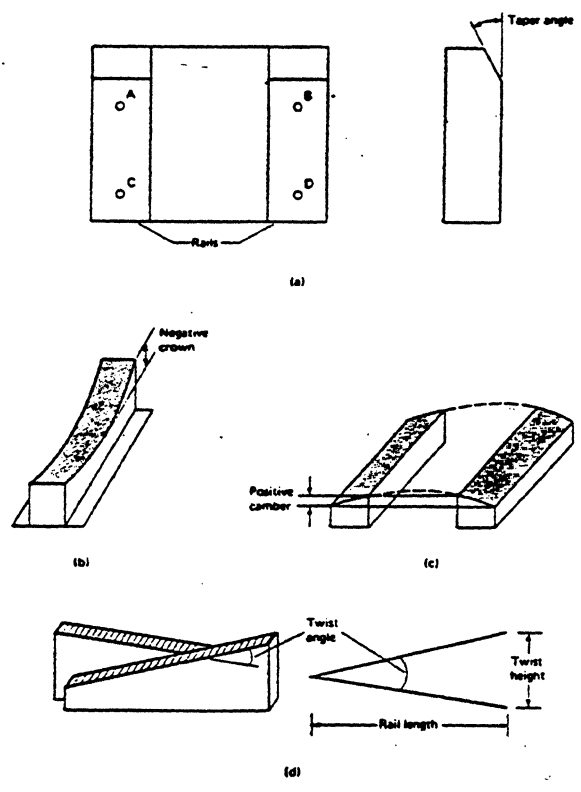


Fig. 2.33. Surface plots of (a) particulate rigid disk A; (b) circumferentially textured (using free-abrasive slurry process) thin-film rigid disk B; (c) circumferentially textured (using fixed-abrasive or tape texturing process) thin-film disk D; (d) untextured thin-film disk C; (e) 3370-type head slider. Radial direction of the disks along horizontal axis.

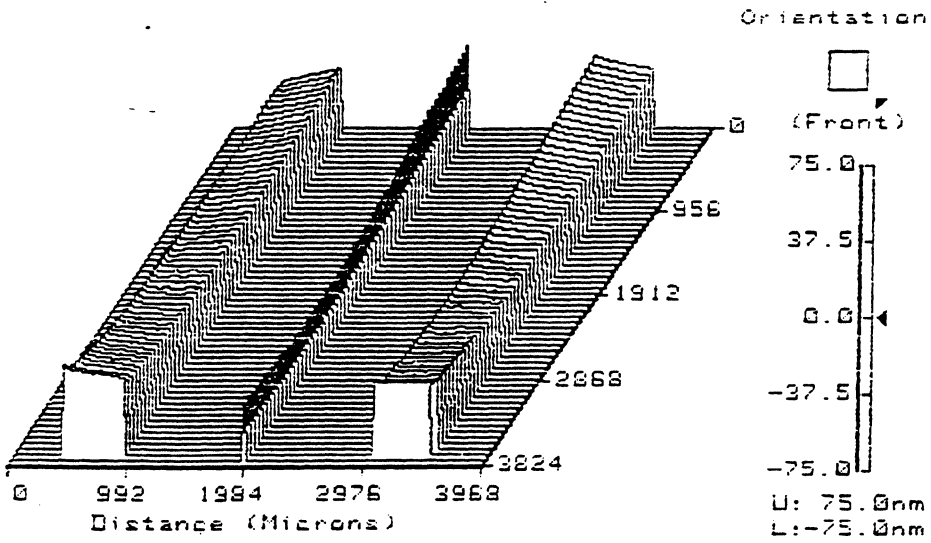
most case - slider is smoother than disk.



a) taper angle - characterize flying
 b) crown + better resolution, station
 c) camber
 d) twist in a two-rail
 magnetic head slider

Fig. 2.36. (a) Three-dimensional surface plot of a magnetic slider at $2.5 \times$ (taper area not shown); (b) profile along a rail length; (c) profile across the two rails. Crown rail 1, 1.97 nm; crown rail 2, 2.66 nm; camber 1, 1.55 nm; camber 2, 2.55 nm; twist, 162 nm; out of flatness, 233 nm.

740550 11:29 03/13/91 -Ref 2.5x
 RMS: 9.15nm SURFACE WVLN: 655.4nm
 RA: 7.24nm Tilt Removed
 P-V: 52.6nm



WYKO

740550 11:29 03/13/91 -Ref 2.5x
 RMS: 8.46nm MAG HEADS WVLN: 655.4nm
 RA: 6.77nm Tilt Removed
 P-V: 51.8nm

The data have been trimmed by 1 pixel.

Crown Heights :	LRA1L	RR1L
	-22.2 nm	-24.0 nm

Twist and Camber :	LRA1L	RR1L
X angle :	0.323 mdeg	-0.803 mdeg
Y angle :	0.211 mdeg	-0.216 mdeg
Length :	3562 um	3573 um
Width :	463 um	480 um

Twist Angle : -0.427 mdeg Twist Height : -26.56 nm
 Camber Angle : 1.126 mdeg Camber Height : 6.60 nm

Flatness : 20.0 nm Most positive : 10.1 nm Most negative : -9.89 nm

Four Point Twist : 3.93 nm

WYKO

Scanning Electron Microscope

General Uses

- Imaging of surface features at 10 to 100,000x: Resolution of features down to 3 to 100 nm, depending on sample
- When equipped with a backscattered detector, microscope allows (1) observation of grain boundaries on unetched samples, (2) domain observation in ferromagnetic materials, (3) evaluation of the crystallographic orientations of grains with diameters down to 2 to 10 μm, and (4) imaging of a second phase on unetched surfaces when the second phase has a different average atomic number
- When suitably modified, the microscope can be used for defect and quality control of semiconductor devices

Examples of Applications

- Examinations of metallographically prepared samples at magnifications well above the useful magnification of the optical microscope
- Examination of fracture surfaces and deeply etched surfaces requiring depth of field well beyond that possible with the optical microscope
- Evaluation of crystallographic orientation of features on a metallographically prepared surface, for example, individual grains, precipitate phases, and dendrites
- Identification of the chemistry of features down to micron sizes on the surface of bulk samples, for example, inclusions, precipitate phases, and wear debris
- Evaluation of chemical composition gradients on the surface of bulk samples over distances approaching 1 μm
- Examination of semiconductor devices for failure analysis, function control, and design verification

Samples

- *Form:* Any solid or liquid having a low vapor pressure ($\geq 10^{-3}$ torr, or 0.13 Pa)

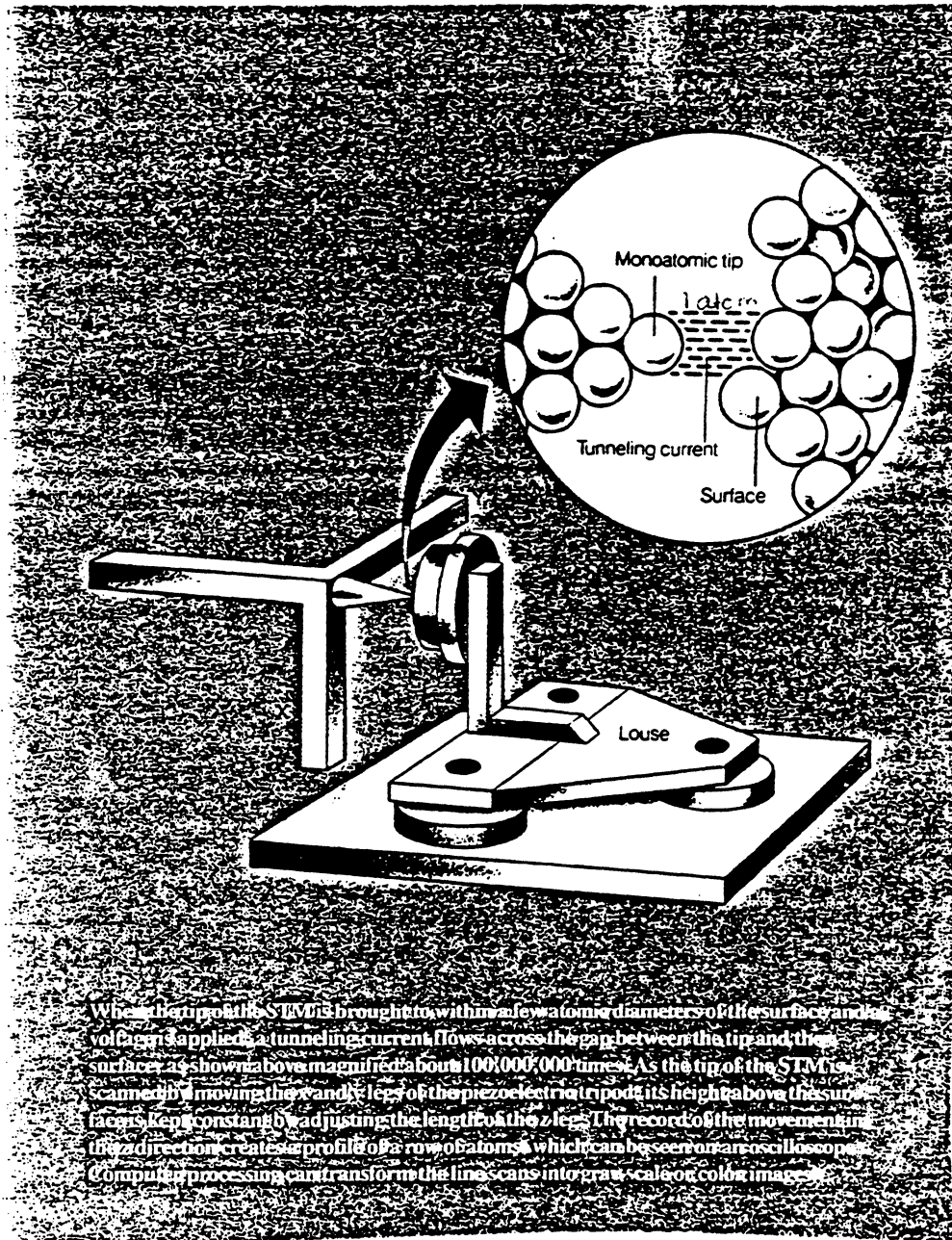
- *Size:* Limited by the scanning electron microscope available. Generally, samples as large as 15 to 20 cm can be placed in the microscope, but regions on such samples that can be examined without repositioning are limited to approximately 4 to 8 cm
- *Preparation:* Standard metallographic polishing and etching techniques are adequate for electrically conducting materials. Nonconducting materials are generally coated with a thin layer of carbon, gold, or gold alloy. Samples must be electrically grounded to the holder, and fine samples, such as powders, can be dispersed on an electrically conducting film, such as a silver paint that has been thoroughly dried. Samples must be free from high vapor pressure liquids, such as water, organic cleaning solutions, and remnant oil-base films

Limitations

- Image quality on relatively flat samples, such as metallographically polished and etched samples, is generally inferior to the optical microscope below 300 to 400x
- Feature resolution, although much better than the optical microscope, is inferior to the transmission electron microscope and the scanning transmission electron microscope

Capabilities of Related Techniques

- *X-ray diffraction:* Provides bulk crystallographic information
- *Optical microscopy:* Faster, less expensive, and provides superior image quality on relatively flat samples at less than 300 to 400x
- *Scanning transmission electron microscopy, Auger electron microscopy:* See Table 3 for comparison
- *Transmission electron microscopy:* Provides information from within the volume of material, such as dislocation images, small angle boundary distribution, and vacancy clusters. Superior resolution, but requires thin samples



can move
x, y, z

When the tip of the STM is brought to within a few atomic diameters of the surface and a voltage is applied, a tunneling current flows across the gap between the tip and the surface as shown above magnified about 100,000,000 times. As the tip of the STM is scanned by moving the x and y legs of the piezoelectric tripod, its height above the surface is kept constant by adjusting the length of the z leg. The record of the movement in the z direction creates a profile of a row of atoms which can be seen on an oscilloscope. Computer processing can transform the line scans into gray scale or color images.

dark field microscopy is for wear, any damage.
particles of $< 0.1 \mu$

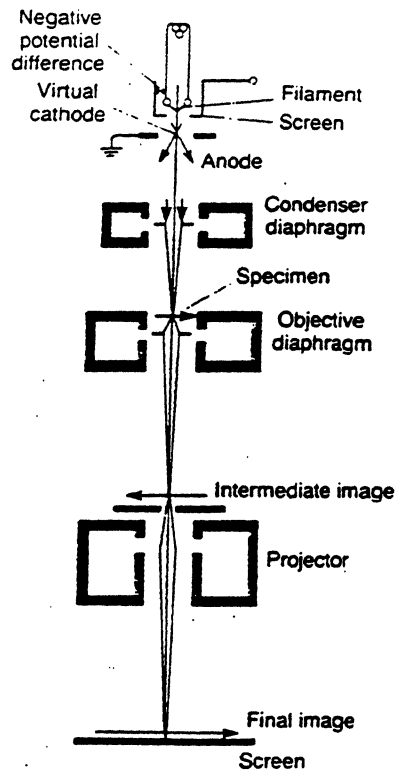
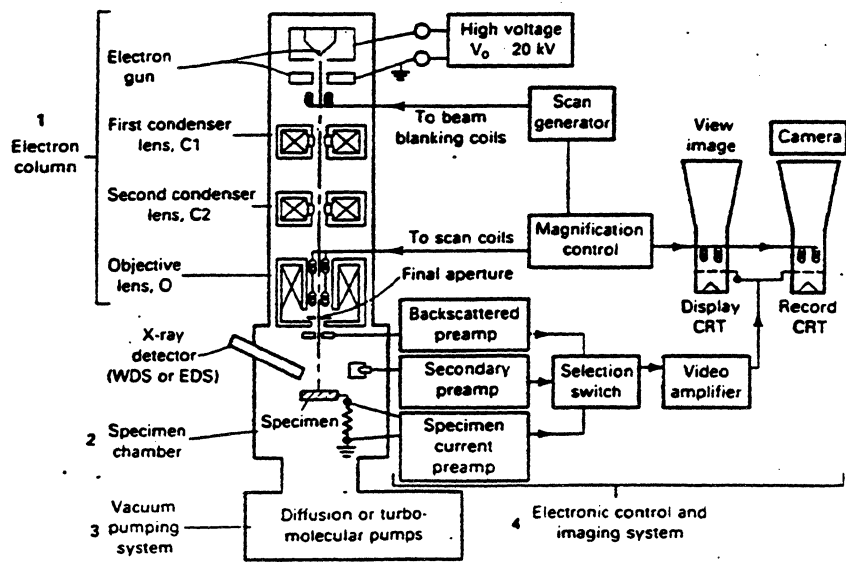


Fig. B.5. Schematic diagram of a transmission electron microscope with electromagnetic optics. *Not applicable.*

Fig. 1 Basic components of the scanning electron microscope

WDS, wavelength-dispersive spectrometer; EDS, energy-dispersive spectrometer; CRT, cathode-ray tube



Effect of mechanical polishing

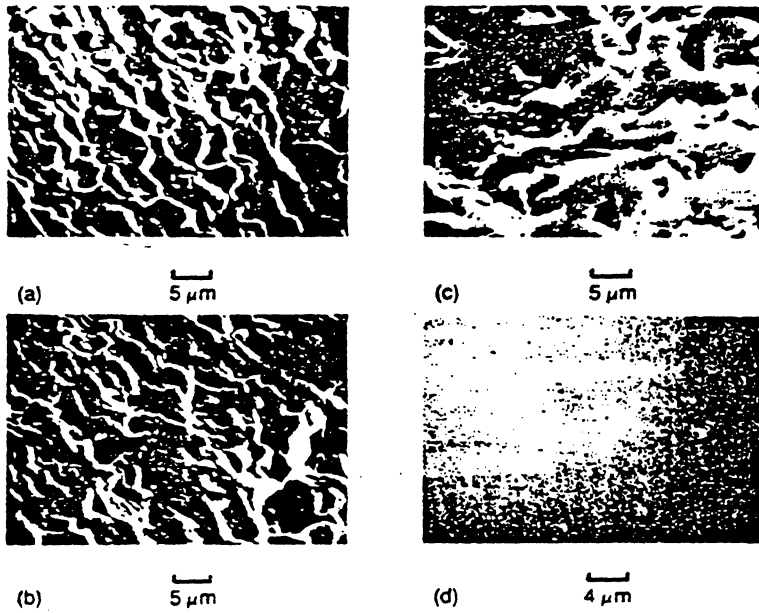


Fig. 10.24. SEM micrographs of Ni-Zn ferrite surfaces lapped for different times: (a) 3 min. (b) 9 min. (c) 15 min. and (d) 60 min (Chandrasekar et al., 1987b).

Effect of chemical etching

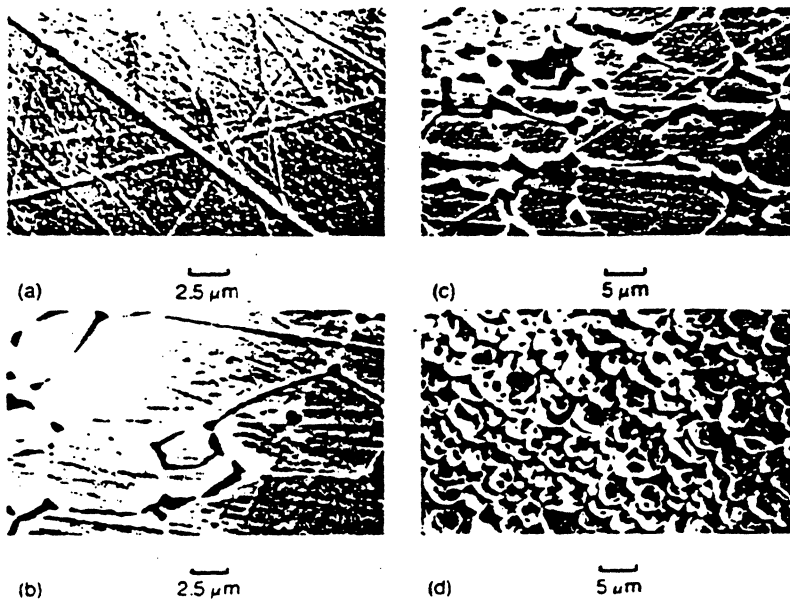
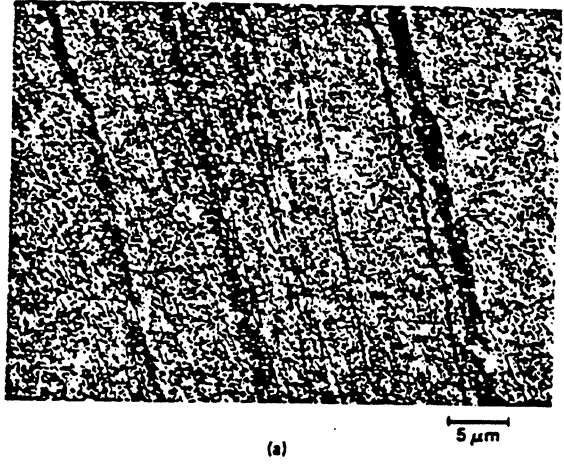
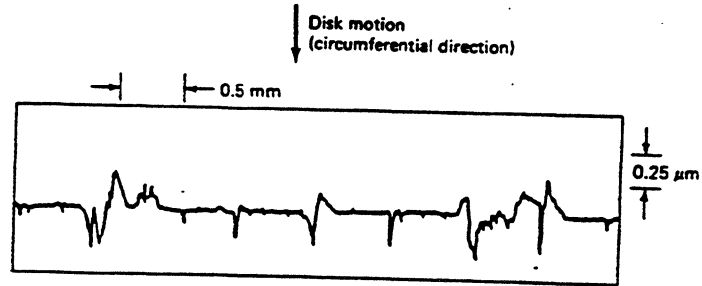


Fig. 10.25. SEM micrographs of lapped Ni-Zn ferrite surfaces after different etching times with orthophosphoric acid: (a) 0.25 min. (b) 0.75 min. (c) 1.5 min. and (d) 15 min. Etching rate ~ 1 μm/min. (Chandrasekar et al., 1987b).

from J. Eng. Industr., Trans., ASME 109, 83 (87)



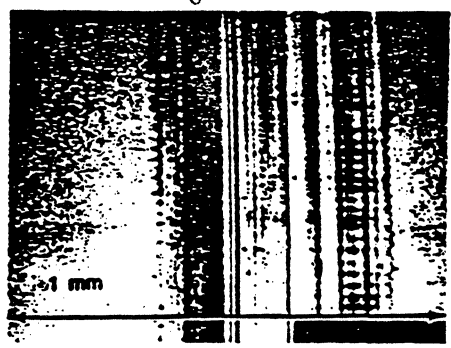
(a)



(b)

Fig. 6.54. (a) SEM micrograph of a worn particulate rigid disk surface against Al_2O_3 -TiC slider after a head crash in CSS. (b) Stylus profile of a worn particulate rigid disk against Al_2O_3 -TiC slider after head crash in CSS.

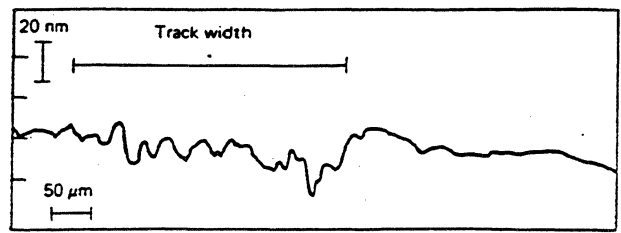
Resolution of SEM $\gamma - 10 \text{ \AA}$



(a)

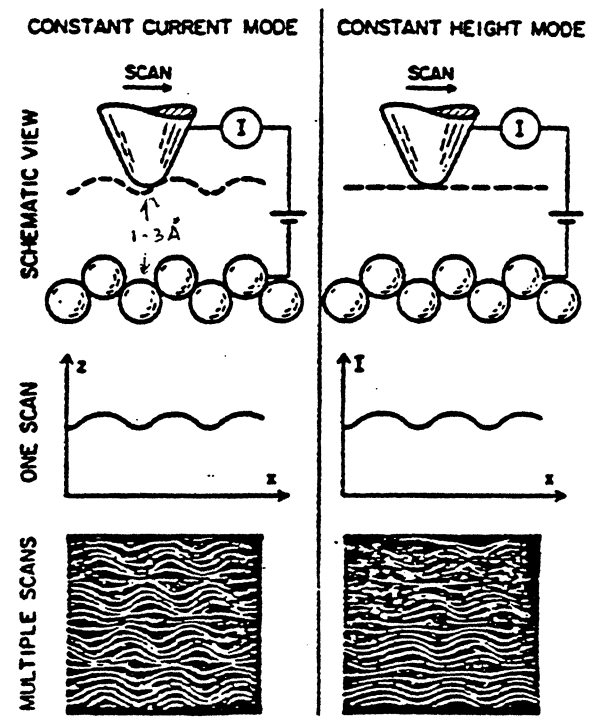
Fig. 6.61. Features of wear tracks on spin-coated SiO_2 film against Al_2O_3 -TiC slider in a low-speed sliding test: (a) SEM micrograph and (b) surface profile across the wear track (Yanagisawa, 1985b).

in "Tribology & Mechanics of Magnetic Recording Systems" Vol. 2 (B. Bhushan & N.S. Eix, eds.) pp. 7-15, SP-19, ASLE, Park Ridge, Illinois.



(b)

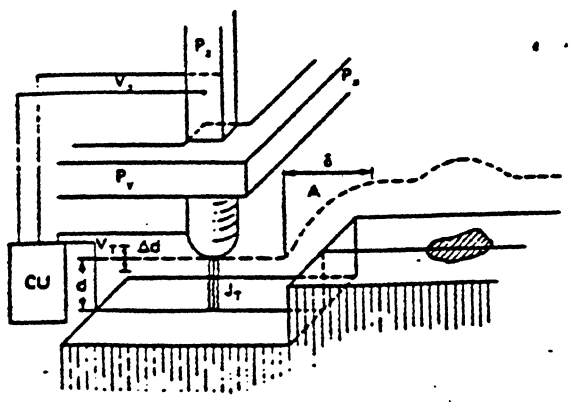
Scanning Tunneling Microscopy (STM)



* Resolution :
 $\lt 0.1 \text{ nm}$
 $\lt 1 \text{ nm}$
 constant height

Scanning tunneling microscope can be operated in either the constant current or the constant height mode. The images are of graphite in air.

- Disadv - Both surfaces should be conductive.
- Adv. - need 1 A to get current.



Principle of the operation of the scanning tunneling microscope

$$J_T \propto V_T \exp(-\pi \phi^2 d)$$

where ϕ = work function
 $A = 1$ if ϕ is in eV and d in Å.

BINNIG, G. ROHRER, H. SURFACE SCI. 126, 236 (83)

Binnig G and Rohrer H. Science 1982

STM of Carbon-Coated Disk

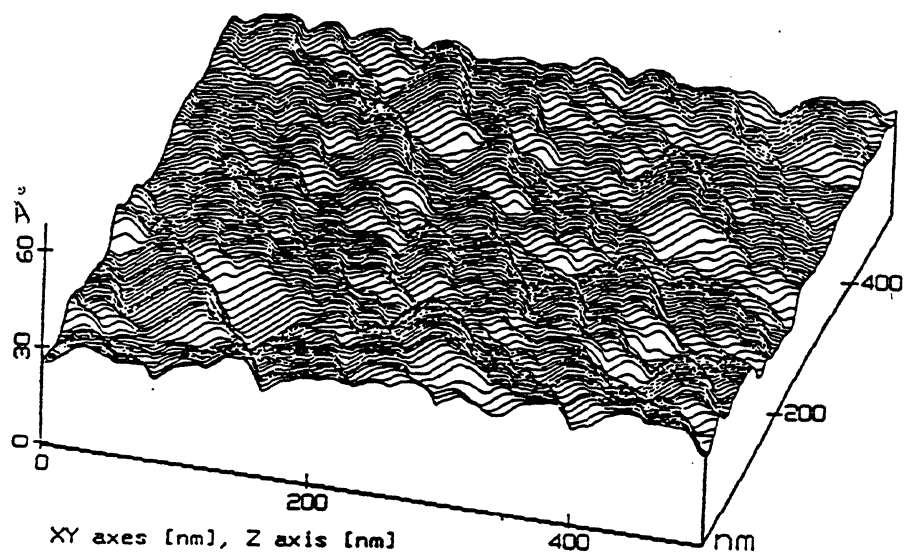


Fig.3 Surface topography of an untextured disk

from Kaneko, R., "Micro-tribological Approach to Head-Medium Interfaces of Magnetic Recording", Proc. 5th Intern. Congress on Tribology, Helsinki, Finland, Vol. 5, 210 (89)

STM of Lubed Disk Surfaces

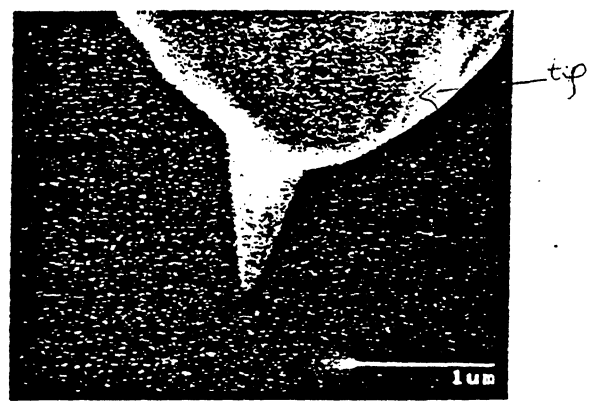


Fig. 1 An electron-beam-deposited tip on etched tungsten

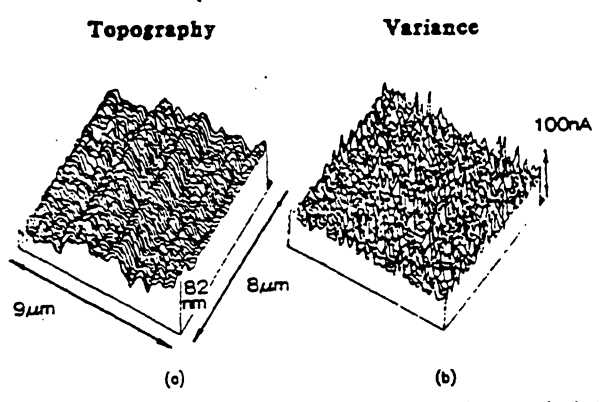


Fig. 2(a) An STM topography image of a rigid disk surface acquired at 1 nA and a bias of 20 mV; (b) current variance image obtained from the same area at a bias of 4 V

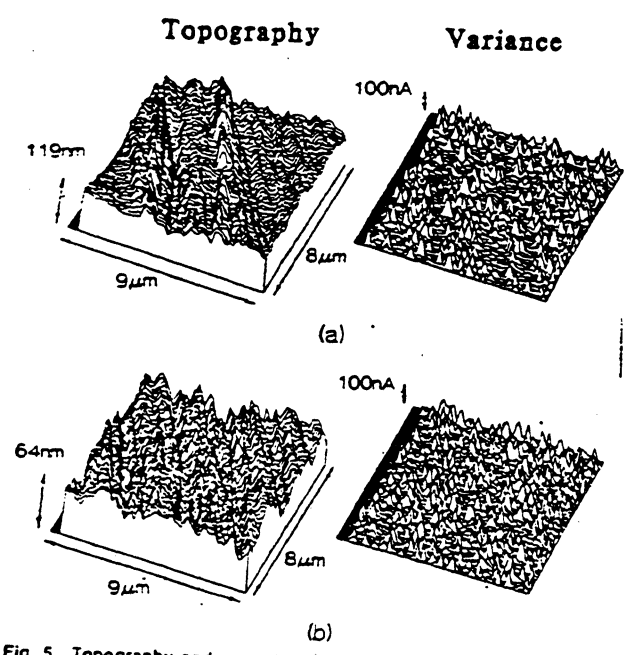


Fig. 5 Topography and current variance images from scratched and untouched regions of untested rigid disk coupons

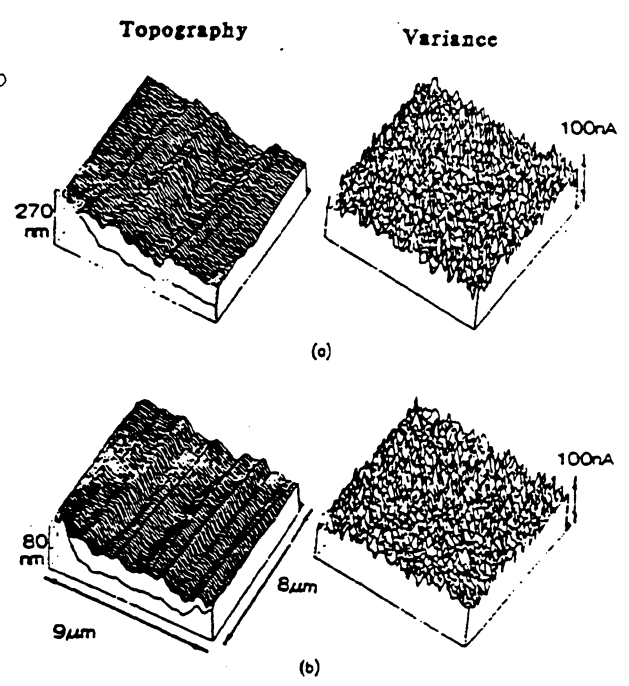
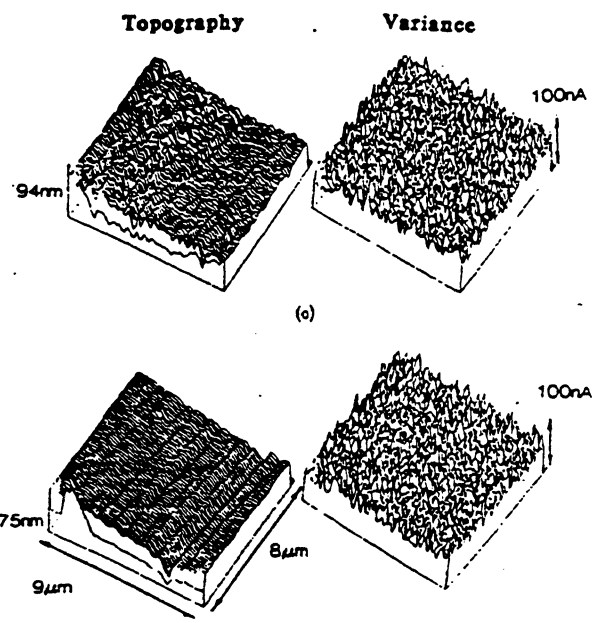
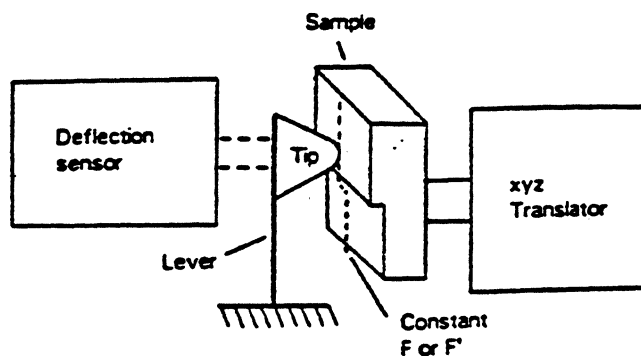


Fig. 3(a) Topography and current variance images obtained on the wear track from a disk tested in dry helium; (b) topography and corresponding current variance image from region away from wear track on the same disk

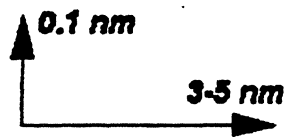


from Srirani, T.S. et al. "The Application of Scanning Tunnelling Microscopy to Study Lubricant Distribution on Magnetic Thin Film Rigid Disks", ASME/STLE TRIB. CONF., TORONTO, CANADA, 1990
 Trib. Conf. Toronto, Canada, Oct 1990

Atomic Force Microscopy (AFM)



Resolution

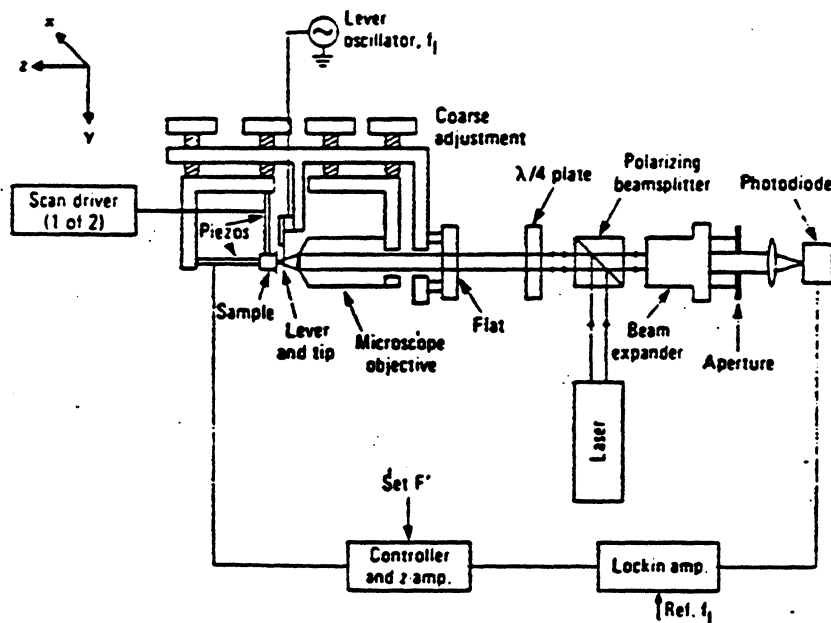


Force $\sim 10^{-10}$ N

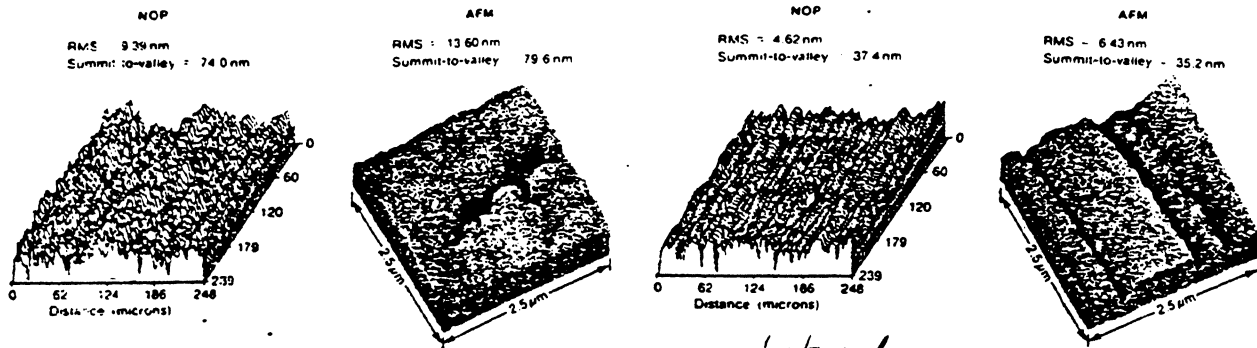
Principle of the operation of the atomic force microscope

Van der Waal Force

Sensor = tunneling current

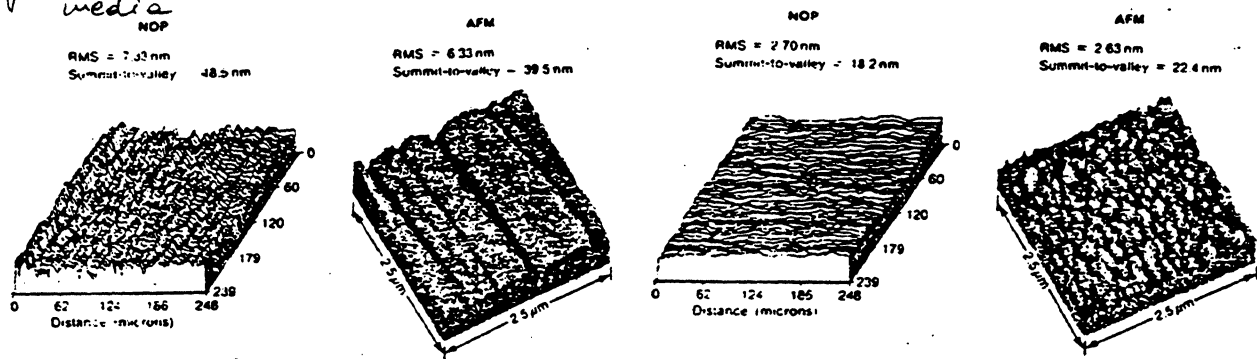


Schematic diagram of the atomic force microscope, which uses optical interference to detect the level deflection (Erlandsson et al., 1988). ←



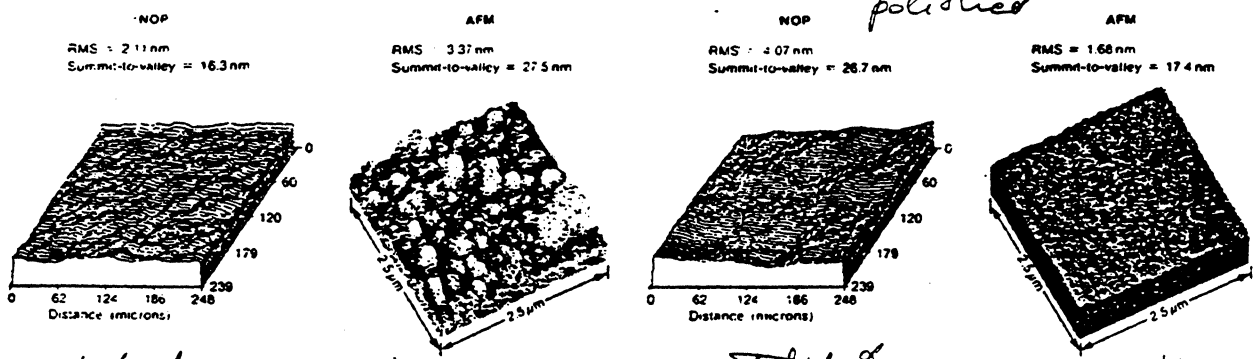
particulate media
Fig. 3(a)

textured
Fig. 3(d)



textured
Fig. 3(b)

Fig. 3(e)



polished
Fig. 3(c)

polished
Fig. 3(f)

slide of γ -Fe₂O₃

Fig. 3 NOP and AFM images of (a) disk A, (b) disk B₁, (c) disk C, (d) disk D, (e) disk E₁, and (f) disk F. The wireframe NOP images are of a 250 μ m square region, and the AFM images are solid grey level images (white is high, black is low) of 2.5 μ m regions of the same disks.

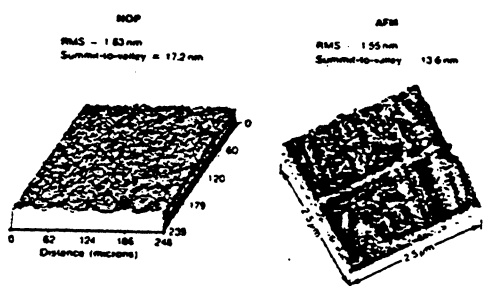


Fig. 4 NOP and AFM images of Al₂O₃-TiC slider
slider

Table 2 Construction of disks and slider

Sample disk designation	Substrate, Al-Mg with	Substrate finish	Construction of magnetic layer	Overcoat
A		Polished	γ -Fe ₂ O ₃ particles in epoxy binder	Perfluoropolyether lubricant (liquid)
B ₁	Ni-P	Textured	Sputtered Co-Pt-Ni film	Sputtered C
C	Ni-P	Polished	Sputtered Co-Ni film	Sputtered SiO ₂
D	Ni-P	Textured	Plated Co-P film	Sputtered C
E ₁	Ni-P	Polished	Plated Co-P film	Sputtered C
F	Alumite	Polished	Sputtered γ -Fe ₂ O ₃ film	Spin coated SiO ₂ (textured) on sputtered SiO ₂
Slider (Al ₂ O ₃ -TiC)				

from Bhushan, B., & Blackman, G.S.,
ASME/STLE Trib. Conf., Toronto, Canada,
Oct. 7-11 1990.

*optical
interfer*

Table 3 Surface topography statistics of various rigid disks and a slider

Roughness Parameter	Disk A		Disk B ₁		Disk C		Disk D		Disk E ₁		Disk F		3370 type slider	
	NOP	AFM	NOP	AFM	NOP	AFM	NOP	AFM	NOP	AFM	NOP	AFM	NOP	AFM
Rms surface height (nm)	9.39	13.6	7.33	6.33	2.11	3.37	4.62	6.43	2.70	2.63	4.07	1.68	1.63	1.55
Rms profile slope x (mrad)	3.73	99.3	4.15	91.5	0.50	76.7	2.40	91.3	0.45	123	0.57	31.1	0.99	13.1
Rms profile slope y (mrad)	1.56	234	0.55	131	0.50	107	0.60	95.0	0.64	147	0.51	27.7	0.61	39.0
Rms surface slope (mrad)	4.03	162	4.17	101	0.70	80.2	2.47	74.3	0.78	96.6	0.75	29.7	1.16	31.4
Rms profile curvature x (1/mm)	3.96	5.36 × 10 ³	5.27	5.96 × 10 ³	0.70	6.5 × 10 ³	2.61	7.1 × 10 ³	0.66	13.4 × 10 ³	0.85	3.29 × 10 ³	1.43	1.27 × 10 ³
Rms profile curvature y (1/mm)	1.57	17.5 × 10 ³	0.67	12.4 × 10 ³	0.69	9.6 × 10 ³	0.52	9.6 × 10 ³	0.73	17.5 × 10 ³	0.79	4.27 × 10 ³	0.79	4.87 × 10 ³
Rms surface curvature (1/mm)	2.16	9.25 × 10 ³	2.67	6.87 × 10 ³	0.35	5.9 × 10 ³	1.35	6.2 × 10 ³	0.53	11.4 × 10 ³	0.64	2.83 × 10 ³	0.84	2.53 × 10 ³
Summit height (nm)														
mean	6	0.41	5	0.71	1	2.8	9	6.9	2	3.9	1	2.6	2	0.15
standard deviation	9	10.5	7	6.7	2	8.8	4	7.1	2	1.1	4	3.7	2	1.4
Summit slope (mrad)														
mean	2.02	71.3	2.13	49.8	0.16	15.6	1.06	22.1	0.21	9.0	0.32	18.3	0.43	10.7
standard deviation	0.96	29.5	2.17	20.7	0.32	12.8	0.53	15.5	0.32	10.6	0.32	11.7	0.32	9.1
Summit curvature (1/mm)														
mean	4.79	6.0 × 10 ³	4.90	4.0 × 10 ³	2.24	6.1 × 10 ³	3.30	7.4 × 10 ³	1.9	11.3 × 10 ³	2.24	3.5 × 10 ³	0.53	1.2 × 10 ³
standard deviation	1.92	2.5 × 10 ³	2.34	0.9 × 10 ³	0.32	0.76 × 10 ³	0.32	2.0 × 10 ³	0.32	1.2 × 10 ³	0.32	1.1 × 10 ³	0.32	0.43 × 10 ³
Summit-to-valley distance (nm)	74.0	79.6	48.5	39.5	16.3	27.5	37.4	35.2	18.2	22.4	26.7	17.4	17.2	13.6
Summit density (1/mm ²)	5.9 × 10 ³	2.4 × 10 ⁶	732	9.1 × 10 ⁶	911	3.5 × 10 ⁶	33	5.0 × 10 ⁶	344	6.4 × 10 ⁶	2.0 × 10 ⁶	3.0 × 10 ⁶	2.4 × 10 ³	13.3 × 10 ⁶

AFM is much more sensitive than optical.
Both are still very useful

~~G.S.P. 124~~

Applications of STM and AFM in Microtribology

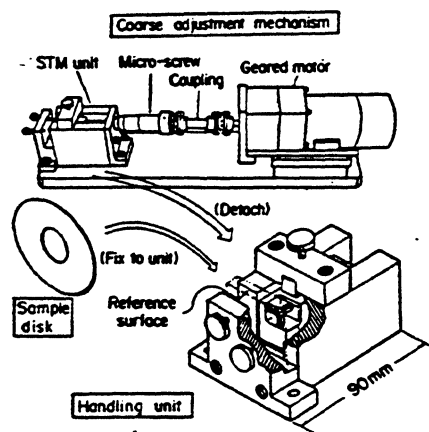


FIG. 1. Simple and easy-to-use STM.

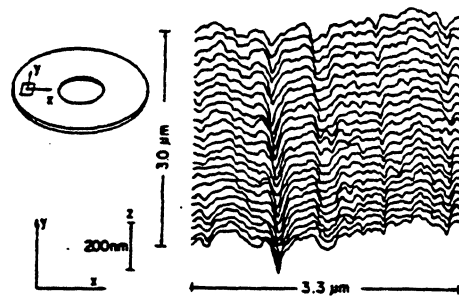


FIG. 2. Example of magnetic disk surface topography measured by the STM.

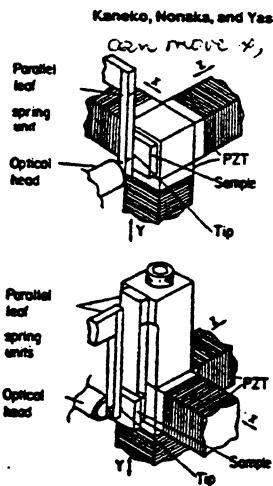


FIG. 3. Schematics of atomic force measuring mechanism for (a) adhesion force and (b) frictional force.

can measure friction
 apply the load
 contact area is very small
 interface is poorly contact

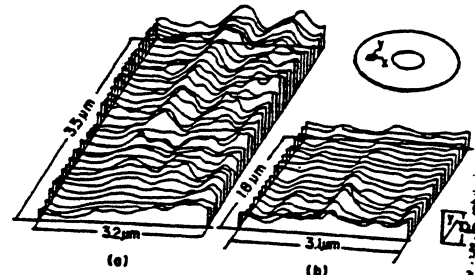


FIG. 5. Frictional forces between (a) carbon sputtered surface or (b) carbon sputtered surface lubricated with perfluoroalkylether and 10-μm radius tungsten tips with zero load.

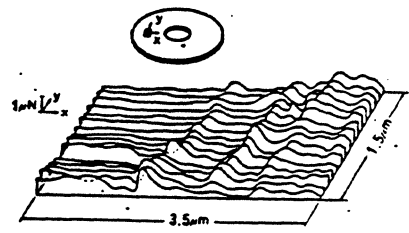


FIG. 4. Distribution of adhesion forces between a carbon sputtered surface and a 5-μm radius tungsten tip.

from Kaneko, K. et al., J. Vac. Sci. Techn., A8, 291 (88)

stylus - silicon, tungsten, glass.

Comparison of roughness measurement methods

Method	Quantitative information	Three-dimensional data	Resolution, nm		On-line measurement capability	Limitations
			Lateral	Vertical		
Stylus instrument	Yes	Questionable	1000-2000	5	No	Contact type, can damage the sample
Optical methods						
Taper sectioning	Yes	No	250	25	No	Destructive, tedious specimen preparation
Light sectioning	Limited	Yes		0.1	No	
Specular reflection	No	No			Yes	
Diffuse reflection (scattering)	Limited	Yes		0.01	Yes	Very smooth surfaces (< 100 nm)
Speckle pattern	Limited	Yes			Yes	Very smooth surfaces (< 100 nm)
Optical interference	Yes	Yes	600-1000	0.2-1	No	Very smooth surfaces (< 200 nm)
Electron microscopy						
Reflection/replication	No	Yes	2-4	10-20	No	
Integration of backscattered signal	Yes	Yes	2-4	10-20	No	
Stereomicroscopy	Yes	Yes	2-4	10-20	No	
Scanning tunneling microscopy	Yes	Yes	0.3	0.02	No	Requires a conducting surface; scans small areas
Atomic force microscopy	Yes	Yes	0.3	0.02	No	
Fluid/electrical	No	No			Yes	Semiquantitative

Measurements of Isolated Asperities

Optical Methods (light scattering)

Glide Test Methods

- * piezoelectric sensors (PZT) *sensor level is compact*
- * magnetoresistive sensors (MR)

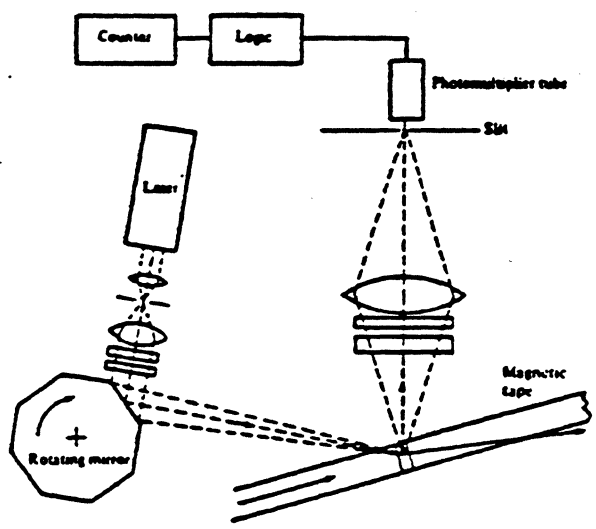
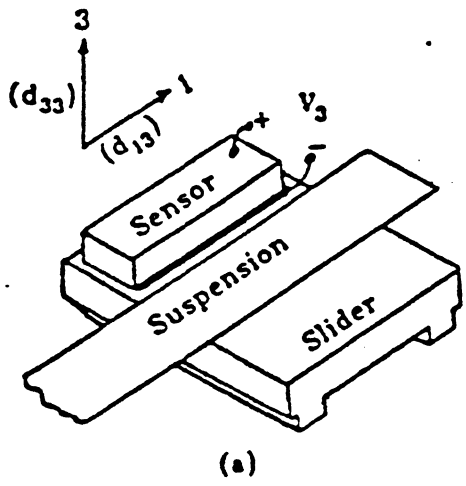


Fig. 2.45. Optical schematic of a grazing incidence laser asperity counter (Grimm, 1979). *not sensitive, good for loose smooth surface.*

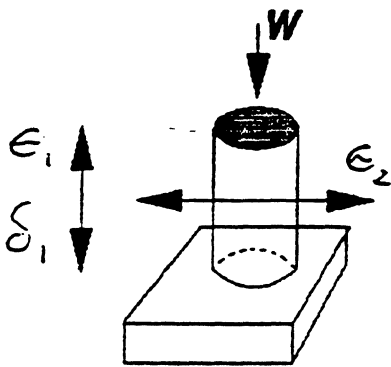


everytime when sensor hit, get a peak.

Fig. 2.47. (a) A PZT sensor mounted on a 3380 slider and (b) an unfiltered and 100-400 kHz filtered PZT signal from a 3380 slider flying over a disk defect (1 ms full trace) (From: C. E. Yeack-Scranton, "Novel Piezoelectric Transducer to Monitor Head-Disk Interactions", IEEE Trans. Magn., vol. MAG-22 c 1986 IEEE.)

Loading of Solids

Basic relations:



when a solid is subjected to load (W), stresses are produced in the solid which increase as the load is increased. These stresses produce deformations which are defined by the strains.

δ_1 = stress in axial direction = $\frac{\text{load } (W)}{\text{cross-sectional area}}$

ϵ_1 = strain in axial direction = $\frac{\text{change in length}}{\text{original length}}$

and

$$\delta_1 = E \epsilon_1$$

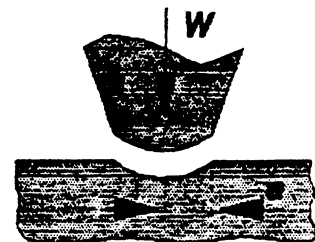
where E is the elastic constant, the Young Modulus

and

$$\epsilon_2 = -\nu \epsilon_1$$

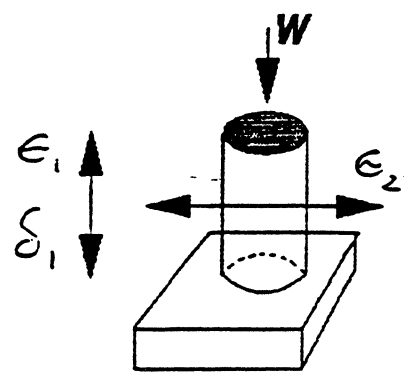
where ν is the Poisson Ratio, and ϵ_2 is the strain in the transverse direction

Yield stress (Y) is the stress state at which the transition from elastic behavior to plastic behavior occurs.
Hardness (H), $H = W/a^2$, the ratio of the load to the surface area of the permanent indentation.



Loading of Solids

Basic relations:



when a solid is subjected to load (W), stresses are produced in the solid which increase as the load is increased. These stresses produce deformations which are defined by the strains.

$$\delta_1 = \text{stress in axial direction} = \frac{\text{load } (W)}{\text{cross-sectional area}}$$

$$\epsilon_1 = \text{strain in axial direction} = \frac{\text{change in length}}{\text{original length}}$$

and

$$\delta_1 = E \epsilon_1$$

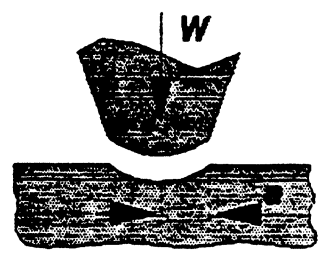
where E is the elastic constant, the Young Modulus

and

$$\epsilon_2 = -\nu \epsilon_1$$

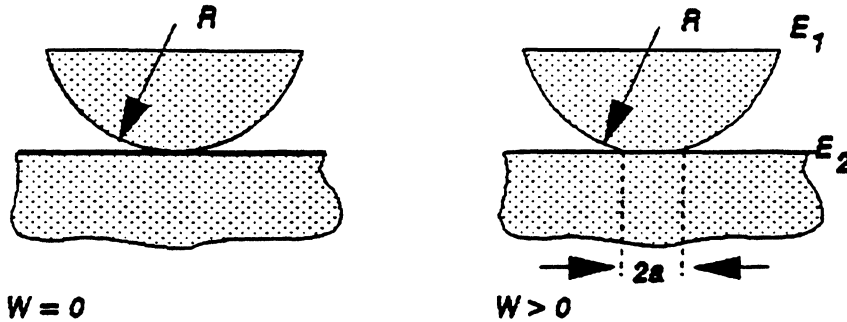
where ν is the Poisson Ratio, and ϵ_2 is the strain in the transverse direction

Yield stress (Y) is the stress state at which the transition from elastic behavior to plastic behavior occurs.
Hardness (H), $H = W/a^2$, the ratio of the load to the surface area of the permanent indentation.



Contact Between a Spherical and Flat Surface

what are the factors that determine the real area over which the load is supported?

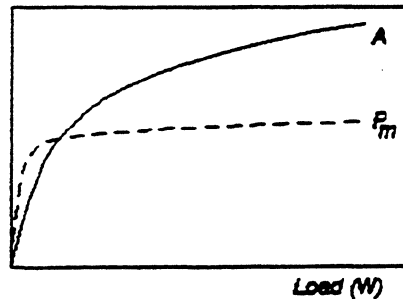


according to Hertz's equation for elastic deformations

$$Q = 1.1 \left\{ \frac{WR}{2} \left(\frac{1}{E_1} + \frac{1}{E_2} \right) \right\}^{1/3} \propto \left(\frac{3WR}{4E^*} \right)^{1/3}$$

at this stage the contact area $A = a^2 \approx W^{2/3}$ and the

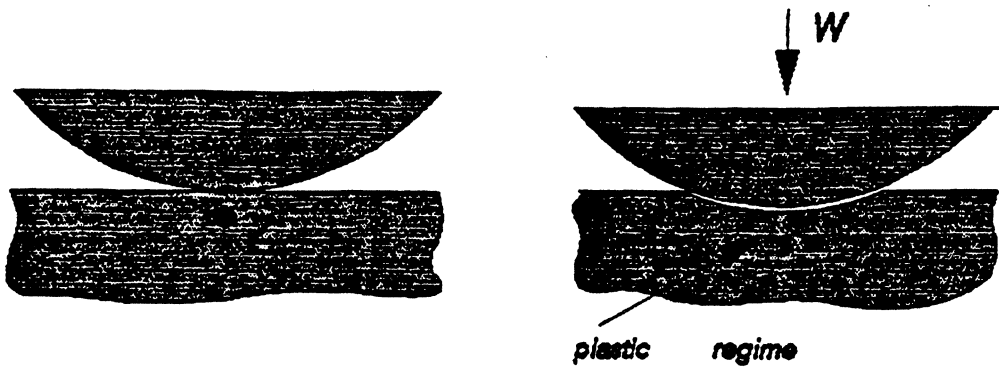
mean pressure over the area of contact $P = W/a^2 \approx W^{1/2}$ $H = 3Y$



variations of A & P_m with load (W) during elastic deformations

However, as the load is increased, the mean pressure P increases until it reaches such a value that at a critical point within the softer material the elastic limit is exceeded. This limit is exceeded when

$$P_m = 1.1Y$$



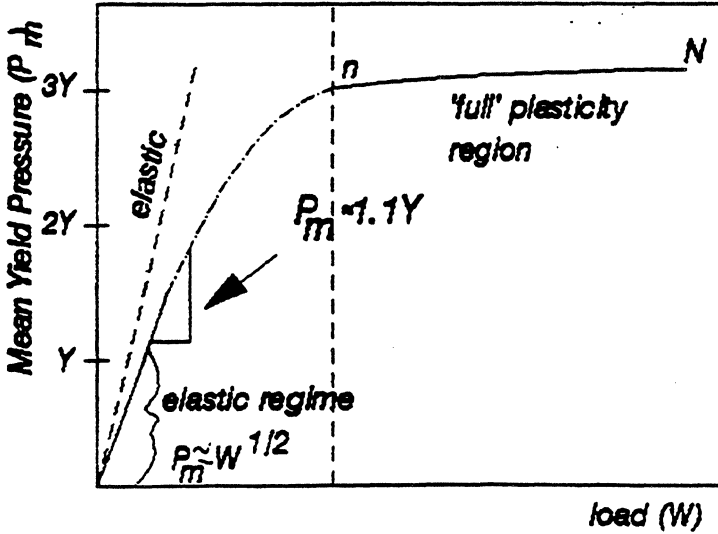
the onset of plasticity occurs at the point z
 (according to Hertz - about 0.6a below the center
 of the circle of contact) below the surface when

the mean pressure
a - radius of contact spot.

$$P_m \approx 1.1Y$$

At a later stage the whole of the material around
 the indentation flows plastically; at this stage

$$P_m \approx 3Y$$



It is interesting to calculate the load (W_L) required to bring the deformation up to the onset of plastic flow ($P_m = 1.1Y$)

$$W_L = 13.1 P_m^3 R^2 (1/E_1 + 1/E_2)$$

if

$$Y = 200 \text{ kg/mm}^2$$

$$P_m = 220 \text{ kg/mm}^2$$

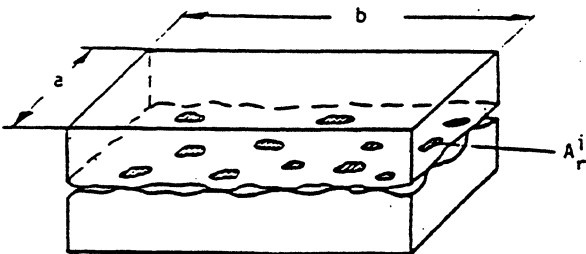
$$E_1 = E_2 = 2 \times 10^{12} \text{ dynes/cm}^2$$

typical for tool steel

then

$W_L = 1.4 \times 10^{-3} \text{ g}$	\rightarrow	for $R = 1 \times 10^{-4} \text{ cm}$
14 g	\rightarrow	for $R = 1 \times 10^{-2} \text{ cm}$
$14 \times 10^4 \text{ g}$	\rightarrow	for $R = 1 \text{ cm}$

Contact of Rough Surfaces



nominal and real area of contact

$$A_o = a \cdot b \gg A_r = \sum_{i=1}^n A_r^i \quad (n: \text{number of contacts})$$

- i) the nominal area of contact, A_o , i.e., the apparent area of overlap of the contacting solids
- ii) the real area of contact, A_r , i.e., the sum of the separate microscopic areas at which the asperities are in contact.

According to Archard (1957), the multipoint contact under elastic deformation can give a real area of contact almost linearly proportional to load (W), i.e.,

$$A = \text{constant } (W/E)^c$$

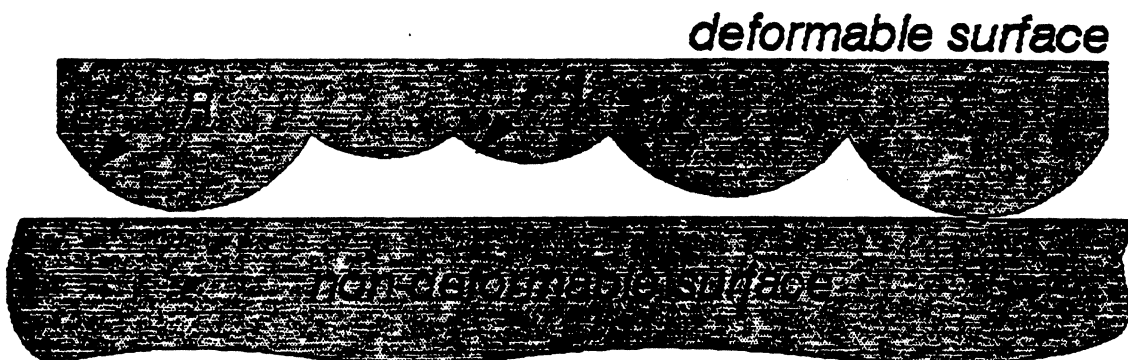
where $4/5 \leq c \leq 44/45$ (depending on the model)

Another extension of the Hertzian theory of an elastic contact between spheres to the case of rough surfaces with Gaussian distribution of peak-heights was made by Greenwood and Williamson (1966)*

They assumed that:

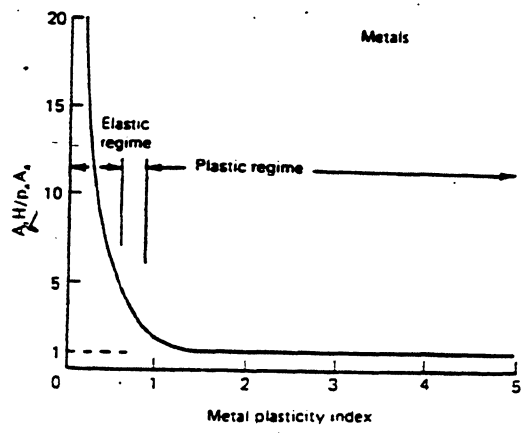
- 1) rough surface is covered with spherical asperities
- 2) asperities' summits have constant radius (R)
- 3) asperities' heights vary randomly, and
- 4) surfaces have Gaussian distribution of peak heights.

*valid only for
static contacts of
contacts with no
frictional stresses*



* Proc. Roy. Soc. Lond. A 296, 330 (1966)

Influence of Plasticity Index on the Real Area of Contact



to minimize friction
and wear the ratio
of the real area of
contact to the apparent
contact should be as
low as possible

i) the plastic contact results in a minimum contact area, but repeated plastic contact leads to wear and undesirable permanent deformations



ii) $E_c (\delta_p / R_p)$ should be as high as possible. The asperities with high E_c and low R_p produce high contact stresses and result in lower A_r for a given load
make surface rougher -> rms higher

$\psi = (E_c / H) (\delta_p / R_p)$

iii) High ψ allows contact with fewer asperities and also results in lower A_r

Caveats

- * when in shear, contacts yield plastically at lower ψ
- * with thin overcoats, yielding is dominated by the modulus and hardness of the substrate

* E, Y and H are functions of strain rate (loading and unloading of the asperity contacts)

1. RMS
2. contact area

Nanoindentation Hardness Apparatus

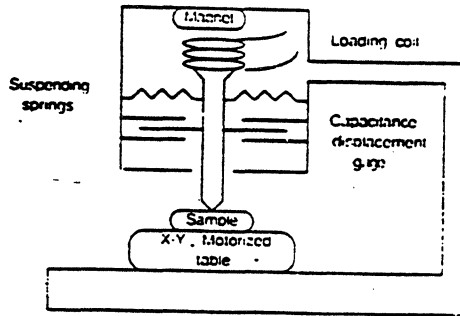
Developed by Pethica (1983)

displacement sensitivity $2-3 \text{ \AA}$
 0.2-0.3 nm

force resolution $\sim 0.5 \mu\text{Newton}$

minimum penetration 15 nm

strain rates 3-6 nm/s



Nanoindenter, Nano Instr.,

Oakridge, Tenn.

characterize the mechanical properties

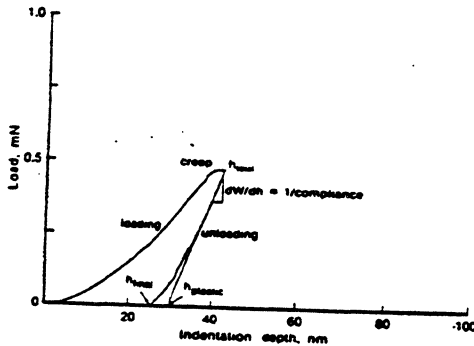


Fig. A.12. Typical load-displacement curve obtained at a 40-nm indentation depth using the nanoindentation apparatus (Pethica et al., 1983) for a thin-film (metal) disk (Al-Mg substrate, 10-20 μm Ni-P, 50-75 nm Co-Pt-Ni, 20-30 nm C, and 1-4 nm perfluoropolyether lubricant) identified as B1 in Chapter 3. Plastic depth is obtained by extrapolating the fitted line to zero load.

the slope of the unloading curve (dW/dh) is used as a measure of the elastic modulus of the thin film

the compliance for the Berkovich indenter (∇)

is given as

$$\frac{dh}{dW} \sim \frac{1}{E_c} \left(\frac{\pi}{A} \right)^{1/2}$$

s - specimen

i - indenter

where

$$\frac{1}{E_c} = \frac{1 - \nu_s^2}{E_s} + \frac{1 - \nu_i^2}{E_i}$$

$$h_{eff} = \left(\frac{area}{24.5} \right)^{1/2}$$

Greenwood & Williamson's Plasticity Index (ψ)

$$\psi = \left(E_c / H \right) \left(\delta_p / R_p \right)^{1/2}$$

E_c : Young Modulus
 H : Hardness
 δ_p : RMS

where E_c is the composite modulus

$$\frac{1}{E_c} = \frac{(1-\nu_1^2)}{E_1} + \frac{(1-\nu_2^2)}{E_2}$$

H is the hardness of softer solid

δ_p is the standard deviation of peak heights distribution

$$\delta_p = \left(\sigma_{p_1}^2 + \sigma_{p_2}^2 \right)^{1/2}$$

$1/R_p$ is the asperity-peak curvature

$$\frac{1}{R_p} = \frac{1}{R_{p_1}} + \frac{1}{R_{p_2}}$$

then

elastic contact if $\psi < 0.6$

and

plastic contact if $\psi > 1$

using G&W analysis, Bhushan derived a relationship

for the real area of contact in the elastic regime:

$$A_{re} \sim 3.2 P_a A_a / E_c \left(\delta_p / R_p \right)^{1/2}$$

$\psi < 0.6$

for plastic contacts:

$$A_{rp} \sim P_a A_a / H$$

$\psi > 1$

B. P. 167

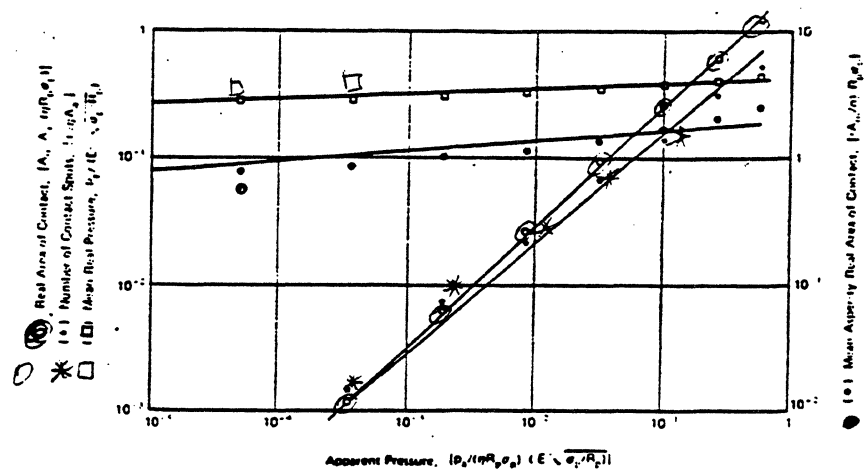


Fig. 3.8. Relationship between mean real pressure, real area of contact, number of contact spots, and mean asperity real area of contact with apparent pressure (Bhushan, 1984a).

Table 3.1. Interplaner separation, mean real pressure, real area of contact, number of contact spots, and mean asperity real area of contact for elastic and plastic contacts

Parameters	Elastic contact ($\psi < 0.6$ or $\psi_p < 1.8$)	Plastic contact* ($\psi > 1$ or $\psi_p > 2.6$)
Interplaner separation	$D = 1.40 [\log(0.57/P_s)]^{0.65}$	
Mean real pressure	$\frac{p_r}{E'(\sigma_p R_p)^{1/2}} = 0.42 P_s^{0.04} \sim 0.32$	$p_r/H = 1^b, 0.5^c, 2^d$
Real area of contact	$\frac{A_{re}}{A_s(\eta R_p \sigma_p)} = 2.40 P_s^{0.40} \sim 3.20 P_s$	$\frac{A_{re}}{A_s} = \frac{P_s^b}{H} \cdot \frac{2P_s^c}{H} \cdot \frac{P_s^d}{2H}$
Number of contact spots	$\frac{n}{\eta A_s} = 1.21 P_s^{0.88} \sim 2.64 P_s = 0.5(D \rightarrow 0)$	$\frac{n}{A_s}$ (in $1/\text{mm}^2$) $\sim 511.11 \zeta (P_s/H)^{0.91} C$
Mean asperity real area of contact	$\frac{A_{re} \cdot n}{R_p \sigma_p} = 2.00 P_s^{0.08} \sim 1.21$	$\frac{A_{re}}{n}$ (in mm^2) $\sim \frac{1.95 \times 10^{-3}}{\zeta} (P_s/H)^{0.06} C$

$P_s = p_s (\eta R_p \sigma_p) E'(\sigma_p R_p)^{1/2} \leq 0.57$

$\zeta = [1. (2\eta)^{1/2} R_p] (E' H)$

^a H = Bulk hardness of the softer material.
^b Based on Bowden and Tabor (1950).
^c Based on Gupta and Cook (1972a).
^d Based on Pullen and Williamson (1972).

and

$$\frac{l_c}{E_c} = \left(\frac{24.5}{\pi}\right)^{1/2} 2h_p \frac{dh}{dw}$$

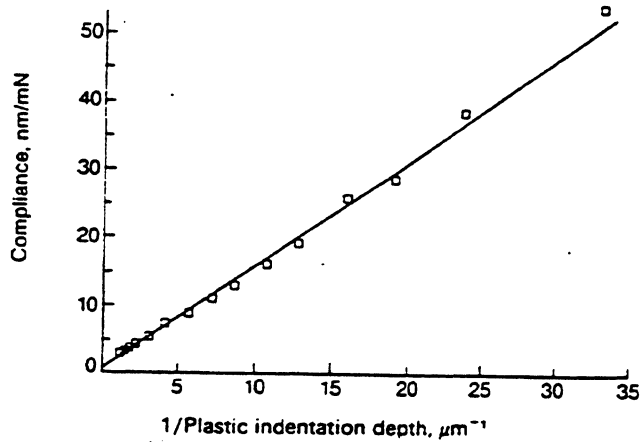


Fig. A.24. Compliance as a function of plastic indentation depth for a thin-film (metal) disk (same as that in Fig. A.12) using the nanoindentation apparatus. A constant modulus with depth would be indicated by the straight line. The deviation indicates a lower modulus near the surface for composite structure.

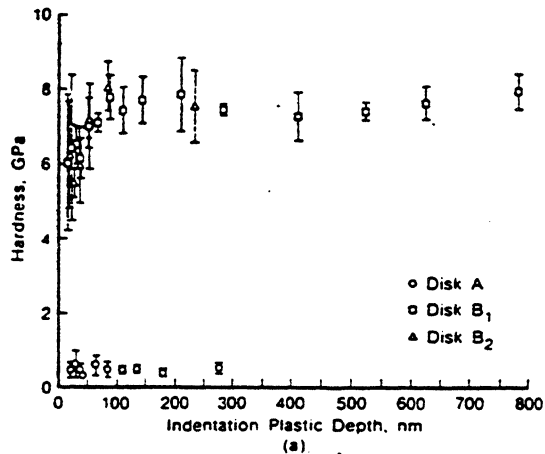
Real Area of Contact of Typical Magnetic Rigid Disks

measurements required:

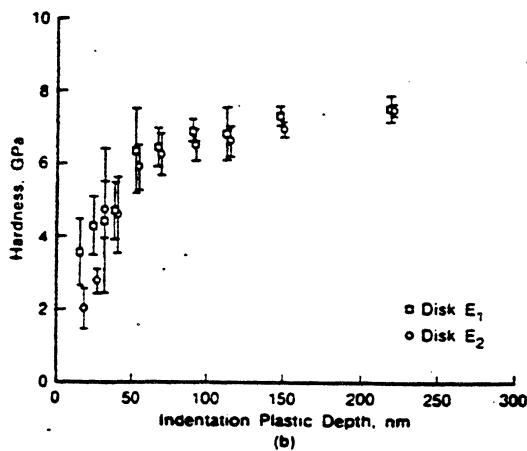
- 1) surface roughness ($\delta_p \pm R_p$). A 3-D optical profiler should be used.*
- ii) Young's modulus (E) and microhardness (H) is obtained using a nanoindentation apparatus developed by Pethica. The Berkovich indenter, a triangular pyramid-shaped diamond, is well applicable for extremely thin films*

Table 3.4. Construction of the rigid disks used

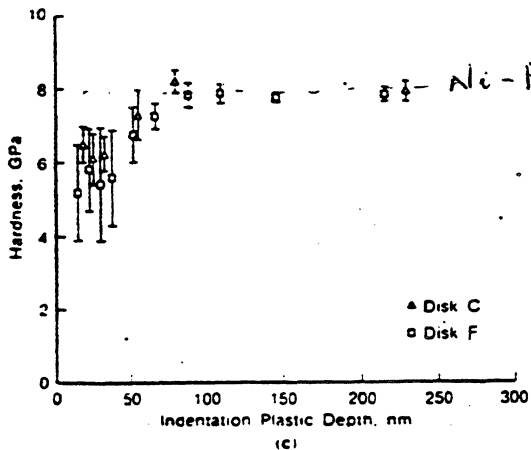
Disk designation	Substrate, Al-Mg with	Substrate finish	Construction of magnetic layer	Overcoat
A	-	Polished	γ -Fe ₂ O ₃ particles in epoxy binder	Perfluoropolyether lubricant (liquid)
B ₁	Ni-P	Textured	Sputtered Co-Pt-Ni film	Sputtered C
B ₂	Ni-P	Textured	Sputtered Co-Pt-Ni film	Sputtered ZrO ₂ -Y ₂ O ₃
C	Ni-P	Polished	Sputtered Co-Ni film	Sputtered SiO ₂
D	Ni-P	Textured	Plated Co-P film	Sputtered C
E ₁	Ni-P	Polished	Plated Co-P film	Sputtered C
E ₂	Ni-P	Polished	Plated Co-P film	None
F	Alumite	Polished	Sputtered γ -Fe ₂ O ₃ film	Spin coated SiO ₂ (textured) on sputtered SiO ₂



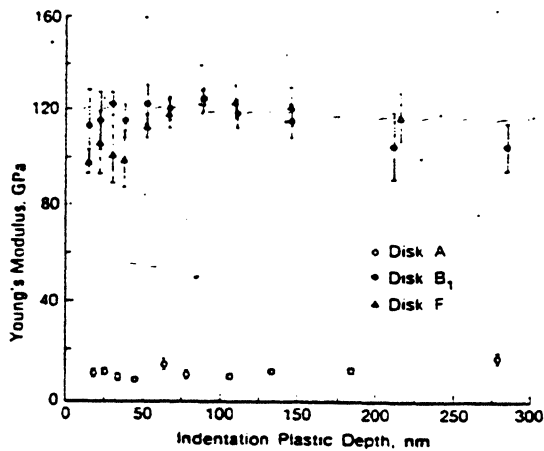
hardness of the particulate disk (A) is seen to be much less than that of the thin-film disk



effect of the overcoat (E₁) on the hardness at small depths is visible



In all cases, the decrease in thickness is seen near the surface with the hardness approaching that of the substrate layer (Ni-P) at large depths



effective Young's modulus of elasticity

observe that:

i) about 120 GPa is obtained for Young's modulus which is less than that measured

for Ni-P alone on the Mg-Al substrate (128 GPa), and

ii) a decrease at larger indentation depths, is due

to a lower stiffness of the Mg-Al substrate (70 GPa) much softer

Table 3.5. Real area of contact calculations for rigid disks

Disk designation* slider	E, GPa	H, GPa	RMS nm	σ_p , nm	1. R_p , 1 mm	ψ	$A_{re} A_p$, 1-GPa	A_p , 1. mN	$A_{re} A_p$, μm^2	r_p , MPa
A	9.4	0.5	9.39	9	4.79	0.267	22.6	9.9	2.3	45
B1	113	6.0	7.33	7	4.90	0.124	4.3	2.5	1.7	239
B2	129	6.2	7.33	7	4.90	0.135	3.8	2.2	1.7	268
C	107	6.2	2.11	2	2.24	0.054	9.6	8.8	1.1	107
D	108	5.5	4.62	4	3.30	0.081	7.1	4.9	1.5	144
F	98	5.2	4.07	4	2.24	0.060	10.3	4.7	2.2	100
Al ₂ O ₃ -TiC slider	448	22.6	1.63	2	0.53					

* Against Al₂O₃-TiC slider.

Real CA

Table 3.6. Young's modulus and microhardness of rigid disks, disk materials, and sliders

Disk designation/slider	Young's modulus, GPa	Hardness, GPa (kg/mm ²)
Disk*		
A	9.4 ± 5	0.5 ± 0.13 (54)
B1	113 ± 15	6.0 ± 1.8 (612)
[B1] ^b	105 ± 10	7.4 ± 0.15 (758)
B2	129 ± 23	6.2 ± 1.6 (632)
C	107 ± 5	6.2 ± 0.5 (632)
D	108 ± 12	5.5 ± 1.7 (564)
E1	77 ± 15	3.5 ± 0.9 (361)
E2	96 ± 15	2.0 ± 0.6 (207)
F	98 ± 5	5.2 ± 1.3 (530)
Disk materials ^c		
Ni-P coating on Si (15 μm)	128 ± 8	5.9-7.8 (600-800)
C overcoat on Si (100 nm)	170 ± 10	10-20 (1020-2040)
Co-Cr alloy coating on Si (180 nm)	191 ± 20	7.8-9.4 (795-958)
Slider		
Al ₂ O ₃ -TiC	450	22.6 (2300) → better performance
Mn-Zn ferrite	122	5.9 (600)

Note that ψ values

are all < 0.6 which

suggests that all contacts

are elastic.

Texture

* At an indentation plastic depth of 15-20 nm and corresponding load of about 0.1 mN.

^b At an indentation plastic depth of 280 nm and corresponding load of 18 mN.

^c At an indentation plastic depth of 35 nm and corresponding load of about 0.5 mN.

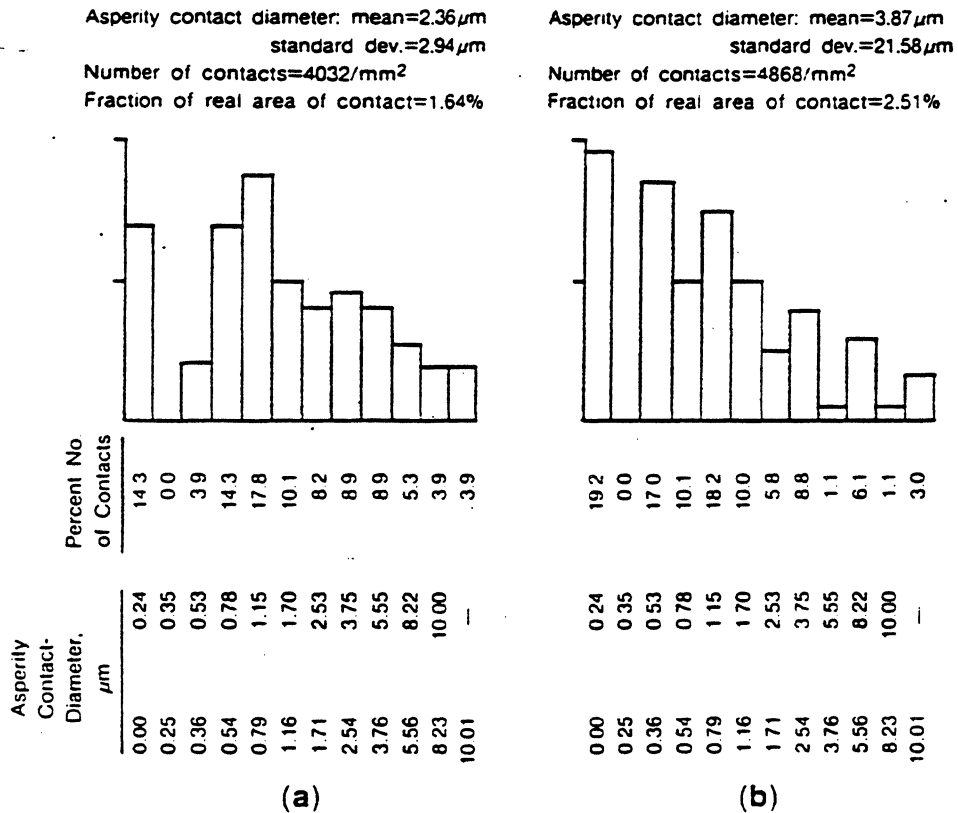


FIG. 10. Log normal distribution of asperity contact diameters for a thin-film disk before and after 60 h of contact time at 0.5 N load. Note the increase in the number of contacting asperities and the real area of contact (Bhushan and Dugger, 1990).

the rate of increase in the area is attributed to the rate-dependant mechanical properties, i.e., viscoelastic and viscoplastic deformations and the normal stress.

Conclusions:

- * *most contacts are definitely elastic ($\psi < 0.6$)*
- * *for wear and magnetic performance considerations it is desirable to design HDI with elastic contacts $E' (d_p/r_p)$ as large as possible ($\psi \sim 0.6$). It is preferable to achieve it by selecting a high E' rather than a high value of $(d_p/r_p)^{1/2}$.*
- * *the effective modulus can be increased by increasing the modulus of the overcoat or of the substrate film.*
- * *hardness effects the wear of the summit caps and should be high and comparable to that of the slider to maintain a low A_r .*
- * *the effective hardness can be increased by increasing the hardness of the substrate.*
- * *the effective hardness should be high and comparable to that of the slider to maintain a low A_r .*

Residual Stresses

Nearly all coatings, by whatever means they are produced, and surface layers of treated parts are found to be in a state of residual stress. Grinding, lapping (magnetic heads) and sputtering of thin films are found to give rise to a considerable amount of residual stresses on the surface.

The stresses may be:

compressive (i.e., the coating would like to expand parallel to the surface)

tensile (i.e., the coating would like to contract)

Compressive stresses are believed to increase hardness of the coatings. They tend to reduce sliding wear, reduce formation of wear particles, and increase fracture strength.

Tensile stresses, in the extreme cases, may lead to cracking and delamination of the coating.

For the ceramics such as magnetic heads, both tensile and compressive residual stresses are undesirable and should be minimized as much as possible.

Techniques used to measure residual stresses involve determination of the stresses by measuring the physical properties of the body that are affected by the presence of these stresses.

The method used to measure residual stresses are:

- 1) deformation (or curvature) methods
- 2) x-ray, electron, and neutron diffraction

Deformation Methods

Disk Method

$$\delta = \frac{\sigma}{r^2} \cdot \frac{E_s}{3(1-\nu_s)} \cdot \frac{t_s^2}{t_c}$$

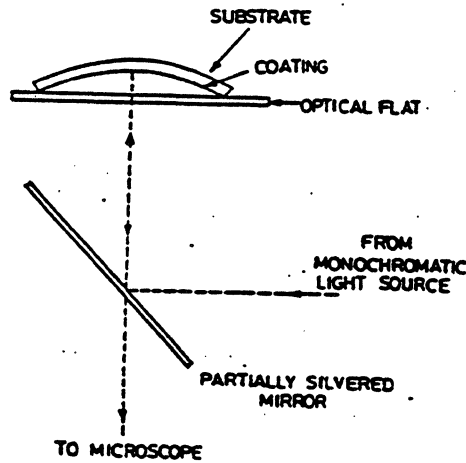


FIGURE 15.25 Schematic diagram for measurement of deflection of the center of a disk plate by optical interference.

t_s = substrate thickness
 t_c = coating thickness
 δ = deflection at the distance r from the center

the above equation

is valid if $t_c \ll t_s$

Applications: stresses in magnetic and overcoat films as produced by the sputtering process.

Beam Methods

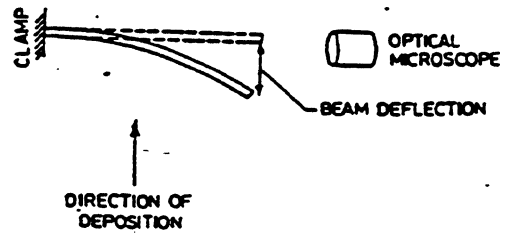


FIGURE 15.26 Schematic diagram for measurement of deflection of the free end of a cantilevered beam by microscopic observations.

Beam methods can be used in situ during the deposition process. Beam deflection can be measured electromechanically or by using capacitive, inductive or interference methods.

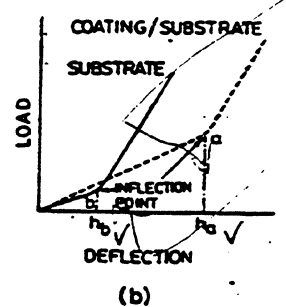
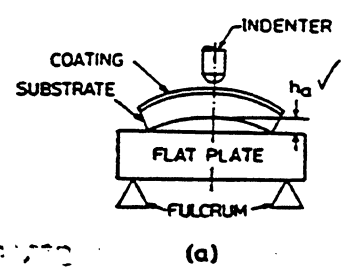


FIGURE 15.28 (a) Schematic diagram of the deflection measurement of a bent beam using a nanoindenter. (b) Load-deflection curve for a warped composite-beam substrate.

$$R = \frac{L^2}{8(h_a - h_b)}$$

L = substrate length

the biaxial stresses on a rectangular substrate according to Stoney equation

$$\sigma_x = \frac{E_s t_s^2}{6 t_c (1 - \nu_s^2)} \left(\frac{1}{R_x} + \nu \frac{1}{R_y} \right)$$

$$\sigma_y = \frac{E_s t_s^2}{6 t_c (1 - \nu_s^2)} \left(\frac{1}{R_y} + \nu \frac{1}{R_x} \right)$$

Microstresses (0.1 to 100nm) effect x-ray diffraction patterns. Raman spectroscopy and ultrasonic methods are also used.

Adhesions of Coatings

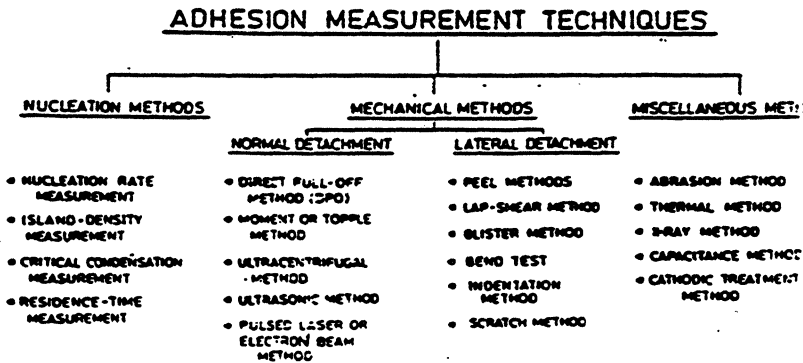


FIGURE 15.30 Classification of coating-to-substrate adhesion measurement techniques.

Direct Pull-off Method

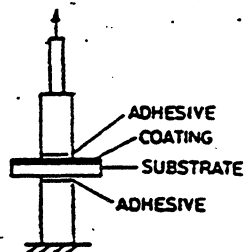
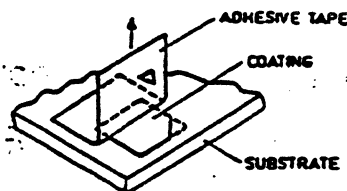


FIGURE 15.31 Schematic illustration of direct pull-off method for adhesion measurements.

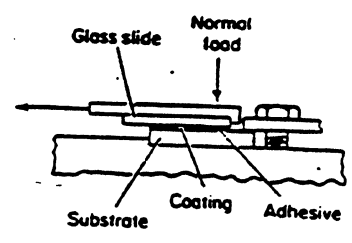
limited by the strength of the adhesive.

Max. strength is about 100 MPa (Eastman 910)



Scotch tape method usually applicable for coating with adhesion strengths less than 0.5 MPa.

Lap - Shear Method



= force required to break
adhesion normalized to the
contact area

Fig. A.30. Schematic illustration of the lap-shear method for measurement of coating-to-substrate adhesion (Mittal, 1976).

$$\sigma_c < 100 \text{ MPa}$$

Indentation Method

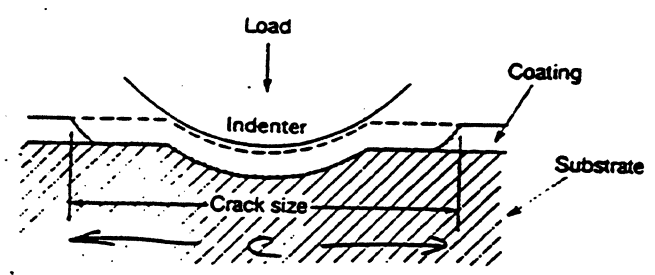


Fig. A.31. Schematic illustration of the indentation method for measurement of coating-to-substrate adhesion.

The minimum load at which the coating fracture is observed is called the critical load and is employed as the measure of the coating adhesion.

$$C = \alpha \left(1 - \frac{W_{cr}}{W} \right) W^{1/4}$$

where

$$\alpha^2 = \frac{\alpha_1 t_c^{3/2} H^{1/2}}{(K_{Ic})_{\text{interface}}}$$

H - mean hardness

fracture toughness

Scratch Method

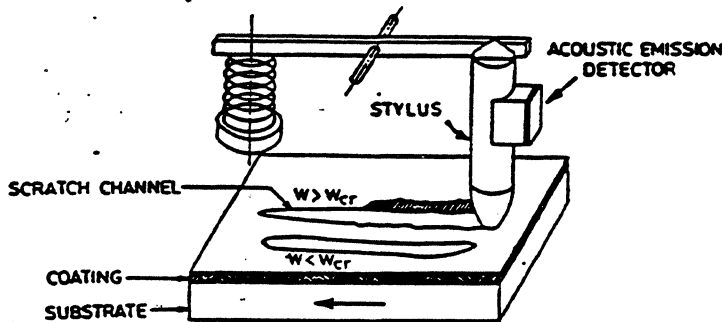


FIGURE 15.39 Schematic illustration of the scratch method for adhesion measurement.

The minimum load or the critical load at which the coating is removed or detached is used to measure the adhesion.

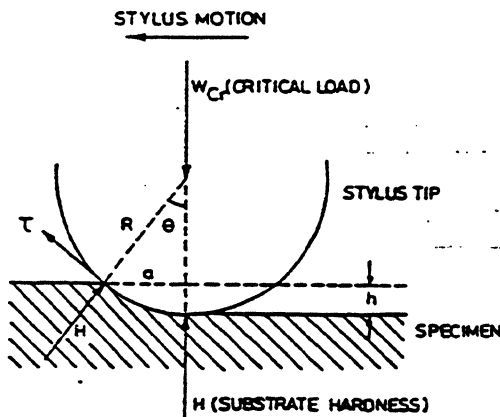


FIGURE 15.40 Geometry of the scratch.

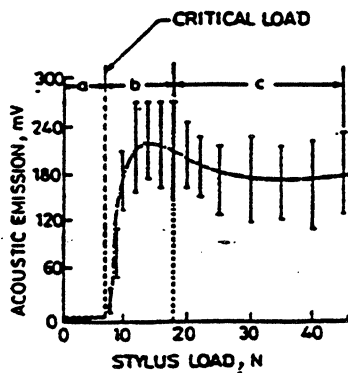
$$H = \frac{W_{cr}}{\pi a^2} \left. \vphantom{\frac{W_{cr}}{\pi a^2}} \right\} \text{SUBSTRATE HARDNESS}$$

ADHESION STRENGTH τ :

$$\tau = H \tan \theta =$$

$$= \frac{W_{cr}}{\pi a^2} \left[\frac{a}{(R^2 - a^2)^{1/2}} \right]$$

or $\tau = W_{cr} / \pi a^2$ if $R \gg a$



the acoustic-emission technique is very sensitive in determining critical load.

MICRO-INDENTATION AND MICRO-SCRATCH TESTS ON SUB-MICRON CARBON FILMS.

T.W. WU*, R.A. BURN*, M.M. CHEN** AND P.S. ALEXOPOULOS*

*IBM Research Division, Almaden Research Center, San Jose, CA 95120.

**IBM General Product Division, San Jose, CA 95139.

ABSTRACT

Micro-indentation and micro-scratch techniques were used to characterize the hardness and the adhesion strength of 0.11 μm thick sputtered carbon films on Silicon substrates. Hardness depth profiles and critical loads were measured using a microindenter under indentation and scratch testing modes, respectively. The carbon film with 6 mtorr argon sputtering pressure shows better practical adhesion (or higher critical load) and slightly higher hardness. The indentation fracture phenomenon observed on the 30 mtorr film is closely related to its poor adhesion. The failure mechanism will also be discussed.

INTRODUCTION

Adhesion is not just an important problem but also a difficult one. Nowadays, extremely thin films ($< 0.1 \mu\text{m}$) are extensively used both in semiconductor and computer storage technologies; therefore, a device which is capable of measuring this critical property of a sub-micron thick film is highly desirable. The characterization of adhesion strength by scratch testing is well established and commonly used in the hard coatings industry [1-4]. However, because of approximately two orders of magnitude difference in the sample thickness, new specifications are required on the potential testing devices, such as the range and the resolution of the applied load, the sensitivity of the acoustic emission detector, the tip radius and quality of the indenter...etc., and these stringent demands mean conventional type scratch testers are not immediately applicable.

In this study, we have modified the existing microindenter developed at the IBM Almaden Research Center [5] to perform not only the micro-indentation but also the micro-scratch tests. Two sub-micron carbon films with different mechanical properties have been used to demonstrate this added capability. Extensive SEM studies were also carried out to understand the failure mechanisms.

EXPERIMENTAL PROCEDURE

Two 0.11 μm thick carbon films were deposited on Si<111> wafers using a DC planar magnetron sputtering system under the same process conditions except for different argon sputtering pressures. The nomenclature, process conditions and some of the sample properties are summarized in Table I. After deposition, the Si wafer was cut into approximately 10 mm square coupons which were mounted on the sample post (2 in Fig.1) for the indentation and scratch tests.

For obtaining the hardness depth profiles, we have performed the continuous load and un-load test and utilized the data processing routine described in the previous report [5]. The indentation rate used for the loading and unloading stages were 4 and 15 nm/sec, respectively. The indenter used for hardness measurement was a 3-sided diamond pyramidal or Berkovich indenter [6].

TABLE I: Some Properties of the Sample Films

Sample ID	Ar-pressure (mtorr)	Residual stress (dyne/cm ²)	Mass Density (g/cm ³)	Hardness (GPa)	Critical load (g)
A	30	-2×10^9 †	1.5 ‡	~23	0.24 ± 0.03
B	6	-6×10^9 †	2.1 ‡	~25	2.98 ± 0.34

† compressive stress, obtained by wafer curvature measurement.

‡ measured by X-ray absorption technique.[11]

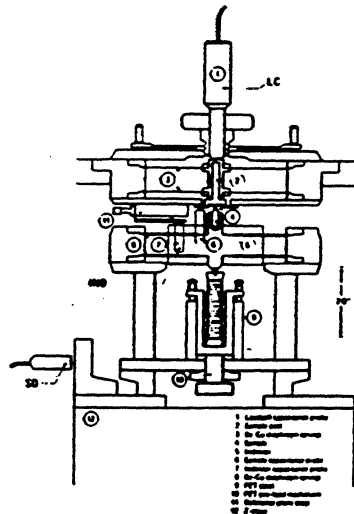


Fig. 1: Schematic diagram of indenter assembly and loadcell assembly. Here IND: indenter probe, LC: loadcell probe and SD: scratch distance probe.

The scratch test can be treated as a combination of two operations, one is the normal indentation process carried out by the indenter assembly, the other is a horizontal motion executed by the precision X-translation stage. Combining the existing capabilities of the microindenter with an additional capacitance probe (SD in Fig. 1) for monitoring the displacement of the X-translation stage, we can perform a scratch test under the following modes:

- (1) Indenter-servo mode: We can have any pre-determined displacement pattern for the indenter motion during the entire scratch process, for instance, a constant indentation speed.
- (2) Loadcell-servo mode: By using the loadcell output (LC) instead of indenter capacitance probe output (IND) as the input signal for the servo system, the microindenter can perform an indentation or a scratch test under a constant loading rate, or hold the applied load constant at any stage.
- (3) Profilometer mode: By locking in the loadcell output at a small constant load via the servo system, usually it is set at 10 mg, then scanning the indenter across the sample surface by moving the X or Y-translation stage. The recorded locus of the indenter tip is then the surface profile. This is a very useful function for measuring the scratch groove depth.

The current version of the microindenter has a range of applied load from a few mg up to 200 g with a load resolution of 3 mg, and a depth resolution of 1 nm. The scratch speed is from 0.5 $\mu\text{m}/\text{sec}$ up to 50 $\mu\text{m}/\text{sec}$ and the scratch length can be up to several mm.

To perform a scratch test, we first place the indenter about 0.1 μm away from the sample surface. This step allows us to begin a scratch with a zero applied load. Second, we set the traveling range and speed of the X-translation stage at 120 μm and 1 $\mu\text{m}/\text{sec}$, respectively, through the controlling program and then start the motion. Finally, the PZT motor is activated to drive the indenter toward the sample surface at a speed of 15 nm/sec. The outputs from three capacitance probes (i.e. IND, LC and SD in Fig. 1) were recorded during the entire period of the scratch process by a standard data acquisition system. The maximum applied load can be adjusted by selecting the indentation speed, the scratch speed or distance. A conical type diamond indenter with nominal 5 μm tip radius has been used for the tests.

A JEOL 840 Scanning Electron Microscope was used for examining the fractography of the scratch tracks. Because of the relatively low electrical conductivity of sputtered carbon films, a 10KV accelerating voltage was used.

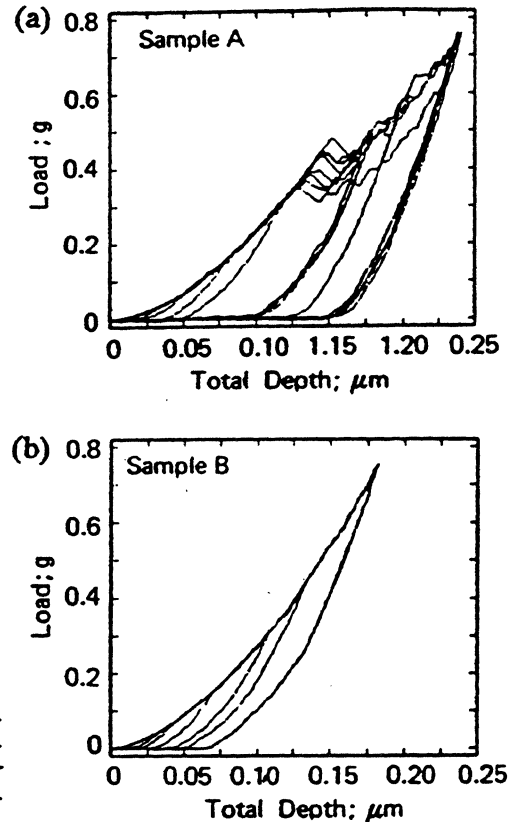


Fig. 2: Indentation loading curves of (a) Sample A and (b) Sample B. Notice the indentation fracture phenomenon shown on (a).

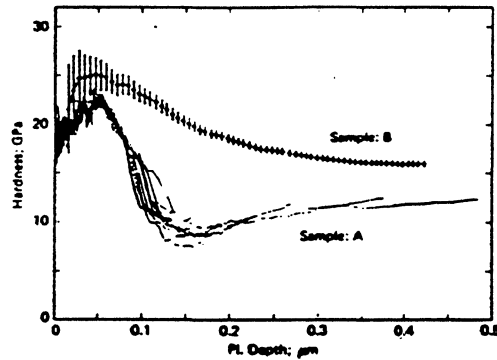


Fig. 3: Hardness depth profiles of Sample A and Sample B.

RESULTS AND DISCUSSION

Micro-indentation and Micro-scratch Tests

Figs. 2a and 2b show the indentation loading curves of Samples A and B, respectively. Sample A shows failure events during the indenting process as the abrupt drops in load as the applied load reaches roughly 0.36 g. In contrast, Sample B simply shows the normal loading patterns up to 7.5g (only range to 0.8 g shown in Fig. 2b). The hardness depth profiles of Samples A and B are shown in Fig. 3. So as not to obscure the indentation fracture phenomenon which occurs for Sample A, we have omitted plotting the final average hardness values and the standard deviation bars which we have shown for Sample B. The profile of Sample A shown in Fig. 3 is simply a superposition of the individual hardness curves obtained from each indentation. The intrinsic hardness of the carbon coatings can be estimated from the first plateaus in the hardness depth profiles [5], and they are ~23 and ~25 GPa for Samples A and B, respectively. The slightly higher hardness of Sample B may be attributed to its higher mass density as verified by X-ray absorption measurements [11]. As expected, both hardness depth profiles approach the hardness of the Si substrate, which is about 16 GPa, at large penetration depth.

The following information can be acquired after scratch testing. (1) The distribution of the applied load along the scratch length. (2) The distribution of the total and the plastic depth along the scratch length. (3) The critical load, which is the applied load corresponding to the first event of failure during the scratch process, such as film cracking or delamination. The critical load is obtained directly from the loadcell output. (4) The scratch hardness (or scratch resistance); by adopting the concept of the Meyer hardness [7], the scratch hardness can be simply defined as $H_{sc} = 9.8 \times [L - (0.5 \times \pi \times (W/2)^2)]$ [10]. Where, H_{sc} : the scratch hardness in GPa. L : the applied load in g. and W : the width of the scratch track in μm .

Figs. 4a and 4b are the scratch loading curves of Samples A and B, respectively. The scratch loading curve is the plot of the scratch load vs. the scratch length. For clarity, we have shifted each scratch loading curve 15 μm apart to prevent overlap. Interestingly enough, we have observed that, in both cases, the first abrupt drop on the scratch load occurs very regularly, although for Sample B it has occurred at much higher load than for Sample A. This implies that a characteristic property of each sample has been detected. If we define the critical load, L_c , as the applied load which is associated with the first occurrence of the load drop on a scratch loading curve, then the average critical loads and their standard deviations for Samples A and B can be calculated. The results are also included in Table I. Because of the high accuracy in monitoring the lateral scratch position, for each scratch we can match the applied load to its corresponding scratch pattern along the entire scratch length.

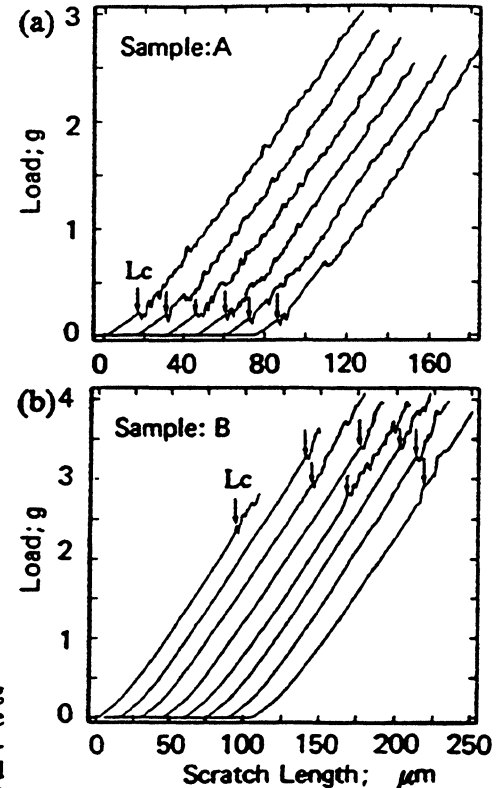


Fig. 4: Scratch loading curves of (a) Sample A, and (b) Sample B. Arrows indicate the positions of the first load drops.

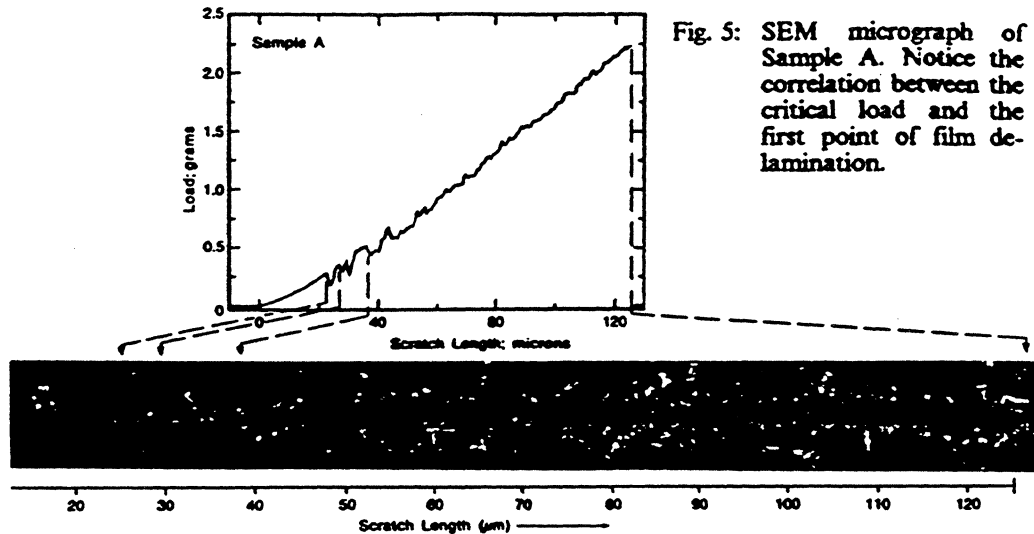


Fig. 5: SEM micrograph of Sample A. Notice the correlation between the critical load and the first point of film delamination.

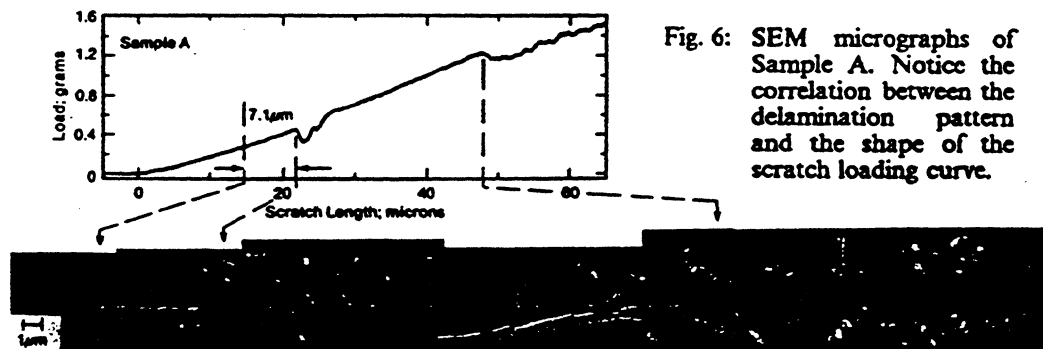


Fig. 6: SEM micrographs of Sample A. Notice the correlation between the delamination pattern and the shape of the scratch loading curve.

Fractography

Figs. 5 and 6 show the correlations between the scratch loading curves and the corresponding scratch morphology of Sample A. Similarly, Figs. 7 and 8 are for Sample B. The following observations can be made; (1) A smooth scratch loading curve was observed before the applied load exceeded the critical value, L_c , which is in contrast to the zig-zag type curve when it exceeded this value. (2) The initiation of film delamination always occurred at the scratch position where the first drop of the applied load was observed. (3) The zig-zag shape of the scratch loading curve is attributed to consecutive delamination of the carbon films. (4) The size of the load drop is proportional to the scale of the film delamination. (5) On Sample B, a set of uniform tensile type cracks [8] were observed along the scratch tracks before the film delamination initiated (see Fig. 8). This suggests that although the carbon film had been fractured, it was still bonded to the Si substrate until the applied load eventually exceeded L_c . The cracking of the film causes only small changes of the loadcell output and hence induces small kinks or ripple structures on the scratch loading curve.

The explanation for observations (1) and (2) may be argued as follows. Because of the high hardness of the carbon film (ref. Table I) and the low friction between the film and the indenter tip, the indenter slides smoothly on the carbon film up to the load level of L_c , and the failure mechanism up to this stage is simply wearing and thinning down the carbon layer. However, when the applied load reaches L_c , the carbon film starts to delaminate and/or flake out of the track. Failure events such as film cracking and delamination inevitably cause a sudden increase of the local compliance of the sample system, which in turn, results in an abrupt drop of the loadcell output. Items (4) and (5) actually can be thought of in terms of the load drop scaling with the amount of elastic energy released during the corresponding failure event. This also implies that there is a limitation to the sensitivity of our detecting scheme, i.e. direct loadcell output measurement. In other words, if we assume that the released energy can be scaled by the delaminated area, then for small scale delamination, say for which the diameter of the coating flakes is smaller than $0.1 \mu\text{m}$, the criterion for L_c determination may not be applicable because the load

Fig. 7: SEM micrograph of Sample B. Notice that the higher critical load corresponds to the later delamination.

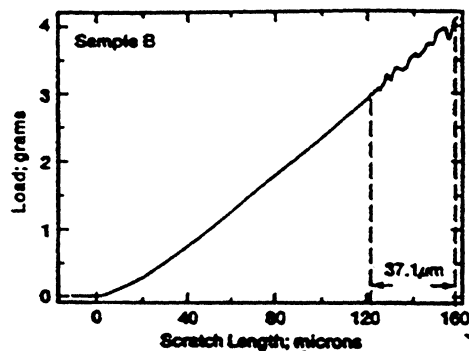
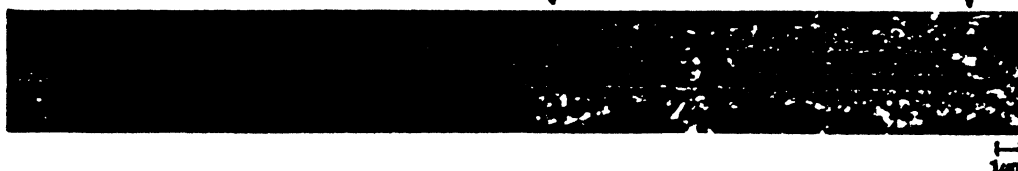
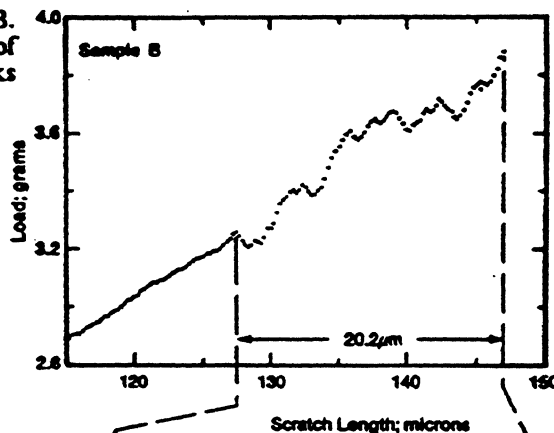


Fig. 8: SEM micrograph of Sample B. Notice that the appearance of the uniform tensile type cracks before film delamination.



drop becomes so small it may not be discernible from the background noise. A similar problem also exists in devices which use the acoustic emission detection scheme. However, locating the delamination spots by high resolution SEM or increasing the loadcell sensitivity are two possible ways to increase the sensitivity.

Figs. 5 through 8 have clearly demonstrated the one-to-one correspondence between the critical load and the first point of film delamination. Based on this fact, it seems reasonable to conclude that the critical load, L_c , as we defined previously does correlate to the practical adhesion strength [9] of the film/substrate interface. It is worthwhile to emphasize that L_c is a quite complicated function, which includes variables such as the hardness, Young's moduli of coating and substrate, the coating thickness, the friction between the indenter and the coating, indenter tip radius, and even the testing conditions such as the scratch speed and loading rate [3,8]. Therefore care must be exercised when attempting to rank adhesion strength using only the critical loads measurements.

Direct Scratch Depth Measurement

The plastic depth profile along a scratch track can be obtained by the following procedure;
(1) Pre-scan: Operating the microindenter in the profilometer mode and then acquiring the

scratch test is often used to evaluate the adhesion strength of the hard carbon films deposited by sputtering onto the magnetic media (see Matsuura et al.)

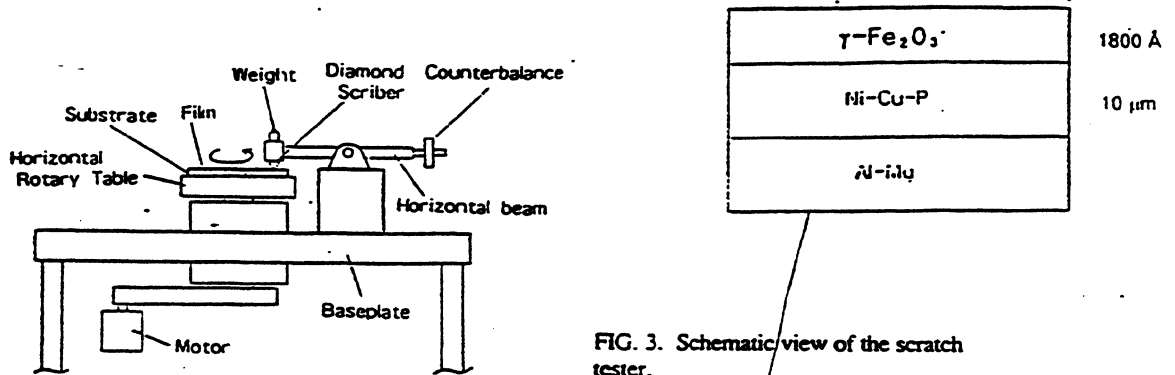


FIG. 3. Schematic view of the scratch tester.

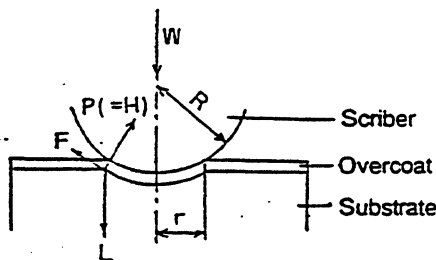
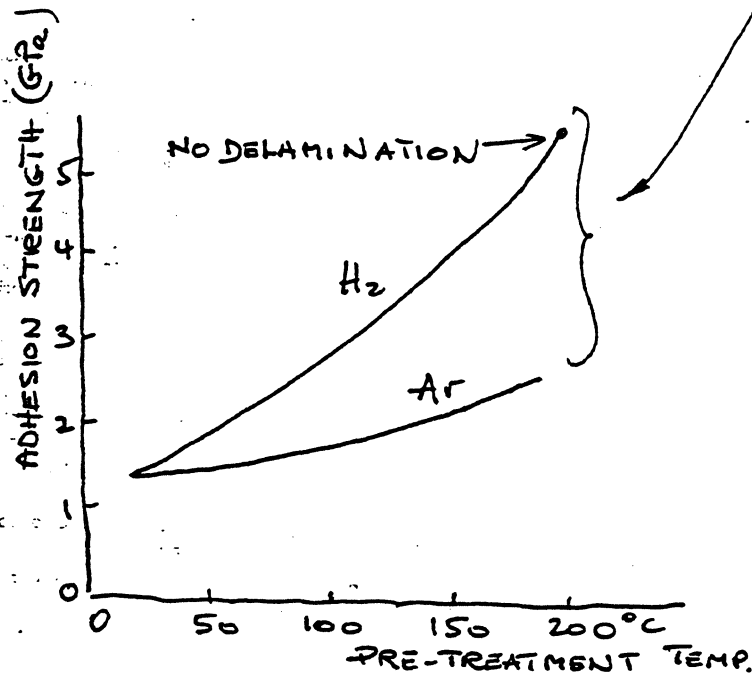


FIG. 4. Benjamin and Weaver's model (1960) in scratch test.



WITH $\gamma\text{-Fe}_2\text{O}_3$,
 $\tau \geq 5 \text{ GPa}$
 (Fe-C formation)
 much higher adhesion.

WITH Co-Ni-Cr
 $\tau \approx 1.6 \text{ GPa}$

(Only physical bonding,
 reduction oxide
 forming carbide)

Cr - adhesive layer - Co
 Cr is control for magnetic
 properties.

10/26/94

COATING-THICKNESS MEASUREMENT TECHNIQUES

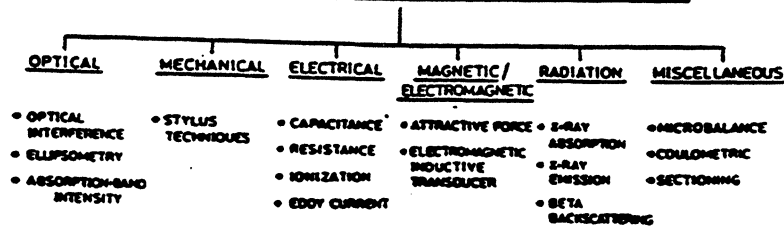
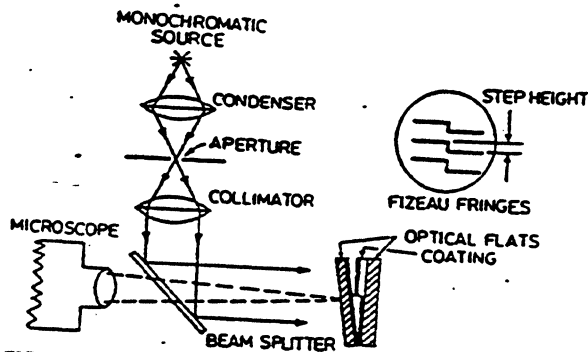


FIGURE 15.1 Classification of coating-thickness measurement techniques.

TABLE 15.1 Comparison of Some Common Thickness-Measurement Techniques

Measurement technique	Coating materials	Thickness range	Accuracy or precision	Remarks
Multiple-beam interference	All	3 nm to 2 μm	-1 nm	Nondestructive; step and highly reflective surface required; most accurate but time consuming
CARIS/VAMFO Ellipsometry	Transparent coatings	40 nm to 20 μm	-1 nm to 0.1%	Nondestructive
	Transparent coatings	1 nm to a few micrometers	-0.1 nm to 0.1%	Nondestructive; mathematics complicated; most accurate, especially with very thin coatings
Stylus	All	3 nm to a few millimeters	5%	Nondestructive; step in the coating required; the coating should be hard enough to resist the penetration of stylus; substrate should be quite smooth and rigid
Resistance	Metals	20 nm to 1 μm	1%	Nondestructive; also used as deposition-rate monitor
Ionization	All	No limit	<0.1 nm s ⁻¹	Only used as vapor deposition rate monitor
Eddy current	Metals on metals provided conductivities are different	1-1000 μm	1%	Nondestructive
Magnetic force/electromagnetic	Coatings or substrate to be magnetic	3-125 μm	1%	Nondestructive; sensitive to the magnetic conditions and properties of the test specimen
X-ray absorption	All	10 nm to 1000 μm	5%	Nondestructive; substrate must produce the characteristic radiations; simple, rapid scan, used in on-line manufacturing
X-ray emission	All	2 nm to 1000 μm	2%	Nondestructive; substrate must not contain any of the elements in the coating material; multicomponent coatings can be measured; simple, rapid scan, used in on-line manufacturing
Beta backscattering	All	10 nm to 50 μm	5%	Nondestructive; coating and substrate material must have difference in atomic number; simple, rapid scan, used in on-line manufacturing
Microbalance (gravimetric)	All	No limit	-0.1 nm cm ⁻²	Used as vapor deposition-rate monitor; simple
Microbalance (momentum type)	All	No limit	-0.1 nm min ⁻¹ per degree rotation	Used as vapor deposition-rate monitor; simple
Oscillating quartz-crystal	All	No limit	<<0.1 nm cm ⁻²	Most commonly used vapor deposition-rate monitor; simple
Coulometric	Metals (must be dissolved anodically)	1 to 50 μm	10%	Destructive; generally used for plated coatings

Thickness Measurements (cont'd)



Interferometric Technique

FIGURE 15.2 Schematic diagram for thickness measurement by multiple-beam optical interferometer using Fizeau method of fringes of constant thickness.

Ellipsometry

optical technique
can correlated with FTIR

Accuracy about 1 Å

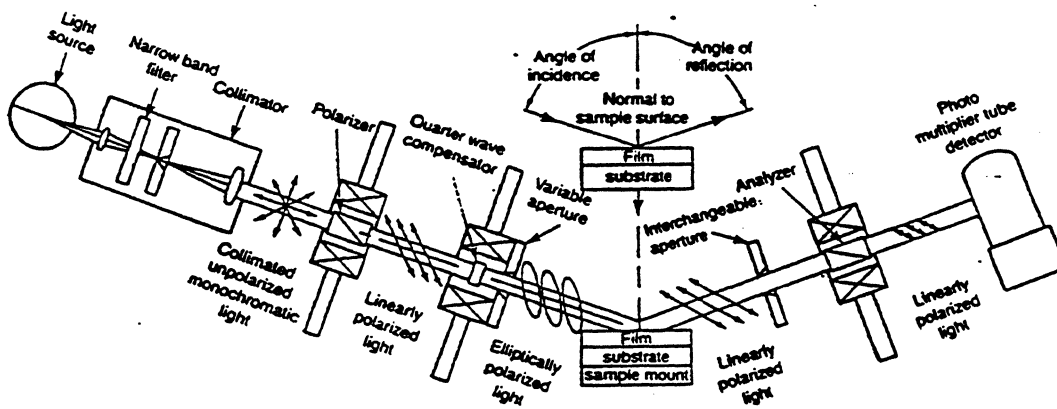


Fig. B.35. Schematic diagram of a manual ellipsometer (Anonymous, 1982).

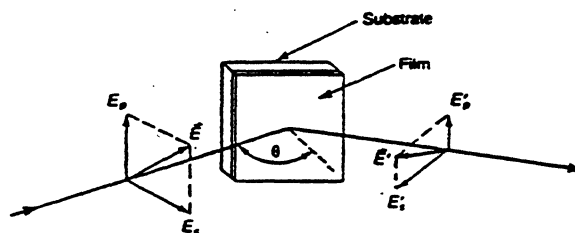


Fig. B.34. A description of the electric field amplitudes in an ellipsometry experiment.

in the absence of surface films, E_p and E_s are in phase and amplitude.

$$\tan \psi_i = \frac{E_p}{E_s}$$

if some film is present, then E_p & E_s are no longer in phase and the reflected light is elliptically polarized.

the ellipsometric parameter ψ is then

$$\psi = \tan^{-1} \left[\left(\frac{E_p'}{E_s'} \right) \left(\frac{E_s}{E_p} \right) \right]$$

and the phase difference $\Delta = \Delta_r - \Delta_i =$

$$\Delta = (\psi_p' - \psi_s') - (\psi_p - \psi_s)$$

ψ_p' - REFLECTED PHASE
 ψ_p - INCIDENT PHASE

In general, at a very small film thickness, Δ is a function of the film thickness and ψ is essentially a constant.

Changes in ψ can be attributed to changes in the structure of the surface layers of the substrate itself.

variation

TABLE 2-II. - VITREOUS SILICA*

Surface history	Polished with Diamond Paste		Polished with Cerium Oxide	
	ψ (in degrees)	Δ	ψ (in degrees)	Δ
Ideal case	3.79	360.00	3.79	360.00
Mech. polish	0.52	290.00	3.79	359.64
etch + growth HF 2 min etch in 10% HF	2.55	334.00	3.77	359.93
4 min etch in 10% HF	3.93	4.00	3.79	0.11
6 min etch in 10% HF	4.16	3.04	3.80	0.29

*Reference 17.

from Vedam, K., "Characterization of Surfaces", Syracuse Univ. Press, p. 503, 1975.

diamond-polished silica have been densified (ref. index 1.53 and thickness of 95 nm). No work hardening observed with cerium oxide.

FTIR can measure very accurately to 5 Å

Surface Analytical Techniques

over 60 techniques are LISTED IN LITERATURE

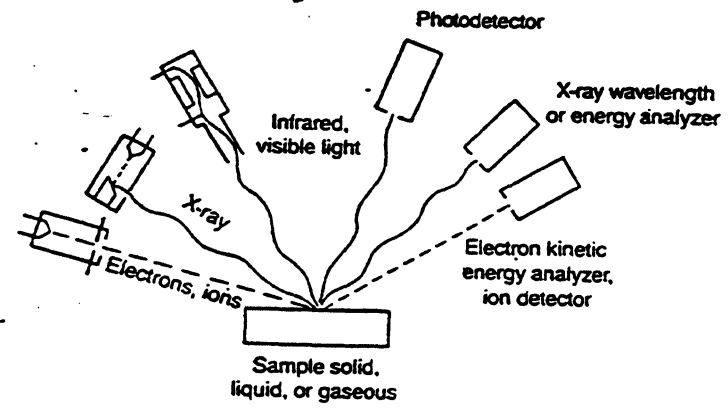


Fig. B.1. Excitation of sample and detection of radiation.

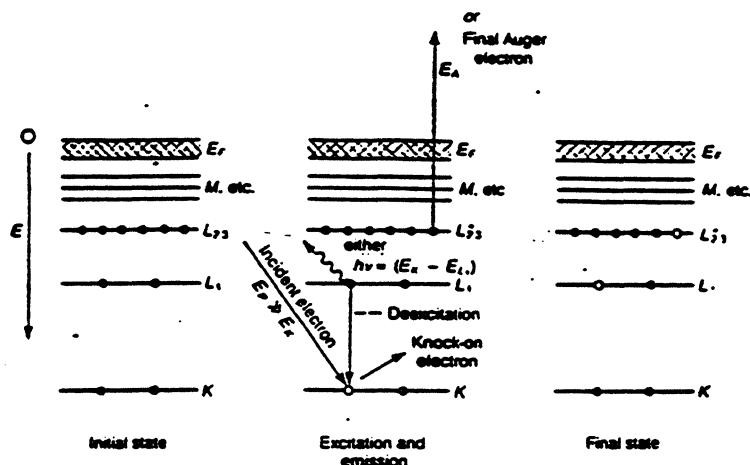
Table B.3. Comparison of the various techniques used for chemical analyses ✓ ✓

Technique	Information*	Elements not covered	Incident radiation			Spatial resolution	Sampling depth, monolayers	Sensitivity (order of)	Results, absolute or comparative		Popularity (1, most popular)
			Type	Energy	Environment ^b				Nondestructive		
1. High-energy beam UHV (primarily for inorganic materials)											
AES	E	H, He	Electron	1-10 keV	UHV	0.2 μm	3	0.3%	Com.	Y	1
EPMA	E	H, He, Li (WD) Z ^c ≤ 9 (ED)	Electron	15-50 keV	UHV	1 μm	1-2 μm	0.05% (1 pg)	Com.	Y	1
ISS	E	H, He	Ion	0.1-10 keV	UHV	1 mm	1	1%	Com.	Y	2
RBS	E	H, He	Ion	1-3 MeV	HV/UHV	1 mm	10-100	1%	Abs.	Y	3
SIMS (static)	C	—	Ion	5-22 keV	UHV	1 μm	2	0.1%	Com.	N	2
SIMS (dynamic imaging)	E	—	—	—	—	0.5 μm	30	1 ppm	Com.	—	—
SIMS (dynamic depth profile)	E	—	—	—	—	50 μm	40	1 ppm	Com.	—	—
XPS	C	H, He	X-ray Cu K, laser	1.5-15 keV	UHV	0.2 mm	3	0.3%	Com.	Y	1
XRF	E	Z ≤ 11 air H, He, Li, Be-vac. (WD)	X-ray (Tungsten lamp)	1-45 keV	HV/air	1-5 mm	50 μm-1 mm	0.05% (< 1 pg)	Com.	Y	2
2. Low-energy beam ambient environment ^d (primarily for organic materials)											
MS	F	N/A ^e	Electron	6-100 eV	HV	N/A	N/A	1 pg	Com.	N	1
NMR	F	N/A	dc magnetic field/rf signal	200-300 MHz	Air	N/A	N/A	0.1 mg	Com.	N	2
FTIR	F	N/A	IR	1 mW	Air	1 x 3 cm	10 ² - 10 ⁴	0.5 nm	Com.	Y	1
RS	F	N/A	Visible	1-2 mW	Air	40 μm	10 ² - 10 ⁴	5-50 nm	Com.	Y	3
ELL	Optical properties, film thickness	N/A	Visible	1-2 mW	Air	10 μm-1 mm	10 ² - 10 ⁴	0.1 nm	Abs.	Y	1

*E, elemental; C, chemical (elemental with binding energy information); and F, functional groups in organic molecules.
^bUHV, ultrahigh vacuum (~ 10⁻¹⁰ Torr); HV, high vacuum (~ 10⁻⁶ Torr).
^cZ, atomic number.
^dExcept MS.
^eN/A, not applicable.

- AES - Auger Electron Spectroscopy
- SIMS - Secondary Ion Mass Spectroscopy
- XPS - x ray Photon Electron Spectroscopy
- MS - Mass Spectroscopy
- FTIR - Fourier Transform Infrared Spectroscopy

Electron Beam Techniques



There are two (2) possible processes:

1. when $h\nu$ or a photon of energy is emitted we have x-ray fluorescence
2. when $h\nu$ is given to a third electron (Auger electron) in the $L_{2,3}$ shell, we have Auger emission.

$$h\nu = (E_K - E_L)$$

Fig. B.13. Schematic energy level diagram of the process of Auger emission and X-ray fluorescence in a solid. Binding energies are measured downward from an assumed level of energy at the Fermi level (E_F) (Briggs and Seah, 1983).

The Auger electron (after Pierre Auger) is ejected from the atom with a well-defined energy E_A , given by

$$E_A = E_K - E_L - E_{L_{2,3}}^*$$

where $E_{L_{2,3}}^*$ is the binding energy of $L_{2,3}$ in the presence of a hole in L_1 .

Auger electrons have energies unique to each atom (except hydrogen and helium).

* Sensitivity ca. 1/100 monolayer

0.3 Å

Escape path ca. 1 nm - 2-3 nm

Spacial resolution ca. 0.2 μm

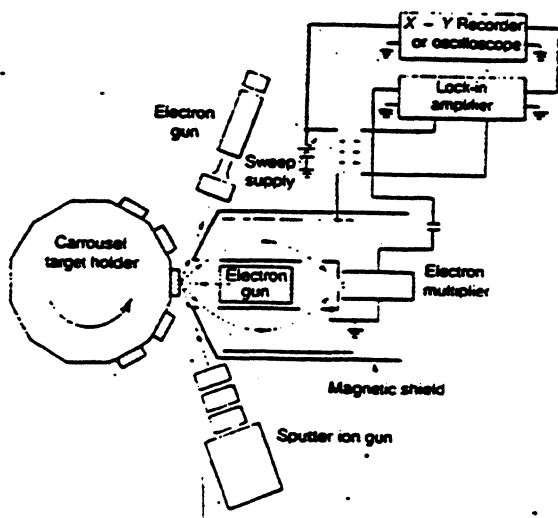
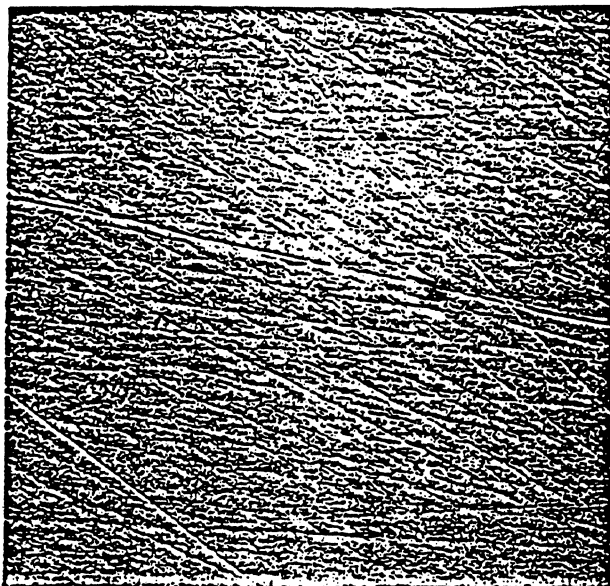
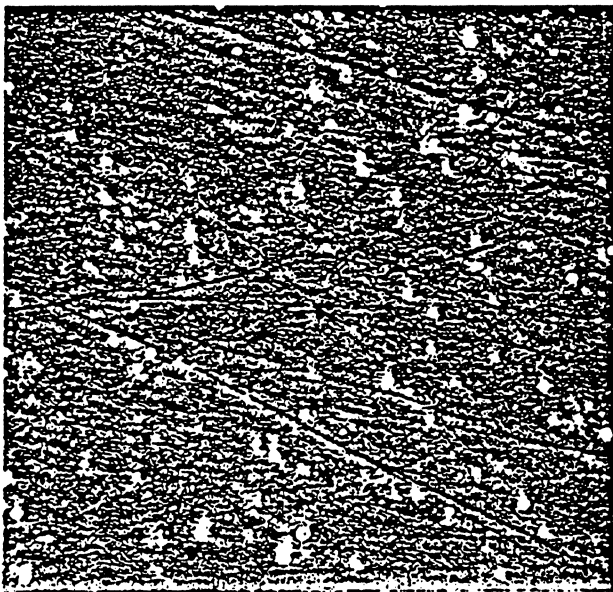


Fig. B.14. Schematic diagram of the cylindrical mirror analyzer as an Auger spectrometer (Czanderna, 1975).



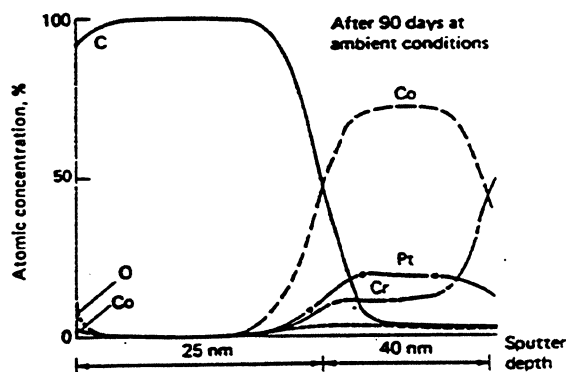
(a)



(b)

Depth Profiling

Ar ions eject neutrals by momentum transfer.
energy range 0.5 to 5 KeV.



spot diameter 1-5 mm
sputtering rates up to 5nm/min

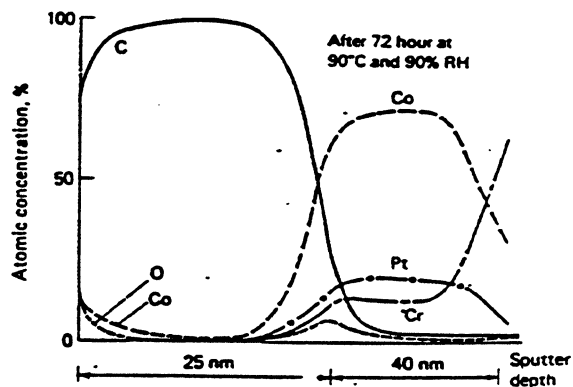


Fig. 6.75. Auger depth profiles of CoCr-Pt rigid disk with carbon overcoat after storage at ambient conditions for 90 days and after environmental stressing at 90°C and 90% RH for 72 hours (Novotny et al., 1987).

IEEE Trans. Magn. MAG-23,3465, 1987

- 1. can measure atoms
- 2. 3D mapping
- 2. cannot get information about chemical bonding.

Fig. 2 Chart of principal Auger electron energies

Open circles indicate the electron energies of the principal Auger peaks from each element. Closed circles represent predominant peaks for each element. Source: Ref 1

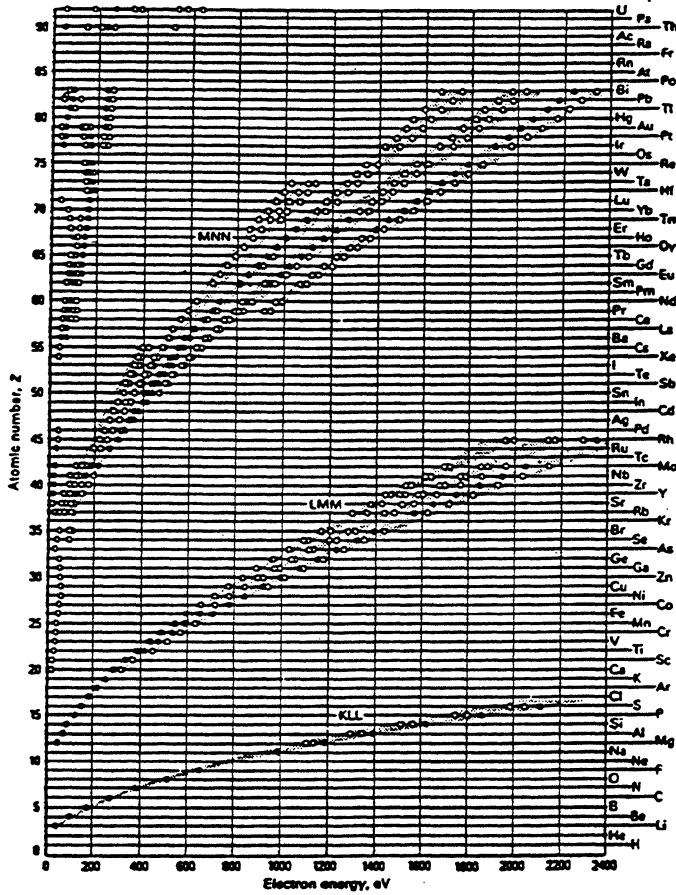


Fig. 4 Experimental measurements of electron escape depths in various elements

Source: Ref 12

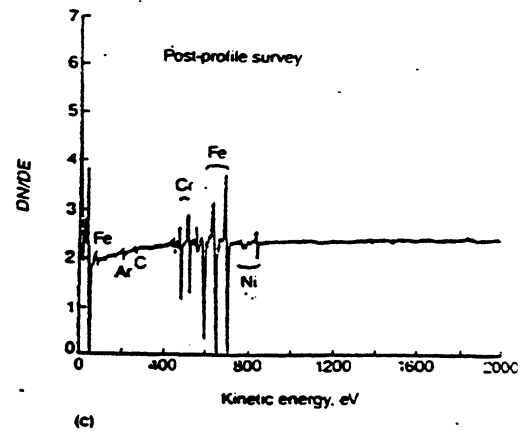
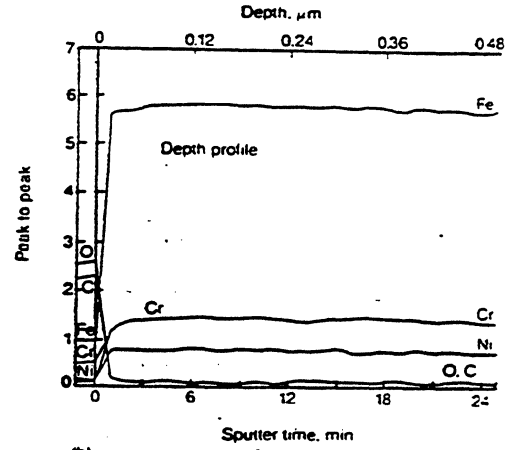
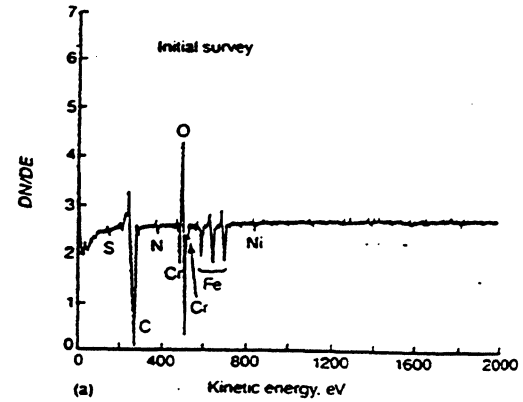
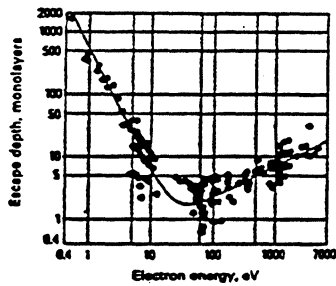
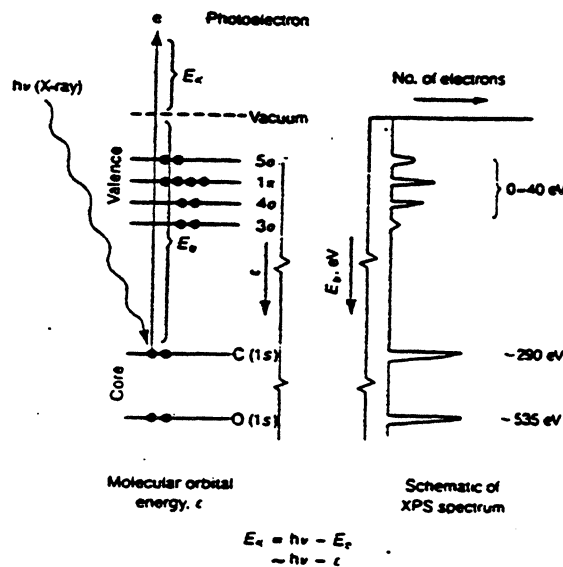


Fig. B.15. Auger electron survey spectra for a 303 stainless steel block: (a) initial survey (b) depth profiles, and (c) post-profile survey (Bhushan et al., 1985).

X-ray Photoelectron Spectroscopy (XPS) or Electron Spectroscopy for Chemical Analysis (ESCA)



$$E_b = h\nu - E_K$$

In this process the X-ray (photons) expels an electron giving up the energy to it.

The binding energy of orbital electrons is

Fig. B.18. Electronic energy level diagram and the resultant XPS spectrum using CO as an example (Casper and Powell, 1982).

characteristic of each atom. However, electron energies are affected by chemical interactions between atoms in the molecule, and as a result, binding information can be also obtained.

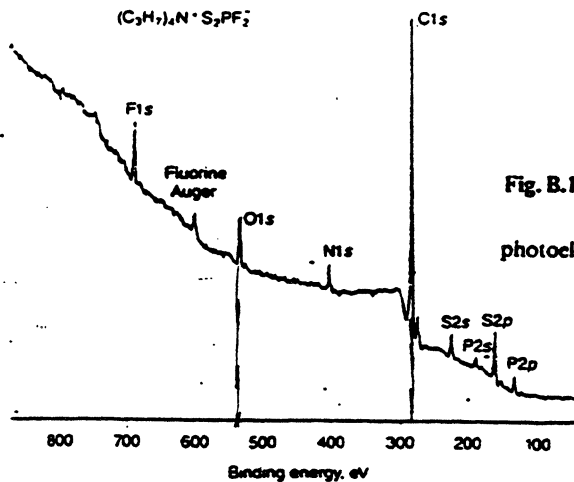
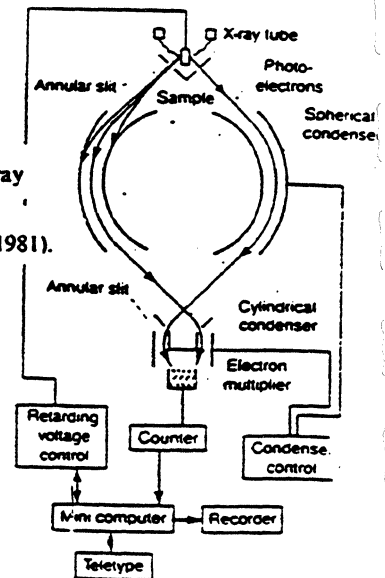
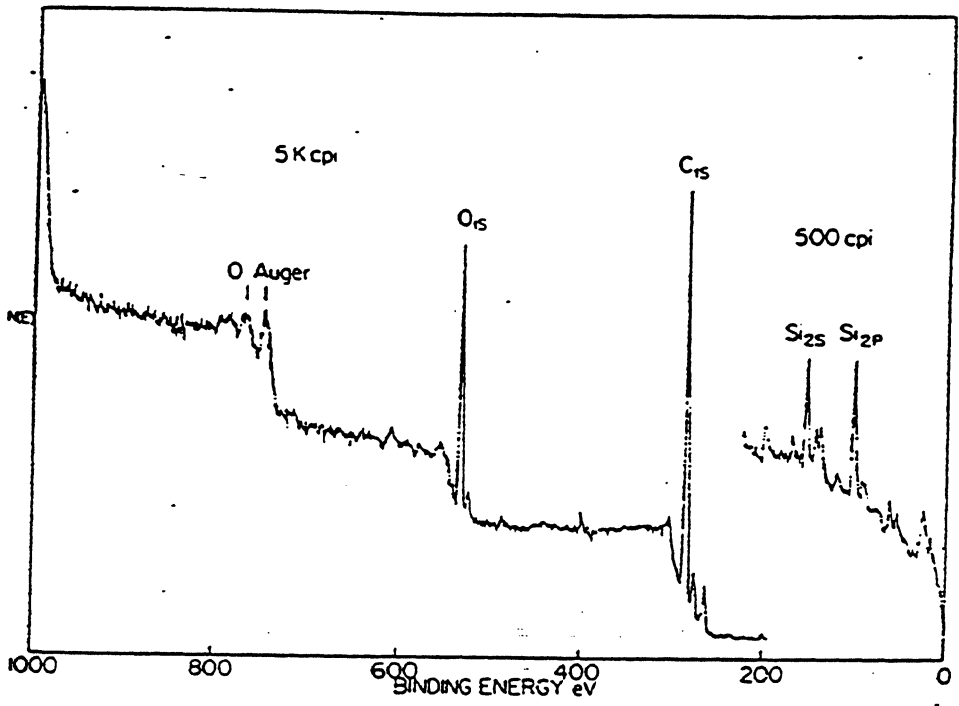


Fig. B.20. XPS spectrum illustrating qualitative elemental identification and their valence states (Czanderna, 1975).

Fig. B.19. Schematic diagram of an X-ray photoelectron spectrometer (Buckley, 1981).



XPS (cont'd)



metal transfer
from the metal
surface to the
polymeric (epoxy)
surface

Figure 6-66. — XPS spectrum of epoxy pin before sliding. Note absence of iron peaks. Silicon peaks indicate that some silicon was transferred from polishing paper to epoxy surface during preparation.

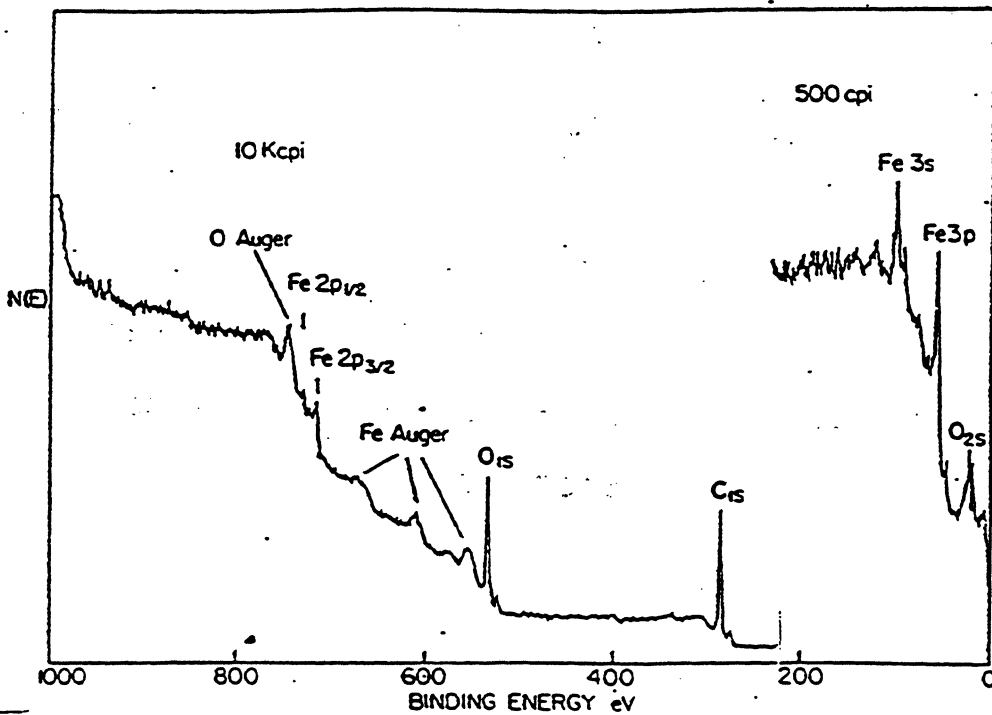


Figure 6-67. — XPS spectrum of epoxy pin after steady-state friction coefficient was

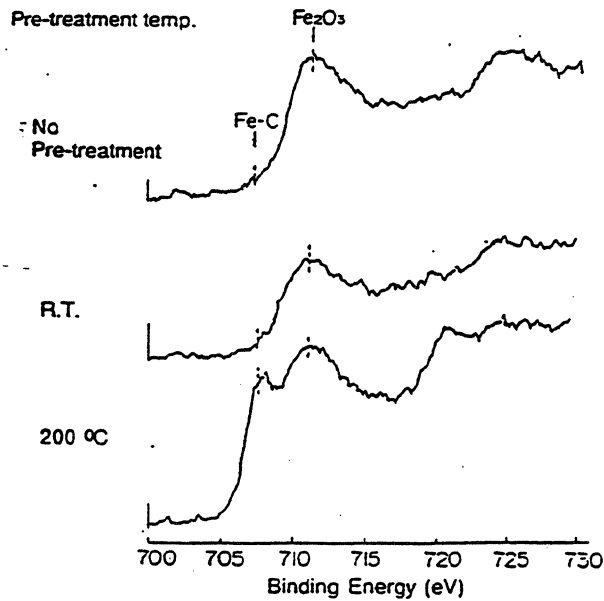


FIG. 8. XPS spectra of Fe_{2p_{3/2}} at the interface of DLC (the CVD processed hard carbon film) and γ -Fe₂O₃ media. The peaks at 707 and 711 eV show Fe-C and γ -Fe₂O₃, respectively. Pretreatment was conducted by hydrogen plasma for 3 min at the temperature shown.

Table 2. Correlation between Fe compound and adhesion strength

Temperature	Gas	Fe compounds	Adhesion strength
RT	No treatment	Fe ₂ O ₃	1.3 ± 0.05
RT	H ₂	Fe ₂ O ₃	1.3 ± 0.05
200°C	H ₂	Fe ₂ O ₃ , Fe-C	>5.0

(from Matsuura et al., *Adv. Info. Storage Syst.*, V2, 69, 1991)

ARXPS (Angle Resolve XPS)

this technique is used to measure distribution of an lubricant on the carbon surface.

Electron intensities as a function of the exit angles

(from ca. 5 to 90 degrees) is measured. This permits to calculate a fraction of the surface area covered by the thin film of the lubricant (escape path).

(from Kimachi, Y., et al., *IEEE Trans., Magn. MAG-23*, 2392, 1987).

Secondary Ion Mass Spectroscopy (SIMS)

Fig. 1 Schematic representation of the principles of SIMS

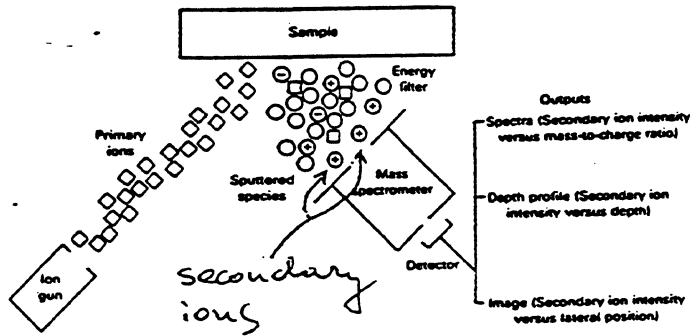
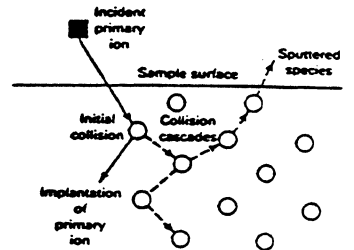


Fig. 2 The physical effects of primary ion bombardment: implantation and sputtering



Primary ions: Ar^+ or O^+ (5-22 KeV)

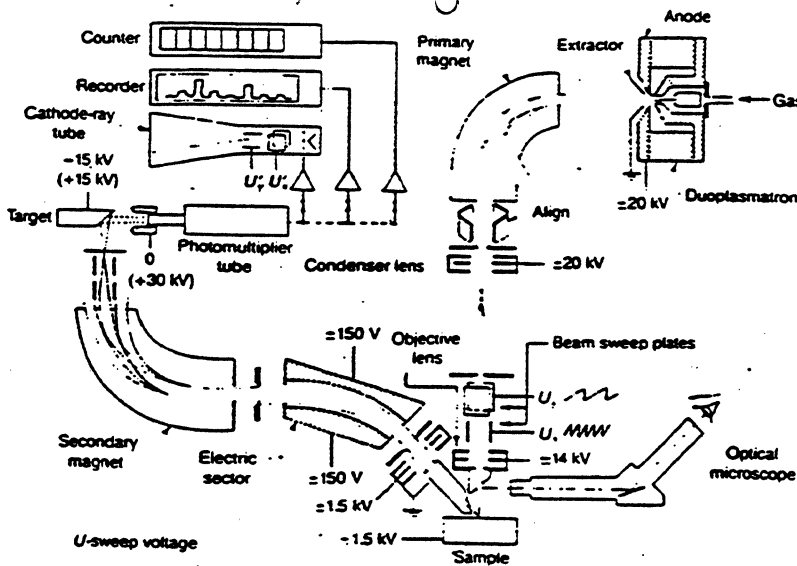
all elements can be detected including isotopes

spacial resolution ca. 1 μm

a fractional portion of the monolayer can be detected and

a sampling depth as small as a few monolayers can be achieved.

can measure porosity too



problem:
charge buildup on
non-conductive solids.

Fig. B.23. Schematic diagram of a SIMS (Willard et al., 1974).

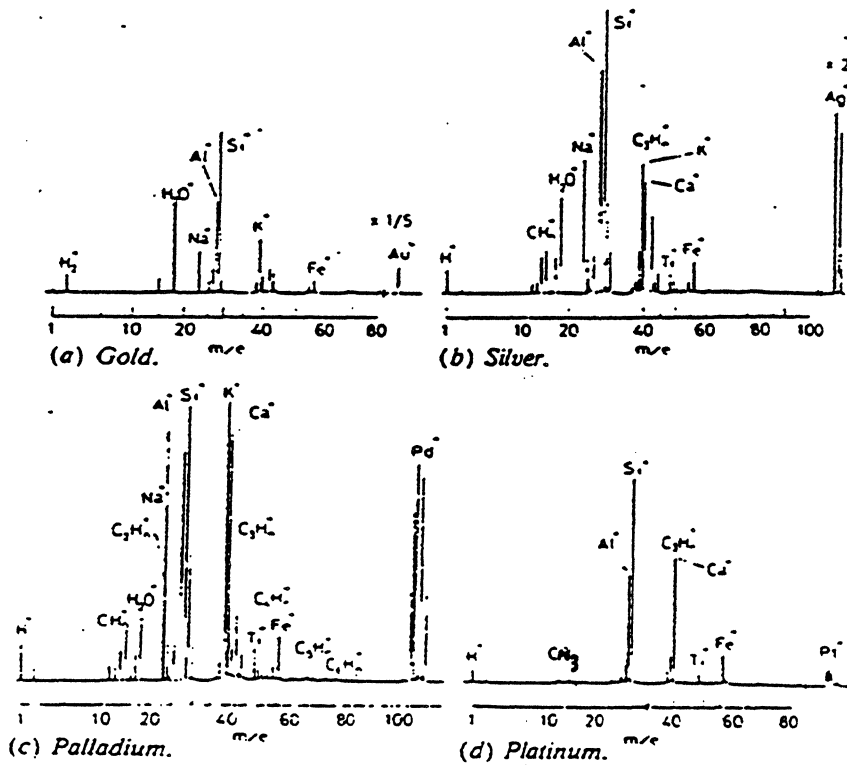
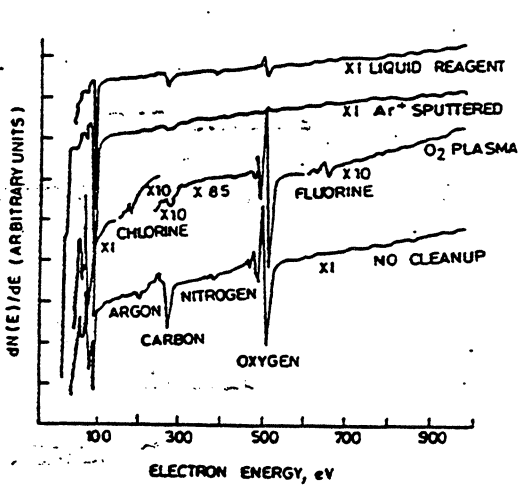


Figure 2-55. — Secondary ion mass spectroscopy (SIMS) spectra of surfaces of SiC abrasive paper used to finish various metals (ref. 52).



(b)

FIGURE 7.3 (a) Typical SIMS and ISS spectra of 1024 Al sheet (i) prior to and (ii) after cleaning procedures. (b) Typical Auger spectra prior to and after several cleaning steps. Liquid reagent cleanup sequence includes deionized water rinse, 10 percent HF acid dip, deionized water rinse, and isopropanol or Freon vapor dry. [Adapted from Yang et al. (1975) and Sparrow (1977).]

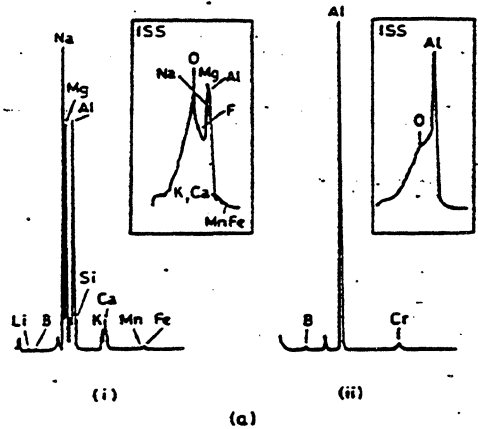
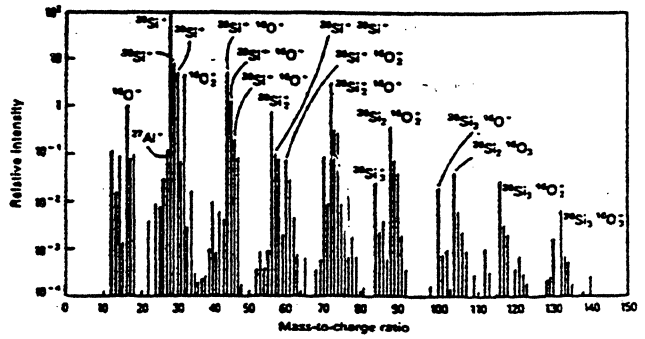


Fig. 6 Positive SIMS spectra (in the form of a bar graph) for high-purity silicon under oxygen bombardment in an ion microscope Source: Ref 10



Mass Spectroscopy (MS)

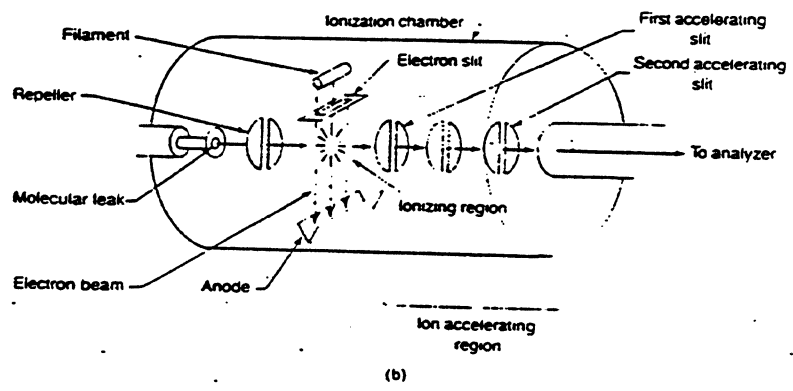
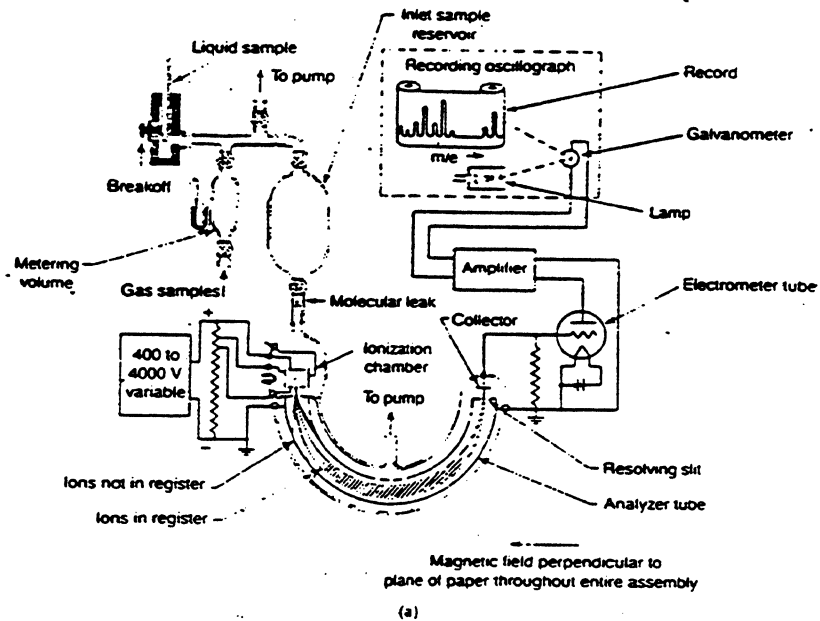


Fig. B.24. (a) Schematic diagram of the Dempster (180°) mass spectrometer and (b) blowup of electron-impact ion source and ion accelerating system (Willard et al., 1974).

$$r = \frac{1}{H} \left(\frac{2Vm}{e} \right)^{1/2}$$

where H is the uniform magnetic field (in G), V - is the mass of ^{accelerating voltage} ions (in g) and e - is the charge (in absolute coulombs)

to obtain the (m/e) spectrum, the accelerating voltage or the magnetic field is varied at a constant rate.

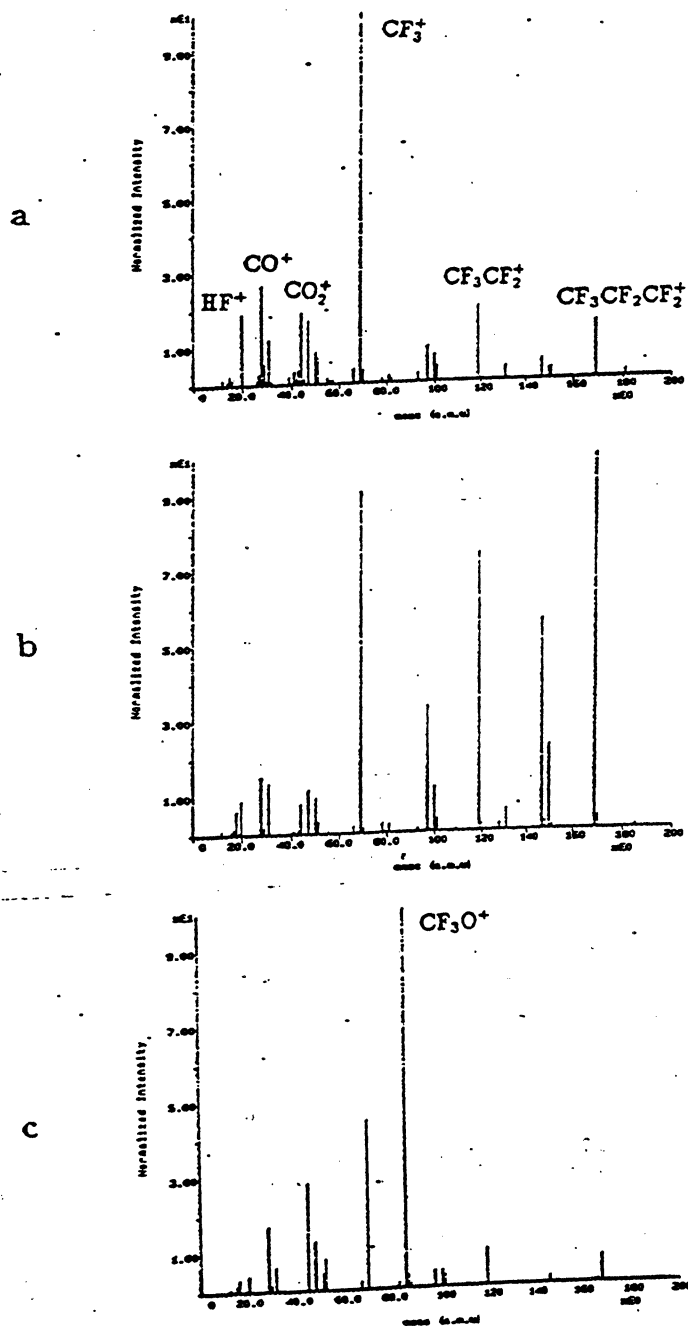


Figure 5. The mass spectrum of the degradation products of Krytox 143 AD after electron bombardment (a), after heating to 450 °C and during wear (c).

from Vurens, G., et al., 'Surface Science Investigations in Tribology', ACS Symp. Series #485, 1992.

Infrared Spectroscopy (IR)

<p>General Uses</p> <ul style="list-style-type: none"> • Identification and structure determination of organic and inorganic materials • Quantitative determination of molecular components in mixtures • Identification of molecular species adsorbed on surfaces • Identification of chromatographic effluents • Determination of molecular orientation • Determination of molecular conformation and stereochemistry <p>Examples of Applications</p> <ul style="list-style-type: none"> • Identification of chemical reaction species; reaction kinetics • Quantitative determination of nontrace components in complex matrices • Determination of molecular orientation in stretched polymer films • Identification of flavor and aroma components • Determination of molecular structure and orientation of thin films deposited on metal substrates (oxidation and corrosion products, soils, adsorbed surfactants, and so on) • Depth profiling of solid samples (granules, powders, fibers, and so on) • Characterization and identification of different phases in solids or liquids <p>Samples</p> <ul style="list-style-type: none"> • Form: Almost any solid, liquid, or gas sample • Size (minimum): Solids—10 ng if it can be ground in a transparent matrix, such as potassium 	<p>bromide; 10-μm diameter for a single particle; 1 to 10 ng if soluble in a volatile solvent (methanol, methylene chloride, chloroform, and so on). Flat metal surfaces—1 by 1 cm (0.4 by 0.4 in.) or larger. Liquids—10 μL if neat, considerably less if soluble in a transparent solvent. Gases—1 to 10 ng</p> <ul style="list-style-type: none"> • Preparation: Minimal or none; may have to grind in a potassium bromide matrix or dissolve in a volatile or infrared-transparent solvent <p>Limitations</p> <ul style="list-style-type: none"> • Little elemental information • Molecule must exhibit a change in dipole moment in one of its vibrational modes upon exposure to infrared radiation • Background solvent or matrix must be relatively transparent in the spectral region of interest <p>Estimated Analysis Time</p> <ul style="list-style-type: none"> • 1 to 10 min per sample <p>Capabilities of Related Techniques</p> <ul style="list-style-type: none"> • Raman spectroscopy: Complementary molecular vibrational information • X-ray fluorescence: Elemental information on bulk samples • X-ray photoelectron spectroscopy: Elemental information on adsorbed species • High-resolution electron energy loss spectroscopy: Molecular vibrational surface information • Mass spectrometry: Molecular weight information • Nuclear magnetic resonance: Additional molecular structure information
--	---

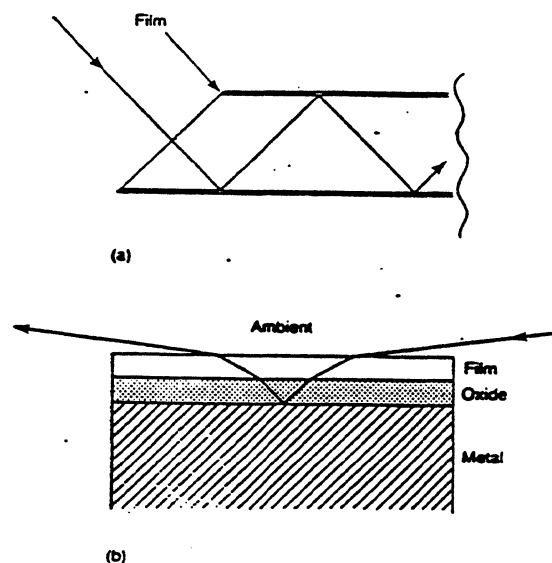


Fig. B.31. Schematic diagram showing the internal reflection and (b) schematic diagram showing the external reflection for an oxide coated metal with an overlayer film.

The spectra range of greatest use covers the frequency range from 200 cm^{-1} to 4000 cm^{-1} (50 to 2.5 μm).

The technique simply involves irradiating the surface with photons

of varying wavelength,

detecting the reflected signal, and looking for the adsorption bands resulting from the interaction of a surface with the IR radiation.

IR (cont'd)

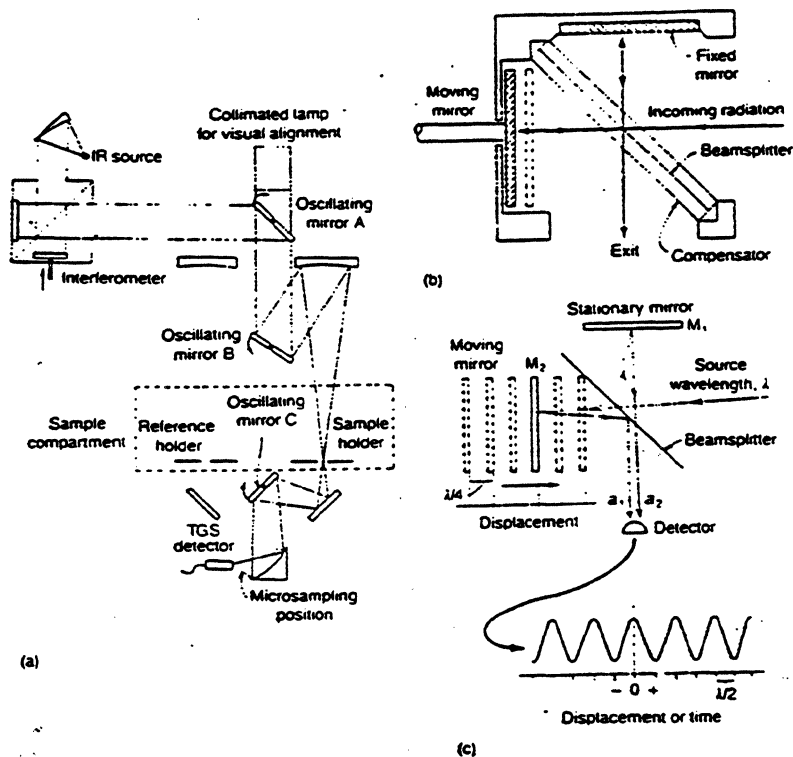


Fig. B.32. (a) Schematic diagram of a Fourier transform infrared spectrometer; (b) simplified diagram of a Michelson interferometer; and (c) mirror movement translated into cosine wave pattern (Willard et al., 1974).

Fourier Transform Infrared Spectroscopy (FTIR) uses an interferometer to modulate the intensity of each wavelength of light at a different audio frequency. Advantages of the FTIR over the dispersive IR spectrometers include a higher S/N ratio (larger no. of scans/ per unit of time) and higher sensitivities.

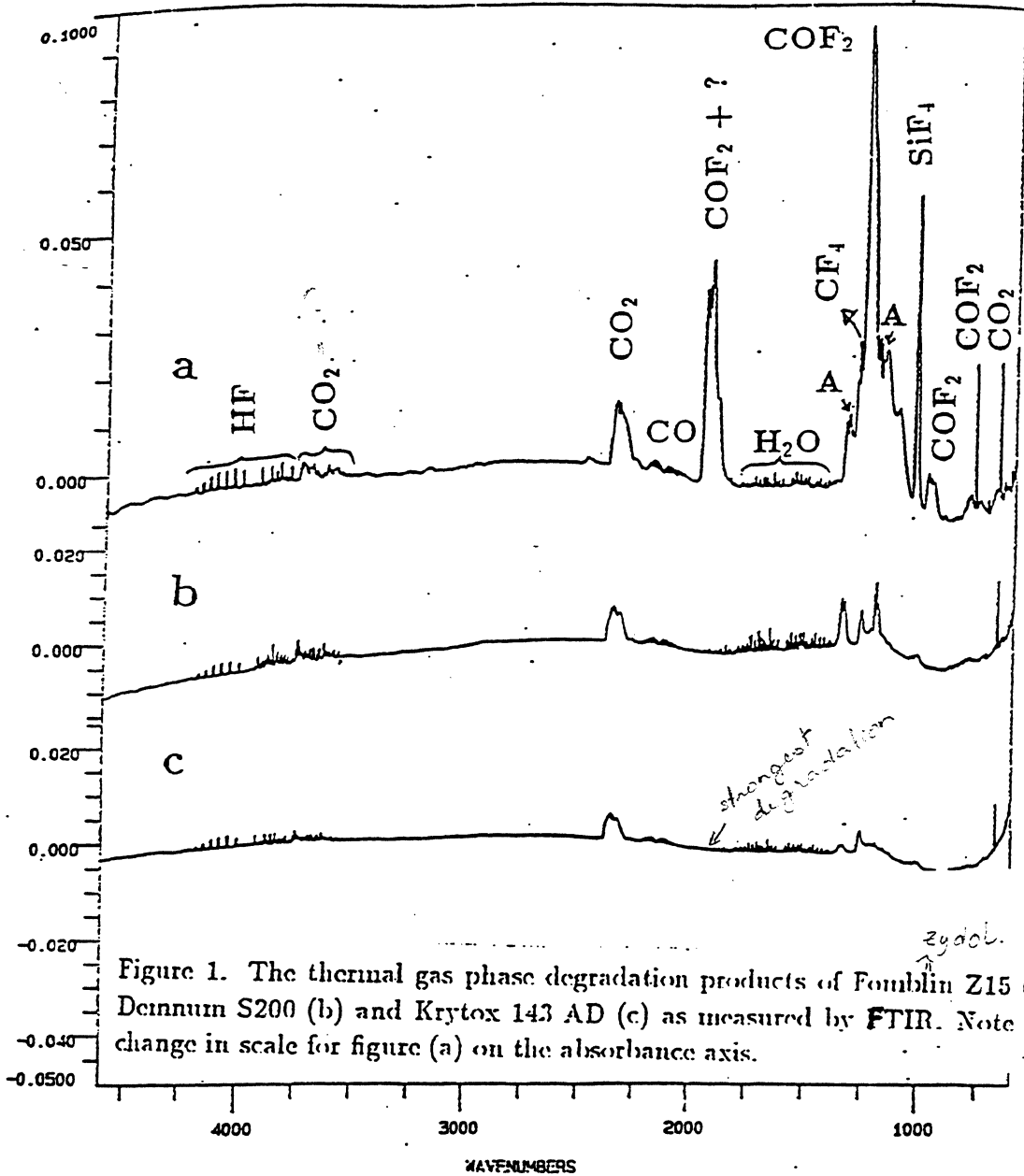


Figure 1. The thermal gas phase degradation products of Fomblin Z15 (a), Demnum S200 (b) and Krytox 143 AD (c) as measured by FTIR. Note the change in scale for figure (a) on the absorbance axis.

from Vurens, G., et al., in "Surface Science Investigations in Tribology", ACS Symp. Series #485, 1992.

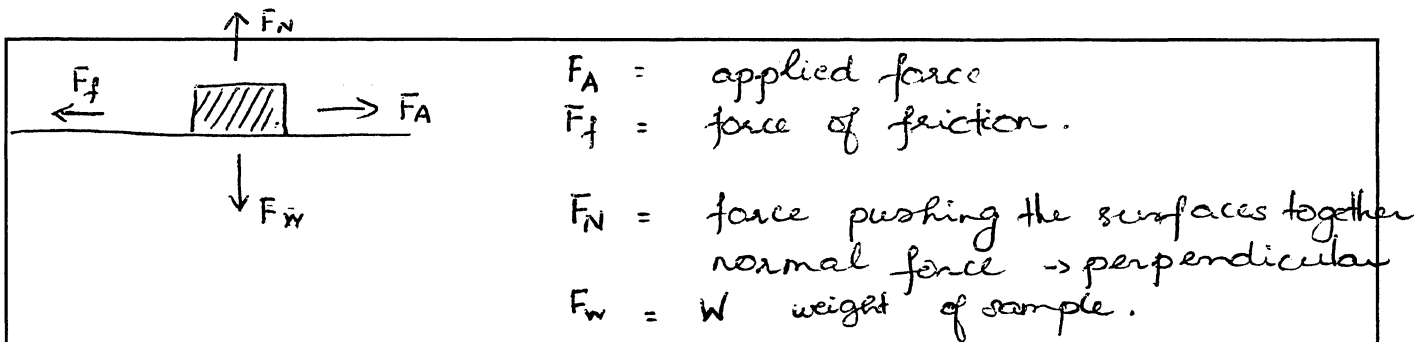
The FTIR technique has been also used for analysis and measurements of the lubricant thickness and also other organics present on the disk surface.

(see Au-Yeung, V., IEEE Trans. Magn. MAG_19, 1662, 1983).

stop at 10/26/94

Quantum™

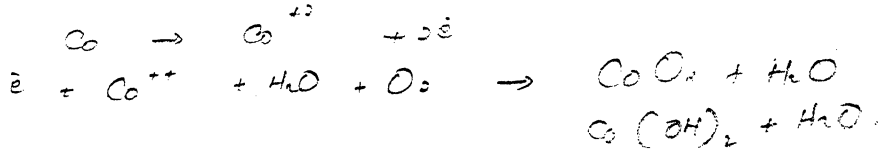
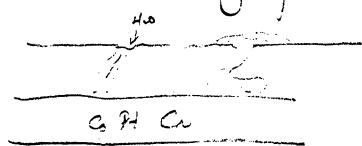
QUANTUM CORPORATION
500 McCarthy Blvd.
Milpitas, CA 95035



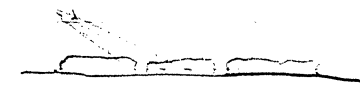
10/26/94.

low M.W. - durability good friction poor - diffuse fast
 high M.W. " poor " good - diffuse slow.
 surface mobility low, they don't move around, they are like monolayers.

interface is failing, because lube is falling apart. or cont. at the gap area.



irradiation



1.2 - rough
 0.2 = smooth - because need to fly very low.

Alumina is a catalyst - degrading the lubricant - falls apart.
 generating free radical - they are very active - reaction with anything from environment
 when lube is degrading - is it degrading the tribology? surfa.
 friction is higher - if lube is degraded.
 create some wear particles \rightarrow low amplitude.
 shorter life time - poor durability, with carbon.
 if no lube - crash -
 if you have wear - vapour - see the wear, \rightarrow H₂O - is there
 can't move because no lube.

* Forces - surface exposure - attractive force, & surface forces * tension

PLANNING

The Importance of Interfaces

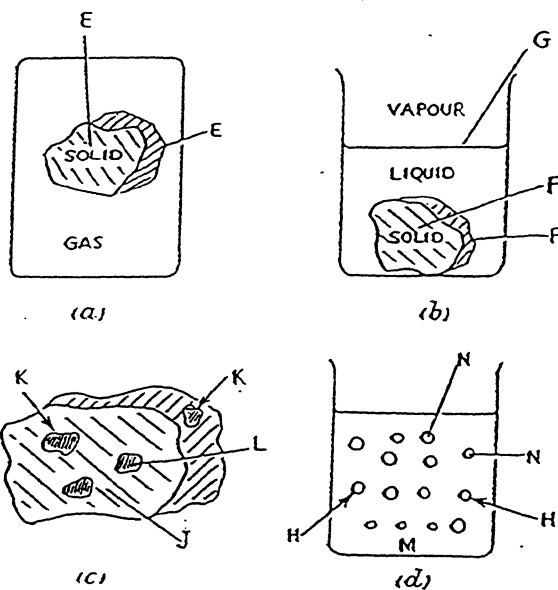
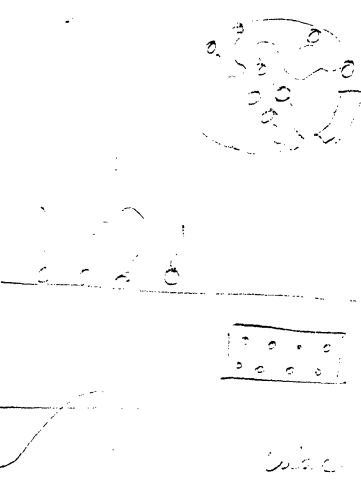


FIG. 1. Diagrammatic representation of different types of interface:

- (a) Solid-gas interface at E, E.
- (b) Solid-liquid interface at F, F and Liquid-vapour interface at G.
- (c) Solid-solid interface at K, K, etc. Lumps of Solid L are embedded in Solid J (e.g., graphite in cast iron).
- (d) Liquid-liquid interface at H, H. Drops of liquid N in liquid M (e.g., oil in water).

If _____ c



wetting take place
it will be very hard

notes - H/C grease

H-C - not compatible with C-F
you will see a tube problem

INTERFACE	PHENOMENA WHOLLY OR PARTLY ARISING THEREFROM, OR WHERE INTERFACE IS SPECIALLY IMPORTANT
SOLID-GAS	Adsorption of gas. Friction. Sublimation. Tensile strength of solid. Dust, smoke (Aerosols). Decomposition of solid to give solid plus gas; chemical reaction of gas with solid. Catalysis.
SOLID-LIQUID	Adsorption of solutes from solution. Electrode processes. Rate of dissolution of solid in liquid. Colloidal sols. Soldering. Wettability; waterproofing. Flotation of minerals. Catalysis.
SOLID-SOLID	Adhesion and cohesion. Friction. Strength of alloys. Reactions between solids.
LIQUID-GAS	Surface tension. Evaporation, distillation. Foams. Mists, fogs.
LIQUID-LIQUID	Emulsions.

notes from H/C can be on the disk.

c surface tension is higher than liquid

G-L. Thumb = solid

liquid.

The forces of nature

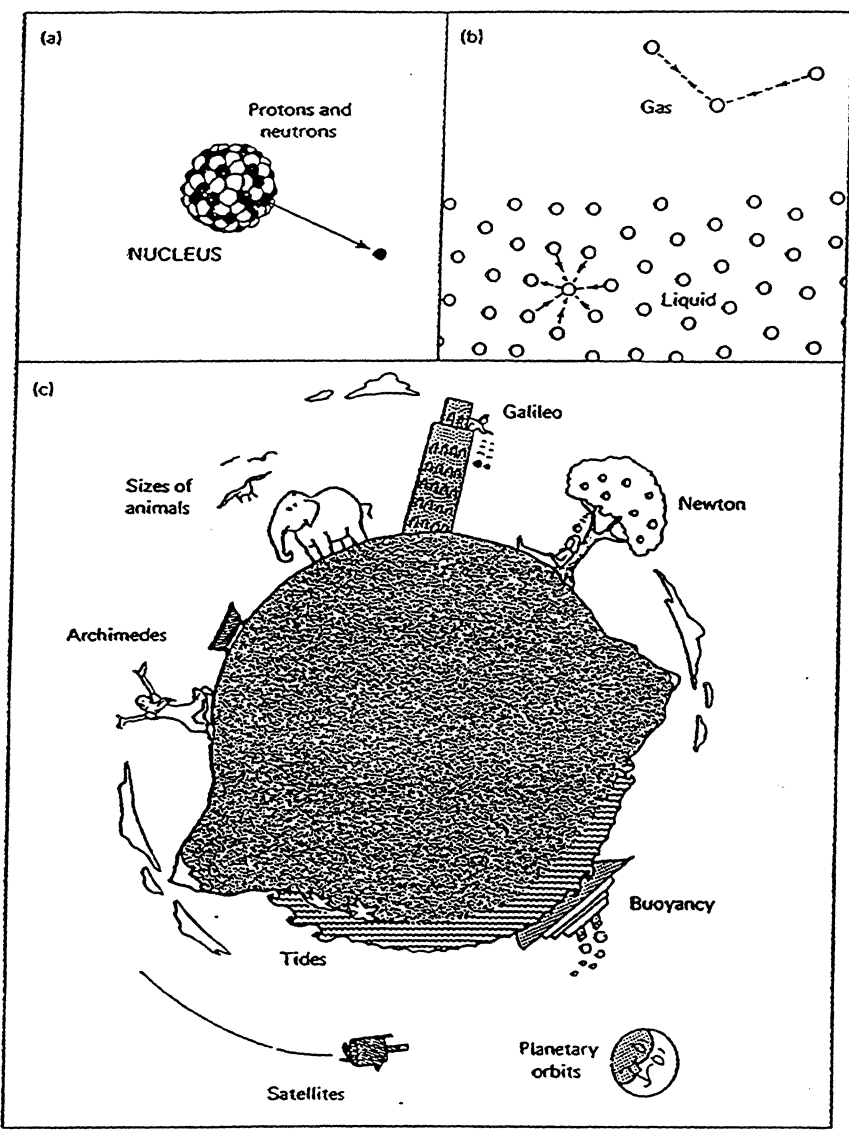


Fig. 1 The forces of nature.
 (a) Strong nuclear interactions hold protons and neutrons together in atomic nuclei. Weak interactions are involved in electron emission (β decay).
 (b) Electrostatic (intermolecular) forces determine the cohesive forces that hold molecules together in solids and liquids.
 (c) Gravitational forces affect tides, falling bodies, and satellites. Gravitational and intermolecular forces acting together determine the maximum possible sizes of mountains, trees, and animals.

from:
 J.N. Israelachvili,

"Intermolecular and Surface Forces", Academic Press, 1985

from J.N. Israelachvili (JNI)

Forces between Molecules

Dutch physicist J.D. van der Waals (1873) included correction terms in the ideal gas law ($PV = nRT$) to account for the effects of attractive forces between molecules

$$(P + a/v^2)(V - b) = nRT$$

in 1903, Mie proposed an interaction potential of the following form

$$V(r) = A/r^n - B/r^m$$

the repulsive term is poorly understood and $n=9$ or $n=12$ works satisfactory in most cases.

For the attractive term, $m=1$ which corresponds to the interaction of two ions (Coulomb's energy).

$m=2$ & $m=3$, correspond to ion-permanent dipole and permanent dipole-permanent dipole interaction.

$m=4$, describes ion induced dipole interaction, and $m=6$, corresponds to dipole-induced dipole and London dispersion forces (see Fig.4 on the next page).

The best known form of the Mie's equation is that known as the Lennard-Jones potential for the interaction between a pair of non-dipolar molecules, such as a pair of inert gas atoms:

$$V(r) = A/r^{12} - B/r^6$$

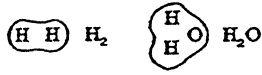
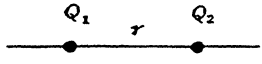
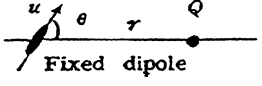
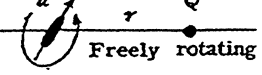
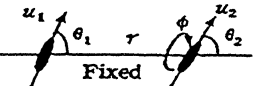
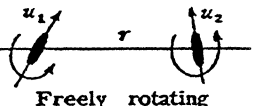
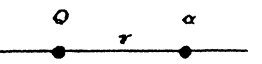
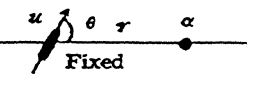
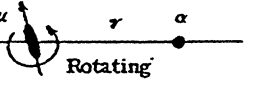
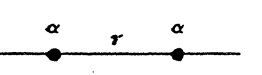
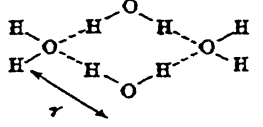
Type of interaction	Interaction energy $w(r)$
Covalent 	Complicated, short range
Charge-charge 	$Q_1 Q_2 / 4\pi\epsilon_0 r$ (Coulomb energy)
Charge-dipole 	$-Qu \cos \theta / 4\pi\epsilon_0 r^2$
	$-Q^2 u^2 / 6(4\pi\epsilon_0)^2 k T r^4$
Dipole-dipole 	$-u_1 u_2 [2 \cos \theta_1 \cos \theta_2 - \sin \theta_1 \sin \theta_2 \cos \phi] / 4\pi\epsilon_0 r^3$
	$-u_1^2 u_2^2 / 3(4\pi\epsilon_0)^2 k T r^6$ (Keesom energy)
Charge-nonpolar 	$-Q^2 \alpha / 2(4\pi\epsilon_0)^2 r^4$
Dipole-nonpolar 	$-u^2 \alpha (1 + 3 \cos^2 \theta) / 2(4\pi\epsilon_0)^2 r^6$
	$-u^2 \alpha / (4\pi\epsilon_0)^2 r^6$ (Debye energy)
Two nonpolar molecules 	$-\left(\frac{3}{4}\right) \frac{h\nu^2}{(4\pi\epsilon_0)^2 r^6}$ (London dispersion energy)
Hydrogen bond 	Complicated, short range, energy roughly proportional to $-1/r^2$

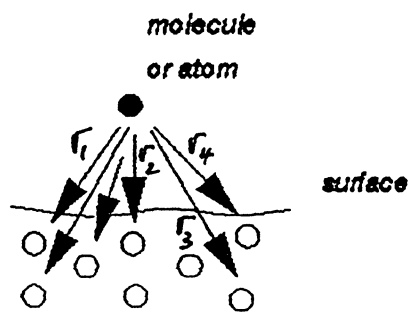
Fig. 4 Common types of interactions between atoms, ions, and molecules in vacuum. $w(r)$ is the interaction free energy (in J); Q , electric charge (C); u , electric dipole moment (C m); α , electric polarizability ($C^2 m^2 J^{-1}$); r , distance between interacting atoms or molecules (m); k , Boltzmann constant ($1.38 \times 10^{-23} J K^{-1}$); T , absolute temperature (K); h , Planck's constant ($6.626 \times 10^{-34} J s$); ν , electronic absorption (ionization) frequency (s^{-1}); ϵ_0 , permittivity of free space ($8.854 \times 10^{-12} C^2 J^{-1} m^{-1}$). The force is obtained by differentiating the energy $w(r)$ with respect to distance r .

from JN1's book

Complications

- a) the L-J potential refers to the interactions of two ions atoms or molecules and the interaction of macroscopic bodies is the result of the summation of all the interactions
- b) the London forces exhibit phenomenon of retardation which is due to coupling of the electromagnetic frequency of the instantaneous dipoles with those induced in neighboring atoms. The transition to fully retarded regime occurs over a range of 30 to 50 nm and the value of m increases to 7.

Attractive Forces at Interfaces



$$W = \sum W_i$$

where $W_i = -B/r^6$
(pair potential)

London replaced sum by

integral

$$W = - \int B r^{-6} N dv \text{ (energy)}$$

where N is the no. of atoms in unit volume at a distance r from the atom. If N is a constant

The net interaction

energy \rightarrow

$$W = -N \pi B / 6 r^3 \left. \begin{array}{l} \text{Force, } F \\ F = \partial W / \partial r = \\ -N \pi B / 2 r^4 \end{array} \right\}$$

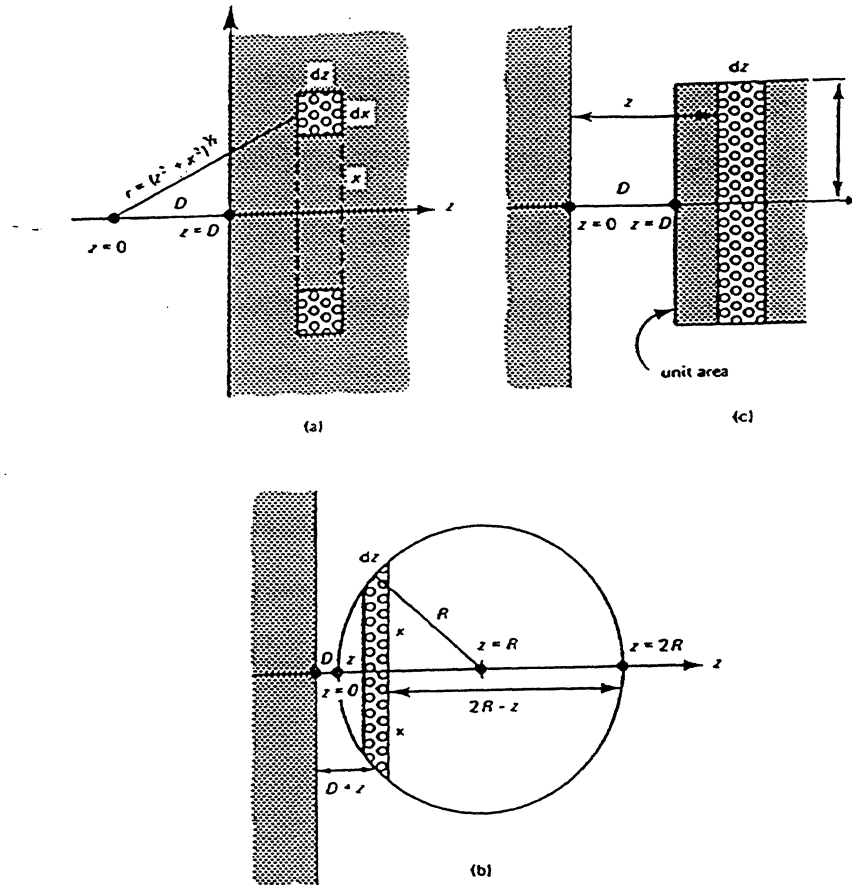


Fig. 25 Methods of summing (integrating) the interaction energies of molecules in different phases to obtain the interaction energies between macroscopic bodies.
 (a) Molecule near a wall.
 (b) A spherical particle near a wall ($R \gg D$).
 (c) Two planar surfaces ($l \gg D$).

to calculate the interaction energy of two planar surfaces separated by a distance in vacuum, a further integration is required over the depth of the second surface which leads to

$$W(D) = -\frac{A}{12\pi D^2}$$

where A is the Hamaker constant ($\sim N$) and N is the number density of atoms.

DERJAGUIN'S APPROXIMATION*

It relates the force law $F(D)$ between two curved surfaces to the interaction energy $W(D)$ of two planar surfaces.

Sphere/plane

$$F(D)_{\text{Sphere}} = 2\pi R W(D)_{\text{plane}}$$

Sphere/sphere

$$R = R_1 = R_2$$

$$F(D) = 2\pi \sqrt{\frac{R_1 R_2}{R_1 + R_2}} W(D)_{\text{plane}}$$

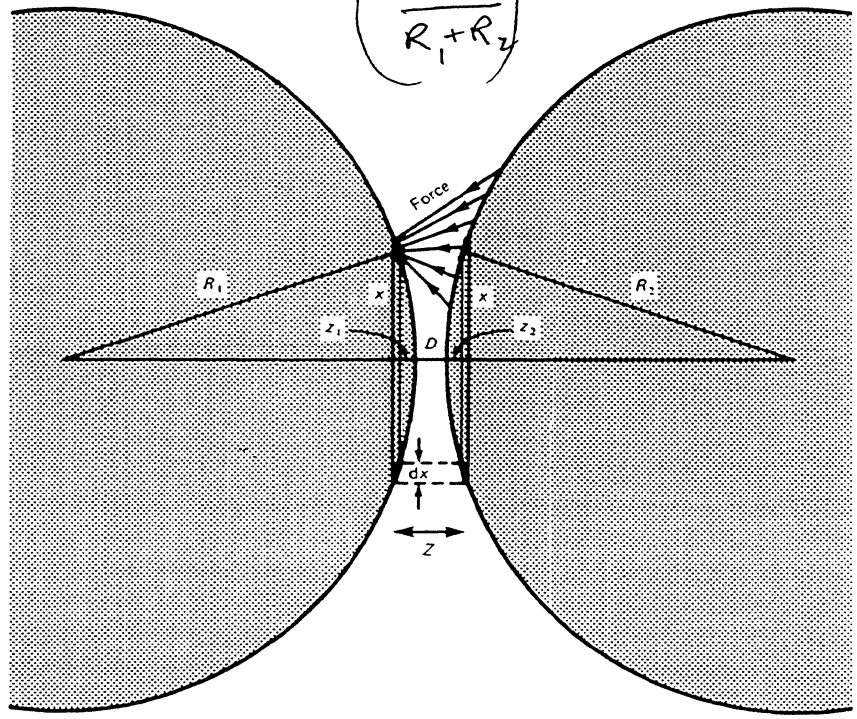


Fig. 26 The Derjaguin approximation (Derjaguin, 1934), which relates the force law $F(D)$ between two spheres to the energy $W(D)$ per unit area of two flat surfaces by $F(D) = 2\pi[R_1 R_2 / (R_1 + R_2)]W(D)$.

* Derjaguin, B.V., Kolloid Zeit. 69, 155 (1934)

EXPERIMENTAL MEASUREMENTS OF INTERMOLECULAR AND SURFACE FORCES.

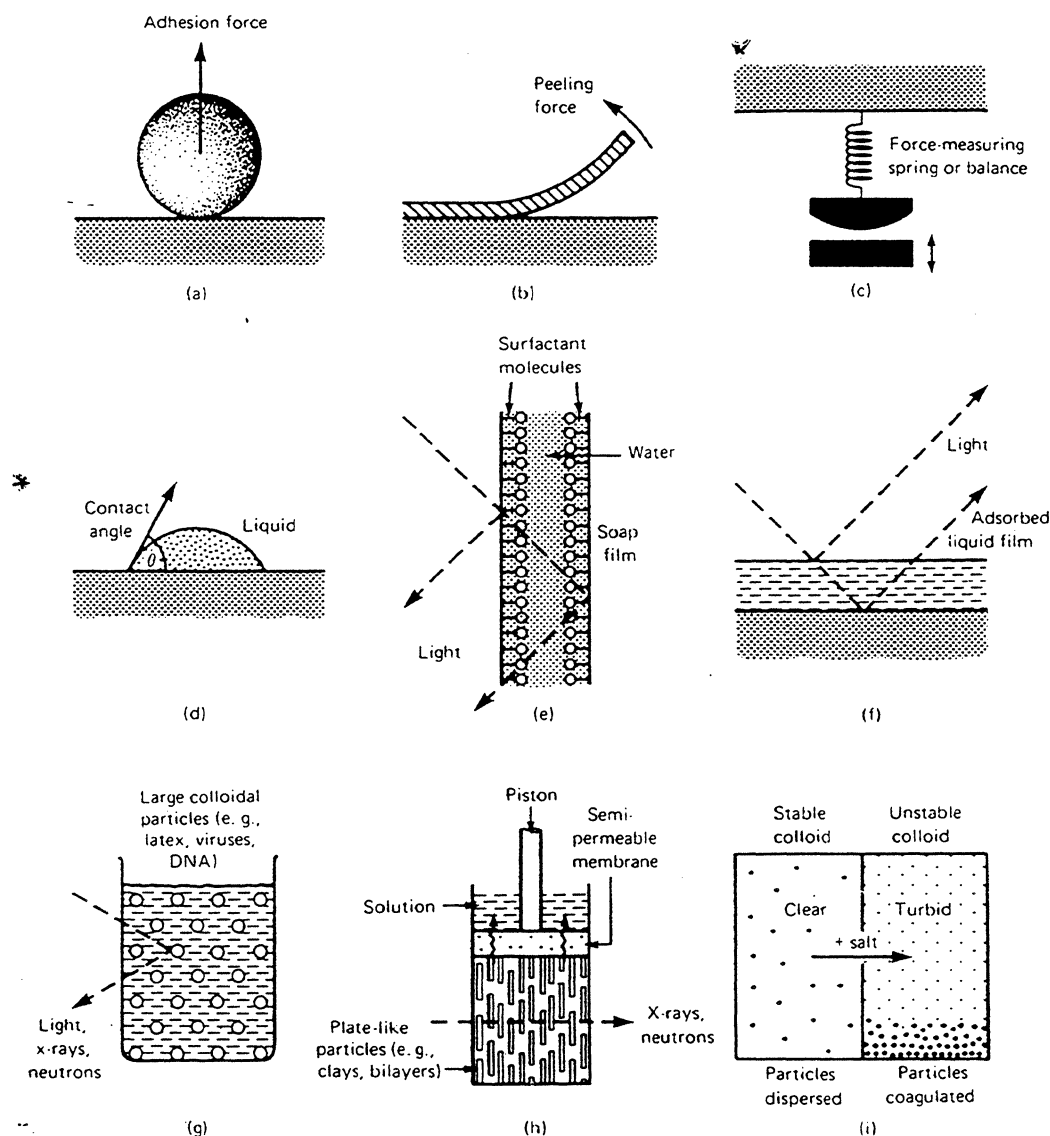


Fig. 28 Different types of measurements that provide information on the forces between particles and surfaces.

(a) Adhesion measurements (practical applications: xerography, aerosols, crop dusting, particle adhesion).

(b) Peeling measurements (practical applications: adhesive tapes, crack propagation).

(c) Direct measurements of force as a function of distance D (practical applications: testing theories of intermolecular forces).

(d) Contact angle measurements (practical applications: detergency, mineral separation processes using froth flotation, nonstick pans, waterproofed fibres).

(e) Equilibrium thicknesses of thin free films (practical applications: soap films, foams).

(f) Equilibrium thickness of thin adsorbed films (practical applications: wetting of hydrophilic surfaces by water, adsorption of molecules from vapour, drainage of liquid layers).

(g) Interparticle spacing in liquids (practical applications: colloidal suspensions, paints, ink, pharmaceutical dispersions).

(h) Sheet-like particle spacings in liquids (practical applications: clay and soil swelling behaviour, microstructure of soaps, biological membrane interactions).

(i) Coagulation studies (practical application: basic experimental technique for testing the stability of colloidal preparations).

Interaction Energy between Bodies of Different Geometries

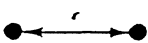

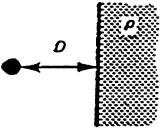
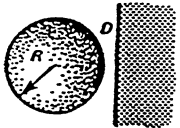
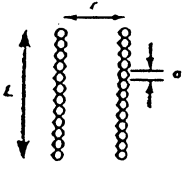
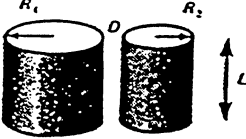
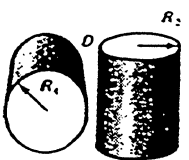
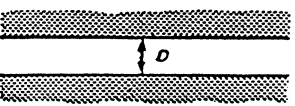
<p>Two atoms</p>  $w = -Cr^6$	<p>Two spheres</p>  $W = \frac{-A}{6D} \frac{R_1 R_2}{(R_1 + R_2)}$
<p>Atom-surface</p>  $w = -\pi C \rho / 6D^3$	<p>Sphere-surface</p>  $W = -AR/6D$
<p>Two parallel chain molecules</p>  $W = -3\pi CL/8a^2 r^2$	<p>Two cylinders</p>  $W = -\frac{AL}{12\sqrt{2}D^{3/2}} \left(\frac{R_1 R_2}{R_1 + R_2} \right)^{3/2}$
<p>Two crossed cylinders</p>  $W = -A\sqrt{R_1 R_2}/6D$	<p>Two surfaces</p>  $W = -A/12\pi D^2 \text{ per unit area}$

Fig. 29 Nonretarded van der Waals interaction free energies between bodies of different geometries calculated on the basis of pairwise additivity. The Hamaker constant A is defined by $A = \pi^2 C \rho_1 \rho_2$, where ρ_1 and ρ_2 are the number of atoms per unit volume in the two bodies and C is the coefficient in the atom-atom pair potential (top left). A more rigorous method of calculating the Hamaker constant in terms of the macroscopic properties of the media is given in Section 11.3. The forces are obtained by differentiating the energies with respect to distance.

A_{12} for various substances immersed in water at 20°C (taken from reference [11])

	$d\gamma^2/\text{mJ m}^{-2}$	A_{12}/J
Polyhexafluoropropylene	18	2×10^{-22}
Paraffin wax	25.5	2×10^{-22}
Polyethylene	35	2×10^{-21}
Polystyrene	44	5×10^{-21}
Copper	60	1.4×10^{-20}
Silver	76	2.5×10^{-20}
Anatase (TiO ₂)	91	3.5×10^{-20}
Iron	98	4×10^{-20}
Iron (III) oxide	107	4.5×10^{-20}
Graphite	110	5×10^{-20}
Tin (IV) oxide	118	5.5×10^{-20}
Silica	123	6×10^{-20}
Rutile (TiO ₂)	143	8×10^{-20}
Mercury	200	1.3×10^{-19}

Strength of van der Waals interactions (air or vacuum)

for two planar surfaces $W = -A/12\pi D^2$

and the adhesion force: $F/\text{unit area} = \partial W / \partial D$

or pressure:

$$\Delta P = A/6\pi D^3 \approx 7 \times 10^8 \text{ N/m}^2$$

$$\approx 7,000 \text{ atm (kg/cm}^2)$$

we used H (Hamaker constant) equal to $1 \times 10^{-19} \text{ J}$ and

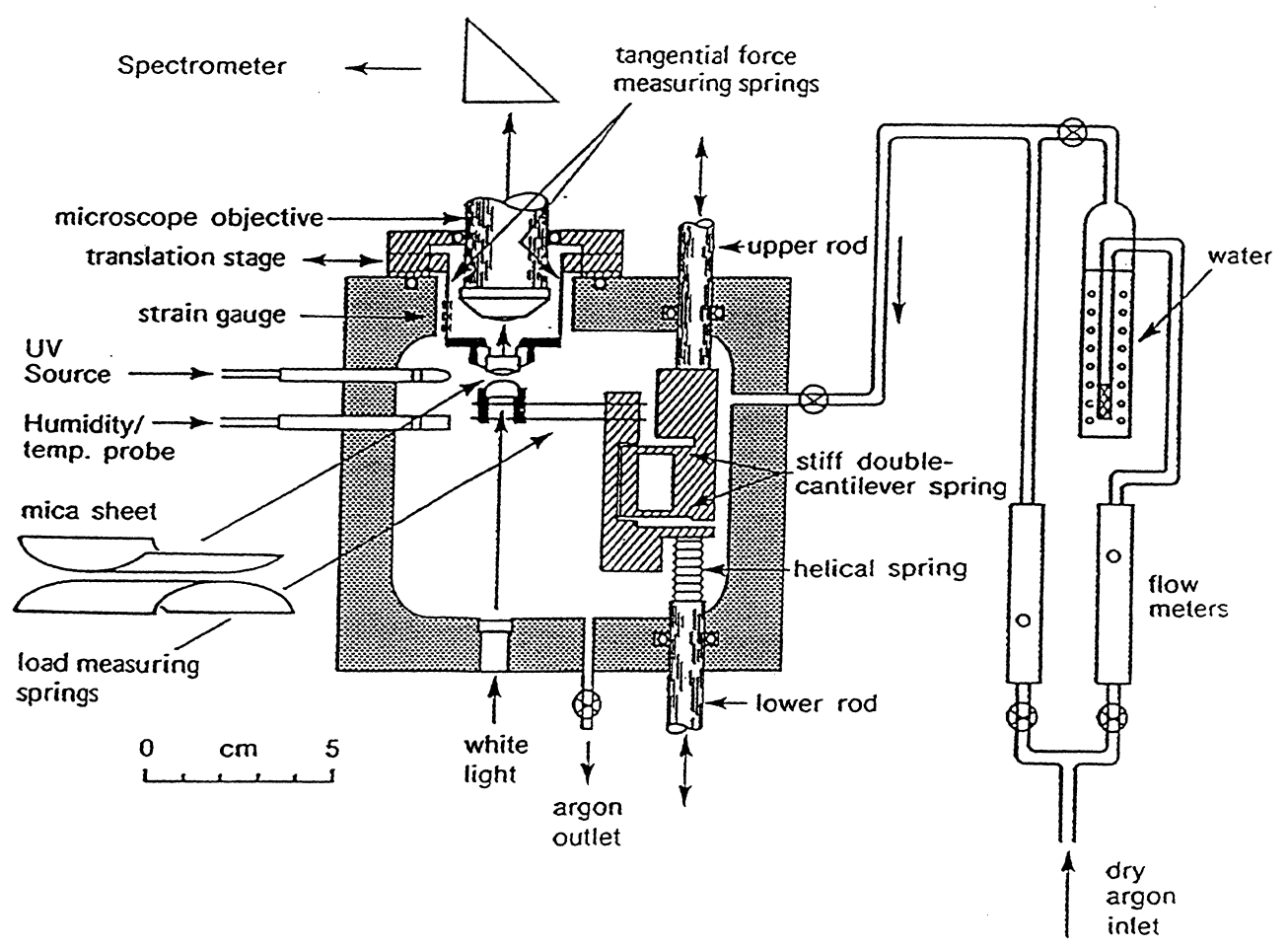
$D = 0.2 \text{ nm}$. (average radius of atom)

thus, for $D = 10 \text{ nm}$

$$\Delta P = 5.3 \times 10^3 \text{ N/m}^2 \approx 0.05 \text{ atm}$$

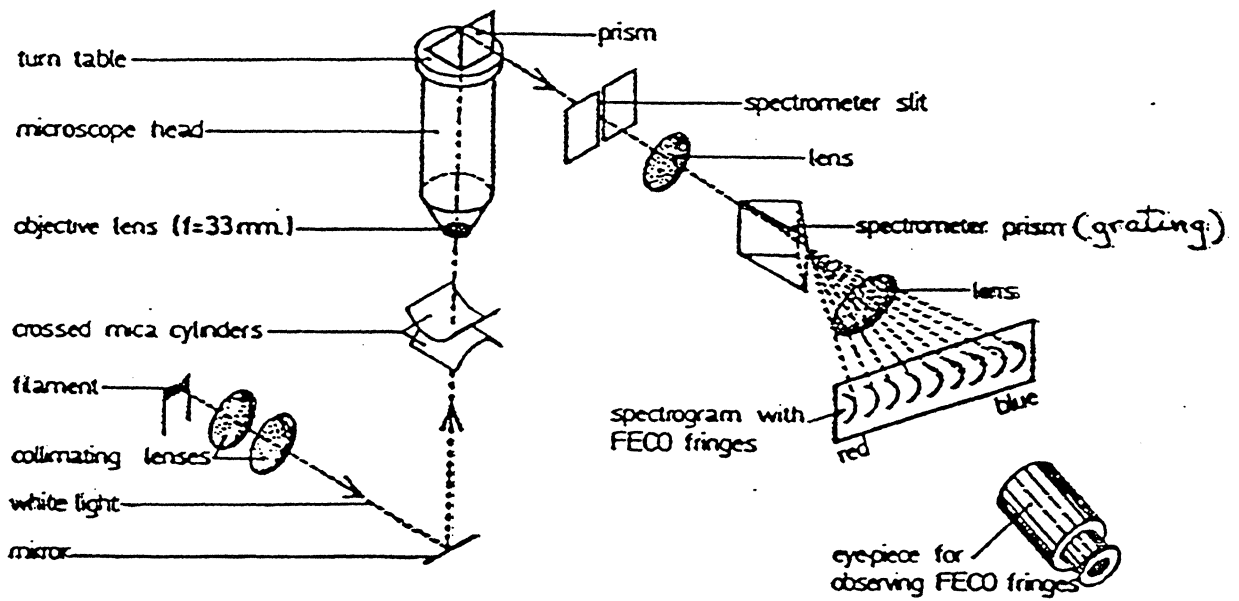
$$\text{or } \approx 50 \text{ g/cm}^2 \rightarrow$$

still significant number



Schematics of Surface Force Apparatus

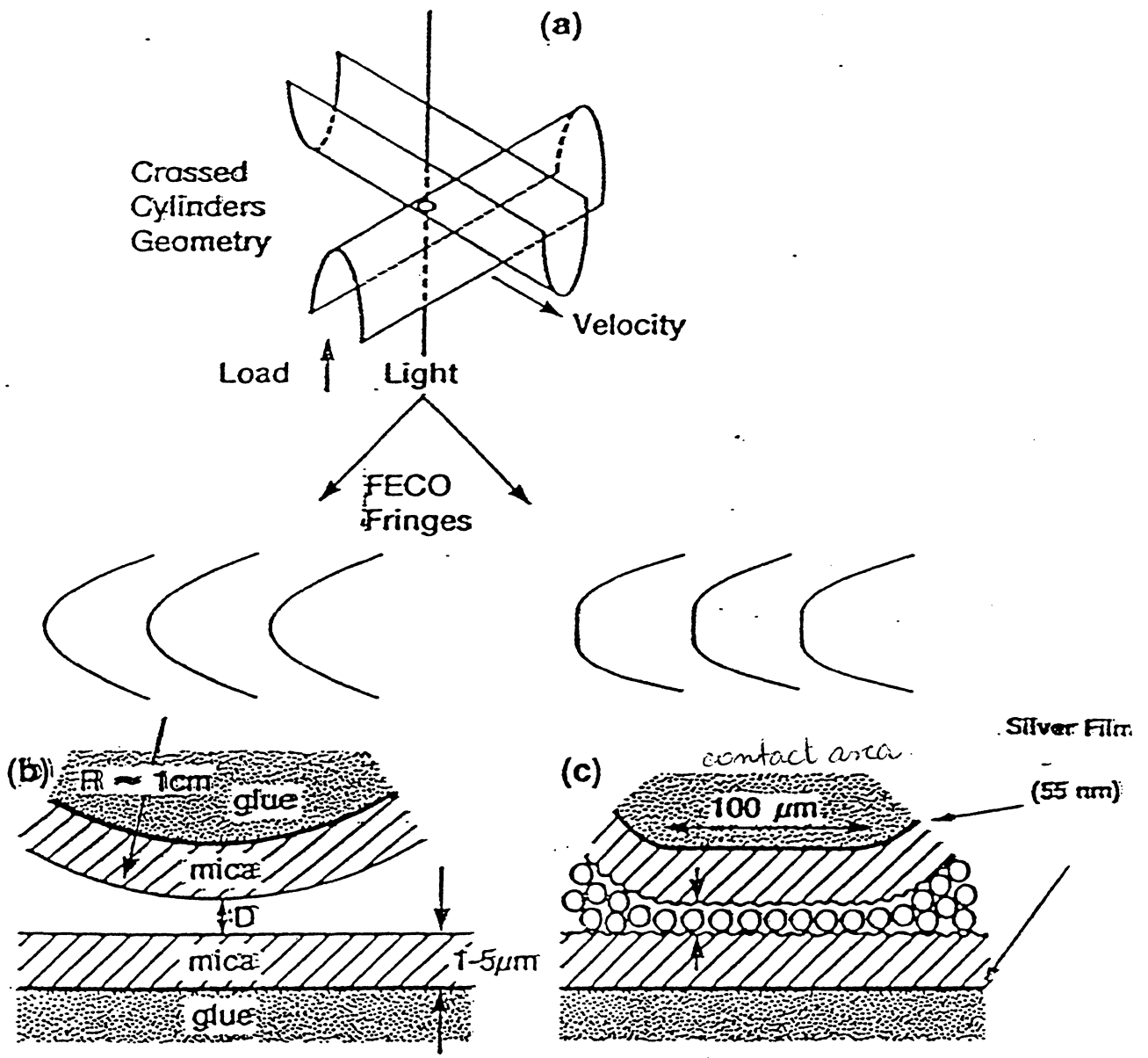
See: Israelchvili, J.N., and Adams, G.E., J. Chem. Soc. Faraday Trans. 174, 975 (1978)
 can measure with an accuracy of 1-2 Å



Optical system.

Journal of Colloid and Interface Science, Vol. 44, No. 2, August 1973

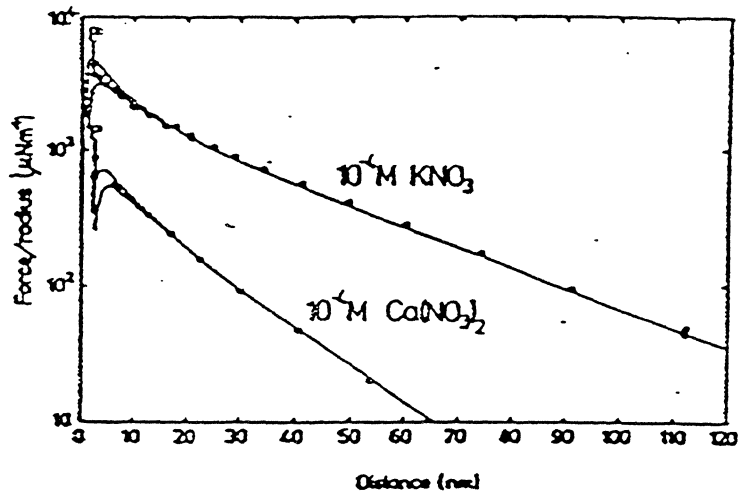
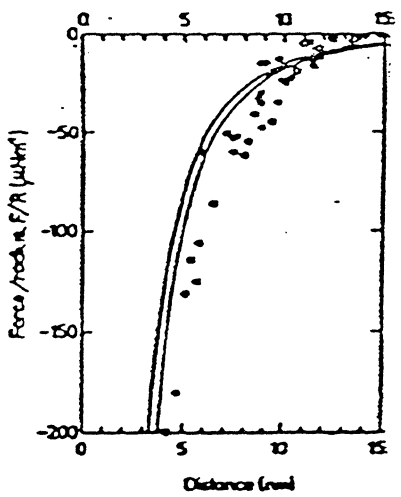
Optical System for SFA



$$F = \gamma A$$

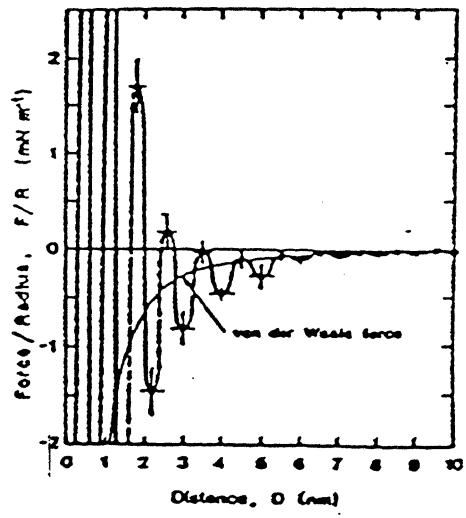
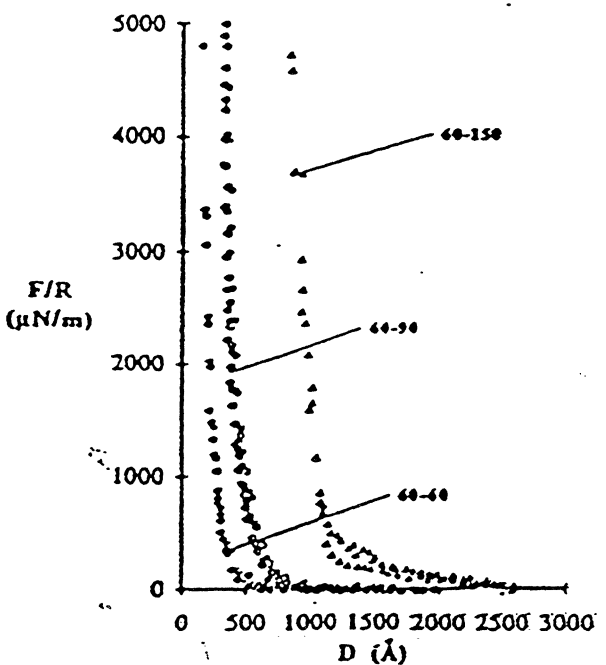
Concept of SFA

EXAMPLES OF SURFACE FORCES



VAN DER WAALS FORCES

ELECTROSTATIC FORCES



STERIC OR ENTROPIC FORCES

STERIC OR ENTROPIC FORCES

STRUCTURAL FORCES

Structural Forces

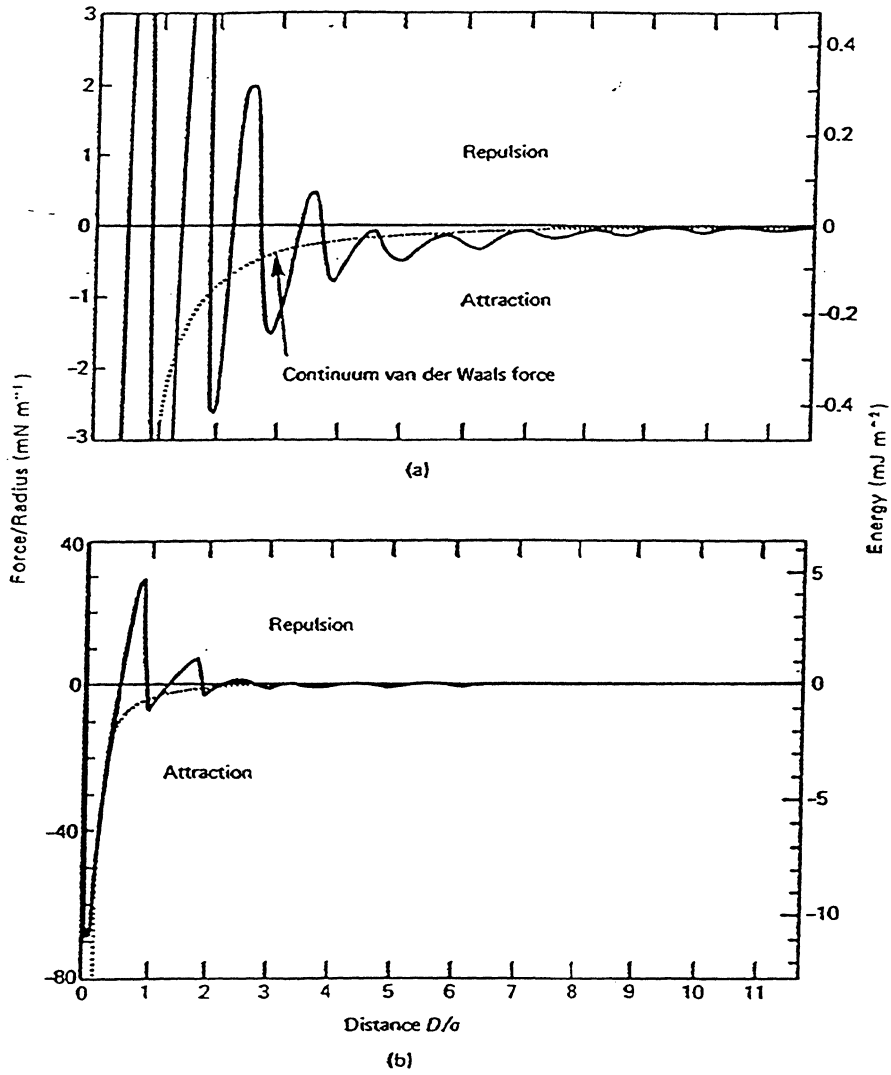
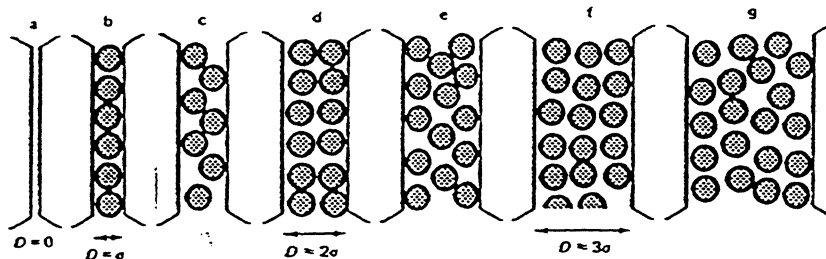


Fig. 52 (a) Measured force F between two curved mica surfaces of radius R (≈ 1 cm) in OMCTS ($\sigma \approx 0.9$ nm) at 22°C . For comparison, the theoretical continuum van der Waals force is also shown.

(b) The full force law plotted on a reduced scale. The right hand ordinate gives the corresponding interaction energy per unit area of two flat surfaces according to the Derjaguin approximation: $W = F/2\pi R$. (From Horn and Israelachvili, 1981.)

This doesn't work with lube and polymer



Attractive vdw Forces

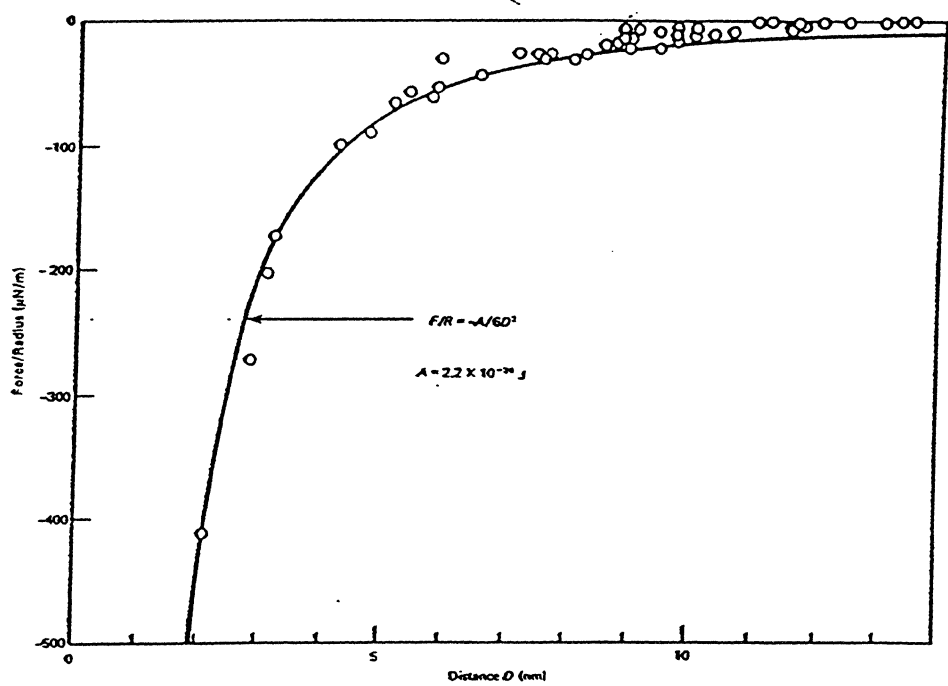
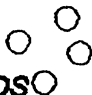

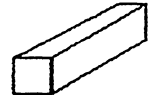


Fig. 34 Attractive van der Waals force F between two curved mica surfaces of radius $R \approx 1 \text{ cm}$ measured in water and aqueous electrolyte solutions. The measured nonretarded Hamaker constant is $A = 22 \times 10^{-20} \text{ J}$. Retardation effects are apparent at distances above 5 nm. [From Israelachvili and Adams (1978) and Israelachvili and Pashley (unpublished).]

Concept of Surface Tension

why rain drops  are not cubes , rods 

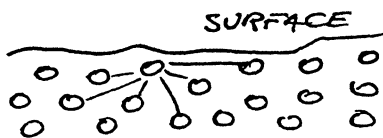
or rectangulars? 

Nature tends to minimize its energy and it is doing so by reducing the ratio of surface to volume.

Condensation of water into droplets results in an energy change associated with the formation of a liquid surface.

This energy increase is termed the surface free energy or the excess surface free energy.

The energy units are in Joules (J) per m^2 .



“surface in a state of lateral tension or surface tension”

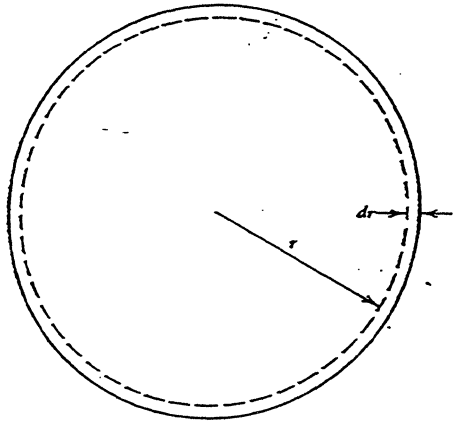
the surface tension unit is mN/m and the symbol is γ .

Customary units are also: $ergs/cm^2$ or $dynes/cm$.

thermodynamically
$$\gamma = \frac{dW}{dA}$$

the surface tension γ is the reversible work, W , required to create a unit area of the surface, A , at constant volume, temperature and chemical potential.

Equation of Young and Laplace



soap bubble

total surface free energy is $4\pi r^2 \gamma$ but on shrinking

r decreases by dr

$$4\pi (r-dr)^2 \gamma = 4\pi r^2 \gamma - 8\pi r dr \gamma + 4\pi dr^2 \gamma$$

($8\pi r dr \gamma$) decreases in surface energy ↓

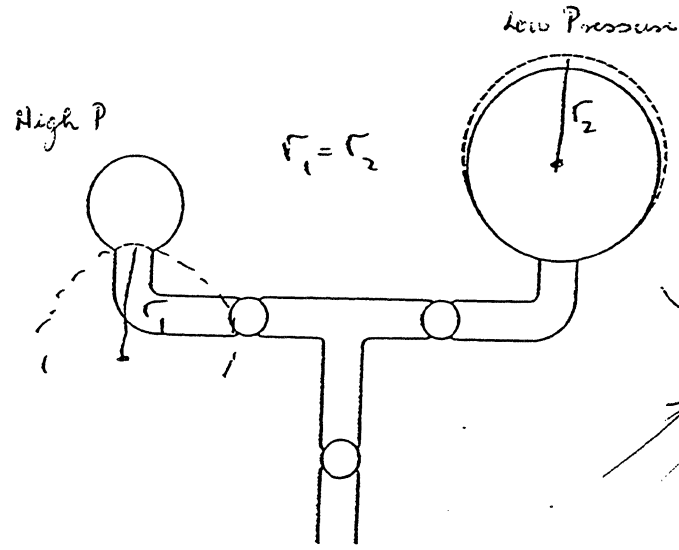
must be balanced by a pressure difference across the film ΔP such that the work against this pressure difference $\Delta P 4\pi r^2 dr$ is equal to the decrease in surface free energy.

$$\Delta P 4\pi r^2 dr = 8\pi r \gamma dr$$

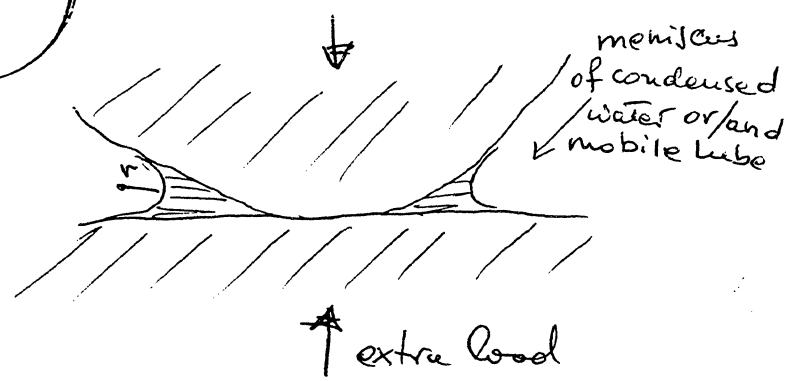
OR

$$\Delta P = 2\gamma / r$$

↑ surface tension



pressure is equilibrated when $r_1 = r_2$



↑ extra load

$$\Delta P = 2\gamma / r$$

depend very much on texture

Fig. II-3. Illustration of the equation of Young and Laplace.

for an elliptical surface

$$\Delta P = \gamma \left(\frac{1}{r_1} + \frac{1}{r_2} \right)$$

Kelvin's Equation

Liquids that wet or have a small contact angle on surfaces will condense from vapor into cracks and pores. At equilibrium the meniscus curvature r is related to the relative vapor pressure p/p_0 by the Kelvin's equation

$$\frac{1}{r} = r_k = \frac{\gamma V}{RT \ln(P/P_0)}$$

where V is the molar volume

$$\Delta G = \int V dP$$

since $\Delta P = 2\gamma/r$

$$\Delta G = 2\gamma V/r$$

but $G = G_0 + RT \ln P$

$$\Delta G = RT \ln(P/P_0)$$

water keep condensing.

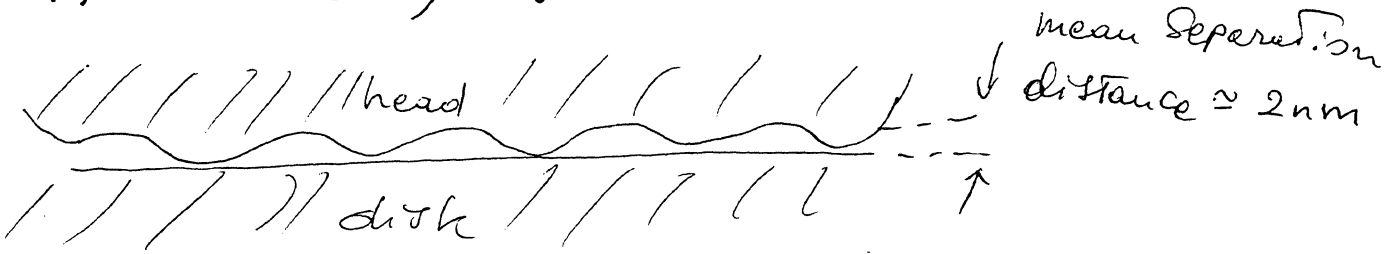
$r \approx \infty$ for $P/P_0 = 1$ 100% RH

$r \approx 10 \text{ nm}$ for $P/P_0 = .9$ 90% RH

$r \approx 1.6 \text{ nm}$ for $P/P_0 = .5$

$r \approx 0.5 \text{ nm}$ for $P/P_0 = .1$

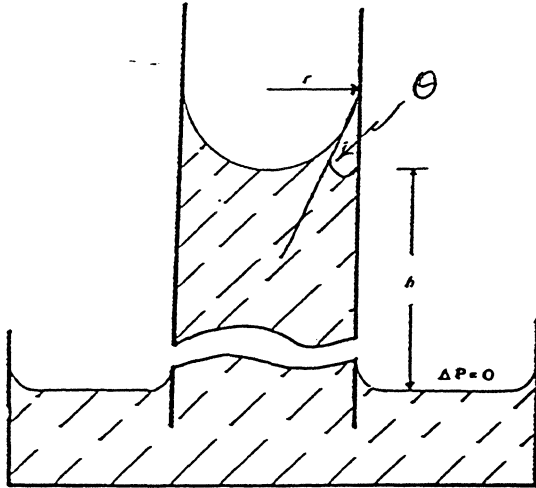
$$\therefore RT \ln(P/P_0) = 2\gamma V/r$$



* gap between the head and the disk can be filled with condensed water at RH between 50% and 90%.*

Measurements of Surface Tension

Capillary Rise Method



Capillary rise (capillary much magnified in relation to dish).

$$\Delta P = 2\gamma/r$$

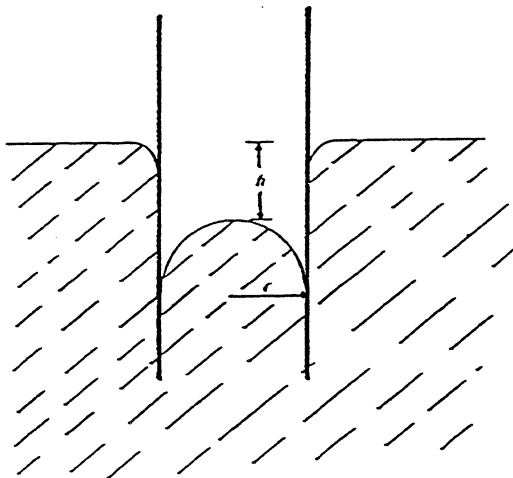
$$\Delta P = \Delta \rho g h =$$

HYDROSTATIC PRESSURE DROP

$$\Delta \rho g h = 2\gamma/r$$

MORE GENERALLY

$$\Delta \rho g h = \frac{2\gamma \cos \theta}{r}$$



Capillary depression.

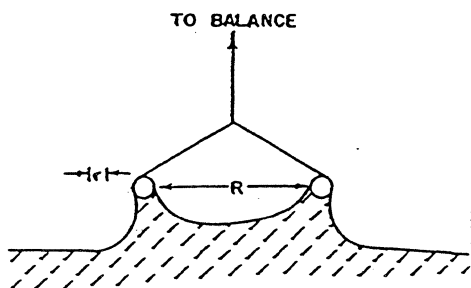
Ring Method

$$W_{tot} = W_{RING} + 4\pi R\gamma$$

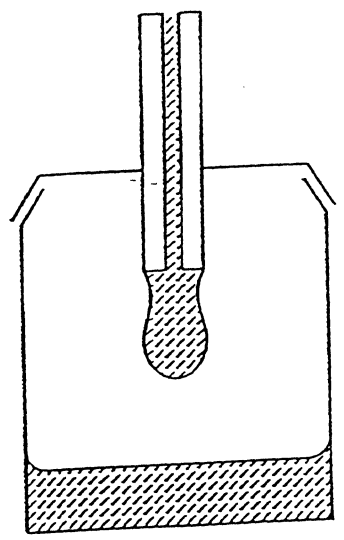
CORRECTION FACTOR f

REQUIRED

$$f = f\left(\frac{R^3}{V}, \frac{R}{r}\right)$$



Drop Weight Method



$$W_t = 2\pi r \gamma \text{ (ideal)}$$

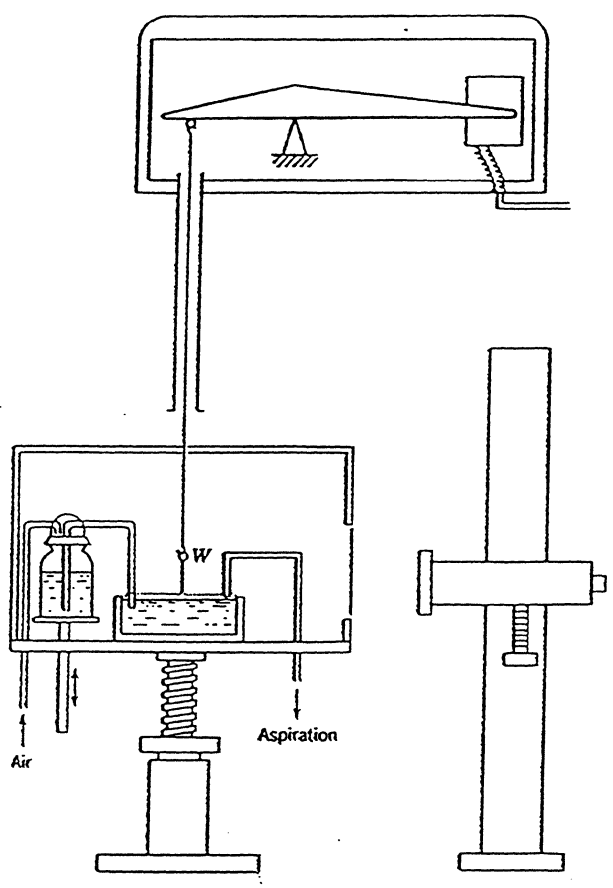
$$W_t' = 2\pi r \gamma f \text{ (less ideal)}$$

where

$$f = f(\sigma/V^{1/3})$$

can measure the cleanliness of disc

Wilhelmy Plate Method



$$W_{t_{TOT}} = W_{t_{PLATE}} + \gamma P$$

WHERE P IS THE PERIMETER

GENERAL EQ.

$$\gamma \cos \theta = \frac{\Delta W_t}{P}$$

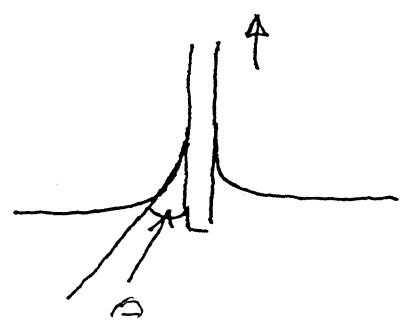
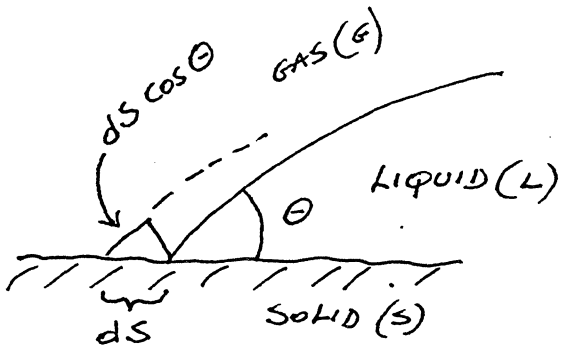


Fig. II-16. Apparatus for measuring the time dependence of interfacial tension from Ref. 40). The air and aspirator connections allow for establishing the desired level of fresh surface. W denotes the Wilhelmy slide, suspended from a Cahn electrobalance with a recorder output.

Spreading Liquids over Solids

The contact angle Θ measurement



distance

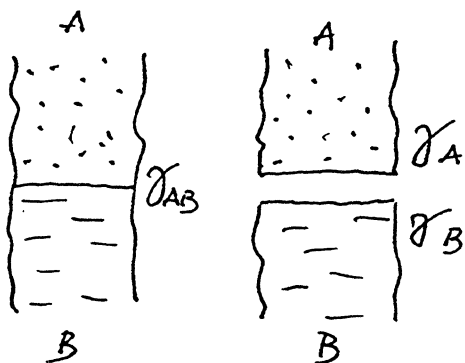
$$\gamma_{SL} dS + \gamma_{LV} dS \cos \Theta -$$

$$\gamma_{SV} dS = 0$$

and $\cos \Theta = \frac{\gamma_{SV} - \gamma_{SL}}{\gamma_{LV}}$

as stated by Young in 1805

Work of Adhesion



$$W_{AB} = \gamma_A + \gamma_B - \gamma_{AB}$$

the work of adhesion is the work required to generate two new surfaces corrected for the energy lost at the original interface

for pure liquids

$$W_A = 2\gamma_A$$

the work of adhesion between a liquid and a solid surface

$$W_{SL} = \gamma_{SV} + \gamma_{LV} - \gamma_{SL}$$

Dupré equation

where γ_{SV} - the surface tension of the solid
against air (or vapor)

γ_{LV} - the surface tension of the liquid
against air (vapor), and

γ_{SL} - the surface tension of the solid
against liquid

using Dupré and Young's equations, we can obtain
for the work of adhesion:

$$W_{SL} = \gamma_{LV} (1 + \cos \theta)$$

Young - Dupré
equation

Therefore, the work of adhesion between a liquid and
a solid can be obtained by measuring the contact angle.

Wetting



Wetting occurs when θ is between 0 and 90 degrees.

At 90°, the attraction of the liquid for the solid is
half that for itself.

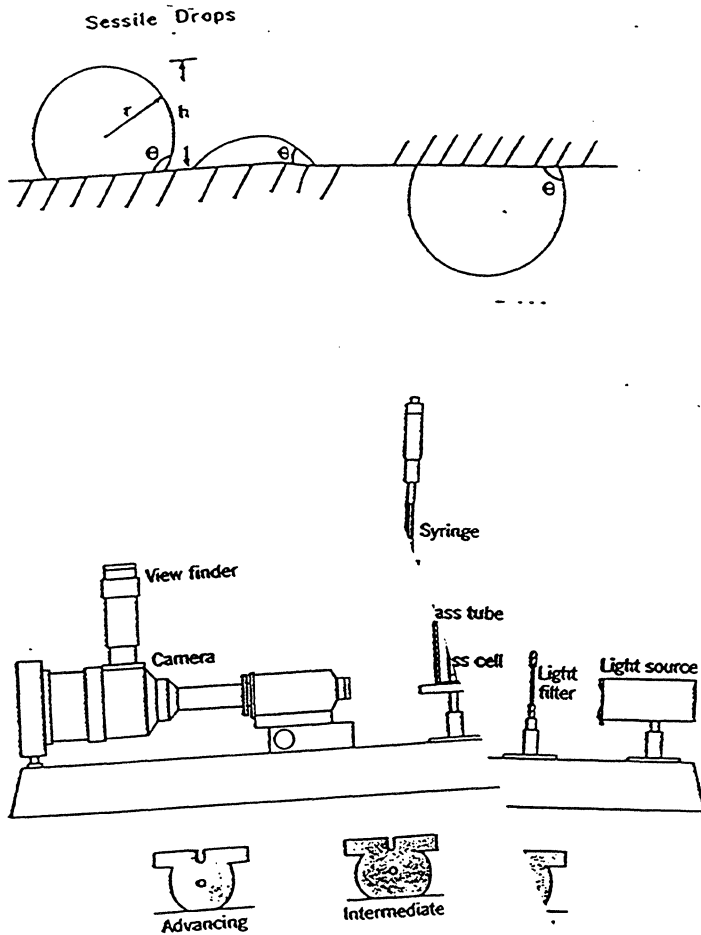
if θ is > 90 no wetting occurs

if $\theta = 0$ liquid spreads

* Thus, spreading occurs when the adhesive energy is greater
than the fluid's cohesion. *

$$W_{SL} \geq 2\gamma_{LV}$$

Measurement of Contact Angle



contact angle θ measured directly by means of a goniometer

easy to obtain receding and advancing angles. Assures that the solid-liquid interface is in equilibrium with the saturated vapor.

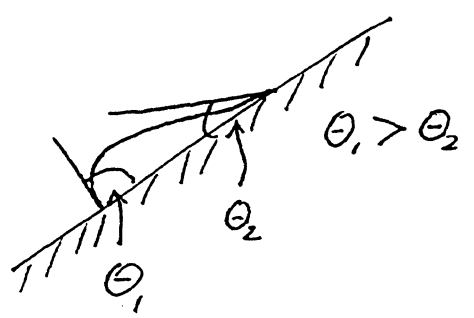
Fig. X-5. The captive bubble method. (Courtesy . Ottewill.)

Apart from energetic considerations of the surface, the contact angle also depends on the surface state, that is, the surface roughness, the manner of preparation, and the degree of oxidation or the level of contamination.

Effect of roughness

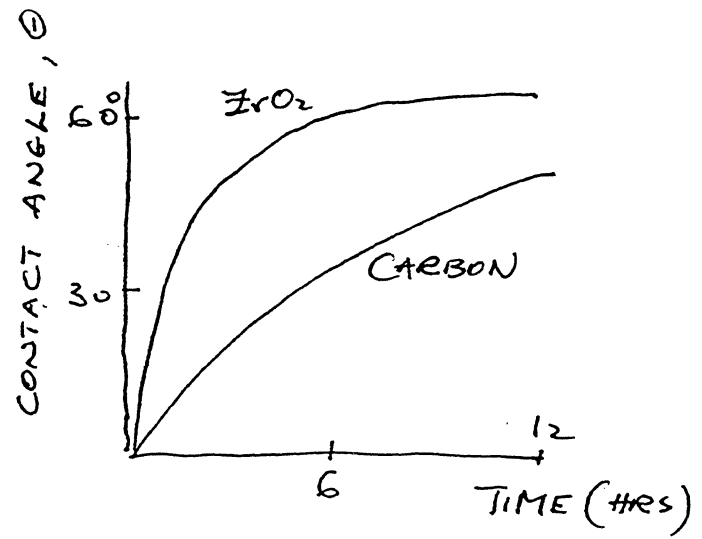


$\cos \theta_r = r \cos \theta_{true}$
where r is the roughness factor that gives the ratio of the true surface area to the projected area.



due to roughness, surface heterogeneity or contamination

Contamination



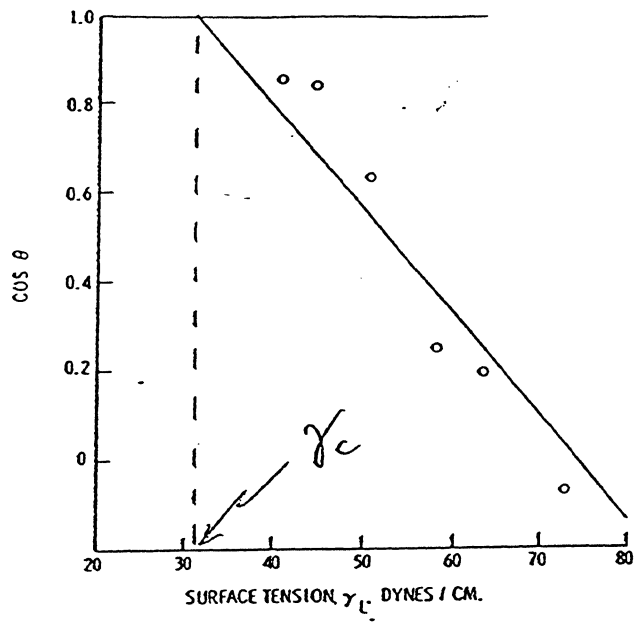
diference in kinetics of adsorption reflects on higher affinity for ZrO_2 (higher surface energy) than for carbon

Advancing contact angle, 20-25°C						
Liquid γ , erg/cm ²	Solid	θ , deg	$d\theta/dT$, deg ^o /K	π^o , erg/cm ²	Reference	
Mercury (484)	PTFE ^a	150			73	
	Glass	128-148			47, 79, 80	
Water (72)	<i>n</i> -H ^b	111			77	
	Paraffin	110			81	
	PTFE ^a	112			81	
			108			73
			98		8.8	82
		FEP ^c	108	-0.05		83
		Polypropylene	108	-0.02		84
		Polyethylene	103	-0.01		85
			96	-0.11		83
			94			86
			93			87
			88		14	88
		Human skin	90			89
			75 ^d			90
		Naphthalene	88 ^e	-0.13		91
		Stibnite (Sb ₂ S ₃)	84			48
		Graphite	86		19	92
					59	93
		Graphon	82			86
		Pyrolytic carbon	72		228	88
	Stearic acid ^f	80		98	88	
	Gold	0			74	
	Platinum	40			86	
	Silver iodide	17			94	
	Glass	Small		ca. 20 ^g	95	
CH ₂ I ₂ (67, 50.8 ^h)	PTFE	85, 88			90, 109	
	Paraffin	61			81	
		60			90	
	Talc	53			50	
	Polyethylene	46, 51.9			90, 109	
		40 ^r			87	
Formamide (58)	FEP ^c	92	-0.06		83	
	Polyethylene	75	-0.01		83	
CS ₂ (ca. 35 ^h)	Ice ⁱ	35	0.35		45	
Benzene (28)	PTFE ^a	46			73	
	<i>n</i> -H ^b	42			77	
	Paraffin	0			96	
	Graphite	0			96	
<i>n</i> -Propanol (23)	PTFE ^a	43		8.8	91	
	Paraffin	22			97	
	Polyethylene	7		5	98	

Zisman's Approach (next page)

This approach allows to predict wetting and spreading from contact angle measurements. The data is plotted as

$\cos \theta$ vs surface tension of a homologous series of liquid to yield γ_c (the critical surface tension)



at $\cos \theta = 1$, the contact angle is zero, and the surface is completely wet

γ_c = critical surface tension for the solid surface

any liquid with $\gamma_{LV} \leq \gamma_c$ will spread over the surface

FIG. 12—WETTING DATA FOR POLYETHYLENE [48]

Dependence of γ_c on the Chemical Composition

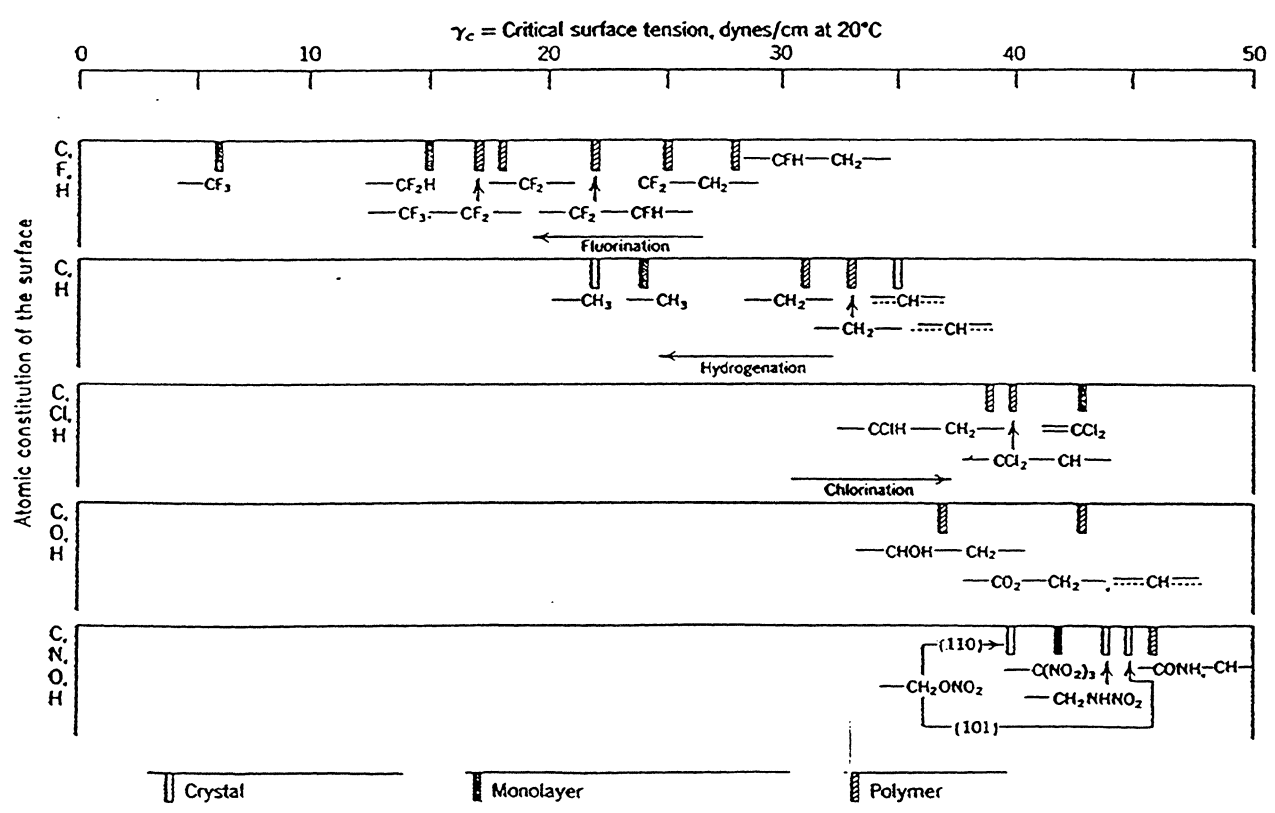


Fig. X-12. The wettability "spectrum" for selected low energy surfaces. (From Ref. 104.)

Fowkes' Approach

Zisman's critical surface tension measurements are only applicable to low energy surfaces such as waxes, polymers or adsorbed monolayers of fatty acids.

By contrast, Fowkes method can be used, in principle, to high energy solids like metals and oxides.

Fowkes postulates that the forces at interfaces can be separated into different components depending on their origin. Thus for water

$$\gamma_{\text{H}_2\text{O}} = \gamma_{\text{H}_2\text{O}}^d + \gamma_{\text{H}_2\text{O}}^h$$

where γ^d is the surface energy arising from dispersion forces (van der waals) and γ^h is the contribution from hydrogen bonding. For mercury (Hg)

$$\gamma_{\text{Hg}} = \gamma_{\text{Hg}}^d + \gamma_{\text{Hg}}^m$$

where γ^m is a contribution from the metallic bonds

and interfacial tension (liquid/liquid or solid/solid)

$$\gamma_{12} = \gamma_1 + \gamma_2 - 2 \sqrt{\gamma_1^d \gamma_2^d}$$

$$\gamma_{SL}^1 = \gamma_S + \gamma_L - 2 \sqrt{\gamma_S^d \gamma_L^d}$$

TABLE I. DETERMINATION OF γ_1^d FOR MERCURY
(Ergs/Sq. Cm. at 20° C.)

Hydrocarbon (No. 2)	γ_1	γ_{12}	γ_1^d
n-Hexane	18.4	378	210
n-Octane	21.8	375	199
n-Nonane	22.8	372	199
Benzene	28.85	363	194
Toluene	28.5	359	208
o-Xylene	30.1	359	200
m-Xylene	28.9	357	211
p-Xylene	28.4	361	203
n-Propylbenzene	29.0	363	194
n-Butylbenzene	29.2	363	193
Average			200 ± 7

$\gamma_1 = 484 \text{ ergs/sq. cm. at } 20^\circ \text{ C.}$
See Reference 11.

the values of $\gamma_{H_2O}^d$ (Table I) and $\gamma_{H_2O}^d$ (Table II) obtained with different hydrocarbons appear to confirm the validity of Fowkes equation

TABLE II. DETERMINATION OF γ_1^d FOR WATER
(Ergs/Sq. Cm. at 20° C.)

Hydrocarbon (No. 2)	γ_1	γ_{12}	γ_1^d
n-Hexane	18.4	51.1	21.8
n-Heptane	20.4	50.2	22.6
n-Octane	21.8	50.8	22.0
n-Decane	23.9	51.2	21.6
n-Tetradecane	25.6	52.2	20.8
Cyclohexane	25.5	50.2	22.7
Decalin	29.9	51.4	22.0
White oil (25°)	28.9	51.3	21.3
Average			21.8 ± 0.7

$\gamma_1 = 72.8 \text{ ergs/sq. cm. at } 20^\circ \text{ C.}$

Dispersion Force Component of the Surface

Energy (γ_s^d)

combining Young's and Fowkes equations

$$\gamma_{LV} \cos \theta = \gamma_{SV} - \gamma_{SL} \quad \text{AND}$$

$$\gamma_{SL} = \gamma_{SV} + \gamma_{LV} - 2\sqrt{\gamma_s^d \gamma_L^d}$$

gives

$$\left\{ \cos \theta = -1 + 2\sqrt{\frac{\gamma_s^d}{\gamma_L^d}} \left(\frac{\sqrt{\gamma_L^d}}{\gamma_L} \right) \right\} \text{ (see next page)}$$

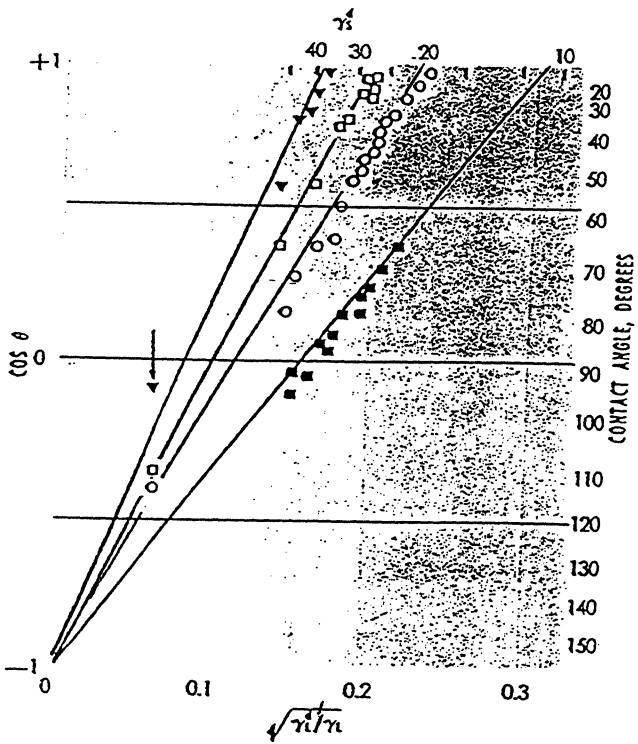


Figure 3. Contact angles of a number of liquids on four low energy surfaces. Triangles refer to polyethylene, open squares to paraffin wax, open circles to $C_{12}H_{24}$, and black squares to fluorododecanoic acid monolayers on platinum. All points below arrow are contact angles with water

Table IV provides a useful guide in comparing the adsorbent properties of materials. For example, it shows that graphite is one of the strongest adsorbents.

TABLE I. SUMMARY OF γ^d VALUES FOR LIQUIDS AND SOLIDS (AT 20°C)

Substance:	γ^d	γ_L	Determined by*:
Liquids:			
Dimethyl siloxanes	16.9 ± 0.5	19.0	θ
Water	21.8 ± 0.7	72.8	γ_{12}
Glycerol	37.2 ± 0.2	64.5	γ_{12}
Formamide	39.5 ± 7	58.2	θ
Mercury	200 ± 7	484	γ_{12}
Hydrocarbons	$\gamma^d = \gamma_L$		
Monolayers on Platinum:			
1- n - $C_{11}F_{23}COOH$	10.4		θ
1- n - $C_9F_{19}COOH$	13.1		θ
1- n - $C_{12}H_{27}NH_2$	22.1		θ
Low Energy Solids:			
Polyhexafluoropropylene	18.0		θ
Polytetrafluoroethylene	19.5		θ
n - $C_{16}H_{34}$ crystals	21.0		θ
Paraffin wax	25.5		θ
Polypropylene	28		$\theta, \Delta G_{ads}$
Polyethylene	35.5		$\theta, \gamma_{L,extrap}$
Polystyrene	44		θ
High Energy Solids:			
Copper	60		ΔG_{ads}
Silver	74		ΔG_{ads}
Barium sulfate	76		ΔG_{ads}
Silica	78		ΔG_{ads}
Anatase (TiO_2)	92		ΔG_{ads}
Graphite	96		$\theta, \Delta G_{ads}, \Delta H_{ads}, \Delta H_{im}$
Lead	99		ΔG_{ads}
Tin	101		ΔG_{ads}
Iron	106		ΔG_{ads}
Iron Oxide	107		ΔG_{ads}

* θ —contact angle
 γ_L —interfacial tension
 ΔG_{ads} —free energy of adsorption (ϵ_s)
 $\gamma_{L,extrap}$ —extrapolation of surface tension from decaled temperatures
 ΔH_{ads} —heat of adsorption
 ΔH_{im} —heat of immersion

TABLE IV. VALUES OF γ_s^d OBTAINED FROM π_s MEASUREMENTS FOR ADSORBED VAPORS

Adsorbent	Adsorbate	Reference	Temperature	π_s	γ_s^d , Ergs/Sq. Cm.
Polypropylene	Nitrogen	(16)	78° K.	12	26
	Argon	(16)	90° K.	13	28.5
Graphite*	Nitrogen	(29)	78° K.	51	123
	n -Heptane	(3, 6, 20)	25° C.	63, 56, 58	* 132, 115, 120
Copper	n -Heptane	(21)	25° C.	29	60
Silver	n -Heptane	(21)	25° C.	37	74
Lead	n -Heptane	(21)	25° C.	49	99
Tin	n -Heptane	(27)	25° C.	50	101
Iron	n -Heptane	(21)	25° C.	53	108
	Argon	(2)	90° K.	47	106
	Nitrogen	(2)	78° K.	40	89
Ferric oxide	n -Heptane	(21)	25° C.	54	107
Anatase (TiO_2)	n -Heptane	(26)	25° C.	46	92
	Butane	(26)	0° C.	43	89
	Nitrogen	(26)	78° K.	56	141
Silica	n -Heptane	(6)	25° C.	39	78

strong adsorbent

The Role of Interfacial Forces in Tribology

- * electrostatic
- * steric
- * van der Waals
- * meniscus
- * viscous

Electrostatic Forces

- * electrostatic forces are produced by electron transfer from one atom to another
- * the amount of charge transfer depends on the contact area, the work function difference, and the density of electronic surface states.

$$\overline{F}_{el} = 4.5 \times 10^{-12} E^2 A_{real}$$

if $A_{real} = 0.15 \text{ mm}^2$ (5% of the apparent area of 3 mm^2)
and $V = 0.3 \text{ volts}$, $h = 3 \text{ nm}$, and $E = V/h = 1 \times 10^6 \text{ V/cm}$.

$$\overline{F}_{el} \approx 60 \text{ mN} \quad (6 \text{ gms})$$

Van der Waals Forces

these forces arise from interactions of permanent or induced dipoles. They are effective from a very large separations (ca. 50 nm) down to interatomic separations (ca. 0.3 nm).

For two parallel plates separated by the distance D , the force per unit area (or the adhesive pressure) is

$$P_{VDW} = H / 6\pi D^3 \quad \text{where } H \approx 1 \times 10^{-19} \text{ J}$$

H high for metals

if $D = 0.3 \text{ nm}$ between plates

$$P_{VDW} = 2 \times 10^8 \text{ N/m}^2 \approx 2,000 \text{ atm}$$

if $D = 1 \text{ nm}$

$$P_{VDW} = 5.3 \times 10^6 \text{ N/m}^2 \approx 53 \text{ atm}$$

if the apparent contact area of the average head is 0.025 cm²

and the real contact area is about 0.5% of the apparent area

($1.25 \times 10^{-4} \text{ cm}^2$), the adhesive pressure is ca. 6.6 grams.

$$1 \text{ nm} = 1 \times 10^{-9} \text{ m}$$

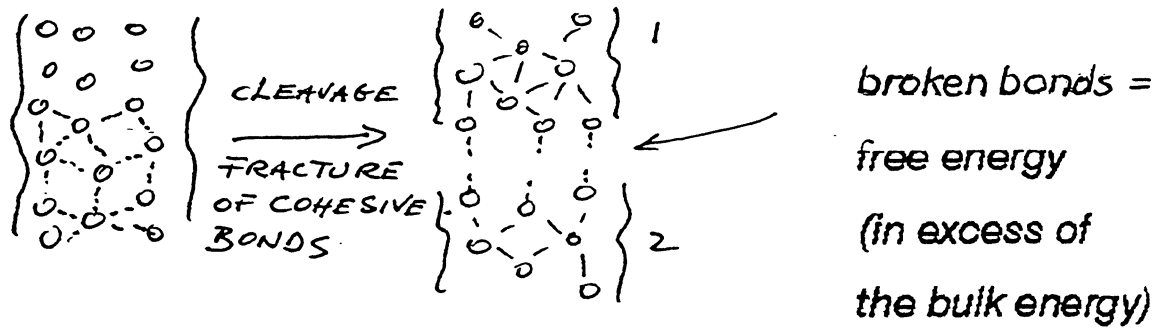
$$\text{J/m} = \text{N}$$

$$\text{J/m}^2 (\text{Joule/meter}^2) = \text{N/m}$$

(Newton/meter)

$$\text{N/m}^2 = \text{Pa} (\text{Pascal})$$

Surface Free Energy in Adhesion



$$\Delta\gamma = \gamma_1 + \gamma_2 - \gamma_{12} \quad \text{work of adhesion}$$

where γ represents the energy that must be applied to separate a unit area of the interface.

Adhesion between elastic solids was analyzed by Fuller and Tabor (1975). They modeled asperity contacts of two rough surfaces following Greenwood and Williamson's approach. The adhesion parameter after Fuller and Tabor predicts that

$$\phi = E_c \sigma_p^{3/2} R_p^{1/2} / R_p \Delta\gamma$$

where E_c is the composite modulus, σ_p is the standard deviation of the summits, and R_p is the composite of mean radii of curvature of the summits.

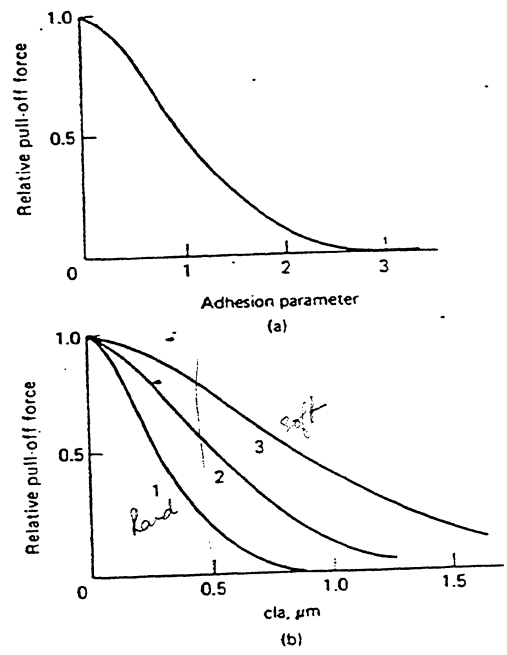


Fig. 4.9. (a) Predicted relative pull-off force as a function of the adhesion parameter (Fuller and Tabor, 1975). (b) Relative pull-off force for smooth rubber spheres in contact with a flat Perspex surface as a function of the cla roughness of the Perspex. Effect of modulus E of the rubber; curve 1, 2.4 MPa; curve 2, 0.68 MPa; curve 3, 0.22 MPa. The pull-off force of smoothest surfaces was a few mN (Fuller and Tabor, 1975).

the adhesion parameter represents the statistical average of a competition between the compressive forces exerted by the higher asperities that are trying to separate the surfaces and the adhesive forces between lower asperities that are trying to hold the surfaces together.

untextured
ultra clean thin film
disk

For $E_c = 100 \text{ GPa}$ (p. 62)

$G_p = 2 \text{ nm} = 20 \text{ \AA}$

$R_p = 500 \text{ \mu m}$

$\Delta \gamma = 1 \text{ N/m}$ (10^3 dynes/cm)
 $= 1 \text{ J/m}^2$

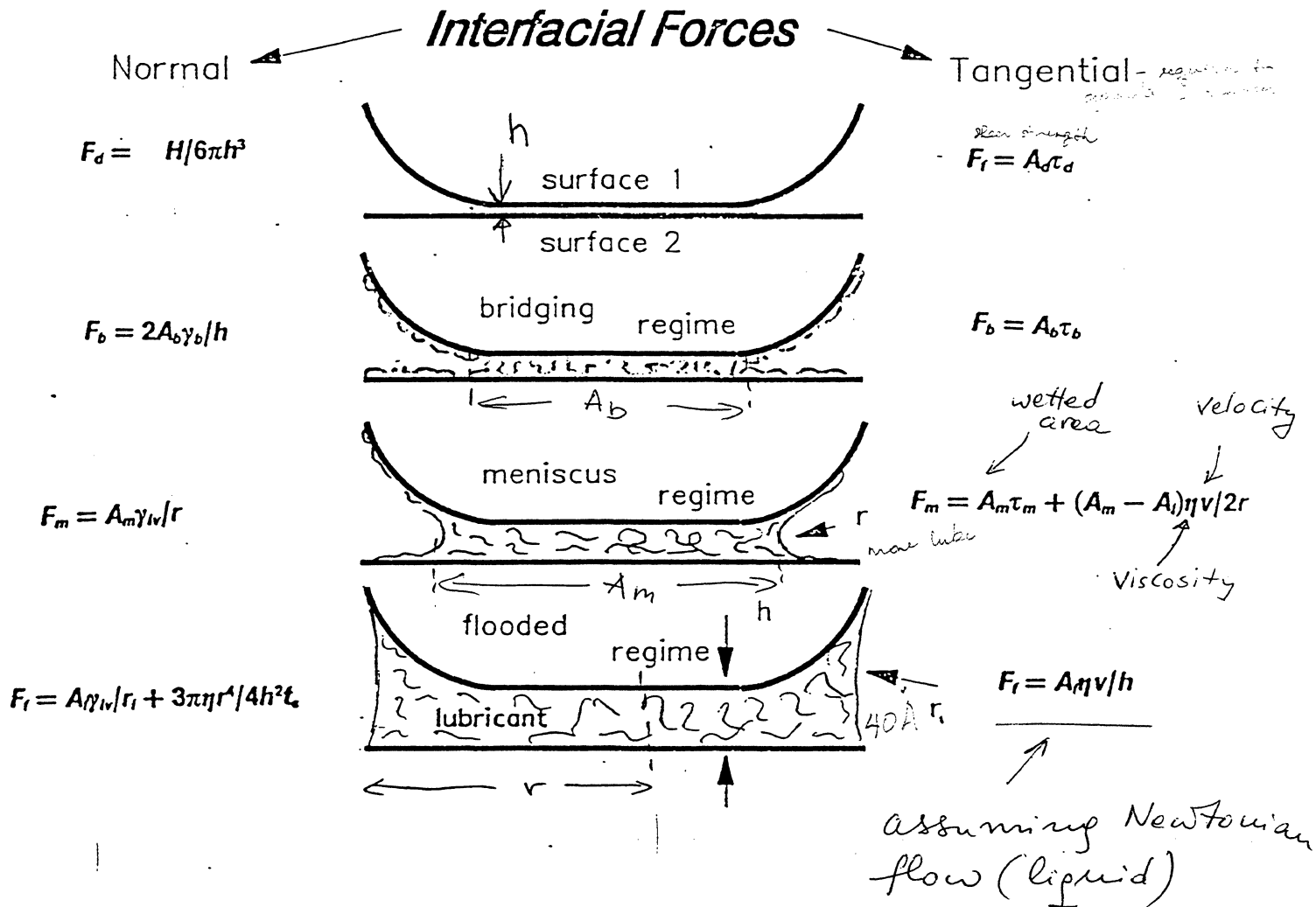
$\Theta = 0.4$

if $\Delta \gamma = 50 \text{ mN/m}$ (lubricant present) $\Theta \neq 8$

thus, solid-solid adhesion is significant especially for smooth surfaces (slider/disk).

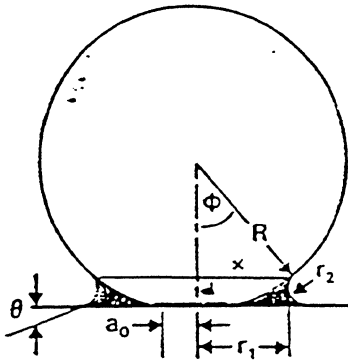
Idealized Geometries

Simplified schematic of the interfacial forces acting between an isolated asperity and a flat surface. Note that different relationships describe forces in normal and tangential directions.



Meniscus Effects

The meniscus forces between a sphere and a flat surface



Laplace pressure:

$$\Delta P = \gamma_{LV} \left(\frac{1}{r_1} + \frac{1}{r_2} \right) \approx \frac{\gamma_{LV}}{r_2}; \quad (r_1 \gg r_2)$$

Since wetted area $\approx \pi x^2 \approx 2\pi R d$

$$F_m = \left(\frac{\gamma_{LV}}{r_2} \right) 2\pi R d$$

For small ϕ , $d \approx 2r \cos \theta$

$$\therefore F_m = 4\pi R \gamma_{LV} \cos \theta$$

$$F_m = 2\pi R \gamma_{LV} (\cos \theta_1 + \cos \theta_2)$$

A (area of the slider)
 ↓
 Surface tension of tube
 ↓

$$F_m = \frac{(0.025 \text{ cm}^2)(21 \text{ dynes/cm})}{100 \times 10^{-8} \text{ cm}}$$

$$= 5.25 \times 10^5 \text{ dynes}$$

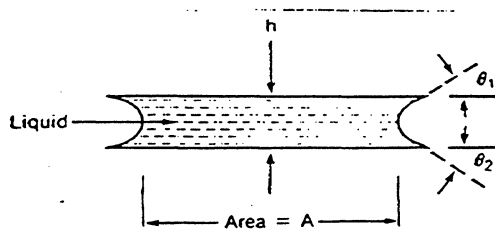
$$\approx 525 \text{ gms}$$

film thickness

$$3 \times 10^3 \text{ dynes} \approx 1 \text{ gm}$$

The meniscus force between two flat surfaces

(given by Rabinowicz 1965)



$$F_m = \frac{A \gamma_{LV}}{h} (\cos \theta_1 + \cos \theta_2)$$

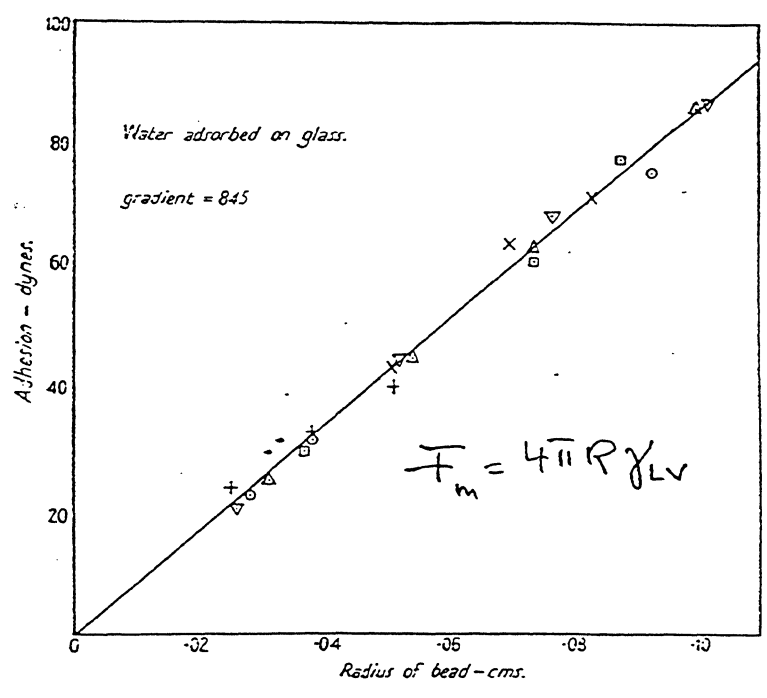


FIG. 108. Adhesion of a spherical glass bead on a flat glass surface in a humid atmosphere. The adhesive force A is directly proportional to the radius of curvature, R , of the bead. The slope of the straight line is a measure of the surface tension of the liquid between the surfaces, and the calculated value is 67 dynes/cm.

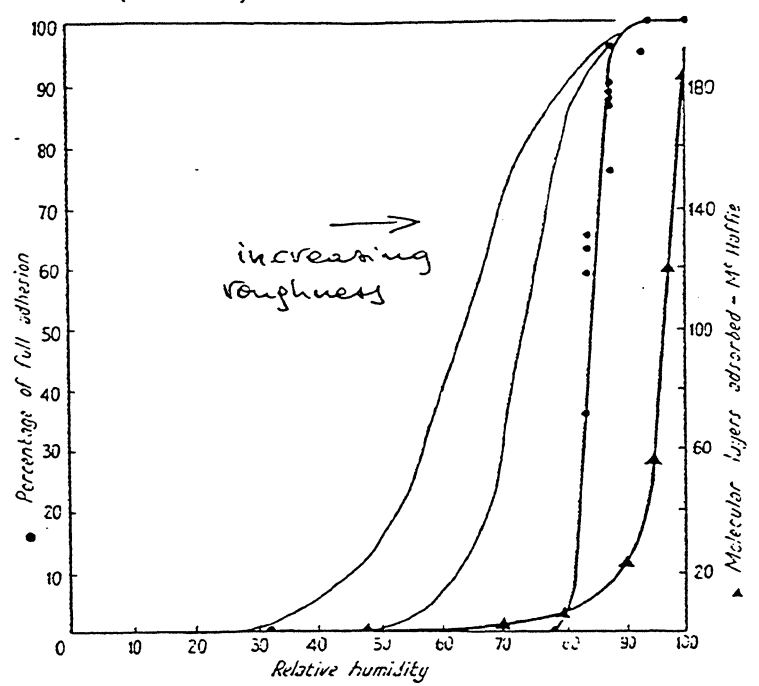
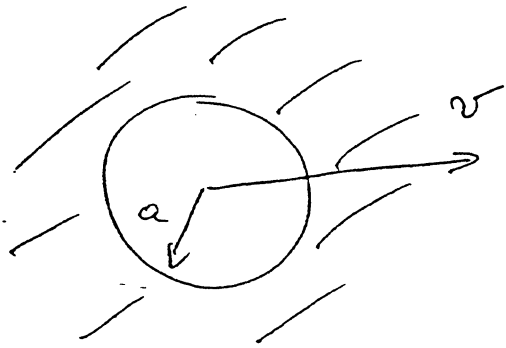


FIG. 109. Adhesion of glass surfaces as a function of the humidity of the surrounding atmosphere. The adhesion rises rapidly at humidities exceeding 80 per cent. saturation (curve ●). There is a close parallel to the results of McHaffie and Lenthal (curve ▲) for the thickness of the water film adsorbed on glass surfaces.

both figures from Bowden & Taber
"The Friction and Lubrication of Solids"
Oxford Press, 1954.

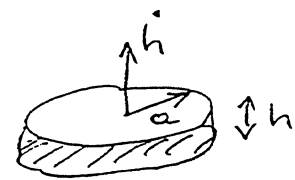
Viscous Forces



$$F_v = 6\pi\eta a v$$



$$F_v = \eta \frac{A v}{d}$$



$$F_v = \frac{3\pi\eta a^4}{4t_s} \left(\frac{1}{h_1^2} - \frac{1}{h_2^2} \right)$$

$$F_v = \eta \cdot f(\text{geometry}, [L]) \cdot \frac{d(\text{displacement})}{dt}$$

$$\int_0^t F_v dt = \eta \int_{\text{Start}}^{\infty} f(\text{geometry}) d(\text{displacement})$$

$$= \underline{I} (\text{impulse})$$

critierum for unsticking against viscous force is that a particular impulse must be exceeded

↖ proportional to η (viscosity)

(from Matthewson, Phil. Mag. A57, 207, 1988)

thus the time integral of the viscous force is

$$\int_{t_m}^{t_s} \bar{F}_v dt = \bar{I}_v \quad (1)$$

and

$$\bar{F}_v = \bar{I}_v / t_s \quad (2)$$

where t_s is the separation time

this is essentially the same formula as given by McFarlane and Tabor (1950)

$$\bar{F}_v = \beta \eta / t_s \quad (3)$$

where β is the proportionality constant (dimension of length²)

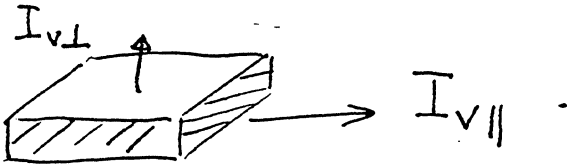
Equation (2) applies when a constant force is applied

When the force increases linearly with time and at some rate

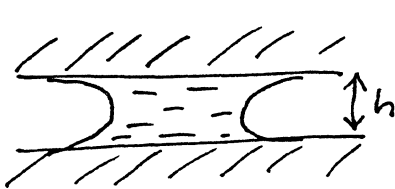
$$\bar{F}_v = \left(2 \dot{F} \bar{I}_v \right)^{1/2} \quad (4)$$

Matthewson derived formulas for the impulse required to separate surfaces in the perpendicular and parallel directions.

note that equations 3 and 4 apply for any geometry separating along any path and geometry and path information is contained in the appropriate expressions



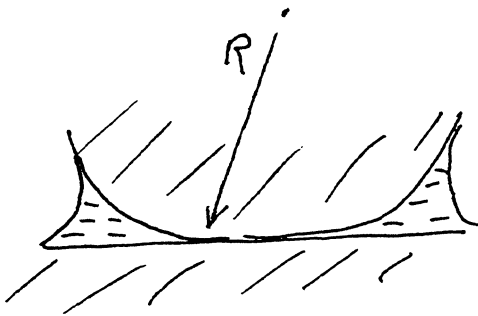
impulse required to separate flat surfaces



$$\bar{I}_{v\perp} = \frac{3\pi\eta a^4}{8h^2} \quad (5)$$

a = equivalent radius of the surface area

$$\bar{I}_{v\parallel} = \frac{16\pi a^3}{3h} \quad (6)$$



$$\bar{I}_{v\perp} = 6\pi\eta R'^2 \ln\left(\frac{t}{2D_0}\right) \quad (7)$$

$$\bar{I}_{v\parallel} = \eta (R'^3 t)^{1/2} \ln\left(\frac{2t}{D_0}\right) \quad (8)$$

where t is the fluid film thickness and D_0 is the distance of the closest approach (combined roughness)

Total Adhesion

for separation in normal direction

$$F_{ad \perp} = F_m + F_{v \perp} \quad (9)$$

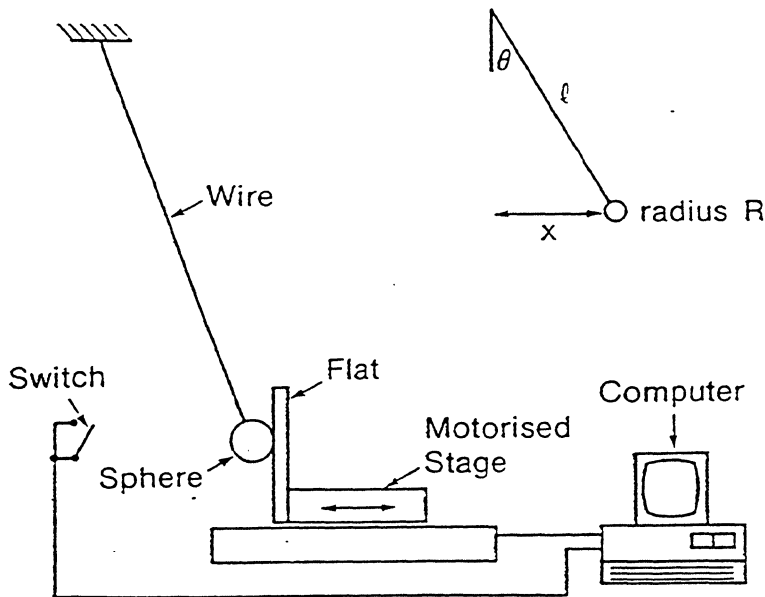
for separation in tangential direction

$$F_{ad \parallel} = \mu (F_m + P) + F_{v \parallel} \quad (10)$$

where P is the externally applied normal load.

The Force Pendulum Apparatus

was used to verified the equations for the case of a sphere separating normally from a flat surface



$$F = mg \tan \theta$$

for small θ

$$F = \frac{mgx}{l} \quad (11)$$

Schematic diagram of the force pendulum apparatus.

from equations 9 and 2

$$\overline{F}_{ad} = \overline{F}_m + \frac{\overline{I}_v L}{t_s} \quad (12)$$

where the separation time is measured as a function of a constant applied force (static experiment).

and from equations 9 and 4

$$\overline{F}_{ad} = \overline{F}_m + \left(\frac{2mg \overline{I}_v v}{\lambda} \right)^{1/2} \quad (13)$$

where the adhesive force is measured as a function of the constant stage velocity, i.e., the applied force is ramped linearly with time.

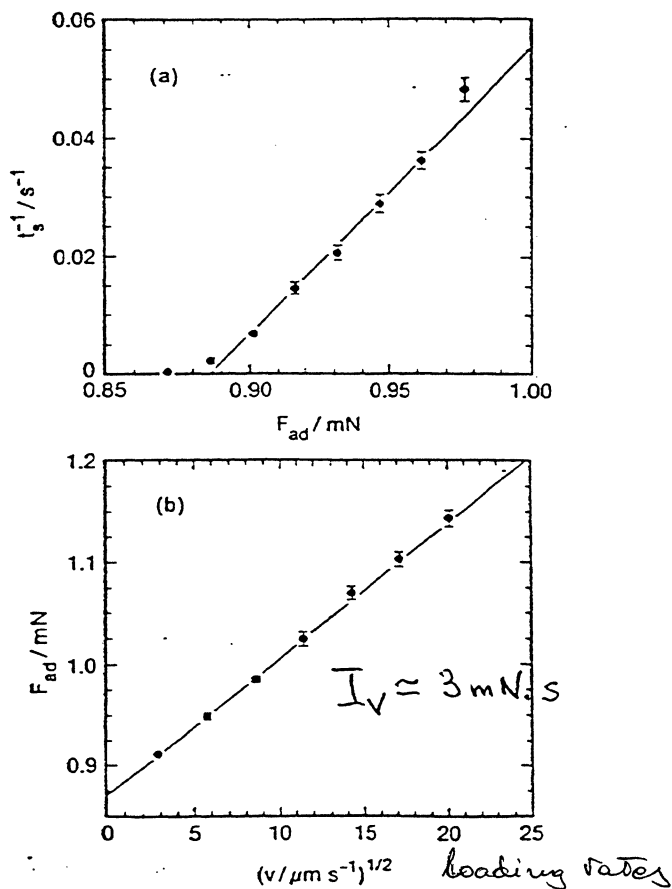


Figure 4. Results of (a) 'static' and (b) 'dynamic' adhesion measurements for a 4 mm radius sphere on abraded glass.

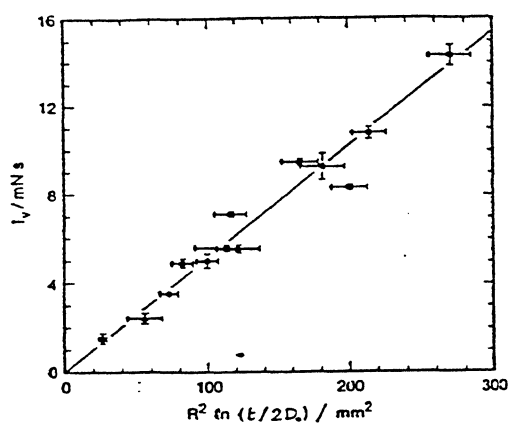


Figure 5. Measurements of the viscous impulse for various surfaces roughnesses, liquid film thicknesses and sphere radii.

testing eq. 7

$$\overline{I_{vL}} = 6\pi\eta R^2 \ln\left(\frac{t}{D_0}\right)$$

the results span four decades in roughness (i.e., D_0), two decades in film thickness and one in sphere radius.

Head - Medium Interface

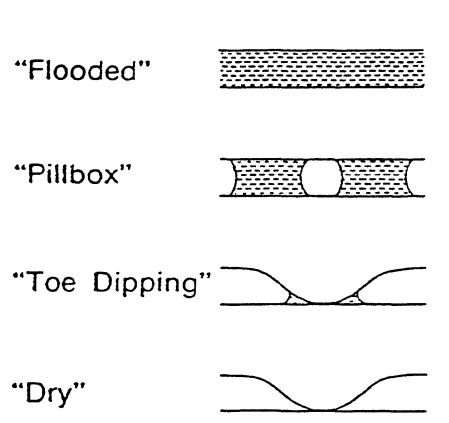


Figure 2. Geometry of the meniscus bridges between two surfaces at different wetting regimes.

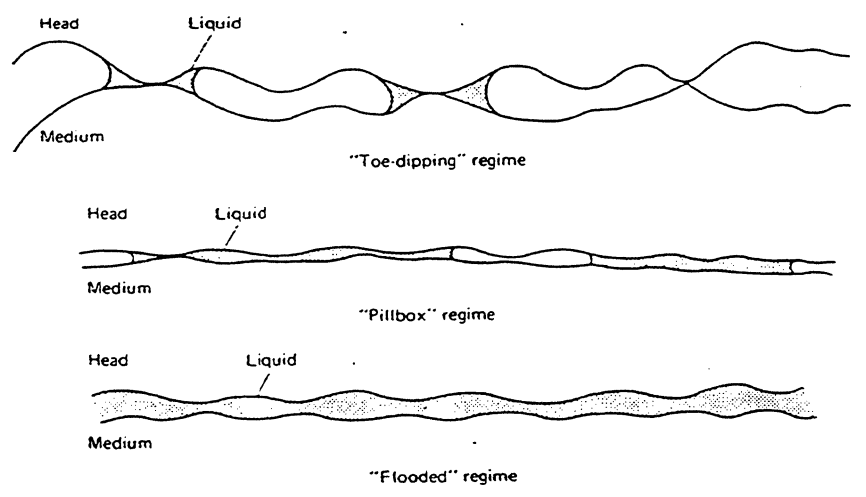


Fig. 4.15. Regimes of different liquid levels in the head-medium interface.

The "Flooded" Regime

(14)
$$\overline{F}_m = \frac{2A \gamma_{LV} \cos \Theta}{h}$$
 } the meniscus force

(15)
$$\overline{F}_v = \frac{\eta A}{h} (L \alpha)^{1/2} e^{-1/2}$$
 } the peak viscous force
 (peak viscous force for constant acceleration α)

where γ is the fluid viscosity, L is the distance the surface need to slide to become unstick and α the start-up linear acceleration.

The "Pillbox" Regime

$$\bar{F}_m = \frac{N 2\pi a^2 \gamma \cos \Theta}{h} \quad (16)$$

and

$$\bar{F}_{V||} = \left(\frac{9}{2} \ddot{F} I_v^2 \right)^{1/3} \quad (17)$$

where $\ddot{F} = k \alpha$

this is the peak viscous force when the applied force accelerates at a constant rate.

α is the start-up acceleration

$$I_{V||} = \frac{16}{3} \frac{\eta a^3}{h} \quad (18)$$

and the total adhesive force for a constant acceleration is

both \bar{F}_m and \bar{F}_s are \sim to no. of pillboxes and their areas

$$\left\{ \begin{array}{l} \bar{F}_s = N \pi a^2 \left(\frac{2\eta \gamma \cos \Theta}{h} \right) \quad (19) \quad \bar{F}_m \gg \bar{F}_v \\ \bar{F}_s = N \pi a^2 \left(\frac{32 \ddot{F} \eta^2}{\pi h^2} \right)^{1/3} \quad (20) \quad \bar{F}_m \ll \bar{F}_v \end{array} \right.$$

The "Toe-Dipping" Regime

$$\bar{F}_m = N (4\pi R \gamma \cos \Theta) \quad (21)$$

and

$$\bar{F}_m \approx \frac{W(\text{load})}{\left[\frac{E' \sigma_p (\sigma_p / R_p)^{1/2}}{16.6 \gamma_{LV} (\cos \Theta_1 + \cos \Theta_2)} \right] - 1} \quad (22)$$

Total Tangential Force

$$F_{ad \parallel} = \mu (F_m + P) + F_{v \parallel} \quad (10)$$

where μ is the true coefficient of friction and is given as

$$\mu \approx 3.2 \frac{\tilde{\tau} R_p^{1/2}}{E_c \sigma_p^{1/2}} \quad (23)$$

where $\tilde{\tau}$ is the mean shear strength of the contact area, E_c is the complex modulus, σ_p and R_p are the composite std. deviations and mean radius of curvature of the summits.

Experimental Results

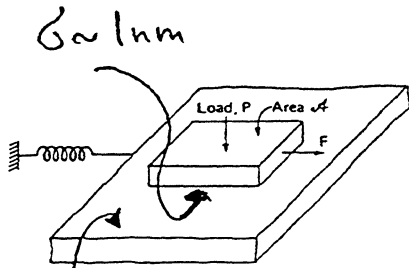


Figure 2 Apparatus for measuring adhesion force.

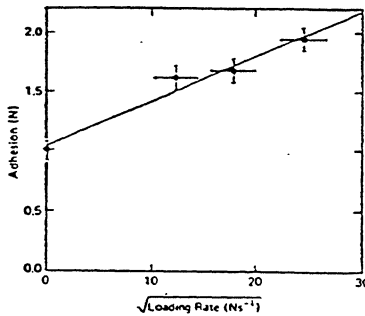


Figure 3 Adhesion as a function of start-up rate.

note a significant increase in adhesion with start-up rate

"high" adhesion surface 2 nm (σ_p)

"low" adhesion surface 5 nm (σ_p)

both surfaces were coated with 2 nm of lubricant.

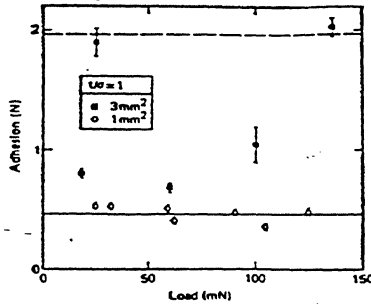


Figure 4 Adhesion as a function of normal load for the "high" adhesive surface.

"High" adhesive surface

$A = 1 \text{ and } 3 \text{ mm}^2$

the adhesion is substantially independent of load.

The interface is operating at the flooded end of the pillbox regime.

$$\zeta_p = 2 \text{ nm}, t = 2 \text{ nm.}$$

↑
lubricant thickness

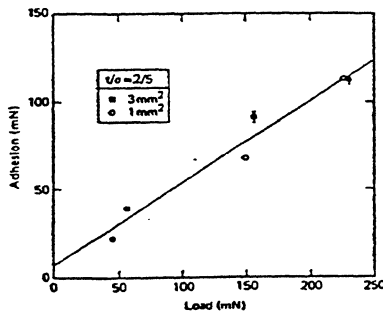


Figure 5 Adhesion as a function of normal load for the "low" adhesive surface.

"Low" adhesive surface

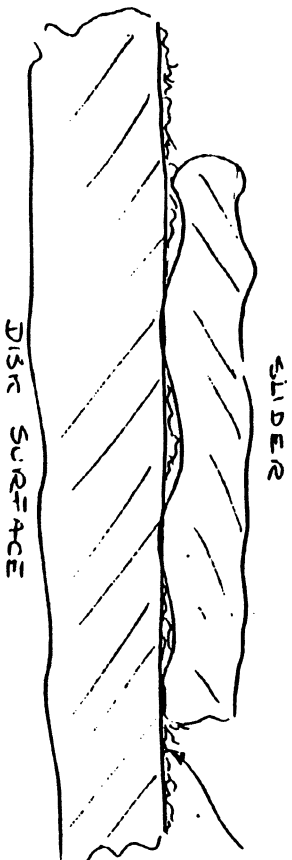
the adhesion is proportional to the normal load and is independent of the apparent contact area

given $\zeta_p = 5 \text{ nm}$ and $t = 2 \text{ nm}$, the results imply that the toe-dipping regime is operative for this interface.

Calculation of Stiction

* The "dry" Regime*

- no molecular lubric present -



shear strength of the "dry" interface $\tau \approx 1.25 \times 10^7 \text{ N/m}^2$

Real contact area $\approx 6.25 \times 10^{-9} \text{ m}^2$ (2025psi the apparent area)

The "stiction" or the static friction F_S is the force required to separate adhesive joints in tangential direction

For smooth surface:

$$F_S = A_{real} \tau$$

Tabor's adhesion theory

and

$$F_S = (6.25 \times 10^{-9} \text{ m}^2) (1.25 \times 10^7 \text{ N/m}^2) = 0.078 \text{ N} \approx 7.8 \text{ g}$$

or according to Amontons law and for smooth surface

$$F_S = \mu_{eff} L$$

Tabor's $L = C_{ad}$

where

if we take

$$R_p = 500 \mu\text{m} = 500 \times 10^{-6} \text{ m}$$

$$\Delta p = 20 \text{ nm} = 20 \times 10^{-9} \text{ m}$$

$$E_c = 100 \text{ GPa} = 100 \times 10^9 \text{ N/m}^2$$

$$\text{and } \tau = 1.25 \times 10^7 \text{ N/m}^2$$

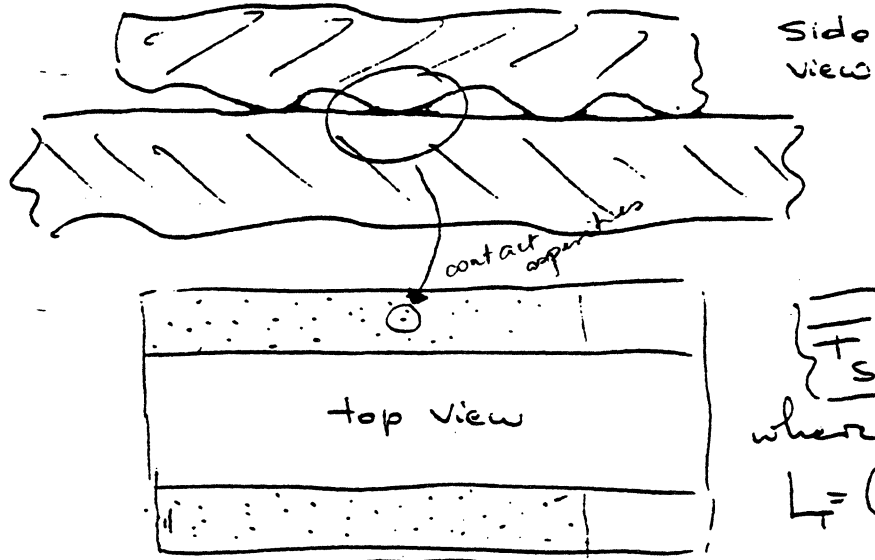
and

$$F_S \approx (0.2) (6 \text{ g } C_{ad}) \approx 1.2 \text{ g}$$

* 3. Bhushan in Tribology, Mechanics of Magn. Storage Devices, Springer-Verlag, 1990, p. 261.

The "Toe-Dipping" Regime

- lubricant thickness less than the peak-to-valley disk roughness -



$$\overline{F}_S = \mu_{\text{eff}} L_{\text{total}}$$

where

$$L_T = (F_m + L_{\text{susp.}})$$

$$F_m = N 4\pi R \gamma \cos \theta$$

$$F_m = (4000)(4\pi)(500 \times 10^{-6})(21 \times 10^{-3})$$

$$F_m = 0.52 \text{ N} = 52 \text{ g}$$

where

$$R = 500 \times 10^{-6} \text{ m}$$

$$\gamma = 21 \times 10^{-3} \text{ N/m}$$

$$N \cong 4000 \text{ (expt.)}$$

calc.

$$N \sim \frac{2.64 L_T}{E_c \sigma_p^{3/2} R_p^{1/2}}$$

and

$$\overline{F}_S = (0.13)(52) = 6.8 \text{ g}$$

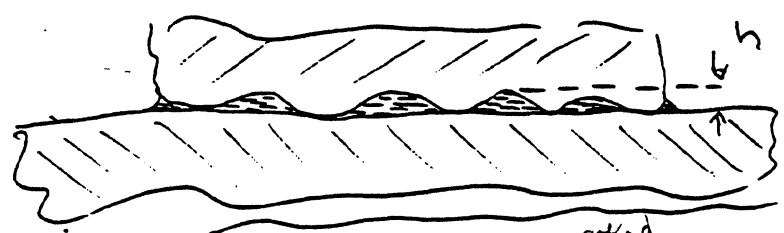
$$\overline{F}_S = (0.2)(52+6) = 11.6 \text{ g}$$

but N is the function of the normal load and will increase as more asperities are brought into contact

3

The "Flooded" Regime

- lubricant thickness \geq surface roughness -
- long rest times -



$h \approx 50$
 $\approx 10 \text{ nm}$

$$F_s = \mu_{\text{eff}} (F_m + F_{\text{preload}}) + F_v \quad \text{viscous resistance}$$

$$F_m = \frac{2 A_{\text{app}} \gamma}{h} = \frac{2 (2.5 \times 10^{-6}) (21 \times 10^{-3})}{(100 \times 10^{-10})} = 10.5 \text{ N} = 1050 \text{ g}$$

$$F_v = \frac{\eta A_{\text{app}}}{1.5 h} (L \alpha)^{1/2}$$

where $\eta = 200 \text{ mPa}\cdot\text{s}$
 $\eta = 200 \text{ mN}\cdot\text{s}/\text{m}^2$
 $A_{\text{app}} = 2.5 \times 10^{-6} \text{ m}^2$
 length of slider $L = .2 \text{ cm} = 2 \times 10^{-3} \text{ m}$
 acceleration $\alpha = 15 \text{ m}/\text{s}^2$

$$F_v = \frac{(200 \times 10^{-3}) (2.5 \times 10^{-6})}{1.5 (100 \times 10^{-10})} \times (2 \times 10^{-3} \times 15)^{1/2}$$

$F_v = 5.2 \text{ N} = 520 \text{ g}$

$\therefore F_s = 0.2 (1050 + 6) + 520 = 731 \text{ g} !$

Note that for $\delta_p = 5 \text{ nm}$ ($h = 25 \text{ nm}$)

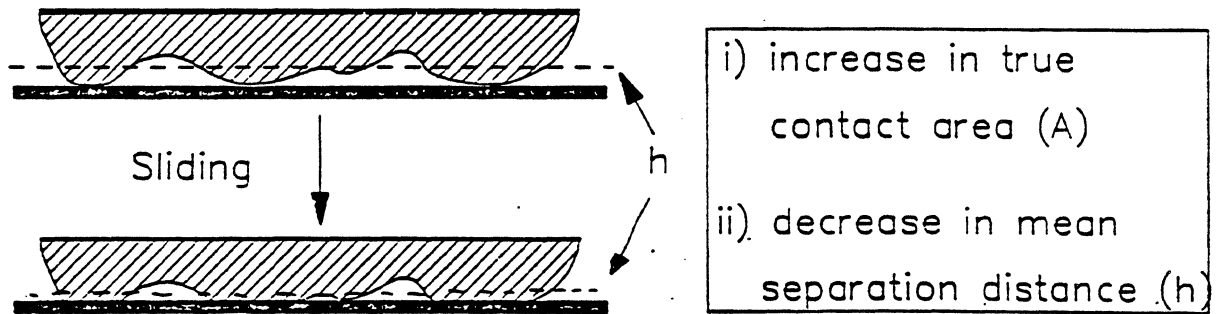
$F_m = 420 \text{ g}$, $F_v = 208 \text{ g}$ and $F_s = 293 \text{ g}$

136

Factors Affecting Stiction

- Rest time
- Humidity and temp.
- Ambient contaminants
- Lubricant thickness more lubc - some adhesion
- Surface roughness
- Mechanical properties of the interface
- Contact Start-Stop (CSS)
- Head slider Area
- Head slider load
- Acceleration of the drive
↑
Viscous Forces depend on acceleration

Effect of Contact Start-Stop (CSS)



Factors affecting:

- i) lubricant properties
(mobility, viscosity, chemical resistance)
- ii) mechanical properties of surfaces
(elastic modulus, E , hardness, H)
- iii) surface topography
(rms, asperity curvature and density)

Measurement of Friction / Stiction in Disk Drives

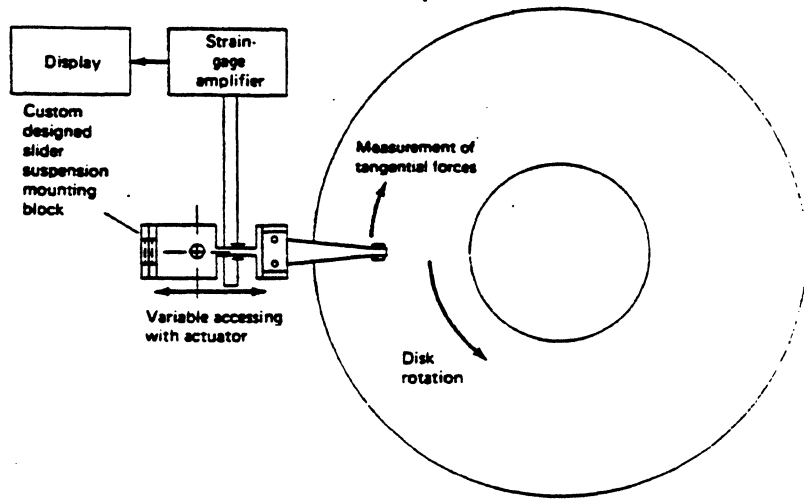
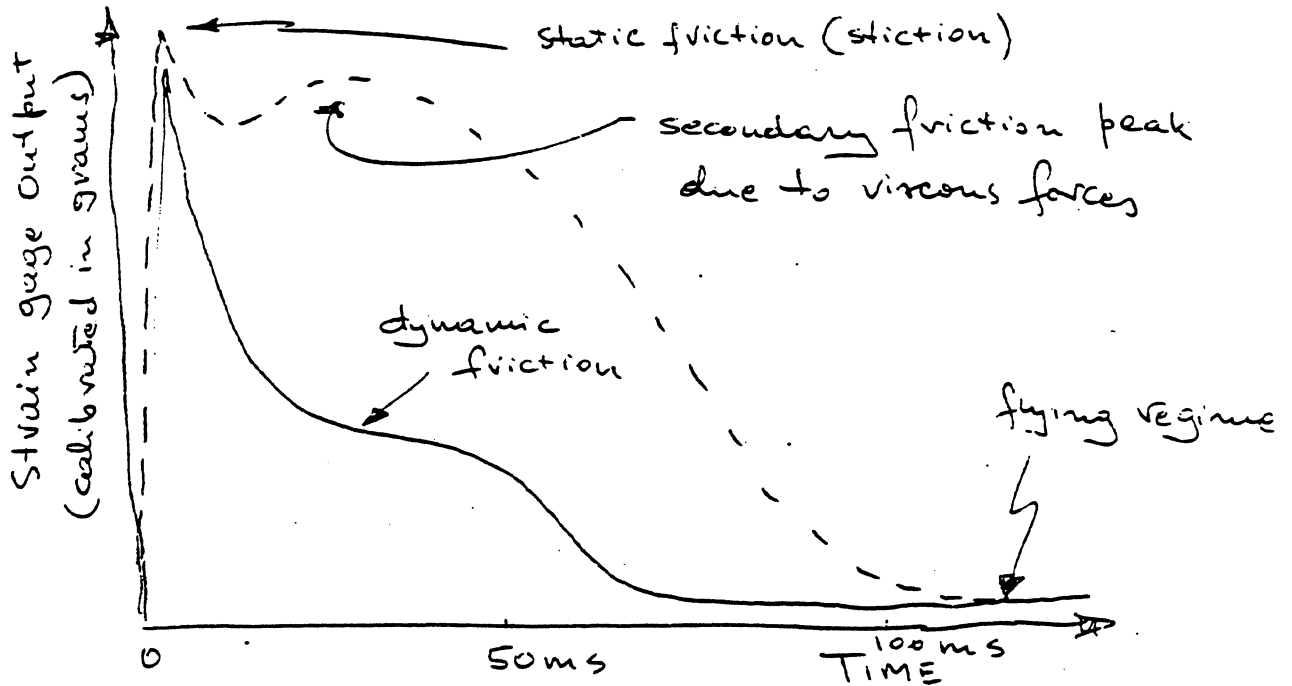


Fig. 4.65. Schematic of a test apparatus for friction measurement at head-disk interfaces.



by Ishikawa et al,
 IEEE Trans. Magn.
 Mag-22, 999 (1986)

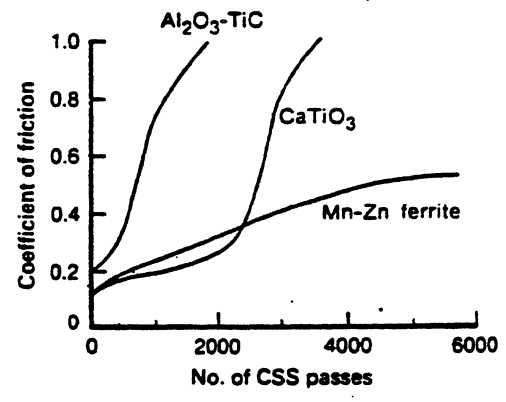


Fig. 4.70. Change of the coefficient of static friction as a function of the number of passes of Mn-Zn ferrite, CaTiO₃, and Al₂O₃-TiC head sliders on a thin-film (metal) rigid disk with sputtered carbon overcoat.

An increase in the friction is believed to be because burnishing of the disk asperities and collection of wear debris accumulated at the interface. Note that burnishing of the disk asperities increases with hardness of the slider material.

Knoop microhardness	Al ₂ O ₃ -TiC
	2300 kg/mm ²
	CaTiO ₃
	950 kg/mm ²
	Mn-Fe
	600 kg/mm ²

With some ceramic overcoats, of higher hardness than carbon, the Al₂O₃-TiC sliders are more compatible.

Interestingly, ZrO₂-Y₂O₃ (~1300 kg/mm²) overcoat shows very low wear comparing to that of carbon (~1200 kg/mm²) when tested against Al₂O₃-TiC. Possible explanation: higher surface energy of ZrO₂-Y₂O₃ results in more effective lubrication of the interface.

Effect of Lubricant Thickness

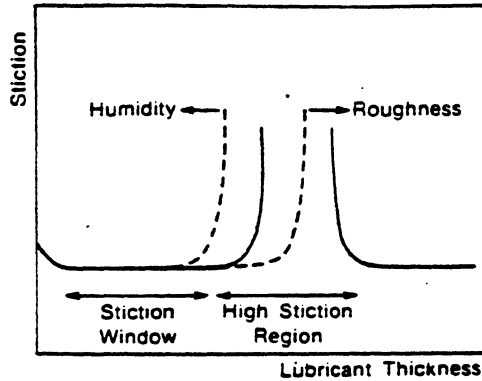


FIG. 13. Hypothetical model of stiction and its dependence on the quantity of lubricant or moisture and surface roughness.

At intermediate levels of the lubricant, the meniscus forces exert the maximum effect.

At lower levels, the range of "the stiction window" depends strongly on the surface roughness and humidity.

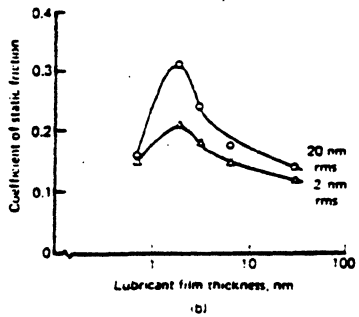
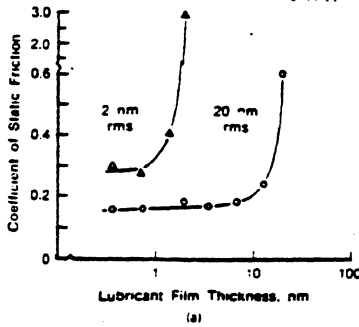


Fig. 4.73. (a) Lubricant thickness dependence on coefficient of static friction for liquid perfluoropolyether on a thin-film (metal) rigid disk at 2 and 20 nm rms surface roughness against an Al₂O₃/TiC slider. (b) Lubricant thickness dependence on the coefficient of static friction for solid lubricant on a thin-film (metal) rigid disk at 2 and 20 nm rms surface roughness against an Al₂O₃/TiC slider (Yanagisawa, 1995a).

in "Tribology and Mechanics of Magn. Storage Systems" (Ed. S. Bhushan), Vol. 2, p 21, SP-19, ASLE, Park Ridge, Ill.

11/9/94

Effect of Humidity

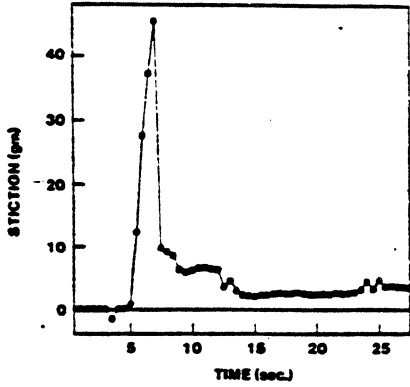


Fig. 5: Force measurement during stiction test

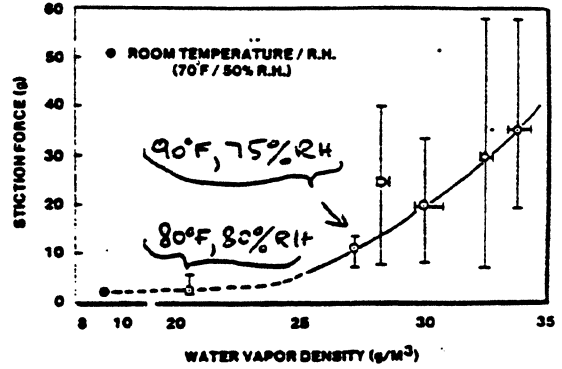


Fig. 6: Stiction tests at different water vapor densities

(Liu & Mee, 1983)
 IEEE Trans. Magn. Mag-19,
 p. 1654 (1983)

With lubricant present and water competing for adsorption sites, the surface tension component of the meniscus forces should be replaced by the interfacial surface tension of the lubricant-water mixture, i.e., $\gamma_{wl} \approx 58 \text{ mN/m}$

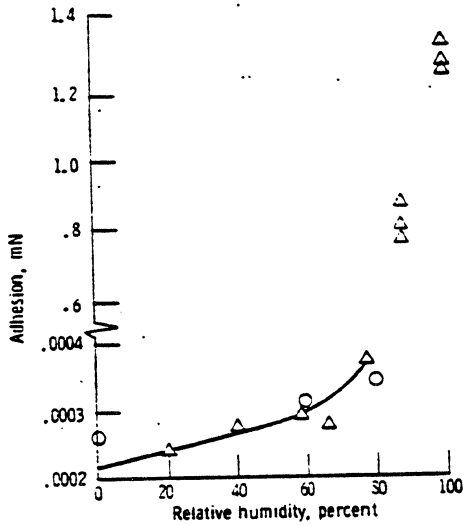
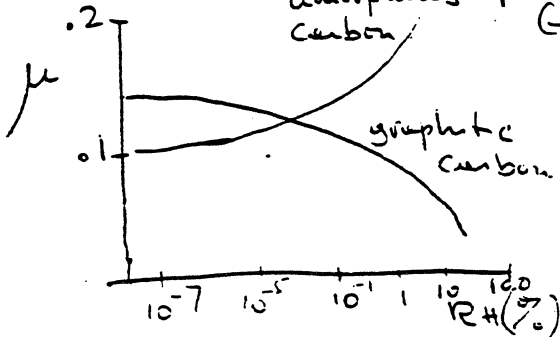


Figure 10.—Adhesion as a function of humidity for a Ni-Zn ferrite pin in elastic contact with a Ni-Zn ferrite flat in nitrogen atmosphere.

(Miyoshi et al., 1983)
~~IEEE Trans. Magn. Mag-19,~~
 amorphous p. 1654
 Carbon (1983)



a decrease in μ for graphitic carbon is due to adsorption of polar gases (water, O_2 , CO_2 , N_2 , etc.) at the edges of the crystallites which weakens the inter-layer bonding

Effect of Rest Time

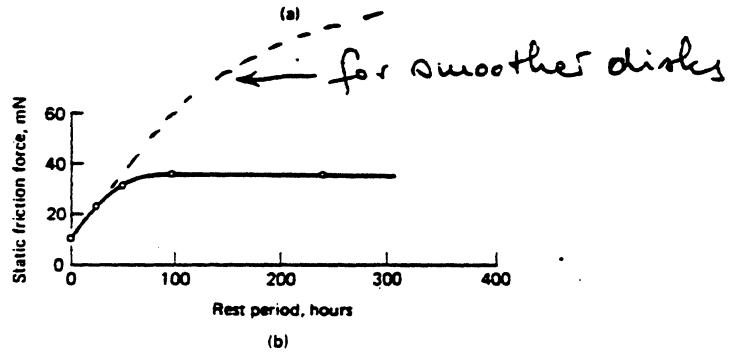
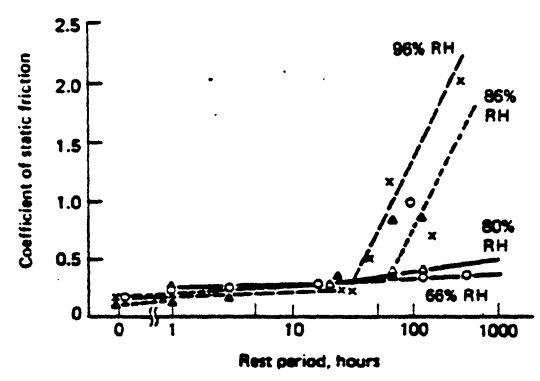


Fig. 4.82. (a) Coefficient of static friction versus rest period at different relative humidities of a particulate rigid disk against a ferrite slider (Togo et al., 1980). (b) Static friction force versus rest period at 25°C/50% RH of a thin-film (metal) disk against a Mn-Zn ferrite slider (Kaneko and Koshimoto, 1982).

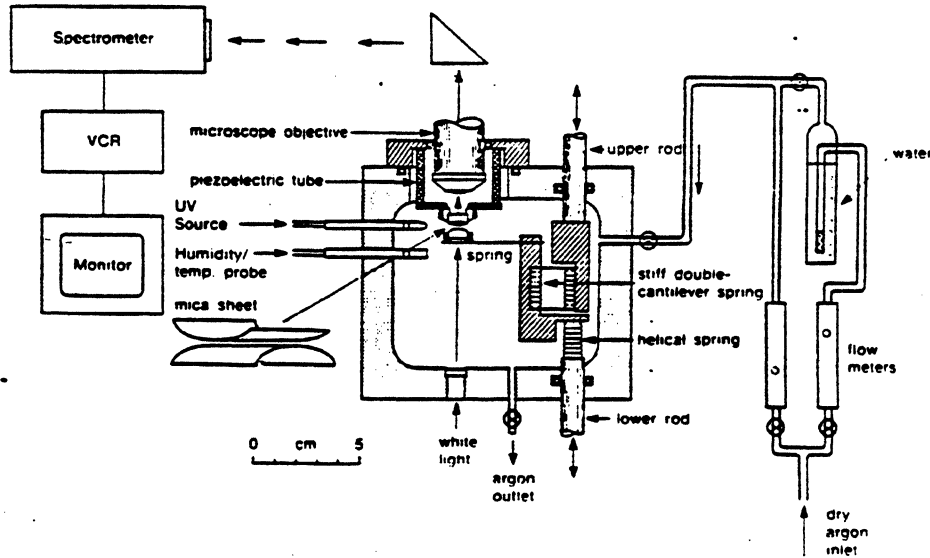
IEEE Trans. Magn.
MAG-18, 1221 (1982)

The source of friction

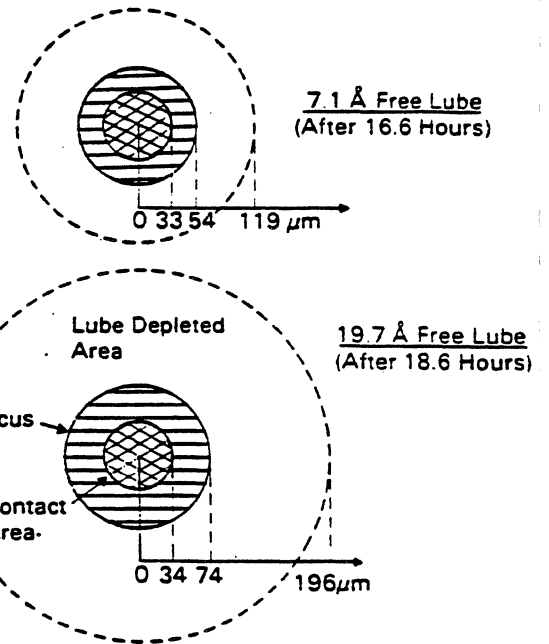
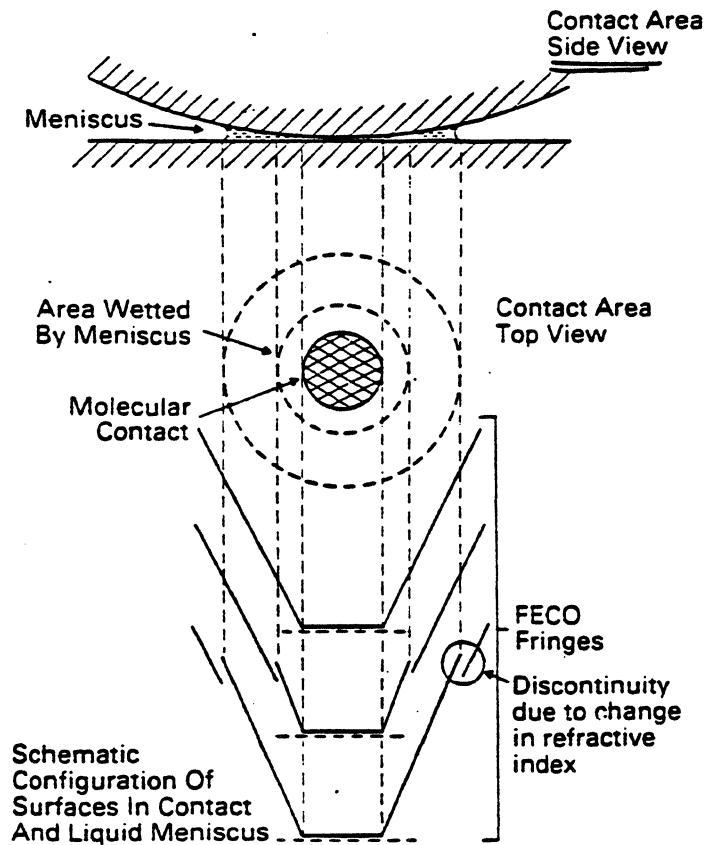
- (1) meniscus / viscous effects
- (2) mechanical deformation of the disk asperities (creep).

Both effects lead to increase in the adhesive forces and high friction.

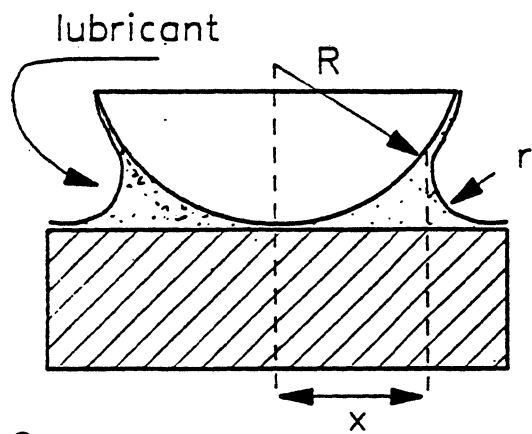
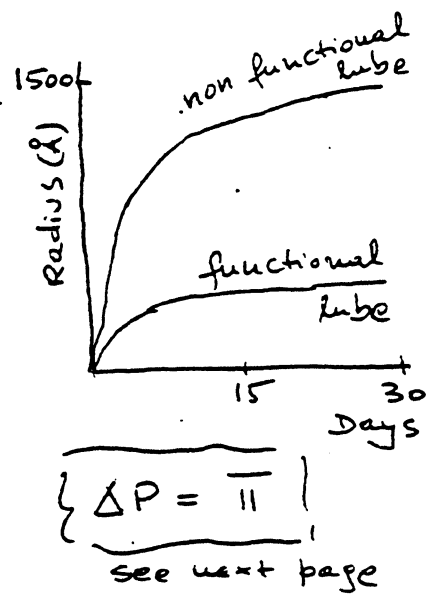
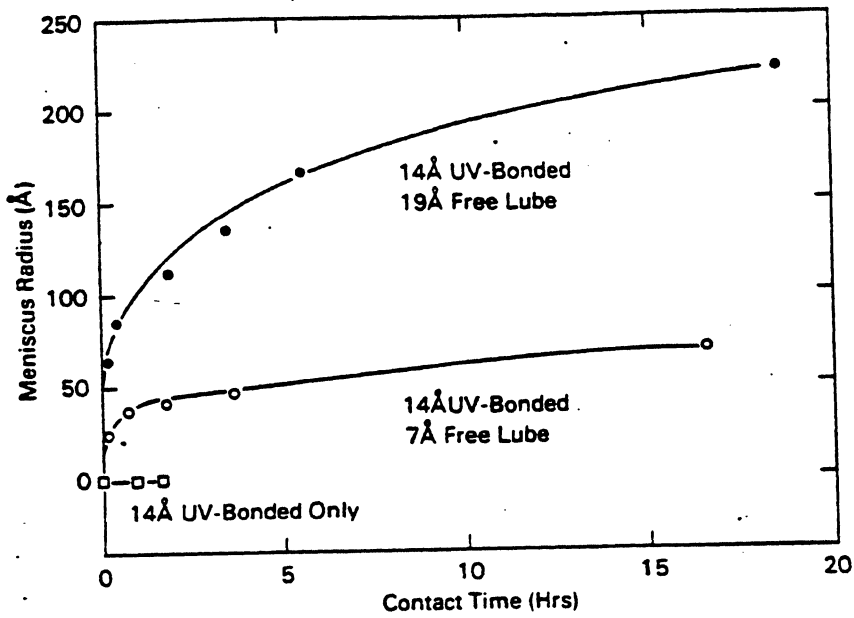
Kinetics of Meniscus Formation



Surface
Force
Apparatus



Top View through
the Contact zone



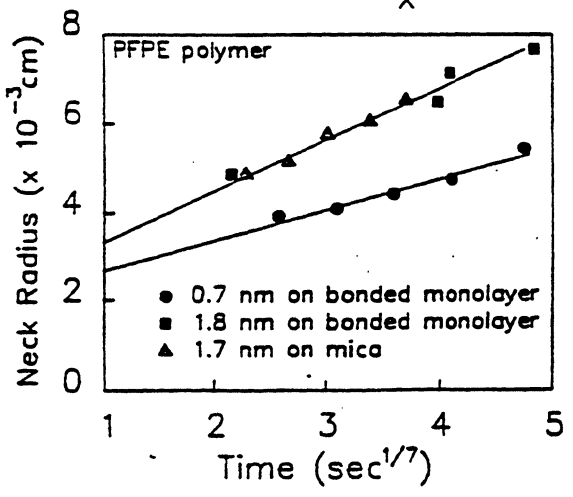
Meniscus Growth Rate

$$\frac{dx}{dt} = 2D_s \delta_s \frac{\gamma_s \Omega}{kT} \left(\frac{2R}{x^2}\right)^3$$

substituting for K and integrating:

$$\frac{x^7}{7} = \frac{16D_s \delta_s \gamma_s \Omega R^3}{kT} t$$

- δ_s = film thickness
- γ_s = surface tension (23 erg/cm²)
- Ω = molecular volume (5x10⁻²³cm³)
- R = surface radius (1.5 cm)
- kT = Boltzman constant (4.12x10⁻¹⁴erg)



$$\text{Slope} = \left(112D_s \delta_s \frac{\gamma_s \Omega}{kT} R^3\right)^{1/7}$$

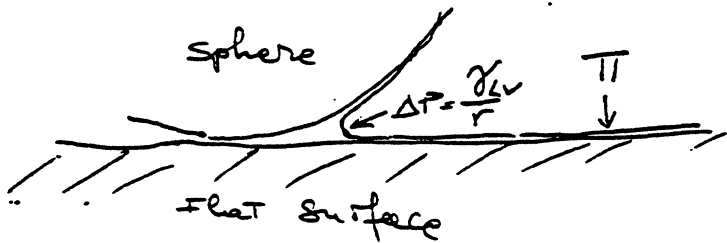
- $D_s \approx 1.2 \times 10^{-12}$ cm²/sec for thicker films
- and
- $D_s \approx 1.1 \times 10^{-14}$ cm²/sec for 7 Å film

(1) G.C.Kuczynski, Trans. AIME 185, 169 (1949)

At equilibrium, when the radius reaches a constant value, the capillary pressure (Laplace) $\Delta P = \frac{\gamma}{r}$ is equal to disjoining pressure Π .

The disjoining pressure :

$$\Pi = \Pi_{VDW} + \Pi_{el} + \Pi_{structural}$$



where

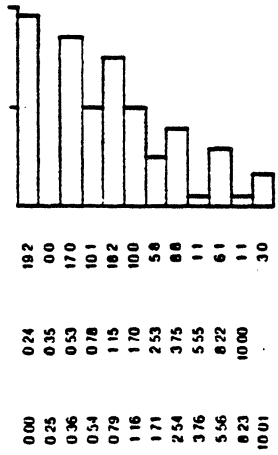
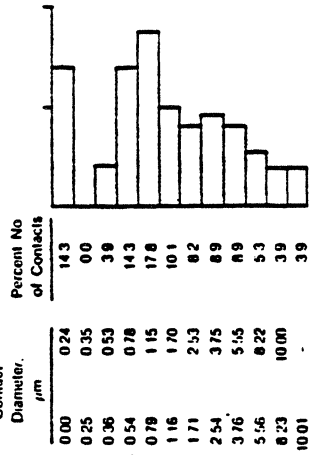
$$\Pi_{VDW} = \frac{H}{6\pi h^3}$$

Π - represents adhesive energy with which the surface attracts the lubricant molecules

Mechanical Deformations

Asperity contact diameter: mean = 2.36 μm
 standard dev = 2.94 μm
 Number of contacts = 4032/mm²
 Fraction of real area of contact = 1.84%

Asperity contact diameter: mean = 3.87 μm
 standard dev = 21.58 μm
 Number of contacts = 4968/mm²
 Fraction of real area of contact = 2.51%



(a)

(b)

FIG. 10. Log normal distribution of asperity contact diameters for a thin-film disk before and after 60 h of contact time at 0.5 N load. Note the increase in the number of contacting asperities and the real area of contact (Bhushan and Dugger, 1990).

the rate of increase in the contact diameter, number of contacts and total real area is attributed to the rate-dependent mechanical properties i.e., viscoelastic and viscoplastic deformations, and the normal stress.

13

145

Fixes to Reduce Stiction

- ✓ low ratio of the mobile to bonded area
- ✓ surface texture: (load/unload band)
- ✓ humidity control in the file
- ✓ positive crowned sliders
- ✓ small sliders
- ✓ low loads
- ✓ load/unload mechanisms

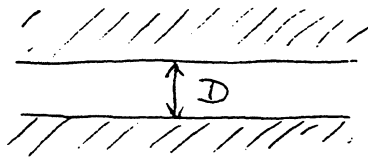
Minor fixes

- ✓ locally heated sliders
- ✓ acoustic excitation of the sliders
- ✓ radial pull
- ✓ slow accelerations

NORMAL FORCES

① Normal load (head load, $L \approx 4 \text{gms}$)

② Van der Waals Forces

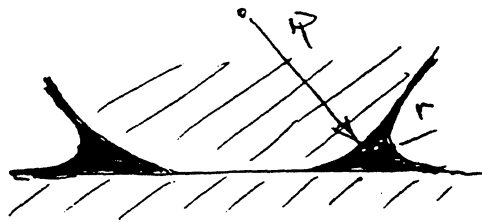


Hamaker
constant

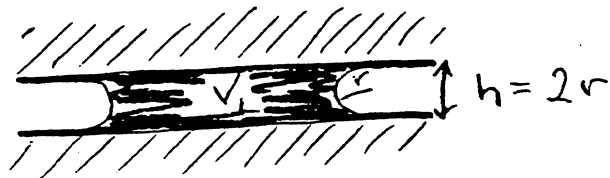
$$F_{vw} = \frac{H}{6\pi D^3} \cdot A_c$$

contact area

③ Meniscus Forces



$$F_m = 4\pi R \gamma \cos \theta$$



$$F_m = \frac{2\gamma_L}{h^2} \cdot V_L = \frac{2\gamma_L}{h} \cdot A_{\text{wetted}}$$

TANGENTIAL FORCES

$$\bar{F}_{TOTAL} = \bar{F}_{STATIC} + \bar{F}_{KINETIC}$$

(STICTION) (DRAG)

STICTION

$$\bar{F}_S = \bar{\tau} A_c$$

but $\bar{\tau}$ & A_c depend on load

$$a^3 = RL/K \text{ (Hertz eq.)}$$

(not applicable)

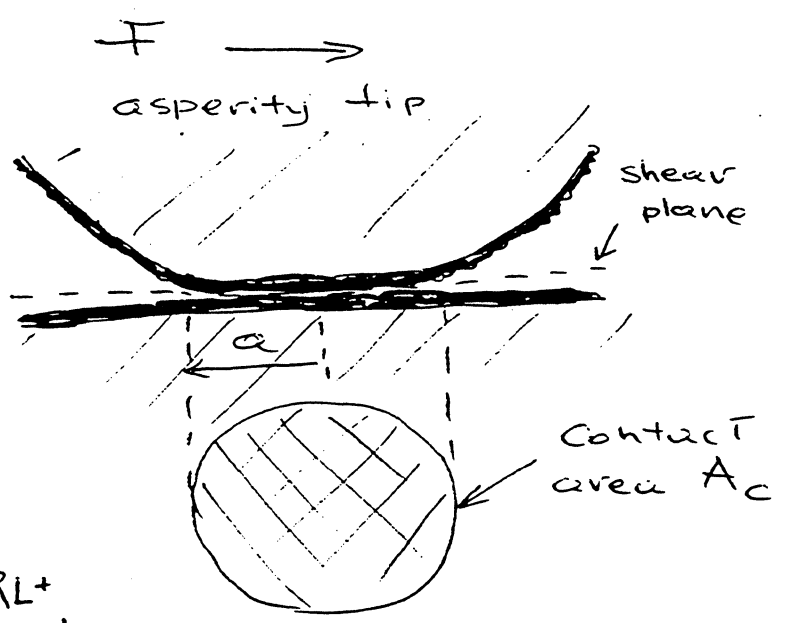
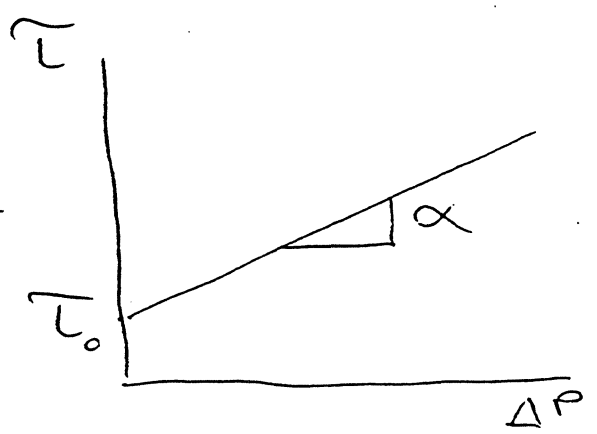
$$a^3 = \frac{R}{K} \left(L + 3\gamma_s \pi R + \sqrt{\{6\gamma_s \pi RL + (3\gamma_s \pi R)^2\}} \right)$$

additional increase in contact area.

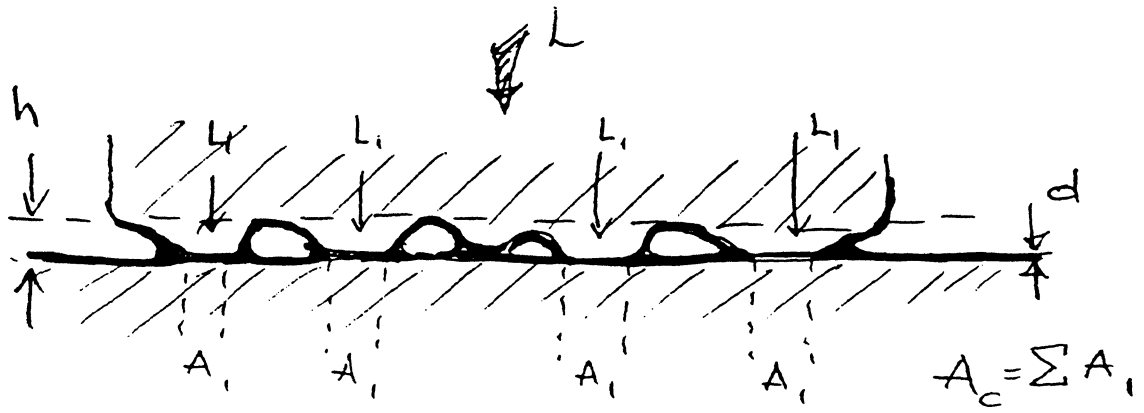
shear strength $\bar{\tau}$ depends on load and surface energy γ_s

$$\bar{\tau} = \bar{\tau}_0 + \alpha \Delta P$$

$\bar{\tau}_0$ & α depend on properties of the lubricant film



(1) Tribology Vol. 111 P. 1-10 $\rho_c = \rho < 1$ and $A = 2.4 \times 10^{-11} \text{ m}^2$



$$\Delta P = \frac{L}{A_c} + \frac{H}{6\pi D^3} + \frac{2\gamma_L}{h^2} \cdot \frac{V_L}{A_c}$$

PRESSURE $\left\{ \begin{array}{l} \text{load} \\ \text{Van der Waals force} \\ \text{meniscus effect} \end{array} \right.$

$$A_c = \sum A_i$$

$$L = \sum L_i$$

$$F_s = \tau A_c = \tau_0 A_c + \alpha A_c \Delta P$$

$$F_s = \tau_0 A_c + \alpha \left(L + \frac{H}{6\pi D^3} \cdot A_c + \frac{2\gamma_L}{h^2} \cdot V_L \right)$$

if $V_L = d_m \cdot A_T$ (+thickness of free lube x geometric contact area)

$$F_s = \tau_0 A_c + \alpha \left(L + \frac{H}{6\pi D^3} \cdot A_c + \frac{2\gamma_L d_m}{h^2} \cdot A_T \right)$$

needed to know:

τ_0 (shear strength at zero load)
 pin-on-disk and surface force app. experiments

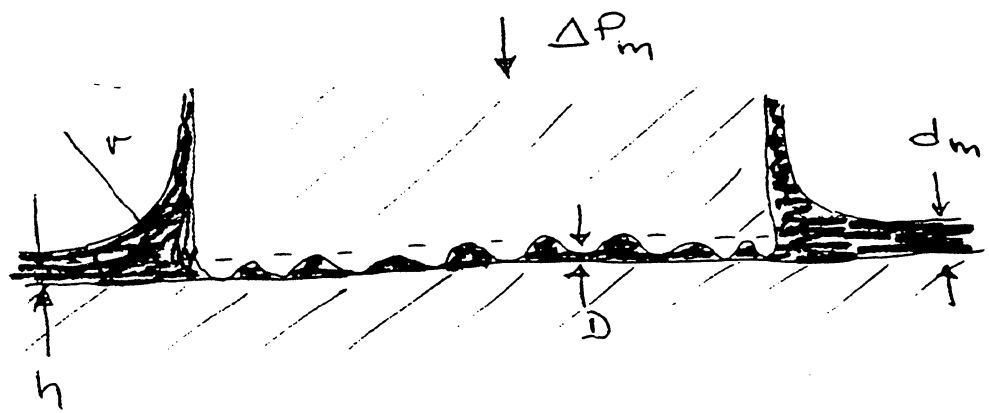
A_c (contact area) no simple technique to measure A_c
 Surface force apparatus (SFA)

H (Hamaker constant)
 SFA, kinetics of meniscus formation
 $\frac{\gamma}{D^3} = \frac{H}{6\pi D^3}$

γ_L (Surface tension)
 Wilhelmy plate technique

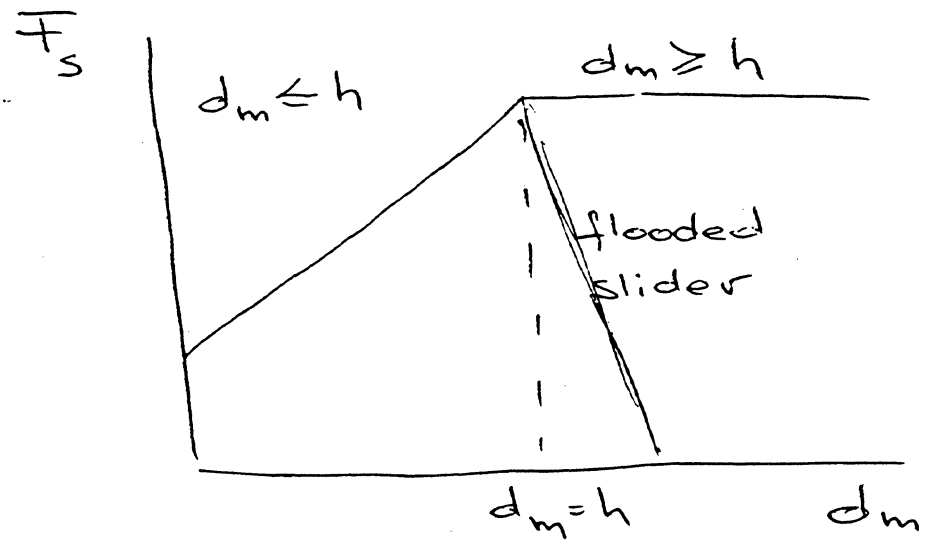
α (pressure coefficient) - pin-on-disk exp't.

What if $d_m > h$



Since $\Delta P_m = \frac{\gamma L}{r} = \frac{\mu}{6\pi d_m^3}$

$$F_s = \tau_o A_c + \alpha \left[L + \frac{\mu A_c}{6\pi} \left(\frac{1}{D^3} + \frac{1}{d_m^3} \right) \right]$$



if $A_T = 1 \text{ mm}^2 (1 \times 10^{-6} \text{ m}^2)$
 $A_c^* = 4.5 \times 10^{-9} \text{ m}^2 (0.5\% \text{ of } A_T)$
 $\tau_o = 2 \times 10^6 \text{ N/m}^2$
 $\alpha = 0.21$

load $L = 4 \text{ gms } (0.04 \text{ N})$

Hamaker constant $H = .75 \times 10^{-20} \text{ J}$

lubricant thickness $D = 15 \text{ \AA } (15 \times 10^{-10} \text{ m})$

viscosity $\gamma_L = 20 \times 10^{-3} \text{ N/m}$

Thickness of free lube $d_m = 10 \text{ \AA } (10 \times 10^{-10} \text{ m})$

average spacing between faces $h = 100 \text{ \AA } \approx 5 \text{ rms } (1 \times 10^{-8} \text{ m})$

At zero load, $L=0$, and no free lube
 bonded monolayer

$F_s = \tau_o A_c = 0.9 \text{ gms } (\text{pin-on-disk})$

True contact area

$\therefore A_c = F_s / \tau_o = .009 \text{ N} / 2 \times 10^6 \text{ N/m}^2 = 4.5 \times 10^{-9} \text{ m}^2$

now

$F_s = \tau_o A_c + \alpha \left(L + \frac{H}{6\pi D^3} A_c + \frac{2\gamma_L d_m}{h^2} A_T \right)$ get lube migration.

$F_s = .157 \text{ N} = 15.7 \text{ gms}$

depend on the free lube thickness

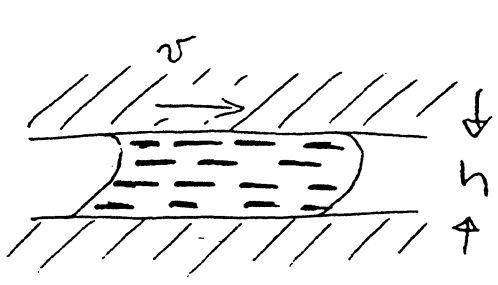
if $d_m = 0 \text{ \AA}$ no meniscus force,

$F_s = .02 \text{ N} = 2 \text{ gms}$

if $d_m = h$ (maximum flooding)

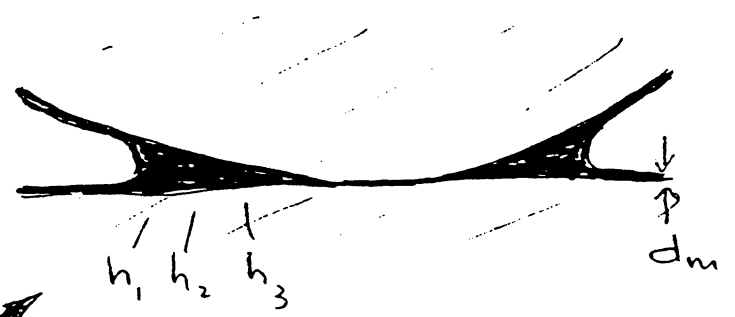
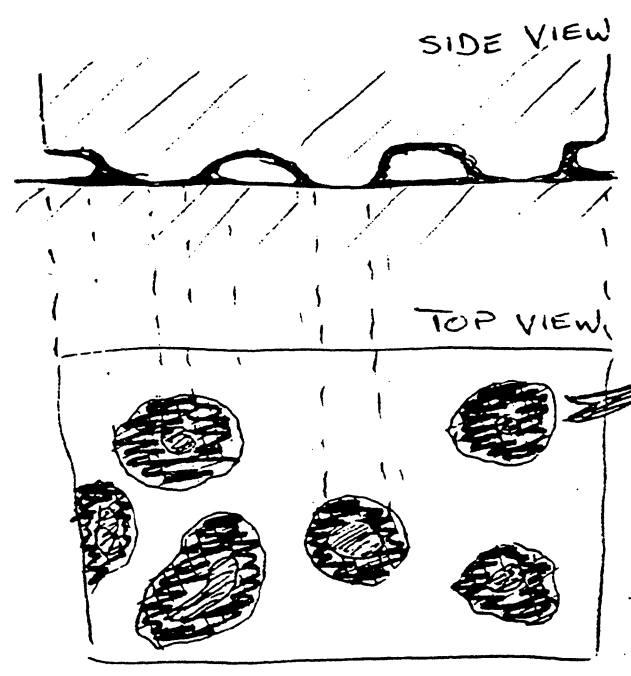
$F_s = 92 \text{ gms}$

DRAG (Viscous Component)



$$F_v = \eta \frac{v}{h} \cdot A_w$$

sliding velocity v
 wetted area A_w
 lube viscosity η
 High viscosity - high resistance



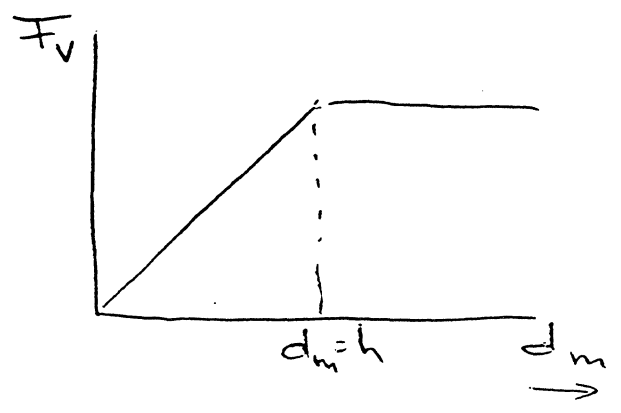
$$F_v = \eta \frac{v}{\sum h} \cdot \sum A_w$$

but since $\eta = f(\text{shear rate } \dot{\gamma} \text{ MWt})$

$$F_v = v \sum_{h=1}^n \left(\eta \cdot \frac{A}{h} \right)$$

assuming $A_w = \frac{V_L}{h} = \frac{d \cdot A_T}{h}$

$$F_v = \eta \frac{v d_m}{h^2} \cdot A_T$$



if $\eta = 20 \times 10^{-3} \text{ N}\cdot\text{s}/\text{m}^2$ (20 cP)

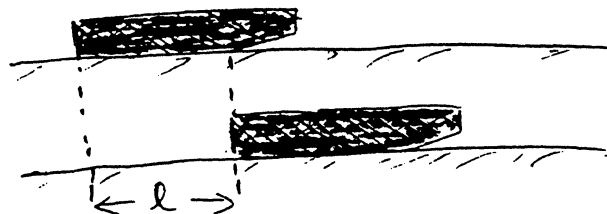
$h = 100 \text{ \AA}$

$A_T = 1 \text{ mm}^2$

$d_m = 10 \text{ \AA}$

$l = 1 \text{ mm}$

$v = 0.14 \text{ m/s}$ at $a = 10 \text{ m/s}^2$

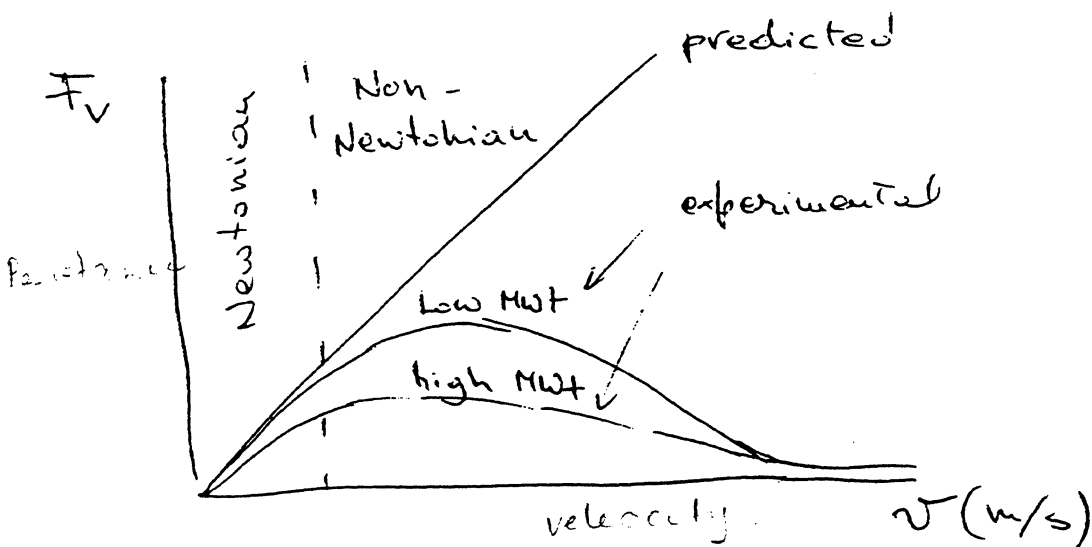


$\therefore \overline{F}_v = \eta \frac{v d_m}{h^2} \cdot A_T = 0.028 \text{ N} = 2.8 \text{ gms}$

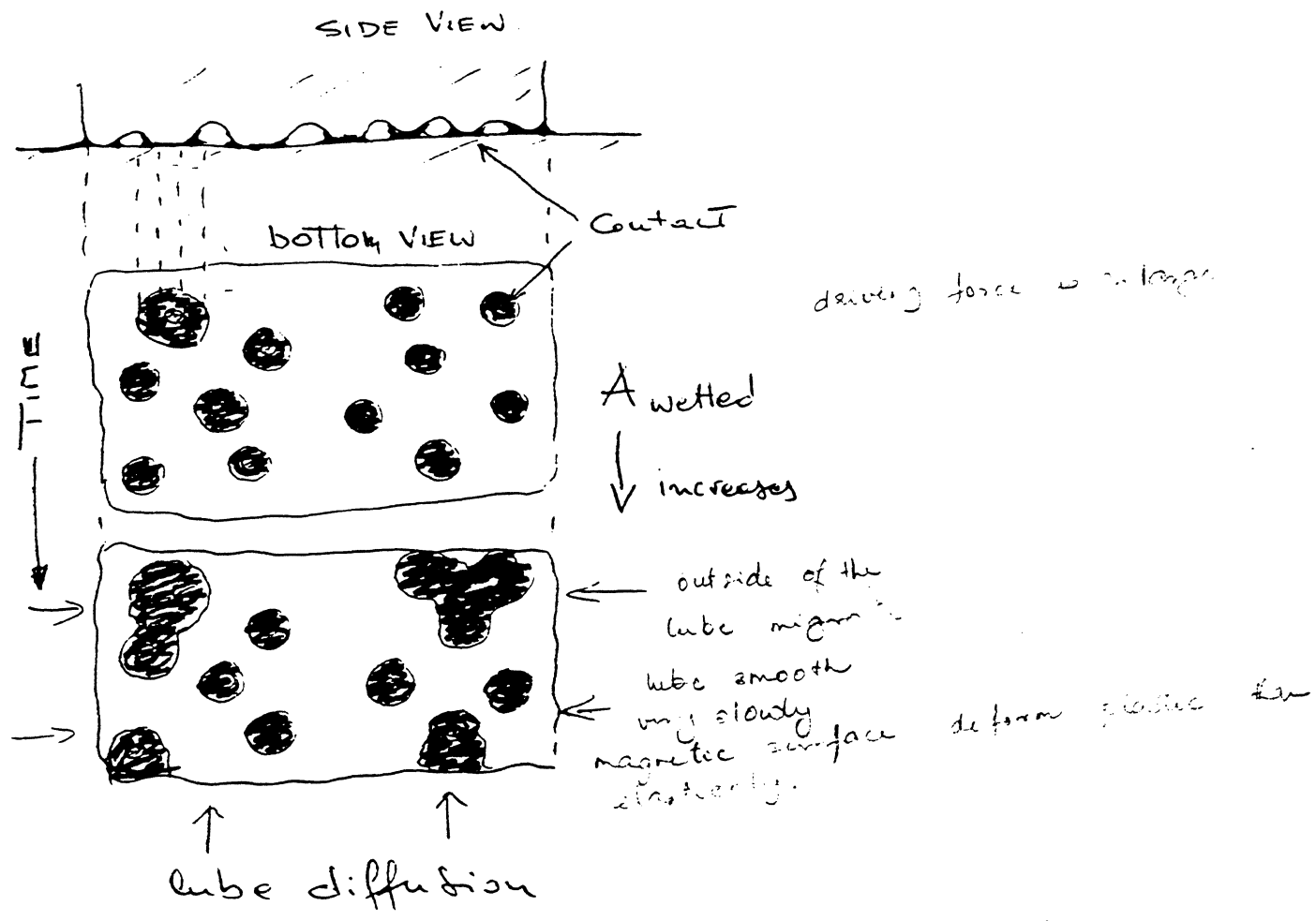
if $d_m = h$

$\overline{F}_v = 28 \text{ gms}$

Non-Newtonian Drag

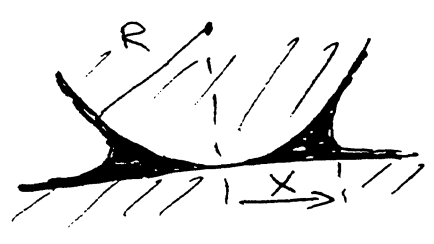


REST STICTION



$$F_s = \tau_0 A_c + \alpha \left(L + \frac{H}{6\pi D^3} A_c + \frac{2\gamma L}{h} A_{\text{wetted}} \right)$$

ISOLATED ASPERITY



$$A_w = \sum x^2 \frac{1}{h}$$

and $x \approx t^{1/4}$

↑ extent of meniscus
times go out pressure increase

FRICTION

FRICTION is the resistance to relative motion of contacting bodies. The degree of friction is expressed as a coefficient of friction μ , which is the ratio of the force F_T required to initiate or sustain relative motion to the normal force F_N that presses the two surfaces together.

The basic law of friction was put forward by Leonardo da Vinci whose notebook illustrates with sketches that:

1) $F_T \propto F_N$ and

2) $\frac{F_T}{F_N}$ is independent of the apparent contact area.

These laws are often referred as Amontons laws after the French army engineer, presented his findings to the Royal Academy in 1699.

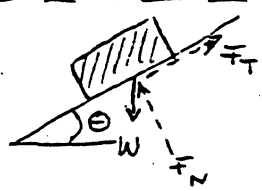
The three quantitative relations are as follows:

I) "The frictional force is directly proportional to the normal load"

$$F_T = \mu F_N$$

this relationship enables us to define a

Coefficient of friction μ . Alternatively,



$$F_T = W \sin \theta$$
$$F_N = W \cos \theta$$

$$\mu = \frac{F_T}{F_N} = \tan \theta$$

the above law can be expressed in terms of a frictional angle θ

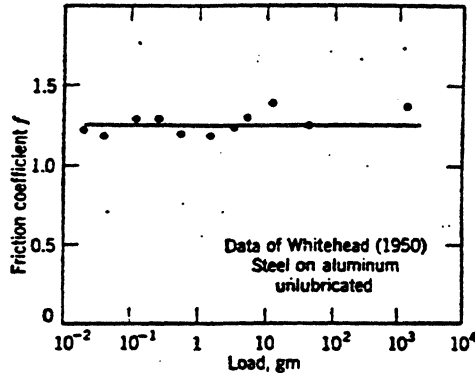


Fig. 4.6. For steel on aluminum, the friction is independent of load over a wide range of loads.

Deviations: occur mostly with very hard materials like diamond or very soft materials like Teflon.

often
$$F_T = c F_N^x$$

where c is a constant and x varies from $\frac{2}{3}$ to 1.

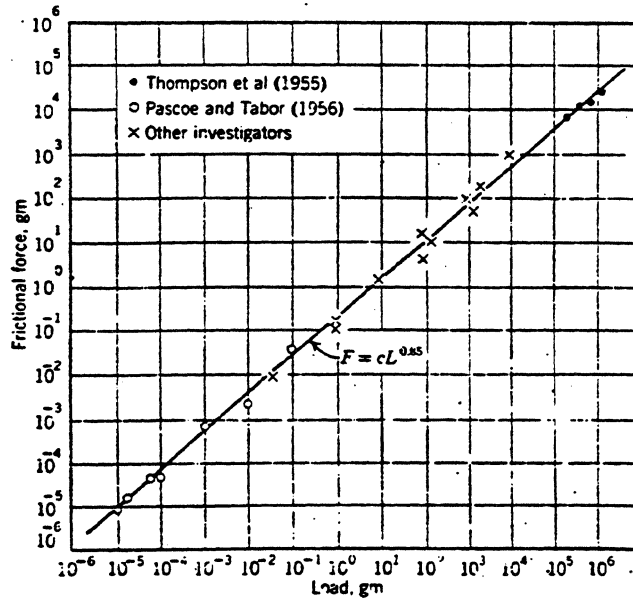


Fig. 4.8. Data collected by Allan (1958) on the effect of load on the friction of Teflon.

Another case is when surface properties (oxide films) contribute to friction significantly. This law does not apply to elastic and viscoelastic materials (such as rubber).

effect of oxide removal

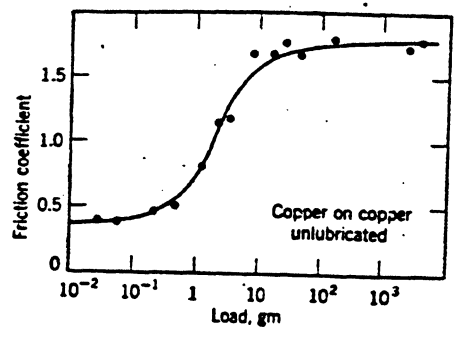
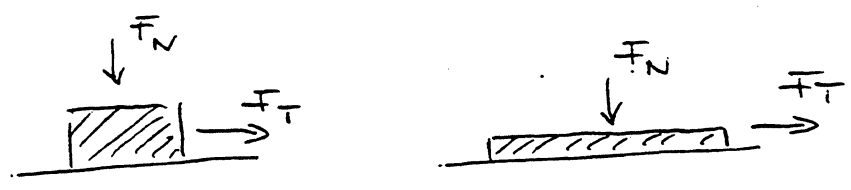


Fig. 4.9. Data of Whitehead (1950) on the variation of the friction of copper with the applied load.

II) "The frictional force is independent of the apparent area of contact".



Thus large and small objects have the same coefficient of friction.

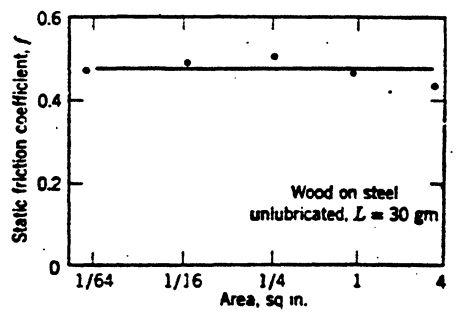
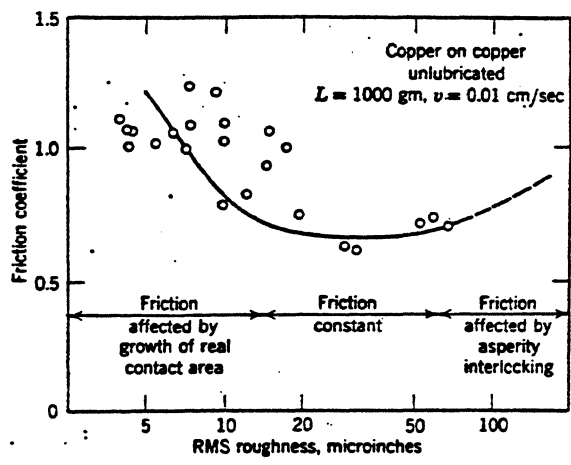


Fig. 4.7. The effect of changes in contact area on the friction of wood on steel. No significant variation is found.

Deviations: occur with very smooth and very clean surfaces. Also at high pressures when $A_r \approx A_{apparent}$ under the conditions of



Conditions of strong interaction between the surfaces takes place, so that the friction becomes independent of the load but \approx to the apparent area of contact (the real area of contact).

Fig. 4.14. Plot of friction against roughness shows a negative slope region caused by excessive junction growth, and a positive region caused by the interlocking of asperities. In between, friction is independent of roughness.

III "The kinetic friction is independent of the velocity of sliding". (3rd Law of Friction provided by Coulomb).

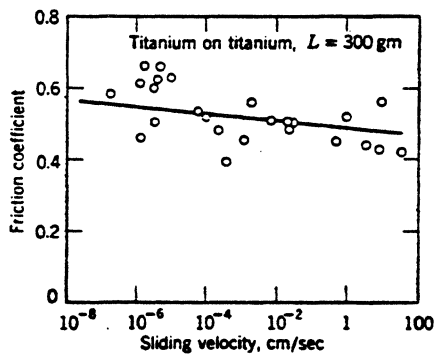


Fig. 4.12. Friction-velocity curve of hard materials has slightly negative slope over wide range.

Usually the slopes of μ vs velocity are fairly small, that the friction coefficient change by just a few percent as the speed is varied by a factor of

Actually, this law is not valid for any material as shown in the next figure.

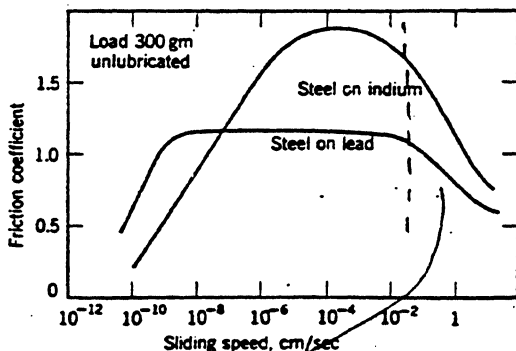


Fig. 4.13. Friction-velocity curve of materials which creep has positive slope at low speeds, negative slope at high speeds.

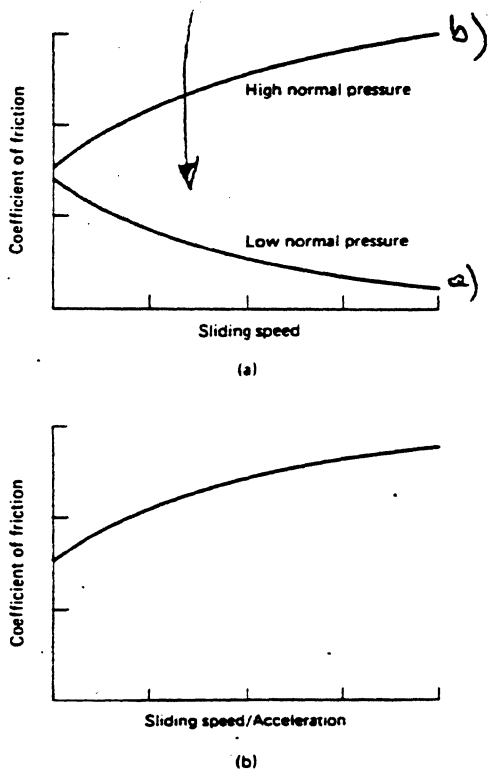


Fig. 4.2. Coefficient of friction as a function of sliding speed in (a) a dry contact and (b) a lubricated contact.

Note, however, that over a speed range of as much as a factor of 10^{10} the friction coefficient varies by a factor of 2

Changes in the sliding speed result in a change in the shear strain rate which can influence the mechanical properties of the mating materials.

a) the strength of many materials is greater at higher shear strain rates which results in a lower real area of contact.

b) high sliding speed can result in high interface temperatures which can reduce the strength of the materials.

c) the stress required to shear the liquid generally increases with an increase in the sliding velocity and the acceleration. For Newtonian fluid

$$\frac{F_T}{A_{real}} = \frac{\eta}{h} v$$

where η = viscosity
 h = film thickness
 v = sliding velocity

The Static Friction Coefficient

It is well known that the friction force req^d to ~~maintain~~ start sliding is usually greater than the force required to maintain sliding.

about 10% increase

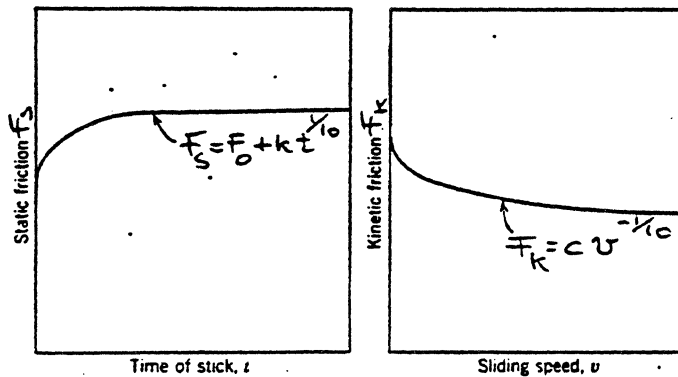
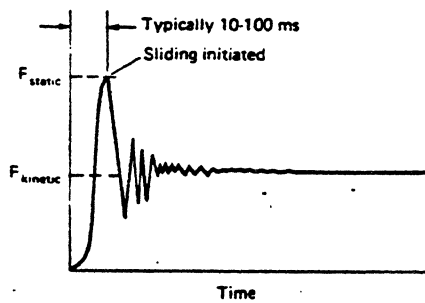


Fig. 4.10. Typical plot of static coefficient as a function of time of stick (Rabinowicz, 1957).

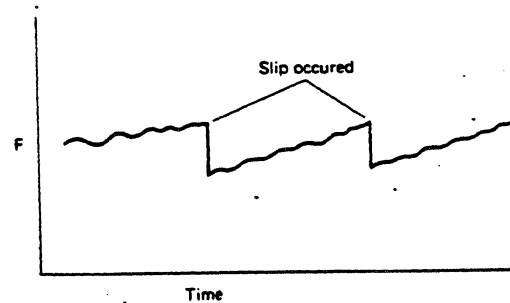
Fig. 4.11. Typical plot of kinetic coefficient as a function of sliding speed (Barwell, 1956).

can hear the noises

The Stick-Slip Phenomena ($F_s \gg F_k$)



Friction force vs time of displacement



Kinetic friction force vs time

All stick-slip processes are caused by the fact that the friction force does not remain constant as a fx of some other variable such as distance time or velocity.

When a tangential force is applied to one of the surfaces, the two remain in adhesive contact until the potential energy of the applied force exceeds the adhesive minima. A rapid "slip" of the two surfaces then occurs and the surfaces continue sliding until the adhesive energy exceeds the kinetic energy. At this point the surfaces stick together again and the cycle is repeated.

Reducing Stick-Slip amplitude

Methods used:

- by i) increased damping
- ii) increased inertia
- iii) increased stiffness of the spring
- iv) choosing a lubricant which results

in $F_s = F_k$ (i.e., boundary lubricant).
 enough lube - to give a sufficient lubricity, lube - is poor

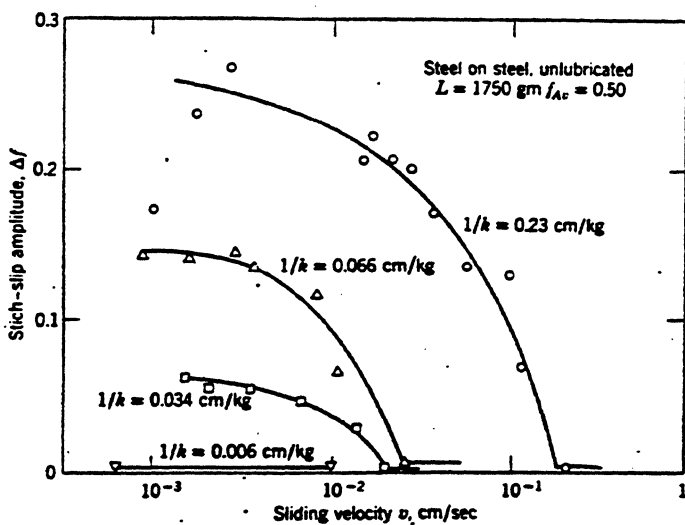
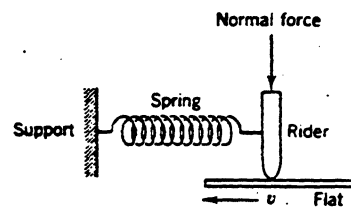


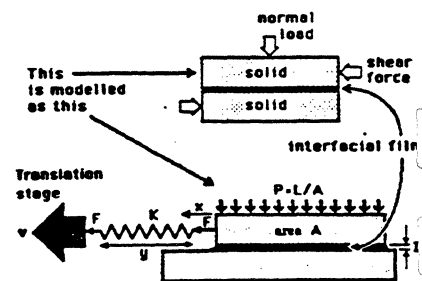
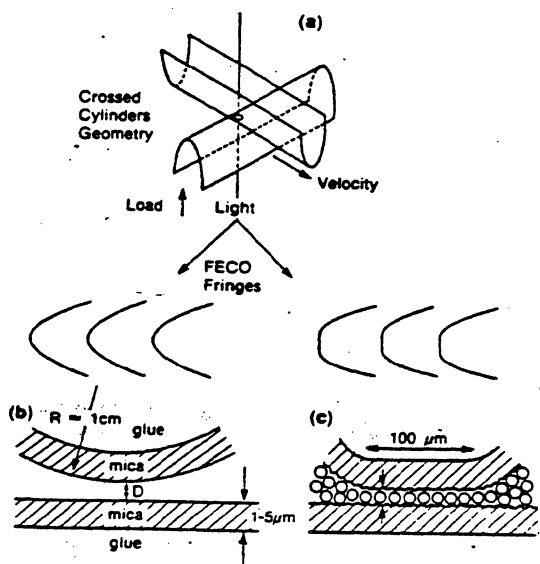
Fig. 4.44. Stick-slip amplitude for various spring stiffnesses.



Representation of a typical friction apparatus.

Velocity at which $\Delta f = c$ correlates with the displacement between the surfaces correspond to $\sim 10^{-3} \text{ cm}$ (size of the junctions in this system).

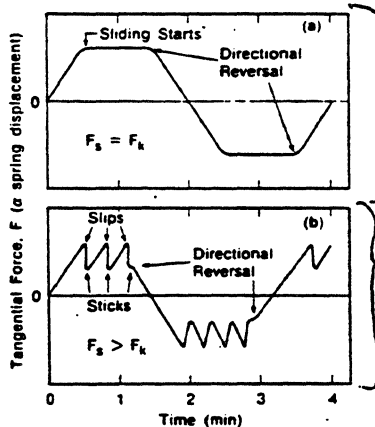
Molecular Aspects of the Stick-Slip Phenomenon



- v Velocity of translation stage
- x Total displacement of upper surface
- v_x Velocity of upper surface ($v_x = dx/dt$)
- K Spring stiffness
- y Spring length
- F Frictional force (spring tension = $K\Delta y$)
- A Contact area
- L Externally applied load
- P Externally applied pressure ($P = L/A$)
- D Thickness of film

Fig. 1. (a) Crossed cylinder configuration of mica sheets, showing formation of the contact area. Schematic drawings of the fringes of equal chromatic order (FECC) observed in the spectrometer are shown for (b) two mica surfaces separated by distance D and (c) two flattened mica surfaces separated by a single monolayer of organic molecules. Typical experimental parameters are as follows: undeformed radius of surfaces (R) from 1 to 2 cm; externally applied loads (L) up to 50 g and down to negative loads; contact diameters ($2r$) up to $100\ \mu\text{m}$; areas (A) up to $10^{-4}\ \text{cm}^2$; sliding velocities (v) up to $40\ \mu\text{m}\ \text{s}^{-1}$; number of liquid layers (n) separating surfaces during sliding from 1 to 4, corresponding to gap thicknesses D up to $25\ \text{\AA}$.

Figure 1. Schematic representation of experimental set-up used to measure shear forces and other dynamic properties of liquids in ultrathin liquid films between two molecularly smooth mica surfaces. The experimental details are given [9].



typical of a "good" lubricant, i.e., bonded PFPE lubes, where $F_s = F_k$

poorly lubricated interface

Fig. 3. Drawings of some typical chart-recorder traces, showing both steady friction (where the static and kinetic friction coefficients, F_s and F_k , are equal) and stick-slip friction where $F_s > F_k$, the stick-slip amplitude being given by $F_s - F_k$. (a) Sliding of mica in ambient environment and (b) while separated by molecules of simple neat liquids. In the latter case, the amplitude and frequency of stick-slip was found to depend on load, sliding velocity and the number of intervening molecular layers [8]. It should be noted that, before each slip, the surfaces are pinned together with the slope of the force vs. time trace proportional to the driving velocity v and the spring constant.

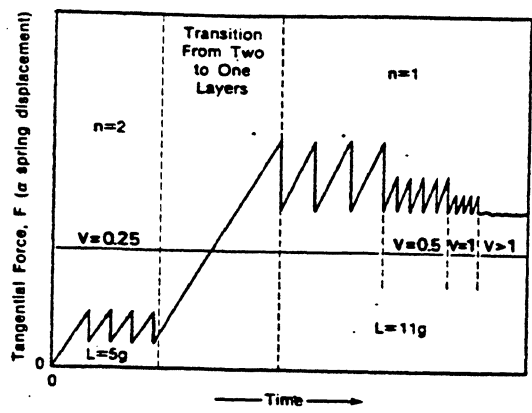


Fig. 1 Chart recorder trace of the frictional force as a function of time after commencement of sliding at various steady state driving velocities, v ($\mu\text{m/s}$), and externally applied loads, L (g). n is the number of liquid OMCTS layers between the surfaces during sliding.

The "Cobblestone Model"

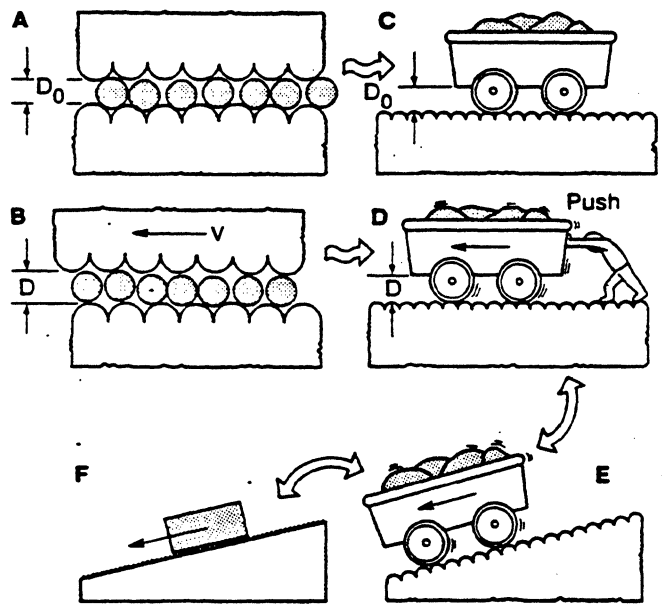


Fig. 4 The "Cobblestone Model". A: At equilibrium, the molecules assume energetically favorable positions, and the surfaces are at their closest separation, D_0 . B: During sliding the surfaces separate a bit ($D > D_0$) so as to allow the intervening molecules to roll-over and allow sliding. C & D: Analogous situation to A & B where cartwheels are pressed down onto a cobblestone road by gravity. E: The "push" of D can be brought about by inclining the road. F: A similar phenomenon occurs for a block of material lying on an inclined plane with sand in between the two surfaces.

$\Delta D F_{ad} = \Delta d F_T =$
 $\epsilon 2 \gamma_s A$ where
 $\epsilon 2 \gamma_s$ is some frac
of the surface energy
and A is the area
of contact. If
 $\Delta D \approx \Delta d \approx 1 \text{ \AA}$ and
 $\epsilon = 0.1$ then
 $F_T/A \approx \frac{\epsilon 2 \gamma_s}{\Delta d} \approx$
 $\approx 5 \times 10^7 \text{ N/m}^2$
measured 2×10^7
for cyclohexane

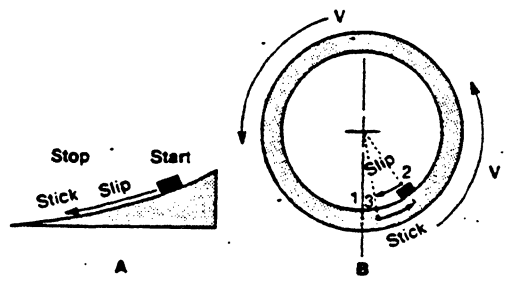
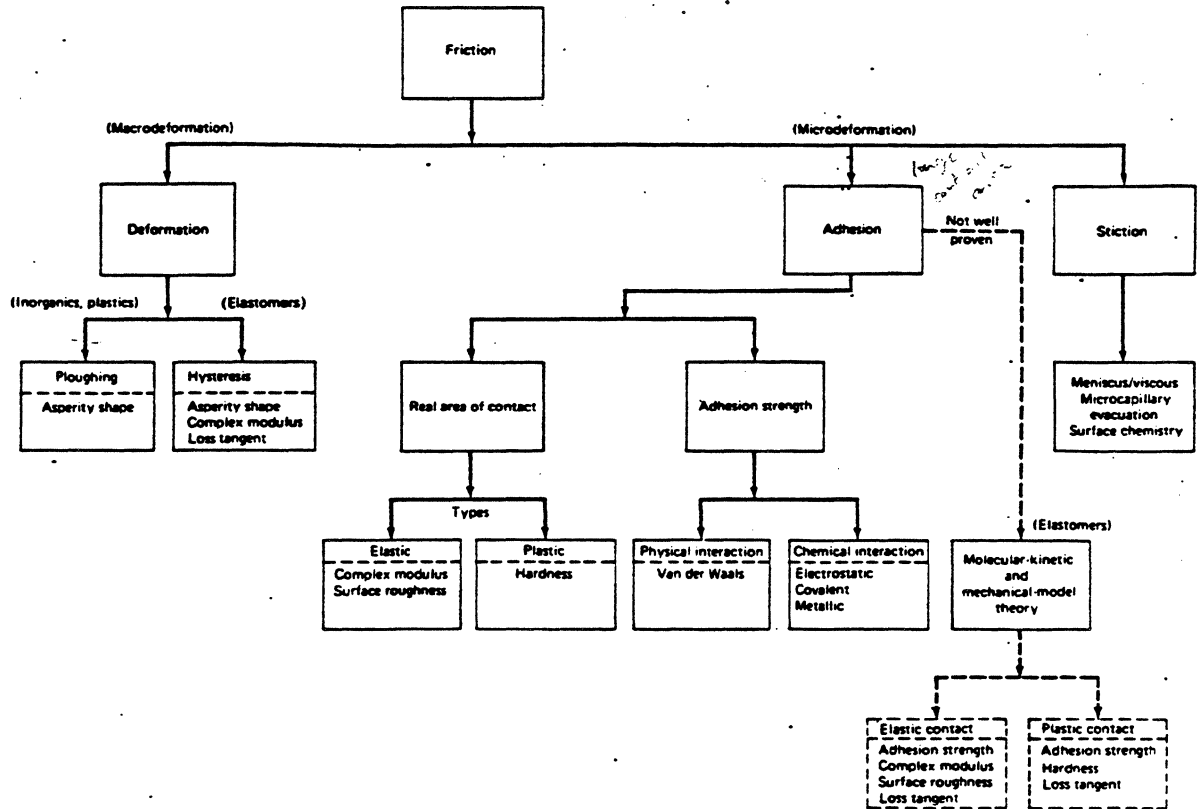


Fig. 5 The "cobblestone" model for stick-slip between two surfaces.

It is likely that the stick-slip phenomenon is a cooperative one, involving the orchestrated movement of all the molecules between the surfaces, especially at the slip.



Basic Mechanism of Friction

$$F_{\text{Total}} = F_{\text{adhesion}} + F_{\text{deformation}}$$

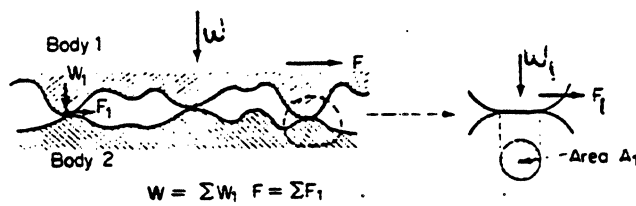


Fig. 3.2. The local asperity contacts between surfaces.

The Simple Adhesion theory

$$A_1 = \frac{W_i}{H} = \frac{\text{load}}{\text{hardness}}$$

$$F_i = A_1 \tau$$

where F_i is the friction force for the junction and τ is the shear strength per unit area which is a property of the material (metal-to-metal contact) or the lubricant film (fully lubricated)

contact area

Since $A_1 = w_1 / H$ and $F_1 = A_1 \tau$

$$F_1 = \frac{w_1 \tau}{H}$$

the friction is thus \propto to the load and is independent of the size of the bodies:

the coefficient of friction μ is then

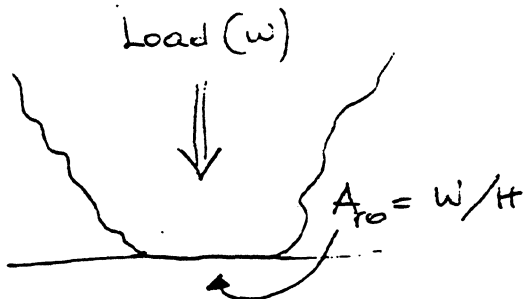
$H \approx 3Y$
 $\tau \approx \frac{1}{2} Y$

$$\mu = F/W = \tau/H$$

since for most materi: $\tau \approx 0.2 H$ so $\mu \approx 0.2$

this is far too small. For clean metals μ is of order of 10-100!

Explanation — junction growth



Under combined normal and tangential stresses the junction area grows according to an empirical law (Tabor, 1950) of the form:

form:

where α has a value of order 9

no good like - τ - high surface roughness

Ratio A_r/A_0

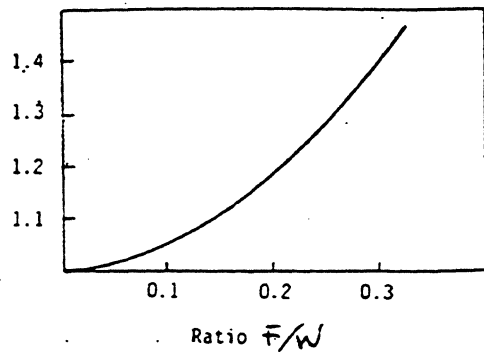


Figure 4.13 Junction growth under combined normal and tangential forces.

Effect of Surface Films

Under what conditions will junction growth be so small that its effect may be neglected?

Analysis shows that a modest reduction in the interfacial strength ($\bar{\tau}$) produce a very large reduction in junction growth.

$$\mu = \frac{F}{W} = \frac{A \bar{\tau}_{tube}}{A H} \approx \frac{\bar{\tau}_{tube}}{H_0} \approx \frac{1}{2} \frac{\bar{\tau}}{H_0} \approx 0.1$$

if, however, the head/disk interface is lubricated with weakly attached (van der Waals forces) lubricant molecules, the combined action of normal and tangential forces can result in the lubricant displacement and a significant increase in contact area and adhesion.

Load Dependence of Simple Friction Laws

from Derjaguin⁽¹⁾

$$F_T = \mu (F_N + F_A) \quad F_A = \text{attractive pull-off force}$$

and from Tabor's theory⁽²⁾

$$F_T = A \bar{\tau} \quad \text{where } \bar{\tau} = f(\text{pressure})$$

where $\bar{\tau} = \bar{\tau}_0 + \alpha P$ where $\alpha = \text{pressure coeff}$

(1) "Adhesion of Solids" Consultants Bureau, N.Y., 1978

(2) "The Adh. & Lubric. of Solids", Part I, Clarendon Press, Oxford, 1951.

and $F_T = A (\tau_0 + \alpha P)$

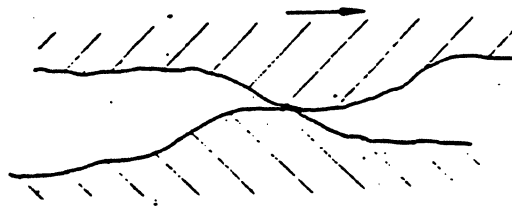
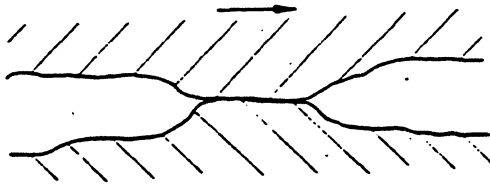
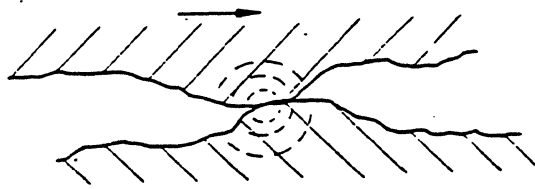
$$F_T = \frac{W}{P} (\tau_0 + \alpha P)$$

or

$$\left\{ \frac{F_T}{W} = \tau_0/P + \alpha = \mu \right\}$$

how lubricant molecule behave as a function of pressure

Microscopic View of Sliding Friction



stage I:
elastic deformation
plastic deformation
ploughing

stage II:
adhesion bonding

stage III:
shearing of junctions
elastic recovery

Schematic
Representation
of a unit
event in
the friction
process

and total macroscopic friction force F_F :

$$F_F = \sum F_1 + \sum F_2 + \sum F_3 + \sum F_4$$

where F_1 = resistance caused by elastic displacement

F_2 = " " " by plastic displacement

F_3 = resistance due to shearing (ploughing)

F_4 = " " " to shearing (adhesion)

The Plowing Component

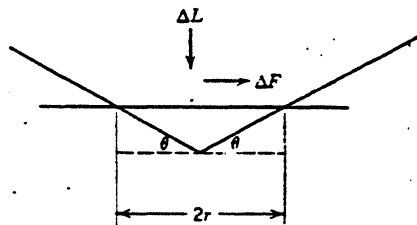


Fig. 4.20. Schematic illustration of a cone pressed into a flat surface. During sliding, a groove is swept out of projected area $r^2 \tan \theta$.

sharp asperities on a hard surface can produce scratches when slid over a soft surface and in addition to the friction force is involved.

During sliding, the penetrated area A_p , swept out is given by

$$A_p = \frac{1}{2} 2r \cdot r \tan \theta = r^2 \tan \theta$$

and $F = A \bar{L} + r^2 \tan \theta$

or $\bar{F} = \bar{L} r^2 + r^2 \tan \theta$

$$L = \bar{L} r^2 H$$

$$\mu = \frac{F}{L} = \frac{\bar{L}}{H} + \frac{\tan \theta}{H}$$

for really rough surfaces (e.g. sand) $\tan \theta \geq 0.2$ or larger and the plowing term is large. Usual $\tan \theta$ is about 0.05 or less, the plowing becomes negligible.

Note: This contribution is significant during disk finishing operation.

Possible effects that can occur between the intersecting asperities leading to energy transmission and dissipation

I. Introduction of mechanical energy into the contact zone

- formation of real area of contact

II. Transformation of mechanical energy

- elastic deformation and elastic hysteresis
- plastic deformation
- ploughing
- adhesion

III. Dissipation of mechanical energy

(a) Thermal transformation

- generation of heat and entropy

(b) Storage

- generation of point defects and dislocations
- strain energy storage
- phase transformations

(c) Emission

- thermal radiation and conduction
- phonons (acoustic waves, noise)
- photons (triboluminescence)
- electrons (exo-electrons)

be very hungry for e
 one of the main
 generate the wear → break the bond.

Storage of Energy

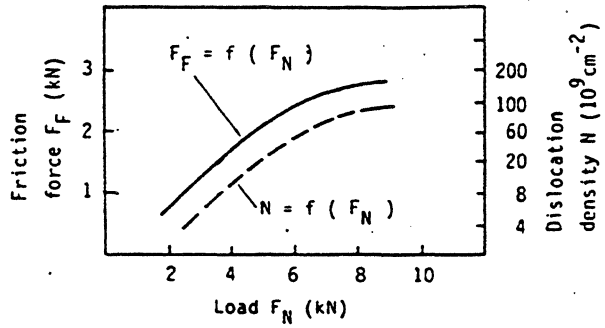


Figure 4.19 Friction force and dislocation density (Ref. 4.73).

density of dislocation is a function of load and elastic and plastic properties of the surfaces. The stored energy usually small accounts for less than 1% of the energy expended in friction.

Emission of Phonons

the generation of friction-induced acoustic waves (consisting of phonons) and the emission of sound. It is connected with processes of elastic deformation and release of asperities.

The frequency of the natural micro-vibrations is determined by the contact stiffness and the mass of the sliding surface. The critical velocity V_{cr} , at which these micro-vibrations vanish is

$$V_{cr} = \frac{\mu \delta l^2}{2\eta \gamma} \quad \text{where}$$

- η - the creep viscosity
- δ - yield strength
- μ - friction coeff.
- γ - ave. height of asperities
- l = ave. spacing of the surface asperities

The absolute amount of energy emitted is only a very small part of the whole F_E

Emission of photons

the tribo-luminescence is well known in physics. It occurs when certain solid bodies are rubbed against each other. Assumed to be due to electrostatic discharges of electrostatic double-layers residing in sheared surface cracks and dislocations. Consumes only a small part of the whole frictional energy.

Emission of electrons (exo-electron emits)

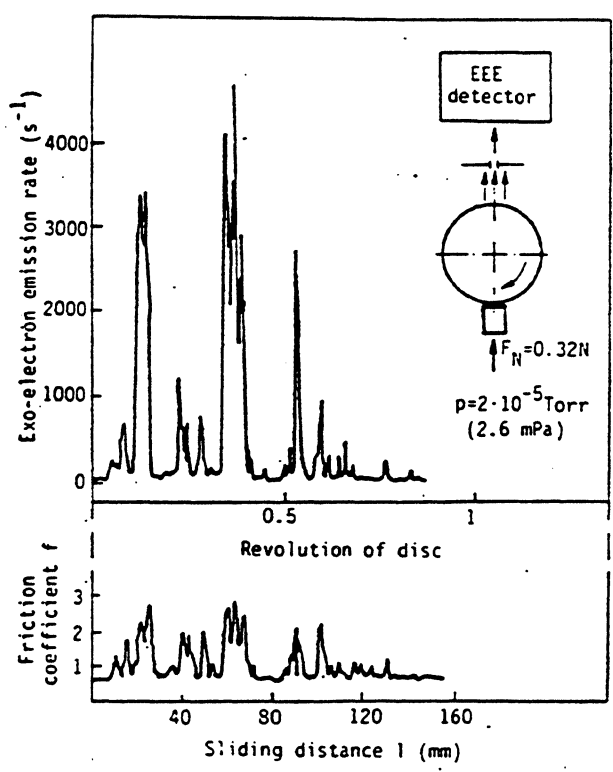


Figure 4.20 Friction coefficient and exo-electron emission rate

in 1940 Kramer noted that electrons are emitted from freshly abraded metallic surfaces.

a complete theory of the electron emission is not yet available.

This process is of great significance to the surface lubrication process where the exo-electrons are known to cause lube degradation and depletion.

The Generation of Heat

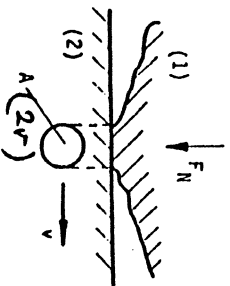


Figure 4.21 Model of a sliding asperity.

This model was used by Archard to calculate the temp. rise on the assumption that the heat is generated at the true contact area and that the heat is conducted away into the bulk by the rubbing members. The theory requires the solution of the equations for the flow of heat into each body. The derived surface temperatures are expressed in terms of the rate of supply of heat, the size and speed of the heat source, and the thermal properties of the material.

In the greatly simplified case and as indicated Speed

- tribo-induced temperature
- i) a bulk temp. rise
- ii) temperature gradient
- iii) local temperature rises or "flash temperature"

$$\Delta T = \frac{\mu F_N v}{4 J r (k_1 + k_2)}$$

where J is the mechanical equiv. heat, and k_1 and k_2 are the thermal conductivities of the two materials.

Problems:

- 1) μ has uncertainty of 30% or thereabouts
- 2) estimation of v can be easily off by a factor of as much as 10.

3) The heat is generated at many junctions (164)
and the load at each junction must be
calculated, and their mutual influence
estimated.

So, it looks like only a fool would try
to calculate the temp. rise produced in
sliding.

According to Rabinowicz, a crude
formula of an order-of-magnitude estimate
of actual surface temperatures is

$$\Delta T = \frac{v}{2} \left(\pm \text{a factor of 3} \right)$$

where ΔT is the flash temperature ($^{\circ}\text{F}$)
and v is the sliding speed in ft/min $60 = 900^{\circ}\text{F}$

$$\Delta T = \frac{308/\text{s} \times 60}{20} = 900^{\circ}\text{F}$$

11/30/94

$$F = A_r \bar{L} = \frac{W}{H} \bar{L} = \frac{W}{6k} \kappa = \frac{W}{6}$$

$$\begin{aligned} \bar{L} &= \frac{1}{2} Y \\ 4 &= 3Y \end{aligned}$$

$$\therefore \mu = \frac{F}{W} = \frac{1}{6} \quad \text{usually } \mu = .3 \text{ to } .7$$

Rebinowich (also JKR)

-- $W_{ab} = \gamma_a + \gamma_b - \gamma_{ab} > 0$ diff energy change

W_{ab} is decreased by bonding

$$A_r = \frac{L}{4} + \frac{2\pi r W_{ab}}{\sin \theta H} \quad \text{geometric factor}$$

$$\mu = \frac{F}{W} \approx \frac{k}{4} \left(1 + \kappa \frac{W_{ab}}{H} \right)$$

Kragelski (1980)

$$\mu = \frac{L_0}{Pr} + \beta + \kappa \alpha_h \sqrt{\frac{h}{r}}$$

$$\beta = \frac{W}{A_r}$$

Quantum™

QUANTUM CORPORATION
500 McCarthy Blvd.
Milpitas, CA 95035

11/1/94

Vector : is a quantity that is represented by both a magnitude and a direction.

Forces are vector quantities

1. Gravitational force - is an attractive force that exists between all objects.
2. Electromagnetic force - give materials their strength, their ability to bend, squeeze, stretch, or scatter. This force results from electric charge.
3. Nuclear force - holds the particles in the nucleus together.
4. Weak Force - a form of electromagnetic force and is involved in the radioactive decay of some nuclei.

Newton's 1st Law: An object with no net force acting on it remains at rest or moves with constant velocity in a straight line.

Newton's 2nd Law: acceleration of an object is directly proportional to the net force on it and inversely proportional to its mass.

$$a = \frac{F}{m} \quad \text{or} \quad F = ma = (1.0 \text{ Kg})(1.0 \text{ m/s}^2) = 1.0 \text{ N}$$

Forces always occur in pairs.

Newton's 3rd Law: - when one object exerts a force on a second force object, the second exerts a force on the first that is equal in magnitude but opposite in direction.

The weight of an object is proportional to its mass.
weight is the gravitational force of an object.

$$\text{The force of gravity} - F = mg.$$

$$W = mg.$$

on the surface of earth, objects that have only the force of gravity acting on them fall downward with an acceleration of $9.80 \frac{\text{m}}{\text{s}^2}$ $g = 9.80 \text{ m/s}^2$

PLANNING

Quantum™

QUANTUM CORPORATION

500 McCarthy Blvd.

Milpitas, CA 95035

11/3/94

Cohesive Force = in real liquids the particles do exert electromagnetic forces of attraction on each other.

The particles of an ideal liquid are totally free to slide over and around one another.

Surface Tension = is a result of the cohesive forces among the particles of a liquid. It is the tendency of the surface of a liquid to contract to the smallest area. S.T. makes liquids form spherical drops. It results from cohesive force.

Adhesion = is the attractive force that acts between particles of different substances, and A.F are electromagnetic in nature.

Elasticity is the ability of an object to return to its original form after external forces are removed.

Transmitted wave = lower velocity, shorter wavelength.

Reflected wave = higher velocity, longer wavelength

PLANNING

Wear

At the most elementary level wear is manifested by a loss of surface material from one or both surfaces when they are subjected to relative motion. Note that although wear clearly occurs at the surface contact which is also the seat of the friction mechanism, the two are not simply related one to the other.

Table 1.1. Friction and wear results for various material combinations.

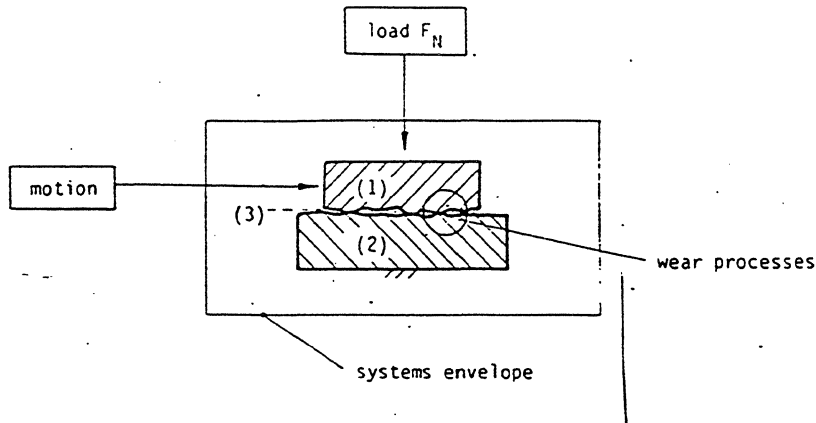
Materials	μ	Wear rate $\text{cm}^3/\text{cm} \times 10^{-12}$
Mild steel on mild steel	0.62	157 000
60/40 Brass on tool steel	0.24	24 000
PTFE on tool steel	0.18	2000
Stellite on tool steel	0.60	320
Stainless steel on tool steel	0.53	270
Polythene on tool steel	0.65	30
Tungsten carbide on itself	0.35	2

Mechanisms of wear

The most common mechanisms are:

- i) adhesive wear,
 - ii) abrasive wear,
 - iii) surface fatigue,
 - iv) tribochemical wear
- degradation of wear,
coarcoat

A simple tribo-mechanical system

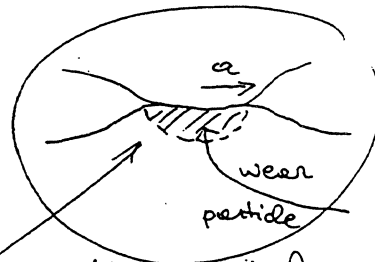
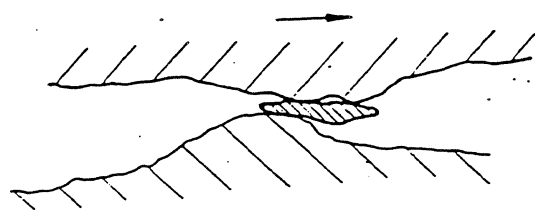
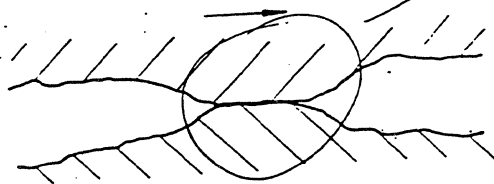
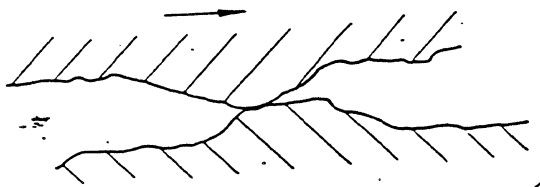


Some "macroscopic rules" of wear under dry sliding conditions

I. The wear rate w , i.e. the volume V of material removed per unit sliding s is proportional to the normal load F_N

$$w = \frac{V}{s} \propto F_N$$

II. The wear rate is independent of the apparent area of contact only real contact area



if $\Delta A = \pi a^2$
and $\Delta s = 2a$
 $\Delta V = \frac{2}{3} \pi a^3$

then it follows that

$$\frac{\Delta V}{\Delta s} = \frac{\Delta A}{3} \text{ and introducing a factor } k,$$

the total wear rate is

$$\frac{V}{s} = \frac{1}{3} k A_r$$

and since

$$A_r \propto \frac{F_N}{E} \quad (\psi < 0.6) \text{ (elastic)}$$

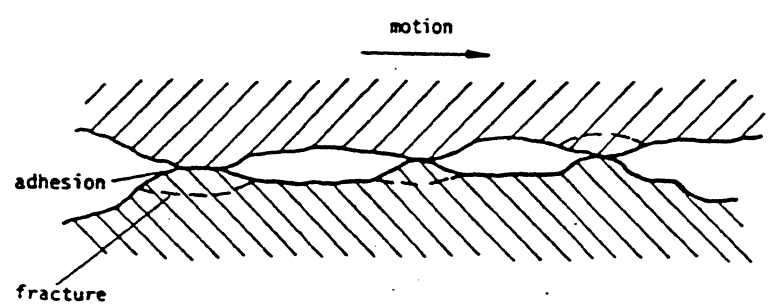
$$A_r \propto \frac{F_N}{H} \quad (\psi > 1) \text{ (plastic)}$$

$$\therefore V \propto k F_N s$$

Criticism

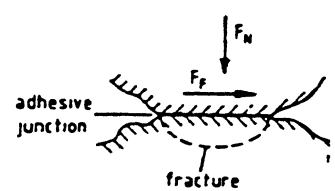
- 1) many exceptions
- 2) violates the conservation law for energy because the actual work done is ~~to~~ several orders of magnitude larger than the fracture energy.
- 3) does not address the plastic deformation process at the interface.

Adhesive Wear Situation



The adhesive wear processes are initiated by the interfacial adhesive junctions which form if solids materials are in contact on an atomic scale.

Adhesive wear mechanisms



- simplest relation:

$$W_v = k \cdot \frac{F_N \cdot s}{H}$$

H : hardness

• Adhesive wear model:

- (i) asperity contact deformation
- (ii) removal of surface films
- (iii) formation of adhesive junctions
- (iv) fracture of junctions and transfer of material
- (v) modification of transferred fragments (e.g. strain energy storage, tribochemical effects)
- (vi) removal of transferred/backtransferred fragments (e.g. by fatigue, fracture, abrasion)

Characteristics of adhesive wear models

- W_v : wear volume
- s : sliding distance
- k : Archard wear coeff. - depend on wear

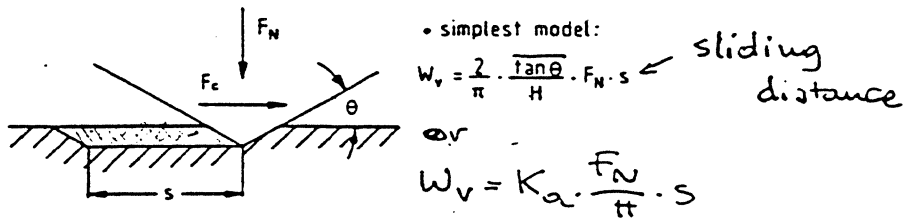
$k \approx$ probability factor which indicates the probability of wear particles being created by the adhesive effects between the populations of asperities on two rubbing surfaces

Abrasive Wear Mechanism

The effect of abrasion occurs in contact situation in which direct physical contact between two surfaces is given where one of the surfaces is considerably harder than the other.

Two general situations:

- i) two-body abrasion, i.e., hard slides and disk softer overcoat.
- ii) three-body abrasion where the hard surface is a third body caught between the two other surfaces.



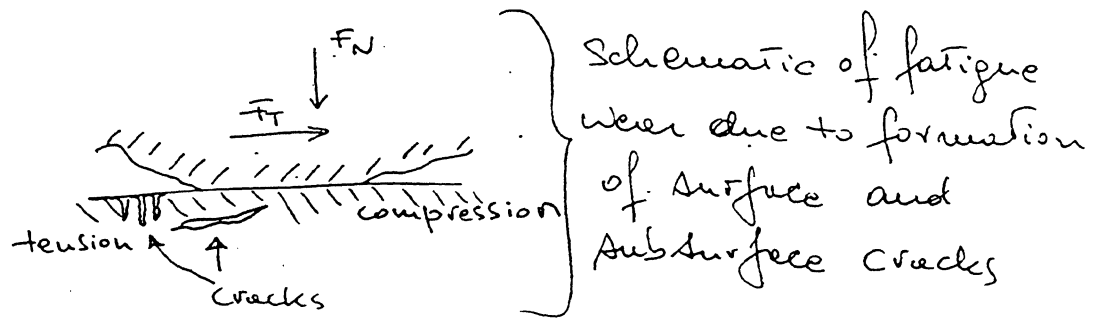
This expression relates the wear volume to the asperity slope ($\tan \theta$, which is weighted average of the $\tan \theta$ values of all the individual cones) of the penetrating abrasive particle, the hardness of the abraded material, and the unit of sliding distance. The eq. bears some resemblance to the Archard eq. (adhesive wear), though one difference is noticeable — K_a is related to the characteristic geometry of the hard asperities as defined by the angle θ .

Criticism

- 1) does not include effects of plastic deformation of the substrate layer. Specifically flowing ϕ , which depends on ductility of material.

Fatigue wear

periodic variations of stresses in a sliding contact can give rise to fatigue failure



* Tribochemical Wear *

due to dynamic interaction between environment and mating material. This interaction leads to a cyclic stepwise process:

- in the first step, the surfaces react with environment, and reaction products are formed on the surface.
- in the second step, attrition of the reaction products occurs as a result of crack formation and/or abrasion in the contact interactions of the materials. Thermal desorption is also possible.

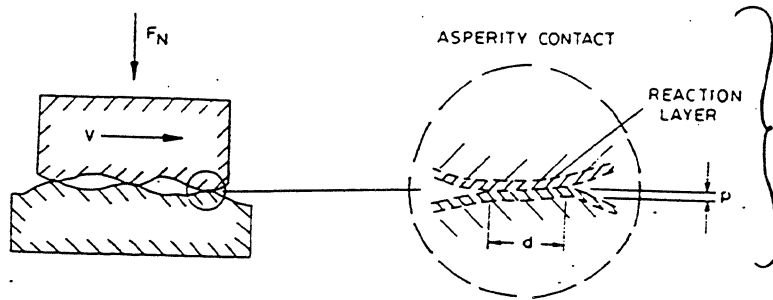
Tribochemical wear hypothesis to explain wear in steels was proposed by Quinn et al. (x)

(x) ASLE Trans. 10, 158 (1967)

the expression is given by

$$W_v = \frac{k''}{\xi^2 \rho^2} \cdot \frac{d}{H} \cdot \frac{F_N}{v} \cdot s$$

- where
- k'' : velocity factor of oxidation
 - d : asperity contact diameter
 - ρ : thickness of reaction layer
 - ξ : critical thickness of reaction layer
 - H : hardness

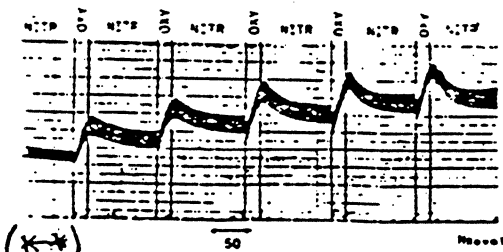


model of
tribochemical
Wear - carbon wear

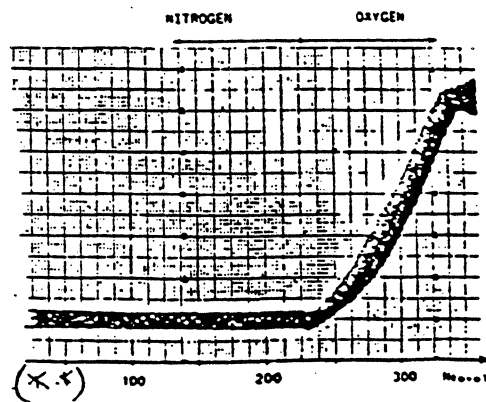
according to Quinn,

- a) the reactivity is increased due to the increased asperity temperature
- b) the mechanical properties of the surface layers are changed: they have tendency to brittle fracture.

oxide the carbon



Friction coefficient between slider and a-C as a function of chemical environment.



Friction coefficient for a $CaTiO_3$ slider on a-C disc at 0.06 m/s in dry nitrogen, then in oxygen.

(*) Marchon B et al. IEEE Trans. 26, 168, 1990

Corrosive wear (non tribological)

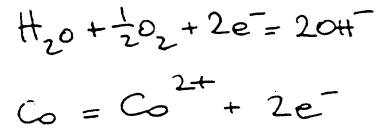
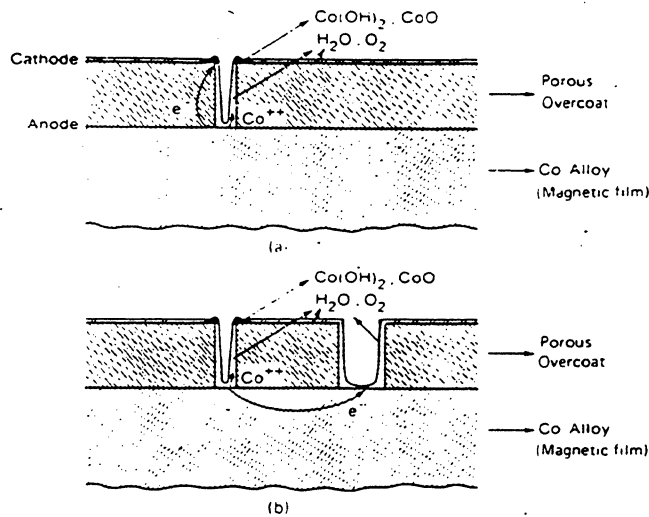
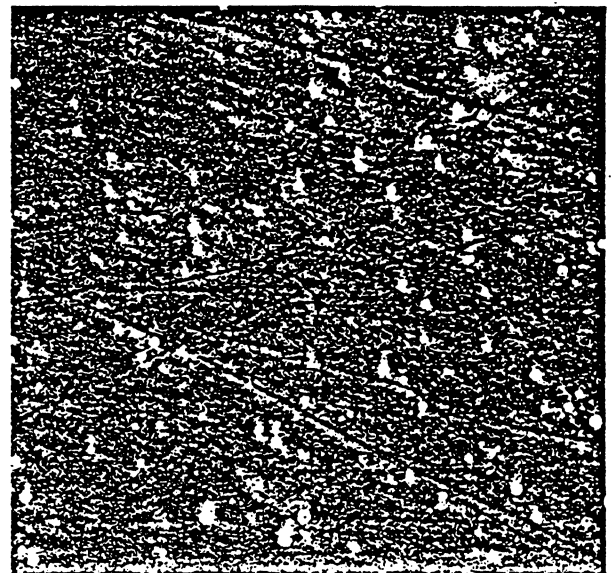
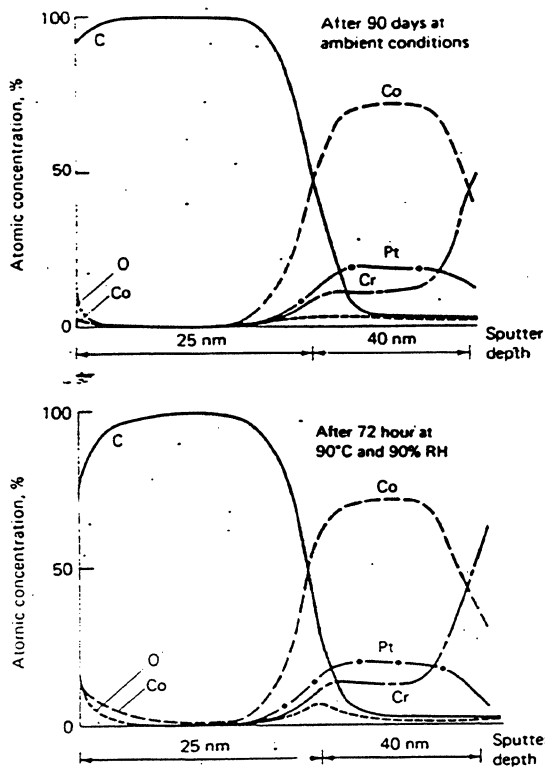


Fig. 6.74. Schematics of electrochemical corrosion mechanism in cobalt-based magnetic films with a porous overcoat (Novotny et al., 1987).

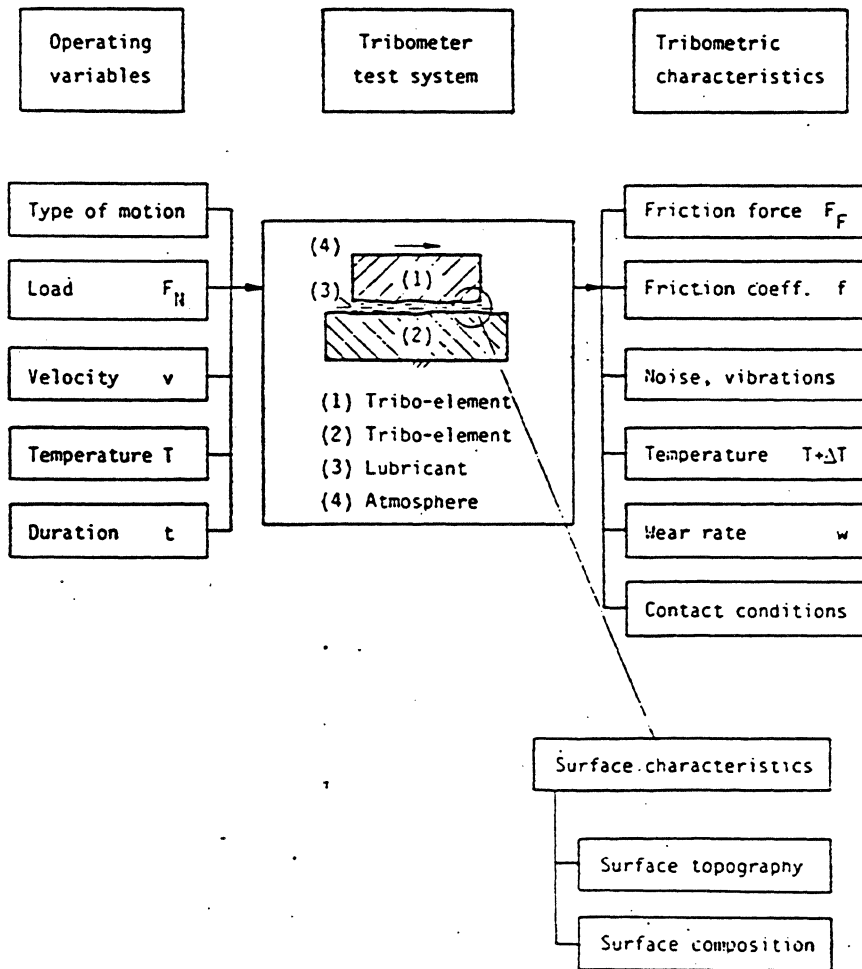


5 μm

Fig. 6.75. Auger depth profiles of CoCr-Pt rigid disk with carbon overcoat after storage at ambient conditions for 90 days and after environmental stressing at 90°C and 90% RH for 72 hours (Novotny et al., 1987).

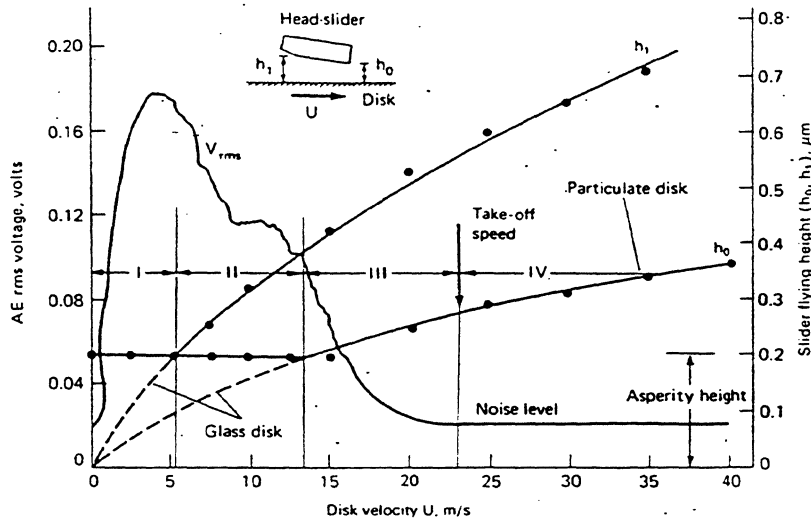
SEM micrograph of NiP/CoP/C film surface after 24 hrs exposure to 10 ppb Cl_2 at 75% RH and 25°C.

Characteristics and Parameters relevant to tribo-testing.



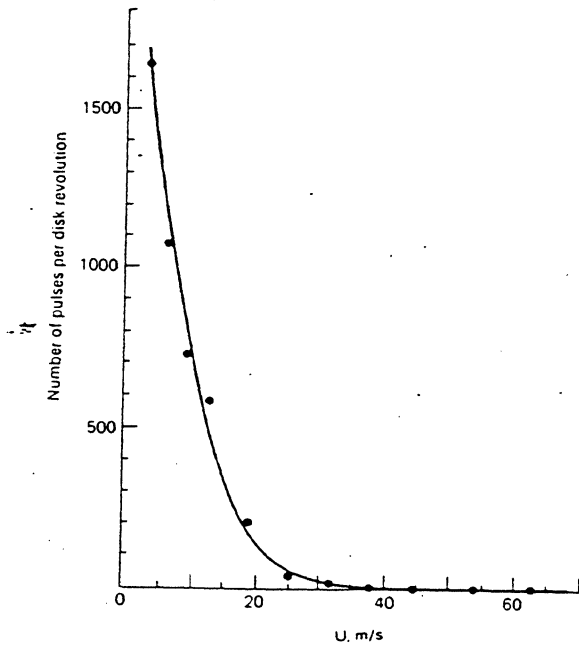
Rigid Disk Wear

— particulate disks —



(a)

during asperity contacts, the disk debris can be generated by adhesive, abrasive, and impact wear.



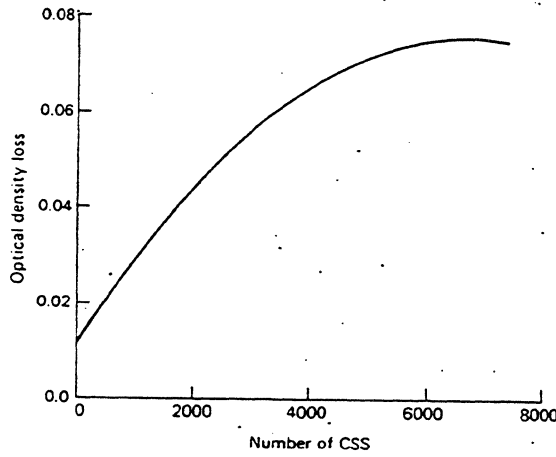
(b)

Most of disk and slider wear occurs below the take-off speed in CSS

Fig. 6.51. (a) AE output and head slider flying heights at the leading and trailing edges as a function of disk velocity on a particulate disk with maximum asperity heights of $0.2 \mu\text{m}$ (Tago et al., 1980). (b) Number of electrical contact pulses as a function of disk velocity for a particulate disk (Tseng and Talke, 1974).

174

Effect of lubricant on wear



Availability of lubricant
 to some extent in general
 slider tend to pick up the
 film from the disk.

Fig. 6.55. Lubricant loss of a particulate rigid disk against Al_2O_3 -TiC slider as a function of the number of CSS (Levy and Wu, 1984).

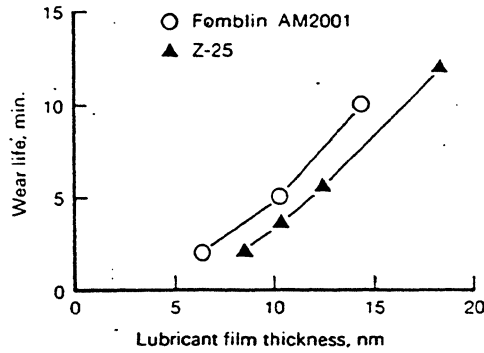


Fig. 6.56. Wear life as a function of lubricant film thickness for two lubricants on a particulate disks slid against a hemispherically ended steel pin (Scarati and Caporiccio, 1987).

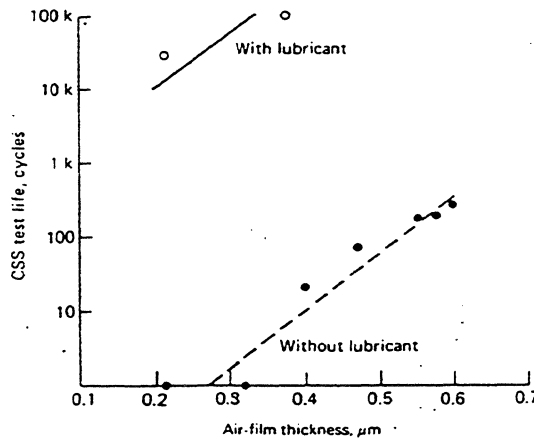


Fig. 6.57. Contact start/stop test life as a function of air-film thickness (at the full speed) for a lubricated and an unlubricated particulate rigid disk surface against a Mn-Zn ferrite slider (Kawakubo et al., 1984).

CSS test

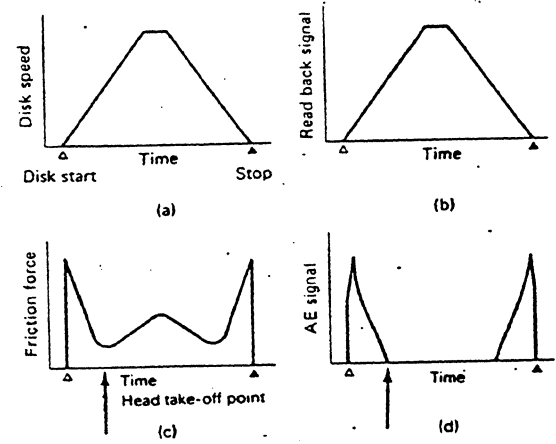


Fig. 6.58. Relation between readback signal, friction force, AE signal, and disk sliding speed in a CSS cycle (Kawakubo et al., 1984).

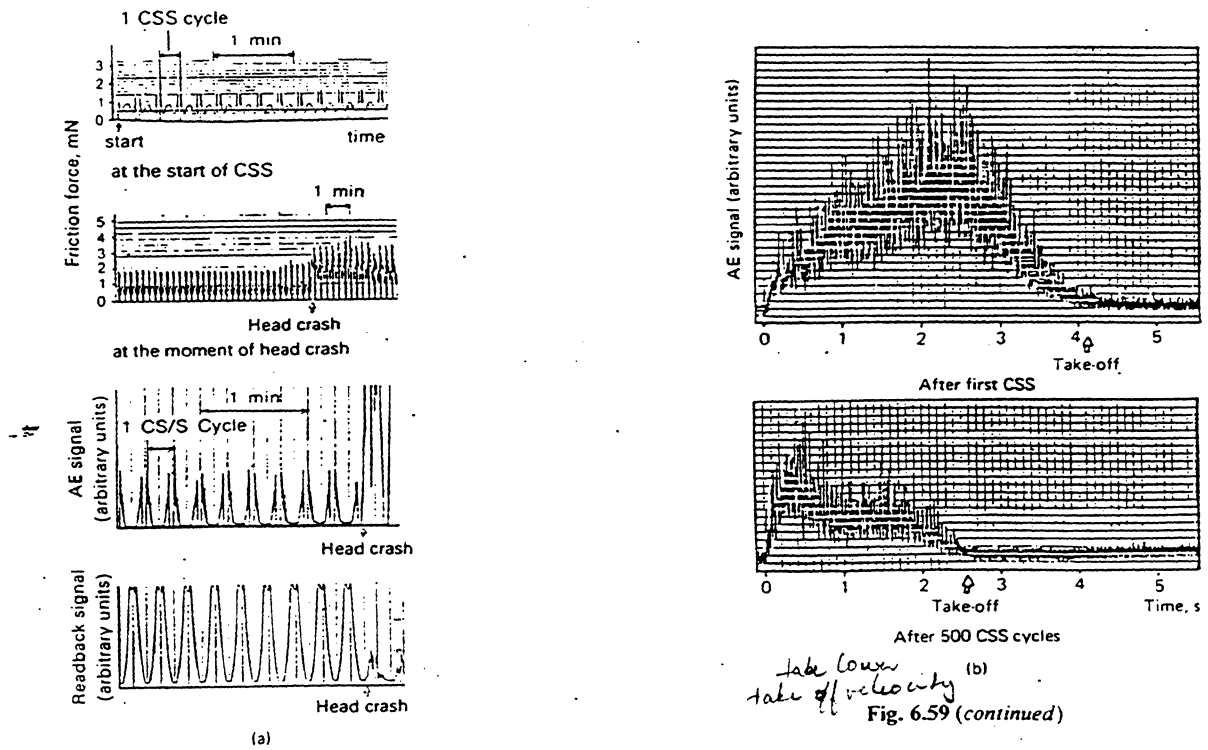


Fig. 6.59. (a) Friction force, AE signal, and readback signal near the head crash in a CSS test (particulate rigid disk without lubricant against Ni-Zn ferrite slider). (b) AE signal at different CSS (particulate rigid disk without lubricant against Ni-Zn ferrite slider) (Kawakubo et al., 1984).

— thin film disks —

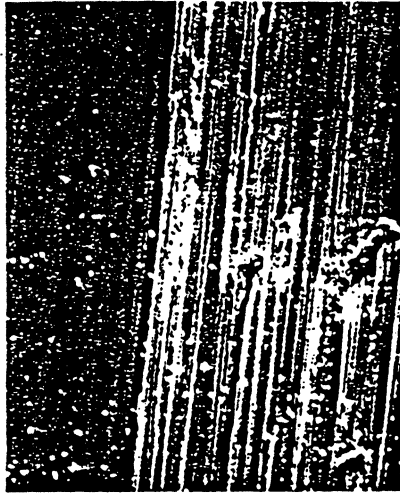


Fig. 6.60. SEM micrograph of wear track on sputtered carbon film against mini-monolithic Mn-Zn ferrite slider after 61,000 CSS (Gatzen et al., 1987).

An HDI can fail from internal degradation (wear debris from HDI wear) and external contamination (wear debris extrinsic to the HDI and particulates from the environ.)

Long durability can be achieved by selecting a hard overcoat and lubricant appropriately and by minimizing the external contamination

Effect of Mechanical properties

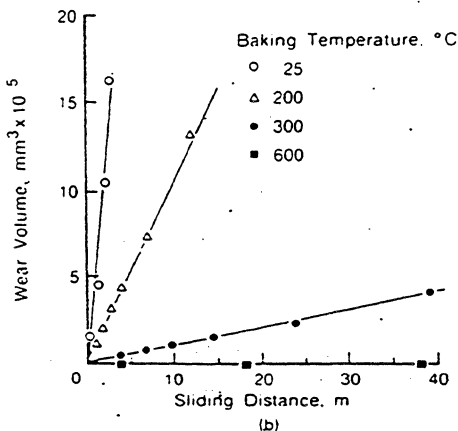
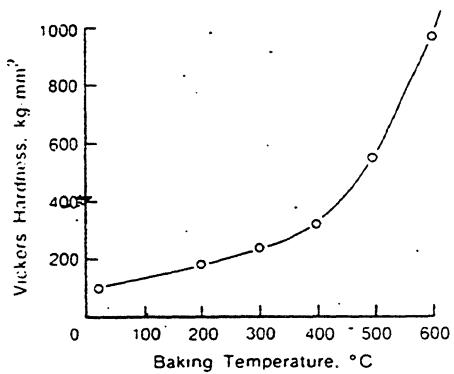


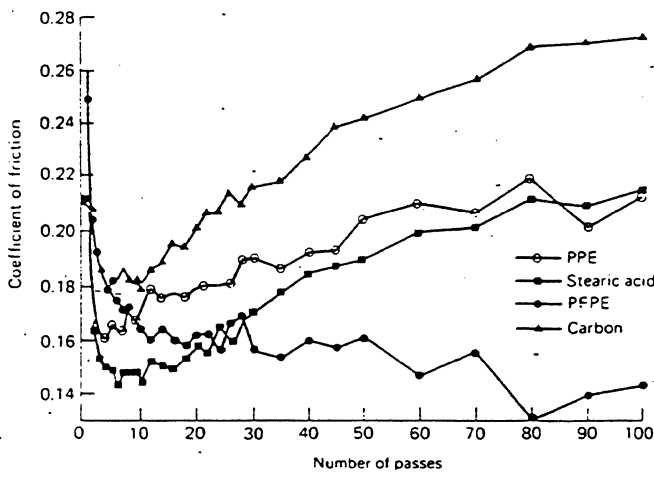
Fig. 6.63. (a) Dependence of Vickers hardness on baking temperature for SiO₂ films. (b) Relation between sliding distance and wear volume for SiO₂ films exposed to air, baked at various temperatures, and slid against Al₂O₃-TiC slider in a low-speed sliding test (Yanagisawa, 1985b).

increase in hardness results in improvement in wear resistance.

Similarly, for carbon overcoats, hardness should be high for increased wear resistance

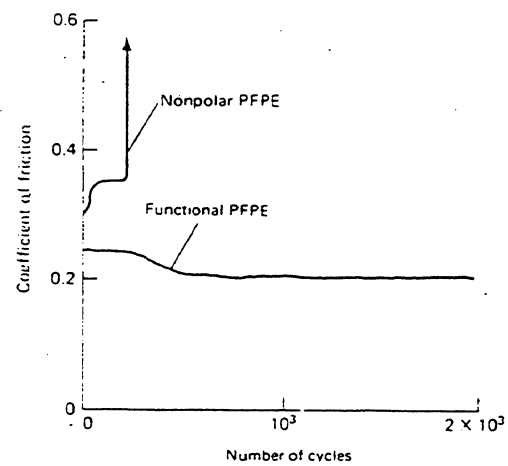
Amorphous carbon films and diamond-like films have hardness in the range 1000-3000 kg/mm²

Effect of Lubricant



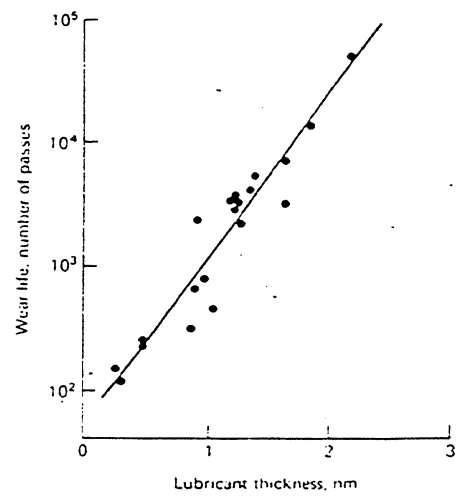
where PPE :
polyphenylether
PFPE :
perfluoropolyether

Fig. 6.65. Relation between number of passes and coefficient of friction for different lubricants on a carbon film. The tests were run against a 440 stainless Steel ball using Bowden-Leben apparatus (Timsit et al., 1987).



shows importance
of lubricant to
adhesion

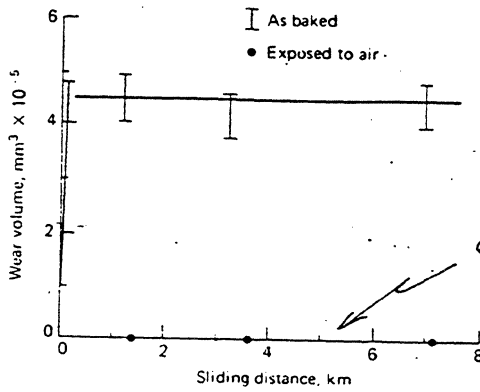
Fig. 6.66. Relation between number of passes and coefficient of friction on thin-film (Co-Ni alloy) disks with an SiO₂ overcoat and two perfluoropolyether lubricants with a 2 nm thickness. The sliding tests were run at 0.5 m/s and 285 mN (Miyamoto et al., 1988).



effect of
lubricant
thickness

Fig. 6.67. Relation between wear life and perfluoropolyether lubricant thickness for a thin-film (oxide) disk with an SiO₂ overcoat. The sliding tests were run at 15 m/s and 5 Torr pressure against an Al₂O₃-TiC slider (Terada et al., 1988).

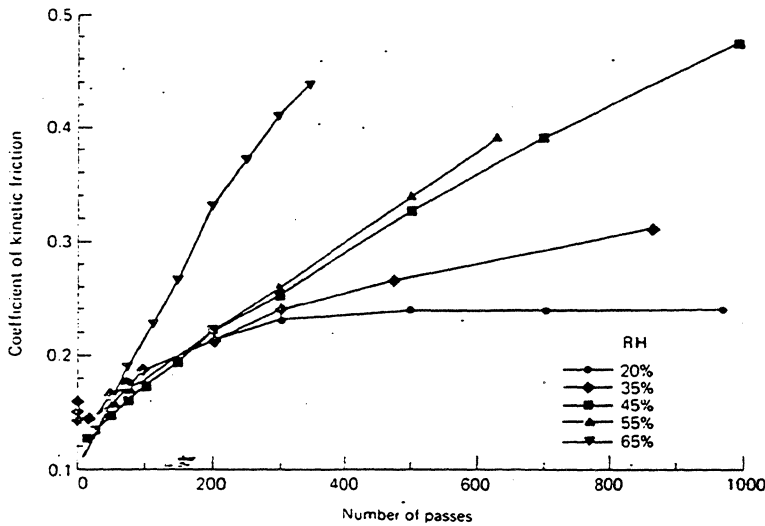
Effect of Environment



organic ambient
contaminants improve
durability

exposed to air for 135 hrs.

Fig. 6.71. Relation between wear volume and sliding distance for as-baked SiO₂ films (at 200 C) and for films exposed to air, slid against an Al₂O₃-TiC slider in a low-speed sliding test (M. Yanagisawa, "Tribological Properties of Spin coated SiO₂ Protective Film on Plated Magnetic Recording Disks", SP-19, ASLE, 1985).



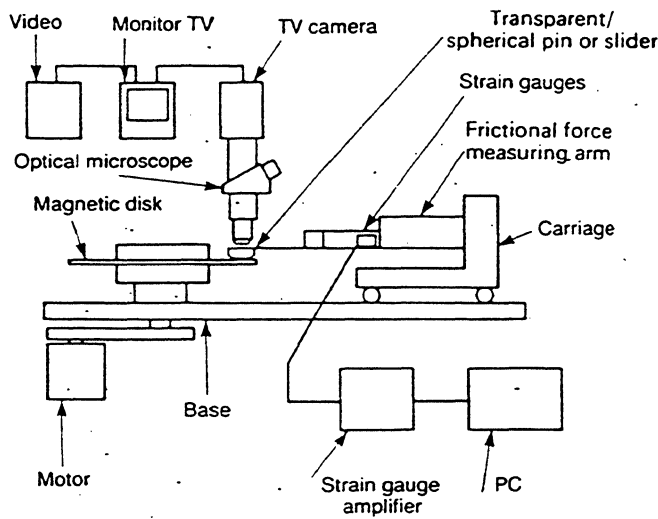
an increase in
friction with humid
is attributed to
displacement of the
lubricant molecules
with water adsorbing
preferentially on
the disk surface

Fig. 6.72. Relation between coefficient of kinetic friction and sliding distance as a function of relative humidity for a thin-film (metal) disk with a carbon overcoat and a perfluoropolyether lubricant against Al₂O₃-TiC slider in a low-speed sliding test (3 to 6 mm/s) (Timsit and Stratford, 1988).

Accelerated Wear Tests

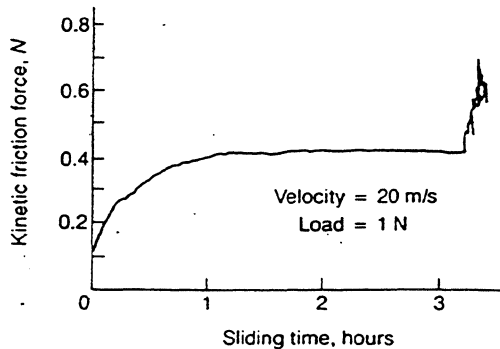
✓ Accelerated Durability Tests (ADT) are used during early development of head sliders and disks. The objective is to determine the relative durability of the disk and head materials in a short test period (on the order of minutes or hours).

Pin-on-Disk Test



Contact stresses very high - wear mechanism may be different from that of the normal head slider-disk interface.

Fig. 7.12. Schematic of transparent/spherical pin- or slider-on-disk durability apparatus (Kawakubo et al., 1986).



The failure is defined when the dynamic friction rises above a certain clip level.

Fig. 7.13. Example of kinetic friction force as a function of sliding time data for a particulate disk from the ADT.

Accelerating Wear Test (AWT)

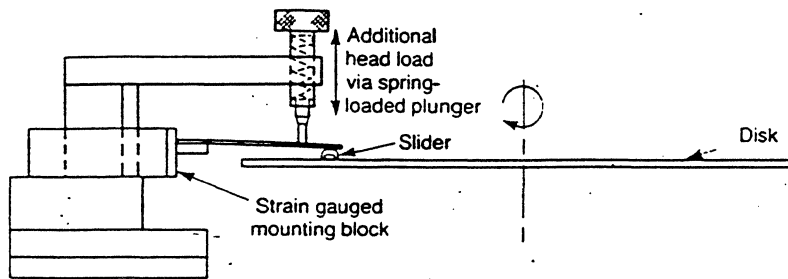
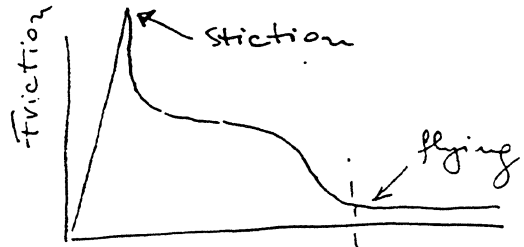
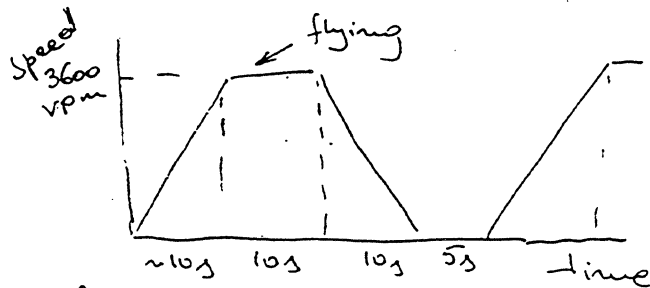


Fig. 7.14. Schematic of the suspension loading arrangement for the slider-on-disk test.

Surface velocity 1 on the take off speed. Suspension load normal (95 or 150 mT or higher (5 to 10x))

✓ Accelerated CSS Test

Simulates start and stop of a single disk or drive.



The CSS life requirement for a disk is usually $> 10K$ (typically $20K$). Static friction after the max. number of CSS for a statistically significant number of files must be low enough to overcome spindle torque.

"The failure is defined to occur when the static friction rises above a certain level or a visible wear track is formed"

Failure Mechanisms in CSS

181

A single-disk test stand is instrumented to give information about head slider-disk contacts, take-off speed, air-film thickness, and particle counts. These measurements allow us to identify precursors to failures that are helpful in identifying failure mechanisms.

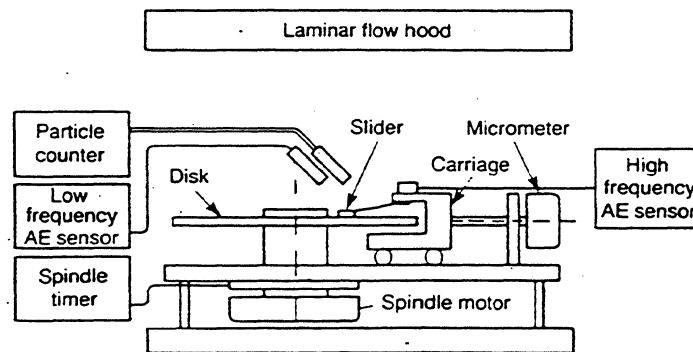


Fig. 7.15. Schematic of the single-disk test stand in a clean bench for CSS or flyability tests (Gatzen et al., 1987).

Regimes of Lubrication

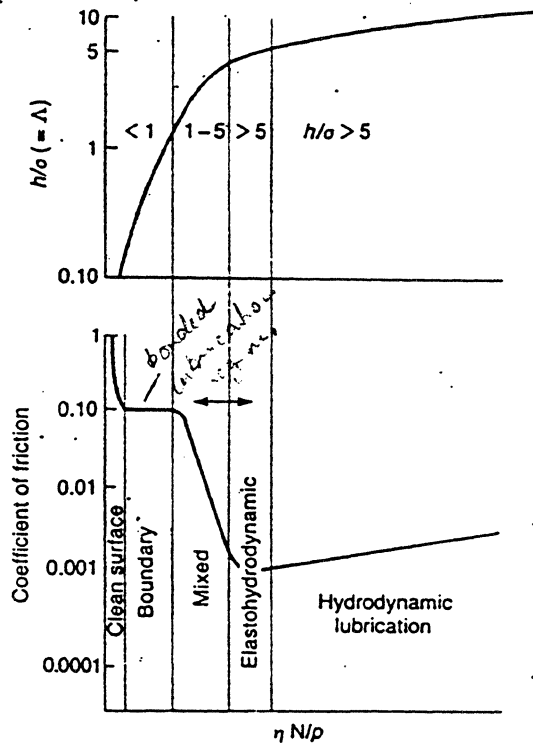
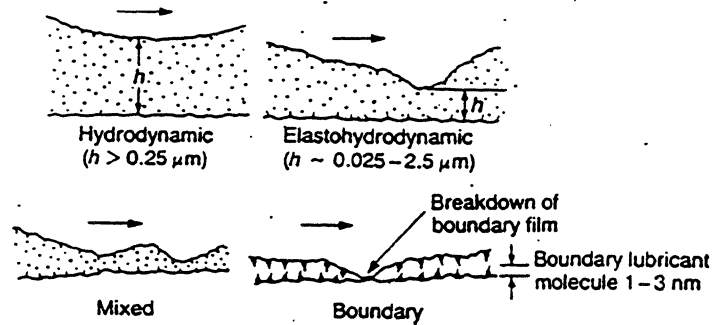


Fig. 8.1. Lubricant film parameter (Λ) and Stribeck curve showing different lubrication regimes observed in fluid lubrication without an external pumping agency.

where $h/\sigma = \frac{\text{mean film thickness}}{\text{composite standard deviation of surface roughnesses}}$

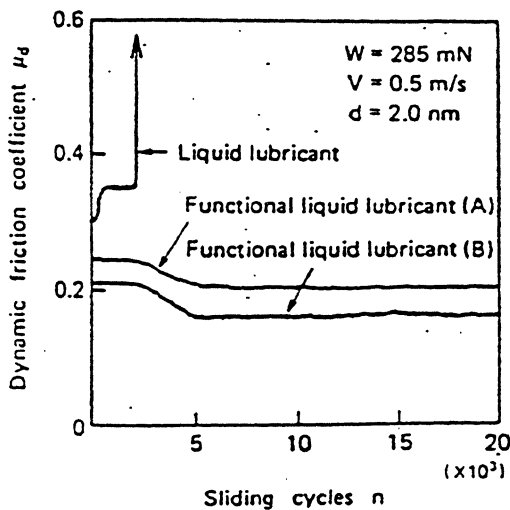
η = viscosity, N = sliding velocity

p = normal pressure

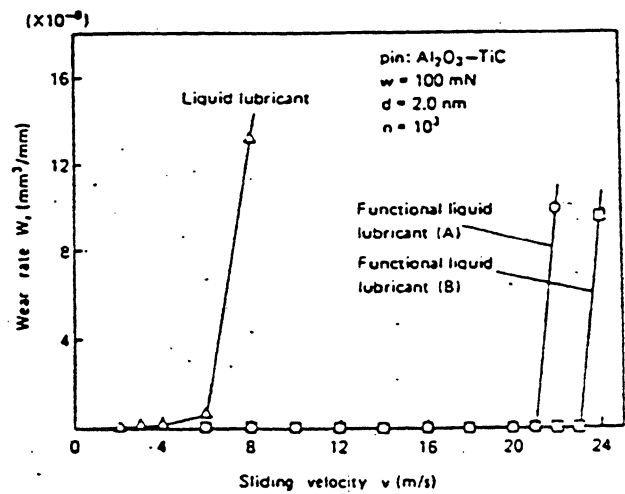
Basic Requirements of Boundary Lubricant

(1) Strong attachment to the surface to resist penetration by surface asperities

	FUNCTIONAL LIQUID LUBRICANT (A)	FUNCTIONAL LIQUID LUBRICANT (B)	LIQUID LUBRICANT
Molecular Weight	2200	2200	2500
Viscosity (cSt) at 20°C	20	80	500
Vapor Pressure (Torr.) at 20°C	1×10^{-4}	2×10^{-4}	2×10^{-6}
Molecular Structure	$\begin{array}{c} \text{CH}_3\text{OOC} \text{---} \\ \quad \quad \quad \\ \quad \quad \quad \text{R}_{11} \\ \quad \quad \quad \\ \text{CH}_3\text{OOC} \text{---} \end{array}$	$\begin{array}{c} \text{HO} \text{---} \text{CH}_2 \text{---} \\ \quad \quad \quad \\ \quad \quad \quad \text{R}_{12} \\ \quad \quad \quad \\ \text{HO} \text{---} \text{CH}_2 \text{---} \end{array}$	$\begin{array}{c} \text{F} \text{---} \text{R}_{13} \text{---} \text{C}_2\text{F}_5 \\ \\ \text{CF}_3 \end{array}$



-Dynamic friction coefficient versus number of sliding cycles in boundary lubrication under a loading force of 285 mN.

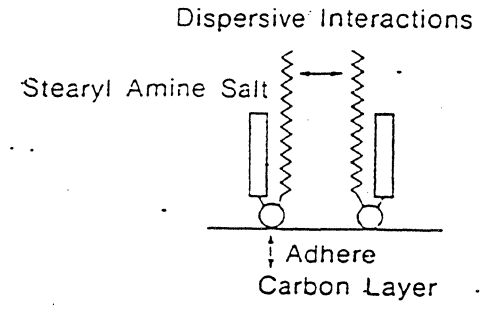
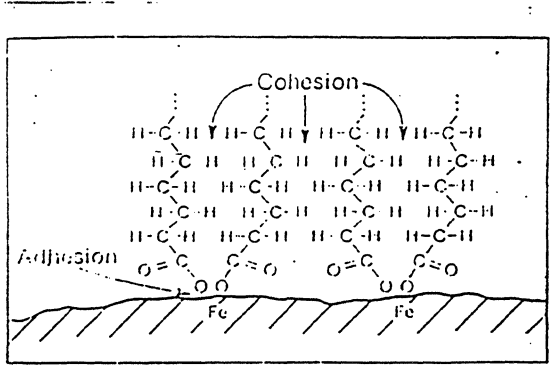


-Relationship between wear rates of disk media coated with 2.0-nm-thick lubricants and sliding velocity under a high loading force of 100 mN.

Yasu Miyamoto et al. Tribol. & Mechanics of Magn. Storage Systems, STLE Sp. Publ., SP-25, 55, 1988

4

(2) Strong lateral attraction between the chains to ensure that shearing takes place between the layers of the lubricant.



- ~ Alkyl chain
- Perfluoro alkyl chain
- Polar group (COO⁻H₃N⁺)

A model for salt type lubricant adsorbed on the carbon layer (from Kondo et. al., 1989).

(3) low shear strength between the layers assures low friction. PFPE lubricants (perfluoropolyethers) exhibit low molecular cohesion and shear strength.

Experimentally bonded lubricants do appear to provide longer wear life compared to unbonded or nonpolar lubricants. However, since these lubricants are bound in place, they suffer from an inability to "heal" after head-disk contacts because there is less lubricant migration across the disk surface compared to liquid lubricants. To alleviate this handicap, the bonded lubricants are often combined with a small amount of free lubricant, which can migrate across the disk surface and replace lubricant loss due to head-disk contacts.

Effect of Adsorbed Gases and Simple Organics

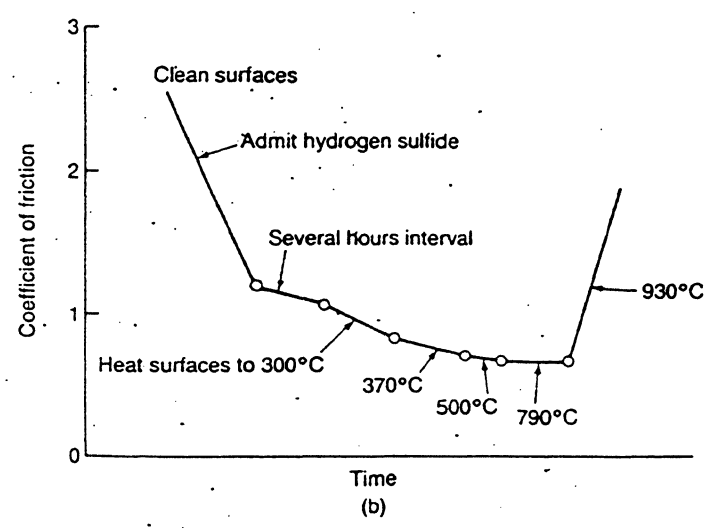
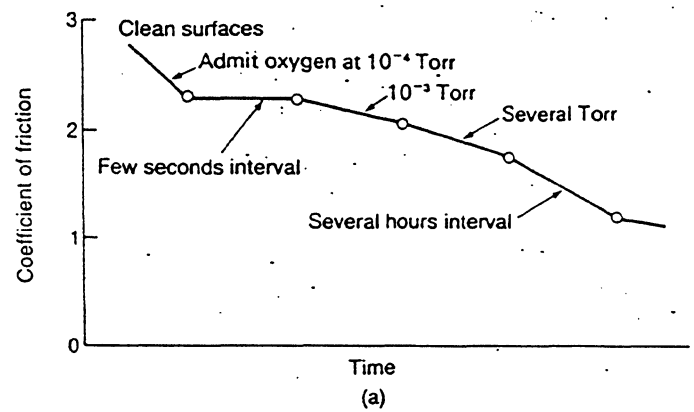
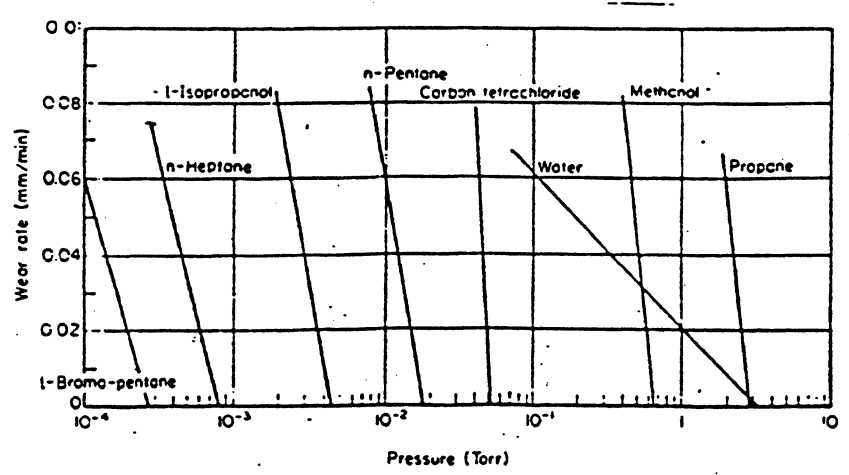
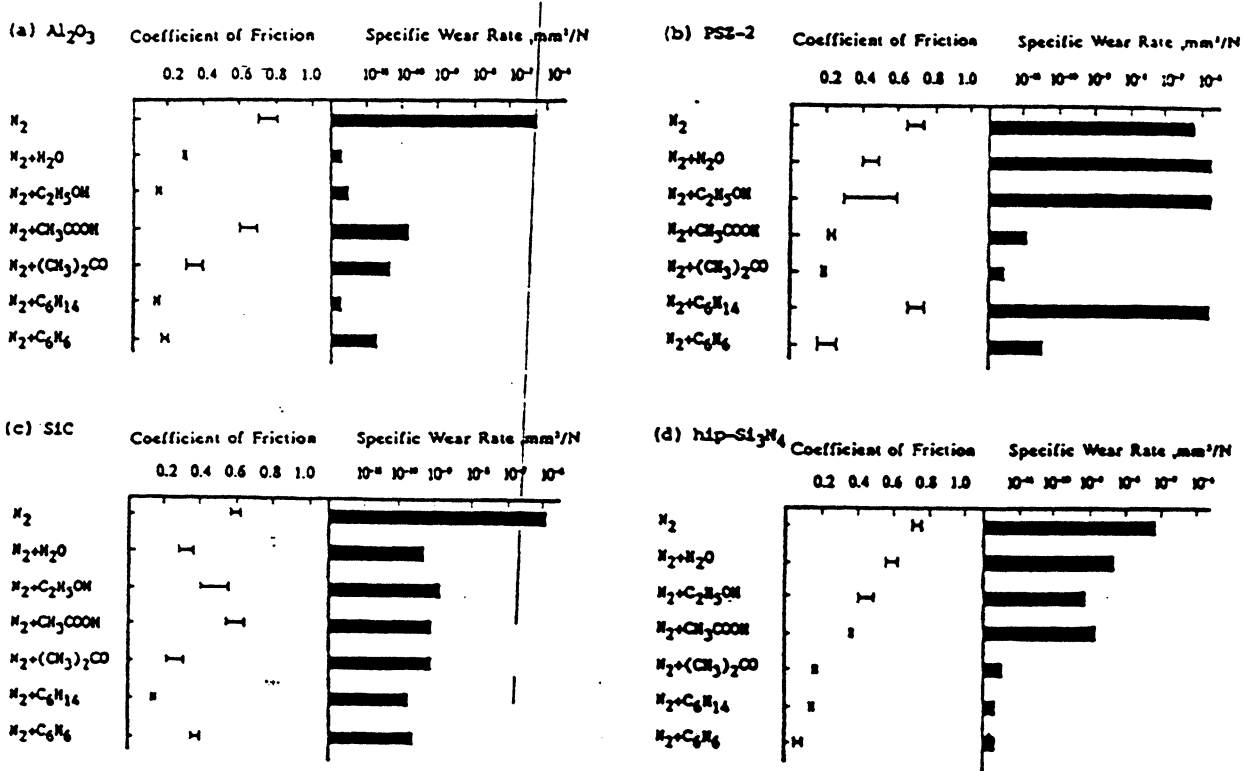


Fig. 8.4. (a) Effect of oxygen on friction of outgassed iron surfaces and (b) effect of hydrogen sulfide on friction of outgassed iron surfaces (Bowden, 1951).

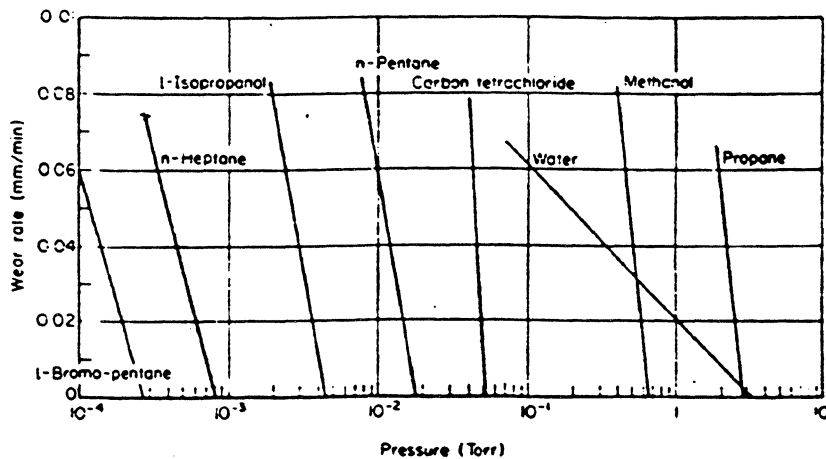


Effects of condensable vapors on wear of graphite. [R. H. Savage and D. L. Schaefer, *J. Appl. Phys.* 27, 136-138 (1956).]

Effect of Simple Organics on Friction and Wear of Ceramics



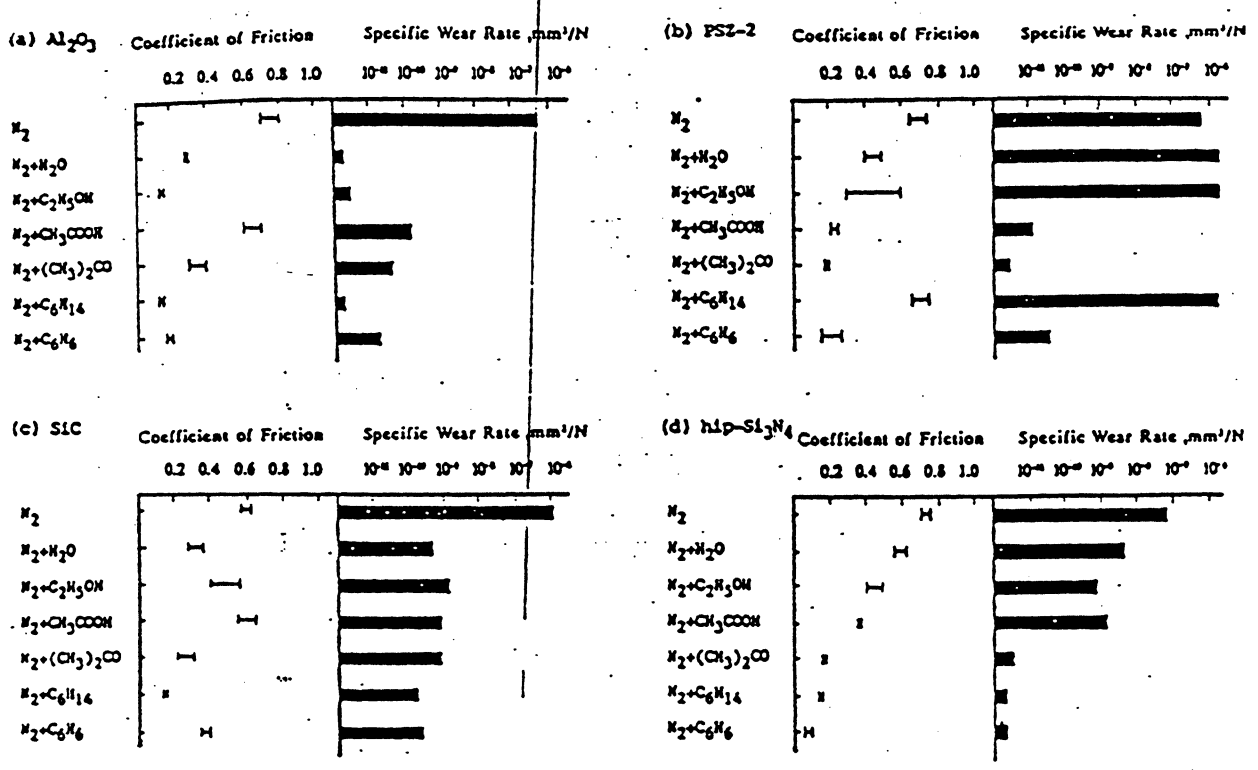
Friction and wear behaviour in nitrogen with various kinds of organic compound: (a) Al₂O₃, (b) PSZ-2, (c) SiC, (d) hip Si₃N₄.



Effects of condensable vapors on wear of graphite. [R. H. Savage and D. L. Schaefer, *J. Appl. Phys.* 27, 136-138 (1956).]

* $\text{C}_2\text{H}_5\text{OH} < \text{C}_6\text{H}_6 < \text{Wear } 134 \text{ } 125 / 1000$

Effect of Simple Organics on Friction and Wear of Ceramics



Friction and wear behaviour in nitrogen with various kinds of organic compound: (a) Al₂O₃, (b) PSZ-2, (c) SiC, (d) hip Si₃N₄.

from Sasaki, S., Wear, 134, 185 (1989)

Effect of Monolayer and Multilayers

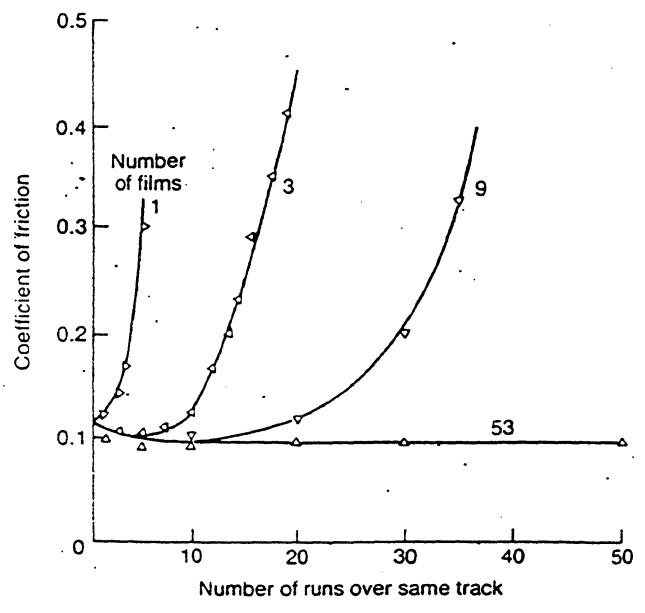


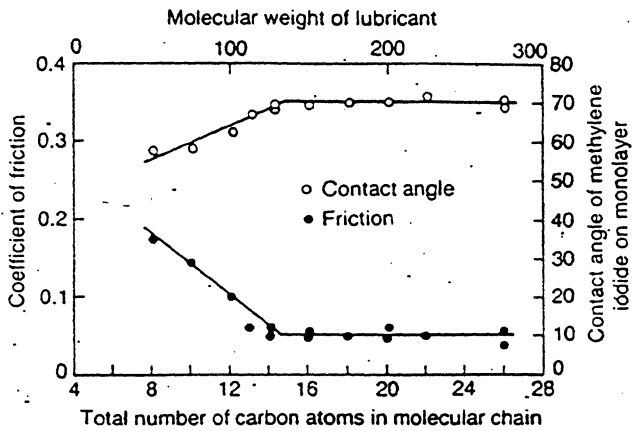
Table 8.1. Shear stress as a function of number of boundary layers trapped between two mica surfaces for octamethylcyclotetrasiloxane (OMCTS)^a and cyclohexane^b

Number of layers	Shear Stress, MPa	
	OMCTS	Cyclohexane
1	8.0 ± 0.5	2.3 ± 0.6 × 10 ⁻¹
2	6.0 ± 1.0	1.0 ± 0.2
3	3.0 ± 1.0	4.3 ± 1.5 × 10 ⁻¹
4	Not measured	2.0 ± 1.0 × 10 ⁻²

^a Molecular diameter ~ 0.85 nm.
^b Molecular diameter ~ 0.5 nm.

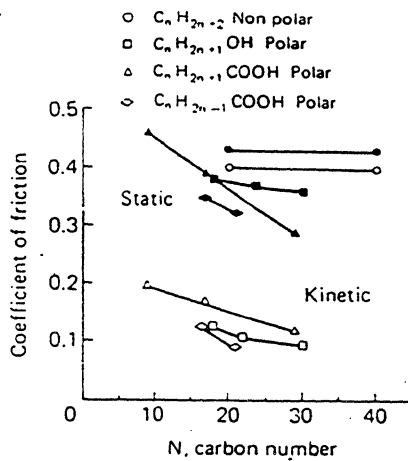
Fig. 8.5. Wear behavior of stearic acid films deposited on stainless steel sliding against stainless steel surface (Bowden and Tabor, 1950).

Effect of chain length (molecular weight)



Similar trends were found for other lubricant films such as paraffins and alcohols.

Fig. 8.7. Effect of chain length (or molecular weight) on coefficient of friction (of stainless steel sliding on glass lubricated with a monolayer of fatty acid) and contact angle (of methyl iodide on condensed monolayers of fatty acids on glass) (Zisman, 1959).



Polar solid lubricants show a decrease in the coefficient of friction with an increase in the number of carbon atoms.

Fig. 4.74. Static and kinetic coefficients of friction as a function of the number of carbon atoms for nonpolar and polar solids on a thin-film rigid disk surface against an Al₂O₃-TiC slider (Yanagisawa, 1985a).

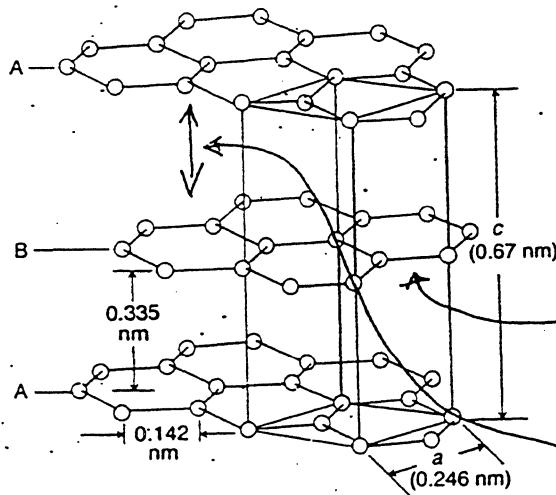
Solid Lubricants

- * Soft materials polyethylene, generally provide low friction and wear and are used at relatively low loads ($< 1 \text{ MPa}$) and low speeds ($< 10 \text{ m/s}$).
- * hard materials tungsten, diamond provide low wear at high loads, speeds and high temperatures for extended periods.

Soft Materials

- * lamellar solids
best known examples are graphite and MoS_2 .

The structure of graphite shows a series of parallel planes or sheets which are relatively far apart.



bond strength $\approx 100 \text{ kcal/g-atom}$

bond strength $\approx \text{a few kcal/g-atom}$

Fig. 8.8. Structure of graphite.

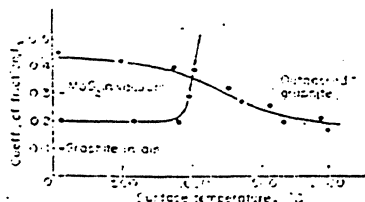


Fig. 8.3. Friction of outgassed polycrystalline graphite as a function of temperature.

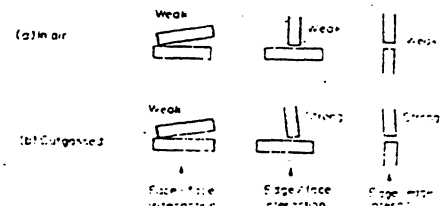


Fig. 8.4. Interaction of edges and cleavage faces in sheets of graphite.

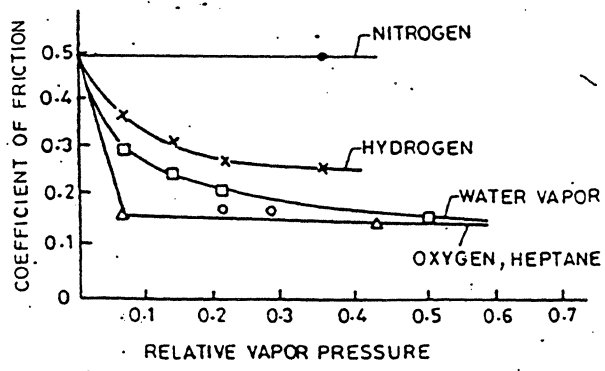


FIGURE 5.3 Effect of environment composition and its vapor pressure on coefficient of friction of graphite sliding against steel. [Adapted from Rowe. (1960).]

For graphite to work effectively as a solid lubricant, however, the presence of moisture or other gaseous contaminants is necessary

* Metal salts

The main interest is in their high-temperature potential. Examples: PbO effective from RT to $\sim 350^\circ C$ and in excess of $500^\circ C$. CaF_2 and CaF_2/Be mixture is effective between 250 and $700^\circ C$.

* Soft metal films

used in rolling element bearings. Examples: In, Pb, Pd, Rh, Ag, Au, Cu & Sn.

* Polymeric films

PTFE (teflon) - polytetrafluoroethylene, polyethylene, polyimide, phenolics, silicones, and epoxies

The low friction of PTFE is attributed to the smooth molecular profile of the polymer chains which, after orientation in early stage of sliding, can then slip easily over each other

* Organic acids (fatty acids)

lauric, myristic, palmitic, and stearic

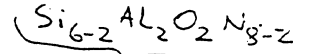
- excellent lubricants but are volatile, unstable at high temperatures, and may be corrosive

Hard Materials

hard materials comprise metals and ceramics.

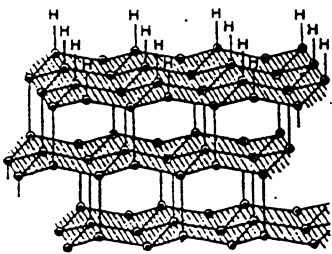
ex. nickel-phosphorous ($Ni_{81}P_{19}$) \neq Ni-B. covalent-bond

The most popular ceramics are:

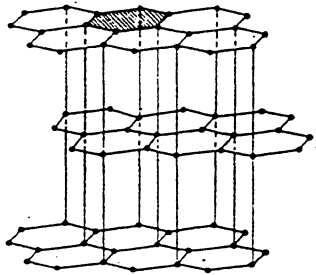


B_4C , TiC , SiC , HfC , Cr_3C_2 , WC , Si_3N_4 , Siolons,
 TiN , Al_2O_3 , Al_2O_3-TiC (87-13%), CrO_2 , $ZrO_2-Y_2O_3$, SiO_2 ,
 TiB_2 , ZrB_2 , $MoSi_2$, and diamond-like carbon.

Diamond Coatings



(a)



(b)

FIGURE 14.66 Schematic diagrams showing the similarities in the crystal structures of: (a) Diamond. (b) Graphite. The hydrogen atoms bonded to the surface carbons depict their role in stabilizing the diamond surface structure.

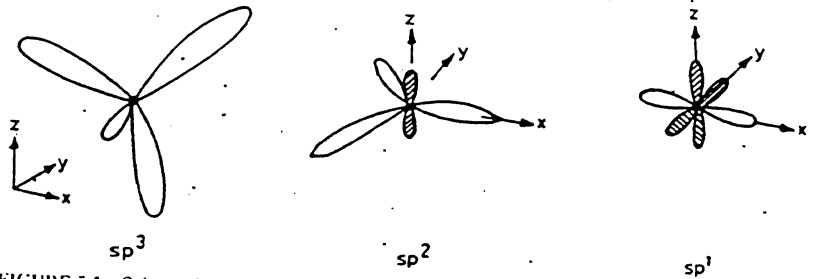


FIGURE 5.1 Schematic representation of sp^3 (diamond), sp^2 (graphite), and sp^1 (hydrocarbons and certain polymers) bonding types of carbon atoms.

sp^3 each of the carbon's four electrons is assigned to a tetrahedrally directed sp^3 hybrid orbital, which then form a strong σ (covalent) bond with an adjacent atom.

sp^2 three of the four electrons are assigned to trigonally directed sp^2 hybrid orbitals, which form the σ bonding plane; the fourth electron lies in a $p_z (p_{\perp})$ orbital laying normal to the σ bonding plane. The p_{\perp} orbital forms weaker bonds (Van der Waals type) with adjacent p_{\perp} orbitals.

lies in a $p_z (p_{\perp})$ orbital laying normal to the σ bonding plane. The p_{\perp} orbital forms weaker bonds (Van der Waals type) with adjacent p_{\perp} orbitals.

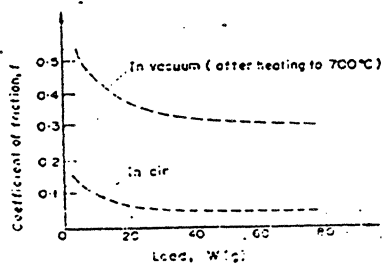


Fig. 5.12. Comparison of friction of diamond surfaces in air and vacuum.

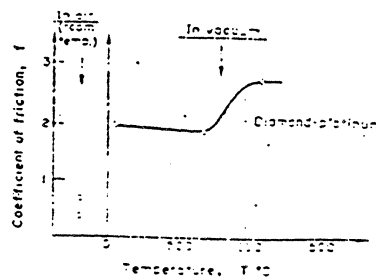


Fig. 5.13. Friction of diamond-on-metal after cleaning in a vacuum.

192

Overcoats for Film Media

- Overcoats provides mechanical protection (tribology, durability), corrosion protection, and electrical insulation.
- Spacing loss considerations limit overcoat thickness to 250-400Å range.
- Typical overcoat materials - amorphous carbon, SiO_2 or ZrO_2 .
- Hardness is usually considered a key parameter, but *effective* hardness is often dominated by substrate and underlying films.

High tensile strength, resistance to brittle fracture and adhesion are also important.

Overcoat should be chemically inert.

- "Others" include TiC , TiN , SiC , BN , Cr_2O_3 , Al_2O_3 .

Diamond-Like Carbons (DLC)

The amorphous carbon coatings with (a-C:H) or without hydrogen (a-C) produced by ion-beam assisted evaporation, sputtering, ion plating, and PECVD processes are very hard and are normally called diamond-like carbon (DLC).

i-C has been proposed as a generic term for these coatings (i for the role of the ions).

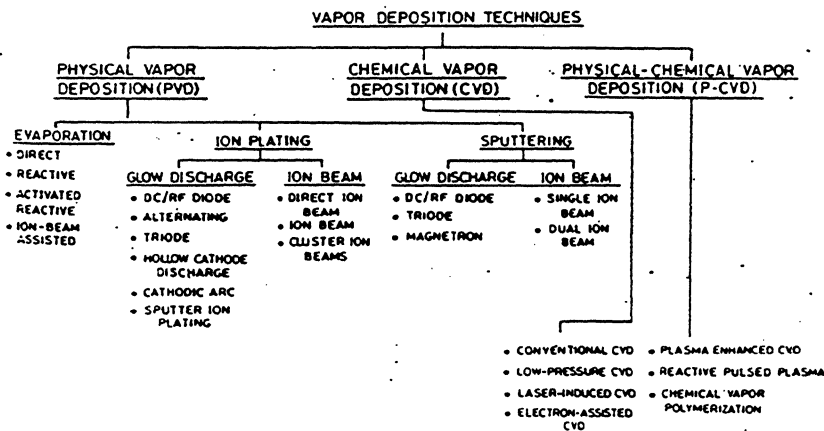
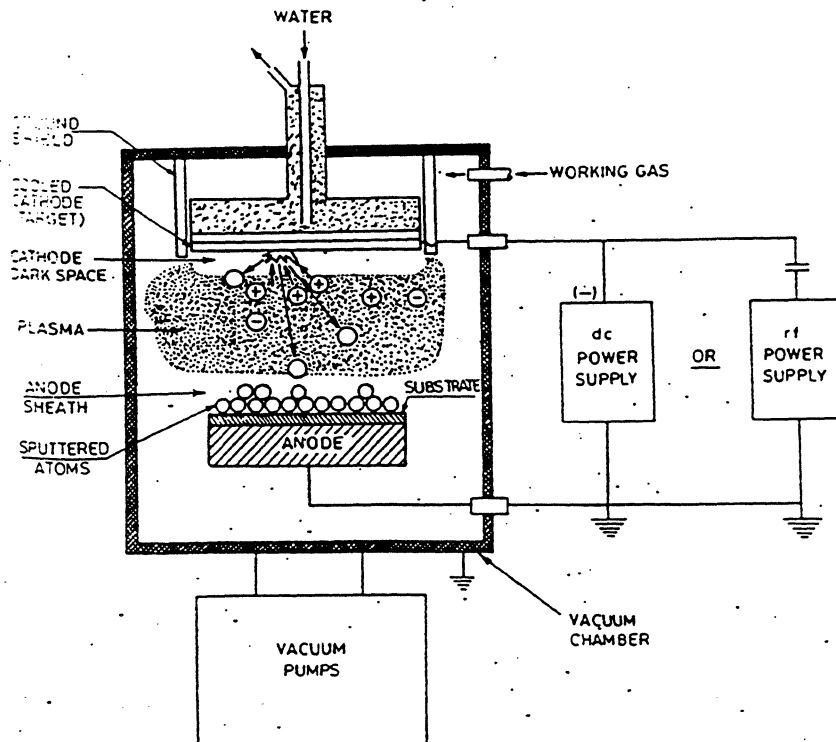


FIGURE 9.1 Classification of coating deposition techniques based on vapor deposition.



Background Gas
Ar, N₂,

FIGURE 9.38 Schematic of a glow-discharge planar diode sputtering system using dc or capacitively coupled rf power supply.

TABLE 9.1 Process Parameters of Various Coating Deposition Techniques Based on Vapor Deposition*

Deposition technique	Type of coating materials	Form of coating material source	Type of substrates	Kinetic energy, eV	Deposition pressure, Pa (torr)	Deposition temperature, °C	Coating thickness range, μm	Deposition rate, μm min ⁻¹	Relative adhesion
Direct evaporation	Essentially any pure metal, many alloys, and compounds, e.g., Al, Au, Ag, Ni, Cr, Ti, Mo, W, stainless steel, Ni-Cr, Pb-Sn, MCrAlY, Al ₂ O ₃ , TiC, TiB ₂	Solid	Any nongassing material	0.1-1	10 ⁻³ -10 ⁻⁶ (10 ⁻⁵ -10 ⁻⁸)	200-1600†	0.1-1000	1-25	Fair at elevated temperature
Activated reactive evaporation (ARE)	Almost any, e.g., Al ₂ O ₃ , SiO ₂ , Y ₂ O ₃ , TiO ₂ , SnO ₂ , In ₂ O ₃ , W ₂ C, TiC, Ni-TiC, ZrC, HfC, VC, NbC, TiC-CO, TiC-Ni, TiN, HfN, CBN, TiB ₂ , ZrB ₂ , TiC-TiB ₂ -Co	Solid	Any nongassing material	5-20	10 ⁻² -1 (10 ⁻⁴ -10 ⁻²)	200-1600†	0.1-1000	1-75	Fair to good at elevated temperature
Glow-discharge ion plating	Almost any, e.g., Au, Ag, Pb, Sn, Pb-Sn, Al, Ni, Cr, Ni-Cr, CoCrAlY, SiO ₂ , Al ₂ O ₃ , Cr ₂ O ₃ , ZrO ₂ , TiO ₂ , WC, TiC, Cr ₃ C ₂ , B ₄ C, TiN, HfN, ZrN, Si ₃ N ₄ , and (TiAl)N	Solid	Substrate must withstand ion bombardment heating	10-100	5 × 10 ⁻¹ -10 (5 × 10 ⁻³ -10 ⁻¹)	100-300	0.02-10	0.02-5	Generally good
Ion beam ion plating	Almost any, e.g., Ni, Al, Au, i-C, Cr-C, Cr-N, TiN, Si ₃ N ₄ , AlN, and (TiAl)N	Solid	Substrate must withstand ion bombardment heating	100-10,000	10 ⁻⁵ -10 ⁻² (10 ⁻⁷ -10 ⁻⁴)	100-500	0.02-10	0.02-2	Excellent

TABLE 9.1 Process Parameters of Various Coating Deposition Techniques Based on Vapor Deposition* (Continued)

Deposition technique	Type of coating materials	Form of coating material source	Type of substrates	Kinetic energy, eV	Deposition pressure, Pa (torr)	Deposition temperature, °C	Coating thickness range, μm	Deposition rate, μm min ⁻¹	Relative adhesion
Glow-discharge sputtering	Essentially any, e.g., Au, Ag, Ni, Cr, Co, Mo, W, Al ₂ O ₃ , ZrO ₂ , Cr ₂ O ₃ , SiO ₂ , TiC, ZrC, HfC, B ₄ C, TiN, ZrN, HfN, Si ₃ N ₄ , CrB ₂ , Mo ₂ B ₃ , Cr ₃ Si ₂ , MoS ₂ , WS ₂ , PTFE, poly(amide-imide)	Solid	Any nongassing material	10-100	5 × 10 ⁻¹ -10 (5 × 10 ⁻³ -10 ⁻¹)	100-300	0.02-10	0.02-2	Generally good
Ion beam sputtering	Almost any, e.g., Ni, Cr, Mo, Ti, W, Zr, Ta, Si, Ni ₃ Al, Nb-Ti, i-C, Al ₂ O ₃ , SiO ₂ , Ta ₂ O ₅ , Cr-C, AlN, Si ₃ N ₄ , i-BN, PTFE	Solid	Any nongassing material	100-10,000	10 ⁻⁵ -10 ⁻² (10 ⁻⁷ -10 ⁻⁴)	100-500	0.02-10	0.02-0.5	Good to excellent
Chemical vapor deposition (CVD)	Essentially any, e.g., Ni, Cr, Mo, Ti, W, Zr, Ta, Si, Cu, Fe, Pt, Al ₂ O ₃ , ZrO ₂ , Cr ₂ O ₃ , SiO ₂ , SnO ₂ , TiC, ZrC, HfC, B ₄ C, Cr ₃ C ₂ , WC, TiN, ZrN, HfN, Si ₃ N ₄ , BN, TiB ₂ , ZrB ₂ , MoB, FeB, TiSi ₂ , MoSi ₂	Solid, liquid, gas/vapor	Any metal or nonmetal that can withstand deposition temperature and chemical attack by plating vapors	0.1-1	10-10 ⁵ (0.1-760)	150-2200	0.5-1000	0.5-25	Excellent
Plasma-enhanced chemical vapor deposition (PECVD)	Essentially any, e.g., Si, Ni, C, diamond, TiO ₂ , TiC, B ₄ C, SiC, TiN, BN, Si ₃ N ₄ , polymers	Solid, liquid, gas/vapor	Any nongassing material that can withstand deposition temperature	10-500	1-500 (10 ⁻² -5)	100-500	0.5-10	0.1-2	Good to excellent

TABLE 9.2 Advantages and Disadvantages of Various Vapor Deposition Techniques

Deposition technique	Advantages	Disadvantages
Direct/reactive evaporation	Simple, cheap, extremely high deposition rates, low pressure, no gas scattering, and incorporation of gas atoms	Low kinetic energy, inadequate adhesion, high substrate temperature for dense coatings, imprecise control of stoichiometry of compound coatings, substrate must generally be rotated for uniform coating
Activated reactive evaporation (ARE)	Extremely high deposition rates, variety of coating compositions, precise control of stoichiometry, better adhesion, denser microstructure than evaporation	High substrate temperature, addition of extra electrode make process slightly complicated as compared to evaporation, substrate must generally be rotated for uniform coating
Glow-discharge ion plating	Simple, excellent adhesion, graded interface, moderately high deposition rate, good coverage of complex shapes	Deposition is complicated due to substrate biasing as compared to sputtering and evaporation and ARE
Ion beam ion plating	Excellent adhesion, very high kinetic energy of ions, fine control of kinetic energy and incident angle of ions possible, low-pressure deposition, no gas atom incorporation	Needs separate ion source, poor throughput, low deposition rates, not suitable for industrial production
Glow-discharge sputtering	Simple, wide choice of coating materials, easy to obtain stoichiometric coatings through optimization of parameters, low substrate temperature, excellent uniformity over complex and large areas, but poor coverage and deep recesses	Relatively low kinetic energy
Ion beam sputtering	Independent control over kinetic energy and current density of ions, directionality control of ion beams, very high-kinetic-energy ion beam leads to excellent adhesion and high density, low deposition pressure, high deposition rates, no gas atom incorporation, no substrate heating, and unique coating properties	Needs separate ion source, cannot be used with very large substrate areas because of small ion beam size (~100-mm diameter)
Chemical vapor deposition	Wide choice of coating materials, extremely high deposition rates, near-theoretical density, controlled grain size, excellent adhesion, relatively uniform coating of complex shapes and over large areas possible	High substrate temperature, low kinetic energy, relatively high cost of starting materials, low utilization of starting materials
Plasma-enhanced chemical vapor deposition	Lower substrate temperatures as compared to CVD, high deposition rates, excellent adhesion due to high kinetic energy, and flexibility of substrate shape and size	More complex as compared to CVD because of inclusion of plasma, strong interaction of plasma with growing coating resulting in somewhat nonuniform deposition; deposition of pure materials very difficult

sputtering approach is the best for practical manufacturing ↑

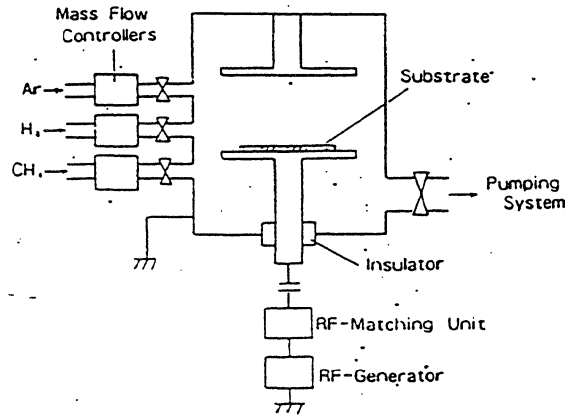


FIG. 1. Schematic view of the RF plasma CVD system.

Chemical Vapor Deposition

TABLE 14.32 Selected Properties of Hard Diamond-like Carbon (a-C, a-C:H) Coatings Applied by Various Plasma Techniques

Deposition conditions								
Deposition technique	Source of carbon	Ion energy	Density, kg m ⁻³	Electrical resistivity, Ω cm	Optical properties	Hardness (HV or HK)	Chemical inertness	References
Sputter deposition (a-C)	Carbon target in rf plasma	rf power 2.2 and 75 W	—	10 ⁻² -10 ³	E _o = 0.8 eV	—	—	Hauser (1977)
	dc magnetron sputtering of a graphite target	Power 10 W	2100-2200	1.5 × 10 ²	n = 2.3 E _o = 0.68 eV	2400 HV	—	Savvides and Window (1985)
		50 W	1900	1.0	n = 2.73 E _o = 0.5	2095 HV	—	
		500 W	1600	0.2	n = 2.95 E _o = 0.4	740 HV	—	
	Carbon target in dc plasma (with simultaneous bombardment of substrate)	1-20 eV	2100-2200	> 10 ¹¹	Reflectance = 0.2 Absorptance = 0.7	—	—	Banks and Rutledge (1982)
* (a-C:H)	Carbon target in rf plasma of hydrogen	—	—	10 ¹²	E _o = 1.4 to 2.8 eV	2000 HV	—	Hiraki et al. (1984)
Ion beam deposition (a-C:H)	Hydrocarbon in dc plasma and Ar ion beam	0.5-1.5-keV	~2000	10 ⁷ -10 ¹⁰	—	4000-6000 HV	—	Weissmantel et al. (1982)
	Carbon target and Ar ion beam	1.2 keV	2250	—	E _o = 0.7 eV	>2000 HV	—	Kaplan et al. (1985)
PECVD deposition (a-C:H)	Hydrocarbon in rf plasma	40-100 eV	—	~10 ¹⁰	n = 2.0	> glass	Resist HF for 40 h	Holland and Ojha (1979)
	Hydrocarbon in dc plasma	50-100 eV	—	—	n = 2.3 at λ = 5 μm	1850 HK	—	Moravec and Orent (1981)
	Hydrocarbon in rf plasma	200 eV	—	—	—	3000 HV	—	Yamamoto et al. (1988)
	Hydrocarbon in rf plasma	0.5-1.5-keV	1500-1800	10 ¹²	n = 1.85 to 2.20 E _o = 1.0 to 1.6 eV	1250-1650	—	Bubbenzer et al. (1983)
	Hydrocarbon in rf plasma	100 eV	—	—	—	2500 HK, modulus of elasticity = 120 MPa	—	Memming et al. (1986)

n = refractive index.
E_o = energy band gap.

Not Hydrogenated

Resistivity is very high

Table 8.11. Structure and properties of some deposited thick ($\geq 1 \mu\text{m}$) diamond-like carbon films

Type of C	Electrical resistivity, $\Omega\cdot\text{cm}$	Microhardness, kg/mm^2	Structure/surface analytical technique(s)	Reference
Ion Plated a-C:H	10^{11}	Able to scratch glass	Polycrystalline background of cubic diamond with a particle size of 5–10 nm with single crystal region up to $5 \mu\text{m}$ \varnothing /X-ray diffraction; surface layer amorphous/electron diffraction	Aisenberg and Chabot (1971) Spencer et al. (1976)
a-C:H	$10^7\text{--}10^9$	4000–6000	Microcrystal of diamond/electron diffraction and energy loss spectroscopy	Weissmantel et al. (1982)
Rf plasma a-C:H	10^{11}		XPS spectra found between diamond and graphite	Berg and Andersson (1979)
a-C:H	10^{12}		XPS spectra found between diamond and graphite	Nyaish and Holland (1984)
a-C:H		1900	Amorphous	Pethica et al. (1985)
a-C:H			Tetrahedrally and trigonally bonded carbon/NMR	Kaplan et al. (1985)
a-C:H		2500 Young's modulus, 0.12 GPa	Amorphous/FTIR	Memming et al. (1986)
a-C:H		3000	Raman spectra found between diamond and graphite	Kurokawa et al. (1987)
Sputtered a-C	10^4	1200–2400	Tetrahedrally and trigonally bonded carbon/optical	Savvides and Window (1985)
a-C:H	10^{12}	1000–2000	Improved diamond-like structure/electron diffraction and Raman	Miyasato et al. (1984)

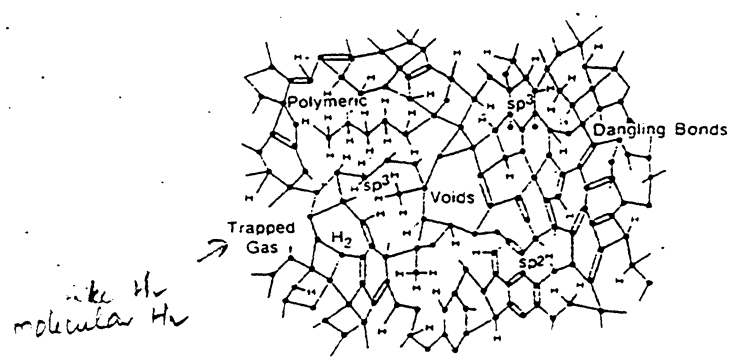


Figure 1. Schematic diagram showing possible atomic configurations in a random network of hydrogenated amorphous carbon.

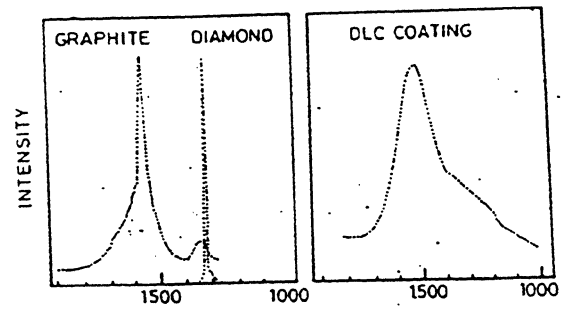


FIGURE 14.63 Raman spectra of single-crystal diamond, single-crystal graphite, and DLC carbon coating on a silicon substrate produced by rf-PECVD. [Adapted from Kurokawa et al. (1987).]

depend on the ratio of sp^3 to sp^2 hybridization.

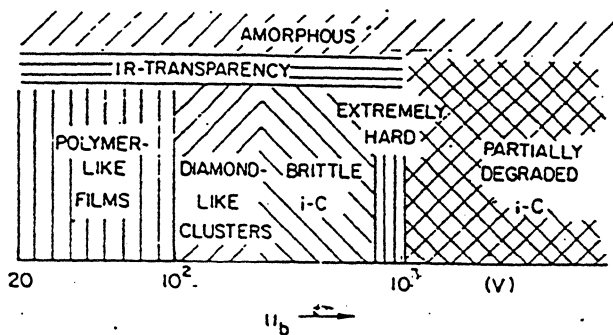


FIG. 14. Schematic representation of general film properties of "diamond-like carbon" films as a function of accelerating voltage, V_a . The films were grown by "ion plating" from benzene (from Ref. 138).

a-C:H coatings from ionized benzene vapor using argon ion beam at acceleration voltage between 0.5 and 1.5 kV

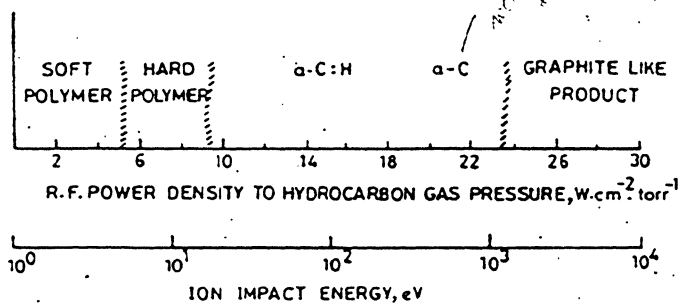


FIGURE 14.61 Characteristic features of DLC carbon coating produced by rf-PECVD on rf power density to hydrocarbon gas pressure and impact energy. [Adapted from Nuyesh and Holland (1980).]

the C-H bonds decrease and C-C bonds increase as the rf power density increases and gas pressure is reduced.

TABLE 14.34 Properties for the Four a-C:H Coatings Produced by rf-PECVD*

Material	Negative self-bias voltage, V	Gas pressure, Pa	Bias volt./ (gas press.) ^{1/2} , V/Pa ^{1/2}	Hydrogen conc., at %	sp ² /sp ³ ratio	Density, kg m ⁻³	Micro-hardness, kg mm ⁻²	Refractive index	Optical band gap, eV
Diamond†	—	—	—	0	0/100	3000-3500	8000-10,400	2.41	5.5
Coating	200	3.2	111	60	10/90	1490	—	1.78	2.05
Coating	400	5.0	180	50	13/87	1500	1200	1.82	1.60
Coating	800	3.6	420	40	20/80	1590	3000	1.93	1.20
Coating	1200	1.9	869	25	38/62	1750	2200	2.10	0.95
Graphite†	—	—	—	0	100/0	2300-2700	Soft	2.8 (1C)	0

* Yamamoto et al. (1988) reported that substrate temperature from -100 to 230°C had little effect on the properties.

† Literature values for bulk diamond and graphite are included for comparisons.

Source: Adapted from Fink et al. (1984), and Yamamoto et al. (1988).

TABLE 14.35 Properties of a-C:H Coatings Produced by PECVD and Ion Beam Sputtering

Material	H ₂ at. %	sp ² /sp ³	Density, kg m ⁻³	Hardness, g to scratch	Optical band gap, eV
Diamond*	0	0/100	3000-3500	Extremely hard	5.5
rf anode PECVD	61	14/86	1020	160	4.1
rf cathode	58	20/80	1170	250	4.0
dc anode	47	50/50	1460	700	1.7
dc cathode	31	60/40	1700	1250	—
Ion beam sputtering (88% H ₂ in Ar)	35	62/38	1530	>2000	1.2
Ion beam (0% H ₂ in Ar)	0	—	2250	>2000	0.7
Graphite*	0	100/0	2300-2700	Soft	0

* Literature values for bulk diamond and graphite are included for comparisons.

Source: Adapted from Kaplan et al. (1985).

Durability & the bonding nature of Carbon overcoats

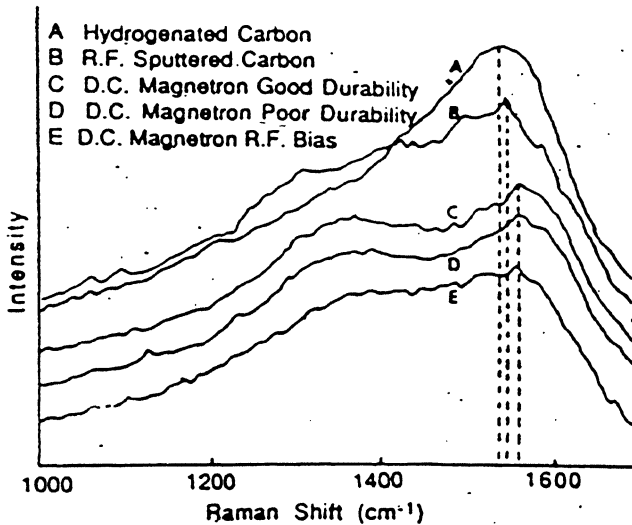


Fig. 2—Raman Spectra Obtained from the Different Carbon Types

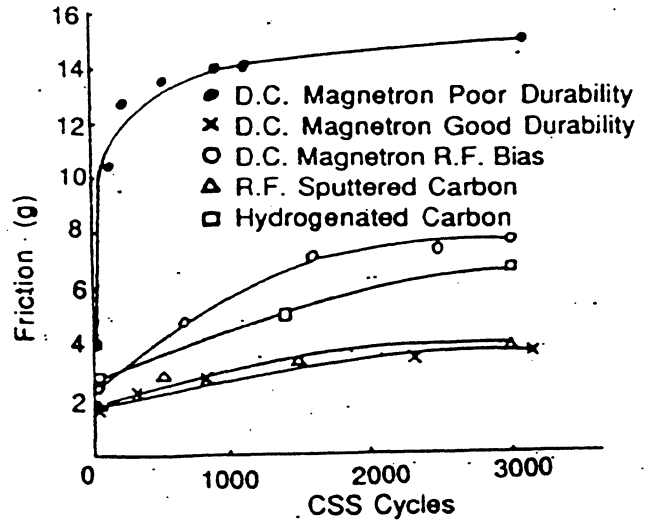


Fig. 1—Friction vs. CSS Cycles for Different Carbon Types Using Ferrite Heads.

Table 1 Peak Frequencies and Intensities Calculated from Raman Data in Figure 2							
File Name	D Peak			G Peak			
	Int. 1	MWMM 1	Freq. 1	Int. 2	MWMM 2	Freq. 2	
A	1993	390	1301	2724	110	1534	2.59
B	1292	295	1349	902	81	1550	5.22
C	2308	224	1359	1804	68	1569	4.21
D	1413	237	1357	1063	66	1571	4.77
E	-	257	1361	-	79	1570	-

A - Hydrogenated Carbon
 B - R.F. Sputtered Carbon
 C - D.C. Magnetron Good Durability
 D - D.C. Magnetron Poor Durability
 E - D.C. Magnetron R.F. Bias

No correlation between slight changes in Raman Spectra & mechanical properties. Difference between ● and × coating attributed to carbon thinning due differential nucleation at the the grain boundaries.

(from S. Smith et al, Seagate Technology)

Effect of Humidity

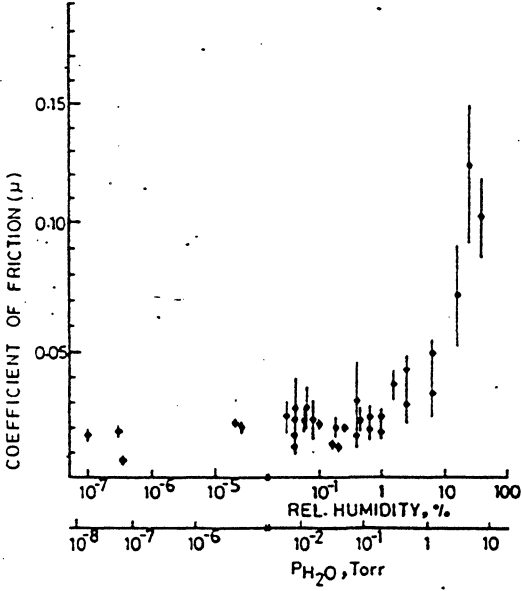


FIGURE 14.65 Coefficient of kinetic friction as a function of water vapor partial pressure (p_{H_2O}) in N_2 atmosphere of a steel pin sliding on an rf-plasma CVD (DLC) carbon coating on a silicon substrate. [Adapted from Enke et al. (1980).]

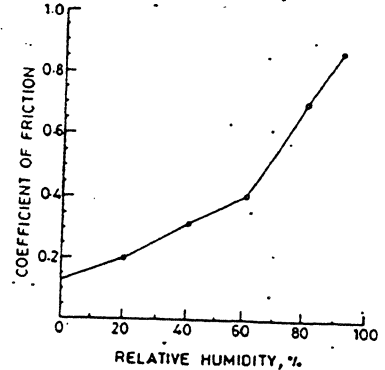


FIGURE 14.57 Coefficient of kinetic friction as a function of relative humidity of an Mn-Zn ferrite slider sliding on dc magnetron-sputtered (DLC) carbon-coated magnetic disk. Normal load = 100 mN; sliding speed = 1 m s^{-1} . [Adapted from Doan and MacKintosh (1988).]

Humidity Insensitive Films

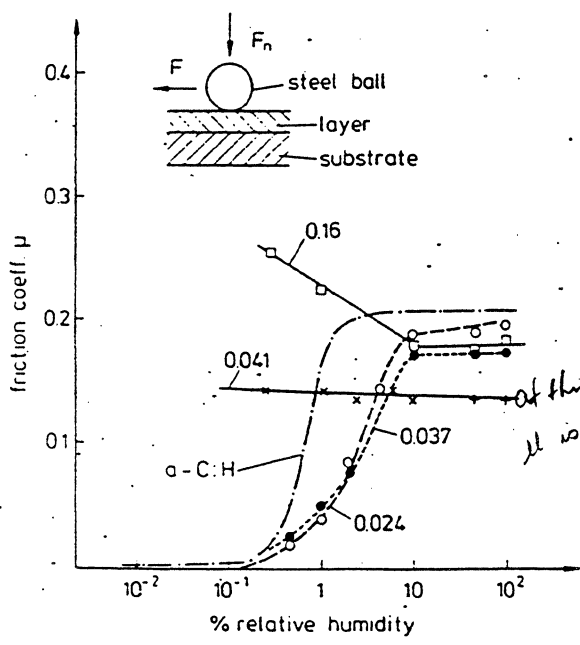


FIG. 1. Friction coefficient vs relative humidity for a-C:H (Fe) at various Fe concentrations at a load $F_n = 0.3 \text{ N}$.

from Dimigen et al., Appl. Phys. Lett., 50, 1057 (1987)

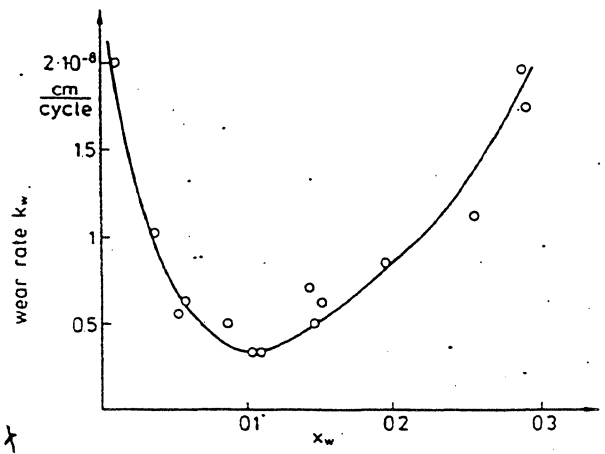


FIG. 2. Wear rate k_w vs mole fraction of tungsten in the a-C:H film; load: $F_n = 0.3 \text{ N}$.

TABLE I. Friction at sliding speed of 10 cm s^{-1} .

Material	Friction μ	
	Humid air 40%	Dry N_2 ~0.2%
a-C:H	0.21	0.02
a-C:H (W) $x = 0.06$	0.19	0.23
a-C:H (Ru) $x = 0.07$	0.15	0.7 (0.06 at $V = 1.6 \text{ cm s}^{-1}$)

at this level it is independent

DISK DURABILITY

To Achieve Durability, Thin Film Media Requires:

1. Surface overcoat (ZrO_2 , carbon)

To provide a hard and wear resistant surface

To reduce risk of crash due to head/disk contact

To provide corrosion protection to the magnetic film

2. A liquid or solid lubricant (free, bonded or partially bonded)

To reduce friction and wear

To provide flyability

3. *Right Roughness*

Liquid Lubricants

Table 8.6. Types of liquid lubricants (oils)

Natural organics	Synthetic organics
Animal fat	Synthetic hydrocarbons (polybutene)
Shark oil	Chlorinated hydrocarbons
Whale oil	Chlorofluorocarbons
Vegetable oils	Esters
Mineral (petroleum oils)	Organic acid
- Paraffinic	Fatty acid
Naphthenic	Dibasic acid (di)
Aromatic	Neopentyl polyol
	Polyglycol ethers
	Fluoro
	Phosphate
	Silicate
	Disiloxane
	Silicones
	Dimethyl
	Phenyl methyl
	Chlorophenyl methyl
	Alkyl methyl
	Fluoro
	Silanes
	Polyphenyl ethers
	Perfluoropolyethers

Animal fats:

historically commonly used lubricants. Usually good boundary lubricants. Poor thermal and oxidative stability tend to break down to give a solid-like deposits.

Mineral oils:

most widely used mainly hydrocarbons (paraffins) in which the carbon atoms are straight or branched chains. Aromatics play an important role in boundary lubrication.

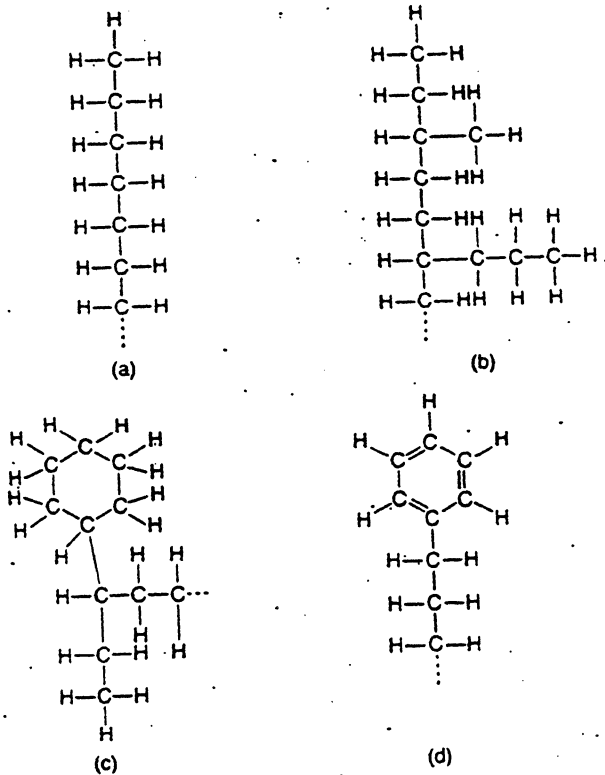


Fig. 8.10. Main types of mineral (petroleum) oils: (a) straight paraffin, (b) branched paraffin, (c) naphthene, and (d) aromatic.

Class	Typical structural formula
Synthetic hydrocarbon (Polybutene)	$(-CH_2-CH_2-CH_2-CH_2-)_n$
Chlorofluorocarbon	$\left[\begin{array}{cc} Cl & F \\ & \\ -C & -C- \\ & \\ F & F \end{array} \right]_n$
Diester	$C_8H_{17}-O-CO-C_8H_{16}-CO-O-C_8H_{17}$
Neopentyl polyol ester	$CH_3-CH_2-C(CH_2OOC-C_8H_{17})_2$
Fatty acid ester	$C_{13}H_{27}-OC(=O)-C_{18}H_{37}$
Polyglycol ether	$HO-(CH_2-CH(CH_3)-O-)_n-H$
Fluoroester	$F(CF_2)_4-CH_2OOC(CF_2)_4-F$
Phosphate ester	$(CH_3-C_6H_4-O)_3P=O$
Silicate ester	$Si(O-C_8H_{17})_4$
Disiloxane	$C_4H_9-O-Si(O-C_4H_9)_2-O-Si(O-C_4H_9)_2-O-C_4H_9$
Silicone	$CH_3-Si(CH_3)_2-O-Si(CH_3)_2-O-Si(CH_3)_2-CH_3$
Silane	$(C_{12}H_{25})_3Si(C_6H_{13})_3$
Polyphenyl ether	
Perfluoroalkyl polyether	$F-CF_2-CF_2-O-CF_2-CF_2$

Fig. 8.11. Typical chemical structure of principal classes of synthetic lubricants (Braithwaite, 1967).

Polybutenes

stability (thermal) limited by the bond energy of the C-C (85 kcal/mole). improve by the use of branched chains and oxidative inhibitors

Chlorofluorocarbons

Cl & F atoms protect the C-C bond and improve stability

Esters

products of an alcohol (R-CH₂OH) and organic acid (R'-COOH).

the ester linkage:
 $R'-O-C(=O)-R-C(=O)-O-R'$
 thermally more stable than hydrocarbons and chlorofluorocarbons

They also exhibit an excellent viscosity-temperature and volatility properties. But they are prone to the acid-catalyzed degradation reactions that can proceed by oxidative, thermal, or hydrolytic mechanisms.

Silicones

high chemical inertness, thermal stability, low volatility but are poor boundary lubricants.

Silanes:

204

a high temperature stability.
they are not polymers

Polyphenyl ethers:

very resistant to oxidation, very low volatility
fair boundary lubricants

Perfluoropolyethers

most promising for high-temperature applications
very low surface tension. Chemically inert.

Table 8.7. Typical properties of commonly used classes of synthetic lubricants (oils)

Lubricants	Thermal stability, °C	Kinematic viscosity (cSt) at, °C					Specific gravity at 20°C	No O ₂ Thermal* conductivity, cal/h m °C	Specific heat at 38°C, cal/g °C	Flash point, °C	Pour point, °C	with O ₂ Oxidative* stability, °C	Vapor pressure at 20°C, Torr
		-20	0	40	100	200							
Mineral oils	135	170	75	19	5.5		0.86	115	0.39	105	-57		10 ⁻⁶ to 10 ⁻²
Diesters	210	193	75	13	3.3	1.1	0.90	132	0.46	230	-60		10 ⁻⁶
Neopentyl polyol esters	230	16	16	15	4.5		0.96			250	-62		10 ⁻⁷
Phosphate esters	240	85	38	11	4		1.09	109	0.42	180	-57		10 ⁻⁷
Silicate esters	250	115	47	12	4	1.3	0.89			185	-65		10 ⁻⁷
Disiloxanes	230	200	100	33	11	3.8	0.93			200	-70		
Silicones													5 x 10 ⁻⁸
Phenyl methyl	280	850	250	74	25	22	1.03	124	0.34	260	-70	240	
Fluoro	260	20,000		190	30	24	1.20			290	-50	220	
Polyphenyl ethers													
4P-3E	430		2500	70	6.3	1.4	1.18	133	0.43	240	-7	290	10 ⁻⁸
5P-4E	430			363	13.1	2.1				290	+4	290	
Perfluoropolyethers													
Fomblin YR	370		8000	515	35		1.92	82	0.24	none	-30	320	10 ⁻⁹
Fomblin Z-25	370	1000	440	150	41		1.87		0.20	none	-67	320	3 x 10 ⁻¹²

Physical and Chemical Properties

#(1) Viscosity

$$\text{absolute viscosity} = \frac{\text{shear stress}}{\text{rate of shear}}$$

expressed in Centipoises (cP = mPa · s)

The Viscosity should change as little as possible within the operating temp. and pressure and should not be temporarily or permanently reduced under high shearing forces. Shear instability (a permanent drop in viscosity) reflects a molecular degradation at very high shear rates. Applicable to magnetic systems where the rate of shear $\dot{\gamma}$ is of the order of 10^9 s^{-1} .

(2) Surface tension *

A liquid with low surface tension and a low contact angle would spread easily on the solid surface and provide good lubrication.

Table 8.9. Surface tension of several base oils

Liquid	Surface tension, dynes/cm (= mN/m)
Water	72
Mineral oils	30-35
Esters	30-35
Methyl silicone	20-22
Perfluoropolyethers	19-21

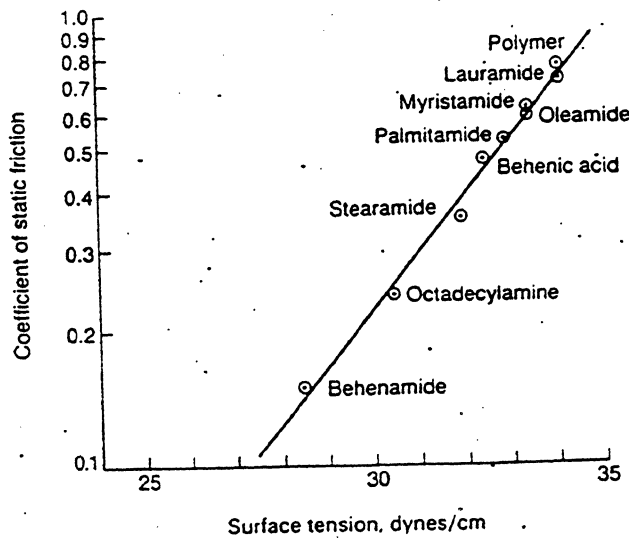


Fig. 8.12. Coefficient of static friction as a function of critical surface tension for several long-chain, solid fatty lubricants in thin coatings of vinylidene chloride-acrylonitrile copolymer (Owens, 1964).

Owens (1964) incorporated about 2% by weight of solid fatty compounds into VCA polymer and showed a good correlation between friction and surface tension.

(3) Thermal Properties

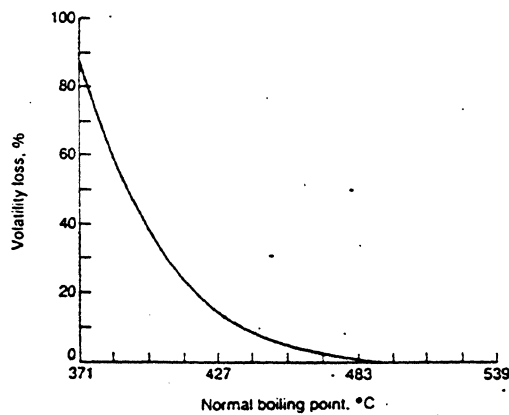
The thermal conductivity and specific heat play important role in heat dissipation from the rubbing asperities.

Continuous frictional heating can result in an oxidation with the formation of high molecular weight degradation products appearing as deposits.

(4) Volatility

is related to molecular weight (or viscosity) the higher the molecular weight, the lower the volatility. It is generally measured as the weight loss from a sample heated under standard conditions of time and temperature.

Perfluoropolyethers (PFPE) have the lowest vapor pressure (10^{-12} to 10^{-9} torr)



An increase in the boiling point from 371 to 430°C results in a decrease in volatility loss from 90 to 10%

Volatility loss is a function of the normal boiling point
(Booser, 1984)

(5) Oxidative Stability

207

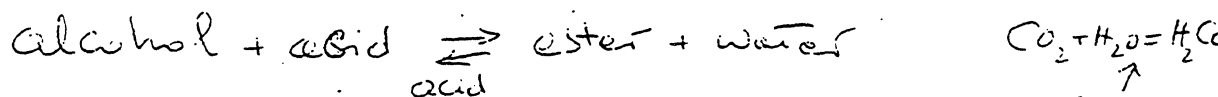
Oxidative stability, the stability of a lubricant in the presence of air or oxygen, is the most important property. Oxidation proceeds in a chain-like autocatalytic fashion that involves formation of organic peroxides which in turn increase the rate even further. Certain metal surfaces and ceramics exert a pronounced catalytic effect in promoting the rate. Inhibitors (anti-oxidant additives) such as aromatic amines, phenols, or alkyl sulfides are not effective when the lubricant is in a molecularly thin film.

(6) Thermal Stability (TS)

is the resistance of the lubricant to either molecular breakdown or rearrangement at elevated temps. in the absence of air. It defines the maximum useful temperature at which the lubricant can be used. TS is related to the strength of the bond between any two atoms in the polymer chain.

TS is also a function of film thickness

(7) Hydrolytic Stability (water resistance)



Since water is available (H^+) and organic acid (CO_2) a heat source (frictional heat) can drive the equilibrium in the reverse direction.

General Properties of Some Classes of Synthetic Lubricants

Lubricant	Viscosity temperature characteristics	Volatility	Oxidation resistance	Thermal stability	Resistance to hydrolysis	Flammability characteristics	Lubrication characteristics	Solvent effect on paints, rubber, etc.	Solubility in petroleum and other synthetics	Improvement additive compatibility	Price range per liter	Typical applications
Chloro-fluoro-carbons	Poor	Some lower, some higher	Excellent	Poor to excellent	Poor to excellent	Excellent	Good to excellent	Widely variable	Generally poor	Widely variable	\$10-100	Nonflammable, extreme oxidation-resistant lubricants for plant processes or devices handling reactive materials
Dibasic-acid esters	Good to excellent	Generally lower	Fair to good	Fair to good	Fair to good	Poor to fair	Fair to good	Pronounced effect	Good to excellent	Generally good	\$2-5	Instrument oils, low-volatility grease bases, special hydraulic fluids, jet-turbine lubricants
Neopentyl polyol esters	Good to excellent	Lower	Good	Good	Fair to good	Poor to fair	Fair to good	Pronounced effect	Good to excellent	Generally good	\$2-5	Instrument oils, low-volatility grease bases, special hydraulic fluids, jet-turbine lubricants
Polyglycol ethers	Good to excellent	Generally lower	Poor to fair	Fair to good	Fair to good	Fair to good	Good	Pronounced effect on paint, small effect on rubber	Fair to good	Generally good	\$1-3	Special hydraulic fluids, forming and drawing lubricants, low-temperature grease base, vacuum-pump lubricants, component of other synthetic lubricant formulations
Phosphate esters	Excellent	Generally lower	Good	Fair to good	Poor to good	Good to excellent	Good to excellent	Pronounced effect	Good to excellent	Generally good	\$2-6	Fire-resistant hydraulic fluids, low-volatility, high-lubricity grease base, lubrication additives in other synthetics, special low-temperature lubricants
Silicate esters	Excellent	Lower	Poor to fair	Good	Poor to fair	Poor to fair	Fair to good	Some effect	Fair to good	Fair to good	\$4-10	Heat-transfer fluids, high-temperature hydraulic fluids, low-volatility, low-viscosity grease bases, components for low-viscosity hydraulic fluids
Silicones	Excellent	Much lower	Good to excellent	Good to excellent	Excellent	Poor to good	Poor to fair	Generally small effect	Poor	Poor	\$20-40	High-temperature bearings, condensation pump lubricant, low-volatility grease base for lightly loaded bearings, damping fluids, devices requiring minimum viscosity change with temperature
Silanes	Fair to good	Much lower	Fair to good	Good to excellent	Good	Poor to fair	Fair to good	Generally small effect	Fair	Fair		Base stocks for high-temperature greases, hydraulic fluids, and engine lubricants; require extensive formulation
Polyphenyl ethers	Poor to fair, generally high pour points	Much lower	Excellent	Excellent	Excellent	Poor to fair	Fair to good	Generally small effect	Fair		\$30-60	High-temperature fluid for reactor coolant, hydraulic applications at very high temperature
Perfluoro polyethers	Good to excellent	Lowest	Excellent	Excellent	Excellent	Poor to fair	Good	Generally small effect	Fair		\$30-60	Base stocks for greases for high-temperature, vacuum and chemical resistance applications; hydraulic fluids for very high temperatures, magnetic rigid disks

* Properties are for typical class members, comparing synthetics with well-refined petroleum products in equal service. For comparative purposes, the petroleum product would rate as fair to good. Exceptions are flammability and volatility where petroleum products would rate poor and lubrication characteristics and hydrolysis where petroleum products would be rated excellent.

Lubricant Selection Criteria

How to select a disk Lubricant?

bonded like - solid
non bonded - mineral oil, plasma

Good boundary lubrication *very thin monolayer*

- Provide adequate wear protection
- Insure long-term flyability

Low surface tension

- Lower stiction force
- Minimize contamination sensitivity

Low volatility

- Reduce loss due to evaporation and air shear

Good surface affinity

1. AFM
2. Rinse with solvent
3. Functional Test

- Provide long-term durability
- Reduce loss due to spin-off and displacement

High thermal/chemical stability

- Prevent catalytic decomposition
- Prevent formation of frictional polymers
- Compatible with other file components

Good hydrolytic and shear stability

- Provide stable interface performance

commercial measurement for

1. time ejection pump

polystyrene } → measure the viscosity
polyethylene } before and after
apply polystyrene
see - decrease the
viscosity
because the polystyrene
fall apart.

Lubrication for Thin Film Disks

Special constraints

- Lack of a disk-based replenishment mechanism
- Conflicting demands for low stiction and high durability
- Enhanced severity of tribological environment

Emphasis

- Role of lubricant molecular structure
- Mechanism of lubricant retention
- Lubricant stability

SURFACE LUBRICATION OF FILM MEDIA

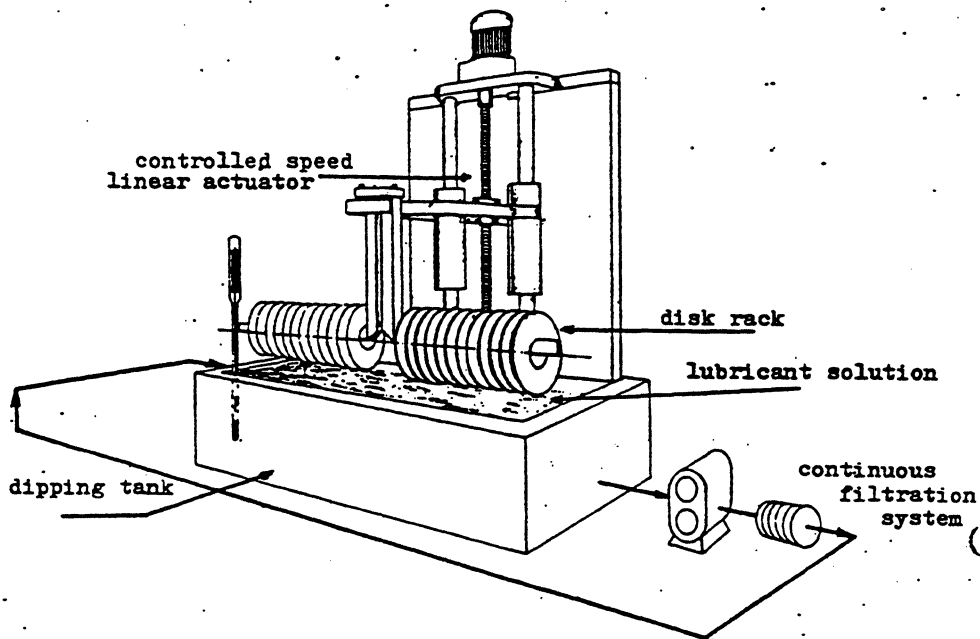
- Film media is generally treated with 5-30Å of surface lubricant for improved durability. In general, lubrication:
 - Reduces wear (particularly at lower humidities)
 - Improves flyability
 - But, lubricant increases stiction/friction
- Lubricants used include hydrocarbons (stearic acid, palmitic acid) and perfluoroethers (Z-15, Z-DOL).

Concerns with hydrocarbon lubricants are volatility, crystallization during cycling, frictional polymer formation, reactivity with head materials.

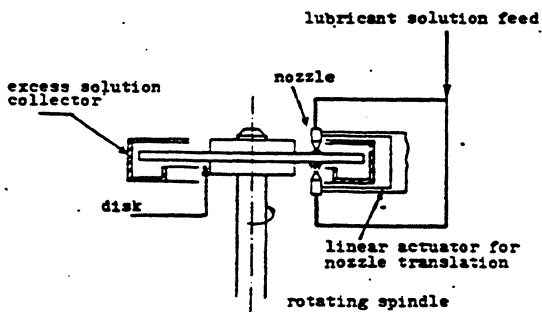
Major concern with perfluoroethers is stiction.

- Lubricants can be applied by:
 1. Spraying
 2. Spin Coating
 3. Dipping
 4. Evaporation
 5. Wiping

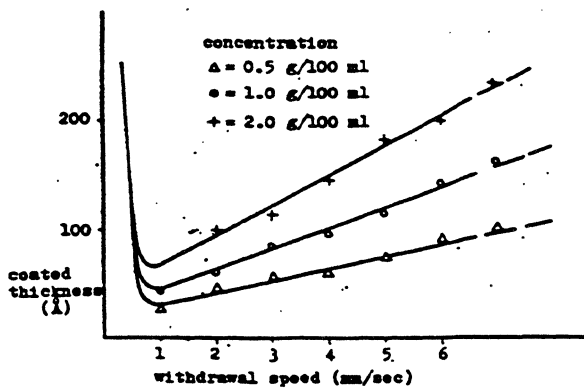
Lubricant Application Methods



Dip coating device



Spin/spray coating device



Typical dip coating calibration graph

Silicone Lubricants

Advantages

- Good thermal/oxidative stability
- Low volatility

Disadvantage

- Generally a poor boundary lubricant –

Review

- Adequate performance on early Winchester particulate disks (*Harker et al. 1981*)
- Poor durability under boundary lubrication conditions (*Cogdell et al. 1987*)
- Good performance on SiO₂ overcoated thin film disks (*Yanagisawa and Sugauma 1978*)
Non functional lubricant.

Conclusion

- Applications are too selective, depending on overcoat type

Hydrocarbon Lubricants

Advantage

- Good boundary lubricant

Disadvantages

- High volatility
- Poor thermal/oxidative stability

Review

- Performance strongly influenced by chain properties (*Yanagisawa 1985; Beltzer and Jahanmir 1987*)
 - Polarity → μ , lube depletion
 - Chain length → μ
 - Chain substituents → coverage, wear protection
- Durability of LB layers of cadmium arachidate is superior to that of physisorbed fluorocarbons on SiO₂ (*Novotny and Swalen 1989*)
- Adequate interface performance achieved using fatty acids with a reservoir device in a thin film disk file (*Gregory et al. 1988*)

Conclusion

- Potential applications only with a replenishment device

TABLE I
LUBRICATING MATERIALS

C	γ -(<i>N</i> -octadecylsuccinylamino)propyltriethoxysilane. $\text{CH}_3(\text{CH}_2)_{17}\text{NHCOCH}_2\text{CH}_2\text{CONH}(\text{CH}_2)_3\text{Si}(\text{OC}_2\text{H}_5)_3$
2C	γ -(<i>N,N</i> -dioctadecylsuccinylamino)propyltriethoxysilane. $[\text{CH}_3(\text{CH}_2)_{17}]_2\text{NCOCH}_2\text{CH}_2\text{CONH}(\text{CH}_2)_3\text{Si}(\text{OC}_2\text{H}_5)_3$
3C	γ -[<i>N</i> -(tris(heptadecyloxymethyl)methylsuccinylamino)propyltriethoxysilane]. $[\text{CH}_3(\text{CH}_2)_{16}\text{COOCH}_2]_3\text{CNHCOCH}_2\text{CH}_2\text{CONH}(\text{CH}_2)_3\text{Si}(\text{OC}_2\text{H}_5)_3$
ODS	mono-octadecyltriethoxysilane. $\text{C}_{18}\text{H}_{37}\text{Si}(\text{OC}_2\text{H}_5)_3$
St	stearic acid. $\text{C}_{17}\text{H}_{33}\text{COOH}$

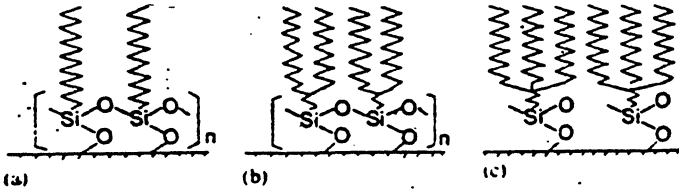


Fig. 1. Structures of monomolecular layers for (a) C, (b) 2C and (c) 3C on the substrates.

Effect of
Lateral and
Normal Bonding

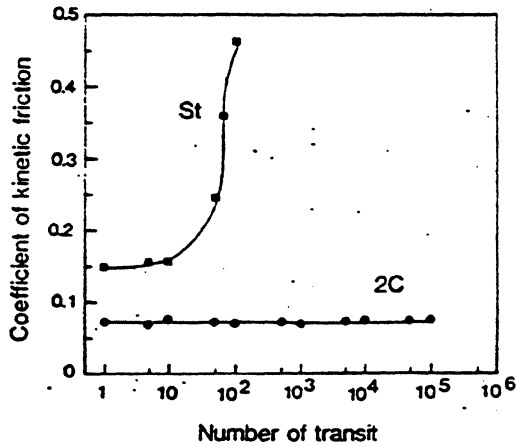


Fig. 4. Continuous frictional performance for 2C and St on glass substrates.

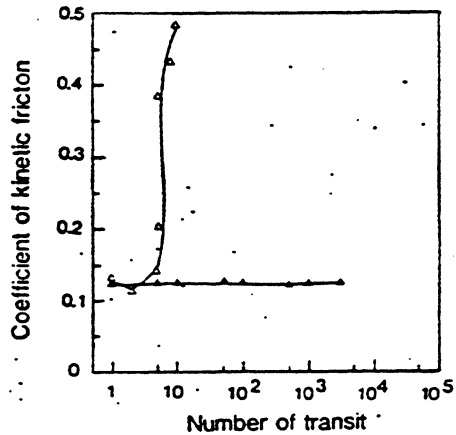


Fig. 5. Continuous frictional performance for 2C on oxidized CoCr (\blacktriangle) and non-oxidized CoCr (\circ) substrates.

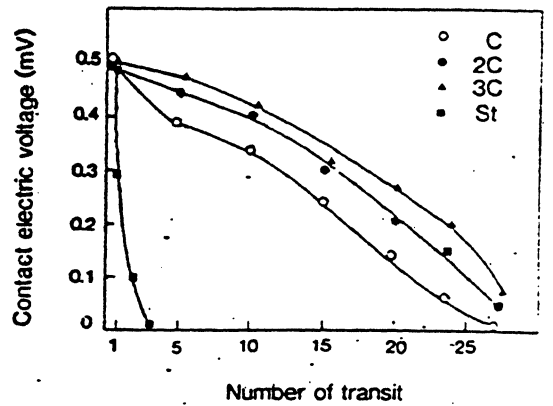
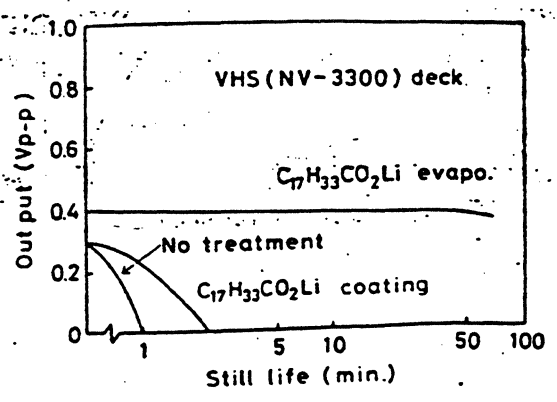


Fig. 3. Wear performance of monolayers for C, 2C, 3C and St on the evaporated aluminum on glass substrates determined by the electrical contact measurements.

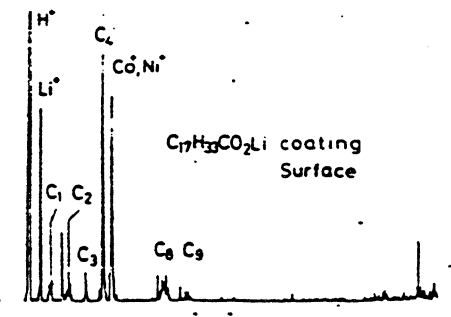
(E. ENDO et al., Thin Solid Films, 28.7, (1989))

Effect of Molecular Ordering



Still life of films treated by various surface treatments.

Lubricant deposited by evaporation in vacuum (Nakamura et al, IEEE Trans on Magn. Mag-20, 833, 1984)



replace

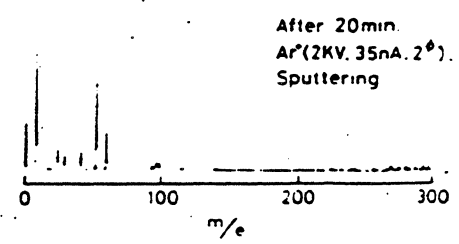
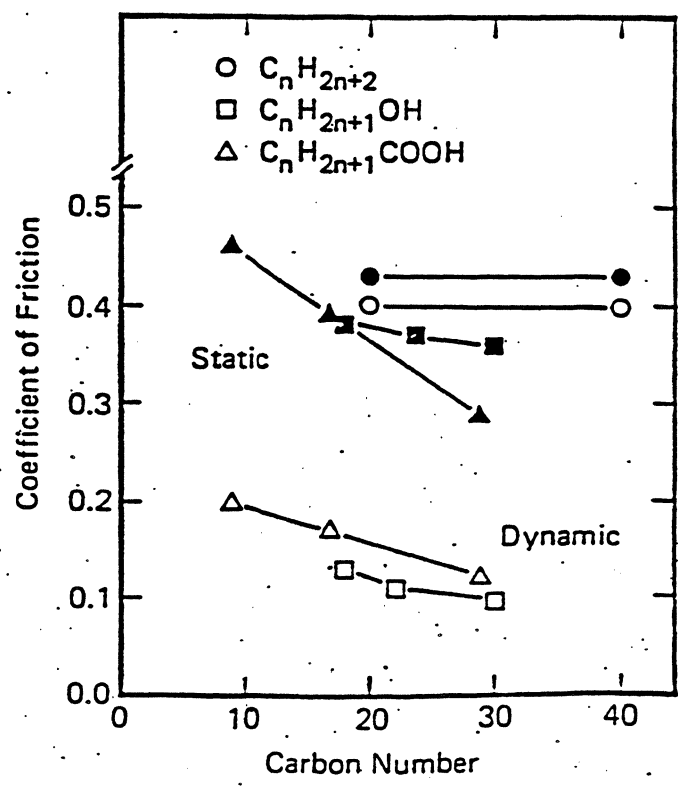


Fig.5. SINS profiles of film treated by coating method of Lithium oleate.



performance is much better with functional groups. Importance of Reactive Groups.

Dynamic and Static friction coefficients as a function of carbon atoms number for non polar and polar lubricants

(Yamaguchi, ST)

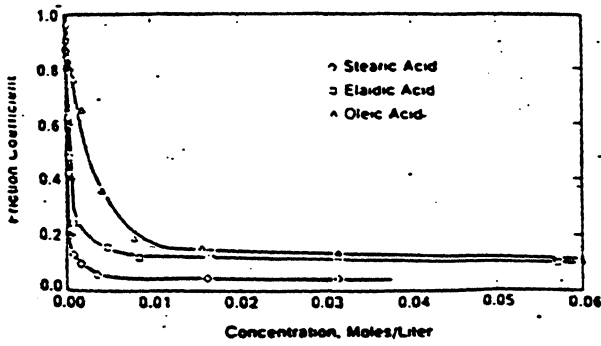


Fig. 1—Friction coefficient data for stearic, elaidic and oleic acids

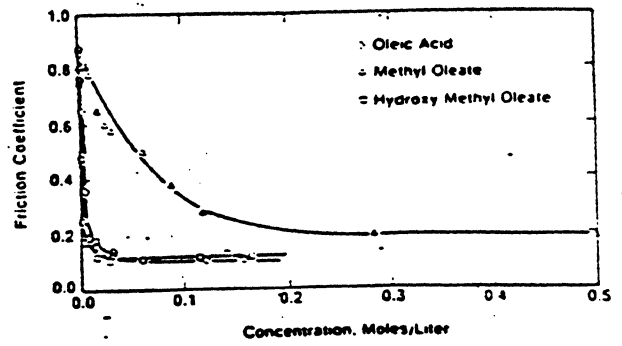


Fig. 3—Friction coefficient data of methyl oleate and 12-hydroxy methyl oleate compared with oleic acid.

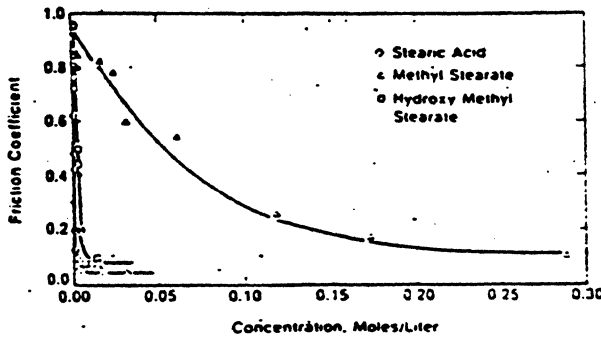


Fig. 2—Friction coefficient data of methyl stearate and 12-hydroxy methyl stearate compared with stearic acid.

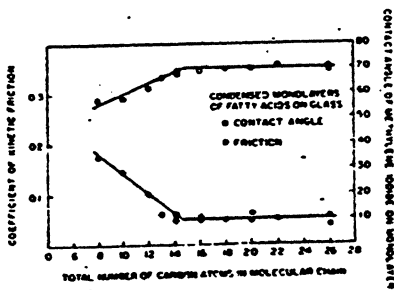
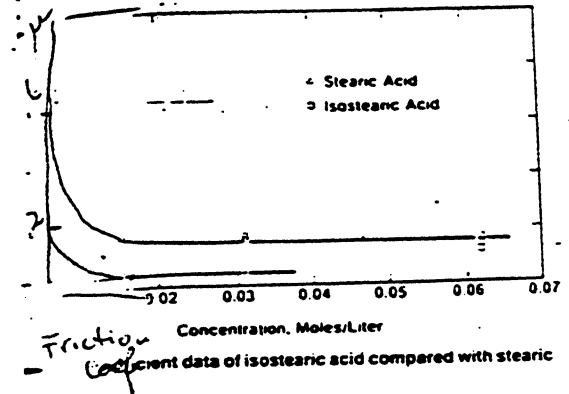


FIG. 11 EFFECT OF CHAIN LENGTH ON KINETIC FRICTION OF STAINLESS STEEL ON GLASS LUBRICATED BY A FATTY-ACID MONOLAYER

The frictional behavior is explained in terms of the compound molecular structure and the structural effects on the adsorption free energy. It is shown that increasing hydrogen bonding tendency of the polar end group or ~~the~~ increasing the attractive chain dispersion interactions, the adsorption energy is increased and the friction coefficient is reduced.

(Jannini & Beltracchi, ASME Trans., Vol. 24, 3, 423, 1935)

8 Boundary Lubrication
with Cadmium Arachidate

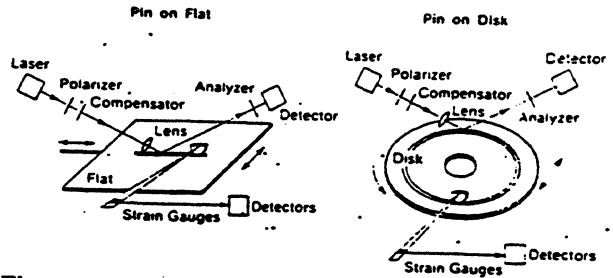
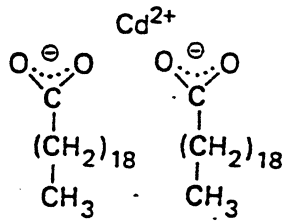
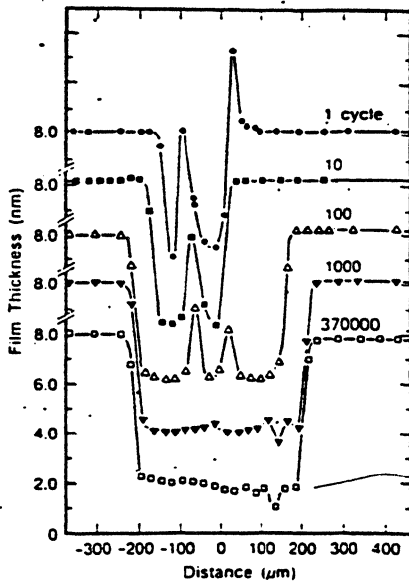


Figure 1. Low-speed pin-on-flat and pin-on-disk tribological setups with in situ scanning microellipsometry to profile wear of LB films.



monolayer thickness

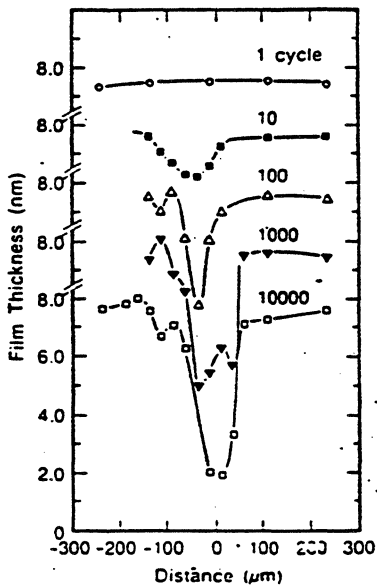


Figure 4. Film thickness profile of three CdA layers on SiO₂/Si as a function of number of sliding cycles: (a, top) the rectangular, ceramic slider with 150-mN load; (b, bottom) hemispherical pin with 3-mN load.

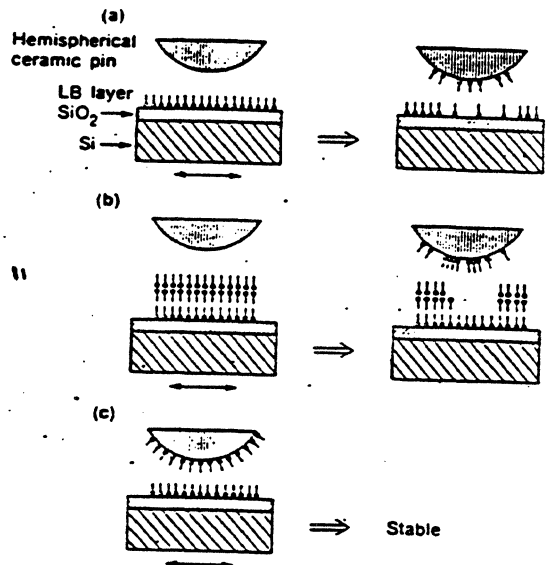


Figure 5. Schematic representation of tribological experiments: (a) with flat or disk coated with an LB monolayer; (b) with flat or disk coated with multilayers; (c) with both surfaces coated with a monolayer.

need monolayer on own side.

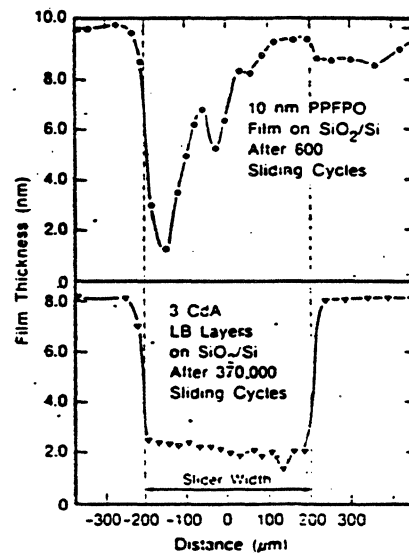


Figure 7. Comparison of film thickness profiles before failure for SiO₂/Si coated with physisorbed PPFPO (poly(perfluoropropylene oxide)) and chemisorbed (three CdA monolayers) lubricants. The rectangular, ceramic slider has a 150-mN load.

*University of Swalen, Hangmu
5,485, 1989*

Effect of Reactive Groups

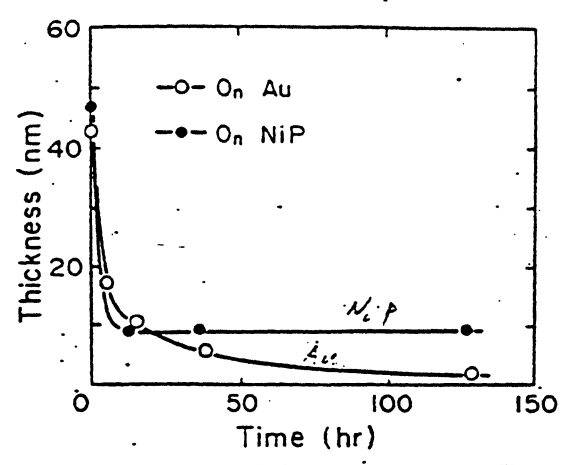


Fig. 6—Thickness depletion for PFPE monocarboxylic acid film on Au surface and on NiP surface with elapsed spinning time.

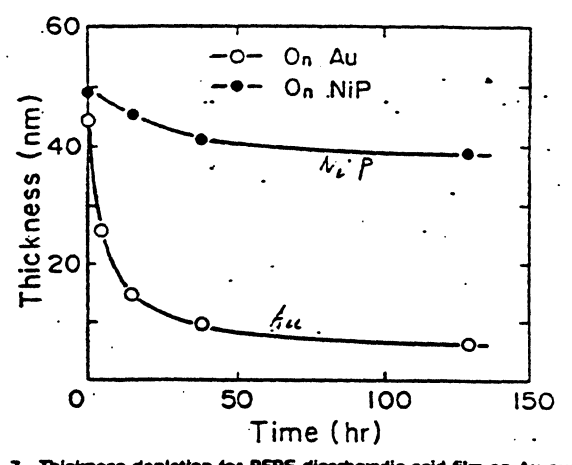


Fig. 7—Thickness depletion for PFPE dicarboxylic acid film on Au surface and on NiP surface with elapsed spinning time.

(M. Yamagisawa, Trib. & Mechanism of Magnetic Storage Systems, vol. IV, 43, 1987)

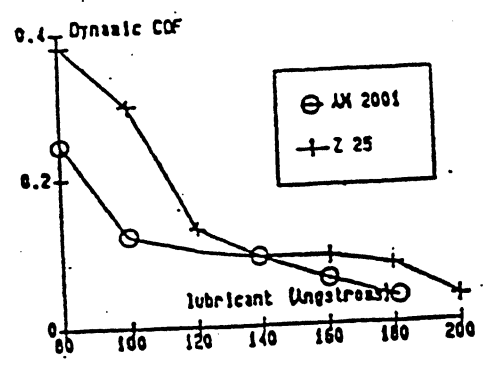


Fig. 2. Dynamic COF vs. amount of lubricant.

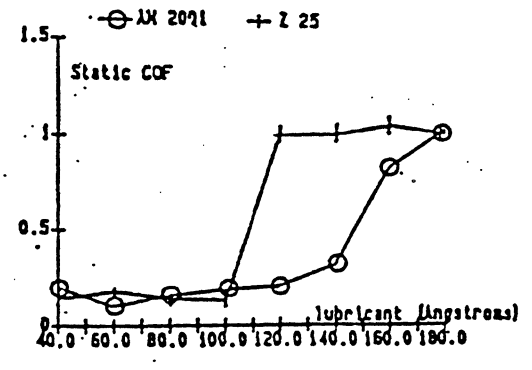


Fig. 4. Static COF vs. amount of lubricant.

(A.M. Scavuti & G. Caporiccio, IEEE Trans. on Magnetics, vol. Mag-23, 106, 1987)

Perfluoropolyether Lubricants

Advantages

- Good boundary lubricant
- High thermal/chemical stability
- Low surface tension
- Low vapor pressure

Disadvantage

- Possibility of autocatalytic degradation
- Not stable fraction of polymer

Review

- Reactive end groups improve lube adhesion
(Caporiccio 1986)
- Functional lubes have significantly lower friction coefficients and better durability than non-functional lubes
(Scarati and Caporiccio 1987; Miyamoto et al. 1988)
- Duplex lube: functional + non-functional
(Barlow et al. 1987; Hoshino et al. 1988)
- Composite lube: solid + liquid
(Reick 1982; Miyamoto et al. 1987)
- Assembled lube: hydrocarbon + perfluoroalkyl chains
(Kondo et al. 1989)

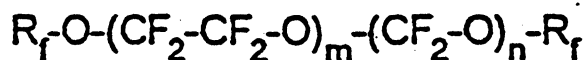
Conclusion

- State-of-the-art rigid disk lubricants

Perfluoropolyether Lubricants

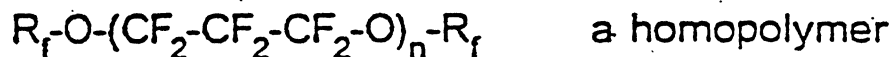
Linear PFPE

- Fomblin Z



where $m/n = 0.6$ to 0.7 a random copolymer

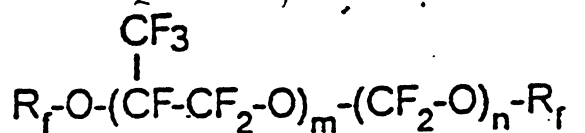
- Demnum



Better stability

Branched PFPE

- Fomblin Y



where $m/n = 20$ to 30 a random copolymer

- Krytox

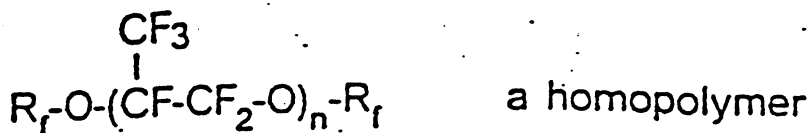


Table 8.10. Typical physical and chemical properties of commonly used perfluoropolyethers

	Fomblin Z-25	Fomblin YR	Krytox 143AD
Absolute viscosity, cP			
25°C	230	1700	
Kinematic viscosity, cSt			
20°C	250	1600	
38°C	150	515	495
Viscosity index, ASTM			
D2270	350	130	145
ASTM slope	0.30	0.58	0.55
Pour point, °C	-67	-25	-29
Specific gravity	1.87	1.92	1.88
Molecular weight			
number, Daltons	12,800	6800	2600
Vapor pressure, Torr			
20°C	3×10^{-12}	1×10^{-9}	2×10^{-9}
60°C	6×10^{-9} (93°C)	5×10^{-7}	6×10^{-8}
Volatility, % wt. loss	0.03 (22 h at 150°C)	1 (22 h at 150°C)	1.4 (6.5 h at 260°C)
Bulk modulus at 20°C, kg/mm ²		9.2×10^3	
Surface tension at 20°C, dynes/cm	24	21	19
Contact angle on a particulate rigid disk, degrees	10	16	12
Thermal conductivity at 38°C, cal/h m °C		82	83
Specific heat, cal/g°C	0.20	0.24	0.22
Coefficient of thermal expansion, /°C		1×10^{-3}	0.9×10^{-3}
Dielectric strength, kV/mm	30		16
Electrical resistivity, Ω·cm	3.9×10^{13}		4.1×10^{14}
Refractive index	1.294	1.304	1.301
Maximum useful temperature in air, °C			
Long term	260	260	260
Short term	320	320	320

* $cP = \frac{cP}{density}$
 * $cSt = \frac{cSt}{density}$

Fomblin Reactive Bifunctional PTFE

Type	Structure	M. W.	Visc.*
Z-DEAL	CH ₃ OOC - (Rf) - COOCH ₃	2200	
Z-DIAC	HOOC - (Rf) - COOH	2200	
Z-DOL	HO - CH ₂ - (Rf) - CH ₂ OH	2200	81 cSt
Z-DISOC	OCN - (R') - (Rf) - (R') - NCO	3000	160 cSt
"AM" Series	R - (Rf) - R ← strongest affinity to C surface	2300	90 cSt

Rf = $-\text{CF}_2\text{O} - (\text{C}_2\text{F}_4\text{O})_n - (\text{CF}_2\text{O})_m - \text{CF}_2 - \left(\text{R}'_f - \text{CH}_2 - \Phi - \overset{\text{O}}{\parallel} \text{C} - \text{CH}_2 \right)$
 R = neutral planar ring groups
 R' = alkylene, cycloalkylene, aromatic groups

FIGURE 7: CENTRIFUGAL CREEPING TESTS

Material: A metal plated 5.25-inch thin-film rigid disk spinning at 3600 rpm for 250 hours.

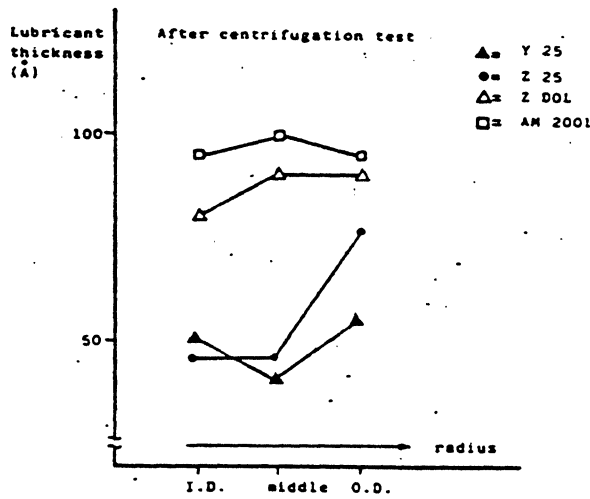
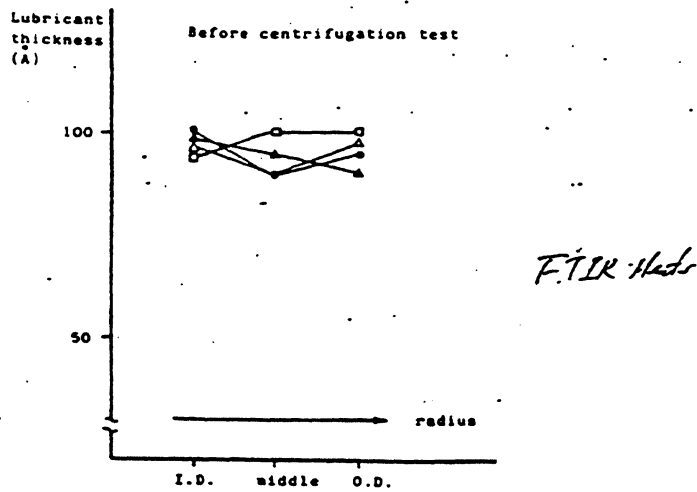
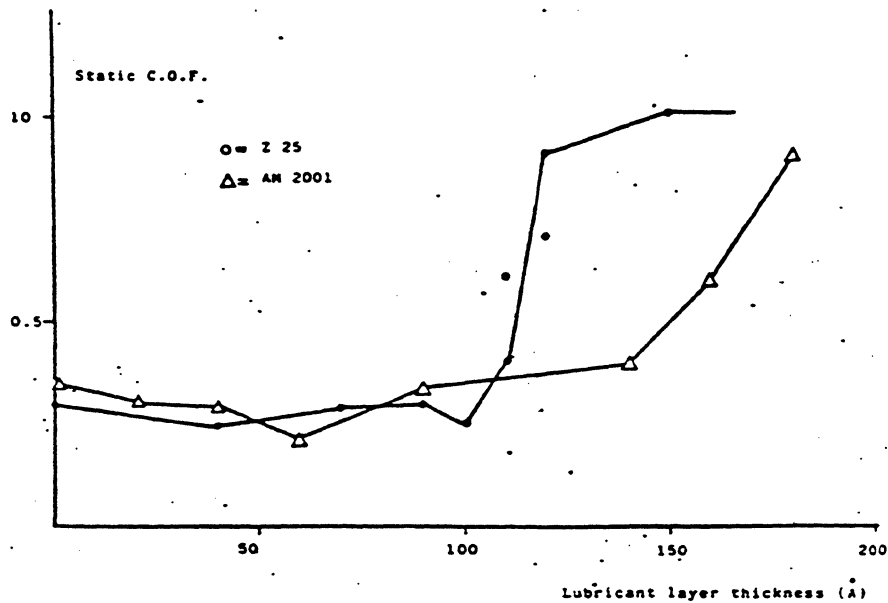


FIGURE 8: STATIC COF AS FUNCTION OF LUBRICANT LAYER THICKNESS

Tests compare 5.25-inch rigid disks with amorphous carbon overcoats and neutral or functional PFPE fluorocarbon overcoats, illustrating the effect of lubricant type and lubricant thickness.



Effect of Molecular Structure

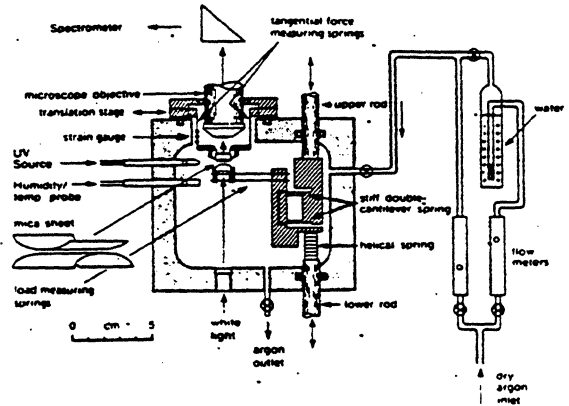
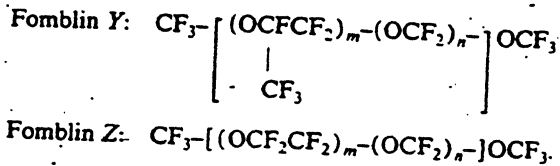


FIG. 1. Schematic drawing of the Shearing Force Apparatus outfitted with a translational stage. The lateral sliding mechanism permits two surfaces to be sheared past each other at various sliding speeds while simultaneously controlling the normal load and measuring the transverse force. The environment is maintained by purging the instrument with argon at the flow rate of 2 cc/min.

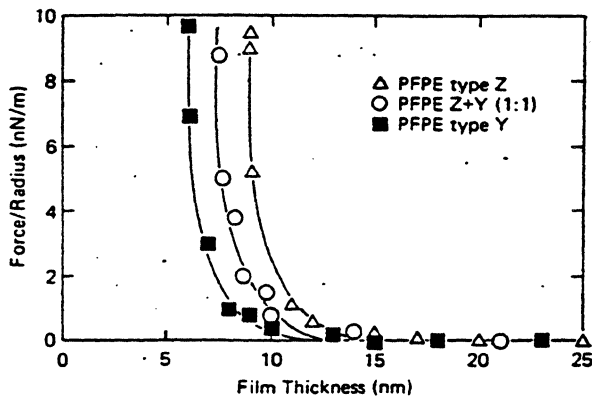


FIG. 2. Measured forces between mica surfaces separated by perfluoropolyether fluids. When compressed under a very large force the two surfaces flatten but do not come any closer than shown by the arrows (referred to as "hard wall"). This hard wall corresponds to a compressed polymer layer at each surface and is equal to 6.4 nm for Y, 7.4 nm for Z + Y blend, and 9 nm for Z type polymers, respectively.

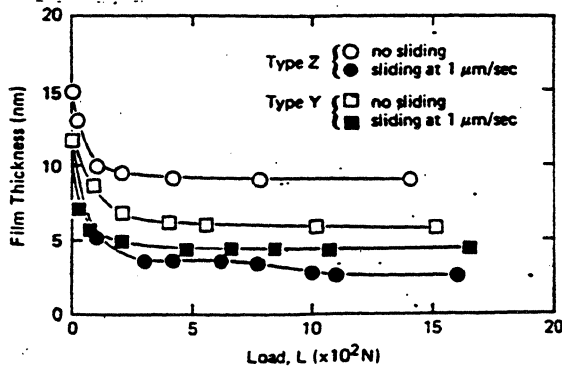


FIG. 3. Measured film thickness vs load. Bottom two curves show respective behavior of polymers Y and Z during sliding. The equilibrium forces for the polymer Y and Z (upper curves) are included to highlight the effect of shear on the film thickness.

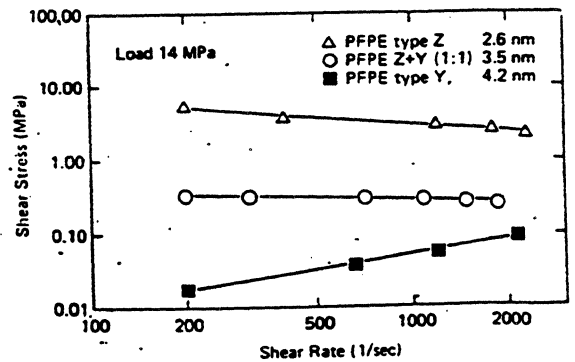


FIG. 4. Shear stress vs shear rate. Shearing of the Z type fluid results in decreasing shear stress with sliding velocity while the opposite holds for the Y type. The 1:1 blend of Z and Y shows an intermediate behavior. It should be noted that the load and thickness were held constant throughout the experiment.

(Howe et al., J. Chem. Phys., Vol. 94, 3, 2347, 1991)

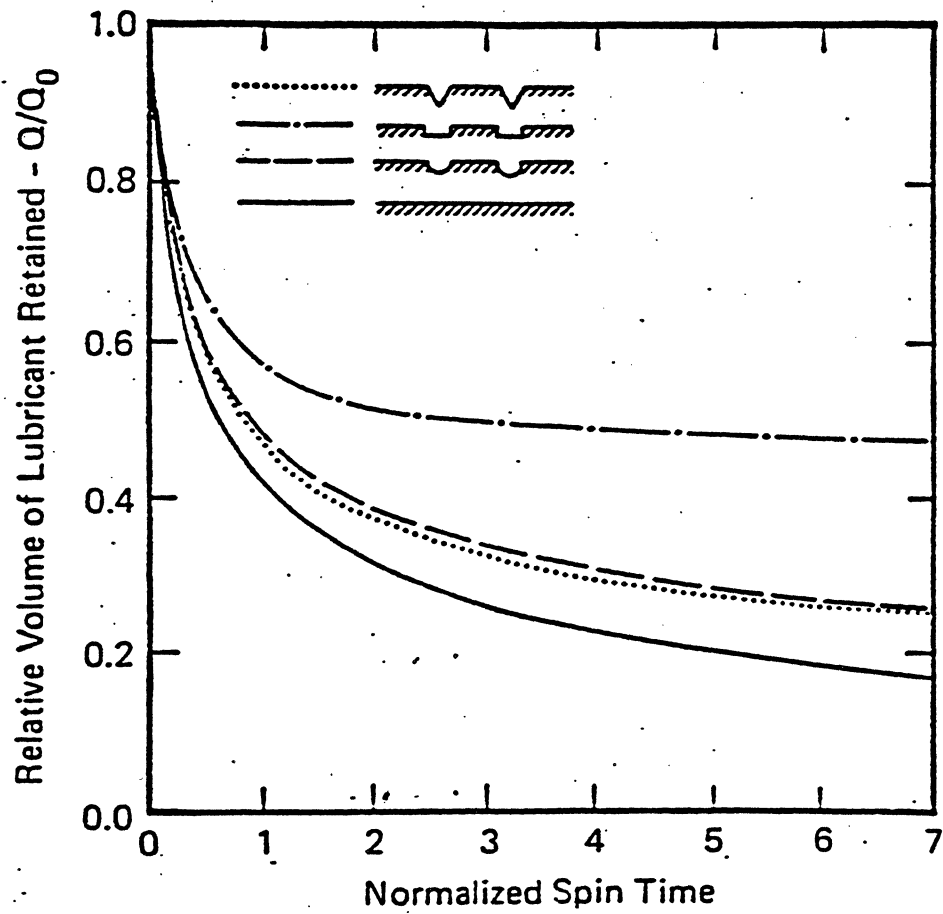
Lubricant Adhesion Enhancement

Disk Surface Texturing

- Mechanical or chemical.
 - Retention affected by shape, frequency, and aspect ratio of topographic features (*Lee 1988*)
 - Decreased friction and stiction (*Doan and Mackintosh 1988; Tasi et al. 1989*)
- Unattractive for higher recording density

Surface Modification Agents

- Create lube-like disk surfaces through chemical bonding
 - Diazo compounds (*Afzali-Ardakani et al. 1984*)
 - Aminosilane molecules (*Hoshino et al. 1988*)
 - Azide compounds (*Kudo et al. 1988*)
- Highly reactive, causing potential head/disk interference
- Used primarily for relatively reactive surfaces and not readily applied to the more inert carbon overcoat

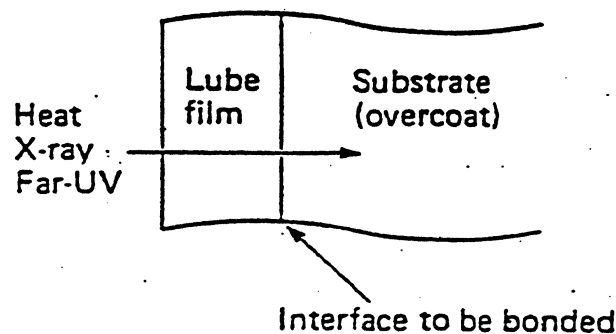


The effect of groove shape on lubricant retention (Icc, 1988).

Lubricant Adhesion Enhancement

Post Lubrication Treatment

- Directly affix lubricant molecules to disk surface



- Heat treatment: elevated temperatures in air
(Caporiccio 1986; Kimachi et al. 1989; Viswanathan 1989)
only works with reactive lubes
- X-ray irradiation: 0.01 ~ 0.1 MeV
(Heidemann and Wirth 1984)
easily decomposes fluoropolymers
- Far-UV irradiation: , 185 and 254 nm in N₂
(Saperstein and Lin 1990)
requires light absorption
- Eliminate lubricant depletion due to spin-off, evaporation and displacement
- Stability of bonding mechanism needs verification

Spin-off depletion

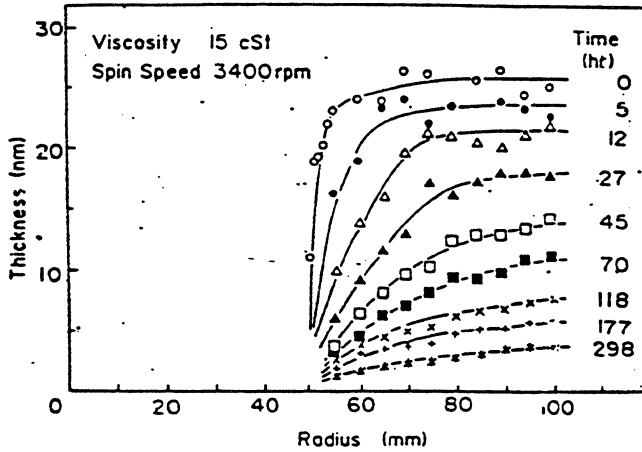


Fig. 2—Successive surface contours for PFPE liquid lubricant (15 cSt) on the rotating magnetic disk at 3400 rpm.

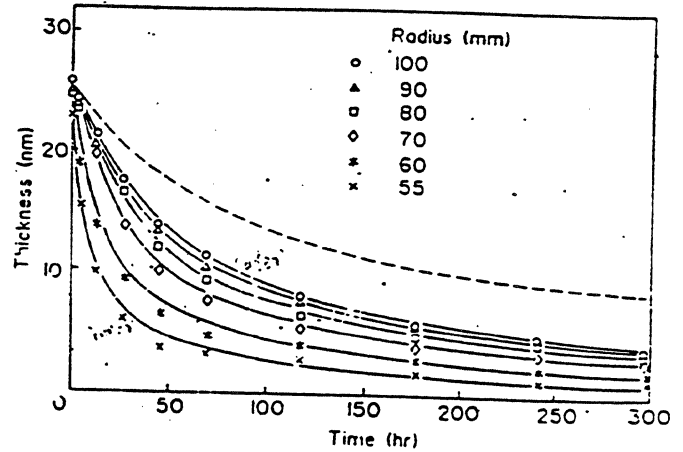


Fig. 3—Depletion for thin liquid film as a function of time at various radii

D. Saperstein & J. Lin

Langmuir, Vol. 6, No. 9, 1990 1523

Table I. Adhesion of the Lubricants after UV Treatment

lubricant	surface	initial thickness, Å	exposure time, min	UV-fixed thickness,* Å
Z-03	carbon	50	10	18 ± 1
Z-15	carbon	50	10	22
Z-25	carbon	50	10	25
YR	carbon	30	10	20
AM2001	carbon	35	10	30
Z-DOL	carbon	35	10	15
Krytox 143AD	carbon	50	10	15
Demnum S100	carbon	50	10	18
Z-15	SiO ₂	50	5	20
Z-15	ZrO ₂	50	5	20
Z-15	Au	50	10	18

* Without UV treatment, <1 Å remains after Freon rinsing except for Z-DOL (2 Å) and AM2001 (4 Å).

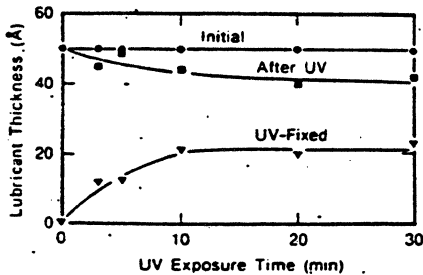


Figure 1. Measured Z-15 thickness on amorphous carbon as a function of UV exposure time: (●) initial thickness ≈ 50 Å; (■) after UV irradiation showing fixed and free lubricant; (▼) after Freon rinse showing UV-fixed thickness only.

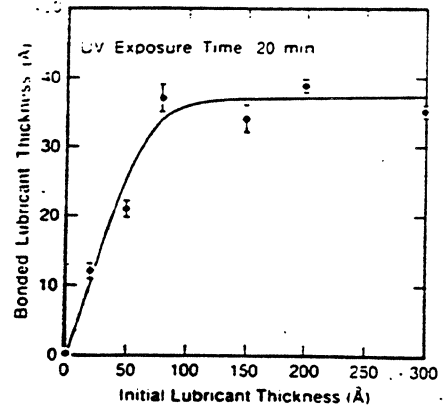


Figure 2. Measured thickness of UV-fixed Z-15 as a function of the initial lubricant thickness on amorphous carbon for a fixed exposure time of 20 min.

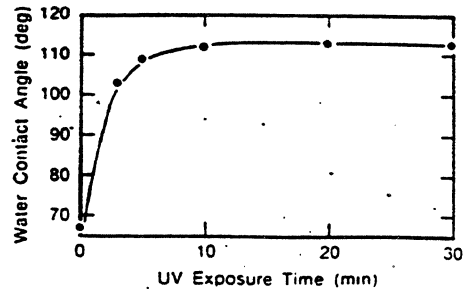


Figure 3. Measured advancing water contact angle of UV-fixed Z-15 on amorphous carbon as a function of the UV exposure time. The initial lubricant thickness was 50 Å.

Table 3: Heat of adsorption and heat of dissolution of the PFPE 1 and 2

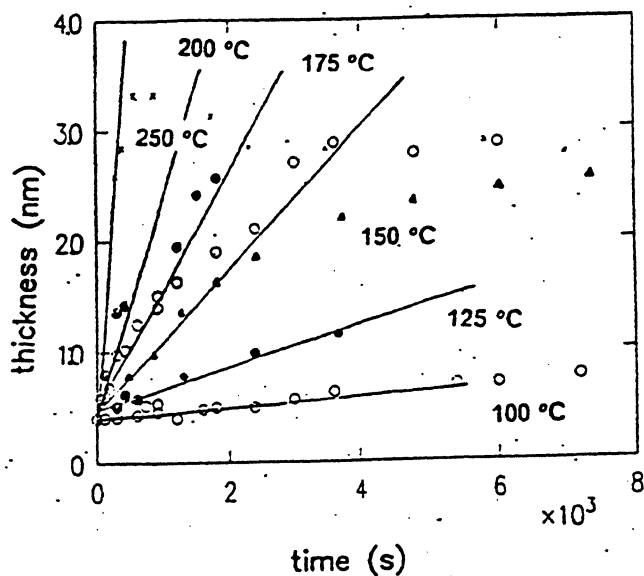
	Heat of adsorption ^{1,2}	Heat of dissolution ¹ in:		
		Freon	CF ₃ OH	C ₈ F ₁₈
ZDOL 1	-64 ± 5	10.1	4.5	6.7
Z03 2a	-33 ± 5	10.0	0.2	5.40
Z15 2b	-33 ± 5	-	-	-
water	-200 ³	-	-	-

¹ in J/g; ± 0.5 J/g² on silica powder (Aerosil, Degussa, 200 m²/g by BET)³ according to ref. (12)

Table 2: Thickness of the perfluoropolyether films attached to various surfaces and activation energy for the attachment

material	thickness (nm)	method of measurement	activation energy
carbon (sputtered)	1.8	FT-IR, XPS, ellips.	5 ± 2
graphite	1.5	XPS	-
silica	2.5	ellips., XPS	15 ± 2
aluminum	4.0	FT-IR	16 ± 4
gold	1.7	ellips.	-
chromium	4.5	FT-IR	14 ± 5
poly(acrylic acid)	2.6	XPS	-
poly(vinyl alcohol)	1.8	XPS	-
polystyrene	<.5	XPS	-

activation energy in kcal/mol



J. Rihe et al. Submitted to J. Chem. Phys.

Kinetics of
Adsorption of
Reactive Lube

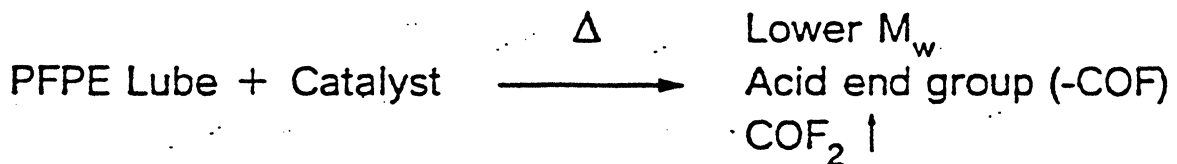
Perfluoropolyether Lubricant Stability

Most PFPE lubes are thermally stable in air up to 350°C

However:

Catalytic Degradation below T_d

(Jones et al. 1983; Carré 1986; Bierschenk et al. 1988;
Mori and Morales 1989; Zehe and Faut 1989)



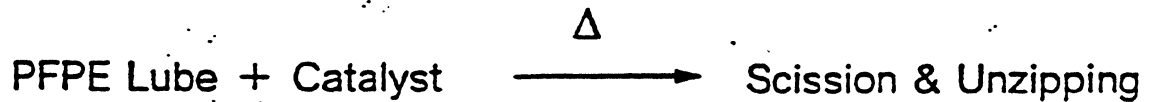
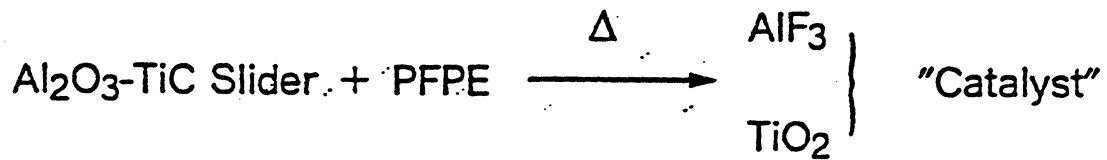
Catalyst: Lewis acids (AlF_3 , FeF_3 , ..)
Metal alloys (Ti, Fe, ..)
Metal oxides (Al_2O_3 , ZrO_2 , ..)

- The presence of $-\text{O}-\text{CF}_2-\text{O}-$ linkages promotes decomposition
Stability: Demnum, Krytox >> Fomblin Z
- During sliding contact, mechanical shear can generate fresh surfaces with catalytic activity, causing lube degradation
- Modified PFPE and additives have been developed for reducing degradation (Jones et al. 1983-1988)

Perfluoropolyether Lubricant Stability

At Head/Disk Interface

During sliding contact at head/disk interface, significant frictional heating may exist (*Suzuki and Kennedy 1989*)



Lube degradation → "autocatalytic" mechanism

- Catalytic nature of slider surface may play a role
- Lube degradation could be system-life-limiting
- Passivation of catalytic activity of file components may be necessary

The Mechanism of Electron Curing of Perfluoropolyethers.

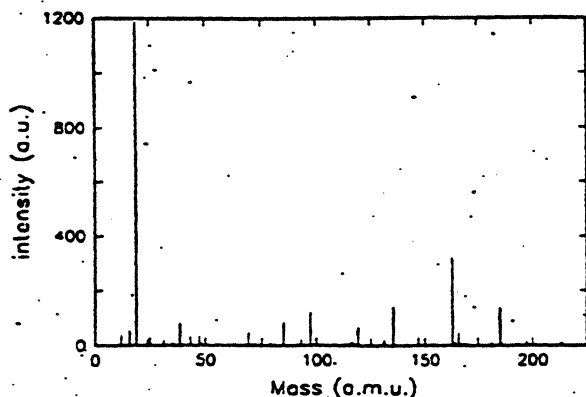
G.H. Vurens
C.S. Gudeman
L.J. Lin
J.S. Foster
TBM Research Division
Almaden Research Center
650 Harry Road
San Jose, CA 95120-6099

Perfluoropolyethers (PFPE's) are a group of polymers widely used as lubricants, dielectric fluids and mechanical and diffusion pump oils. PFPE's are chemically and physically very stable materials. They show an accelerated decomposition in contact with Lewis acid surfaces¹⁻³ but only at elevated temperatures. At room temperature PFPE's are sensitive to low energy electrons⁴, high energy electrons⁵, x-rays⁶, γ-rays⁷ and ion beams⁸.

The decomposition of gas phase PFPE's by low energy (10-90 eV) electrons has been studied by D'Anna et al.⁴. They show that there is a threshold of 14 eV before positive ions can be formed from a PFPE molecule during electron bombardment. In this paper we show that perfluoropolyethers can be crosslinked with low energy electrons of energy below 14 eV. In fact decomposition of the PFPE's occurs into negative ions and radicals with all electron energies used (1 - 20 eV).

The experiments have been performed using several different commercially available PFPE's: Fomblin[®] Y and Z and Demnum[®], all with a variety of different chain lengths. Fomblin Y is a random copolymer of CF₂CF(CF₃)O and CF₂O groups. Fomblin Z is a random copolymer of CF₂CF₂O and CF₂O groups and Demnum is a homopolymer consisting of CF₂CF₂CF₂O groups.

The negative ion spectrum emitted from Demnum DMS-200 under low energy electron bombardment is shown in figure 1. Most of the signal consists of F⁻ ions. It is known from gas phase experiments⁹ that low energy electrons have strong interactions with perfluorinated molecules. The electron attaches itself to the perfluorinated molecule generating a negative ion resonance state, which can decay in several different ways. The re-emission of an electron is the most obvious way in which the negative ion resonance state can decay. The results is the elastic scattering of the electron by the perfluorinated molecule. Dissociation is another very favourable decay path for the negative ion resonance state of perfluorinated molecules. This process, dissociative electron attachment is effectively the initiation step of the crosslinking of the PFPE. PFPE's dissociate into a F⁻ ion and a radical. The radical formed can then crosslink the polymer by propagation and termination steps. Evidence for the crosslinking is the re-



duced solubility of the PFPE's in freon and perfluorooctane, while the FTIR spectra of the PFPE's before and after electron bombardment are identical.

Besides F⁻ ion emission there are other decomposition products observed in the negative ion spectra due to dissociative electron attachment. The peak with the highest intensity is always F⁻, followed by CF₂⁻ if CF₃ sidegroups are present (e.g. Fomblin Y series). Then negatively charged monomer species are observed. PFPE's consisting of C_nF_{2n}O groups will emit C_nF_{2n-1}O⁻ and C_nF_{2n-2}O⁻ species upon low energy electron bombardment. The species containing 2 oxygen atoms has a higher intensity than the species containing only 1 oxygen atom, except for n = 1. Also many smaller negatively charged fragments are emitted (see figure 1). The apparent rearrangement of the atoms in the monomer species emitted is not understood at this time.

We conclude that low energy electrons are able to crosslink perfluoropolyethers. The crosslinking is initiated by a dissociative electron attachment process in which the PFPE molecule dissociates into negative ion and a radical. The radical left behind then propagates and terminates to form a crosslinked polymer.

REFERENCES

- 1) W.R. Jones, K.J.L. Paclorek, D.H. Harris, M.F. Smythe, J.H. Nakahara and R.H. Kratzer, *Ind. Eng. Chem. Prod. Res. Dev.* 24 (1985) 417.
- 2) W. Morales, NASA Tech. Memorandum 87221 (1986).
- 3) M.J. Zehe and O.D. Faut, NASA Tech. Memorandum 101962 (1989).
- 4) E. D'Anna, G. Leggieri, A. Luches and A. Perrone, *J. Vac. Sci. Technol. A* 5 (1987) 3436.
- 5) J. Pacansky, R.J. Waltman and M. Maier, *J. Phys. Chem.* 91 (1987) 1225.
- 6) S. Mori and W. Morales, NASA Tech. Paper 2910 (1989).
- 7) A.E. Petrenko and V.I. Tupikov, *Khim. Vys. Energ.* 18 (1984) 423.
- 8) J.W. Coburn and H.F. Winters, *J. Appl. Phys.* 60 (1986) 3309.
- 9) D. Sianesi and R. Fontanelli, US Patent 3,665,041 (1972).
- 10) Y. Ohsaka, T. Tohzuka and S. Takaki, *European Patent Appl.* 0,148,482 (1985).
- 11) L.G. Christophorou (Ed.), *Electron-Molecule Interactions and their applications*, Academic Press, 1984.

ACS Polymers
Preprints, 1990

Future Challenges

Development of a lubricant for contact recording

Contact chemistry

- Thermal/catalytic effect
- Tribo-electric effect
- Mechanical shear effect

Characterization of surface interactions

Interface specific measurements

- Atomic force microscope
- Surface forces apparatus
- Secondary ion mass spectrometry
- Angle resolved X-ray photoelectron spectroscopy
- X-ray reflectivity
- Surface derivatization

The Role of Disk Carbon and Slider on Water Adsorption

M. Smullen¹, J. K. Lee, A. Chao, and J. Enguero
Conner Peripherals, San Jose, California, 95134-2128, U.S.A.

Abstract - Water adsorption was measured on carbon overcoated, thin film magnetic recording disks and magnetic recording heads. Measurements were made using an ellipsometer with a humidity chamber mounted on the sample stage. Water adsorption is dependent primarily on the hydrogen content of the carbon overcoat, for both lubed and unlubed disks. Water adsorption is independent of the lube type and thickness, except when the carbon overcoat has a low hydrogen content. In the latter case, water adsorption depends on the functional endgroup of the lube and slightly on lube thickness. Water adsorption on magnetic recording heads depends on both the head composition and its surface roughness.

INTRODUCTION

There is a continuing demand for higher storage densities in magnetic recording disk drives. High density can be achieved by flying the magnetic recording head at low fly heights. However, this requires smoother disk and head surfaces. One problem with smooth surfaces is increased friction and stiction. Another factor that causes high friction and stiction is exposure of the disk drive to high relative humidity (RH). These two factors will interact and increase the likelihood of liquid induced adhesion, as disk drive manufacturers begin to incorporate smoother disks and heads into their products. Therefore, it is important to study the properties of disk and head materials in relation to high RH exposure.

There have been many studies on the effects of RH on friction and stiction [1]-[14]. They have shown that adhesion between the disk and head at high RH depends on a buildup of adsorbed water on the disk and head surfaces. Some of these studies include the effects of surface roughness and lubricant on water adsorption, stiction, and friction. In this paper, we studied the role of the type of carbon and slider on water adsorption. Different types carbons were fabricated by varying their hydrogen content. The sliders were composed of different ceramics, which are commonly used as the head materials in disk drives.

EXPERIMENTAL

An ellipsometer was used to measure the thickness of adsorbed water on the disks and heads. The wavelength of the ellipsometer light source was 632 nm and the incident angle was set at 70°. An RH chamber was built on the stage of the ellipsometer. The RH in the chamber was controlled by mixing streams of dry air and air saturated with water vapor. Temperature of the chamber was controlled at 22±2°C. Both

Manuscript received April 4, 1994.

¹ Now with Quantum corporation.

JERRY J.K. LEE
(408) 456-4557 PHONE
(408) 456-3947 FAX
3061 ZANKER RD. MS 5306
SAN JOSE CA 95124-7178

the RH and temperature were measured with a calibrated meter.

The thickness of the adsorbed water was measured using a single transparent layer program. It has been shown that errors due to using the single versus a multilayer program are less than 6% [12], [13]. The refractive index and extinction coefficient of water were assumed to be 1.33 and 0.0, respectively. The refractive index and extinction coefficient of the disks and heads were measured at 0% RH, before measurements at higher RH. The procedure was to place the sample in the chamber, adjust the RH, wait 5 minutes, and then measure the thickness of the adsorbed water layer.

Five types of disks were tested in this study. Each disk had a different hydrogen concentration in its carbon overcoat. All other layers in the disks and the substrate were the same. The hydrogen concentration was varied by adjusting the C_2H_2 concentration of the argon- C_2H_2 gas mixture in the carbon sputtering chamber. This process produced disks at C_2H_2 concentrations of 0, 5, 10, 20, and 30%. All disks had a surface roughness of 4.0 nm. Water adsorption was measured on both lubed and unlubed disks. Disks were lubed with Fombin Z-25, AM2001, and Z-dol. The lube thicknesses ranged from 0.2 to 4.0 nm.

Three types of heads were evaluated. One was composed of Al_2O_3 -TiC (70%-30%), while the other two were composed of different compositions $CaTiO_3$. $CaTiO_3$ heads had the same amount of CaO, TiO_2 , Al_2O_3 , NiO, and SiO_2 , but differed in their BaO and ZnO content. Each of the $CaTiO_3$ heads was also finished at two surface roughnesses.

RESULTS

Fig. 1 shows the water adsorption on the unlubed disks. The adsorbed water thickness increased with RH and C_2H_2 concentration in the argon- C_2H_2 gas mixture. The one

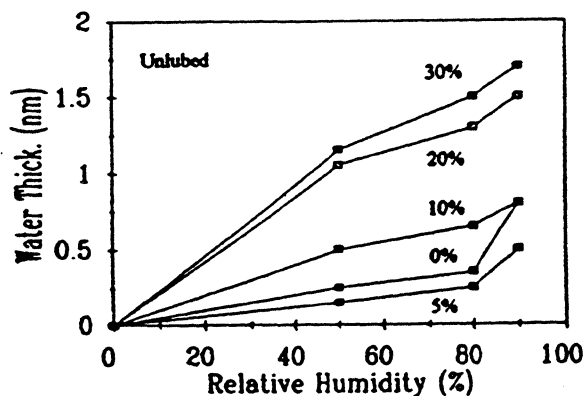


Fig. 1. Adsorbed water thickness on disks, with different carbon overcoats, versus relative humidity. The carbon overcoats were produced with C_2H_2 concentrations of 0, 5, 10, 20, 30% in the sputtering gas. The disks were unlubed.

exception was the 5% C_2H_2 , which showed less water adsorption than 0% C_2H_2 . Fig. 2, 3, and 4 show water adsorption as a function of lube thickness and C_2H_2 concentration for Fomblin Z-25, AM2001, and Z-dol lubes, respectively. Data in these figures were collected at 90% RH. The adsorbed water thickness is independent of lube thickness at C_2H_2 concentrations above 5% for Z-25 and above 10% for AM2001 and Z-dol. Fig. 5 shows the adsorbed water thickness at 90% RH, with a 2.0 nm thick lube on the disks. At 0% C_2H_2 concentration, disks lubed with Z-dol adsorb significantly more water than those lubed with Z-25 or AM2001. However, at higher C_2H_2 concentrations, this difference decreases. The general trend is that disks lubed with Z-dol adsorb the most water, followed by disks lubed with AM2001 and Z-25.

Fig. 6 shows the results of water adsorption on heads. The Al_2O_3 -TiC head adsorbs the most water. For the $CaTiO_3$ heads, a comparison of curves 2 versus 4, and 3 versus 5 shows that heads with higher surface roughnesses adsorb more water. A comparison of curves 4 versus 5 shows that there is not much difference in water adsorption among the two different $CaTiO_3$ compositions.

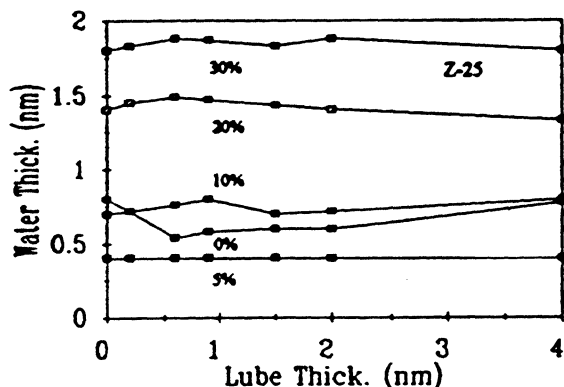


Fig. 2. Adsorbed water thickness on disks with carbons sputtered in C_2H_2 concentrations of 0, 5, 10, 20, and 30% versus Fomblin Z-25 lube thickness. The relative humidity was 90%.

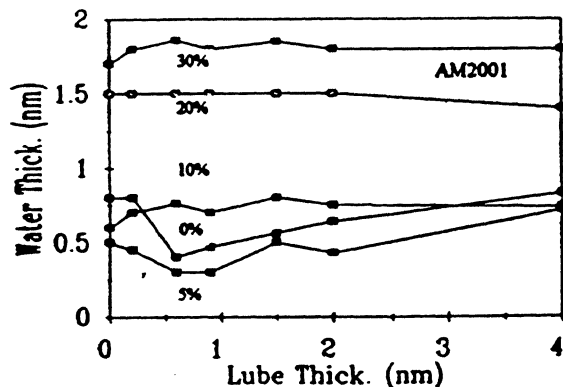


Fig. 3. Adsorbed water thickness on disks with carbons sputtered in C_2H_2 concentrations of 0, 5, 10, 20, and 30% versus Fomblin AM2001 lube thickness. The relative humidity was 90%.

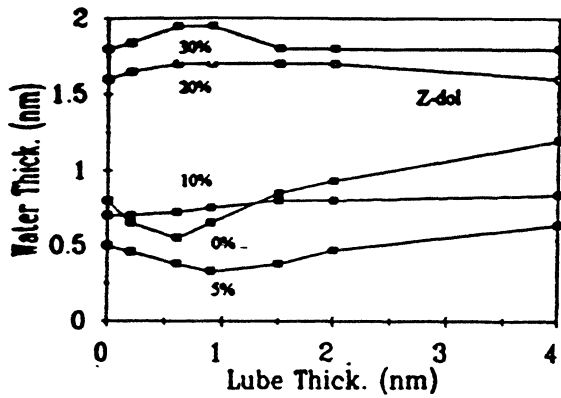


Fig. 4. Adsorbed water thickness on disks with carbons sputtered in C₂H₂ concentrations of 0, 5, 10, 20, and 30% versus Fomblin Z-dol lube thickness. The relative humidity was 90%.

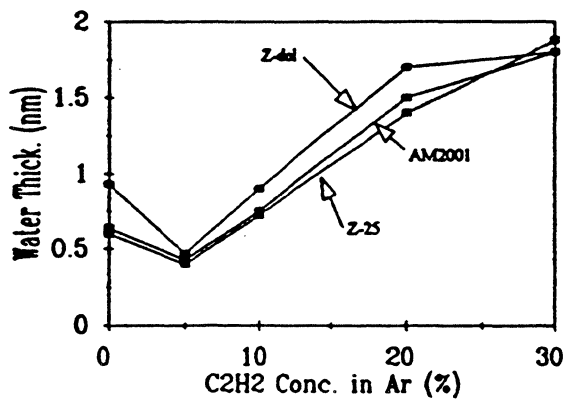


Fig. 5. Adsorbed water thickness on disks with Fomblin Z-25, AM2001, and Z-dol lubes versus the disk sputtering gas C₂H₂ concentration. The relative humidity was 90%.

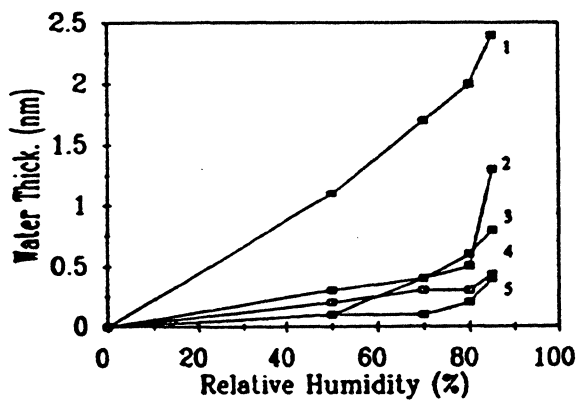


Fig. 6. Adsorbed water thickness on heads versus relative humidity. Al₂O₃-TiC (1), CaTiO₃-composition 1, Rt=32.2 nm (2), CaTiO₃-composition 2, Rt=26.4 nm (3), CaTiO₃-composition 1, Rt=19.4 nm (4), and CaTiO₃-composition 2, Rt=19.4 nm (5).

DISCUSSION

Water is a polar adsorbate and it forms a stronger hydrogen bond with nitrogen, oxygen or fluorine than with other atoms. Because of the hydrogen bonding tendency of water, the adsorption of water is sensitive to the degree of polarity of the adsorbent surface [15]. For example, the amount of water adsorbed on carbon has been shown to increase with the oxygen content of the carbon [16]. The polar groups in this case were chemisorbed oxygen, OH, and COOH. In Fig. 1, the adsorbed water thickness increased with the hydrogen content of the carbon films. At 0% C_2H_2 , oxygen chemisorbs onto the carbon surface, passivating the carbon dangling bonds [17] and providing some sites for water adsorption. Hydrogen in the carbon films at higher C_2H_2 concentrations not only passivates the carbon dangling bonds but it also is incorporated into the carbon structure as sp^2 and sp^3 C-H bonds [18]-[20]. This makes the carbon more polar, producing more sites for hydrogen bonding and thicker adsorbed water layers. The reduction in adsorbed water thickness between 0 and 5% C_2H_2 may be due to the superposition of curves for decreasing oxygen sites and increasing hydrogen sites versus C_2H_2 concentration.

As seen in Fig. 2 through 5, lube has a minor influence on the water adsorption characteristics of these disks. It does exert some influence on disks with low hydrogen contents. The minimum in the 0 and 5% C_2H_2 curves at one monolayer of lube has been explained in [12] and [13]. At one monolayer, the disk surface becomes the least polar due to the lube coverage. With thicker lubes, the unattached functional end groups of the lube provide more water adsorption sites. The fact that a minimum also occurs with Z-25, which has no functional end group, shows that the lube molecule backbone may also provide water adsorption sites. Disks lubed with Z-dol were found to adsorb the most water. The higher adsorption characteristics of Z-dol may be due to its type of endgroup, OH, which favors water adsorption [14]. At higher hydrogen contents, the abundance of water adsorption sites in the carbon overwhelms the lube influence. Therefore, there is no dependence on lube thickness. In all cases, adsorbed water penetrates the lube and reaches the disk surface as shown in [1]. Diffusion was the proposed mechanism, in that study. It is unfortunate that higher hydrogen content carbons adsorb more water because the hydrogen also gives these carbons better wear resistance and friction properties[21].

The higher water adsorption characteristics of the Al_2O_3 -TiC versus the $CaTiO_3$ head are probably due to the presence of the Al_2O_3 phase. This is to be expected since Al_2O_3 is a good adsorber of water and other chemicals, and is used in chemical

filters. It was found that the rougher CaTiO_3 heads adsorbed more water. This is also to be expected since increased roughness increases surface area.

CONCLUSIONS

Water adsorption on carbon overcoated, thin film disks is dependent primarily on the hydrogen content of the carbon overcoat. This is the case for both lubed and unlubed disks. Water adsorption is independent of the lube type and thickness, unless the carbon overcoat has a low hydrogen content. In this latter case, water adsorption depends on the functional endgroup of the lube and slightly on lube thickness. Water adsorption on magnetic recording heads depends on both the head composition and its surface roughness. Al_2O_3 -TiC heads adsorb more water than CaTiO_3 heads, and rougher heads adsorb more water than smoother heads.

REFERENCES

- [1] C. C. Liu and P. B. Mee, *IEEE Tran. Mag.*, vol. 19, no. 5, pp. 1659-1661, 1983.
- [2] H. Dimigen and H. Hubach, *Philips Tech. Rev.*, vol. 41, pp.186-197, 1983-1984.
- [3] R. Menning, H. J. Tolle and P.E. Wierenga, *Thin Solid Films*, vol. 143, pp. 31-41, 1986.
- [4] T. Q. Donn and N. D. Mackintosh, *STLE SP-25*, vol. 5, pp. 6-11, 1988.
- [5] K. Miyoshi, D. H. Buckley, T. Kusada, C. Maeda and B. Bhushan, *STLE SP-25*, vol. 5, pp. 12-16, 1988.
- [6] R. S. Timsit and G. H. Stratford, *STLE SP-25*, vol. 5, pp. 17-23, 1988.
- [7] Z. Li, E. Rabinowicz and N. Saka, *STLE SP-26*, pp.64-70, 1989.
- [8] T. Miyamoto, Y. Ando, S. Hirono, and I. Sato, *J. Mag. Soc. Jap.*, vol. 13, supplement no. S1, pp.207-211, 1989.
- [9] B. Bhushan and M. T. Dugger, *J. Tribology*, vol. 112, pp. 217-223, 1990.
- [10] Y. Li and F. E. Talke, *IEEE Trans. Mag.*, vol. 26, no. 5, pp. 2487-2489, 1990.
- [11] Y. Li and F. E. Talke, *STLE SP-26*, pp. 79-84, 1990.
- [12] H. Tian and T. Matsudaira, *IEEE Trans. Mag.*, vol. 28, no. 5, pp. 2530-2532, 1992.
- [13] H. Tian and T. Matsudaira, *J. Trib.*, vol. 115, pp. 28-35, 1993.
- [14] K. Merchant and S. Smith, *IEEE Trans. Mag.*, vol. 29, no. 6, pp. 3930-3932, 1993.
- [15] S. J. Gregg and K. S. W. Sing, *Adsorption, Surface Area and Porsity*, 2nd ed., Academic, 1982, pp.263.
- [16] A. V. Kiselev and N. V. Kovaleva, *Izvest. Akad. Nauk S.S.S.R., Otd. Khim. Nauk.*, 955 (trans), 1959.
- [17] B. Marchon, M. R. Khan, N. Heiman, P. Percire, and A. Lautie, *IEEE Trans. Mag.*, vol. 26, no. 5, pp. 2670-2672, 1990.
- [18] B. Dischler, A. Eubenzler and P. Koidl, *Solid State Comm.*, vol. 48, no. 2, pp. 105-108, 1983.
- [19] H. Tsai and D. B. Bogy, *J. Vac. Sci. Tech. A*, vol. 5, no. 6, pp.3287-3312, 1987.
- [20] J. K. Lee, M. Smallen, J. Enguero, H. J. Lee, and A. Chao, *IEEE Trans. Mag.*, vol. 29, no. 1, 1993.
- [21] H. J. Lee, R. Zubeck, D. Hollars, J. K. Lee, M. Smallen, and A. Chao, *J. Vac. Sci. Tech. A*, vol. 11, no. 6, pp. 3007-3013, 1993.

Home-Made Preprint

(Session 5B 12:00 N)

The Role of Relative Humidity, Surface Roughness and Liquid Build-Up on Static Friction Behavior of the Head/Disk Interface

Hong Tian

Takeo Matsudaira

Hoya Electronics Corporation
960 Rincon Circle
San Jose, CA 95131

Stiction at the head/disk interface has become one of the major concerns as smoother surfaces are required to achieve lower flying heights of magnetic heads over magnetic disks. In this paper, static friction forces on three types of disk samples with different surface roughness values were measured at various relative humidities. It was found that static friction coefficients were well correlated with total thickness of liquid (lubricant and adsorbed water) at the head/disk interface. The experimental data also agreed fairly well with the calculated values based on a proposed stiction model. It is implied in the stiction model that the bearing ratio or the shape of asperity height distribution, especially the part of high asperities, determines the stiction force. Moreover, long-term stiction was investigated on the unlubricated disk surfaces at 80% relative humidity and on the lubricated disks at 5% relative humidity to separate the effects of water build-up and lubricant build-up at the head/disk interface. It appears that long-term stiction occurs only when enough mobile lubricant is present and the thickness of liquid at the head/disk interface is close to a critical thickness value which is related to surface roughness values.

INTRODUCTION

The ever-increasing demand for higher storage densities requires smooth surfaces to achieve ultra low flying heights of magnetic heads over magnetic rigid disks. However, the smooth surfaces generally have a larger real area of contact and consequently higher friction (Bhushan and Doerner, 1989). Another major concern over the smooth surfaces is the stiction at the head/disk interfaces due to meniscus effect of a liquid. Several studies have contributed to our understanding of the stiction at the head/disk interface. Liu and Mee (1983) were among the earliest studies in this area. They found that stiction occurred at the head/disk interface when relative humidity was high, due to water condensation on disk surfaces. Later, Li, Rabinowicz and Saka (1989) observed severe stiction at the head/disk interface at relative humidities over 80 percent. They also suggested that thickness of lubricant should be controlled below the combined peak-to-valley surface roughness of disks and heads to avoid severe stiction. Water adsorption data on disk surfaces as a function of relative humidity have been reported by Miyamoto et al. (1989) and by Li, Trauner and Talke (1990). It was found that thickness of adsorbed water on unlubricated disk

surfaces increased considerably when relative humidity was over 85% and that stiction measurements qualitatively agreed with the thickness of adsorbed water on disk surfaces. However, little information is available for water adsorption on head surfaces as relative humidity changes.

Recently another important issue was raised by Gitis et al. (1991) and by Koka et al. (1991). During long period of head-disk contact, migration or diffusion of mobile lubricants around contacting asperities enhances the meniscus effect of lubricant. Consequently long-term stiction occurs. On the other hand, one of the advantages of the mobile or free lubricant on disk surfaces is its ability to recover after being sheared by a sliding head. The mobility of lubricant is important to durability of the head/disk interface because surface migration of lubricants is the only way for thin film disks to obtain resupply of lubricant. To achieve high mechanical durability of the head/disk interface, therefore, it is essential to understand the relationship among short-term and long-term stiction, surface roughness, and thickness of liquid at the head/disk interface.

In a recent study by authors (Tian and Matsudaira, 1992), the static friction on very smooth disk surfaces was measured at various relative humidities. It was found that the static friction coefficients were better correlated with the total thickness of liquid (lubricant and adsorbed water) on both the head and the disk surfaces, compared with the

correlation between the friction coefficients and the total thickness of liquid on disk surfaces only or the total thickness of water at the head/disk interface. In this study, the correlation between the static friction and the total thickness of liquid at the head/disk interface was examined on three types of disks with different surface roughness values. A stiction model was also proposed to analyze the experimental data. Thus the objective of this study is to identify a critical thickness of liquid for given surface roughness distributions. Moreover, the effects of water build-up and lubricant build-up on long-term stiction were also investigated in the light of surface roughness.

EXPERIMENTAL

Three types of thin film disks with sputtered carbon overcoats (about 25 nm thick) were used in the study. Glass substrates with isotropic surface roughness patterns were used for Type A and Type B disks. Aluminum substrates which has circumferential textures were used for Type C disks. Surface roughness was measured using a surface profilometer (Taylor-Hobson: Talystep). The stylus has an extremely fine knife-edge tip, nominally 0.1 μm wide in the direction of measurements and 1.5 μm across. The roughness values of the disk surfaces are listed in Table 1, including R_a (average), R_q (rms), R_z (five-point average peak-to-valley), R_p (mean-to-peak) and R (Average asperity radius). Conventional IBM 3370-type two-rail taper-flat sliders (fabricated from $\text{Al}_2\text{O}_3\text{-TiC}$) were used as testing heads. The head size is 2.85 mm x 2.2 mm and the total flat area of the slider rails is 1.58 mm^2 . The roughness values of the head surfaces are also listed in Table 1. A perfluoropolyether (Montefluos: Fomblin AM2001) was used as a liquid lubricant. Surface tension of the lubricant is 25 dyne/cm and its viscosity is 90 cSt @ 20°C (Caporiccio, 1986). Thickness of lubricant was measured by an ellipsometer and by a Fourier transform infrared (FT-IR) spectrometer.

Thickness of adsorbed water on the head and the disk surfaces was measured using an ellipsometer. The sample was placed in a humidity-controlled chamber which was sitting on a sample stage of the ellipsometer. It was assumed that thickness of adsorbed water at two percent relative humidity (2% RH) is negligible. This assumption is consis-

tent with the measurements by Li et al. (1990). Optical indices of the sample surface at 2% RH were taken as a reference point. Then the humidity inside the chamber was controlled at a desired level. The optical indices of the sample surface were measured again and the thickness of adsorbed water was calculated using a single-transparent-layer program. The refractive index of water was assumed to be 1.33. Errors in measuring water thickness, which is caused by using the single-layer program for lubricated disks (refractive index of lubricant is 1.3), were evaluated to be less than 6 percent compared with the measurements using the multi-layer programs. Each measurement was taken after sample surfaces were exposed to a given relative humidity environment for about twenty minutes.

A friction tester was set up in another humidity-controlled chamber. The relative humidity was monitored by a humidity sensor which provides an output to a process controller. Two independent valves, which were regulated by the process controller, controlled the passing of a moist air and a dry air into the chamber to maintain the relative humidity at a given value within $\pm 1\%$ error range. The static friction force was determined as the maximum force value during the start-up of disk rotation at an acceleration of 5 mm/s^2 . At each relative humidity condition, the static friction was measured in twenty minutes after heads were loaded on disk surfaces. All the experiments were conducted at room temperature (20-23 °C) in a clean room (Class 100) environment.

RESULTS

Static Friction Coefficient and Relative Humidity

Figure 1 shows static friction coefficients versus relative humidity for three types of disks. For the Type A disks which had small surface roughness (Fig. 1a), the static friction coefficient at 50% relative humidity (RH) was slightly lower than that at 2% RH when no lubricant was applied on the disk surface. Then the static friction coefficient increased as relative humidity further increased. For the Type A lubricated disks, however, static friction coefficient increased monotonically with relative humidity. At 2% RH, the effect of adsorbed water was negligible. A thin layer of lubricant (about 0.7 nm thick) effectively reduced friction from 0.35 to 0.18. But excess lubricant resulted in even higher friction (up to 0.9 for 2.0 nm thick lubricant). At higher relative humidities (50% RH above), the static friction of the lubricated disks was higher than that of the unlubricated disks. Apparently the effectiveness of lubricant in reducing friction was offset by the meniscus effect of liquid which includes the lubricant and the excessive water adsorbed on the head and the disk surfaces at high relative humidities. For the Type B and the Type C disks (Figs. 1b and 1c, respectively), the similar trend was observed as in case of the Type A disks, but the values of static friction coefficient were much smaller, especially at high relative humidities.

To clearly demonstrate the effect of lubricant alone on the static friction of these three types of disks, we plotted the

Table 1 Surface Roughness and Properties of Heads and Disks*

	R_a (nm)	R_q (nm)	R_z (nm)	R_p (nm)	R (μm)	E (Gpa)
Type A	0.64	0.84	4.10	3.02	34	90
Type B	6.18	7.76	32.01	20.73	13	90
Type C	13.24	15.37	80.25	42.54	21	85
Head	1.91	2.38	8.82	4.37	52	450

* Elastic modulus values are from various references.

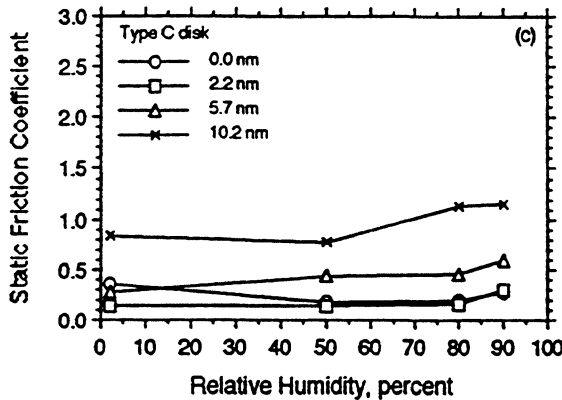
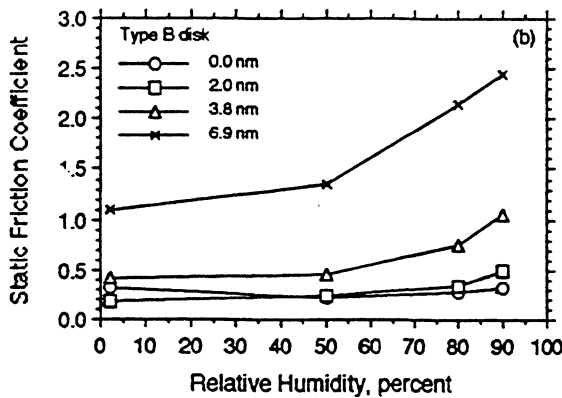
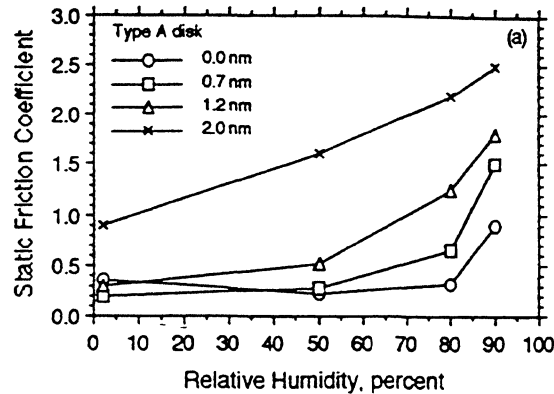


Fig. 1 Static friction coefficient versus relative humidity for three types of disks with various thicknesses of lubricant.

static friction coefficient at 2% RH versus thickness of lubricant as shown in Fig. 2. The static friction coefficient reached a minimum at around 2 nm thick lubricant for the Type B and the Type C disks, but at around 0.6 nm for the Type A disks. Miyamoto et al. (1990) used an Atomic Probe Microscope to measure the interaction forces between a tungsten tip and lubricated disks. They found that as thickness of lubricant increased, the interaction force decreased until reaching a minimum at about 2 nm thick lubricant. Further increase in the thickness of lubricant resulted in an increase of the interaction force. One explanation for the minimum friction value is as follows. A too thin lubricant

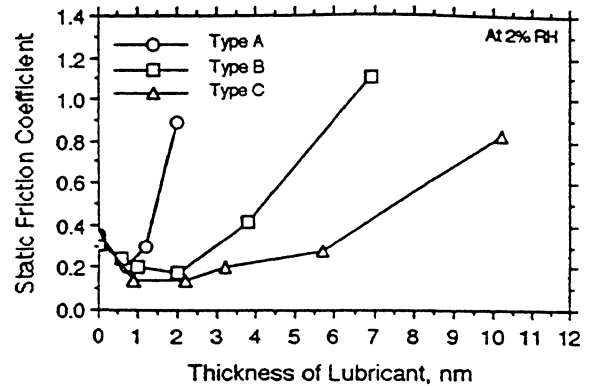


Fig. 2 Static friction coefficient versus thickness of lubricant for three types of disks at 2 percent relative humidity

layer leaves the surface not covered completely so that solid-solid contact still contributes to high friction. But a too thick lubricant layer brings about an additional meniscus force to the interaction force, which also causes higher friction. Thus a proper amount of lubricant will effectively reduce the friction to a minimum. We observed this minimum friction at 1~2 nm thick lubricant only for relatively rough surfaces (Type B and Type C). For the Type A disks which had rather smooth surfaces, however, the thickness of lubricant corresponding to the minimum friction is much smaller, about 0.6 nm. The reason is that the meniscus effect of lubricant on the smooth surfaces may become a dominant factor even when thickness of lubricant is small.

It is well known that adsorption films and/or contaminations are unavoidable unless surfaces are carefully cleaned and degassed in ultra high vacuums (Bowden and Throssell, 1951). If the surfaces are perfectly clean and ductile, the friction coefficient will be enormous and of order of unity (Tabor, 1981). From our experiments and from the literature (Timsit and Stratford, 1988; Li et al., 1990; Streater et al., 1990), the static friction coefficients on unlubricated disks with carbon overcoats are usually around 0.2-0.4, even at very low relative humidities. These observations indicate the presence of some kind of adsorbed surface film which reduces the adhesive strength of contacting asperities. Consequently a lower static friction was obtained in the experiments, just as well reported in the literature for metal surfaces (Rabinowicz, 1965; Gao and Kuhlmann-Wilsdorf, 1990). Nevertheless, a thin layer (a monolayer or a few layers) of lubricant will effectively reduce the interfacial strength of contacting asperities, which in turn reduces friction.

Total Thickness of Liquid at the Head/Disk Interface

Figure 3 shows thickness of adsorbed water on the head surface and on the unlubricated disk surfaces as a function of relative humidity. The thickness of adsorbed water increased, as expected, with relative humidity. Figure 4 shows thickness of adsorbed water as a function of lubricant thickness at

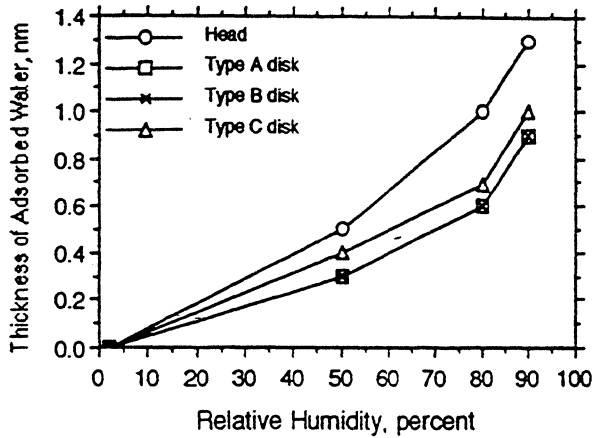


Fig. 3 Thickness of adsorbed water on the head surface and on the three types of unlubricated disk surfaces versus relative humidity.

various relative humidities. The lubricated disks adsorbed slightly less water than the unlubricated disks when the lubricant was thin. When the lubricant was thick, the lubricated disk adsorbed a little more water. One explanation is as follows: When the amount of lubricant is just enough to cover a disk surface, the disk adsorbs the least amount of water because the disk surface becomes hydrophobic due to lubrication. When an excess amount of lubricant is on the surface, however, the functional end groups of the excess lubricant attract water molecules instead of interacting with the disk surface. Thus more water is adsorbed on the disk with a thick lubricant layer.

Since all the measurements were taken on the virgin surfaces, the amount of lubricant transferred to the head surfaces was negligible. Thus the total thickness of liquid at the head/disk interfaces was the sum of the lubricant thickness on the disk surface, the adsorbed water thickness on the disk surface and adsorbed water thickness on the head surface. Figure 5 shows the static friction coefficient data versus the total thickness of liquid at the head/disk interface for three types of disks. The best fitting exponential curves were also plotted in the figure. Apparently the static friction coefficient increased with the thickness of liquid at the head/disk interfaces for all three types of disks. The Type A disks with a small surface roughness showed a quick increase in friction as increasing thickness of lubricant. When the thickness of liquid was over 2 nm, the friction coefficient increased very rapidly. For the Type B disks, the friction coefficient increased moderately with the thickness of liquid until the total thickness of liquid was about 4 nm. Then the friction coefficient increased significantly afterwards. For the Type C disks which have a large surface roughness, the friction coefficient increased, as expected, rather slowly with the thickness of liquid. Nevertheless, when the thickness of liquid was over 8 nm, the friction coefficient was over 0.5 even on the Type C disk surfaces.

The increase in static friction with the thickness of liquid is caused by the meniscus effect of liquid. However, there are

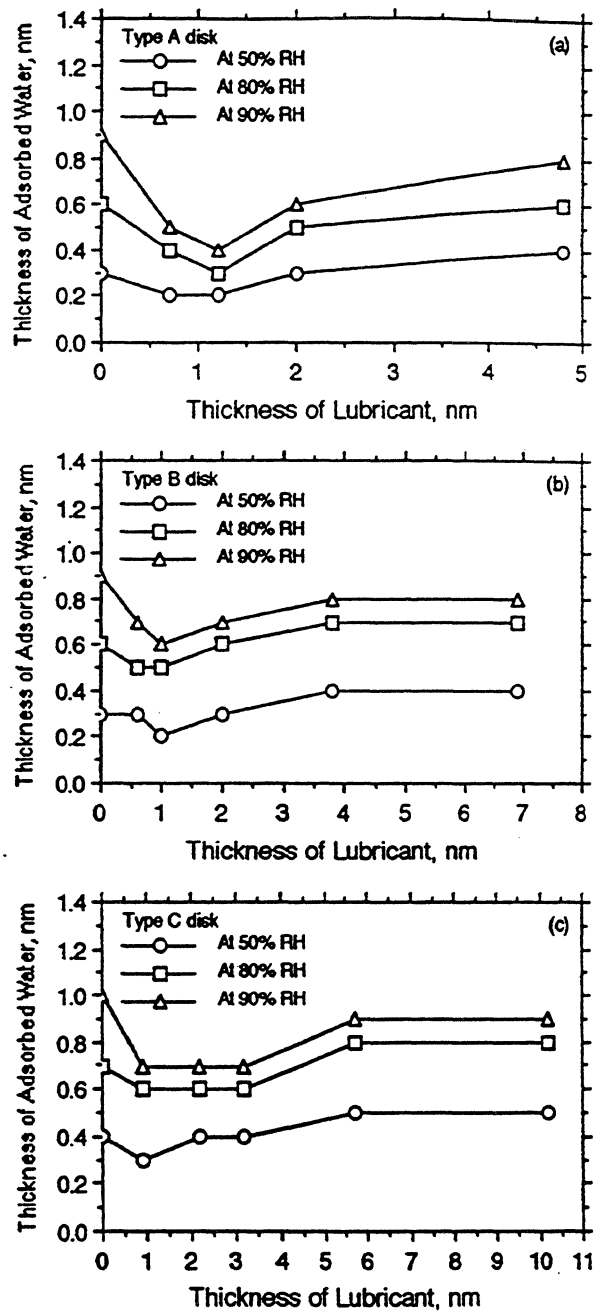


Fig. 4 Thickness of adsorbed water versus thickness of lubricant for three types of disks at various relative humidities

no apparent critical thickness values beyond which the meniscus effect of liquid becomes predominant. There is also no clear definition in this nature about the critical thickness value of liquid. Just for convenience, we chose the friction coefficient of 0.5 as a threshold and the thickness of liquid at this point is a critical thickness value. Although this threshold is an arbitrary value, the friction coefficient does increase with the thickness of liquid much more rapidly when friction coefficient is above 0.5 (see Figure 5). Moreover, because the lowest value of friction coefficient on three types of disks is

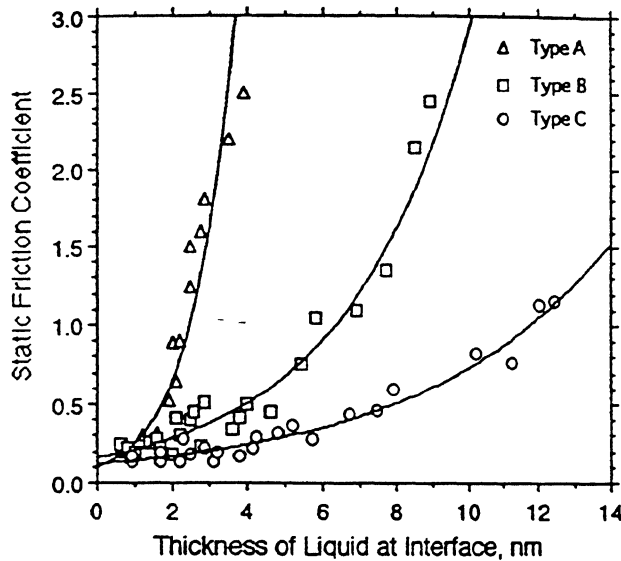


Fig. 5 Static friction coefficient versus the total thickness of liquid at the head/disk interface for three types of disks. The solid lines are the best fitting exponential curves

around 0.2, we can say that the meniscus effect of liquid contributes at least half of the total friction when the friction coefficient is above 0.5. Accordingly, the critical thickness values for the Types A, B, and C disks are about 2, 4, and 8 nm, respectively.

Long-Term Stiction
Water Build-up at the Head/Disk Interface

Figure 6a shows the thickness of adsorbed water on the Type A and the Type B unlubricated disk surfaces at 80% RH as a function of sitting time. Apparently the thicknesses of adsorbed water on both disk surfaces were relatively stable during a long period of exposure to 80% RH. Figure 6b shows the static friction coefficients at 80% RH as a function of head contacting time. For the Type A disks, the friction coefficient increased significantly with the contact time, while only a moderate increase in friction coefficient was obtained for the Type B disks. This is obviously due to the roughness difference of the two disks. The more quantitative way to explain the results in Figure 6 is to compare the initial thickness of adsorbed water at the head/disk interface with the critical thickness values of liquid for the Type A and the Type B disks. The initial thickness of adsorbed water at 80% RH is about 1.6 nm for both the Type A and the Type B unlubricated disks (see Figure 3), which includes 0.6 nm on the disk surface and 1.0 nm on the head surface. Since the disk surfaces do not adsorb more water as the contact time increases, any changes in the friction are mainly due to water build-up at the head/disk interface. For the Type A disks, the initial thickness of adsorbed water (1.6 nm) was very close to the critical thickness value (2 nm). Thus a small amount of

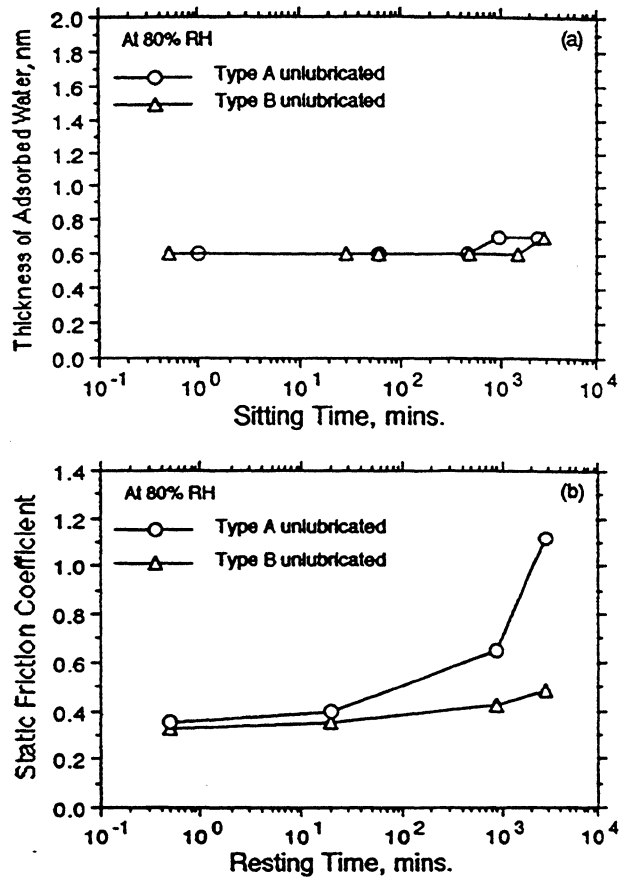


Fig. 6 (a) Thickness of adsorbed water on the Type A and the Type B unlubricated disks versus sitting time at 80% relative humidity; (b) static friction coefficient versus the time of head resting on the Type A and the Type B unlubricated disks at 80% relative humidity

water build-up would result in a significant increase in friction. Indeed, the static friction coefficient increased up to 1.1 after about 3,000 minutes (2 days) of head contact. It can be seen from Figure 5 that about 2.5 nm thick of liquid at the head/disk interface will give a friction coefficient of 1.1. Thus we can estimate that the thickness of adsorbed water building up at the head/disk interface is about 2.5 nm, that is, increased by 0.9 nm after 3,000 minutes of head contact. For the Type B disks, by contrast, the initial thickness of adsorbed water (1.6 nm) was far below the critical thickness value (4 nm). Thus the water build-up had much less effect on friction. The static friction coefficient increased, as expected, only marginally with the contact time.

Lubricant Build-up at the Head/Disk Interface

When a lubricant with functional end groups adsorbs on a solid surface, it will first form a strongly adsorbed lubricant layer (bonded or immobile lubricant), and then form more loose multilayers of the lubricant (mobile lubricant). One

way to determine thickness values of the bonded lubricant and the mobile lubricant is to measure the residual thickness of lubricant after the disk is rinsed with a Freon solvent. We measured the residual thickness of lubricant AM2001 on the three types of disk surfaces using FT-IP. The average residual thickness of lubricant was about 0.5-0.7 nm. Thus the thickness of mobile lubricant on disk surfaces used in the present study should be around the initial thickness of lubricant minus 0.6 nm.

Figure 7a shows the static friction coefficients on the Type A lubricated disks as a function of head resting time. The relative humidity was controlled at 5% so that the effect of adsorbed water was insignificant. Three thickness values of lubricant were chosen for this experiment, 0.6 nm, 1.2 nm, and 2.2 nm. The disk with 0.6 nm thick lubricant had the bonded lubricant only. Thus the lubricant did not migrate and no lubricant build-up was expected. Indeed, Figure 7a shows that the friction coefficient remained unchanged during the head contact. The disk with 1.2 nm thick lubricant had about 0.6 nm thick bonded lubricant and about 0.6 nm thick mobile lubricant on the disk surface. However, the thickness of lubricant was far below the critical thickness for the Type A disks (2 nm). Therefore, little increase in the static friction was obtained. When enough mobile lubricant (0.6 nm bonded plus 1.6 nm mobile) was on the disk surfaces, the initial static friction was already high and a considerable increase in the static friction was observed after a long period of head contact. This is because that the thickness of lubricant (2.2 nm) was already greater than the critical thickness value. Apparently that occurrence of long-term stiction requires not only that mobile lubricant is present on disk surfaces but also that thickness of lubricant is close to a critical thickness value.

To further confirm this finding, we did the same kind of experiments with the Type B disks. Figure 7b shows the static friction coefficient versus the head resting time for the Type B disks. The disk with 2.8 nm thick lubricant had about 2.2 nm thick mobile lubricant on the disk surface. But no significant increase in static friction was observed over a long period of head contact. This is because the initial thickness of lubricant (2.8 nm) is far below the critical thickness value for the Type B disks (4 nm). Even the lubricant slowly migrated or diffused into the contact regions, meniscus effect of lubricant would not be significant until the thickness of lubricant was close to the critical thickness value. The other disk with 6.9 nm thick lubricant had about 6.3 nm thick mobile lubricant available and the initial thickness of lubricant was larger than the critical thickness value. The initial friction was already high and a significant increase in the static friction was observed over a long period of contact. Availability of a large amount of mobile lubricant on the disk surface and a high initial thickness of lubricant contributed to the long-term friction increase. Comparing the friction coefficient value after about 4,000 minutes (3 days) of contact in Figure 7b with the data points in Figure 5, we can estimate that about 10 nm thick lubricant was building up at the head/disk interface for the

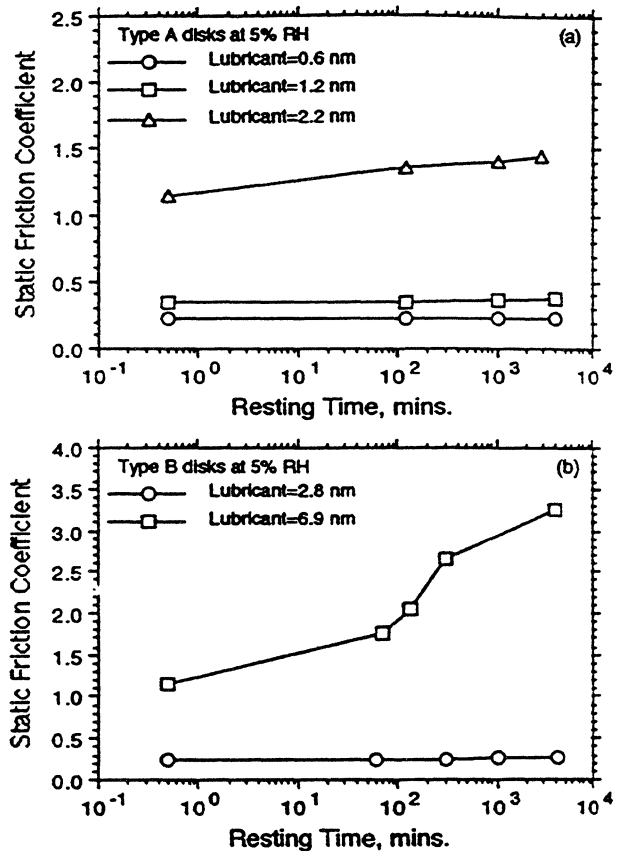


Fig. 7 Static friction coefficient versus the time of head resting on (a) the Type A lubricated disks and (b) the Type B lubricated disks at 5% relative humidity

disk with 6.9 nm thick initial lubricant after about 4,000 minutes of contact.

DISCUSSIONS

When a hemispherical surface of radius R is in contact with a flat surface and a drop of liquid is introduced at the point of contact, surface tension effects will arise. The pressure inside the liquid is lower than that outside the liquid by an amount of γ/r' , where γ is surface energy of the liquid and r' is the radius of curvature of the liquid surface. Rabinowicz (1965) has shown that the adhesion force (meniscus force), p_m , due to the pressure difference is given by

$$p_m = 4\pi R\gamma \cos\alpha \quad (1)$$

where α is angle of contact between liquid and solid. In the case of the hemisphere adjacent to a flat surface (Figure 8a), the meniscus force is given by (Israelachvili, 1985):

$$p_m = \frac{4\pi R\gamma \cos\alpha}{1 + \frac{b}{h-b}} \quad (2)$$

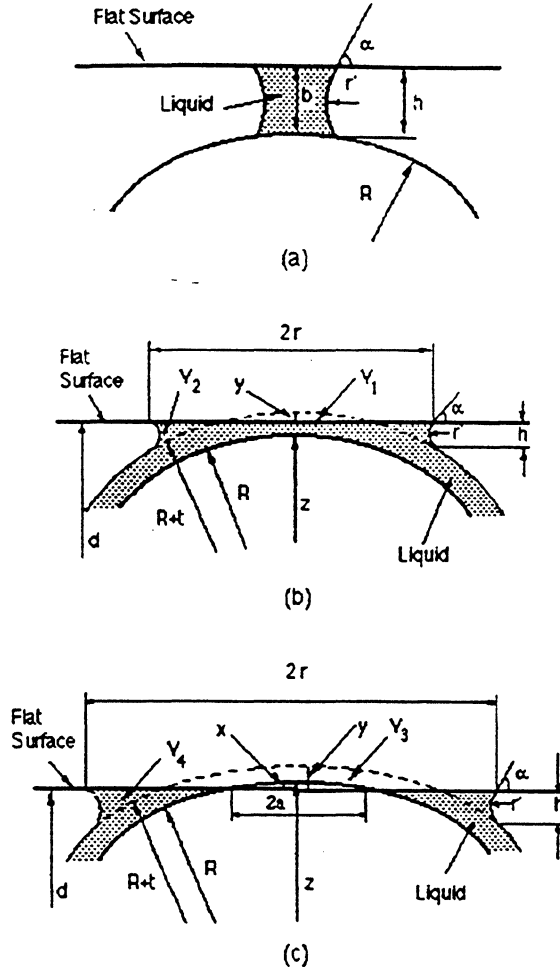


Fig. 8 Schematics of (a) an isolated meniscus; (b) a non-contact but wetted asperity; and (c) a contact asperity

where b is the separation between the sphere and the flat surface and h is a geometric length related to the curvature of the meniscus. Obviously equation (2) becomes equation (1) when $b=0$.

Recently Li and Talke (1990) have developed an analytical stiction model in which the equation (2) was incorporated into the Greenwood-Williamson surface model (Greenwood and Williamson, 1966). They predicted the effect of humidity on stiction as a function of a number of factors. Later Koka et al. (1991) pointed out that the actual peak height distributions rather than the Gaussian distribution should be used in the model to obtain a good correlation with experimental data. Equation (2), which was used by Li and Talke (1990) for calculating the meniscus force, is for the case of an isolated meniscus, i.e., a drop of liquid is introduced between two surfaces after the two surfaces are pressed into contact or close to contact. In an actual head/disk interface, however, disk surfaces are already covered with a layer of lubricant and a layer of adsorbed water before a head contact. Then the contact area wetted by the liquid is greater

than the value calculated from equation (2) because some of the liquid is squeezed out. Therefore a larger stiction force will arise.

Assume that a flat surface is in contact with a rough surface which uniformly covered with a liquid layer. The asperity height of the rough surface is described by a distribution function $\varphi(z)$, where z is the asperity height from the mean plane. Further it is assumed that all asperities are spherical with a constant radius R . When the two surfaces are pressed together under a normal force P , a meniscus force will arise. The meniscus force consists of two parts: one about non-contact but wetted asperities (Figure 8b) and the other about contact asperities (Figure 8c). d is the distance between the flat surface and the mean plane of the rough surface; t is thickness of the liquid layer; α is the angle of contact between the liquid and the solid.

The meniscus force between a flat surface and one non-contact but wetted asperity, p_{mn} , is equal to the wetted area (πr^2) times the pressure difference γ/r' (Figure 8b):

$$p_{mn} = \pi r^2 \frac{\gamma}{r'} \quad (3)$$

By using simple geometrical relationship,

$$r^2 \approx 2(R+t)(h+y), \quad r' \approx \frac{h}{(1+\cos\alpha)}, \quad R \gg t$$

we can rewrite the equation (3) as

$$p_{mn} = 2\pi R\gamma (1+\cos\alpha) \left(1 + \frac{y}{h}\right) \quad (4)$$

Similarly, the meniscus between a flat surface and one contact asperity, p_{mc} , is equal to the wetted area ($\pi r^2 - \pi a^2$) times the pressure difference γ/r' (Figure 8c):

$$p_{mc} = (\pi r^2 - \pi a^2) \frac{\gamma}{r'} \quad (5)$$

Using the above geometrical relationship and $a \approx 2Rx$, we can rewrite the equation (5) as:

$$p_{mc} = 2\pi R\gamma (1+\cos\alpha) \left(1 + \frac{y-x}{h}\right) \quad (6)$$

Since $R \gg t$, $|d-z|$, y , then the selected geometric volumes of liquid (see Figures 8b and 8c) are given by

$$V_1 = \frac{1}{3}\pi r y^2 [3(R+t) - y] \approx \pi R y^2 \quad (7)$$

$$V_2 \approx \frac{1}{2}h [2\pi(R+t)(h+y) - 2\pi(R+t)y] \approx \pi R h^2 \quad (8)$$

$$V_3 = \frac{1}{3}\pi r y^2 [3(R+t) - y] - \frac{1}{3}\pi x^2 (3R - x) \approx \pi R (y^2 - x^2) \quad (9)$$

$$V_4 \approx \frac{1}{2}h [2\pi(R+t)(h+y) - 2\pi(R+t)y] \approx \pi R h^2 \quad (10)$$

Since the liquid is incompressible, the volume of the liquid must be conserved, i.e., $V_1=V_2$, $V_3=V_4$. Then the following equations can be obtained:

$$\begin{aligned} h &= y && \text{for the non-contact asperity} \\ h^2 &= y^2 - x^2 && \text{for the contact asperity} \end{aligned}$$

If the deformation of contact asperities is considered, then $x=0$. Thus the equation (4) and the equation (6) becomes the same equation:

$$P_m = P_{m0} = P_{mc} = 4\pi R\gamma (1 + \cos\alpha) \quad (11)$$

Then the total meniscus force over the apparent contact area A_0 is given by

$$P_m = 4\pi R\gamma (1 + \cos\alpha) A_0 \eta \int_{d-t}^{\infty} \varphi(z) dz \quad (12)$$

η is the areal density of asperity and is determined by using the following relationship (Bhushan and Doerner, 1989):

$$\sigma R \eta \approx 0.04 \quad (13)$$

where σ is the standard deviation of the distribution function $\varphi(z)$. d is calculated by solving the following equation numerically (Greenwood and Williamson, 1966):

$$P = \frac{4\sqrt{R} A_0 \eta E'}{3} \int_d^{\infty} (z-d)^{3/2} \varphi(z) dz \quad (14)$$

where E' is effective elastic modulus of the two contact surfaces. Then the friction force, F , is given by (Li and Talke, 1990)

$$F = A_r s_r + P_m f_m \quad (15)$$

where s_r is average shear strength of asperities; f_m is the friction coefficient associated with the meniscus force P_m ; A_r is the real contact area given by (Greenwood and Williamson, 1966)

$$A_r = \pi R A_0 \eta \int_d^{\infty} (z-d) \varphi(z) dz \quad (16)$$

Figure 9 shows the actual asperity height distributions for the head and the three types of disk surfaces. Since the actual asperity height distributions do not strictly follow the Gaussian distribution, we cannot convert the head and the disk into a flat surface against a rough surface. Therefore, in our calculations, we consider the disk (for head/Type A disk interface) or the head (for head/Type B or C disk interfaces) as a flat surface. The parameters used in the calculations are as follows: $P=6.5$ grams; $f_m=0.2$; $A_0=1.58$ mm²; $\gamma_{\text{water}}=0.07$ N/m; $\gamma_{\text{lubricant}}=0.025$ N/m; $\alpha_{\text{water}}=60^\circ$; $\alpha_{\text{lubricant}}=0^\circ$. The wetting angle of the lubricant is very small and the contact angle of water on unlubricated or lubricated disk surfaces with carbon overcoats is around 60° , as reported in a previous study (Tian and Matsudaira, 1992) and also in the literature (Caporiccio, 1986; Saperstein and Lin, 1990). Figure 10 shows the experimental data and the model predictions based on the actual asperity height distributions. Three sets of experimental data were plotted: the unlubricated disks at various relative humidities (adsorbed water), the lubricated

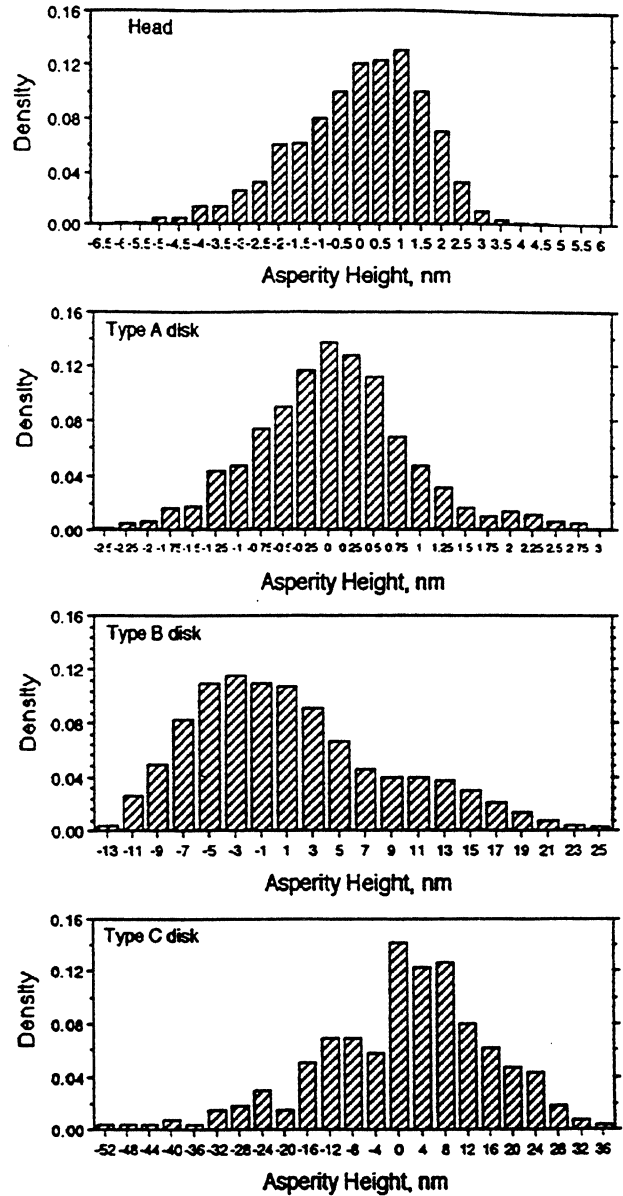


Fig. 9 Histograms of the head and three types of disk surfaces

disks at 2% RH (lubricant) and lubricated disks at various relative humidities (lubricant + water). Apparently the model can only describe a single layer of liquid (lubricant or adsorbed water) at the head/disk interface. Nevertheless, we calculated the friction coefficient based on the model assuming that the liquid layer is a pure lubricant or a pure adsorbed water, and plotted the calculated values in Figure 10. It seems that the calculated values agree fairly well with the experimental data of the Type B and the Type C disks. The calculated values for the Type A disks are higher than the experimental data. The discrepancy may be caused by treating the Type A disks as flat surfaces. The surface roughness of the Type A disks is smaller but not negligible compared with the surface roughness of the head. For the Type B and

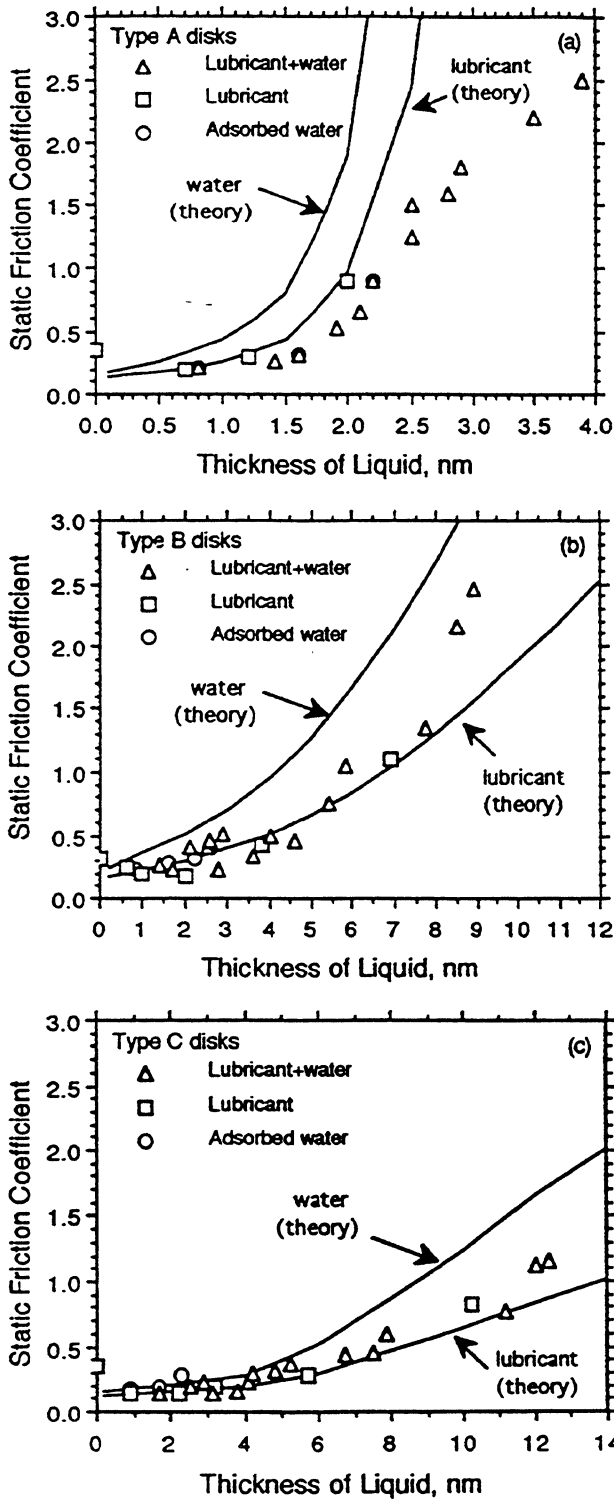


Fig. 10 Experimental data and the model predictions for (a) Type A disks; (b) Type b disks; and (c) Type C disks

the Type C disks, however, the roughness of the head is insignificant and thus the head surface can be treated as a flat surface.

The predictions from the proposed stiction model tell us that friction increases with thickness of liquid. This is not quite true when a small amount of liquid exists at the head/disk interface. It was shown in Figures 1 and 2 that a small amount of water or lubricant at the head/disk interface actually reduces friction. Equation (12) also tells us that the effect of a layer of thin lubricant is different from the effect of a layer of adsorbed water with a same thickness value. The meniscus force depends on two properties of the liquid, the surface energy γ and the contact angle α . According to equation (12), the meniscus force due to the adsorbed water is about 2 times of the meniscus force due to the lubricant of same thickness. However, when the thickness of liquid is small, our experimental results shows that the difference between the adsorbed water and the lubricant is small.

One important implication from Equation (12) is that for a given distribution of asperity height $\phi(z)$, the meniscus force is simply proportional to the bearing ratio which is calculated based on a new parameter, $d-t$, instead of the separation parameter d only. In other words, the distribution shape of the high asperity part is directly related to the meniscus force. Therefore a small number of high asperities will effectively minimize meniscus effect of liquid at the head/disk interface.

CONCLUSIONS

- (1) The static friction coefficients were well correlated with the total thickness of liquid at the head/disk interface for three types of disks with different surface roughness values. When the liquid at the head/disk interface is below the critical thickness value which is related to surface roughness values, the meniscus effect of the liquid is insignificant. When the thickness of liquid is larger than the critical value, the static friction increases drastically as increasing thickness of the liquid.
- (2) The thickness of adsorbed water on the disk surfaces does not change much during a long exposure to an 80% relative humidity. However, when the initial thickness of adsorbed water at the head/disk interface is close to the critical thickness value, static friction increases with the head contact time due to the water build-up at the contacting asperities.
- (3) Presence of the mobile lubricant does not necessarily cause long-term stiction. Long-term stiction occurs only when enough mobile lubricant is present and the thickness of liquid at the head/disk interface is close to a critical thickness value, which is related to surface roughness values.
- (4) The meniscus force is directly related to the bearing ratio of surface roughness in the proposed stiction model. The calculated values based on the model agree fairly well with the experimental data.

REFERENCES

Bhushan, B. and Doerner, M. F., 1989, "Role of Mechanical Properties and Surface Texture in the Real Area of Contact of Magnetic Rigid Disks," *J. Tribology*, Vol. 111, pp. 452-458.

Bowden, F. P. and Throssell, W. R., 1951, "Adsorption of Water Vapour on Solid Surfaces," *Proc. Roy. Soc. of London*, A209, pp. 297-308.

Caporiccio, G., 1986, "A New Series of Lubricants for Magnetic Recording Media from Bifunctional Perfluoropolyether Derivatives," *Symposium on Memory and Advanced Recording Technologies*, San Jose, CA, USA.

Gao, C. and Kuhlmann-Wilsdorf, D., 1990, "Adsorption Films, Humidity, Stick-Slip and Resistance of Sliding Contacts," *IEEE Trans. Components Hybrids and Manufacturing Technology*, Vol. 14, pp. 37-44.

Gitis, N. V., Volpe, L., and Sonnenfeld, R. (1991), "Long-Term Stiction at the Magnetic Thin-Film Disk-Slider Interface," *Adv. Info. Storage Syst.*, ASME, Vol. 3, pp. 91-105.

Greenwood, J. A. and Williamson, J. P. B., 1966, "Contact of Nominally Flat Surfaces," *Proc. Roy. Soc., London*, A295, pp. 300-319.

Koka, R., Viswanathan, K. V., and Rothchild, W., 1991, "Influence of Roughness on Head/Disk Stiction Induced By a Mobile Lubricant Film," *Adv. Info. Storage Syst.*, ASME, Vol. 3, pp. 117-126.

Li, Y., Trauner, D., and Talke, F. E., 1990, "The Effect of Humidity on Stiction and Friction at the Head/Disk Interface," *IEEE Trans. on Magnetics*, Vol. 26 (5), pp. 2487-2489.

Li, Y. and Talke, F. E., 1990, "A Model for the Effect of Humidity on Stiction of the Head/Disk Interface," *Tribology and Mechanics of Magnetic Storage Systems*, STLE SP-29, pp. 79-84.

Li, Z., Rabinowicz, E. and Saka, N., 1989, "The Stiction between Magnetic Recording Head and Thin Film Disks," *Tribology and Mechanics of Magnetic Storage Systems*, STLE SP-26, pp. 64-70.

Liu, C. C. and Mee, P. B., 1983, "Stiction at the Winchester Head-Disk Interface," *IEEE Transaction on Magnetics*, Vol. Mag-19, pp. 1659-1661.

Miyamoto, T., Ando, Y., Hirono, S., and Sato, I., 1989, "Influence of Relative Humidity on Friction Characteristics of Thin Film Disk Media," *J. Mag. Soc. Japan*, Vol. 13, Supplement No. S1, pp. 207-211.

Miyamoto, T., Kaneko, R., and Ando, Y., 1990, "Interaction Force between Thin Film Disk Media and Elastic Solids Investigated by Atomic Force Microscopy," *J. Tribology*, Vol. 112, pp. 567-572.

Rabinowicz, E., 1965, *Friction and Wear of Materials*, John Wiley & Sons, Inc., New York.

Saperstein, D. D. and Lin, L. J., 1990, "Improved Surface Adhesion and Coverage of Perfluoropolyether Lubricants Following Far-UV Irradiation," *Langmuir*, Vol. 6 (9), pp. 1522-1524.

Streator, J. L., Bhushan, B. and Bogy, D. B., 1991, "Lubricant Performance in Magnetic Thin Film Disks With Carbon Overcoat - Part I: Dynamic and Static friction," *J. of Tribology*, Vol. 113, pp. 22-31.

Tabor, D., 1981, "Friction - The Present State of Our Understanding," *ASME Journal of Lubrication Technology*, Vol. 103, pp. 169-179.

Tian, H. and Matsudaira, T., 1992, "Effect of Relative Humidity on Friction Behavior of the Head/Disk Interface," presented at INTERMAG '92, St. Louis, Missouri, April 13-16.

Timsit, R. S. and Stratford, G., 1988, "Effect of Humidity on Friction at Magnetic-Head/Hard-Disk Interfaces," *Tribology and Mechanics of Magnetic Storage Systems*, STLE SP-25, pp. 17-23.

Nomenclature

a	Radius of contact
A_0	Total flat area of the slider rails (apparent contact area)
A_r	Real contact area
d	Distance between a flat surface and the mean plane of a rough surface
E	Elastic modulus
E'	Effective elastic modulus of two contact surfaces
F	Friction force
f_m	Friction coefficient associated with a meniscus
h	Geometric length related to curvature of a meniscus
P	Normal force
P_m	Meniscus force of a single meniscus
P_{mc}	Meniscus force of a contact asperity
P_{mn}	Meniscus force of a non-contact but wetted asperity
P_m	Total meniscus force
r	Geometric radius of wetted asperity
r'	Curvature radius of a meniscus
R	Radius of asperity
s_r	Average shear strength of asperities
t	Thickness of liquid
V_i	Geometric volume ($i=1,2,3,4$)
x, y	Geometric length
z	Asperity height from the mean plane of a rough surface
α	angle of contact between a liquid and a solid
γ	Surface energy of liquid
η	Areal density of asperity
$\phi(z)$	Distribution function of asperity height

Pin-on-disk tribology of thin-film magnetic recording disks

T. E. Karis and V. J. Novotny

IBM Research Division, IBM Magnetic Recording Institute, Almaden Research Center,
650 Harry Road, San Jose, California 95120-6099

(Received 18 January 1989; accepted for publication 2 June 1989)

Tribological studies of friction and wear were performed on carbon overcoated thin-film magnetic recording media with pin-on-disk tests. Scanning microellipsometry was employed to measure the wear of carbon overcoats on rigid magnetic media. Severe wear produced after the carbon film wore through was measured by mechanical profilometry. The wear rate of the carbon is three orders of magnitude lower than that of the underlying metallic layers and is nearly proportional to slider load. Micrographs of the wear tracks and the magnitude of the wear coefficient from the Archard wear equation indicate three-body abrasive wear.

I. INTRODUCTION

An important task in the development of thin-film magnetic recording media is the formation of a mechanically durable and stable disk surface.^{1,2} Metal magnetic media without protective films have very poor wear resistance.³ Because of this, the magnetic layers are usually overcoated with films providing wear and corrosion protection. Cobalt based magnetic films between 40 and 100 nm are deposited on the substrate consisting of a nickel-phosphorus layer 10–20 μm thick on an aluminum-magnesium alloy disk. The cobalt alloy is normally overcoated with a carbon or silicon dioxide protective film 20–100 nm thick. In this study, the wear of thin-film disks produced by the contact sliding of a spherical cap probe against the rotating disk under a wide range of loads is examined using a pin-on-disk apparatus,^{4,5} and scanning microellipsometry⁶ is employed to measure the wear at early stages before the protective carbon layer has worn through. Later stages of wear are measured by mechanical profilometry. Raman spectroscopy⁷ can also measure wear of mechanical overcoats.

This tribological study had the following objectives: First, to develop a test to quantitatively evaluate the tribology of the thin-film magnetic recording media. Second, to set up methods to measure the wear with depth sensitivity better than 1 nm and spatial resolution of at least 20 μm . Third, to compare the wear of the carbon overcoat with the wear of the underlying magnetic layers, and to examine the dependence of the wear on load. Finally, to identify the prevailing wear mechanism in these media from the magnitude of the wear coefficient and optical micrographs.

II. EXPERIMENT

A. Apparatus

The pin-on-disk (POD) apparatus consists of a spindle that rotates the disk and a dual-air slide probe mount⁴ that maintains the probe tip in contact with the disk under the desired load. In this apparatus, air slides are used to isolate the vertical and tangential motions of the probe. (An air slide allows motion only along the axis of the slide through its housing.) The vertical air slide on which the probe is mounted is held perpendicular to the disk surface and moves freely in the vertical direction to follow any disk runout.

Weights are added to the top of the vertical slide to obtain the desired normal load. The vertical air slide housing is mounted on the end of another air slide with its axis of motion perpendicular to that of the vertical slide and tangential to the sliding direction. This is called the tangential air slide. The tangential air slide is held centered at equilibrium by opposing springs.

The displacements of the tangential air slide from its equilibrium position due to the friction force is measured to within $\pm 5 \mu\text{m}$ by a fiber optic sensor that converts the displacement to a voltage. This tangential force signal is low-pass RC filtered at 1 Hz. A personal computer (PC) with an interface card periodically monitors this voltage and converts it to the friction coefficient with an accuracy of 0.02.

Test duration and disk rotation rate are also controlled through the PC. The rotation rate is within the range of 25–100 rad s^{-1} , the rotational velocity is 1–6 m s^{-1} , and the normal load is within the range of 0.05–1 N.

B. Materials

Spherical cap Al_2O_3 (75 wt. %) + TiC ceramic test probes with a 10-cm radius of curvature are used. Tests are done on unlubricated sputtered carbon overcoated thin-film 133-mm (5 $\frac{1}{4}$ -in.) diam magnetic recording disks. Since the purpose of this study was to develop the measurement methodology for overcoats, no attempt was made to further characterize the disks. The root-mean-square roughness of the disk and probe surface is typically 2 and 5 nm, respectively.

C. Procedure

Each test is carried out with a new or thoroughly cleaned probe. The probes are fastened onto the bottom of the vertical air slide with cyanoacrylate adhesive and cleaned with Freon solvent to remove any grease. The probe tip is centered on the surface of the disk by adjusting set screws on the tangential air slide mount.

After the probe is positioned at the desired radial location and aligned, the tangential force calibration is done. The probe is raised off the disk by propping up the vertical air slide, the fiber optic sensor is zeroed, and known weights are suspended from the tangential air slide with nylon line strung over an air bearing pulley to obtain the voltage corre-

sponding to two tangential loads. These calibration loads and corresponding voltages are then input to the PC. Once rotation has begun, the probe is gently lowered to the disk surface. The wear tracks are maintained at least 5 mm apart and tests on the same surface are run from outside to inside diameter to avoid contamination by debris from previous tracks.

D. Analysis

After a given number of sliding cycles, the wear of the overcoat can be evaluated by scanning microellipsometry with the set up sketched in Fig. 1. Ellipsometry⁸ is based on measurement of changes in the polarization of monochromatic polarized light caused by reflection from the surface. When polarized light is reflected from a surface, changes in the relative phases and amplitudes of the electric field vectors parallel and perpendicular to the plane of incidence occur. These changes determine two angles Ψ and Δ which can be related to two unknown optical parameters such as the real and imaginary parts of the refractive index of the substrate n_s and k_s , the real and imaginary part of the refractive index of the film n , and k or n and film thickness d by relations

$$\Psi = f_1(n_s, k_s, n, k, d, \phi, \lambda), \quad (1)$$

$$\Delta = f_2(n_s, k_s, n, k, d, \phi, \lambda), \quad (2)$$

where f_1 and f_2 are functions derived from properties of reflected light,⁹ ϕ is the angle of incidence, and λ is the wavelength of light.

The complex multilayer structure of the film disk can be treated as a single film over the substrate characterized by the effective optical constants. The magnetic layer is usually thick enough that the contributions of underlying layers are minor. The measured optical constants of the substrate (including the magnetic layer rich in cobalt) from Eqs. (1) and (2) are included in Table I together with the real and imaginary parts of the refractive index of carbon. The imaginary part is determined by optical spectroscopy. These values for the carbon film are comparable to those reported by Tsai *et al.*¹⁰ For profiling of wear tracks the laser beam of the ellipsometer is focused into a spot. The sample is scanned at 10-, 25-, or 50- μm steps across the wear track to profile it. During profiling the refractive index is constant and the unknown carbon thickness d is determined from Eqs. (1) and (2). The

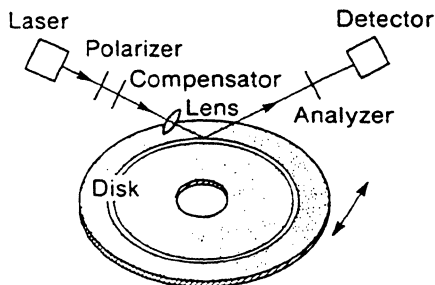


FIG. 1. A schematic drawing of scanning microellipsometry as used to profile the wear track in the overcoat.

TABLE I. The optical constants measured by ellipsometry and optical spectroscopy at $\lambda = 633 \text{ nm}$.

Parameter	Value
Real part of magnetic film refractive index, n_s	2.3
Imaginary part of magnetic film refractive index, k_s	4.4
Real part of carbon film refractive index, n	2.0
Imaginary part of carbon film refractive index, k	0.6

thickness resolution is 0.1 nm, as determined from calibration with Langmuir-Blodgett layers of known thickness. The elliptical spot size is $20 \times 60 \mu\text{m}$, hence the sampled area is approximately $1000 \mu\text{m}^2$. A typical ellipsometer trace across the wear track is shown in Fig. 2(a).

Another instrument used to analyze the wear track was the surface mechanical profilometer. In measuring surface roughness with a profilometer, the surface irregularities are traced when a stylus is moved slowly across the surface. A typical profilometer trace is shown in Fig. 2(b). The profilometer is capable of detecting changes in depth of approximately 10 nm with spatial resolution of $1 \mu\text{m}^2$.

The apparent difference in the surface roughness height outside the track between Fig. 2(a) (ellipsometer) and Fig. 2(b) (profilometer) is due to the difference in the spatial resolution between the two measurement techniques. With a $1000\text{-}\mu\text{m}^2$ spot area, the ellipsometer averages out the local

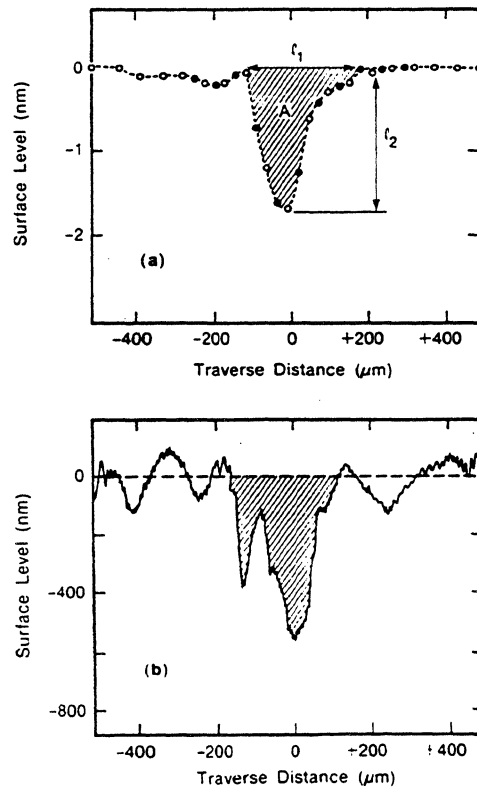


FIG. 2. An example of the wear track measurement by (a) ellipsometer and an illustration of the parameters used to characterize wear traces, and (b) profilometer. The regions outside the wear track indicate the typical surface roughness.

variations in the surface roughness height which are detected by the $1\text{-}\mu\text{m}^2$ spatial resolution of the profilometer. Most of the wear tracks were not deep enough to be detected by the profilometer and measurements were done with the ellipsometer. However, on some of the larger, more prominent tracks, the carbon layer of the disk had apparently been worn through and ellipsometry was no longer applicable. In these cases the mechanical profilometer was necessary for the wear track measurement.

Whether the profilometer or ellipsometer is employed to measure the profile of the wear scar, the track width l_1 , maximum depth l_2 , and cross-sectional area A are measured from the profile. The relation of these parameters to the profile is schematically illustrated in Fig. 2(a). Width l_1 is estimated from the trace, maximum depth l_2 is the difference between the estimated surface level and the deepest groove in the track, and the area A is measured by integration. The wear volume V is obtained by multiplying the profile area A and track circumference.¹¹

For most of the tests the cross section of the wear scar was measured in each quadrant around the circumference to test the uniformity of the track. Typical variation in the wear parameters around the circumference of the track is illustrated in Fig. 3. This variation is attributed to the statistical nature of the wear initiation and propagation. Wear initiates at some point around the track which contains a flaw or loose particle. Wear track growth then propagates around the circumference in an irregular manner, determined by the dynamics of debris transfer between the probe and the overcoat and debris expulsion from the track. Hence, it is natural to observe some variation in the parameters measured to characterize the wear around the circumference of a track. Owing to the irregular character of the grooves and ridges within the wear track, the cross-sectional area is not equal to the area of the segment defined by the radius of the probe and the maximum depth. Variation in the cross-sectional area is

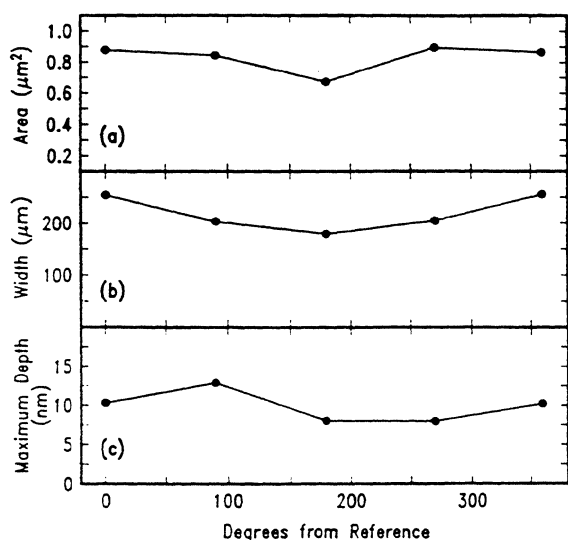


FIG. 3. An example of variation in (a) the cross-sectional area, (b) track width, and (c) maximum depth around the circumference of a track.

significant and obscures the effect of minor changes in the wear produced by small variation in the test conditions. However, if the test conditions are varied substantially, the orders of magnitude difference in the resulting wear is much larger than the error due to nonuniformity around the circumference of the track.

III. RESULTS

During all runs, the friction coefficient was recorded at 60-s intervals. A typical friction trace is shown in Fig. 4. All tests were done at ambient conditions and no systematic variation in the friction coefficient is found with load, velocity, or relative humidity in the range of 45%–60%. In general, the friction coefficient gradually increases with increasing time or number of cycles. The initial dynamic friction coefficients are around 0.1–0.15 and they reach a 0.3–0.4 value before carbon failure. An increase in the friction coefficient is attributed to a rise in the frictional energy dissipation at the interface, which may occur due to a larger real area of contact accompanying removal of asperities.

To characterize the wear, a wear rate is calculated from the cross-sectional area of the track A and the number of sliding cycles m . The wear rate R is defined as

$$R = \frac{V}{S} = \frac{2\pi r A}{2\pi r m} = \frac{A}{m}, \quad (3)$$

where V is the wear volume, S is the distance traveled, and r is radial location.

In one set of tests, the load was held constant at 0.15 N with an increasing number of cycles on each of three disks with different carbon layers. The results of the tests on these

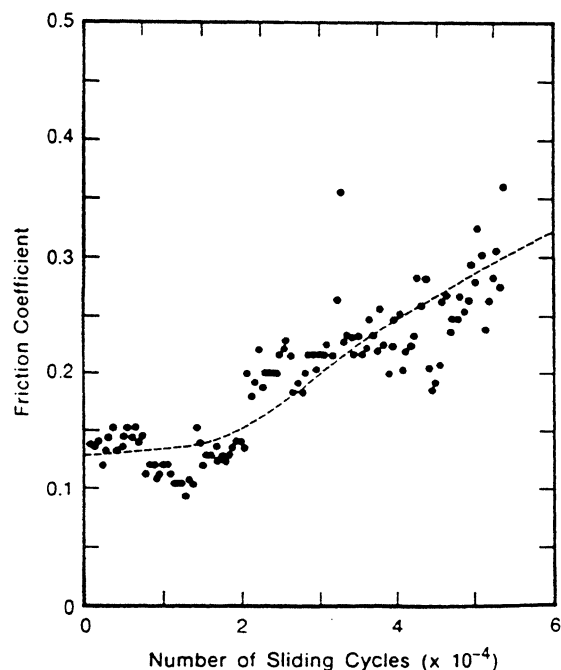


FIG. 4. The typical dynamic friction coefficient during a test run with carbon overcoat. The failure of this overcoat occurred in 2×10^5 sliding cycles.

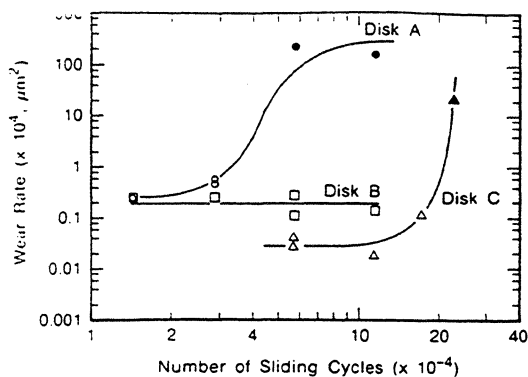


FIG. 5. The wear rate on three different carbon overcoated thin-film recording disks under a 0.15-N load. The open symbols correspond to wear of the overcoat while the solid symbols correspond to wear of the underlying layers.

three disks, referred to as disk A, B and C, are shown in Fig. 5, and the typical data are given in Table II. No significant wear of the spherical cap probe during the wear of carbon was observed. In the cases of severe wear, debris was found on the probe near the point of contact. Wear rate differences between the three disks reflect the sensitivity of mechanical durability to the sputtering conditions during overcoat deposition.

As an aid to understanding the wear process, it is useful to measure the dependence of the wear rate on load. Tests were done on another set of thin-film recording disks under loads of 0.05, 0.15, 0.3, 0.5, and 1 N. Although there is considerable variation in the wear rate, reasonably smooth load dependence results were obtained by averaging the data. The wear rate as a function of slider load is shown in Fig. 6.

IV. DISCUSSION

The results shown in Fig. 5, obtained with a 0.15-N load, show considerable variation in the wear rate. Initially the wear rate is low and fairly constant during wear of the carbon film. Once the carbon film has worn through, the wear rate sharply increases as wear proceeds through the magnetic layer. The wear in this regime is evident with disks A and C and is identified by the solid symbols. Following this transition region, the wear rate levels off at this higher value as shown by the two solid points for disk A.

In practice, the wear regime of interest is before the

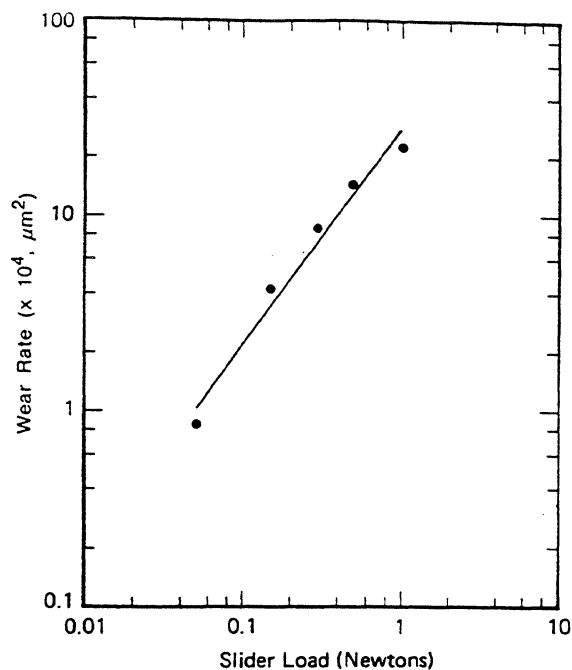


FIG. 6. The average wear rate of the overcoat as a function of the slider load.

overcoat is completely removed. The series of tests at different loads was designed to cover this region of initial wear to further study the tribology of the protective overcoat. One means of attempting to determine the wear mechanism is to calculate the wear coefficient by Archard's law¹²⁻¹⁴

$$K = \frac{pV}{WS} = \frac{pR}{W}, \quad (4)$$

where K is the wear coefficient, W is the load, and p is the indentation hardness. The physical interpretation of K is that it is a probability factor, a measure of the probability of wear particle formation at each asperity interaction. If a single wear mechanism is dominant over a given range of load, the wear coefficient should be independent of the load. A least-squares fit to the data in Fig. 6 gives (with a 90% confidence interval)

$$R = \alpha W^{1.1 \pm 0.2}, \quad (5)$$

where $\alpha = 2.8 \times 10^{-3} \mu\text{m}^2/\text{N}$. Within the limits of measurement error and over this range of load, the wear rate is proportional to the load. The indentation hardness of the carbon overcoat was measured to be approximately 22 GPa. Taking the wear rate to be proportional to the load, the wear coefficient

TABLE II. Typical wear data obtained by averaging several runs with a 0.15-N load on disk B. Δ 's are 90% confidence half intervals.

Number of cycles ($\times 10^{-4}$)	Width		Depth		Area		Wear rate ($\times 10^4 \mu\text{m}^2$)	Wear coefficient ($\times 10^5$)
	l_1 (μm)	Δ (μm)	l_2 (nm)	Δ (nm)	A (μm^2)	Δ (μm^2)		
1.40					not detectable			
2.86	200	40	9.4	3	0.73	0.2	0.25	0.37
5.73	240	30	10.0	4	1.10	0.5	0.20	0.33
11.50	260	100	14.0	3	1.60	0.8	0.14	0.20

cient is $K = 5.5 \times 10^{-5}$. This wear coefficient is within the range reported by Rabinowicz¹⁵ for ceramic sliders on unlubricated particulate disks. A comparison can then be made with wear coefficients observed for other sliding situations to speculate on the type of wear being observed in the POD test on film disks. For unlubricated three-body abrasive wear¹³ K varies from 10^{-5} to 5×10^{-3} , which includes the value for K found in this study.

Optical micrographs of the worn carbon overcoat are shown in Fig. 7. In Fig. 7(a) the track is difficult to distinguish, but in Fig. 7(b) the track appears as a series of grooves in the surface. Grooves along the track were also noticed in the ellipsometer and profilometer traces shown in Fig. 2. Given the magnitude of the wear coefficient and the observed grooves, it seems that the wear is mildly abrasive. The likely wear mechanism is that some wear particles are generated and give rise to three-body abrasive wear with a low-to-moderate abrasive concentration. The micrographs also indicate the difficulty in quantitatively measuring the track width by optical microscopy. Roughness in the track can affect the microellipsometric thickness, but roughness is estimated to introduce at most a 1–2 nm uncertainty in our results.

It should be pointed out that the wear rate varies over orders of magnitude between different disks. This is apparent from the data in Fig. 5, and from comparison of the wear rate in Fig. 5 with that in Fig. 6. Since the measured hardness of the carbon does not vary by more than a factor of 2, the orders of magnitude difference between wear rates is attributed to variation in the wear coefficient. Typical values of the wear coefficient for disk B are listed in the last column of Table II. These are an order of magnitude below the wear coefficient on the disks used in the load dependence study. The overcoats on disks A, B, and C and the disks in the load dependence study were produced by different sputtering methods. This variation serves to illustrate the main point of this study, that the POD test, in conjunction with ellipsometry and profilometry, can detect differences in the wear coefficient of thin films. In general, with mild wear, the wear coefficient is a function of surface topography and mechani-

cal properties. For example, K is affected by the fatigue and fracture properties, areal density, geometry of asperities, and the film adhesion.¹⁴

One further and very interesting observation is the relation of the wear track width to the depth. This relation can be calculated with the mensuration formula for the chord length l_1 and rise l_2 of a circle with radius r ,

$$l_1 \approx 2\sqrt{2rl_2} \quad (6)$$

when $l_2 \ll 2r$. For example, the values of l_1 , calculated from l_2 in Table II are 87, 90, and 106 μm (top to bottom).

The Hertzian contact area of the spherical cap probe on a flat surface may also be considered.¹⁶ The contact radius a is given by the Hertz equation

$$a^3 = 3rF(k_1 + k_2)/4, \quad (7)$$

where F is the total force on the contact, including adhesion forces, and

$$k_i = (1 - \nu_i^2)/E_i, \quad i = 1, 2 \quad (8)$$

are the elastic constants of the two materials with their respective Poisson's ratios ν_i and Young's moduli E_i . Taking $E_1 = 100$ GPa, $\nu_1 = 0.25$, $E_2 = 450$ GPa, and $\nu_2 = 0.25$ for the disk and slider, respectively, the load of 0.15 N and estimated adhesion force of 0.03 N, $l_1 = 2a \approx 110$ μm , in agreement with the geometric calculation, but roughly two times lower than the observed track widths.

The tracks wider than expected from the measured depth are attributed to the tangential displacement of the slider oscillating about its equilibrium position. Since the slider is mounted on a vertical air slide, it is able to follow disk runout. However, the vertical air slide is mounted on a tangential air slide that is held in place by centering springs. The tangential air slide undergoes a small oscillatory displacement at its natural frequency.⁴ It is this small amplitude oscillatory displacement that widens the track beyond that expected from the measured depth. This phenomenon should not affect the results because the measured track cross sectional areas are used to calculate the wear volume.

Since the pin-on-disk test provides reasonable values for the wear coefficient, we suggest that it can be used for process optimization and control of the thin-film coating tribology. Several factors should be considered in the design of test procedure. If the ellipsometer is to be used one should consider that different types of carbon may have optical constants that differ from those in Table I. To determine the wear coefficient K , the wear rate R in Eq. (3) should be measured over a range of slider load from 0.05 to 1 N as shown in Fig. 6. If the wear rate is proportional to the load, then the wear coefficient can be calculated from the slope of the line and the hardness with Eq. (4). Changes in the slope of wear rate as a function of load are indicative of a different wear mechanism.¹⁴ The hardness should also be measured for each type of overcoat with a microindentation hardness tester using an indentation depth much smaller than the film thickness. In addition, the number of sliding cycles to run at a given load must be determined. Although no dependence of the wear rate on sliding velocity is observed, the sliding velocity is limited at the low end by the turntable motor and at the high end by bouncing of the probe off disk runout and

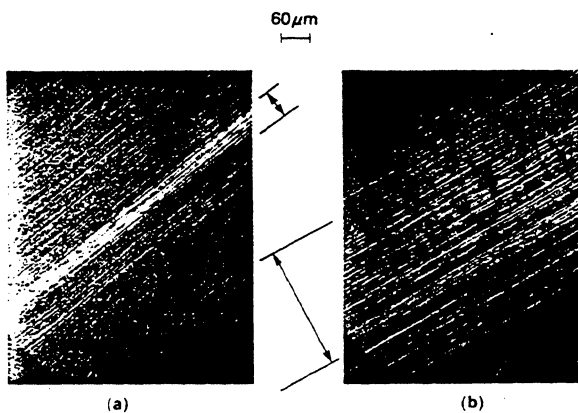


FIG. 7. Optical micrographs of the wear scar on the overcoat illustrating (a) mild wear and (b) severe wear. The apparent wear tracks are indicated, but optical micrographs do not provide reliable track width measurements.

development of an air bearing. To study only wear of the overcoat, the amount of wear produced must be sufficient to measure with the ellipsometer but not so much that the overcoat is completely worn through. In this study, the test with a 0.05-N load was run from 3.7 to 14.3×10^3 cycles and with a 1-N load from 0.07 to 7.4×10^3 cycles. Notice also that since the ellipsometer measures only the overcoat thickness, the observed tracks cannot be due to plastic deformation of the surface, and must result from partial removal of the overcoat.

V. CONCLUSIONS

Pin-on-disk tribology of carbon overcoated thin-film magnetic recording disks in conjunction with scanning microellipsometry and profilometry provides a measurement of the wear volume and the wear coefficient of the carbon overcoat. This method may be employed as a tool to further understanding of the wear mechanism and to evaluate processing conditions giving mechanically durable media.

From the results obtained in this study, it appears that the carbon overcoat wear is three-body abrasive wear. This shows indirectly that the carbon layer has a very good adhesion to the magnetic layer. Once this protective film has worn away, wear proceeds into the magnetic layer and substrate at a much higher rate.

ACKNOWLEDGMENTS

The authors would like to express their gratitude to L. Huang for carrying out many of the tests and analyses. Dur-

ing this study, L. Huang was supported by the IBM N111 MSE co-op program. Gratitude is expressed to A. Kao for supplying some of the disks and the use of his mechanical profilometer and T-W. Wu for the microindentation hardness measurement.

- ¹M. Ishikawa, N. Tani, T. Yamada, Y. Ota, K. Nakamura, and A. Itoh, IEEE Trans. Magn. **MAG-22**, 999 (1986).
- ²Y. Nakatsuka, H. Tanaka, T. Kyoizumi, and Y. Abe. IEEE Trans. Magn. **MAG-22**, 1002 (1986).
- ³T. Croll, ASLE SP-19, 1 (1985).
- ⁴L. Aylward and T. Karis, ASLE SP-19, 93 (1985).
- ⁵Y. Kawakubo, H. Ishihara, Z. Tsutsumi, and J. Shimizu. ASLE SP-21, 118 (1986).
- ⁶V. J. Novotny, J. D. Swalen, and J. P. Rabe, Langmuir **5**, 418 (1989); Y. Hu and F. E. Talke, ASLE SP-25, 43 (1988).
- ⁷G. McClelland, H. Seki, and D. Bullock, Wear **116**, 381 (1987).
- ⁸M. Born and E. Wolf, *Principles of Optics* (Pergamon, New York, 1959).
- ⁹F. McCrackin, "A FORTRAN Program for Analysis of Ellipsometer Measurements," NBS-TN-479, U.S. Department of Commerce, NTIS, 1969 (unpublished).
- ¹⁰H.-C. Tsai, D. B. Bogy, M. K. Kundmann, D. K. Veirs, M. R. Hilton, and S. T. Mayer, J. Vac. Sci. Technol. A **6**, 2307 (1988).
- ¹¹F. Yost, Wear **92**, 135 (1983).
- ¹²J. Archard, J. Appl. Phys. **24**, 981 (1953).
- ¹³E. Rabinowicz, ASME Trans. J. Lubr. Technol. **103**, 188 (1981).
- ¹⁴J. Halling, ASME Trans. J. Lubr. Technol. **105**, 212 (1983).
- ¹⁵E. Rabinowicz, ASLE SP-21, 1 (1986).
- ¹⁶H. Hertz, *Miscellaneous Papers* (Macmillan, London, 1896), p. 146.

Correlation Between Contact Start/Stop and Constant Speed Drag Testing in Magnetic Head-Disk Tribology

S. K. Ganapathi¹

F. E. Talke

Center for Magnetic Recording Research,
University of California, San Diego
LaJolla, CA 92093-0401

A model to establish the correlation between wear in constant speed drag testing and contact start/stop testing is developed. The model is based on the Archard wear equation and uses the quasi-steady Kita-Kogure-Mitsuya model for the transition of a slider from sliding to flying to calculate the velocity dependent contact force between the slider and disk during start/stop. Experimental results for the wear of a zirconia overcoated disk are obtained for both start/stop and constant speed drag testing as a function of the number of repeated cycles using optical profilometry. The correlation between predictions and experimental data shows good agreement for up to at least 10,000 cycles of sliding.

Introduction

Two types of tests are generally used to evaluate the durability of the magnetic head-disk interface. One is the constant speed drag test, in which the head is maintained in contact with the disk at a constant speed and load. The disk velocity is chosen to be low enough to ensure that the head does not fly during rotation. The second is a contact start/stop (CSS) test in which the head rests on the disk when the disk is not rotating but flies on the disk when the disk is rotating at its operating speed. During the acceleration of the disk, the head starts flying over the disk at the so-called "take-off" velocity due to the formation of a hydrodynamic air bearing. As the velocity of the disk decreases during spin down, the head "lands" on the disk, and stays in contact until the disk comes to rest.

Since in a constant speed drag test the slider is always in contact with the disk, wear occurs as long as there is relative motion between the head and the disk. In a CSS test, however, wear occurs predominantly during start-up and shut-down of the disk, i.e., during the time that the air bearing is not fully developed. A further difference between the CSS test and the drag test is that in the drag test the contact force between the head and the disk is constant as a function of time, while in the CSS test, the contact force decreases as a function of increasing velocity, until the head starts flying. When the head flies, the contact force between the head and the disk is zero.

Although the CSS test simulates more closely the conditions in a disk drive, it takes more time to perform. In view of the differences between the constant speed drag test and the CSS test, it is apparent that a need exists to determine whether and to what degree the constant speed drag test can simulate the

durability of the head disk interface. This paper examines the differences between the constant speed drag test and the CSS test, and establishes a correlation between wear during start/stop and constant speed drag testing in the case of a zirconia overcoated disk. Although the zirconia overcoated disk is not as widely used as a carbon overcoated disk in the industry, we chose it because we found that in contrast to the carbon overcoated disk, it wears more gradually. Many investigators have studied the wear of carbon overcoated disks (e.g., Yamaguchi et al., 1988; Lee, et al., 1989; Suzuki and Kennedy, 1989; Dugger et al., 1990), but zirconia has been less well researched (Yamashita et al., 1988).

The Kita-Kogure-Mitsuya model (Kita et al., 1984) is used to simulate the transition of the slider from sliding to flying and to determine the variation of the contact force between the slider and the disk during start-up and spin-down. The time dependent contact force is used in an Archard-type wear equation to predict the wear depth as a function of the number of repeated cycles. The predictions agree well with experimentally measured values of the wear depth by optical profilometry up to about 10,000 cycles of sliding, but deviate at larger number of revolutions.

Theory

Archard (1953) proposed a model of wear for two surfaces in sliding contact according to which the wear volume W of the softer material is proportional to the contact load F , the distance of sliding s and inversely proportional to the hardness of the softer material H , i.e.,

$$W = k \frac{Fs}{H} \quad (1)$$

For adhesive and abrasive wear, the dimensionless wear coefficient k denotes the probability that a wear particle is formed

¹Current address: Applied Magnetics Corporation, 75 Robin Hill Road, Goleta, CA 93117.

Contributed by the Tribology Division for publication in the JOURNAL OF TRIBOLOGY. Manuscript received by the Tribology Division February 14, 1992; revised manuscript received October 1992.

during asperity contacts. The wear coefficient has been documented for various material combinations sliding under different conditions (for example, see Rabinowicz, 1965).

In the following analysis, we assume that wear proceeds gradually with the number of cycles. There is evidence in the literature (Ganapathi et al., 1992) that wear is localized in many regions of the disk. However, this localization in the form of cracks and pits occurs in regions that are on the order of 1 μm in length. In comparison to the circumference of the wear track, the combined area of these regions of localized wear is negligible. In this paper, only the issue of the uniform wear of the overcoat is addressed, and the non-uniform localized wear mentioned above is not taken into account. This treatment is justified for a zirconia overcoated disk which shows a decreased tendency for localized wear.

Constant Speed Drag Testing. For a constant speed drag test, the applied force F_s and the distance of sliding s are known, while H is constant, i.e., the wear volume is

$$W = cF_s s \quad (2)$$

where the constant $c = k/H$ is assumed to be constant throughout the test.

Denoting the width of the wear track by d , the length of the wear track by $2\pi r$ (where r is the radius of the wear track on the disk), and assuming that the overcoat material is softer than the slider material, we obtain the wear depth z as a function of the number of cycles n as

$$z = cF_s n / d \quad (3)$$

Contact Start/Stop Testing. In a contact start/stop test, when the disk is at rest, the applied suspension force is fully supported by the contact force at the head disk interface. When the disk rotates at its operating speed, an air bearing exists and the suspension load is supported completely by the air bearing. During the transition from sliding to flying, the contact force between the slider and the disk decreases as the disk velocity increases.

If the air-bearing force developed during the transition from sliding to flying is denoted by $F_d(t)$, and the applied suspension force is F_s , then the contact force $F_c(t)$ during the transition from sliding to flying is given by $F_c(t) = F_s - F_d(t)$. Hence, the incremental wear volume dW for a sliding distance ds during the transition from sliding to flying is given by

$$\begin{aligned} dW &= cF_c(t) ds \\ &= cF_c(t) \left(\frac{ds}{dt} \right) dt \\ &= cF_c(t) v(t) dt \end{aligned} \quad (4)$$

We have assumed above that both " H " and " k " vary identically for the drag and CSS test. This assumption may appear restrictive at first; however, in this paper we are mainly interested in determining whether the experimental data for the CSS and drag test can be modeled by a simple Archard equation. Thus, agreement of the theoretical predictions with our experimental results would indicate that it is justifiable to use the above assumptions while disagreement would indicate that H and k may be different for the two tests.

For a disk accelerating with a constant angular acceleration α , the velocity at radius r is $v = \alpha r t$ and Eq. (4) becomes

$$dW = cF_c(t) \alpha r t dt \quad (5)$$

Thus, the total amount of wear W during one start-up is given by

$$W = c\alpha r \int_0^{t_s} F_c(t) t dt \quad (6)$$

where t_s denotes the time from the beginning of motion at $t = 0$ to the time at which the slider starts flying. For the

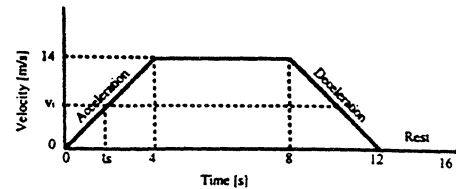


Fig. 1 Typical velocity-time profile for CSS testing

quasi-steady model under consideration, the contact force varies with velocity in the same way for both the spin-up and spin-down phases of a start/stop cycle. Therefore, the total amount of wear for one start/stop cycle is twice that of the spin-up phase.

Since the contact force varies along the track during take-off and landing, the wear depth for a single spin-up or spin-down of the disk is not uniform along the wear track. However, the wear depth may be averaged by assuming that the slider starts at random positions along the wear track for each cycle. Thus, the average wear depth of a track after n start/stop cycles is given by

$$z = \frac{n c \alpha \int_0^{t_s} F_c(t) t dt}{\pi d} \quad (7)$$

From Eq. (3) and (7), the ratio of the wear depth in a contact start/stop test and a constant speed drag test after a given number of cycles is given by

$$\frac{z(\text{CSS})}{z(\text{Drag})} = \frac{\alpha \int_0^{t_s} F_c(t) t dt}{\pi F_s} \quad (8)$$

Experimental Procedure

Constant speed drag tests and CSS tests were conducted using commercially available ferrite heads and 95 mm diameter zirconia overcoated disks. The overcoat thickness was on the order of 25–30 nm. The disks were textured but not lubricated. A load of 0.093 N (9.5g) was used for the tests. A typical velocity-time profile for the CSS test is shown in Fig. 1. The wear tests were stopped after a predetermined number of cycles, and the mean decrease in thickness of the overcoat in the wear track was measured by non-contact optical profilometry using a 2.5X objective lens. Several measurements were made at different angular positions along each wear track and the depth of the track was averaged over these measurements. The disk was reinserted in the CSS tester and the test was continued on the same track. A new head and disk were used whenever the conditions of sliding were changed.

Determination of Takeoff Velocity. An acoustic emission technique was used to determine the takeoff velocity v_t of the head. The method followed was similar to that described by Benson et al. (1988) and Kita et al. (1984). A typical variation of the acoustic emission RMS (AE RMS) voltage as a function of velocity from a zirconia disk for an applied load of 0.093 N is shown in Fig. 2. We observe that the RMS voltage decreases to a low value for velocities greater than about 1.6 m/s, indicating that the slider flies at velocities greater than this value. When the applied suspension load is decreased to 0.068 N, the slider takes off at a velocity of 1.25 m/s.

Model for Predicting the Variation of Contact Load With Velocity. In order to calculate the amount of wear for the contact start/stop test, the variation of the contact load with time, or equivalently, velocity is needed. Following Kita, et al. (1984), we assume a quasi-steady model for the transition of the slider from sliding to flying (Fig. 3), and calculate the

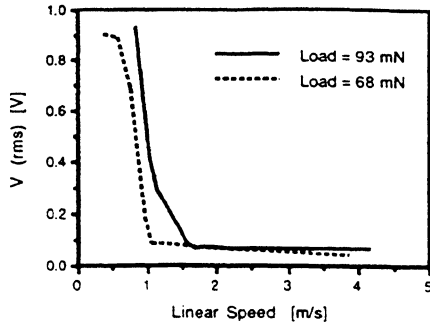


Fig. 2 AE signal as a function of velocity for a zirconia overcoated disk

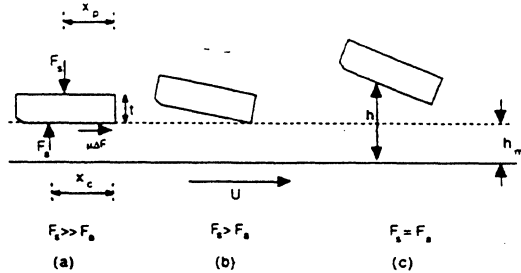


Fig. 3 Quasi-steady model for the transition of a slider from sliding to flying (Kita et al., 1984).

air bearing pressure at each velocity up to the takeoff velocity, making the following assumptions:

1. The slider is in static equilibrium during its transition from sliding to flying and all dynamics effects are neglected.
2. During the transition, the slider is supported on the peaks of the asperities of the disk, i.e., at low velocities, the slider "rests" along its full length on the disk asperities (Fig. 3(a)); at intermediate velocities, the slider begins to pitch, and only the trailing edge of the slider is in contact with the asperities (Fig. 3(b)); and at high velocities, the slider flies over the disk surface (Fig. 3(c)).
3. The air bearing force on the slider in the low and intermediate velocity regimes is calculated as if the trailing edge of the slider were flying at a distance h_m over a perfectly smooth surface.

4. The Reynolds equation modified for first order slip is applicable for calculation of the air bearing force during the transition from sliding to flying, i.e., the air bearing force is calculated based on the fictitious flying height h_m .

To determine h_m , the following procedure is used. The take-off velocity is first determined by the acoustic emission technique described above. At the takeoff velocity, the air bearing force on the slider must be equal and opposite to the applied suspension force. Furthermore, to maintain equilibrium of moments, the pitch angle of the slider must be such that the air bearing force acts through the pivot point. The above two conditions of force and moments equilibrium are now solved simultaneously with the Reynolds equation at the takeoff velocity to determine h_m and the pitch angle θ . In practice, the values of h_m and θ are obtained by an iterative numerical solution of the Reynolds equation. Once the value of h_m is determined, the Reynolds equation is solved for values of the velocity below the takeoff velocity to obtain the air bearing force as a function of velocity. At each velocity, the pitch angle is adjusted to maintain moment equilibrium of the slider.

Applying the above model, we found for a take-off velocity of 1.6 m/s that the value of h_m is approximately 34 nm for a Winchester 3380 type slider. Using this value of h_m , the variation of contact force with time during the transition from sliding to flying of a Winchester 3380 type slider is shown in Fig. 4 for angular accelerations of 188 rad/s², 97 rad/s² and 63 rad/s², respectively. We observe that the time of contact t ,

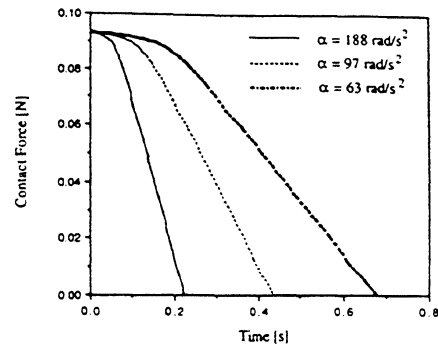


Fig. 4 Variation of contact force as a function of time during the transition from sliding to flying in a CSS test using different angular accelerations

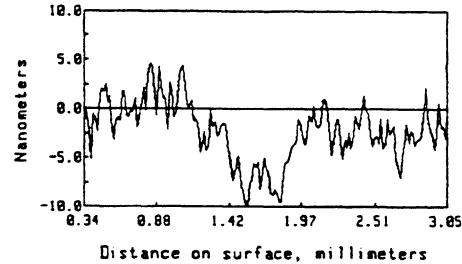


Fig. 5 Profile across a wear track using an optical profiler

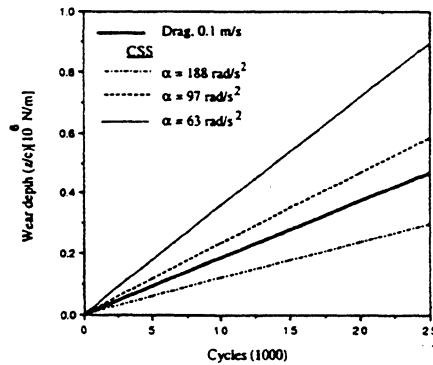


Fig. 6 Computed wear depth normalized with wear constant c as a function of the number of cycles

between the head and the disk decreases as the angular acceleration increases. Numerical integration of Eq. (7) using the contact force profile of Fig. 4 yields the average wear depth along a track as a function of the number of cycles and the constant c .

Results

An example of the measurement of the wear depth by an optical profiler is shown in Fig. 5. The wear depth divided by the wear constant c , i.e., (z/c) , as predicted by our model is shown in Fig. 6 for both the constant speed drag test and the CSS test as a function of the number of cycles.

The experimentally measured wear depths under the same conditions are shown in Fig. 7. The wear depth for a given acceleration increases linearly at first with the number of cycles, but after about 10,000 cycles, the rate of wear decreases. The initial linear increase with sliding distance is intuitively in accordance with Archard's law. The measured decrease in wear rate at larger number of cycles will be discussed later.

We also observe that the wear depth for a given number of cycles decreases with increasing acceleration, as is intuitively expected. Experimental measurements of the wear depth for the drag test at 0.1 m/s and the start/stop test at accelerations of 97 rad/s² and 63 rad/s² are shown in Fig. 7. We observe

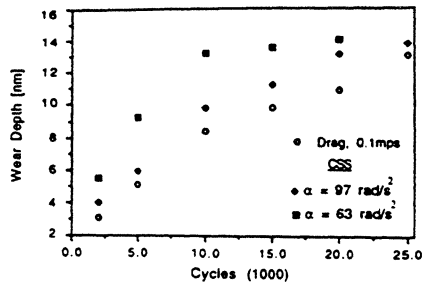


Fig. 7 Experimentally measured wear depths for the drag and CSS tests as a function of the number of cycles

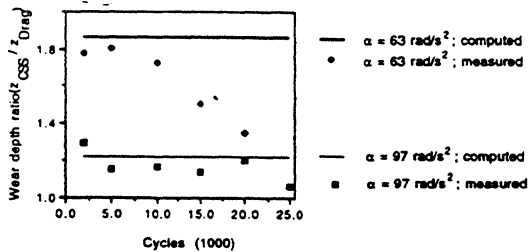


Fig. 8 Ratio of wear depth (z_{CSS}/z_{Drag}) in a CSS test and drag test as a function of the number of cycles

that the wear depth in the CSS test is greater than that in the drag test for both the angular accelerations considered, and that the wear depth in the CSS test is larger for the 63 rad/s^2 test than that for the 97 rad/s^2 test.

In Fig. 8, we have plotted the ratio of the wear depths in the CSS test and the constant speed drag test conducted at 0.1 m/s as a function of the number of cycles using Eq. (8) and the data of Fig. 7. We observe good agreement between the predicted and the experimental results up to about 10,000 cycles of sliding, the agreement being better for the higher acceleration test. Furthermore, we note that the wear depth ratio decreases as the angular acceleration increases, indicating that the wear depth in a CSS test increases as the angular acceleration decreases.

Discussion

The correlation between the wear depth predicted by the model and the experimental measurements of the wear depth decreases for sliding distances greater than about 10,000 cycles for the low acceleration test, but remains good up to 20,000 cycles for the high acceleration test. We also note that as the angular acceleration/deceleration during a start-stop test increases, the wear depth for a given number of cycles decreases. This is to be expected, since the slider is in contact with the disk for shorter periods of time as the acceleration increases. From our data, we extrapolate that at an angular acceleration of about 120 rad/s^2 , the wear depth in the CSS test is approximately equal to that in the constant speed drag test conducted at 0.1 m/s .

The correlation between the computed and experimental data suggests that wear of a zirconia overcoat during drag and CSS testing can be well explained by means of Archard's equation as long as care is taken to account for the velocity dependent contact force in the CSS test. For the disk accelerations used in our experiment (97 rad/s^2 and 63 rad/s^2), the wear depth of the overcoat was found to be higher in the CSS test than in the constant speed drag test. If the disk acceleration is increased, say to 190 rad/s^2 , we predict from Fig. 6 that the wear depth for this acceleration is approximately 60 percent of the wear depth from a constant speed drag tests.

The good agreement between experimental results and theoretical predictions also indicates that our assumptions con-

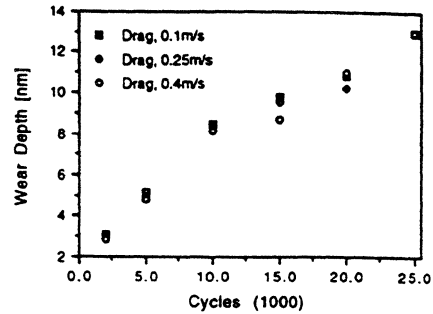


Fig. 9 Wear depth as a function of the number of cycles in a drag test at low velocities

cerning the constancy of H and k in the wear equations for constant speed drag and contact start stop testing are justified.

The increasing discrepancy at large number of cycles and low accelerations appears to be related to several factors. First, at very large sliding distances, the assumptions in Archard's wear model are less likely to be satisfied, since the operative wear mechanism may involve a combination of several individual wear phenomena, making the wear characteristics nonlinear. Another possible reason for the deviation at large distances and low accelerations may arise from the measurement limitations of optical profilometry as discussed by Li and Talke (1990); as the overcoat thickness decreases in the wear track with an increasing number of cycles of sliding, the underlying magnetic layer increasingly contributes to the phase shift of the reflected beam, making the optical wear depth measurement increasingly more suspect. Since this error increases with the amount of wear of the overcoat, the deviation between theory and experiment sets in at a smaller number of cycles as the acceleration decreases. In principle it is possible to overcome this problem by using a mechanical profilometer, since it is dependent only on the surface profile, rather than on the thickness of the layer. However, stylus profilometers permit only line scans across the width of the wear track, and their resolution is less than that of optical profilers. An optical profiler offers the advantage of area scans at various regions of the wear track which can then be averaged. It is possible to obtain better resolution with an atomic force microscope (AFM), but this instrument suffers from the limitation that it can only sample very small areas at a time, and cannot cover the entire wear track. Moreover, determination of the wear track region is very difficult with an AFM.

It is interesting to examine the measurement of the decrease in the wear track depth with time. As mentioned earlier, the measured wear depth is an average across the wear track of the various pixels in an optical profiler trace. The physical interpretation of this averaged wear depth is that some peaks in the surface profile get deformed and truncated during sliding contact. This removal of peaks causes new peaks to be exposed, which again go through the process of deformation and truncation. The average depth of the wear track therefore increases with the number of cycles and this is demonstrated by the example profile of the wear track shown in Fig. 5. This is a direct consequence of the fact that the head slides on the highest peaks of the disk.

The contact force profile at an angular acceleration of 97 rad/s^2 shown in Fig. 4 indicates that the contact force between the head and the disk is almost constant in the initial stages of sliding. This implies that at low velocities (below $\sim 0.4 \text{ m/s}$) the air bearing force developed is very small. Therefore, the wear depth versus the number of cycles in a constant speed drag test should show little dependence on the velocity in this velocity regime. In order to verify this point experimentally, we conducted drag tests at different velocities up to 0.4 m/s and measured the wear depth as a function of the number of cycles. The results, shown in Fig. 9, indicate that the wear

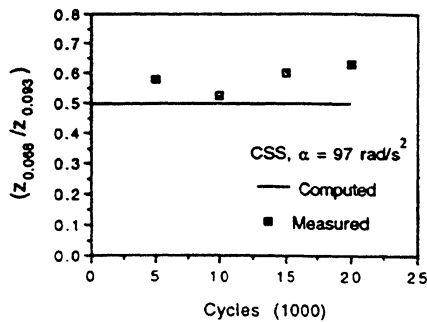


Fig. 10 Wear depth ratio ($Z_{0.068}/Z_{0.093}$) as a function of the number of cycles for loads of 0.068 N and 0.093 N

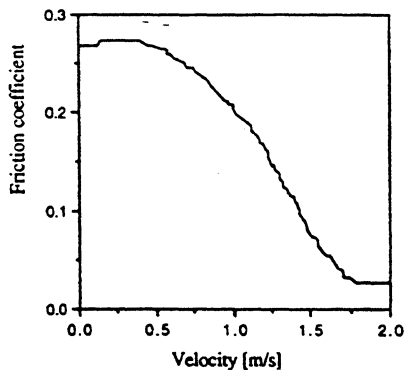


Fig. 11 Variation of friction coefficient as a function of velocity (from Trauner et al., 1990)

depth at a given number of cycles is indeed nearly independent of velocity for velocities below 0.4 m/s, further indicating the usefulness of our model.

In order to further test our model, we conducted wear tests in the CSS mode at an applied suspension load of 68 mN (7g). According to the analysis presented above, load affects the wear depth in two ways. First, since the wear depth is directly proportional to the load, the wear depth is expected to decrease with decreasing load. Second, a smaller suspension load causes a decrease in the takeoff velocity, thereby decreasing the time of contact between the slider and disk and consequently, the amount of wear. Figure 10 shows the wear depth as a function of the number of cycles for the two loads of 0.068 N and 0.093N. Good agreement between the predictions and the experimental results for sliding up to 20,000 cycles is observed. In particular, a decrease in load of 27 percent (from 0.093N to 0.068N) decreases the wear rate by 50 percent.

In addition to the above tests to verify the usefulness of our model, it is possible to verify the validity of the results of Fig. 4 using friction measurements at the head-disk interface. Earlier experiments in this laboratory (Trauner et al., 1990) indicate that the friction coefficient, when plotted as a function of velocity, shows a behavior as shown in Fig. 11, i.e., the friction coefficient is initially constant, then decreases and reaches a minimum at the take-off velocity. In Fig. 11, the friction coefficient was computed by Trauner et al. (1990) by dividing the experimentally measured frictional force by the [constant] applied suspension force. The variation of the friction coefficient as shown in Fig. 11 is typical for the transition from sliding to hydrodynamic flying, but is predicated on calculation of the friction coefficient based on the contact force at zero sliding velocity. However, in the absence of hydrodynamic effects, one finds in most friction tests that the coefficient of friction is nearly independent of the sliding speed. It is therefore justifiable to assume that even in the presence of hydrodynamic lubrication, the "true" friction coefficient,

i.e., the friction coefficient calculated by dividing the instantaneous frictional force by the instantaneous normal force at that velocity, should remain constant. Thus, if the "true" friction coefficient of friction is assumed to be constant, the data in Fig. 11 can also be interpreted as the variation of the contact force with sliding velocity. Comparing Fig. 11 with the variation of the contact force calculated from the Kita-Kogure-Mitsuya model (Fig. 4), we observe that the experimentally measured variation of the normal force closely follows the variation of the normal force as predicted by the model. This agreement further indicates that the results of our model are well supported by experimental results.

Summary and Conclusions

In this study, a model is developed to predict the wear depth of magnetic rigid disk overcoats in a constant speed drag test and a contact start/stop test using Archard's law and the quasi-steady Kita-Kogure-Mitsuya model for the transition of a slider from sliding to flying. The model is used to compare the effectiveness of the constant speed drag test in predicting the results from a CSS test. The model takes into account the fact that in a CSS test the contact load between the head and the disk varies as a function of velocity during start-up and shut-down of the disk drive, while it remains constant in a drag test. The correlation between predictions and experimental measurements of wear depth depends on the load and acceleration used in the tests, but good agreement is found up to at least 10,000 cycles. The results indicate that a decrease in the wear rate of the overcoat can be achieved by both a reduction in the suspension load of the slider and an increase in the acceleration/deceleration of the disk during start-up and shut-down.

Acknowledgments

The authors would like to thank C. A. Lacey for helpful discussions and Prof. D. B. Bogy for the use of his air bearing simulator.

References

- Archard, J. F., 1953, "Contact and Rubbing of Flat Surfaces," *J. Appl. Phys.*, Vol. 24, pp. 981-988.
- Benson, R. C., Sundaram, R., and Talke, F. E., 1988, "A Study of Acoustic Emission from the Slider/Disk Interface in a 5 1/4 Inch Hard Disk Drive," *Tribology and Mechanics of Magnetic Storage Systems*, STLE SP-25, pp. 87-93.
- Dugger, M. T., Chung, Y. W., Bhushan, B., and Rothschild, W., 1990, "Friction, Wear and Interfacial Chemistry in Thin Film Magnetic Rigid Disk Files," *ASME JOURNAL OF TRIBOLOGY*, Vol. 112, pp. 238-245.
- Ganapathi, S. K., Balanson, R. D., and Talke, F. E., 1992, "SEM Studies of Wear Mechanisms in Magnetic Thin Film Disks With Different Overcoats," *ASME JOURNAL OF TRIBOLOGY*, Vol. 114, pp. 263-269.
- Kita, T., Kogure, K., and Mitsuya, Y., 1984, "Wear of the Flying Head of a Magnetic Disk File in Mixed Lubrication," *Tribology and Mechanics of Magnetic Storage Systems*, STLE SP-16, Vol. 1, pp. 35-40.
- Lee, H. J., Hempstead, R. D., and Weiss, J., 1989, "Study of Head and Disk Interface in Contact Start Stop Test," *IEEE Trans. Magn.*, Vol. 25, pp. 3722-3724.
- Li, Y., and Talke, F. E., 1990, "Limitations and Corrections of Optical Profilometry in Surface Characterization of Carbon Overcoated Magnetic Recording Disks," *Trans. ASME*, Vol. 112, pp. 670-677.
- Rabinowicz, E., 1980, "Wear Coefficients-Metals," *Wear Control Handbook*, ASME Press, New York, pp. 475-506.
- Suzuki, S., and Kennedy, F. E., 1989, "Incipient Damage on Thin Film Magnetic Disks and its Detection with a Corrosion Test," *Tribology and Mechanics of Magnetic Storage Systems*, Vol. VI, STLE SP-26, pp. 111-119.
- Trauner, D., Li, Y., and Talke, F. E., 1990, "Frictional Behavior of Magnetic Recording Disks," *IEEE Trans. Magn.*, Vol. 26, pp. 150-152.
- Yamaguchi, H., Tsukamoto, Y., and Yanagisawa, M., 1988, "Mechanical Properties and Durability of Sputtered Carbon Protective Overcoats for Rigid Magnetic Disks," *Tribology and Mechanics of Magnetic Storage Systems*, Vol. V, STLE SP-25, pp. 82-86.
- Yamashita, T., Chen, G. L., Shir, J., and Chen, T., 1988, "Sputtered Zirconia Overcoat with Superior Corrosion Protection and Mechanical Performance in Thin Rigid Disk Application," *IEEE Trans. Mag.*, Vol. 24, pp. 2629-2634.



M. T. Dugger

Y. W. Chung

Department of Materials Science and
Engineering and Center for
Engineering Tribology,
Northwestern University,
Evanston, IL 60208

B. Bhushan¹

Department of Mechanical Engineering,
University of California,
Berkeley, CA 94720
Fellow ASME

W. Rothschild

IBM Application Business Systems Division,
Rochester, MN 55901

Friction, Wear, and Interfacial Chemistry in Thin-Film Magnetic Rigid Disk Files

We present results of a study of hemispherical pins of manganese-zinc ferrite sliding against rigid disks composed of thin films of a sputtered cobalt-nickel-platinum alloy and carbon, with perfluoropolyether as the topical lubricant. The contact life, as marked by the total distance slid to the point at which the coefficient of friction increases rapidly over the steady state value, is much longer in air with 50 percent relative humidity than in dry air or vacuum. The wear debris generated in humid air is much finer and is enriched with cobalt on its surface. In dry air and vacuum, the debris is substantially larger than one micron and tends to be enriched with nickel on its surface. We present a hypothesis which explains the wear mechanisms in various operating environments.

Introduction

There is physical separation between a rigid disk surface and the read/write head by hydrodynamic action during steady-state operation, provided there is no particulate contamination, and friction remains very low. However, during startup and shutdown, the relative speed between the disk and head are insufficient to maintain the air bearing and surfaces are in direct sliding contact. Since the friction force in sliding increases with the real contact area, some degree of roughness is desired to minimize the contact area and consequently friction [1] at low interfacial speeds. Lower flying heights required by the push toward higher recording densities can also lead to asperity contact during disk access or in the presence of contaminant particles. To reduce wear during start/stop operations and isolated asperity contacts, hard coatings and/or topical lubricant layers (solid and liquid) are employed. The effect of the environment on the wear mechanisms of this multilayer structure is at present not well understood. In addition, such issues as wear-induced composition changes and lubricant redistribution on the surface have not been addressed. The objective of this paper is to examine the chemical and morphological changes on the sliding surfaces that accompany changes in the contact life, and investigate the role of the environment on contact durability. Results of wear studies and proposed failure mechanisms are discussed. The rigid disk file selected for this study consists of a 70–90 nm thick cobalt-nickel-platinum magnetic layer over a polished NiP coating 10–20 μm thick, on a 5086 aluminum alloy substrate. A 20–30 nm thick sputtered amorphous carbon film covers the

magnetic layer and 1–4 nm of perfluoropolyether lubricant is placed on top of this overcoat.

In order to perform contact sliding experiments over a range of speed and load conditions, a hemispherically ended pin instead of a slider was used for accelerated wear studies. The wear tests were conducted in controlled environments to simulate operation in various ambient atmospheres.

Experimental

Pin-on-disk sliding experiments were performed using hemispherical pins of manganese-zinc ferrite (a slider material) to simulate conditions present during contact start/stop operations. Since lower linear speeds were used (1–4 m/s) than in actual files in order to maintain direct contact of the surfaces, the pin radius of curvature and applied load were selected to produce contact stress as close as possible to those of the real file environment. Experiments were carried out in an environmental tribo-chamber that allows control of the ambient test atmosphere and incorporates a variety of surface analysis techniques. The tribo-chamber is shown schematically in Fig. 1(a). The system is evacuated by a high capacity pump so that vacuum conditions can be achieved in the presence of small amounts of lubricant with relatively short pumping cycles. The system incorporates a leak valve for controlled gas dosing, an ion gun for sputtering, and a horizontal rotating turntable which is driven through a ferrofluid drive and is capable of sliding speeds of up to 10 m/s. A tribometer beam (Fig. 1(b)), which can deliver normal loads of 0.049 to 2 N, is outfitted with semiconductor strain gauges (gauge factor 115) whose outputs are read by an analog-to-digital converter in a microcomputer. Accuracy in the applied load is estimated at ± 5 mN with a resolution of 1 mN. Analytical equipment includes in-situ Auger electron spectroscopy (AES), an aluminum K_{α} X-ray source for X-ray photoelectron spectroscopy (XPS) and a windowless solid-state X-ray detector

¹On sabbatical from IBM Research Division, Almaden Research Center, 650 Harry Road, San Jose, CA 95120

Contributed by the Tribology Division of THE AMERICAN SOCIETY OF MECHANICAL ENGINEERS for presentation at the STLE/ASME Joint Tribology Conference, Fort Lauderdale, Fla., October 16–19, 1989. Manuscript received by the Tribology Division March 9, 1989. Paper No. 89-Trib-37.

Copies will be available until January 1991.

for sampling the disk composition at greater depth using energy dispersive X-ray analysis (EDX).

Sample Preparation. Pins of manganese-zinc ferrite 3.2 mm × 3.2 mm × 12 mm were cut from hot-pressed ferrite bricks using a diamond saw. Hemispherical caps of 50 mm radius of curvature were ground on one end of the pins in a lathe using concave grinding dies and silicon carbide abrasive papers. Care was taken not to use the near-surface regions of the ferrite bricks (1-2 mm) in preparing the pins to avoid large porosity or other surface inhomogeneities. Polishing was continued with diamond abrasives and colloidal alumina down to 0.05 μm grit size. Density measured by the Archimedes technique was 99.77 percent of theoretical, with 0.2 percent closed porosity and 0.02 percent open porosity. Pins were ultrasonically cleaned in freon and stored in a desiccator. Commercial disks with a circumferential texture (rms surface height = 7.3 nm, Bhushan and Doerner, 1989) were used. All disks were from the same lot. The same side was always used for testing, and disks were stored in clean, sealed containers until ready for use.

Friction and Wear Testing. Disk and pin specimens were transferred to the testing chamber through a front access port, where a high-efficiency particle filter maintained class 100 or better clean room conditions. The disk was clamped to the turntable at the hub and the pin was mounted at the end of the tribometer beam. The chamber was evacuated without baking to a pressure of 1.33 to 2.00 × 10⁻⁶ Pa (approximately 24 hours pumping time). For humid air testing, the chamber was backfilled at the conclusion of this evacuation cycle with air that passed through a desiccant column (silica gel), cold trap

(dry ice + acetone, -78°C) to remove water vapor, and a salt solution (saturated Ca(NO₃)₂ · 4H₂O) to generate 51 percent relative humidity at room temperature (24.5°C). In the case of dry air testing, the last stage was bypassed. The desired normal load at the pin was adjusted to between 50 and 150 mN. The speed control was set to give a sliding speed of 1 or 4 m/s at the test radius. The friction coefficient was measured at regular intervals (50 ms to 5 s, depending on the environment) until the onset of failure as evidenced by a rapid and irreversible increase in the friction coefficient. The contact life was taken as the total distance slid to failure.

Analysis. Elemental analysis of the top approximately 5 atomic layers was performed using electron-excited Auger electron spectroscopy. Auger analyses were performed in derivative sector field sweeping mode using a hemispherical analyzer at a primary electron energy of 3 keV and a beam current of 0.6 to 0.75 μA. Chemical state information over approximately the same depth range was obtained ex-situ using small spot X-ray photoelectron spectroscopy. Investigation of the surface morphology and elemental analysis at greater depths was performed in a scanning electron microscope with energy dispersive X-ray analysis. Topography and distribution of lubricant at the sub-micron level was examined with a scanning tunneling microscope (STM).

Results

Accelerated Wear Tests. Due to the number and desired range of variables to be tested, factorial analysis and fractional replication were used to determine which variable(s) exhibited the greatest influence on the contact life. Two levels of speed: 1 and 4 ± 0.1 m/s, three levels of applied normal load: 49, 98 and 147 ± 1 mN, and three environments: 2.00 ± 0.7 × 10⁻⁶ Pa, dry air at atmospheric pressure (partial pressure of water vapor = 7.5 × 10⁻² Pa) and air with 50 percent relative humidity at atmospheric pressure (partial pressure of water vapor = 1.5 × 10³ Pa), were tested at room temperature (24 ± 2°C). A typical contact life test consists of an initial run-in period in which the larger asperities are worn down, accompanied by a slight decrease in kinetic friction coefficient as a better "fit" is established between the sliding surfaces. A steady-state period usually follows, the length of which depends upon the severity of the testing conditions. Failure occurs with a sudden increase in the kinetic friction coefficient, at which point the test is stopped as the surfaces begin to wear catastrophically.

Figure 2 shows the results of friction tests to date. As can be seen, the test environment is the most important factor deter-

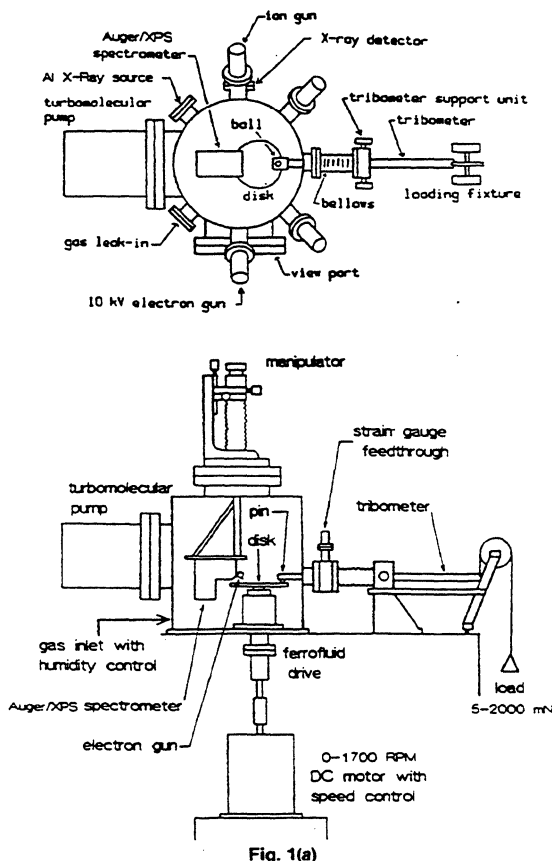


Fig. 1(a)

Fig. 1(b)

Fig. 1 Schematic illustration of (a) the tribo-testing chamber used and (b) the tribometer beam.

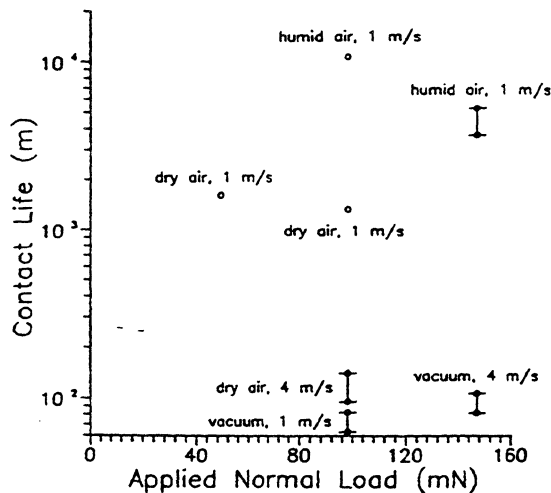


Fig. 2 Summary of contact life as a function of load, speed, and environment tests. Data generally fall in three regimes with humid air giving the longest contact life, vacuum the shortest and dry air intermediate.

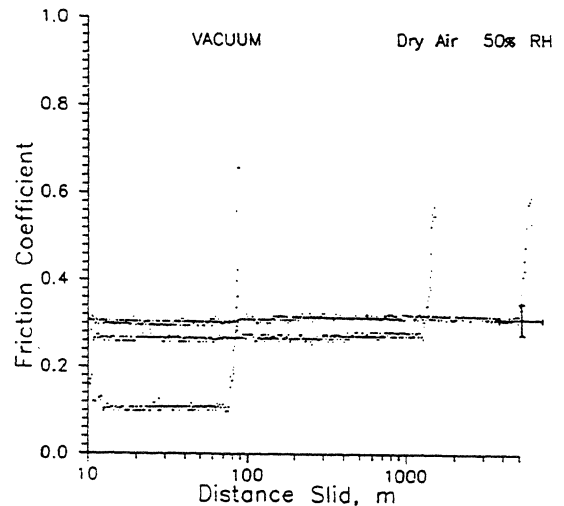


Fig. 3 Representation of the trends in kinetic friction coefficient and contact life with environment at 98 mN applied normal load and 1 m/s sliding speed.

mining contact life over the range of variables tested. For example, at a load of 98 mN and sliding speed of 1 m/s run at 50 percent relative humidity, the specimen survived greater than 10,000 meters of sliding before an increase in kinetic friction coefficient and a visible wear track was observed. Under the same conditions, sliding in dry air produced a contact life of approximately 1300 meters, while in vacuum the life was reduced to less than 100 meters. This comparison is shown in Fig. 3. It is important to note that this dramatic reduction in contact life in vacuum is not due to the volatilization of the lubricant since in all runs (including dry air and humid air) the testing chamber was evacuated to between 1.33 and 2.00×10^{-6} Pa after specimen introduction. Friction coefficients were in the range of 0.1 to 0.3 in all cases and were slightly higher for tests in humid air. This trend has been seen previously in carbon-coated thin film media [2, 3], and appears to be a characteristic of the amorphous carbon film [4-6]. This is in contrast to the behavior of graphite and diamond, whose friction coefficients (in contact with iron) decrease with increasing relative humidity [6].

Microscopy and Surface Composition. Scanning electron microscopic examination of the wear scars on the pin and disk revealed morphology markedly dependent on the testing environment. This is illustrated in Figs. 4(a) to 4(c). Characteristic of post-failure surfaces in vacuum and dry air is severe damage to the disk surface (Figs. 4(a) and 4(b)) with the pin from the vacuum test also exhibiting extensive damage, including intergranular fracture and grain pull-out. In both cases there is also material transferred from the disk to the pin. In humid air, however, the contact area on the pin is covered with very fine (about 1 μm) particles in a dark film (low atomic number), with fine particles on either side of the worn area (Fig. 4(c) and Fig. 7, to be discussed later). SEM examination of the disk wear track shows that (i) the wear damage is small and (ii) the track is covered by a layer with low atomic number contrast, suggesting a carbonaceous deposit.

An investigation of topography on the sub-micron scale was conducted using scanning tunneling microscopy (STM). A sharp metallic tip mounted on a three-axis piezoelectric translator is brought to within a nanometer of the specimen surface and a bias voltage is applied. Under these conditions, electrons can tunnel across the gap creating a current that depends exponentially upon the tip/sample separation. As the tip is rastered over the surface, it must be moved up and down

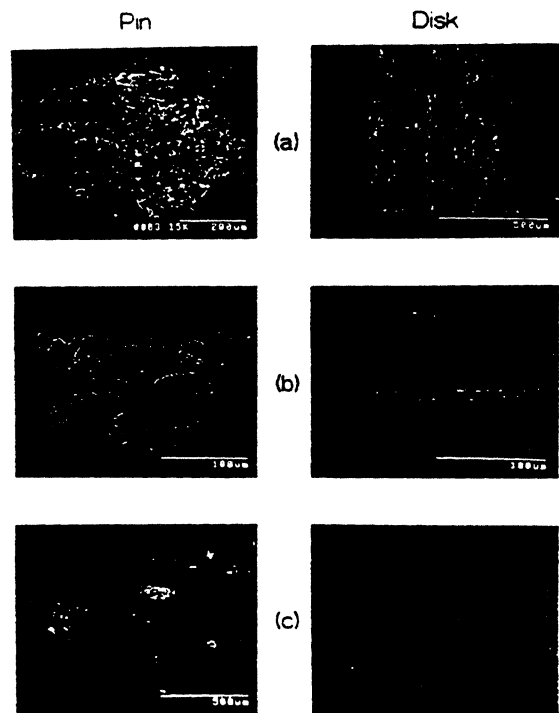


Fig. 4 SEM micrographs of pin and disk surfaces run to failure at 98 mN normal load, 1 m/s in (a) vacuum, (b) dry air, and (c) humid air.

to maintain constant tunneling current. The voltage fluctuations required on the vertical axis of the piezoelectric translator to maintain constant tip/surface separation give a high resolution image of the surface topography. The STM allows noncontact, real time imaging of the nanometer-scale surface roughness typical of thin film rigid disks directly, rather than building up a two dimensional image from many traces of a stylus profilometer or employing stereomicroscopy on SEM micrographs. The lateral resolution also exceeds that of optical profilometers. Figure 5 illustrates the topography of the untested as well as wear track regions on disks tested to failure in vacuum and humid air over a 5 μm scan area. The general observation is that compared to the untested disk surface (Fig. 5(a)), the surfaces of vacuum (and dry air) tested disks become rougher (Fig. 5(b)) while in humid air the finer

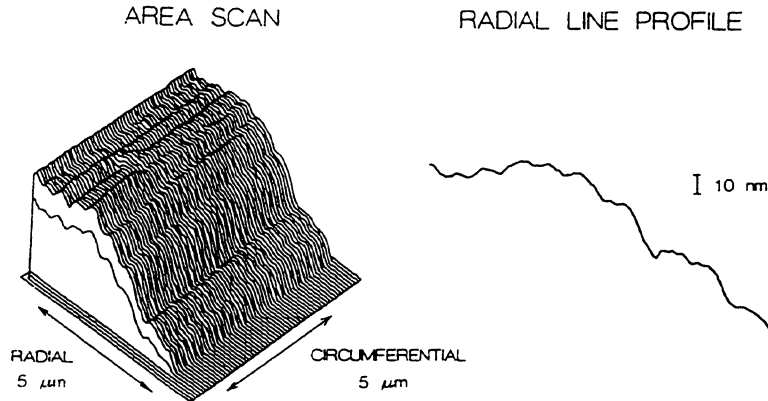


Fig. 5(a)

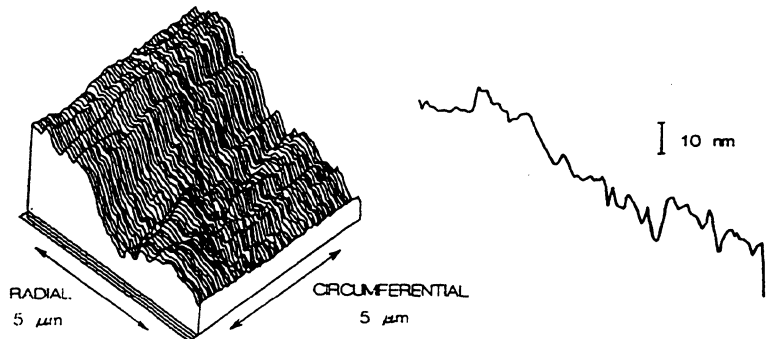


Fig. 5(b)

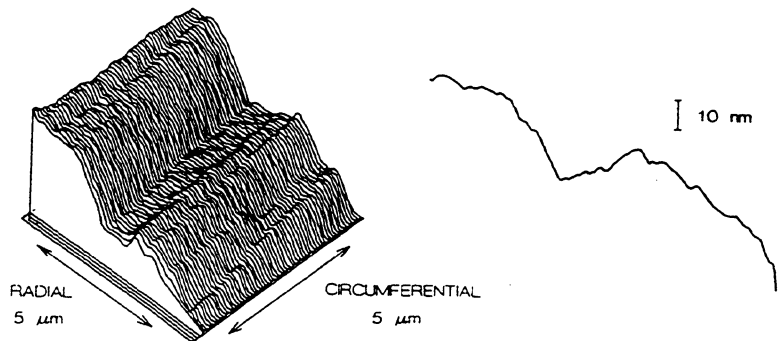


Fig. 5(c)

Fig. 5 Two-dimensional surface profiles using the scanning tunneling microscope on (a) the untested disk surface; (b) on wear tracks after testing at 98 mN applied normal load, 1 m/s sliding speed in vacuum and (c) in air at 50 percent relative humidity. The line scans indicate a general roughening of the surface after testing in vacuum and smoothing after testing in humid air.

grooves in the surface disappear, leaving a surface roughness of longer wavelength (Fig. 5(c)). This qualitative picture of how the topography changes on a small scale is consistent with observations of the worn areas in the SEM. A disadvantage is that because of its high resolution and limited horizontal scan range, statistically meaningful surface roughness parameters can only be obtained from many images.

In an effort to track the evolution of wear debris and deter-

mine its origin, friction tests were repeated at fractions of the expected contact life at 98 mN applied load and 1 m/s sliding speed in each environment. Figure 6 shows wear debris collected on the pin of specimens run to 33 percent of their expected lives in vacuum, dry air, and humid air and analysis by EDX of the wear debris composition.

In vacuum, there was no observable grain pull-out or intergranular fracture in the ferrite at 33 and 68 percent of the

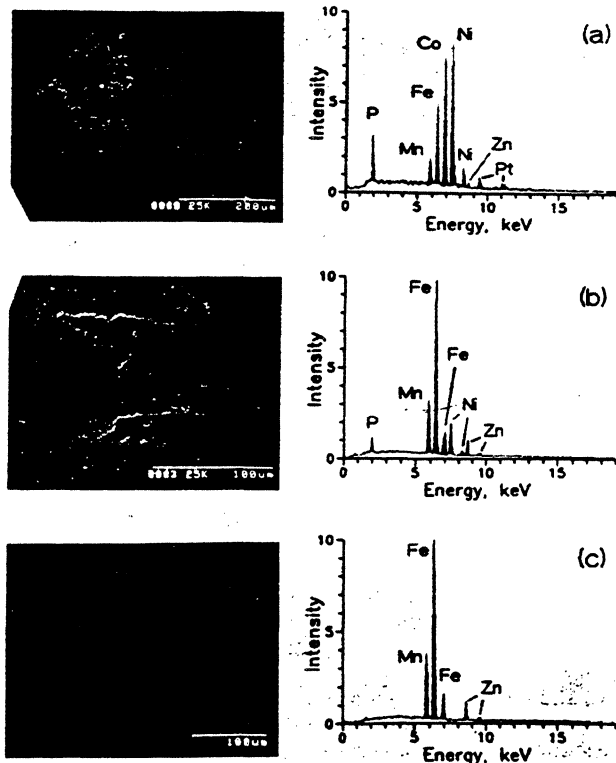
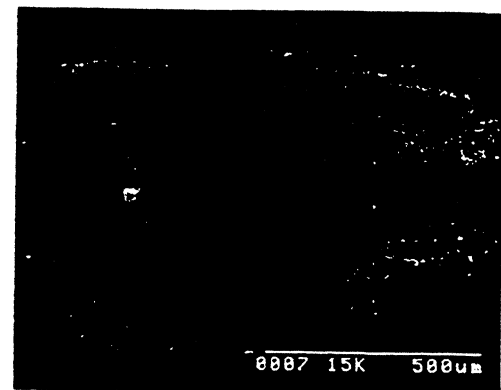


Fig. 6 SEM micrographs of wear debris on pin surfaces and EDX spectra of this debris after running to 33 percent of the expected contact life in (a) vacuum, (b) dry air, and (c) humid air.

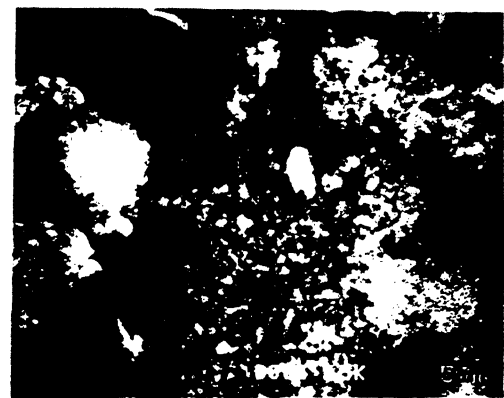
contact life as there was at failure, indicating that the severe damage sustained by the ferrite occurs over a short period near the end of the test. Fine ferrite debris about $1\ \mu\text{m}$ in size appears at the trailing edge of the wear scar on the pin. The majority of wear particles found at 33 percent of the contact life are 5 to $30\ \mu\text{m}$ in size. The wear particles are composed essentially of the disk magnetic layer with some phosphorus also present. This indicates that damage on the disk already extends beyond the media layer and into the underlying NiP buffer layer.

In dry air, very fine particles ($\leq 0.5\ \mu\text{m}$) appear around the contact zone on the pin early in sliding (33 percent of life). These particles exhibit the characteristic spectrum of the ferrite, with some nickel and phosphorus present. The cobalt K_{α} peak overlaps iron K_{β} , but the iron K_{α} to K_{β} intensity ratio in this material of about 5.8 is appropriate for these peaks, indicating that the concentration of cobalt in these particles is much less than the approximately 80 percent present in the magnetic layer. Later in life (68 percent and failure), wear particles $10\ \mu\text{m}$ and larger consisting of the magnetic layer are found on the pin surface.

In humid air a black, carbon-rich deposit believed to be a transfer film from the carbon overcoat or a reaction product from the lubricant is present at the apparent area of contact on the pin surface. The area covered by this deposit increases steadily throughout the life of the contact. No macroscopic damage to the ferrite was observed even after failure, but fine ferrite wear debris on the order of $1\ \mu\text{m}$ in size is present at the trailing edge of the contact spot on the pin as early as 10 percent of the expected contact life. It is not possible to quantify the amount of this debris present at later stages of sliding due to the appearance of the very fine particles forming a pseudo-continuous film to the sides and at the trailing edge of the wear scar, as shown in Fig. 7(a). As demonstrated in Fig. 7(b), the particles are generally much less than a micron in diameter.



(a)



(b)

Fig. 7 SEM micrograph of the overall distribution of wear debris on the pin from a test at 98 mN applied normal load, 1 m/s sliding speed in (a) humid air, and (b) the size of debris in the contact zone.

Additional experiments were performed in each environment in an attempt to determine the role played by the small ferrite debris generated early in sliding in the failure of the contact. In this case, the pin and disk specimens were prepared as described previously, and the test chamber was brought to the desired ambient atmosphere (after an initial outgassing period as described for the other tests). At 98 mN applied normal load and 1 m/s sliding speed, sliding was maintained for 10 percent of the anticipated contact life based on the earlier tests to failure. The chamber was then opened and the pin surface cleaned with a freon-saturated lint-free cotton wiper. It is important to note that this cleaning was done *without removing the pin from the clamping fixture* so that exact alignment of the pin and the disk would be maintained. The tribometer beam was stepped in to a new track on the disk to avoid any ferrite debris that may have been transferred to the disk. The outgassing treatment was repeated and the ambient test atmosphere prepared. The specimens were then tested to failure under the same conditions used for run-in. The results are presented in Table 1. No change in contact life with run-in was observed for tests in vacuum and dry air, suggesting a failure mechanism that does not depend on the presence of hard, abrasive particles, such as solid/solid adhesion. Adhesion of ferrite to transition metal surfaces has been previously observed in vacuum [7], and was found to depend on the chemical activity of the metal surface. More active metal surfaces (quantified by the percentage d-bond character) exhibited larger adhesion to ferrite, and this interfacial bond was found to be in general stronger than the cohesive bond in the

Table 1 The influence of cleaning after run-in on contact life

Environment	Contact Life $\pm \sigma$ (km) no cleaning	Contact Life $\pm \sigma$ (km) cleaned after run-in
vacuum	0.07 \pm 0.01	0.08*
dry air	1.44 \pm 0.14	1.20*
50% RH air	6.39 \pm 2.91	25.83 \pm 4.79

*Single measurement. All others are the result of at least three individual experiments.

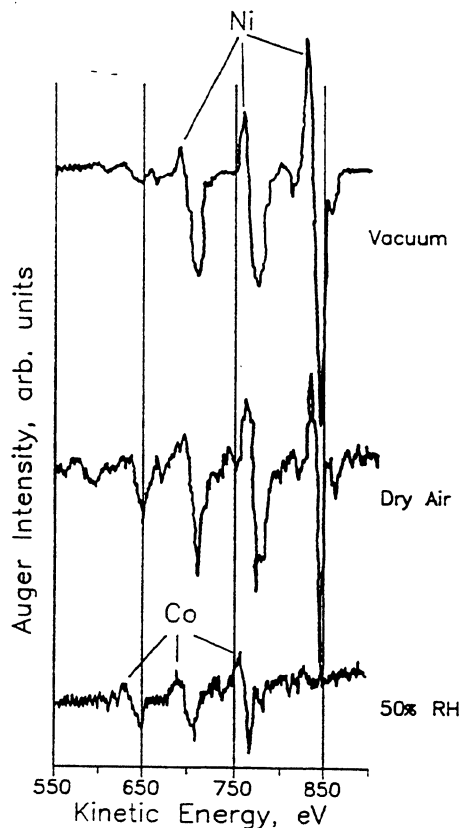


Fig. 8 Auger spectra in the energy range of 550 to 900 eV on disk wear tracks from tests run to failure in each environment at 98 mN applied normal load and 1 m/s sliding speed.

metal, resulting in metal transfer to the ferrite. In humid air, a statistically significant increase in contact life was observed when the ferrite debris generated early in sliding was removed. This suggests that burnishing of the pin surface to flatten large asperities, and removal of this debris from the contact zone, reduces abrasive wear and ploughing of the overcoat and magnetic layers and extends the contact life.

Auger analyses of worn disk surfaces from dry air and vacuum runs shown in Fig. 8 reveal the components of the magnetic layer, indicating that the lubricant and carbon films have indeed been broken through. The specimen surface run in vacuum was composed primarily of nickel, whereas that run in dry air was also nickel-rich but contained relatively more cobalt. Analysis of the wear track from a test in humid air to failure was difficult due to severe attenuation of all but the hydrocarbon peaks, but a high resolution scan of the energy range where peaks from the magnetic alloy should lie revealed only cobalt (bottom spectrum in Fig. 8). Any evidence of nickel in the wear track was completely absent.

The ex-situ XPS spectra taken in small spot ($\sim 300 \mu\text{m}$) mode on a disk track tested to failure in 50 percent relative humidity reveals the presence of strong peaks from the lubricant layer (fluorine, carbon, and oxygen) as shown in Fig. 9.

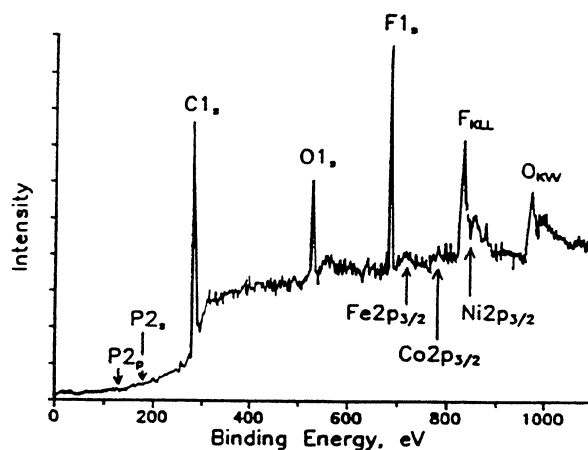


Fig. 9 XPS spectrum from a 300 μm spot on the disk wear track from a test at 98 mN applied normal load, 1 m/s sliding speed in humid air. Locations of elements present in this system are indicated.

This indicates that the lubricant has not evaporated from the surface during the evacuation cycle. In fact, the lubricant has survived one evacuation cycle for wear testing, and a second evacuation cycle after introduction into the small spot XPS chamber.

An additional imaging mode was used on the scanning tunneling microscope to investigate the uniformity of lubricant distribution on the disk surface. In the normal (topography) imaging mode, the tip is scanned over the surface (~ 10 seconds per 128×128 point array) and the tip height adjusted to maintain a constant tunneling current. In an alternate imaging mode, many readings of the tunneling current are recorded at each point. When the tip is located over a region of the surface that is covered by a species of poor conductivity, the surface of this insulating region will begin to accumulate charge. This decreases the voltage bias between the tip and the surface and suppresses tunneling. When sufficient charge has accumulated in the surface layer of this region to create a voltage gradient across the insulator which exceeds the dielectric strength of the material, it will discharge into the conducting substrate. Mapping of the amplitude of such tunneling current fluctuations as a function of position is known as variance imaging. Data acquisition speed is reduced (~ 60 seconds per 128×128 point array), but the current fluctuation map gives an indication of the relative conductivity of different regions of the surface. Figure 10 shows both the topography and variance image of the same (untested) region of the disk surface. Comparison between the topography and variance indicates that "low" areas on the surface are also those exhibiting a high degree of tunneling current fluctuation. One reasonable explanation is that the lubricant (an insulator) is not uniformly distributed, but rather accumulates as "pools" in the lower areas of the disk surface. Nonuniform lubricant distribution on unused disk surfaces can be the result of "spin off" during the finishing process, where radial air shear from the hub to the outer edge has been observed to cause migration and loss of lubricant films down to 1 nm thick [8]. Lubricant tends to remain preferentially in the low regions of the surface that are somewhat protected from air shear. On used disks, constant "wiping" of the disk surface by the slider rails during start/stop operations can redistribute the lubricant. Such pooling of lubricant may leave asperity tips unprotected and lead to a higher probability of disk damage during contact at these points.

Discussion

Flash heating due to dissipation of frictional energy can cause degradation of the lubricant layer by dissociation,

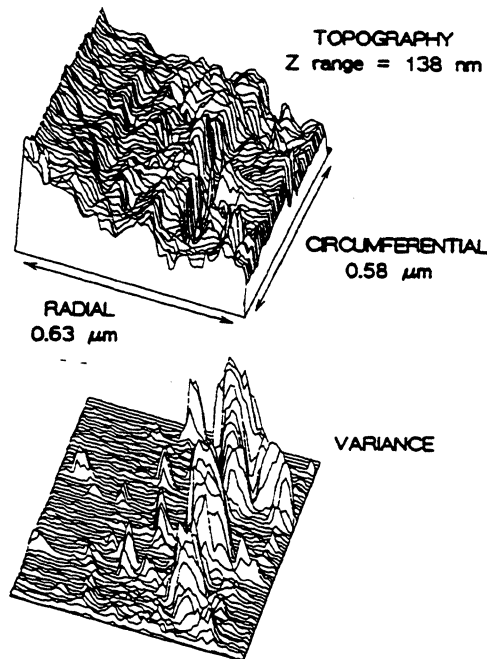


Fig. 10 STM topography and variance image from an untested disk surface

desorption, or oxidation. Under some conditions, frictional heating can be great enough to activate processes such as diffusion and recrystallization in the media layer. Detailed thermal analysis based on heat generation and dissipation at the interface [9] as well as modeling of asperity contact growth during sliding for ferrites in contact with magnetic tape [10] yield a modest 10°C maximum temperature rise at the tape-head interface, but a possible 900°C maximum temperature rise for a head-magnetic particle ($\gamma\text{-Fe}_2\text{O}_3$ or CrO_2) contact. Clearly the interfacial temperature rise is extremely sensitive to the mechanical and thermal properties of the contacting bodies. The case of the thin-film disk is complicated by the fact that it is a multilayer structure with very thin layers. The mechanical properties of the surface layers of such a structure have only recently been investigated [1]. The nominal contact stress in this work is a factor of about 3700 greater than that in Bhushan's [10] 900°C head/particle contact temperature estimate, but the sliding speed and friction coefficient are lower. In addition, the thermal diffusivity for a thin metal film on a metallic substrate is expected to be greater than that for an oxide particle, which will also reduce the flash temperature. While we recognize that there are driving forces for chemical changes within the Hertzian elastic contact zone even at room temperature, any temperature rise can have a dramatic effect on the tribochemical reactions at the interface since many of the processes depend exponentially on temperature.

We must now ask what processes may be activated under these conditions. Segregation of alloy components and impurities has been observed previously in sliding contact on steel surfaces [11]. In the case of Co-Ni alloys, recent experimental work using low energy Auger peaks [12] has shown that nickel segregates to the surface of Co-Ni alloys in vacuum over the entire composition range, as predicted by embedded atom calculations for the 50-50 percent alloy for which the surface layer was found to be about 90 percent Ni at 800 K [13]. On the other hand, since the heat of formation for Co_3O_4 (-71 kcal/mole of Co) is more negative than that for NiO (-57 kcal/mole), oxidation-induced segregation of cobalt is expected to occur in oxidizing environments [14].

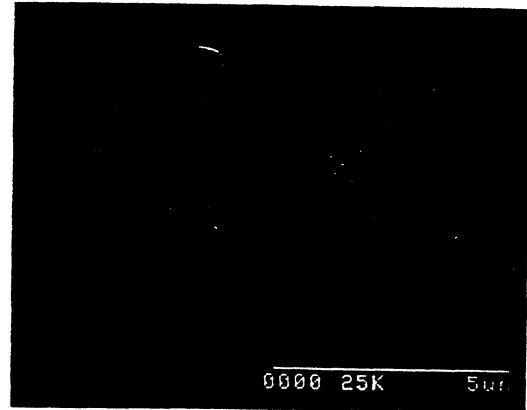


Fig. 11 SEM micrograph of an isolated metallic wear particle on the pin from a test at 98 mN applied normal load, 1 m/s sliding speed in vacuum, showing evidence of agglomeration

There is additional evidence in the literature for the migration of cobalt in magnetic alloy layers at high humidity [15]. This is in exact agreement with our observations.

Based on the results of this work, a consistent picture begins to emerge. When testing starts, fine ($\sim 1\ \mu\text{m}$) ferrite wear particles are generated in the contact zone as the larger asperities on the pin are worn down. The lubricant can offer little protection against such hard, abrasive particles at the contact stresses encountered here. Repeated passage of these particles through the contact zone gradually wears through the overcoat layer. Metallic wear particles are created either by chemical interaction between the ferrite and the Co-Ni alloy (adhesive wear) or by mechanical shearing of asperities. In vacuum, frictional heating may cause segregation of nickel to the surface of wear debris from the Co-Ni alloy. Driven by the high surface free energy of nickel, small wear particles may agglomerate to produce large wear fragments that lead to catastrophic failure. It is known from the literature [16] that there is a size effect on wear rate. There is a dramatic increase in wear rate above a particle size of about $1\ \mu\text{m}$. We believe that rapid agglomeration to particle sizes of greater than a few microns is responsible for the reduction in contact life in vacuum and dry air. Figure 12 is an SEM micrograph taken on the ferrite pin after sliding for 33 percent of the contact life in vacuum at 98 mN applied load and 1 m/s sliding speed, showing a typical wear particle. It is apparent that the wear particle is an aggregate of many smaller ones. EDX analysis reveals the presence of elements from the magnetic layer. In humid environments, oxidation-induced segregation of cobalt is expected, in agreement with the observed enrichment of cobalt found in the wear debris. These cobalt oxide covered particles are expected to have lower surface free energies than pure cobalt or nickel. The thermodynamic driving force towards agglomeration is therefore reduced. It is well known that oxides generally sinter more slowly than do metallic alloys. Therefore, wear particles remain small and do not cause severe damage to the disk. Also, humid air seems to facilitate the formation of the black carbonaceous deposit on the pins and disks. The film is never observed in vacuum. In dry air, it forms much more slowly, as evidenced by the state of film formation from specimens tested to 33 percent of their anticipated contact lives.

It is clear that large wear particles are undesirable for successful performance of the system. In addition, the presence of small ferrite wear debris in all environments tested may initiate the failure process by creating the initial magnetic alloy wear debris which later agglomerates in the case of vacuum and dry air. If the ferrite debris is generated by the first few passes of the pin due to shearing of the largest asperities, we

may expect to see a dramatic difference in contact life once these particles are removed if media wear is caused by ploughing of the ferrite particles. The results of tests in each environment presented earlier where the pin was cleaned after a 10 percent run-in show that this treatment does not change the contact life in a statistically significant way in vacuum or dry air. This implies that either ferrite particles are generated continuously or that some other phenomenon, such as ferrite/media layer adhesion, is responsible for creating the metallic wear particles. The contact life in humid air increased by more than a factor of four after run-in and cleaning of the pin. This result may indicate that in this environment, since oxygen is readily available to reduce the driving force for adhesion, the ferrite debris plays a more important role in the eventual failure of the contact. Our observations here lead to several recommendations to improve the contact life of the actual head/thin-film disk system in all environments. First, reduce the probability of forming fine ferrite wear debris in early stages of sliding by employing a slider with higher surface toughness. This may be accomplished by surface alloying the slider material to place the surface region in compression. Alloying of alumina with chromia on the surface has been demonstrated to produce a factor of two increase in toughness and a factor of ten decrease in wear rate against 52100 steel [17]. Also, alumina and chromia are chemically more stable than ferrite, thereby lowering the tendency of chemical interaction with cobalt or nickel. The asperity flash temperature should be minimized to reduce the driving force for agglomeration and degradation of the lubricant. This is accomplished with the use of higher thermal conductivity materials. Again, alumina is a better material than ferrite in this respect. More thermally stable lubricant species may be provided on the surface that resist decomposition or desorption in the event of local heating. Lubricant molecules with proper functional groups can be attached to the overcoat to offer these degradation-resistant properties. Finally, in the event that wear of the magnetic layer does occur, it is important to oxidize this debris as soon as possible to reduce the tendency toward agglomeration. This may not be possible with dry atmospheric oxygen at concentrated asperity contacts, as demonstrated here. However, one possible solution is to use an oxide overcoat which absorbs water vapor from the atmosphere (such as silica), thereby providing a local source of water vapor upon mild heating at contact points where metallic wear debris will be generated. This will increase the local partial pressure of water vapor and hence the probability of oxidation. As the oxide exits from the contact zone, it has time to be re-hydrated by absorbing water from the ambient, thus providing a continuous supply of water vapor to the contact.

Summary

The variation of surface layers in the sliding of manganese-zinc ferrite pins on Co-Ni-Pt sputtered thin-film disks has been explored in vacuum, dry air, and 50 percent relative humidity air using a device with surface analytical capabilities. Observed differences in total distance slid to failure between air, vacuum, and humid air runs and examination of the surface chemistry and morphology suggest different failure modes for the three environments. The major findings may be summarized as follows:

1 In vacuum, agglomeration of fine metallic wear debris leads to large particles which cause catastrophic wear and a short contact sliding life. Similar results are obtained in dry air, with some increase in contact life.

2) In humid air, oxidation of wear debris at the disk surface suppresses agglomeration and leads to fine, cobalt-rich wear debris that is not very damaging to the contact. Contact life is increased by approximately a factor of four over dry air and a factor of ninety over vacuum.

3) These differences in contact life are not due to volatilization of the lubricant because all specimens receive the same treatment prior to friction testing, and lubricant species are observed on disk wear tracks by XPS after testing.

4) Auger spectra indicate nickel-rich disk wear tracks in vacuum and dry air that may be due to delamination of the magnetic layer, exposing NiP from the underlying buffer layer. In humid air, however, surface analysis indicates oxidation-induced segregation of cobalt to the disk surface.

5) Fine ferrite wear debris found in the early stages of sliding in all environments may initiate formation of metallic wear particles.

6) STM imaging of the disk reveals that the lubricant distribution on the surface may be quite nonuniform, leaving asperities exposed. Improved bonding of the lubricant to the disk surface may provide a more uniform initial coverage and increase resistance to thermal degradation and desorption.

Acknowledgments

The work reported in this paper was supported by a research contract from IBM Corporation. We wish to thank Ralph Scheidecker of the Application Business Systems Division for technical support and guidance. Thanks also to Kathy Wahl of Northwestern's Center for Engineering Tribology for performing some of the EDX analyses.

References

- 1 Bhushan, B., and Doerner, M. F., "Role of Mechanical Properties and Surface Texture in the Real Area of Contact of Magnetic Rigid Disks," *ASME JOURNAL OF TRIBOLOGY*, Vol. 111, 1989, pp. 452-458.
- 2 Doan, T., and MacKintosh, N. D., "Frictional Behavior of Rigid Disk C-Overcoats," *Tribology and Mechanics of Magnetic Storage Systems*, Vol. 5, Eds. B. Bhushan and N. S. Eiss, STLE, Park Ridge, IL, 1988, pp. 6-11.
- 3 Timsit, R. S., and Stratford, G., "Effects of Humidity on Friction at Magnetic-Head/Hard-Disk Interfaces," *Tribology and Mechanics of Magnetic Storage Systems*, Vol. 5, Eds. B. Bhushan and N. S. Eiss, STLE, Park Ridge, IL, 1988.
- 4 Enke, K., Dimigen, H., and Hübsch, H., "Frictional Properties of Diamondlike Carbon Layers," *Appl. Phys. Lett.*, Vol. 36, No. 4, 1980, pp. 291-292.
- 5 Dimigen, H., and Hübsch, H., "Applying Low-Friction Wear-Resistant Thin Solid Films by Physical Vapor Deposition," *Philips Tech. Rev.*, Vol. 41, No. 6, 1983/84, pp. 186-197.
- 6 Memming, R., Tolle, H. J., and Wierenga, P. E., "Properties of Polymeric Layers of Hydrogenated Amorphous Carbon Produced by a Plasma-Activated Chemical Vapor Deposition Process II: Tribological and Mechanical Properties," *Thin Solid Films*, Vol. 143, 1986, pp. 31-41.
- 7 Miyoshi, K., and Buckley, D. H., "Adhesion and Friction of Transition Metals in Contact with Non-Metallic Hard Materials," *Wear*, Vol. 77, 1982, pp. 253-264.
- 8 Bhushan, B., *Tribology and Mechanics of Magnetic Storage Devices*, Springer Verlag, New York, 1989.
- 9 Bhushan, B., "Magnetic Head-Media Interface Temperatures. Part 1—Analysis," *ASME JOURNAL OF TRIBOLOGY*, Vol. 109, 1987, pp. 243-251.
- 10 Bhushan, B., "Magnetic Head-Media Interface Temperatures. Part 2—Application to Magnetic Tapes," *ASME JOURNAL OF TRIBOLOGY*, Vol. 109, 1987, pp. 252-256.
- 11 Dugger, M. T., and Chung, Y. W., "Exploring Failure Mechanisms of Lubricated 52100 Steel Contacts," in *New Materials Approaches to Tribology: Theory and Applications*, edited by L. E. Pope, L. Fehrenbacher, and W. O. Winer, 1989.
- 12 Hajcsar, E. E., Dawson, P. T., and Smeltzer, W. W., "Surface Segregation and Preferential Sputtering in Co-Ni Alloys: Computer Simulations of Auger Spectra," *Surf. Int. Anal.*, Vol. 10, 1987, pp. 343-348.
- 13 Underhill, P. R., "An Embedded Atom Calculation of Surface Segregation in Co-Ni Alloys," *Surf. Sci.*, Vol. 195, 1988, pp. 557-565.
- 14 Lupis, C. H. P., *Chemical Thermodynamics of Materials*, North-Holland, New York, 1983.
- 15 Novotny, V., Itnyre, G., Homola, A., and Franco, L., "Corrosion of Thin-Film Cobalt Based Magnetic Recording Media," *IEEE Trans. Mag.*, MAG-23, No. 5, 1987, pp. 3645-3647.
- 16 Rabinowicz, E., "The Tribology of Magnetic Recording Systems—An Overview," *Tribology and Mechanics of Magnetic Storage Systems*, Vol. 3, Eds. B. Bhushan and N. S. Eiss, STLE, Park Ridge, IL, 1986.
- 17 Gangopadhyay, A. K., Fine, M. E., and Cheng, H. S., "Friction and Wear Characteristics of Titanium and Chromium Doped Polycrystalline Alumina," *Lub. Engr.*, Vol. 44, 1988, p. 330.

Printed in U.S.A.

Transparent Pin Wear Test on Thin-Film Magnetic Disk

Youichi Kawakubo

Mechanical Engineering Research
Laboratory,
Hitachi, Ltd.,
Tsuchiura, Ibaraki, 300 Japan

Yotsuo Yahisa

Data Storage and Retrieval Systems Division,
Hitachi, Ltd.,
Odawara, Kanagawa, 256 Japan

Pin-on-disk wear tests on thin-film magnetic disks were performed using transparent materials. Quartz glass (QG), transparent zirconia (TZ), sapphire (SA), and synthesized diamond (DI) were used as pin materials. In addition to friction, sliding condition and pin wear were continuously monitored with video camera. Simultaneous friction measurement and video monitoring showed that friction dropped when wear debris intruded between pin and disk surfaces. Pin wear, from the measured diameter of wear scar on spherical pins, increased in the order of DI, SA, QG, and TZ. This order of pin wear does not coincide with that of the pin bulk hardness. Disk lifetime increased in the order of TZ, QG, SA, and DI, and the smaller the pin wear, the longer the disk lifetime.

Introduction

Head-disk spacing must be reduced to increase the recording density of rigid disk storage systems, and near-contact/contact recording technologies have been proposed for this purpose (Yeack-Scranton et al., 1990; Hamilton et al., 1991). Because these technologies require head-disk spacing of less than 50 nm, head-disk wear is inevitable. Materials at the head-disk sliding interface must therefore be carefully studied so that head-disk wear can be reduced. The sliding interface of thin-film disk is usually a carbon overcoat with lubricant, but heads are made from a wider variety of materials. It is thus very important to investigate the wear characteristics and failure mode with various head materials. Near-contact/contact recording heads will be smaller than present floating heads (Hamilton et al., 1991). Head contact area will then be orders of magnitude smaller than the disk recording area. If the specific wear volume of head and disk materials are in the same range, the head wear depth would be orders of magnitude larger than the disk wear depth. This makes the reduction of head wear more important.

Head wear on magnetic recording disks was first studied on particulate coated disks (Talke and Tseng, 1974). Accelerated wear tests using spherical pins were then developed, because of very low head wear (Talke and Su, 1975; Kita et al., 1984; Kawakubo et al., 1986). On thin-film magnetic disks, multi-phase materials like $\text{Al}_2\text{O}_3\text{-TiC}$ were shown to exhibit more variation in friction than single-phase materials (Chu et al., 1990), and single-crystal diamond was reported to show the lowest friction against thin-film disks (Chandrasekar and Bhushan, 1991). Enhancement of wear durability by carbon overcoats on head rails has also been reported recently (Bogy et al., 1993). In these papers, the sliding characteristics of head

materials were studied by measuring friction, but wear characteristics of head materials were neither measured nor directly compared in those studies. We recently reported that a transparent pin wear test on thin-film disk is a good technique for measuring pin wear and for directly comparing it with friction (Kawakubo and Yahisa, 1993a). Transparent pin materials, such as quartz glass, transparent zirconia, and single-crystal sapphire, have been studied (Kawakubo and Yahisa, 1993b). The present work included a synthesized diamond as a pin material. Sliding conditions, failure process, friction, wear, and disk lifetime, were compared for those pin materials.

Experiments

Pin-on-disk type sliding wear tests were performed with a pin placed on a test disk surface (Kawakubo et al., 1986). The sliding condition was monitored through a hole at the back of the sliding position and recorded with an optical microscope, a TV camera, and a videorecorder with 540 nm wave length monochromatic light. The test load was 200 mN and the sliding speed was 20 m/s. All tests were performed in a class 100 environment at 23 to 26°C and with 40 to 60 percent RH.

Tests disks were 1.9 mm thick thin-film disks with 224 mm diameter. They had about 10 μm of textured Ni-P underlayer on an aluminum substrate, and then 250 nm Cr underlayer, 60 nm magnetic film, and 30 nm carbon overcoat film were deposited. A liquid perfluoropolyether lubricant was applied on top. Test pin materials were quartz glass (QG), transparent zirconia (TZ), single-crystal sapphire (SA), and single-crystal diamond (DI). Their characteristics are listed in Table 1. The surface curvature radius of the pins was polished to 19 mm except for the 10 mm of the DI pins because of the difficulty in polishing. The back surfaces of the pins were polished in order to make them transparent.

The wear scar diameters D of the pins were measured from the photographs taken from the back of the pins while sliding. It was confirmed that the wear scar diameters D were the same as those measured from the sliding surface after sliding tests.

Contributed by the Tribology Division of THE AMERICAN SOCIETY OF MECHANICAL ENGINEERS for presentation at the ASME/STLE Tribology Conference, Maui, Hawaii, October 16-19, 1994. Manuscript received by the Tribology Division February 21, 1994; revised manuscript received by July 11, 1994. Paper No. 94-Trib-45. Associate Technical Editor: A. K. Menon.
Copies will be available until March 1996.

Table 1 Test pins

	Materials	Knoop hardness	Surface curvature radius	Remarks
QG	Quartz glass	7 GPa	19 mm	
TZ	Transparent zirconia	12	19	82ZrO ₂ -8Y ₂ O ₃ -10TiO ₂
SA	Synthesized sapphire	20	19	<0001> direction of (1120) surface
DI	Synthesized diamond	80	10	<100>, <110> direction of (100) surface

Because D was much smaller than the surface curvature radius R of the pins, the apparent wear volume V_a was calculated using the following equation (Talke, 1972).

$$\bar{V}_a = \pi D^4 / 64 R \quad (1)$$

In photographs of the contact before sliding, however, there was a dark 0th order Newton ring because of the elastic deformation. If Eq. (1) were applied directly to those photos, pin wear volume before sliding would have a finite false value. To compensate for this effect of elastic deformation, the apparent elastic deformation volume V_0 before sliding was calculated from the diameter D_0 of the 0th order Newton ring before sliding using the following equation.

$$V_0 = \pi D_0^4 / 64 R \quad (2)$$

The wear volume V was then calculated from

$$V = V_a - V_0. \quad (3)$$

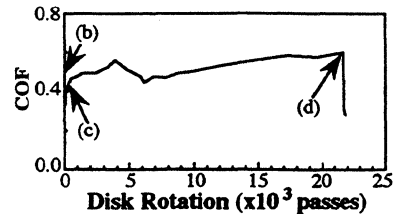
The disk lifetime was determined by the adhesion of metal film to the pin surface, since the adhesion of metal film from the disk was a sign of the disk carbon overcoat failure.

Results

Typical sliding conditions and the coefficient of friction (COF) change during a wear test with QG pin are shown in Fig. 1. As shown in Fig. 1(a), the COF increased rapidly to a little more than 0.4 at the start of the test. It then increased and decreased randomly between 0.4 and 0.6 until 22×10^3 passes, when the disk failure took place. The 0th order circle at the center in Fig. 1(b) shows the elastic deformation before sliding. As shown in Fig. 1(c), the center circle became wider after 100 sliding passes, showing the wear of the pin sliding point. With more test passes, the pin wear scar diameter increased, and the wear debris accumulation and the wear scar on the disk appeared and increased. As shown in Fig. 1(d), the width of the wear scar on the disk just before the disk failure was similar to that of the wear debris adhered on the pin surface.

Typical sliding conditions and the COF change during a wear test with a TZ pin are shown in Fig. 2. As shown in Fig. 2(a), the initial COF was about 0.35, and it soon decreased to 0.25. It again increased to 0.35 until the disk failure took place at 1.1×10^3 passes. The Newton rings in Figs. 2(b) to (d) are obscure because of the poor transmissivity of the TZ pin. As shown in Fig. 2(c), the 0th order circle diameter of the TZ pin after 100 passes was larger than that of the QG pin in Fig. 1(c). As shown in Fig. 2(d), the wear scar on the disk surface just before the disk failure by the TZ pin was less clear than that by the QG pin in Fig. 1(d). A white spot at the leading edge of the TZ pin showing a wear particle intrusion was observed just before the disk failure as in Fig. 2(d) (pointed by an arrow). Metal film adhesion followed at the place of the particle intrusion.

Typical sliding conditions and the COF change during a wear test with an SA pin are shown in Fig. 3. As shown in Fig. 3(a), the COF started from 0.25 and increased gradually to about 0.5. Then, it decreased to 0.35 at about 9×10^3 passes and increased again to 0.45 until disk failure took place at 16×10^3 passes. As shown in Fig. 3(c), the 0th order circle



(a) Coefficient of Friction



(b) Before Sliding



(c) After 100 passes



(d) After 22×10^3 passes
Just before disk failure



Fig. 1 Sliding conditions of QG pin ($R=19$ mm)

diameter of the SA pin after 500 passes was smaller than that of the QG pin after 100 passes in Fig. 1(c). The sliding condition at 9.3×10^3 passes when the COF dropped in Fig. 3(a) is shown in Fig. 3(d). Black debris was formed in the middle of the center circle and the color of the surrounding circle was lighter than that of Fig. 3(c). This shows that the black debris separated and lifted the SA pin surface from the disk. As shown in Fig. 3(e), the wear debris accumulation on the pin surface and the wear scar on the disk surface were similar to those with the QG pin in Fig. 1(d).

Typical sliding conditions and the COF change during a wear test with a DI pin slid in <100> direction are shown in Fig. 4. As shown in Fig. 4(a), the COF started from 0.12 and increased monotonically to about 0.6. As shown in Figs. 4(c), very little wear debris was found on the DI pin surface about 1000 passes. And as shown in Fig. 4(d), the adhesion of the

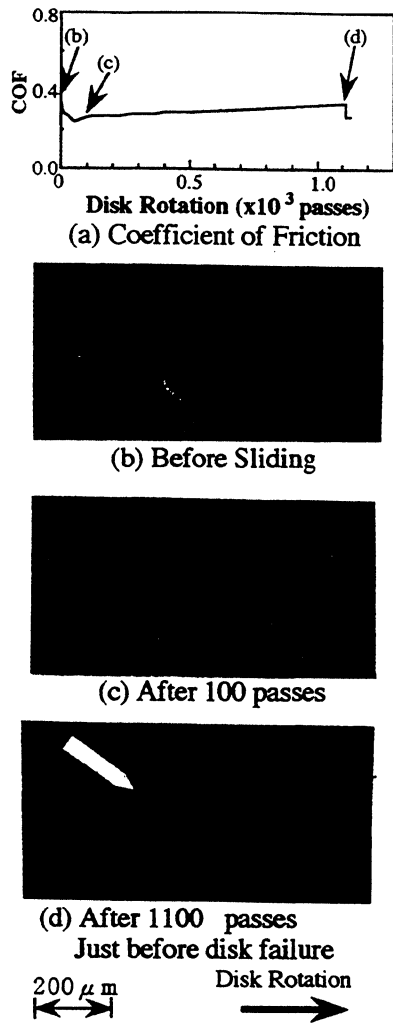


Fig. 2 Sliding conditions of TZ pin ($R=19$ mm)

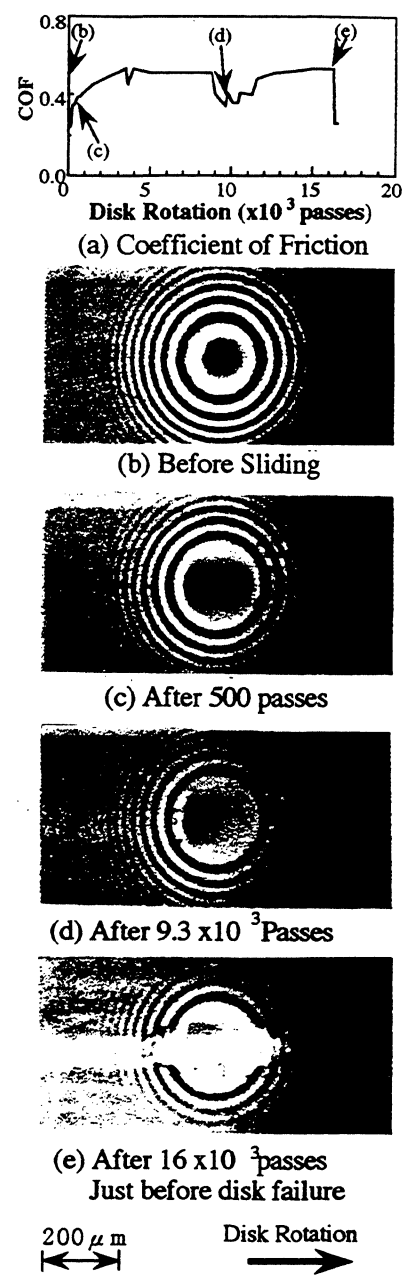


Fig. 3 Sliding conditions of SA pin ($R=19$ mm)

metal film was not found on the DI pin until the test was stopped at about 50×10^3 passes.

Friction change patterns during wear tests are shown in Fig. 5. Large scattering and sharp drops were found in Figs. 4(a) and (c) like those in Figs. 1(a) and 3(a) with the QG and the SA pins. Simultaneous friction measurement and sliding condition monitored showed that COF dropped at wear debris intrusion between pin and disk surfaces as shown in Fig. 3(d). Two curves of the DI pin in $\langle 100 \rangle$ and $\langle 110 \rangle$ directions in Fig. 5(d) were almost identical to each other. Figure 5 shows that the COF changed quite similar within each pin material. The COF curves in Fig. 5 were stopped at disk failure or at a certain test passes before disk failure. The disk lifetimes were 21.7, 22.1, 19.8, 2.8 and 2.9×10^3 passes for the QG pins, 2.6, 1.5, 1.1, 0.73, and 0.55×10^3 passes for the TZ pins, and 21.5, 16.1, and 2.4×10^3 passes for the SA pins. Some tests were stopped before failure, at 22.9, 21.0, and 20.2×10^3 passes for the SA pins and at about 50×10^3 passes for both sliding directions of the DI pin. All the tests with lifetime less than 3×10^3 passes showed similar sliding pattern with that shown in Fig. 2.

Pin wear volume calculated from pin wear scar diameters are shown in Fig. 6. For the TZ and the QG pins, the wear volume increased gradually and disk failure occurred while the wear volume was increasing. For the SA pins, the wear volume increased at the beginning, but after 3×10^3 passes, it increased very slowly or became almost constant until disk failure. This

coincided with the adhesion of wear debris on the SA pin surfaces. For the DI pin, the wear volume increased from about $1 \times 10^{-7} \text{ mm}^3$ at the beginning to $5 \times 10^{-7} \text{ mm}^3$ at 50×10^3 passes. They were more than an order of magnitude smaller than those of other pin materials tested. The pin wear increased in the order of DI, SA, QG, and TZ.

Discussion

From Figs. 1 to 4, it is clear that the pin wear debris had large effects on sliding conditions. The changes of the COF with the QG and the SA pins after several hundred passes were attributed to the results of wear debris intrusion at the pin-disk interface. The changes in lifetime also seemed to be due to the effects of wear debris adhesion on the pin surfaces. It was also found from the observation of the SA pin sliding conditions that the SA pin was lifted by wear debris after 3×10^3 passes and that the debris slid against the disk surface. This

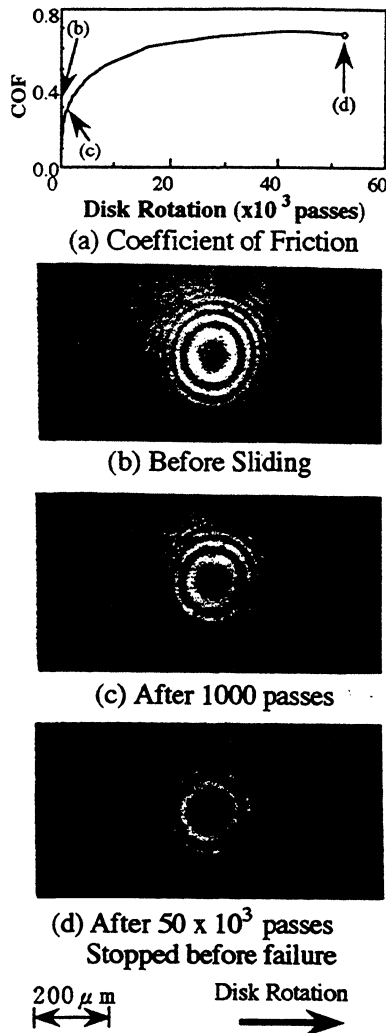


Fig. 4 Sliding conditions of DI pin ($R = 10$ mm, $\langle 100 \rangle$ direction)

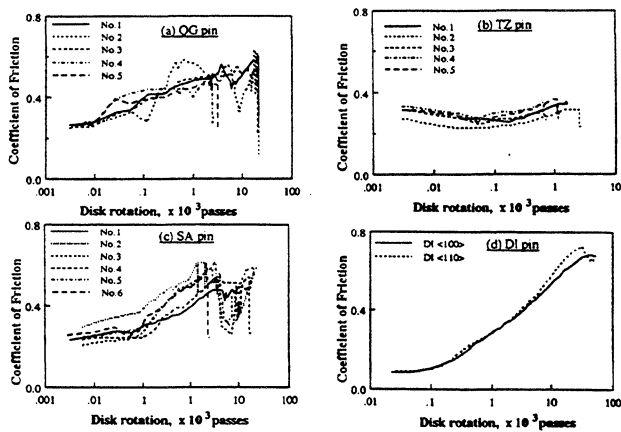


Fig. 5 Coefficient of friction change during transparent pin sliding test

seemed to be the reason for very small or almost no wear of SA pin after that. The wear volume of the DI pin was the lowest in this study and very little wear debris was found on the DI pin sliding surface. This coincided with the similar low COF reported in a previous paper (Chandrasekar and Bhushan, 1991). This is probably the reason for the monotonic COF increase with the DI pin shown in Fig. 4(a) and the identical COF increase of two tests in Fig. 5(d).

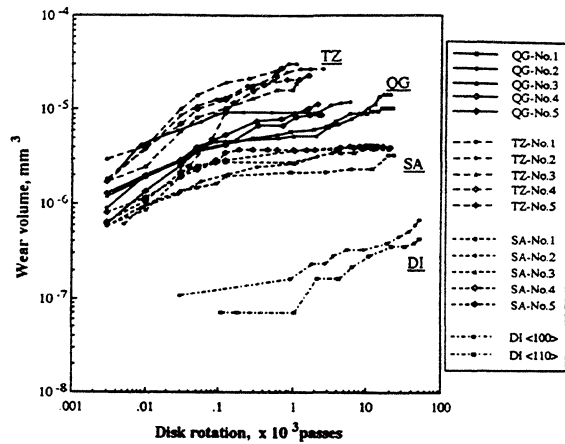


Fig. 6 Wear volume change during transparent pin sliding test

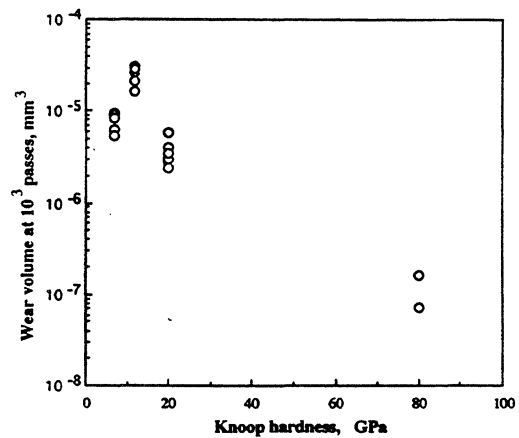


Fig. 7 Effects of pin bulk hardness on wear volume at 1000 passes during transparent pin sliding test

The effects of the pin bulk hardness on wear volume at 10^3 passes are shown in Fig. 7. Pin wear volume increases in the order of DI, SA, QG, and TZ. This order does not coincide with that of the pin bulk hardness in decreasing order, DI, SA, TZ, and QG. The difference between those two orders is the position of TZ. If the data of TZ were excluded, Fig. 7 would show that the harder the pin, the smaller the pin wear. In this study, only TZ was a multiphase material and the three remaining materials were all single-phase materials. This seems to be the reason why the wear volume of TZ was larger than that of the other pin materials in this study. This coincided with results from an earlier report, which said that, in general, the single-phase slider materials showed lower wear than the multi-phase materials (Chu et al., 1990).

The effects of the pin bulk hardness of the disk lifetime are shown in Fig. 8. From the scattering range of the above data, it was found that the disk lifetime increased in the order of TZ, QG, SA, and DI. This order does not coincide with that of the pin bulk hardness in increasing order, QG, TZ, SA, and DI. In fact, an inverse relation between the orders of pin wear volume and the disk lifetime is clear from Figs. 7 and 8. The relationship between pin wear volume and the disk lifetime is therefore plotted in Fig. 9, which shows that the smaller the pin wear, the longer the lifetime. The reason for the above relationship was supposed to be to the fact that the hardness of the thin-film disk surface was similar to the bulk hardness of the pin materials and that the carbon overcoat is very thin. More study is necessary to confirm this. Fig. 9 clearly shows that the pin wear (and, hence, the head wear) should be as

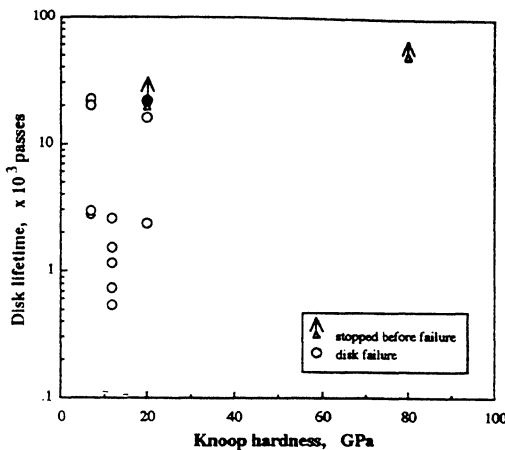


Fig. 8 Effect of pin bulk hardness on disk lifetime during transparent pin wear test

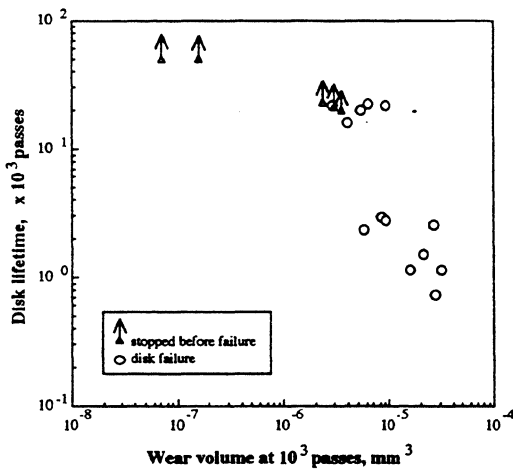


Fig. 9 Relation between wear volume at 1000 passes and disk lifetime during transparent pin wear test

small as possible for high reliability. An earlier report emphasized the importance of wear particle generation and recommended the use of materials with little tendency to produce wear debris (Hedenqvist, 1992). This recommendation is consistent with the results of the present study.

It was shown that the transparent pin sliding test reported here is very useful to analyze the sliding characteristics. Sliding tests using transparent glass disks with carbon overcoat and lubricant on top would also be a good tool to analyze real head sliding characteristics.

Conclusions

Pin-on-disk wear tests on a thin-film magnetic disk were studied. Transparent pin materials—quartz glass (QG), transparent zirconia (TZ), sapphire (SA), and diamond (DI)—were used for pins. In addition to friction, sliding conditions and pin wear were continuously monitored with a video.

A close relation between wear debris intrusion and friction drop was shown by simultaneous observation of friction and sliding conditions. Pin wear increased in the order of DI, SA, QG, and TZ. This order of the pin wear did not coincide with that of the pin bulk hardness in decreasing order, DI, SA, TZ, and QG, probably because TZ is a multi-phase material. This shows the importance of the direct wear measurement of head materials. Disk lifetime increased in the order of TZ, QG, SA, and DI, and the smaller the pin wear, the longer the disk lifetime.

Acknowledgments

The authors are thankful to Professors Yoshitsugu Kimura of the University of Tokyo, Koji Katoh of the Tohoku University, and Sigeyuki Mori of the Iwate University for their stimulating discussions. Thanks are also due to Akihiro Gotoh, Yuuichi Ohtani, Yoshiyuki Kajiki, and Norikazu Tsumita for the help in preparing pin and disk samples.

References

- Bogy, D. B., Yun, S., and Knapp, B., 1993, "Enhancement of HDI Wear Durability by Use of Carbon Overcoats on the Slider's Rails," *Proc. TMR* 93, Sept., pp. D5.
- Chandrasekar, S., and Bhushan, B., 1991, "Friction and Wear of Ceramics for Magnetic Recording Applications-Part II: Friction Measurements," *ASME JOURNAL OF TRIBOLOGY*, Vol. 113, pp. 313-317.
- Chu, M., DeJonghe, L., and Bhushan, B., 1990, "Wear Behavior of Ceramic Sliders in Sliding Contact with Rigid Magnetic Thin-Film Disks," *STLE Special Publications*, SP-29, pp. 9-16.
- Hamilton, H., Anderson, R., and Goodson, K., 1991, "Contact Perpendicular Recording on Rigid Media," *IEEE Trans. on Mag.*, Vol. 27, pp. 4921-4926.
- Hedenqvist, P., Olsson, M., Hogmark, S., and Bhushan, B., 1992, "Tribological Studies of Various Magnetic Heads and Thin-Film Rigid Disks," *Wear*, Vol. 153, pp. 65-78.
- Kawakubo, Y., Ishihara, H., Tsutsumi, Z., and Shimizu, J., 1986, "Spherical Pin Sliding Test on Coated Magnetic Recording Disks," *ASLE Special Publications*, SP-21, pp. 118-124.
- Kawakubo, Y., and Yahisa, Y., 1993a, "Wear Analysis Using Transparent Pins on Thin-Film Disks," *Proc. JAST Tribology Conf.*, (Tokyo), pp. 47-48 (in Japanese).
- Kawakubo, Y., and Yahisa, Y., 1993b, "Wear Analysis Using Transparent Pins on Thin-Film Disks (2), -Effects of Pin Materials," *Proc. JAST Tribology Conf.*, (Nagoya), pp. 395-398 (in Japanese).
- Kita, T., Kogure, K., and Mitsuya, Y., 1984, "Wear of the Flying Head of a Magnetic Disk File in Mixed Lubrication," *ASLE Special Publications*, SP-16, pp. 35-40.
- Talke, F. E., 1972, "An Autoradiographic Investigation of Material Transfer and Wear during High Speed/Low Sliding," *Wear*, Vol. 22, pp. 69-82.
- Talke, F. E., and Tseng, R. C., 1974, "An Investigation of Wear and Material Transfer in Magnetic Recording Disk Files," *Wear*, Vol. 28, pp. 15-27.
- Talke, F. E., and Su, J. L., 1975, "The Mechanism of Wear in Magnetic Recording Disk Files," *Tribology International*, Vol. 8, pp. 15-20.
- Yeack-Scranton, C. E., Etzold, K. F., Khanna, V. D., and Praino, A. P., 1990, "An Active Slider for Practical Contact Recording," *IEEE Trans. on Mag.*, Vol. 26, pp. 2478-2483.

Friction and Wear of Ceramics for Magnetic Recording Applications— Part II: Friction Measurements

S: Chandrasekar

School of Industrial Engineering,
Purdue University,
W. Lafayette, Ind. 47907
Mem. ASME

Bharat Bhushan¹

Department of Mechanical Engineering,
University of California,
Berkeley, California 94720
Fellow ASME

Friction and wear experiments have been conducted under lightly loaded conditions (less than 0.1 MPa) on a number of single crystal and polycrystalline ceramics in sliding contact against magnetic thin-film hard disk and against themselves in order to compare their tribological behavior. The ceramics studied range from single crystal diamond and sapphire to polycrystalline engineering ceramics such as manganese-zinc ferrite, alumina-titanium carbide, and zirconia. The results are analyzed in the context of earlier work on the friction and wear of these ceramics under lightly loaded conditions which has been recently reviewed by Chandrasekar and Bhushan (1990).

1 Introduction

Conventional hard disk magnetic storage systems utilize the relative motion of a hard disk against a stationary or moving read/write magnetic head (Mee and Daniel, 1987; Bhushan, 1989). The magnetic head material, the slider, is usually made of a ceramic; ceramics that are currently in use include Mn-Zn ferrite, alumina-titanium carbide, and calcium titanate. The magnetic thin-film rigid disk usually consists of several layers of thin-films deposited on a thin disk substrate. The layers contain, among other things, the magnetic medium, overcoat and a liquid lubricant. Typically, under steady-state operating conditions, an air bearing of thickness ~ 0.15 to $0.4 \mu\text{m}$ is formed between the head and the disk, thereby preventing direct contact between the two. The average interface contact pressures between head and disk are typically around 7 to 14 kPa (1-2 psi). Depending on the type of head-disk system, the head usually starts to fly and leaves the disk surface at speeds ranging from 2 to 15 m/s. The operating speeds are about 10 to 60 m/s (~ 3600 rpm). Physical contact between head and disk occurs below the flying speed, during start and stop and sometimes at isolated asperities during flying.

The need for improving the storage density and resolution of read/write magnetic recording systems has necessitated research into systems with ultra-low flying gaps, typically $< 0.1 \mu\text{m}$. In this regime, the friction and wear of magnetic disk and head at the contact zones is of even greater interest. A critical need exists for the development of head-slider materials and disk surfaces, which would have a low coefficient of friction between head and disk; this in turn would minimize localized heating and contact temperatures, starting and steady-state

power requirements, and high wear of both head and disk materials. A more durable and ultra-high density magnetic recording system could possibly emerge.

In this regard, we recently reviewed (Chandrasekar and Bhushan (1990)) the friction and wear of ceramics under lightly loaded and marginally lubricated sliding conditions which are similar to those prevailing in magnetic recording systems. Based on this, several ceramics were identified as potential slider materials. In this paper we report results of friction experiments on several of these ceramic materials when in sliding contact with a magnetic disk. Coefficient of friction measurements were also carried out for several of these ceramics in sliding contact against themselves at light loads ($\sim 0.06 \text{ N/mm}^2$). The purpose of these measurements was to see if there were any similarities between the frictional behavior of ceramics in contact with a magnetic disk and ceramics in contact with themselves, under similar lightly loaded conditions. Similar studies on head-tape contacts are described in Bhushan et al. (1984) and Bhushan (1990). The experimental results are analyzed in the context of the results of earlier studies on the state of ceramic friction which are summarized in Part I (Chandrasekar and Bhushan, 1990).

2 Experiments

2.1 Description of Apparatus and Experimental Details. The experimental apparatus used in the study of the friction and wear of various ceramics in sliding contact with magnetic disk is shown schematically in Fig. 1. In this apparatus, disks of 95 mm (3.5 in.) diameter could be rotated at speeds of up to 8000 rpm. The ceramic sliders were glued onto a 3380 type suspension (which applies 0.15N of normal load), and mounted on a crossed I-beam fixture as shown in Fig. 1. The sliders were positioned at a distance of 25 mm from the center of the disk. The crossed I-beam fixture was instrumented with semiconductor strain gauges to measure the normal and frictional forces exerted on the ceramic slider. The semiconductor gauges had a gauge factor (= ratio of fractional change in resistance

¹On sabbatical from IBM Research Division, Almaden Research Center, San Jose, Calif., 95120-6099.

Contributed by the Tribology Division of THE AMERICAN SOCIETY OF MECHANICAL ENGINEERS for presentation at the Joint ASME/STLE Tribology Conference, Toronto, Canada, October 7-10. Manuscript received by the Tribology Division August 23, 1989; revised manuscript received May 7, 1990. Paper No. 90-Trib-8. Associate Editor: T. Larsen-Basse.

Copies will be available until January 1992.

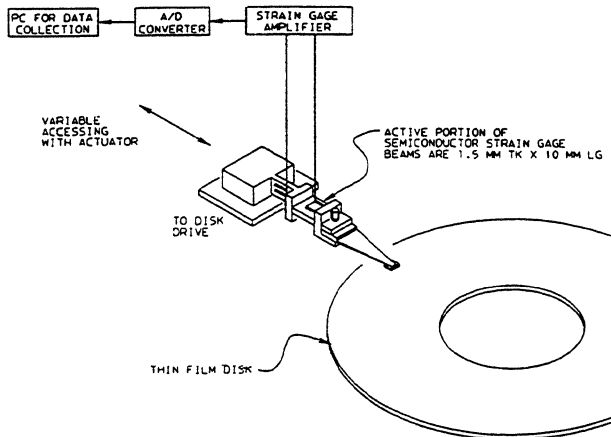


Fig. 1 Schematic of a friction and wear apparatus with the crossed I-beam configuration used in the force measurements

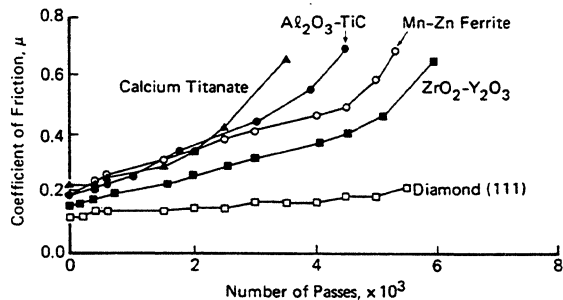


Fig. 2 Variation in the coefficient of friction of three ceramic sliders in contact with thin-film magnetic disk (surface roughness = 7 nm rms) with number of sliding passes. External load = 0.15 N, 800 rpm, slider location is along radius at a distance of 25 mm from center (sliding velocity = 2.1 m/s). Each data point is an average of four runs.

to the strain) of 115. Frictional forces as small as 1 mN could be measured with this arrangement. The disk structure consisted of a circumferentially textured Al-Mg alloy substrate with a 10-20 μm thick electroless plated Ni-P coating, 25-70 nm thick magnetic coating (Co-Pt-Ni), 20-30 nm thick diamond-like carbon coating, and 0.5-4 nm thick perfluoropolyether lubricant coating (Bhushan and Doerner, 1989). The surface roughness of the finished disk surface was 7.3 nm rms and 48.5 nm peak to valley distance. Six different ceramics – single crystal diamond with (111) plane as the slider face, polycrystalline Mn-Zn ferrite, 70 wt percent alumina – 30 wt percent titanium carbide (N-58), calcium titanate, partially-stabilized zirconia (7-8 wt percent Y_2O_3), and silicon nitride – were used as slider materials in friction studies against a thin-film magnetic disk. The physical properties of these ceramics are given in Chandrasekar and Bhushan (1990). The diamond slider face was approximately square with nominal dimensions of $2 \times 2 \times 1$ mm, while the other ceramic sliders had a geometry typical of commercial heads with an rms roughness of about 1.6 nm and peak-to-valley distance of approximately 17.0 nm. In the ceramic-against-ceramic friction experiments, the ceramic slider was typically in the form of a $2 \text{ mm} \times 2 \text{ mm}$ flat (except in the case of Si_3N_4 (5 mm diameter sphere)) and was mounted on a cross I-beam as in Fig. 1. The other ceramic member was in the form of a rectangular flat which was mounted onto the table of a computer numerically controlled (CNC) milling machine. The length of the flat in the direction of sliding was at least 10 mm in all cases except for single crystal SiC (~4mm long flat) and diamond (~2.2 mm long flat). The crossed I-beam was instrumented with semiconductor strain gauges for normal and frictional force measurements.

Table 1 Initial coefficient of friction for various ceramics in sliding contact with thin-film magnetic disk. (External load = 0.15 N, 1000 rpm, slider at 25 mm along radius from center.)

Ceramic slider material	Coefficient of friction, μ
Polycrystalline Mn-Zn ferrite	0.19
Alumina titanium carbide	0.19
Calcium titanate	0.21
Partially-stabilized zirconia	0.15
Silicon nitride	0.22
Single crystal Diamond (111)	0.13

Table 2 Number of passes beyond which there is a steep increase in the coefficient of friction of various ceramic-magnetic disk contacts. (External load = 0.15 N, 800 rpm, slider at 25 mm along radius from center; each value is an average of four runs.)

Slider material	Number of passes
Polycrystalline Mn-Zn ferrite	~ 4500
Alumina-titanium carbide	~ 3500
Calcium titanate	~ 1500
Partially-stabilized zirconia	~ 5000
Diamond (111)	Not seen even after 5500

The I-beam was kept stationary, while the flat mounted on the CNC machine table was moved relative to the ceramic member fixed to the I-beam. In the case of friction experiments with diamond, the diamond flat was mounted on a motorized linear slide to attain speeds lower than those achievable with the CNC machine table.

2.2 Friction of Ceramics Against Thin-Film Disk. Table 1 gives the measured coefficient of friction values for these ceramics when in sliding contact with a magnetic disk. The measured values shown here are those obtained immediately after the slider has been brought into contact with the disk. Amongst the ceramics listed in Table 1, single crystal diamond has the lowest coefficient of friction ($\mu \sim 0.12$ to 0.13) followed by partially stabilized zirconia ($\mu \sim 0.15$), the remaining ceramics all have an initial coefficient of friction close to 0.2 when in contact with the disk. There was no significant change in the initial coefficient of friction when the rotational speed of the disk was varied in the range of 600 to 1200 rpm.

With increasing number of passes, the coefficient of friction between the ceramics and the disk material was generally found to increase as shown in Fig. 2. This increase was, however, small for single crystal diamond even after it had been in contact with the disk for about 5500 passes. The number of passes after which a significant increase in the coefficient of friction occurred is shown in Table 2 for various slider materials. Calcium titanate, in general, exhibited a poor behavior in this regard, that is a significant increase in the coefficient of friction occurred after a smaller number of passes in comparison with the other sliders. Diamond was the best in terms of durability in this context, with the coefficient of friction remaining low even after 5500 passes. Often, when a significant increase in the coefficient of friction occurred and the test was stopped, faint scratch marks were to be seen on the disk surface.

2.3 Friction of Ceramic in Sliding Contact With Itself. Figure 3(a) shows the measured coefficient of friction for the ceramics in sliding contact with themselves. The coefficient of friction is lowest for diamond-on-diamond ($\mu \sim 0.1$) and highest for polycrystalline Mn-Zn ferrite on Mn-Zn ferrite

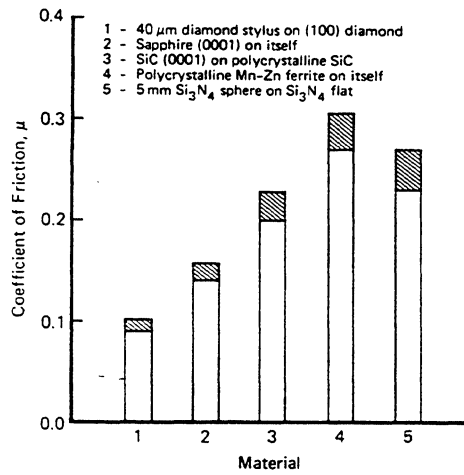


Fig. 3(a)

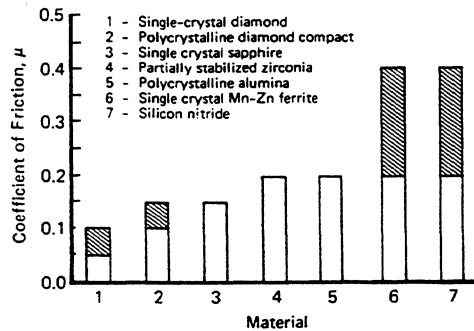


Fig. 3(b)

Fig. 3 Coefficient of friction of various ceramics in sliding contact against themselves. (a) Our experimental results. Sliding velocity = 0.1 mm/s in all cases except diamond where velocity = 0.033 mm/s, external load = 0.25 N, and (b) summary of experimental results of various materials sliding against themselves from literature. Shaded regions denote a range in μ (Chandrasekar and Bhushan, 1989).

($\mu \sim 0.3$). The cross-hatched regions in the figure are the observed scatter in the measured values of the coefficient of friction. The variation in the coefficient of friction observed in the present experiments follow a trend similar to values reported in the literature at room temperature and under lightly loaded conditions, which are summarized in Fig. 3(b) from Chandrasekar and Bhushan (1989). The actual magnitudes are different, reflecting the differences in geometry and conditions of sliding. It should be pointed out that at normal loads much greater than those reported here and over extended periods of sliding, significantly higher coefficients of friction (e.g., 0.7 for Si_3N_4 on Si_3N_4 and 0.8 for PSZ on PSZ) have also been reported for Si_3N_4 and partially stabilized zirconia; see, for example, Ishigaki et al. (1986) and Hannink et al. (1984).

2.4 Friction of Diamond on Diamond. From our experiments, we see that under lightly-loaded conditions, single crystal diamond has consistently shown a lower coefficient of friction than other ceramics while sliding against a magnetic disk. However, since humidity, load and sliding velocity have varying degrees of influence on the friction coefficient, it was decided to embark on a systematic investigation of the friction of single crystal diamond as a function of these variables. Preliminary results are reported here. We also refer the reader to Chandrasekar and Bhushan (1989) which summarizes the pioneering studies on diamond-diamond friction of Seal, Tabor, Wilks and their co-workers.

Two conical diamond styli with hemispherical tips of radius 40 μm and 100 μm and of an unspecified orientation were slid against the (100) face of a single crystal diamond flat (~ 2.2

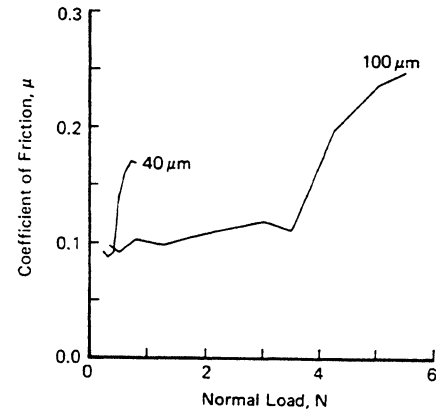


Fig. 4 Effect of normal load on the friction of diamond styli on diamond (100) flat. Diamond stylus tip radius, 40 μm and 100 μm , sliding velocity = 0.033 mm/s. (Note the sharp increase in coefficient of friction beyond a certain normal load.)

Table 3 Variation in the coefficient of friction (μ) between diamond stylus (40 μm radius) and (100) diamond flat with relative sliding velocity

Sliding speed [mm/s]	μ_{dry}	μ_{water}
0.017	0.103 ± 0.006	0.093 ± 0.008
0.033	0.093 ± 0.006	0.109 ± 0.007
0.050	0.108 ± 0.007	0.088 ± 0.01

mm \times 2.2 mm \times 1.5 mm thick), the latter being mounted on a motorized linear slide. The effect of relative sliding velocity and normal load on the coefficient of diamond-diamond friction was investigated. In addition, the experimental results obtained with these 2 styli also enabled comparisons to be made in a load regime with the theoretical predictions of Lawn (1967), and Enomoto and Tabor (1981).

Table 3 shows the measured values of coefficient of friction during dry sliding contact (relative humidity ~ 54 percent) and in the presence of water (surfaces flooded with water). The coefficient of friction is relatively low (~ 0.1) and a simple statistical analysis of the data using hypothesis testing showed that there is no statistically significant difference between the friction in air and water under these conditions. The experimental results are in agreement with the conclusions of Seal (1958) and Casey and Wilks (1973) who showed that water did not have any noticeable effect on the diamond-diamond friction. However, their experiments were conducted at much lower sliding velocities, typically a few micrometers per second.

In contrast to relative sliding speed, the normal load does have an important effect on the friction of diamond-on-diamond. Figure 4 shows the variation of μ with normal load for diamond styli of two different radii; over a certain critical range of the normal load - which is 0.4 to 0.6 N for the 40 μm stylus - the frictional coefficient increases significantly, see Fig. 4. Seal (1958) and Enomoto and Tabor (1981) were amongst the early workers to observe such a transition in the coefficient of diamond friction. Enomoto and Tabor attributed this to the onset of sub-surface cracking and demonstrated the onset of this sub-surface damage using cathodoluminescence studies.

Discussion

The coefficient of friction measurements show that under lightly-loaded conditions, single crystal diamond sliders had the smallest coefficient of friction against a thin-film magnetic disk in air, see Fig. 2 and Table 1. Furthermore, the coefficient of friction of the diamond (111) surface did not increase significantly even after 5500 passes of sliding as shown in Fig. 2. This is in contrast to a relatively rapid increase in the coef-

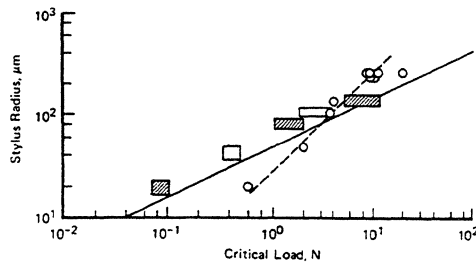


Fig. 5 Plot of critical load W_c against stylus radius, where W_c is load at which a marked rise in coefficient of friction or surface damage occurs on diamond (100) surface. \circ , Seal's (1958) data for crack initiation in sliding on (100) diamond. \cdots , line drawn through Seal's data; \cdots , Lawn's (1967) theoretical curves for the onset of Hertzian fracture in diamond assuming an existing crack size of $0.5 \mu\text{m}$; \blacksquare , Enomoto and Tabor's (1981) results of friction coefficient of diamond; \square , present study.

efficient of friction for calcium titanate, alumina-titanium carbide and Mn-Zn ferrite after about 1500 to 4500 passes of sliding in air in Fig. 2. These are all commonly used slider materials. Our survey of the literature reveals that these are some of the first reported results on the low coefficient of friction for diamond sliding against a magnetic disk. Besides diamond, partially stabilized zirconia (PSZ) also had a small coefficient of friction ($\mu \sim 0.15$) and this coefficient increased significantly only after 5000 passes sliding. Its friction and wear behavior was therefore much better than that of calcium titanate, alumina-titanium carbide and Mn-Zn ferrite.

Because of its high hardness relative to the disk material, it was thought at the outset that diamond would abrade away the disk surface and that subsequently a higher coefficient of friction would result in comparison to the other ceramics. However, this was not observed in the experiments. Under these lightly loaded conditions (< 0.1 Mpa mean contact pressure), adhesion is expected to be the most important contribution to friction. It appears therefore that the adhesion between the diamond and the disk material is much smaller than for other ceramics. A possible reason for this is due to the nature of the diamond surface.

It is known that the diamond surface is covered by carbon atoms with free dangling bonds (Schlossin et al., 1966; Sappok and Boehm, 1968; Spear, 1989). These bonds have a great affinity for hydrogen and the adsorption of hydrogen on the diamond surface has been shown to reduce the adhesion and friction between diamond and metal surfaces (Pepper, 1982a,b). With regard to the diamond-disk system, the strong adsorption of hydrogen on the diamond surface would create a hydrocarbon-like layer. Since the disk surface contains a hydrocarbon lubricant, the interfacial contact would be between two hydrocarbon layers which would result in low adhesion and friction. It is necessary that if the above mechanism is to be operative, the hydrocarbon layer, if one exists, on the diamond surface remain intact during sliding. At the low contact pressures prevalent in our experiments, this is a likely possibility. More evidence for the existence of a hydrocarbon-like layer on the diamond surface comes from the recent work of Feng (1989) and Feng and Wang (1989). They have observed a waxy debris similar to that reported by Seal (1958) generated by the sliding of diamond-on-diamond. The waxy debris was found to contain a significant fraction of hydrogen-rich material and about 10 percent by volume of graphite. This furthers the hydrogen adsorption hypothesis. We propose to systematically pursue this aspect in the near future.

The ceramic-ceramic sliding contact studies carried out at low interfacial pressures have some implications on the selection of slider materials for magnetic recording. Single crystal sapphire, as shown in Fig. 3(a) has a coefficient of friction of about 0.13 to 0.15 when sliding against itself. This is smaller than the friction coefficient of any of the other ceramic-ceramic

contacts studied, with the sole exception of diamond. Sapphire may be a potentially good choice as a slider material. The measured friction coefficients given in Fig. 3(a) compare well with values reported for these systems at somewhat greater normal pressures by other investigators (e.g., Buckley, 1981); see Fig. 3(b) for a summary of these results.

The measurements of diamond-on-diamond friction show that the coefficient of friction is little affected by humidity and sliding velocity. In the former context, Field (1979) reports that the strength of diamond is relatively unaffected by humidity. This is to be contrasted with reductions in the strength of several ceramics observed at high humidity (Kingery et al., 1983). The marginal changes in the friction of diamond with increasing humidity are noteworthy for magnetic recording systems, where sliders can be subjected to a variety of environments.

Our experimental observations in Fig. 4 with two different (tip radius) diamond styli sliding against a diamond flat show that there is a transition in the friction coefficient from a lower to a higher value when the normal force is increased. This is in keeping with the observations of Enomoto and Tabor (1981) who used styli of different tip radius than those used in the present study. This increase in the friction coefficient was attributed to the onset of cracking in diamond at a threshold value of the normal force.

Enomoto and Tabor (1981) analyzed the onset of surface damage using Lawn's earlier analysis (Lawn, 1967) of cone or ring crack formation underneath a sliding spherical indenter, which derived an expression for the critical load for onset of brittle fracture. This is henceforth termed Hertzian fracture. Their experimentally measured critical loads for the transition in the coefficient of friction were in reasonably good agreement with Lawn's predicted critical load for Hertzian fracture in diamond. It is interesting to analyze our experimental results in the context of Frank and Lawn (1966), Lawn (1967), Seal (1958) and Enomoto and Tabor (1981). In Fig. 5, the experimentally observed values for the critical load at which the coefficient of friction of diamond underwent a transition are plotted as a function of the diamond stylus-tip radius; this is a summary of the experimental results of Seal (1958), Enomoto and Tabor (1981) and our study. The solid heavy line is the theoretical curve due to Lawn for the threshold of Hertzian fracture under conditions of elastic contact. It is based on the assumption of an average elastic modulus, an average surface energy for the diamond surface, an average coefficient of friction ($\mu \sim 0.12$) and a surface crack size of $0.5 \mu\text{m}$. It is seen that our data which is shown as unshaded blocks in Fig. 5, for the critical load for transition from a lower to a higher coefficient of friction falls somewhat to the left of the theoretical curve of Lawn. However, the qualitative agreement is very good and provides further validation of the theory of surface damage induced changes in the friction coefficient, as enunciated by Enomoto and Tabor (1981). Similar changes in the friction coefficient have also been observed by Skinner et al. (1971) for a tungsten stylus sliding on single crystal graphite. The exact mechanism by which surface damage induces a change in the friction coefficient in this load range is not well understood.

4 Conclusions

Friction experiments have been conducted on several ceramics during sliding contact against a magnetic hard disk and against themselves, under lightly-loaded conditions in air. Single crystal diamond has the lowest coefficient of friction during sliding contact against these mating materials. We report some of the first results on a low coefficient of friction for single-crystal diamond against a magnetic disk. Furthermore, the increase in the coefficient of friction of diamond during sliding contact against a magnetic disk was relatively small even after

5500 passes, in contrast to other ceramics such as calcium titanate, alumina-titanium carbide, Mn-Zn ferrite, and partially-stabilized zirconia. Single crystal sapphire and silicon carbide also have lower friction coefficients compared to other polycrystalline ceramics, during sliding contact against themselves.

Experiments on diamond-diamond sliding show that sliding velocities in the range of 1 to 3 millimeters per minute had no significant effect on the coefficient of diamond-on-diamond friction. However, there was an increase in this friction coefficient with increasing normal load. The normal forces at which the increase in the friction occurred was higher for a 100 μm radius diamond stylus than for a 40 μm stylus in contact with a diamond flat. These observations agree with Enomoto and Tabor (1981), and Seal (1953); the critical loads at which the transition occurred for these styli was close to the theoretically predicted loads for onset of brittle fracture in single crystal diamond by Lawn (1967) and Frank and Lawn (1967). The experimental results, thereby, further reinforce the theoretical prediction of the dependence of a transition in the friction coefficient on the onset of Hertzian fracture in diamond.

5 Acknowledgments

Chandrasekar would like to acknowledge the School of Industrial Engineering and a grant from the National Science Foundation Program in Materials Engineering and Processing (MSM 8706919A1) used in partial support of this work. The authors would like to acknowledge valuable discussions and help from Bo Breczoczky and Haj Seki of the IBM Almaden Research Center. Part of the experimental work was carried out when Chandrasekar was a visiting scientist at the IBM Almaden Research Center. Chandrasekar would like to acknowledge the Norton Company for donating silicon nitride and zirconia samples and Union Carbide for the sapphire samples.

References

Bhushan, B., 1990, *Tribology and Mechanics of Magnetic Storage Devices*, Springer-Verlag, New York.

- Bhushan, B., Sharma, B. S., and Bradshaw, R. L., 1984, "Friction in Magnetic Tapes: Assessment of Relevant Theory," *ASLE Trans.*, Vol. 27, pp 33-44.
- Bhushan, B., and Doerner, M. F., 1989, "Role of Mechanical Properties and Surface Texture in the Real Area of Contact of Magnetic Rigid Disks," *ASME JOURNAL OF TRIBOLOGY*, Vol. 111, pp. 452-458.
- Buckley, D., 1981, *Surface Effects in Adhesion Friction and Lubrication*, Elsevier, Amsterdam.
- Carslaw, H. S., and Jaeger, J. C., 1952, *Conduction of Heat in Solids*, Oxford University Press, U.K.
- Casey, M., and Wilks, J., 1973, "The Friction of Diamond Sliding on Polished Cube Faces of Diamond," *J. Phys. D. Appl. Phys.*, Vol. 6, pp. 1772-1781.
- Chandrasekar, S., and Bhushan, B., 1990, "Friction and Wear of Ceramics for Magnetic Recording Applications, Part I: A Review," *ASME JOURNAL OF TRIBOLOGY*, Vol. 112, pp. 1-16.
- Enomoto, Y., and Tabor, D., 1981, "The Frictional Anisotropy of Diamond," *Proc. R. Soc. London, Series A373*, pp. 405-417.
- Feng, Z., 1989, Cavendish Laboratory, University of Cambridge, U.K. Private communication.
- Feng, Z., and Wang, Z., 1989, "The Analysis of Wear Debris Generated During Diamond Sliding on Diamond," Poster presentation at Diamond Conference, Bristol, U.K.
- Field, J. E., 1979, *The Properties of Diamond*, Academic Press, New York.
- Frank, F. C., and Lawn, B. R., (1967), "On the Theory of Hertzian Fracture," *Proc. R. Soc. London, Series A299*, pp. 291-306.
- Gitzen, W., 1970, *Alumina as a Ceramic Material*, American Ceram. Soc., Columbus, Ohio.
- Hannink, R. H. J., Murray, M. J., and Scott, H. G., 1984, "Friction and Wear of Partially Stabilized Zirconia: Basic Science and Practical Applications," Vol. 100, pp. 355-366.
- Ishigaki, H., Kawaguchi, I., Iwasa, M., and Toibana, Y., 1986, "Friction and Wear of Hot Pressed Silicon Nitride and Other Ceramics," *ASME JOURNAL OF TRIBOLOGY*, Vol. 108, pp. 514-519.
- Kingery, W., Bowen, H., and Uhlmann, D., 1983, *Introduction to Ceramics* (3rd Ed.), Wiley, New York.
- Lawn, B. R., 1967, "Partial Cone Crack Formation in a Brittle Material Loaded with a Sliding Spherical Indenter," *Proc. R. Soc. London, Series A299*, pp. 307-316.
- Pepper, S., 1982a, "Effect of Electronic Structure of the Diamond Surface on the Strength of Diamond-Metal Interface," *J. Vac. Sci. Technol.*, Vol. 20, pp. 643-647.
- Pepper, S., 1982b, "Transformation of the Diamond (110) Surface," *J. Vac. Sci. Technol.*, Vol. 20, pp. 213-217.
- Sappok, R., and Boehm, H., 1986, *Carbon*, Vol. 6, pp. 283-296.
- Schlossin, H., Van Reynveld, W., and Harris, W., 1966, *Proc. First. Int. Conf. Rock Mech.*, Lisbon, p. 119.
- Skinner, J., Gane, N., and Tabor, D., 1971, "Microfriction of Graphite," *Nature (Phys. Sci.)*, Vol. 232, pp. 195-196.
- Spear, K. E., 1989, "Diamond: Ceramic Coating of the Future," *J. Am. Ceram. Society*, Vol. 72, No. 2, pp. 171-179.
- Seal, M., 1958, "The Friction of Single Crystal Diamond," *Proc. R. Soc. (London), Series A249*, pp. 379-389.

Stang 12/14/91

STRUCTURE AND MECHANICAL PROPERTIES OF HYDROGENATED CARBON FILMS PREPARED BY MAGNETRON SPUTTERING

B. Marchon, P.N. Vo, Mahbub R. Khan
Seagate Magnetics, Fremont, CA 94538

J.W. Ager III
Center for Advanced Materials, Lawrence Berkeley Laboratory, Berkeley, CA 94720

Abstract - Hydrogenated thin carbon films have been prepared by DC-magnetron sputtering in an hydrogen-containing Argon atmosphere. A monotonic decrease in friction buildup as well as an increase in abrasion resistance is observed for increasing hydrogen proportion in Argon, from 0 to 5%. At the same time, Raman data shows higher sp^3 character and an increase in hydrogen content in the film, as monitored with FTIR, is observed. Resistivity measurements also show a transition from conductor to insulator. For very high hydrogen content, the film becomes increasingly softer. These data are attributed to an initial increase in the sp^3/sp^2 bonding ratio, followed by a loss of three-dimensional cross-linking eventually leading to polymerization.

INTRODUCTION

The mechanical performance of thin films used as wear-resistant overcoats is critical for the reliability of a Winchester disc-drive [1]. In the particular case of carbon films, the structure-property relationship and its relevance to magnetic media has attracted a lot of interest in the past decade [2]. Numerous papers have reported on the mechanical properties of carbon films and their dependence on preparation conditions [3-6]. In particular, hydrogenated carbon films (a-C:H), prepared from ion-assisted Chemical Vapor Deposition have been shown to demonstrate good tribological properties in applications such as overcoats on magnetic media [7]. For films prepared by DC magnetron sputtering [3], hydrogen can be incorporated by introducing it directly in the plasma [8]. This technique has been reported to enhance the friction and wear properties of the carbon film [9,10], without being detrimental to magnetic properties in an in-line system [9].

In this paper, carbon overcoats prepared in a DC sputtering system containing various amount of hydrogen (from 0 to 5%) are prepared and their tribology is evaluated. Raman spectroscopy, electrical resistivity, and Infrared Spectra showing gradual changes in the film structure are also reported.

EXPERIMENTAL

Films of 25nm thickness were deposited on untextured 95mm discs. Hydrogen was premixed with Argon in quantities of 0 (pure Argon), 1, 2, 3, and 5%. Total sputtering pressure was set to 10 and 20mT. Friction buildup was measured in a drag test at 25 RPM, using a thin film head (5g load) on unlubricated discs. Abrasive wear tests were performed using a SiC abrasive tape loaded at 6 psi, against a rotating disc for one minute. Raman spectroscopy was performed using the 488nm line of an Argon ion laser at a power of 35mW. Decomposition of the Raman spectra into "G" and "D" peaks (see below) was performed with a customized curve-fitting program, using Gaussian peak shape and a linear background. FTIR spectra were recorded on a Nicolet spectrometer. Resistivity measurements were performed with a four-point probe, on films deposited on glass slides. Because the films are very thin, only resistivity values lower than 20 Ω .cm could be measured.

RESULTS

Figure 1 shows the results of the drag tests on unhydrogenated and 5% hydrogen sample. The rate of frictional buildup is significantly slower for the hydrogenated sample. Variations of the rate of frictional buildup, expressed in gram/turn, vs. hydrogen content during sputtering are reproduced in Figure 2. Total sputtering pressure of 20 mTorr leads to slower buildup than 10 mTorr. Furthermore, there is a monotonic decrease of frictional buildup with increasing hydrogen content during sputtering. In Figure 3 are reproduced (after abrasive wear test, expressed as the number of scratches per millimeter on the disc surface after the test. Addition of hydrogen also improves the durability of the film continuously, with lower pressure giving better results in agreement with previous density [11].

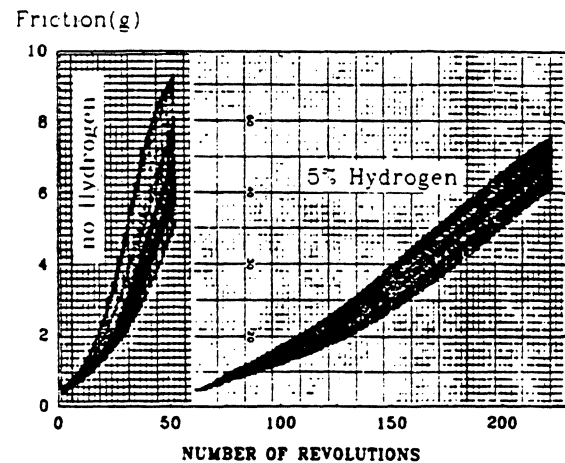


Figure 1: Drag tests (25RPM) on non-hydrogenated and hydrogenated (5% H₂ in Ar) carbon films.

The Raman spectra of the samples sputtered at a total pressure 10mTorr are reproduced in Figure 4. The two peaks at around 1350 ("D") and 1560 cm⁻¹ ("G"), characteristic of carbon thin films [12], show changes in position and intensity. In particular, the "G" peak position shifts down from ca. 1575 to 1555 cm⁻¹ when going from 0 to 5% hydrogen (Figure 5, left). At the same time, the intensity of the "D" peak, as measured by the intensity ratio I(D)/I(G) of the two peaks, decreases from ca. 1.4 to 0.7 (Figure 5, right). At the same hydrogen proportion, changing the total sputtering pressure from 10 to 20 mTorr does not significantly affect Raman spectra. Similar changes in the Raman spectra of DC-magnetron sputtered hydrogenated carbon films had been reported previously [13].

Manuscript received April 15, 1991

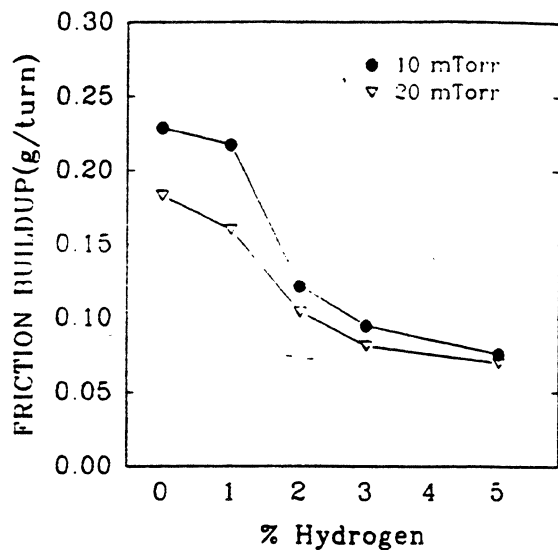


Figure 2: Friction buildup vs hydrogen content during sputtering.

Figure 6 shows FTIR spectra in the 2400-3400 cm^{-1} region, for the films sputtered at 10 mTorr. A steady increase in the amount of hydrogen in the film can be monitored by the increase in the intensity of the peak at around 2900 cm^{-1} , attributed to a stretching of the CH bond [14]. No clear distinction between vibrations arising from sp^2 or sp^3 bonded carbon [14] can be detected.

Addition of hydrogen also increases electrical resistivity (Figure 7). A clear transition from conductor (no hydrogen) to quasi insulator can be observed, in agreement with Cho et al. [13]. Films sputtered at 20mTorr have higher resistivity than those prepared at 10mTorr.

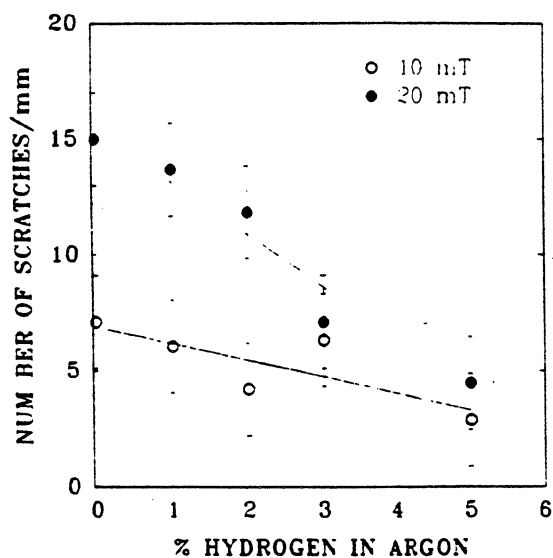


Figure 3: Resistance to abrasion vs hydrogen content during sputtering.

DISCUSSION

According to theoretical work by Beeman et al. [15], a shift of the Raman "G" peak to lower frequency indicates a greater sp^3/sp^2 bonding ratio. According to Figures 4 and 5 (left), addition of hydrogen during sputtering therefore increases the number of four-fold coordinated carbon atoms. At the same time, the total number and/or size of graphitic microdomains, as measured by the $I(\text{D})/I(\text{G})$ intensity ratio [16], is reduced (Figures 4 and 5 right). Friction buildup during slow speed drag test has been associated to sp^2 bonded carbon atoms, through a tribochemical wear mechanism with ambient oxygen [17]. Increase of the sp^3/sp^2 bonding ratio in the carbon film is therefore expected to slow down rates of friction buildup, and this is confirmed in Figures 1 and 2, and is consistent with earlier studies [18].

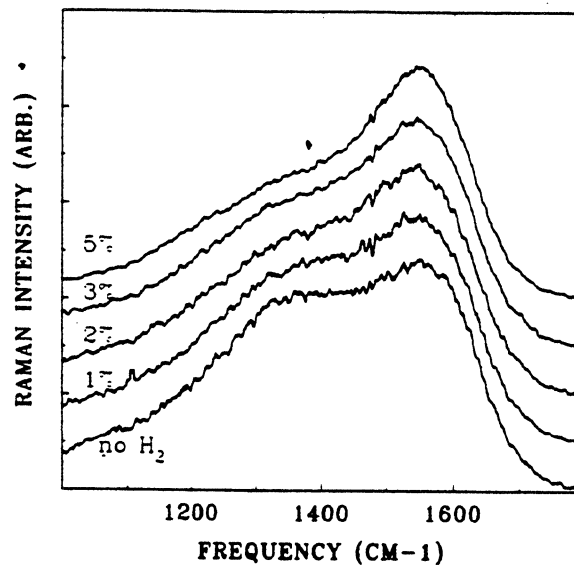


Figure 4: Raman spectra of carbon films sputtered at 10mTorr with various hydrogen content.

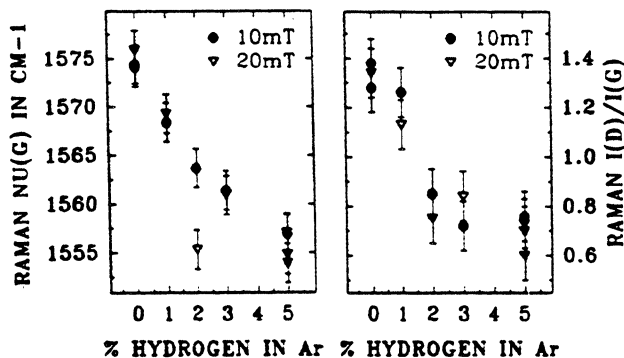


Figure 5: left: Raman "G" band position and right: $I(\text{D})/I(\text{G})$ intensity ratio vs hydrogen content during sputtering.

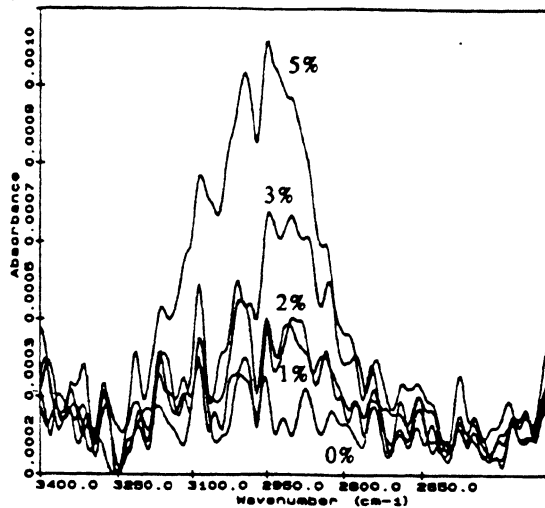


Figure 6: FTIR in the 2400-3200 cm^{-1} region for films sputtered at 10 mTorr.

As for resistance to abrasion, Figure 4 demonstrates that hydrogen addition improves the abrasive wear properties of the film, which seems to contradict previous studies reporting a lowering of film hardness with hydrogen [13,19]. However, the resistance to abrasion as quantified by our particular test, is likely to involve contributions of film toughness, internal stress and adhesion, as well as hardness. Only a careful estimate of all these mechanical parameters could therefore allow to assess our experimental data precisely. Finally, the reduction in abrasive wear for films of lower I(D)/I(G) ratios is in apparent disagreement with earlier work showing better durability for films of higher "D" band intensity [18]. This study however, was performed on unhydrogenated films, and it may not apply to the set of samples described here. The better mechanical properties as reported here will therefore simply be ascribed to a more diamond-like character for increasing hydrogen content, as monitored by the FTIR data in Figure 6. Hydrogen is believed to induce sp^3 from sp^2 , graphite-like, carbon-carbon bonding. Resistivity data from Figure 7 is also consistent with this model. For very high hydrogen content ($>20\%$), the film becomes increasingly soft, with a Raman spectrum showing a high fluorescence background (data not shown here). Such characteristics can be attributed to a transition to a polymeric structure, as hydrogen slowly destroys the three-dimensional carbon network [19].

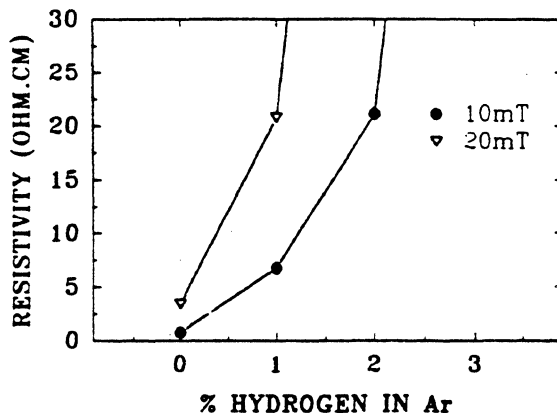


Figure 7: Film resistivity vs hydrogen content during sputtering.

CONCLUSIONS

Addition of hydrogen (up to 5%) in Argon during DC magnetron sputtering has been shown to enhance friction and wear properties of carbon overcoat of thin film media. In the 0-5% range reported here, monotonic decrease in friction buildup and abrasive wear rate have been observed. This improvement in mechanical properties has been monitored with Raman spectroscopy, FTIR and resistivity measurements. A transition from graphite-like to more diamond-like and eventually polymer-like for increasing hydrogen content is proposed to account for the data.

ACKNOWLEDGMENTS

We thank to B. Ho, J. Norton, and R. Jacobs for sample preparations and evaluations. The authors also acknowledge Grangette for Raman measurements. This work was supported, in part, by the Director, Office of Energy Research, US Department of Energy, under contract No. DE-AC03-76SF00098.

REFERENCES

- [1] B. Bhushan, "Tribology and Mechanics of Magnetic Storage Devices", Springer Verlag (1990).
- [2] H.C. Tsai and D.B. Bogy, *J. Vac. Sci. Technol. A*, **5**, 321 (1987).
- [3] N. Savvides and B. Window, *J. Vac. Sci. Technol. A*, **3**, 2386 (1985).
- [4] S. Hoshino et al., *J. Appl. Phys.*, **65**, 1918 (1989).
- [5] K. Enke, *Thin Solid Films*, **80**, 227 (1981).
- [6] R. Memming, H.J. Tolle, and P.E. Wierenga, *Thin Solid Films*, **143**, 31 (1986).
- [7] H.J. Lee and J.R. Weiss, Contributed Paper HA-06 InterMag '90.
- [8] D.R. McKenzie, R.C. McPhedran, L.C. Botten, N. Savvides, and R.P. Netterfield, *Appl. Opt.*, **21**, 361 (1982).
- [9] J.K. Howard, US Patent# 4,778,582 (1988).
- [10] Y. Mehmandoust, H.C. Tsai, H. Samani, and A. Eltough, Contributed Paper HA-07 to InterMag '90.
- [11] L.P. Franco, *J. Vac. Sci. Technol. A*, **8**, 1344 (1990).
- [12] H. Seki, *Surf. Coat. Technol.*, **37**, 161 (1989).
- [13] N.H. Cho, K.M. Krishnan, D.K. Veirs, M.D. Rubin, C.I. Hopper, B. Bhushan, and D.B. Bogy, *J. Mat. Res.*, **5**, 25 (1990).
- [14] J.W. Zou, K. Schmidt, K. Reichelt, and B. Dischler, *Appl. Phys.*, **67**, 487 (1990).
- [15] D. Beeman, R. Lynds, and M.R. Anderson, *Phys. Rev. B*, **30**, 870 (1988).
- [16] R.O. Dillon, J.A. Woollam, and V. Katkanant, *Phys. Rev. B*, **29**, 3482 (1984).
- [17] B. Marchon, N. Heiman, and M.R. Khan, *IEEE Trans Magn.*, **26**, 168 (1990).
- [18] B. Marchon, N. Heiman, M.R. Khan, A. Lautié, J.V. Ager, and D.K. Veirs, *J. Appl. Phys.*, in press.
- [19] F. Jansen and M.A. Machonkin, *Thin Solid Films*, **140**, 2 (1986).



The Society shall not be responsible for statements or opinions advanced in papers or in discussion at meetings of the Society or of its Divisions or Sections, or printed in its publications. Discussion is printed only if the paper is published in an ASME Journal. Papers are available from ASME for fifteen months after the meeting.
Printed in USA.

Transparent Pin Wear Test on Thin-Film Magnetic Disk

Youichi Kawakubo

Mechanical Engineering Research
Laboratory,
Hitachi, Ltd.,
Tsuchiura, Ibaraki, 300 Japan

Yotsuo Yahisa

Data Storage and Retrieval Systems Division,
Hitachi, Ltd.,
Odawara, Kanagawa, 256 Japan

Pin-on-disk wear tests on thin-film magnetic disks were performed using transparent materials. Quartz glass (QG), transparent zirconia (TZ), sapphire (SA), and synthesized diamond (DI) were used as pin materials. In addition to friction, sliding condition and pin wear were continuously monitored with video camera. Simultaneous friction measurement and video monitoring showed that friction dropped when wear debris intruded between pin and disk surfaces. Pin wear, from the measured diameter of wear scar on spherical pins, increased in the order of DI, SA, QG, and TZ. This order of pin wear does not coincide with that of the pin bulk hardness. Disk lifetime increased in the order of TZ, QG, SA, and DI, and the smaller the pin wear, the longer the disk lifetime.

Introduction

Head-disk spacing must be reduced to increase the recording density of rigid disk storage systems, and near-contact/contact recording technologies have been proposed for this purpose (Yeack-Scranton et al., 1990; Hamilton et al., 1991). Because these technologies require head-disk spacing of less than 50 nm, head-disk wear is inevitable. Materials at the head-disk sliding interface must therefore be carefully studied so that head-disk wear can be reduced. The sliding interface of thin-film disk is usually a carbon overcoat with lubricant, but heads are made from a wider variety of materials. It is thus very important to investigate the wear characteristics and failure mode with various head materials. Near-contact/contact recording heads will be smaller than present floating heads (Hamilton et al., 1991). Head contact area will then be orders of magnitude smaller than the disk recording area. If the specific wear volume of head and disk materials are in the same range, the head wear depth would be orders of magnitude larger than the disk wear depth. This makes the reduction of head wear more important.

Head wear on magnetic recording disks was first studied on particulate coated disks (Talke and Tseng, 1974). Accelerated wear tests using spherical pins were then developed, because of very low head wear (Talke and Su, 1975; Kita et al., 1984; Kawakubo et al., 1986). On thin-film magnetic disks, multi-phase materials like Al_2O_3 -TiC were shown to exhibit more variation in friction than single-phase materials (Chu et al., 1990), and single-crystal diamond was reported to show the lowest friction against thin-film disks (Chandrasekar and Bhushan, 1991). Enhancement of wear durability by carbon overcoats on head rails has also been reported recently (Bogy et al., 1993). In these papers, the sliding characteristics of head

materials were studied by measuring friction, but wear characteristics of head materials were neither measured nor directly compared in those studies. We recently reported that a transparent pin wear test on thin-film disk is a good technique for measuring pin wear and for directly comparing it with friction (Kawakubo and Yahisa, 1993a). Transparent pin materials, such as quartz glass, transparent zirconia, and single-crystal sapphire, have been studied (Kawakubo and Yahisa, 1993b). The present work included a synthesized diamond as a pin material. Sliding conditions, failure process, friction, wear, and disk lifetime, were compared for those pin materials.

Experiments

Pin-on-disk type sliding wear tests were performed with a pin placed on a test disk surface (Kawakubo et al., 1986). The sliding condition was monitored through a hole at the back of the sliding position and recorded with an optical microscope, a TV camera, and a videorecorder with 540 nm wave length monochromatic light. The test load was 200 mN and the sliding speed was 20 m/s. All tests were performed in a class 100 environment at 23 to 26°C and with 40 to 60 percent RH.

Tests disks were 1.9 mm thick thin-film disks with 224 mm diameter. They had about 10 μ m of textured Ni-P underlayer on an aluminum substrate, and then 250 nm Cr underlayer, 60 nm magnetic film, and 30 nm carbon overcoat film were deposited. A liquid perfluoropolyether lubricant was applied on top. Test pin materials were quartz glass (QG), transparent zirconia (TZ), single-crystal sapphire (SA), and single-crystal diamond (DI). Their characteristics are listed in Table 1. The surface curvature radius of the pins was polished to 19 mm except for the 10 mm of the DI pins because of the difficulty in polishing. The back surfaces of the pins were polished in order to make them transparent.

The wear scar diameters D of the pins were measured from the photographs taken from the back of the pins while sliding. It was confirmed that the wear scar diameters D were the same as those measured from the sliding surface after sliding tests.

Contributed by the Tribology Division of THE AMERICAN SOCIETY OF MECHANICAL ENGINEERS for presentation at the ASME/STLE Tribology Conference, Maui, Hawaii, October 16-19, 1994. Manuscript received by the Tribology Division February 21, 1994; revised manuscript received by July 11, 1994. Paper No. 94-Trib-45. Associate Technical Editor: A. K. Menon.
Copies will be available until March 1996.

Table 1 Test pins

	Materials	Knoop hardness	Surface curvature radius	Remarks
QG	Quartz glass	7 GPa	19 mm	
TZ	Transparent zirconia	12	19	8ZrO ₂ -8Y ₂ O ₃ -10TiO ₂
SA	Synthesized sapphire	20	19	<0001> direction of (1120) surface
DI	Synthesized diamond	80	10	<100>, <110> direction of (100) surface

Because D was much smaller than the surface curvature radius R of the pins, the apparent wear volume V_a was calculated using the following equation (Talke, 1972).

$$V_a = \pi D^4 / 64 R \quad (1)$$

In photographs of the contact before sliding, however, there was a dark 0th order Newton ring because of the elastic deformation. If Eq. (1) were applied directly to those photos, pin wear volume before sliding would have a finite false value. To compensate for this effect of elastic deformation, the apparent elastic deformation volume V_0 before sliding was calculated from the diameter D_0 of the 0th order Newton ring before sliding using the following equation.

$$V_0 = \pi D_0^4 / 64 R \quad (2)$$

The wear volume V was then calculated from

$$V = V_a - V_0 \quad (3)$$

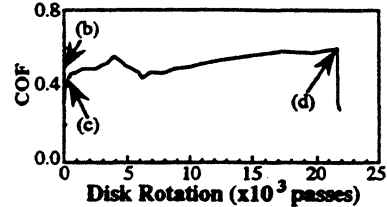
The disk lifetime was determined by the adhesion of metal film to the pin surface, since the adhesion of metal film from the disk was a sign of the disk carbon overcoat failure.

Results

Typical sliding conditions and the coefficient of friction (COF) change during a wear test with QG pin are shown in Fig. 1. As shown in Fig. 1(a), the COF increased rapidly to a little more than 0.4 at the start of the test. It then increased and decreased randomly between 0.4 and 0.6 until 22×10^3 passes, when the disk failure took place. The 0th order circle at the center in Fig. 1(b) shows the elastic deformation before sliding. As shown in Fig. 1(c), the center circle became wider after 100 sliding passes, showing the wear of the pin sliding point. With more test passes, the pin wear scar diameter increased, and the wear debris accumulation and the wear scar on the disk appeared and increased. As shown in Fig. 1(d), the width of the wear scar on the disk just before the disk failure was similar to that of the wear debris adhered on the pin surface.

Typical sliding conditions and the COF change during a wear test with a TZ pin are shown in Fig. 2. As shown in Fig. 2(a), the initial COF was about 0.35, and it soon decreased to 0.25. It again increased to 0.35 until the disk failure took place at 1.1×10^3 passes. The Newton rings in Figs. 2(b) to (d) are obscure because of the poor transmissivity of the TZ pin. As shown in Fig. 2(c), the 0th order circle diameter of the TZ pin after 100 passes was larger than that of the QG pin in Fig. 1(c). As shown in Fig. 2(d), the wear scar on the disk surface just before the disk failure by the TZ pin was less clear than that by the QG pin in Fig. 1(d). A white spot at the leading edge of the TZ pin showing a wear particle intrusion was observed just before the disk failure as in Fig. 2(d) (pointed by an arrow). Metal film adhesion followed at the place of the particle intrusion.

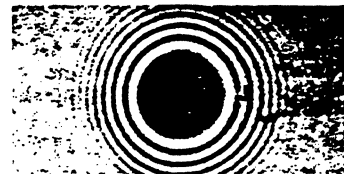
Typical sliding conditions and the COF change during a wear test with an SA pin are shown in Fig. 3. As shown in Fig. 3(a), the COF started from 0.25 and increased gradually to about 0.5. Then, it decreased to 0.35 at about 9×10^3 passes and increased again to 0.45 until disk failure took place at 16×10^3 passes. As shown in Fig. 3(c), the 0th order circle



(a) Coefficient of Friction



(b) Before Sliding



(c) After 100 passes



(d) After 22×10^3 passes
Just before disk failure



Fig. 1 Sliding conditions of QG pin ($R = 19$ mm)

diameter of the SA pin after 500 passes was smaller than that of the QG pin after 100 passes in Fig. 1(c). The sliding condition at 9.3×10^3 passes when the COF dropped in Fig. 3(a) is shown in Fig. 3(d). Black debris was formed in the middle of the center circle and the color of the surrounding circle was lighter than that of Fig. 3(c). This shows that the black debris separated and lifted the SA pin surface from the disk. As shown in Fig. 3(e), the wear debris accumulation on the pin surface and the wear scar on the disk surface were similar to those with the QG pin in Fig. 1(d).

Typical sliding conditions and the COF change during a wear test with a DI pin slid in <100> direction are shown in Fig. 4. As shown in Fig. 4(a), the COF started from 0.12 and increased monotonically to about 0.6. As shown in Figs. 4(c), very little wear debris was found on the DI pin surface about 1000 passes. And as shown in Fig. 4(d), the adhesion of the

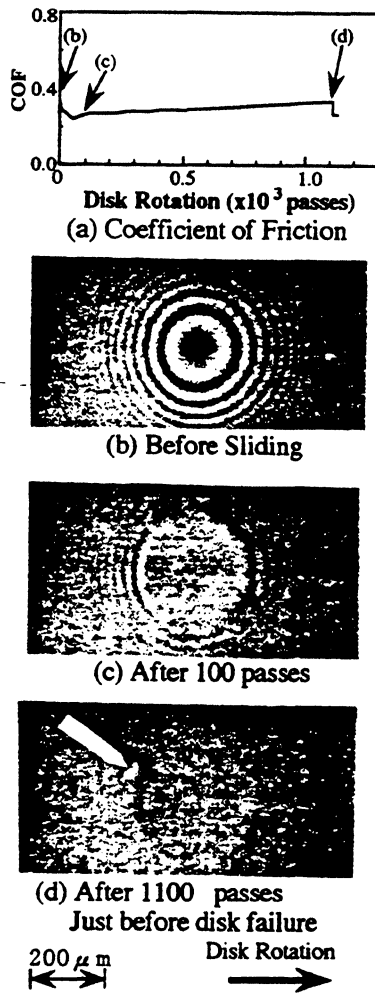


Fig. 2 Sliding conditions of TZ pin ($R=19$ mm)

metal film was not found on the DI pin until the test was stopped at about 50×10^3 passes.

Friction change patterns during wear tests are shown in Fig. 5. Large scattering and sharp drops were found in Figs. 4(a) and (c) like those in Figs. 1(a) and 3(a) with the QG and the SA pins. Simultaneous friction measurement and sliding condition monitored showed that COF dropped at wear debris intrusion between pin and disk surfaces as shown in Fig. 3(d). Two curves of the DI pin in $\langle 100 \rangle$ and $\langle 110 \rangle$ directions in Fig. 5(d) were almost identical to each other. Figure 5 shows that the COF changed quite similar within each pin material. The COF curves in Fig. 5 were stopped at disk failure or at a certain test passes before disk failure. The disk lifetimes were 21.7 , 22.1 , 19.8 , 2.8 and 2.9×10^3 passes for the QG pins, 2.6 , 1.5 , 1.1 , 0.73 , and 0.55×10^3 passes for the TZ pins, and 21.5 , 16.1 , and 2.4×10^3 passes for the SA pins. Some tests were stopped before failure, at 22.9 , 21.0 , and 20.2×10^3 passes for the SA pins and at about 50×10^3 passes for both sliding directions of the DI pin. All the tests with lifetime less than 3×10^3 passes showed similar sliding pattern with that shown in Fig. 2.

Pin wear volume calculated from pin wear scar diameters are shown in Fig. 6. For the TZ and the QG pins, the wear volume increased gradually and disk failure occurred while the wear volume was increasing. For the SA pins, the wear volume increased at the beginning, but after 3×10^3 passes, it increased very slowly or became almost constant until disk failure. This

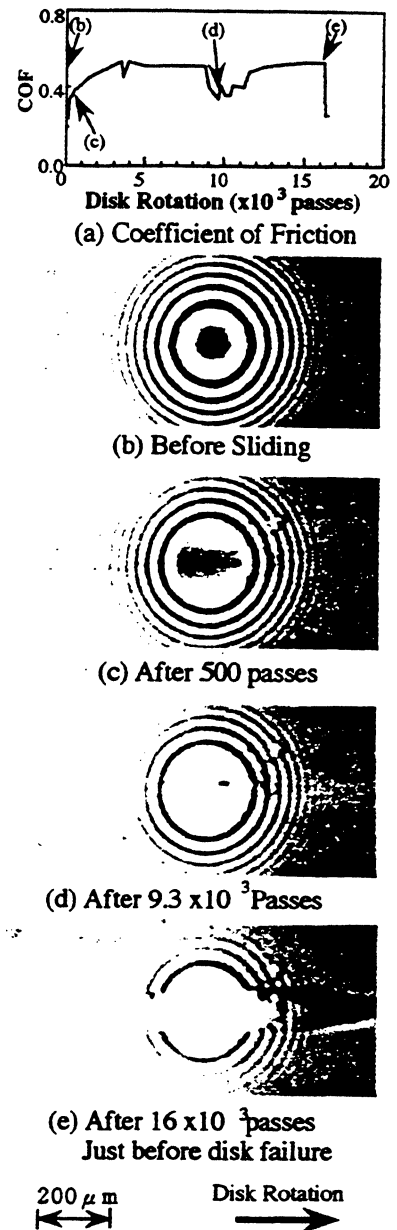


Fig. 3 Sliding conditions of SA pin ($R=19$ mm)

coincided with the adhesion of wear debris on the SA pin surfaces. For the DI pin, the wear volume increased from about $1 \times 10^{-7} \text{ mm}^3$ at the beginning to $5 \times 10^{-7} \text{ mm}^3$ at 50×10^3 passes. They were more than an order of magnitude smaller than those of other pin materials tested. The pin wear increased in the order of DI, SA, QG, and TZ.

Discussion

From Figs. 1 to 4, it is clear that the pin wear debris had large effects on sliding conditions. The changes of the COF with the QG and the SA pins after several hundred passes were attributed to the results of wear debris intrusion at the pin-disk interface. The changes in lifetime also seemed to be due to the effects of wear debris adhesion on the pin surfaces. It was also found from the observation of the SA pin sliding conditions that the SA pin was lifted by wear debris after 3×10^3 passes and that the debris slid against the disk surface. This

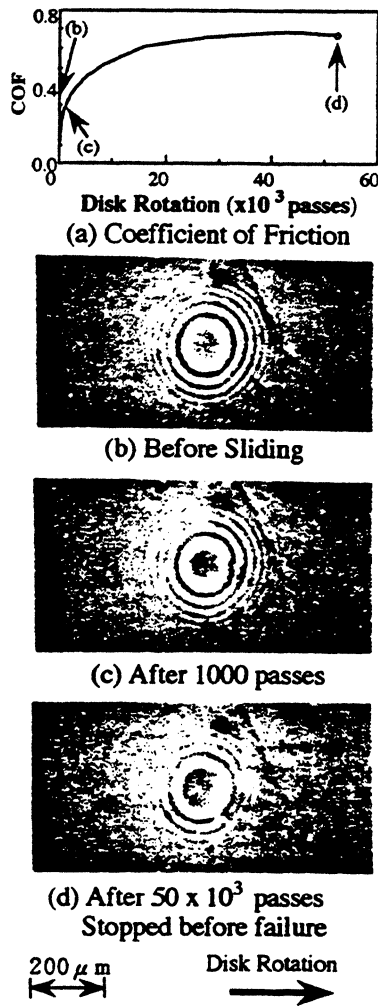


Fig. 4 Sliding conditions of DI pin ($R = 10$ mm, $\langle 100 \rangle$ direction)

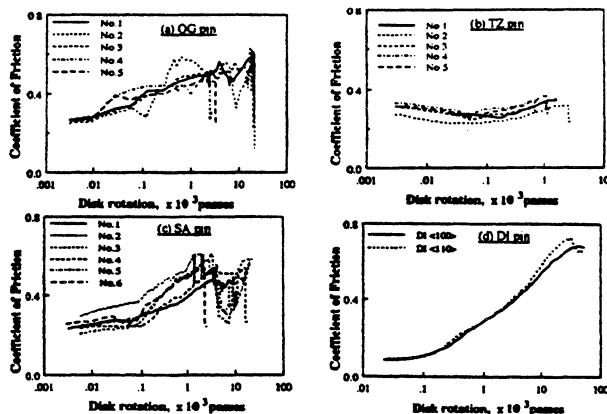


Fig. 5 Coefficient of friction change during transparent pin sliding test

seemed to be the reason for very small or almost no wear of SA pin after that. The wear volume of the DI pin was the lowest in this study and very little wear debris was found on the DI pin sliding surface. This coincided with the similar low COF reported in a previous paper (Chandrasekar and Bhushan, 1991). This is probably the reason for the monotonic COF increase with the DI pin shown in Fig. 4(a) and the identical COF increase of two tests in Fig. 5(d).

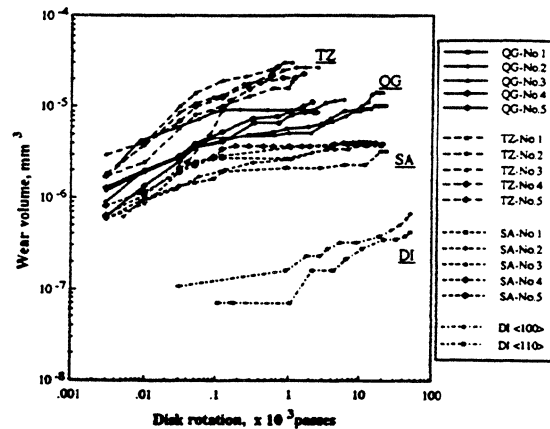


Fig. 6 Wear volume change during transparent pin sliding test

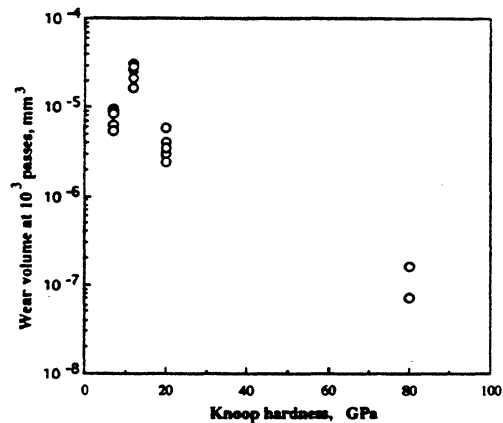


Fig. 7 Effects of pin bulk hardness on wear volume at 1000 passes during transparent pin sliding test

The effects of the pin bulk hardness on wear volume at 10^3 passes are shown in Fig. 7. Pin wear volume increases in the order of DI, SA, QG, and TZ. This order does not coincide with that of the pin bulk hardness in decreasing order, DI, SA, TZ, and QG. The difference between those two orders is the position of TZ. If the data of TZ were excluded, Fig. 7 would show that the harder the pin, the smaller the pin wear. In this study, only TZ was a multiphase material and the three remaining materials were all single-phase materials. This seems to be the reason why the wear volume of TZ was larger than that of the other pin materials in this study. This coincided with results from an earlier report, which said that, in general, the single-phase slider materials showed lower wear than the multi-phase materials (Chu et al., 1990).

The effects of the pin bulk hardness of the disk lifetime are shown in Fig. 8. From the scattering range of the above data, it was found that the disk lifetime increased in the order of TZ, QG, SA, and DI. This order does not coincide with that of the pin bulk hardness in increasing order, QG, TZ, SA, and DI. In fact, an inverse relation between the orders of pin wear volume and the disk lifetime is clear from Figs. 7 and 8. The relationship between pin wear volume and the disk lifetime is therefore plotted in Fig. 9, which shows that the smaller the pin wear, the longer the lifetime. The reason for the above relationship was supposed to be to the fact that the hardness of the thin-film disk surface was similar to the bulk hardness of the pin materials and that the carbon overcoat is very thin. More study is necessary to confirm this. Fig. 9 clearly shows that the pin wear (and, hence, the head wear) should be as

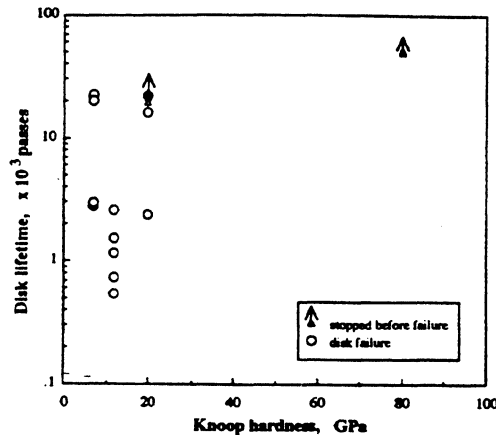


Fig. 8 Effect of pin bulk hardness on disk lifetime during transparent pin wear test

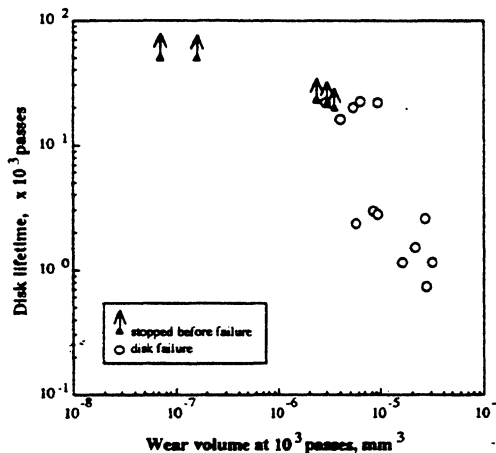


Fig. 9 Relation between wear volume at 1000 passes and disk lifetime during transparent pin wear test

small as possible for high reliability. An earlier report emphasized the importance of wear particle generation and recommended the use of materials with little tendency to produce wear debris (Hedenqvist, 1992). This recommendation is consistent with the results of the present study.

It was shown that the transparent pin sliding test reported here is very useful to analyze the sliding characteristics. Sliding tests using transparent glass disks with carbon overcoat and lubricant on top would also be a good tool to analyze real head sliding characteristics.

Conclusions

Pin-on-disk wear tests on a thin-film magnetic disk were studied. Transparent pin materials—quartz glass (QG), transparent zirconia (TZ), sapphire (SA), and diamond (DI)—were used for pins. In addition to friction, sliding conditions and pin wear were continuously monitored with a video.

A close relation between wear debris intrusion and friction drop was shown by simultaneous observation of friction and sliding conditions. Pin wear increased in the order of DI, SA, QG, and TZ. This order of the pin wear did not coincide with that of the pin bulk hardness in decreasing order, DI, SA, TZ, and QG, probably because TZ is a multi-phase material. This shows the importance of the direct wear measurement of head materials. Disk lifetime increased in the order of TZ, QG, SA, and DI, and the smaller the pin wear, the longer the disk lifetime.

Acknowledgments

The authors are thankful to Professors Yoshitsugu Kimura of the University of Tokyo, Koji Katoh of the Tohoku University, and Sigeyuki Mori of the Iwate University for their stimulating discussions. Thanks are also due to Akihiro Gotoh, Yuuichi Ohtani, Yoshiyuki Kajiki, and Norikazu Tsumita for the help in preparing pin and disk samples.

References

- Bogy, D. B., Yun, S., and Knapp, B., 1993, "Enhancement of HDI Wear Durability by Use of Carbon Overcoats on the Slider's Rails," *Proc. TMRC 93*, Sept., pp. D5.
- Chandrasekar, S., and Bhushan, B., 1991, "Friction and Wear of Ceramics for Magnetic Recording Applications-Part II: Friction Measurements," *ASME JOURNAL OF TRIBOLOGY*, Vol. 113, pp. 313-317.
- Chu, M., DeJonghe, L., and Bhushan, B., 1990, "Wear Behavior of Ceramic Sliders in Sliding Contact with Rigid Magnetic Thin-Film Disks," *STLE Special Publications*, SP-29, pp. 9-16.
- Hamilton, H., Anderson, R., and Goodson, K., 1991, "Contact Perpendicular Recording on Rigid Media," *IEEE Trans. on Mag.*, Vol. 27, pp. 4921-4926.
- Hedenqvist, P., Olsson, M., Hogmark, S., and Bhushan, B., 1992, "Tribological Studies of Various Magnetic Heads and Thin-Film Rigid Disks," *Wear*, Vol. 153, pp. 65-78.
- Kawakubo, Y., Ishihara, H., Tsutsumi, Z., and Shimizu, J., 1986, "Spherical Pin Sliding Test on Coated Magnetic Recording Disks," *ASLE Special Publications*, SP-21, pp. 118-124.
- Kawakubo, Y., and Yahisa, Y., 1993a, "Wear Analysis Using Transparent Pins on Thin-Film Disks," *Proc. JAST Tribology Conf.*, (Tokyo), pp. 47-48 (in Japanese).
- Kawakubo, Y., and Yahisa, Y., 1993b, "Wear Analysis Using Transparent Pins on Thin-Film Disks (2). -Effects of Pin Materials," *Proc. JAST Tribology Conf.*, (Nagoya), pp. 395-398 (in Japanese).
- Kita, T., Kogure, K., and Mitsuya, Y., 1984, "Wear of the Flying Head of a Magnetic Disk File in Mixed Lubrication," *ASLE Special Publications*, SP-16, pp. 35-40.
- Talke, F. E., 1972, "An Autoradiographic Investigation of Material Transfer and Wear during High Speed/Low Sliding," *Wear*, Vol. 22, pp. 69-82.
- Talke, F. E., and Tseng, R. C., 1974, "An Investigation of Wear and Material Transfer in Magnetic Recording Disk Files," *Wear*, Vol. 28, pp. 15-27.
- Talke, F. E., and Su, J. L., 1975, "The Mechanism of Wear in Magnetic Recording Disk Files," *Tribology International*, Vol. 8, pp. 15-20.
- Yeack-Scranton, C. E., Etzold, K. F., Khanna, V. D., and Praino, A. P., 1990, "An Active Slider for Practical Contact Recording," *IEEE Trans. on Mag.*, Vol. 26, pp. 2478-2483.

sendo

Tsui Wai

CARBON-COATED HARD DISK FAILURE IN CONTACT-START-STOP TESTS[©]

KOJI NAMURA, HITOSHI OTA, KAZUHIKO INANAGA
Advanced Mechanical System Dept., Central Research Laboratory
Mitsubishi Electric Corporation 1-1, Tsukaguchi-Honmachi 8-Chome, Amagasaki, Hyogo 661, Japan
NOBUO OHMAE (Member, STLE)
Dept. of Precision Engineering, Faculty of Engineering
Osaka University, Yamada-Oka, Suita, Osaka 565, Japan

The failure mechanism of carbon-coated hard disks was investigated by contact-start-stop (CSS) tests. The CSS tests were carried out with Al₂O₃-TiC sliders and unlubricated carbon-coated hard magnetic disks at relatively low humidities which do not cause slider stiction. Effects of the rise time of disk velocity and the number of CSS cycles on disk failure were investigated. After etching the tested disk, cracks existing below the disk surface were observed by SEM and AES.

From these investigations, the following observations have been made:

- 1. Wear of the carbon coating is negligibly small until an abrupt disk failure occurs*
- 2. The number of CSS cycles to failure decreases when the rise time increase*
- 3. Fatigue cracks occur within the magnetic media and propagate to the surface*
- 4. Fatigue cracks also propagate in-plane at the boundaries of individual layers*
- 5. The fatigue cracks lead to an abrupt failure.*

INTRODUCTION

In rigid disk drives, developments toward higher density data storage led to smaller flying heights between a disk and a recording head (1). To achieve reliable low flying height, the contact-start-stop systems (CSS) have been widely adopted. In CSS systems, when the disk is being started or stopped, sliding contact occurs between the disk and slider surface. As a result, lubricant or a protective overcoat layer is essential to reduce mechanical damage and wear. The lubricant and protective layers must not only satisfy the requirement of good resistance to wear and corrosion but also be thin enough to accomplish high recording density. And hence, investigations on the tribological properties of liquid and solid lubricants are reported (2), (3). When liquid lubricant is coated on thin film recording media, lubricant thickness decreases on account of sliding contact. Recently, from the viewpoint of mass production, the practical application of sputtered carbon films is investigated (4), (5)

because the process is compatible with the sputter-carbon deposition of thin film recording media. However, there is uncertainty concerning the wear properties of carbon coated thin film disks.

The aims of this study are to investigate the failure mechanism of carbon coated thin film disks. CSS tests at different rise times of disk rotation were conducted. The changes in disk surface were observed by scanning electron microscope and surface profilometer before and after the disk failure. Worn disk surfaces were sputter-etched, and a scanning electron microscope was used to observe the cracks below the surface and to identify the mechanisms of disk failures.

EXPERIMENT

Experimental Apparatus

Figure 1 shows a schematic view of the experimental apparatus. The experimental apparatus consists of two systems; disk drive system and slider support system.

A disk is attached to a spindle motor with a clamp which has a pin to determine a disk position. An encoder is attached to the end shaft of a spindle motor to control the starting position of the disk and the disk rotational speed.

A suspension arm, which holds the slider, is installed on the holder. The holder is supported with a support plate through a parallel spring type load cell. An acoustic emission (AE) sensor is installed on the (distal) end of the holder to monitor the change of contact conditions between slider and disk. The holder is set on micro-stages to determine the radial position of the slider.

Tested Disk and Slider

Disk construction is shown in Fig. 2. A Ni-P layer was plated on the Al substrate. The magnetic layer (Co-Cr and permalloy) and carbon layer were deposited on the Ni-P layer by sputtering. The thickness of the carbon layer is about 20–30 nm. No lubricant was coated on the carbon layer. A taper-flat type slider made of sintered Al₂O₃ and TiC was used for the experiment.

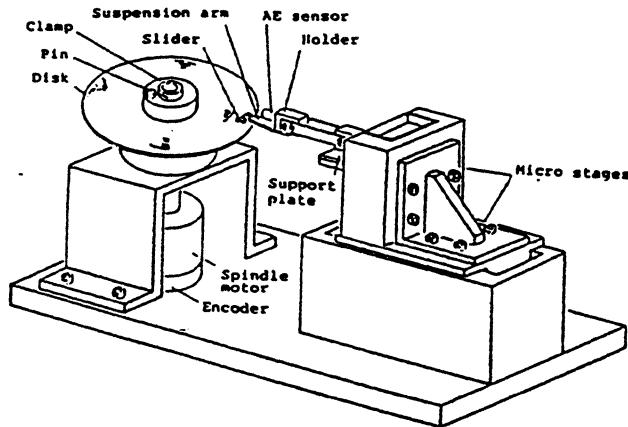


Fig. 1—Schematic view of experimental apparatus

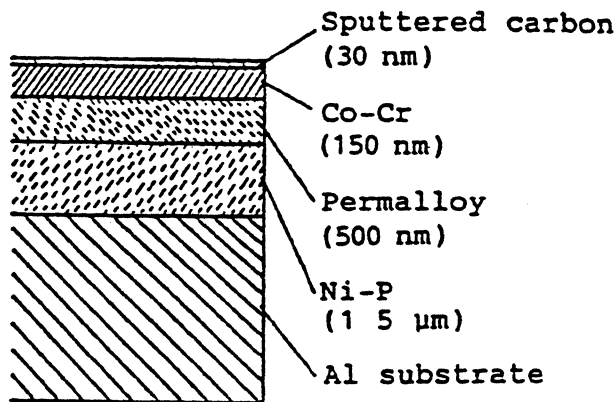


Fig. 2—Disk construction

Experimental Method and Conditions

A disk was attached with a clamp to the spindle motor within the accuracy of 5 μm for both circumferential and radial directions. The disk position was adjusted so that each start-stop cycle started with the slider and disk in the same relative position.

After pressing a slider to a disk with a vertical micro-stage at a load of 50 mN, the disk was rotated to the starting position at a relatively slow speed. Then, the disk was driven with the velocity-time pattern shown in Fig. 3. The relative speed of the slider was set at 10 m/s to obtain a flying height of the slider of 0.15 μm. The deceleration time was the same as the acceleration time, and these values were varied from 2 to 24 s.

AE signals and disk rotational speed during one CSS cycle were recorded every 100 CSS cycles. Surface roughness of the disk was measured with a non-contacting surface profilometer at every 500 CSS cycles to investigate the degree of wear of the disk. To detect disk wear precisely, it is necessary to measure the surface profile at the same location. A pair of indentations were made with a micro-hardness tester at both the outer and inner peripheries of the track that the slider glided on, and the surface profile was measured after adjusting the sensor position of the surface profilometer to trace the pair of indentations.

Experiments were performed in a clean chamber with the following conditions; dust level was below class 100, and

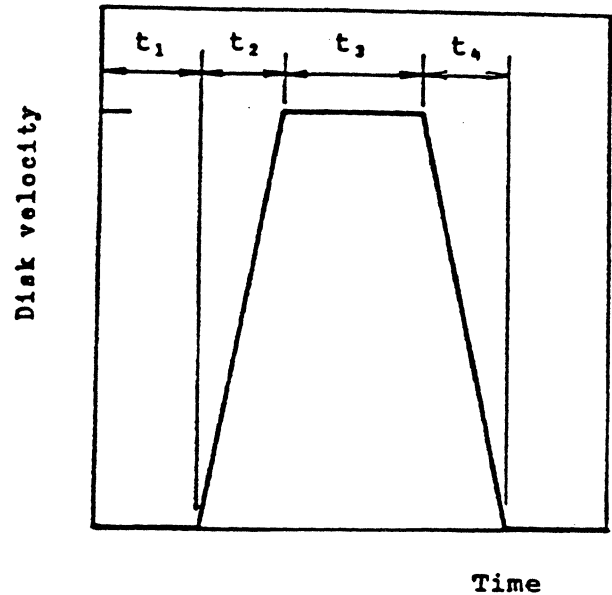


Fig. 3—Velocity-time relation of the disk

fluctuations of the relative humidity and temperature were within 5 percent and 1 degree, respectively. To prevent slider stiction, the relative humidity was set at 15–20 percent.

Lifetime of the disk was defined as the time when the depth of damage became larger than the thickness of the carbon layer, because output signal level decreased if the damage reached the magnetic layer.

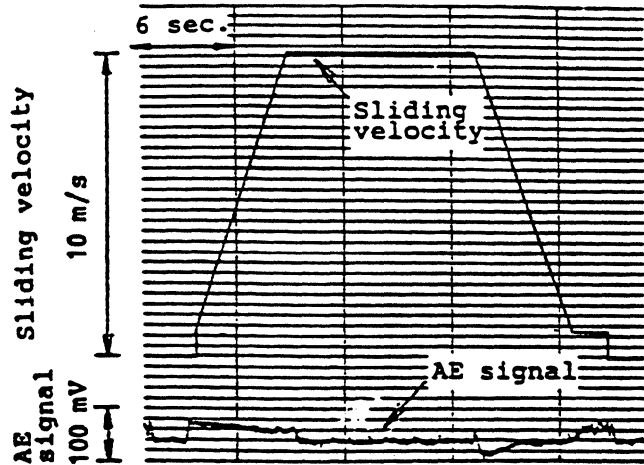
Disks which had been damaged were sputter-etched by Ar. After etching a certain volume, etched disks were observed using the scanning electron microscope (SEM) and auger electron microscopy (AES). Etching depth was estimated by the auger spectrum. As defect distribution in a layer was considered to differ from that at a boundary of layers, subsurface defects were observed at the following positions; the boundary between the carbon and Co-Cr layer, within the Co-Cr, the boundary between the Co-Cr and permalloy layer, within the permalloy, and at the boundary between permalloy and the Ni-P layer.

RESULTS AND DISCUSSION

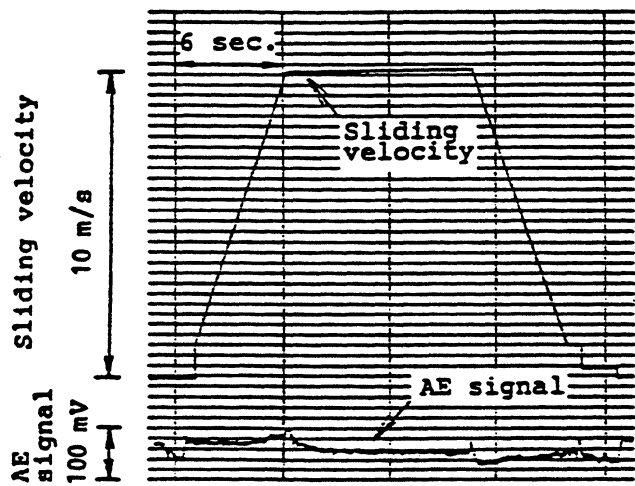
Changes of disk surface roughness and AE output signals

Figure 4 shows typical AE signals and sliding velocities during a CSS cycle whose rise time is 6 s. The number of CSS cycles is normalized with the maximum number of the CSS cycles obtained for a series of experiments. From Fig. 4, AE signal does not change below normalized CSS number of 0.92 which is about 97 percent of the tested disk life (0.95).

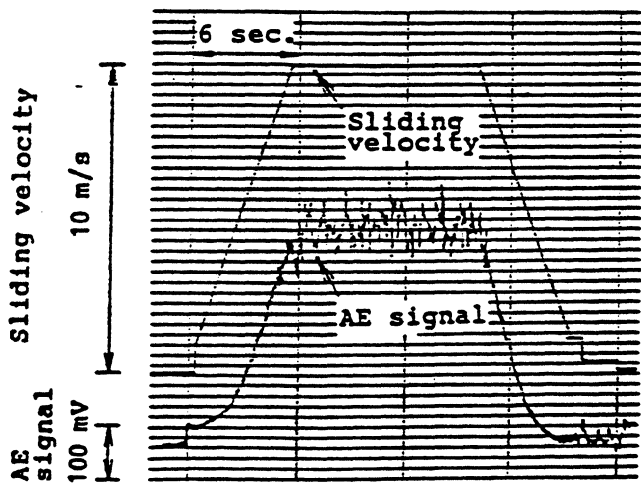
Sliding velocity is obtained from disk revolution signals which are generated every rotation. AE signal fluctuates during the positioning of the disk to the starting point. The following was found from the measurements of AE signal: fluctuation level of AE signals during a CSS cycle is smaller than that during the positioning of the disk at a slow speed. The AE signal level increases rapidly just before a disk failure occurs.



(a) 1 cycle of CSS



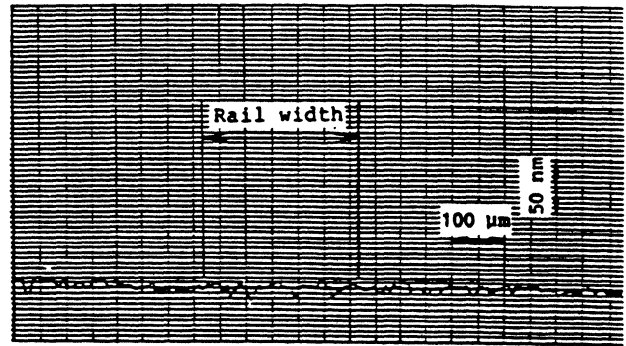
(b) Normalized CSS cycle, 0.92



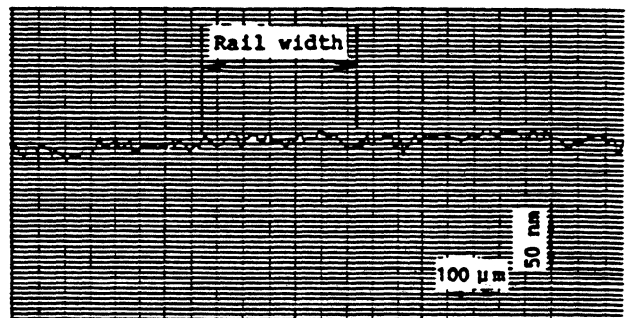
(c) Normalized CSS cycle, 0.95

Fig. 4—Typical AE signals as a function of CSS cycles

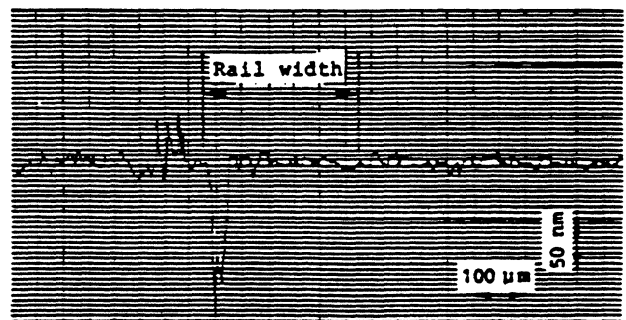
Figure 5 shows surface profiles of tested disks at the same normalized CSS cycles as those in Fig. 4. Surface profile fluctuates within the resolution of a surface profilometer



(a) 1 cycle of CSS



(b) Normalized CSS cycle, 0.92



(c) Normalized CSS cycle, 0.95

Fig. 5—Surface profile of tested disk

(3 nm) as shown in Fig. 5. Clear wear trace could not be detected below the normalized CSS cycles of 0.92.

The width of the deep scratch is about 50 μm ; that is one-order narrower than the width of the slider. The depth of the deep scratch measured at the normalized CSS cycles of 0.95 reaches to more than 0.1 μm , and wear debris deposits on the disk (left side of the deep scratch).

These results lead to the following conclusions: wear of carbon is negligibly small during a CSS test under the condition that relative humidity is comparatively low and slider stiction does not occur. Furthermore from Figs. 4 and 5, the disk failure occurs abruptly.

Macro Observation of Slider and Disk Surface

Slider Surface

Figure 6 is a scanning electron micrograph of a slider surface and its surface profile after the normalized CSS cycles of 0.15. Clear scratches or severely worn portions are

not observed, but some parts of the surface are coated with adhered material. Thickness of the adhered material is less than 5 nm from the measurement of surface profile shown in Fig. 6. The thickness of the adhered material is the same order as the surface roughness of the disk and smaller than the depth of the deep scratch. The adhered material may consist mainly of carbon detached from the disk.

From these results, it is difficult to consider that adhered material on the slider (shown in Fig. 6) scratches the disk surface and produces a deep valley as designated in Fig. 5(c).

Disk Surface

Figure 7 shows scanning electron micrographs of a failed disk surface at the rise time of 6 s (a) and 24 s (b). An arrow indicates the rotational direction of the disk.

The width of the deep scratch is about 30–40 μm and is small compared with the slider width. These deep scratches were observed within the sliding track.

Edge and bottom portion of the deep scratch for a rise time of 6 s is very similar to that for 24 s:

1. Many small cracks are observed at the boundary of the non-defect and deep scratch zones. These cracks seem to be separated from the edge of the deep scratch.
2. Scratched and flaked traces are observed at the bottom of the deep scratch.

Accordingly, the disk failure occurs by the same mechanisms for the rise times of 6 to 24 s. The failed disks at a rise time of 6 s are observed in detail in the following sections.

Micro Observation of Failed Disks

Surface Cracks

Figure 8 shows a scanning electron micrograph of a failed

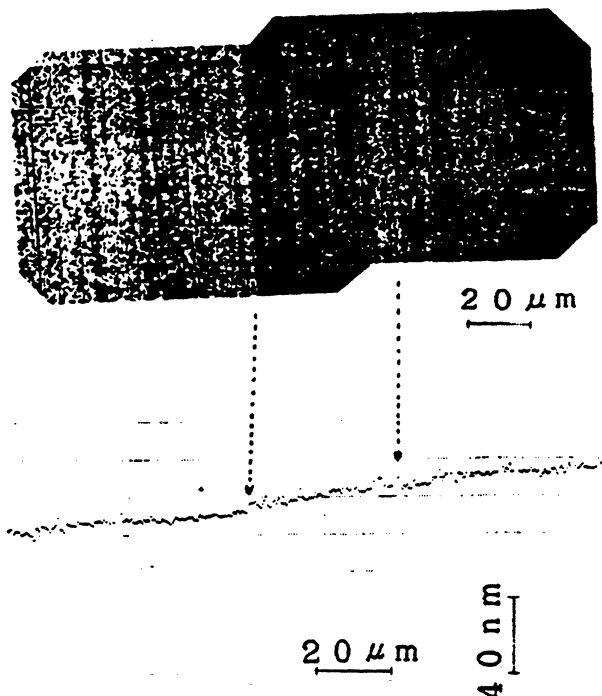


Fig. 6—Scanning electron micrograph of slider surface and its surface profile.

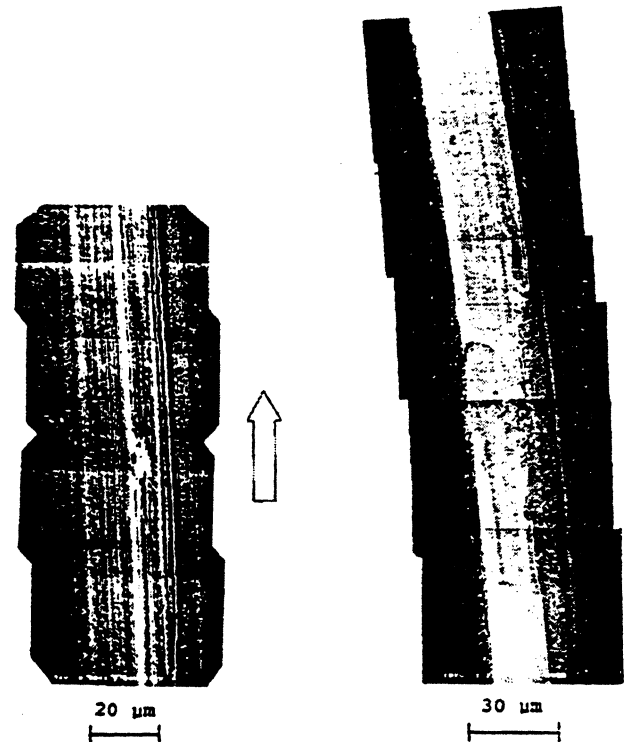


Fig. 7—Scanning electron micrograph of failed disk surface.
(a) Rise time of 6 s
(b) Rise time of 24 s

disk surface enlarged at the edge portion of the deep scratch at the rise time of 6 s. Parallel small cracks are observed just separated from the deep scratch. Paying attention to the parallel cracks, the following 4 regions are defined: Region I is the failed region, regions II and IV are the non-damaged region, and region III is the region that contains parallel cracks at about 2 μm from the edge of the deep scratch.

Parallel cracks are about 4 μm in length and some cracks join each other in region III. The angle between the parallel cracks and slider rotating direction is about 45 degrees. Although similar cracks to the parallel cracks are observed at region I, these were not frequently detected at region III because of plastic flow caused by the scratch traces. The crack length at region I is about 20 μm , and cracks at region I are roughly parallel to those at region III.

Auger spectra from the failed disk are also shown in Figs. 8(b) and (c). Figs. 8(b) and (c) were obtained from point A of region IV and point B of region I, respectively.

Only carbon was detected from region IV from Fig. 8(b). On the other hand, cobalt and chromium were detected from region I. This means that the deep scratch reaches the Co-Cr layer at point B. Carbon is still detected at point B. The following factors are considered in realizing that carbon was detected from region IV: Wear debris consisting of carbon and Co-Cr scratch the disk surface. Part of the wear debris may adhere to a disk, and then carbon is detected from the adhesive wear debris.

Subsurface Cracks

SEM observations in the preceding section suggest that the cracks observed in both regions I and III occur by the same mechanism. Therefore, extensions of the cracks, which

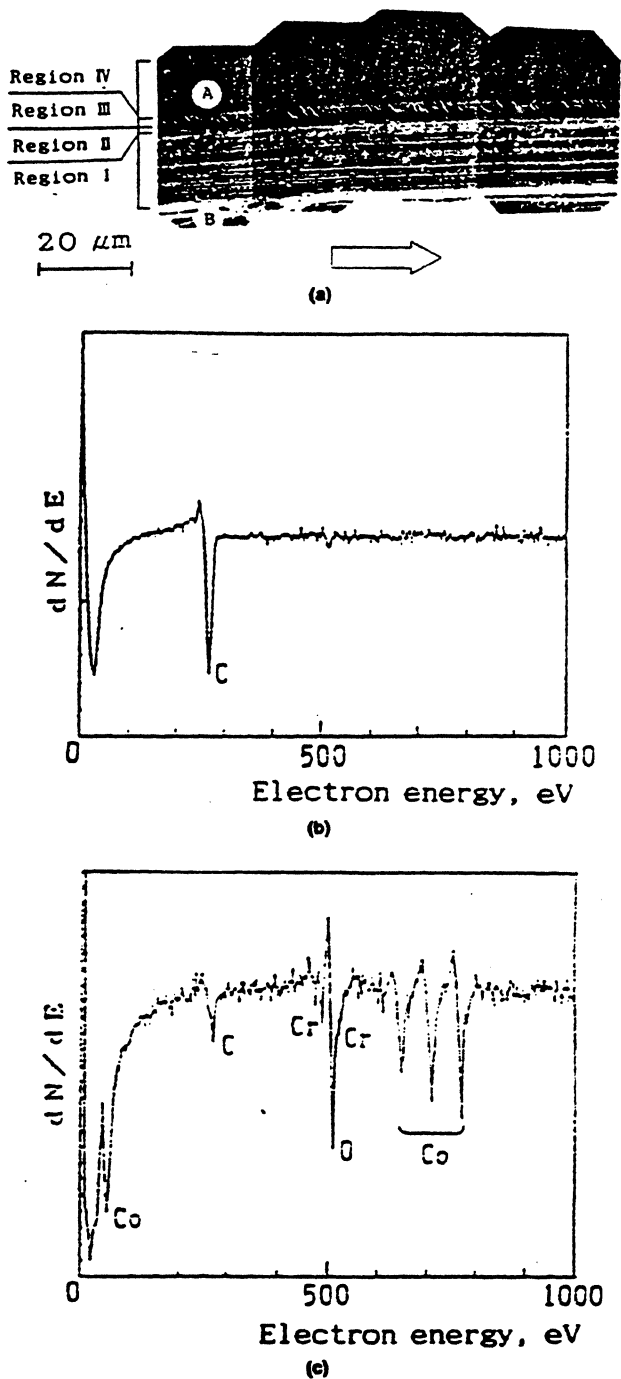


Fig. 8—Scanning electron micrograph and Auger spectra from failed disk.
 (a) Scanning electron micrograph of a failed disk enlarged at the edge portion of the deep scratch shown in Fig. 7(a)
 (b) Auger spectrum at point A in Fig. 8(a)
 (c) Auger spectrum at point B in Fig. 8(a)

were observed in both regions I and III, were investigated at the subsurface of the disk. Failed disks were sputter-etched by Ar to the following depths; (a) the boundary between the carbon and Co-Cr layer, (b) approximately the middle of the Co-Cr layer, (c) the boundary between the Co-Cr and permalloy layer, (d) approximately the middle of the permalloy layer, (e) the boundary between the permalloy and Ni-P layer.

Etched surfaces were observed with SEM at every etching stage as shown in Figs. 9(a)–(e), respectively. Etching depth was estimated by monitoring the Auger spectrum at point A in Fig. 8. Region I is etched to the Co-Cr layer at both Figs. 9(a) and (b), etched to the permalloy layer at both Figs. 9(c) and (d), and etched to the Ni-P layer at Fig. 9(e). Regions I to IV shown in Fig. 9 correspond to those in Fig. 8. From Fig. 9(a), cracks are observed only at regions I and III and not observed at region II near the boundary between the carbon and Co-Cr layer.

On the other hand, cracks are observed at region II when the disk is etched to the Co-Cr layer through the boundary between the Co-Cr and permalloy layer. A continuous crack is observed from region I to III and its length reaches about 30 μm .

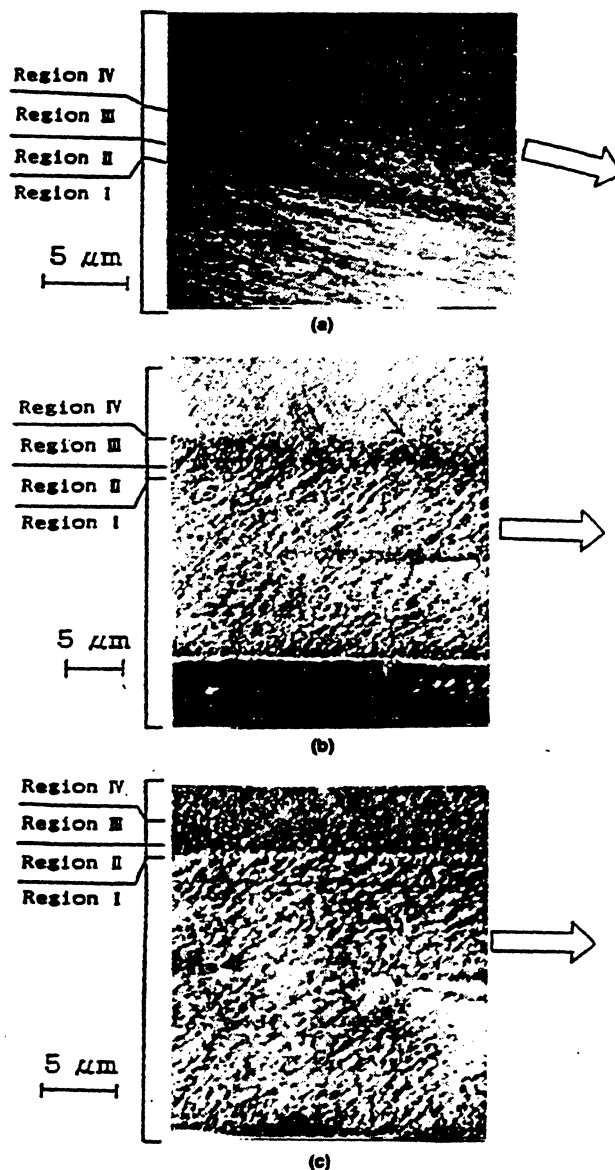


Fig. 9—Scanning electron micrographs of a failed disk after etching;
 (a) Boundary between carbon and Co-Cr
 (b) Approximately the middle of Co-Cr
 (c) Boundary between Co-Cr and permalloy

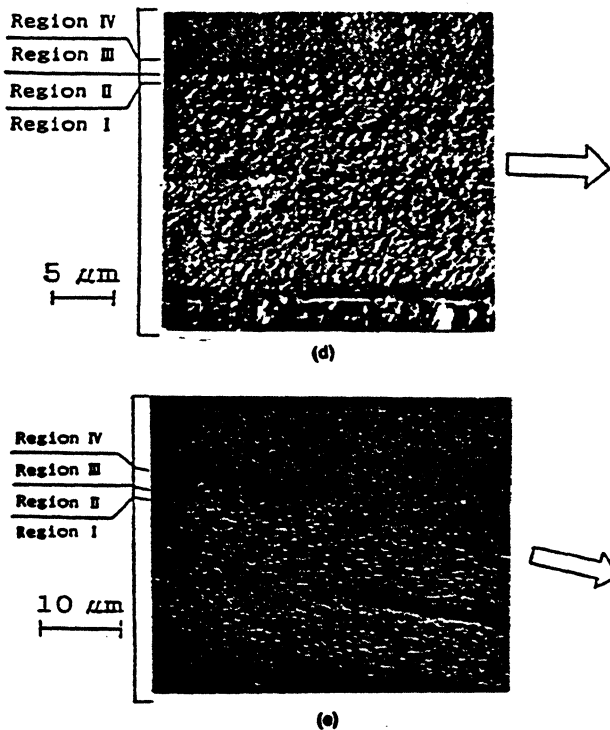


Fig. 9—continued

- (d) Approximately the middle of permalloy
 (e) Boundary between permalloy and Ni-P

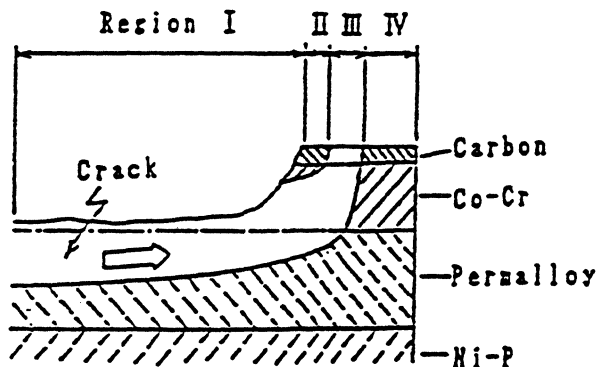


Fig. 10—Schematic diagram of crack propagation

When the etching proceeds to the permalloy layer as shown in Fig. 9(d), previous cracks are observed only at regions I and II, and not observed at region III. Etching further to the boundary between the permalloy and Ni-P layer, previous cracks are not observed as shown in Fig. 9(e). From these results, the cracks are found to extend beneath the deep scratch. Cracks reach the surface at the outer edge of the deep scratch and also propagate along the thickness direction to the permalloy layer beneath the deep scratch.

In comparison with Figs. 9(a) and (b), the micrographs' contrast of region III near the boundary between the carbon and Co-Cr layer is different from that of regions II and IV. On the contrary, the difference in micrographs' contrast is not observed at the Co-Cr layer. The same phenomena are found in Figs. 9(c) and (d) that the contrast of regions II and III is different from that of region IV at the boundary

between the Co-Cr and permalloy layers. Clear contrast is not observed at the permalloy layer. It is known that contrast irregularity of SEM photographs means the differences in elements and/or surface roughnesses.

These results suggest that defects occur at boundaries of the cracked region.

Generation Mechanism of Subsurface Cracks

The area that contains the crack at the etched disk is schematically illustrated in Fig. 10. Observation results of crack existence area at regions II and III reveal that the crack extends obliquely in the depth direction. Normal and traction load act on a disk from the slider. The extension of a circular subsurface crack under normal and traction loads has been investigated analytically with a fracture mechanics approach (6): The circular subsurface crack propagates mainly Mode 2 under the repeated loading, and the leading crack tip extends toward the surface. The crack propagation pattern at regions II and III shown in Fig. 10 is similar to that of the leading crack tip. Therefore, subsurface cracks seem to extend first along the extended plane of the crack face (region I) and then extend toward the surface (regions II and III).

Figure 11(a) shows the scanning electron microphotograph of another type of disk failure considered to be caused by flaking, and a surface profile is also recorded in Fig. 11(b). It is found from Figs. 11(a) and (b) that the depth of the deep scratch is $0.4 \mu\text{m}$, that the bottom profile of the deep scratch is nearly flat, and that the wear debris scratches the disk. A different defect is observed at the right side of the deep scratch. The surface profile indicates that a lump of wear debris falls off the disk. The fallen wear debris penetrates between slider and disk, and adheres to the disk pressed with the slider. The height of adhered material is higher than the flying height of the slider, and this kind of surface damage leads to a head crash.

From these results, it is considered that such disk failure as pitting or flaking occurs abruptly when the fatigue crack reaches the surface, or the fatigue crack extends along the extended plane of the crack face.

Effect of Rise Time on CSS Lifetime

Figure 12 shows the relationship between normalized CSS cycle to failure and rise time of disk. From Fig. 12, CSS lifetime is found to decrease with an increase in the rise time of disk.

The following two factors acting on the disk must be considered at the start of the disk; static friction coefficient between the slider and disk, and dynamic load factor (DLF) of the slider which gives the maximum spring reactive force under the dynamic condition defined by the disturbance (7).

Friction coefficient μ is the largest at the start, and DLF decreases with an increase in the rise times. If the dynamic load at starting is dominant for a disk failure, CSS lifetime would almost be constant. This does not agree with the experimental results shown in Fig. 12. If repeated rubbing is dominant for disk failure, CSS lifetime would decrease with an increase in the rise time. It would be obvious that when a rise time is long, the disk surface undergoes re-

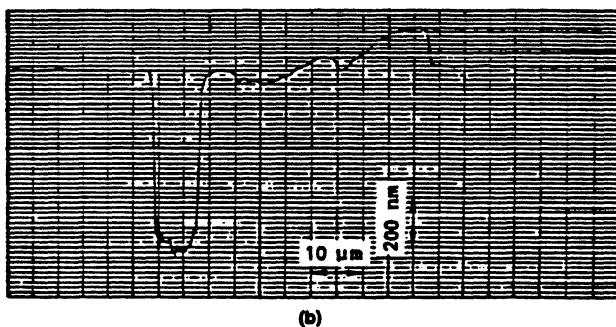
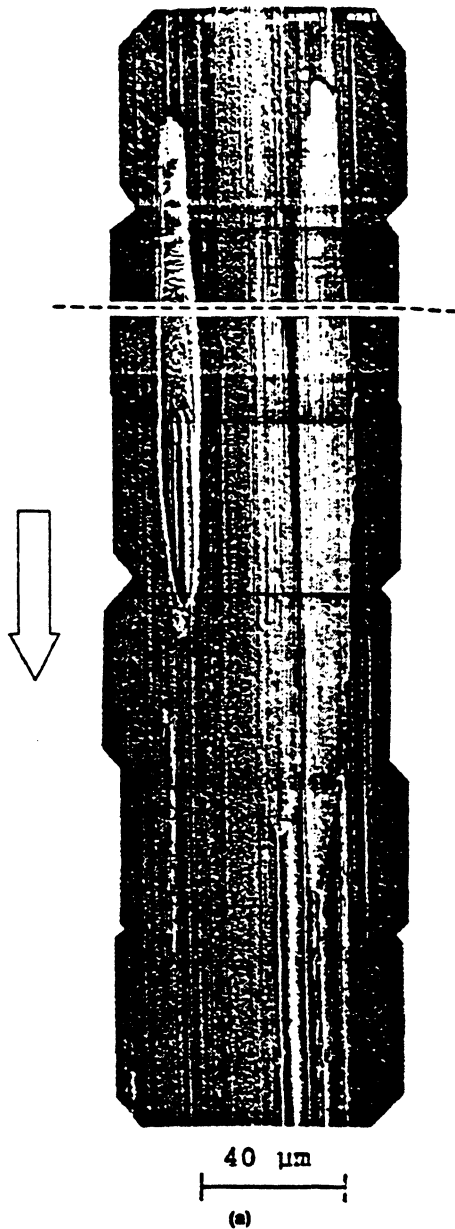


Fig. 11—Flaking failure and its surface profile.
(a) Entire view of the failure
(b) Surface profile

peated rubbing by many times. Therefore, it is mentioned that the effect of cyclic friction force is greater than that of the number of CSS on propagating fatigue cracks.

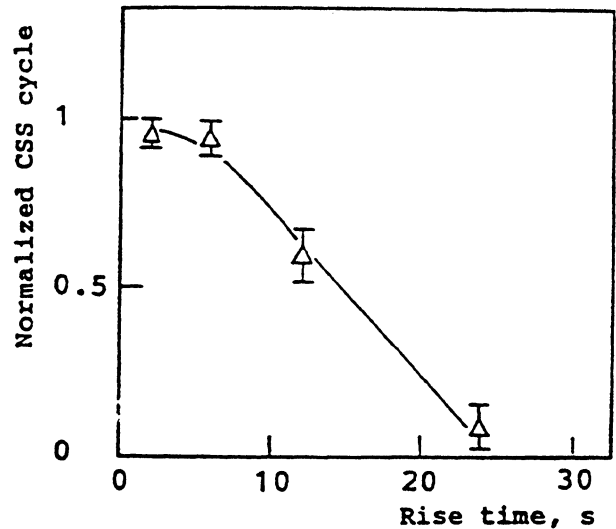


Fig. 12—Relationship between CSS cycles to failure and rise time of disk

CONCLUSIONS

The failure mechanism of carbon-coated hard disks during CSS tests was investigated experimentally. From these investigations, the following conclusions were made:

1. Wear of carbon is negligibly small during a CSS test under the conditions of low relative humidity, which decreased suction of the slider.
2. Disk failure occurs abruptly by the following mechanism: Fatigue cracks are produced in the disk with repeated CSS cycles. The cracks extend in-plane and propagate toward the disk surface. When the crack reaches a boundary, the crack extends in both the in-plane direction along the boundary and in the surface direction.
3. Flaking occurs abruptly when the crack reaches the surface, or extends long enough along the extended plane of the crack face.
4. CSS lifetime decreases with an increase in the rise time. This means that, to propagate the crack, cyclic load caused by the glide of a slider is more dominant than forces acting at the start.

REFERENCES

- (1) Mallinson, J. C., "The Next Decade in Magnetic Recording," *IEEE Trans. Mag. Mag-21*, pp 1217-1220 (1985).
- (2) Yanagisawa, M., "Lubricating on Plated Magnetic Recording Disks," *ASLE SP-19*, pp 16-20 (1985).
- (3) Hu, Y. and Talke, F. E., "A Study of Lubricant Loss in the Rail of a Magnetic Recording Slider Using Ellipsometry," *Tribology and Mechanics of Magnetic Storage Systems, V, STLE SP-25*, pp 43-48 (1988).
- (4) Duan, T. Q. and Mackintosh, N. D., "The Frictional Behavior of Rigid-Disk Carbon Overcoats," *Tribology and Mechanics of Magnetic Storage System, 5, STLE, SP-25*, pp 6-11 (1988).
- (5) Timsit, R. S. and Stratford, G., "Effect of Humidity on Friction at Magnetic-Head/Hard-disk Interfaces," *Tribology and Mechanics of Magnetic Storage System, 5, STLE, SP-25*, pp 17-23 (1988).
- (6) Kaneta, M. et al., "Growth Mechanism of Subsurface Crack Due to Hertzian Contact," *Trans. ASME, J. Tribol.*, 108, pp 134-139 (1986).
- (7) Harris, C. M. and Crede, C. E., *Shock and Vibration Handbook*, Second Edition, McGraw-Hill, 42-12 (1976).

Adsorption of Perfluoro-Polyethers on Carbon Surfaces[©]

M. YANAGISAWA
NEC Corporation
Kawasaki 216 Japan

In order to further the ability to design tribologically reliable disk media, fundamental properties of adsorption, interaction between lubricant and overcoats and mobility of adsorbed lubricants were investigated for perfluorinated polyether (PFPE) lubricants on carbon surfaces. A variety of oxygen-containing functional groups and unpaired electrons, i.e. dangling bonds, were detected on carbon surfaces. These dangling bonds were found to be the effective adsorption sites for PFPE lubricants. Intra-molecular mobility for a PFPE diol on an amorphous carbon surface was studied using nuclear magnetic resonance (NMR). Thin film viscosities for molecular segments were derived from relaxation time. The viscosity near the hydroxyl segment was determined to be 6.3 times as large as that for a bulk lubricant at 20°C. However, the mobility for the segments in a main chain was found to be similar to that for liquid PFPE. The magnitude of the interaction, evaluated by heat of adsorption, increases with an increasing density of dangling bonds and with an increasing hydrophilic affinity for functional groups in lubricants.

KEY WORDS

Carbon, Magnetic Data Storage, Surface Films, Lubricant Analytical Techniques

INTRODUCTION

Maintaining the current industry trend in recording density improvement will require continued reduction in head/media separation. Decreased head/media separation places progressively more severe constraints on the boundary lubrication system. It is therefore essential to the development of an improved fundamental understanding of the behavior of lubricant molecules in the head/media interface in order to maintain the reliability of future magnetic disk systems. Achieving an appropriate molecular design, based on the

molecular conformation, interaction with slider and overcoat surfaces, and an understanding of the boundary lubrication mechanism, is a systematic way to reach the goal.

Previous work reported the static and dynamic conformations of adsorbed PFPE derivatives on plated magnetic disks overcoated with Sol-gel SiO₂ (1), (2) referenced to basic data for bulk lubricants. For example, PFPE with hydroxyl groups (PFPE diol) adsorbs to silanol groups on the sol-gel SiO₂ surface through hydroxyl groups. Main chains in PFPE diol molecules orient parallel to the overcoat surface. Changes in frequencies and relative intensities of IR peaks with film thickness suggested that the conformation of PFPE derivatives on SiO₂ surfaces is unlike bulk conformation, with polymer chains extended preferentially along the surface (3). Studies of the molecular conformation of lubricants on carbon surfaces of sputtered disks by STM (4) and IR (5) report that a benzene ring in PFPE lubricants with phenoxy or piperonyl groups interacts with the carbon surface. However, adsorption sites on the carbon surface have not been identified.

Dynamic behavior for molecularly thin lubricants, particularly, a film viscosity, are interesting and important issues in investigating replenishment mechanisms (6)-(8), spin-off calculations (9), (10) or boundary lubrication mechanisms. Several methods for measuring thin film viscosity have been reported. For example, the surface diffusion for PFPE on a magnetic disk surface was measured by an ellipsometry (11), (12). Shearing stress and a shear rate for a PFPE film between mica surfaces were measured by interferometry (13). The report suggested that the effective viscosities of PFPE films with several nonometers in thickness was several orders of magnitude larger than their corresponding bulk values. Therefore, the film viscosity on the disk surface can be different than that for intermediate lubricants located between the head and the disk surfaces. Furthermore, there has been no report published on the molecular mobility of PFPE lubricant for intra-molecular segments.

Structural and mechanical properties of carbon films determined by various measurement methods have been reported (14), (15). A variety of functional groups has been determined to exist on carbon surfaces (16). However, there

Presented as a Society of Tribologists and Lubrication Engineers paper at the ASME/STLE Tribology Conference in Lehigh, PA, October 14-20, 1994
Final manuscript approved August 8, 1994

have been no reports specifying which functional group is the effective adsorption site for PFPE lubricant molecules.

This study reports on adsorption sites of carbon surfaces, adsorption energy between carbon surfaces and lubricant molecules, and intra-molecular mobility for thin PFPE lubricant layers on disk surfaces through various analytical measurements.

EXPERIMENTAL

The primary lubricant investigated in this work was perfluoropolyether with hydroxyl groups (PFPE diol):



The average molecular weight and viscosity of PFPE diol are 2000 and 0.96 cm²/s at 20°C, respectively.

In addition to PFPE diol, several other PFPE derivatives, such as nonfunctional group, ester, and piperonyl, are examined for an interaction energy to carbon surfaces.

Various carbon surfaces from graphite to diamond were prepared for adsorbent in order to evaluate adsorption sites. Graphite and diamond powders have pure sp² and sp³ structures, respectively. CVD carbon powder, prepared by grinding a chemically vapor-deposited carbon target for sputtering, shows high graphitic structure, as shown in Fig. 1(a). Amorphous carbon powder was prepared through carbonizing by baking resin powders at 800°C. The amorphous carbon powder has mixed structures with sp² and sp³. G band and D band in Raman spectrum of the amorphous carbon are similar to those of sputtered carbon, as shown in Fig. 1(b). Sputtered carbon powder was prepared by collecting from sputtering chambers, in which carbon films had been deposited without hydrogen gas. The conventional BET method was applied to measure a specific surface area of the carbon powders.

Lubricants were coated on the carbon surfaces by mixing the carbon powders with PFPE lubricant solution, whose concentration corresponds to desired thickness. The lubricant solution was prepared by dissolving PFPE diol into 1,1,2-trichloro-1,2,2-trifluoro ethane solvent. The PFPE lubricant was adsorbed on the carbon surfaces after the solvent was removed in vacuum at room temperature. The thickness of adsorbed lubricants was calculated from the specific surface area of adsorbent and the adsorption quantity, derived from the weight change before and after the adsorption. Neither rinsing nor draining was introduced. There is no excess lubricant in the sample because whole lubricant was coated to a molecularly thin film on carbon powders after the solvent was evaporated.

Functional groups on carbon surfaces were analyzed by X-ray photoelectron spectroscopy (XPS) and electron spin resonance (ESR). Oxygen-containing functional groups such as -COO-, >C=O, →C-O- can be analyzed by C_{1s} spectra. However, spectra of -COO- cannot distinguish between carboxyl (-COOH) and ester (-COOR) groups. Further, spectra of →C-O- cannot distinguish between hydroxyl (→COH) and ether (→C-O-C←) groups. Par-

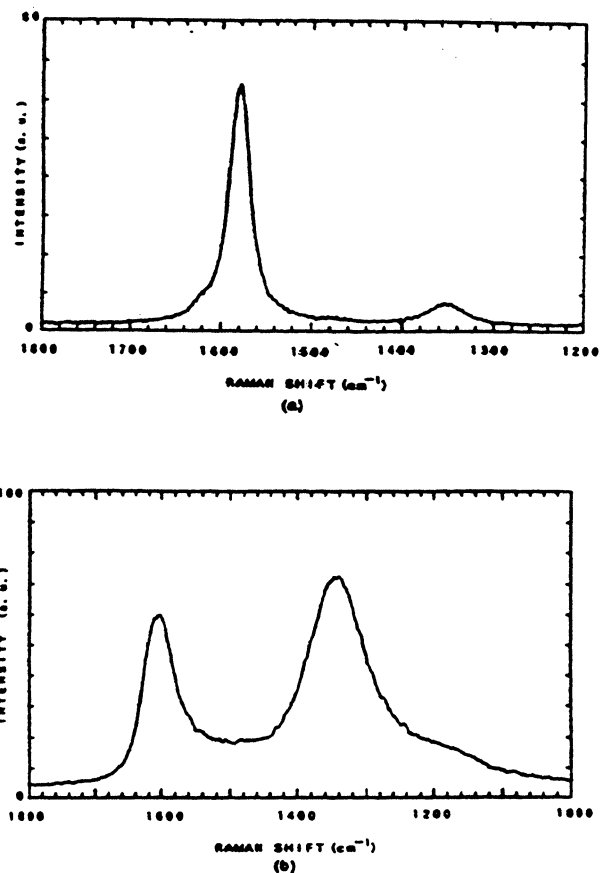
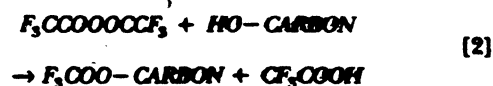
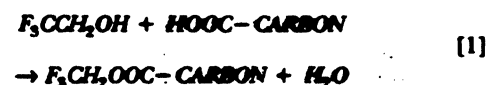


Fig. 1—Raman spectra.
(a) for CVD carbon
(b) for amorphous carbon

ticularly, carboxylic and hydroxyl groups should be noticed because they show so strong affinity as major adsorption sites.

The chemical modification method (17), (18) is applied to identify carboxylic and hydroxyl groups from XPS spectra. When a carbon surface is exposed in trifluoro-ethanol (TFE) and trifluoro-acetic anhydride (TFAA) vapor, the TFE or the TFAA alternatively react with the carboxyl group or the hydroxyl group on the carbon surface, respectively, as shown in the following chemical reactions.



Reaction rate (modification rate) is derived from standard surfaces, polyacrylic acid (PAA) and polyvinyl alcohol (PVA). The carboxyl group and the hydroxyl group on carbon surfaces are quantitatively analyzed from the reaction rates and XPS spectra of chemically modified groups.

ESR spectra were measured to analyze for dangling bonds, considered to be major adsorption sites on carbon surfaces. The ESR spectrometer was used with magnetic fields of 336.5

± 25.0 mT. Mn^{2+} in MgO is used as an external standard material.

Nuclear magnetic resonance (NMR) was used to measure intra-molecular mobility of PFPE lubricants on carbon surfaces. The detail theory for derivation and measurement of lubricant film viscosity from relaxation times of nuclei is described in Ref. (2).

The FT-NMR spectrometer, equipped with a 6.34-T super-conduction magnet, was used with resonance frequency of 270.0 MHz and pulse width of 6μ s. Hexafluoro benzene and tetramethyl silane were used as the standard material for ^{19}F and 1H , respectively. The nuclei, proton (1H) and fluorine (^{19}F), were selected for measurement of the spectra and a spin lattice relaxation time, T_1 . The solid mode NMR was used with the CP-MAS (Cross-Polarization Magic Angle Spinning) technique (19) with MAS rotational speed of 5kHz to measure NMR spectra and T_1 for thin PFPE diol films on carbon surfaces. The molecular mobility at the end groups was obtained through 1H measurement. The molecular mobility at the main chain was obtained from the nuclei ^{19}F . T_1 relaxation times were measured by an inversion recovery method. The magnetization, $-M_0$, inverted by a 180 degree pulse, recovered through the zero-crossing point to the magnetization, $+M_0$, in the thermal equilibrium. The magnetization, $M(t)$, at a certain time, t , is shown as the following equation.

$$M(t) = M_0(1 - 2\exp(-t/T_1)) \quad [3]$$

T_1 is calculated from the slope of $\ln(M(t))$ vs. t diagram, where $M(t)$ is proportional to the intensity of the NMR spectrum. Relaxation times at various temperatures were measured by the time-dependent spectrum intensity, when the temperature of the sample holder was controlled.

The magnitude of adsorption between the carbon surfaces and the lubricants is indicated by the heat of adsorption. The heat of adsorption is measured by the flow micro-calorimeter (1), in which the temperature change, caused by adsorption or desorption, is measured using thermistors. The adsorption occurs in carbon powders of adsorbent when the adsorbate (lubricant) solution is introduced. The desorption occurs, when the carrier flow is switched from adsorbate solution to solvent. The heat of adsorption is defined as the difference between the endotherm value of the adsorption process and the exotherm value of the desorption process.

$$H_{ads} = H_{end} - H_{ex} \quad [4]$$

H_{ads} shows the component of chemisorption in the heat of adsorption.

RESULTS AND DISCUSSION

Interaction between Adsorption Sites on Carbon Surfaces and Lubricant Molecules

Hydrophilic adsorption sites are analyzed by XPS. Figure 2 shows XPS spectra of C_{1s} on the sputtered carbon surface. Peaks, derived from separation, are assigned to conjugated double bonds, $\rightarrow CO-$, $>C=O$, and $-COO-$ from the high

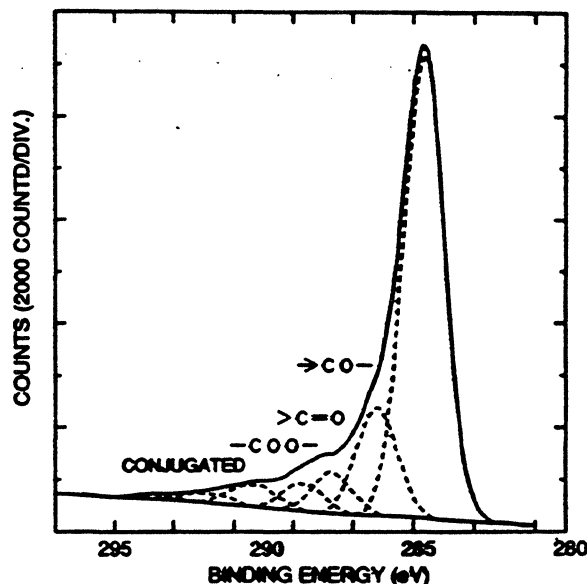
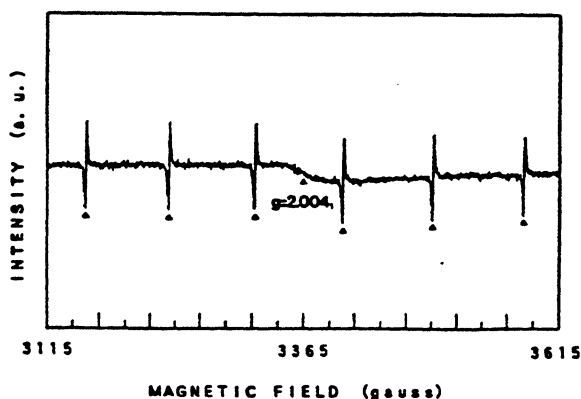
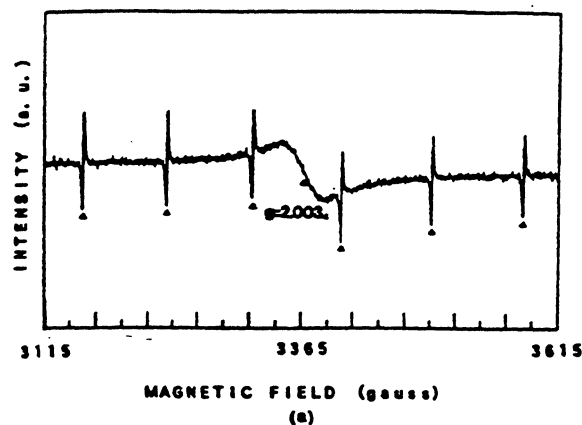


Fig. 2— C_{1s} -XPS spectra for sputtered carbon surface.

TABLE I—FUNCTIONAL GROUPS RATIO TO TOTAL CARBON, ANALYZED BY XPS WITH CHEMICAL MODIFICATION

FUNCTIONAL GROUPS		% OF TOTAL CARBON	INORGANIC CHARACTER NUMBERS
Ether	$\rightarrow C-O-C\leftarrow$	15.7	20
Conjugated	$>C=C-C\leftarrow$	7.0	2
Carbonyl	$>C=O$	6.0	65
Ester	$-COOR$	3.5	60
Carboxyl	$-COOH$	0.5	150
Hydroxyl	$\rightarrow COH$	0.3	100

bonding energy side. Many oxygen-containing functional groups are found on the sputtered carbon surface. Table I shows the ratio of these functional groups to total carbon, measured by the chemical modification method. There are many functional groups such as carbonyls, esters, ethers, or conjugated double bonds, which may show weak bondability. The bondability among themselves is shown by an inorganic character number which is defined in Ref. (20). The inorganic character number shows the relative magnitude of association between functional groups. The distance between the boiling point curve of a methane series hydrocarbons and the curve of saturated, univalent, primary straight-chain alcohol is taken as an inorganic character number of 100. The inorganic character numbers of carboxyl, hydroxyl, carbonyl, ester, and ether, conjugated double bond are 150, 100, 65, 60, 20, and 2, respectively. According to these values, carbonyls, esters, ethers, or conjugated double bonds show weak bondability, compared with hydroxyl or carboxyl groups. If the hydrophilic hydroxyl group is selected for the functional group of PFPE, the inorganic character number is considered to be an appropriate index showing bondability between lubricants and carbon surfaces, although there is no data on



(b)
Electron spin Spectroscopy

Fig. 3—ESR spectra.

(a) for amorphous carbon
(b) for amorphous carbon with PFPE diol lubricant

the inorganic character number between different functional groups.

Table 1 also shows that there is only a small amount, 0.8%, of functional groups such as carboxyl and hydroxyl groups, that are expected to show strong affinity for the lubricant because of their large inorganic character number. Similar results were reported in the previous work (18). Therefore, the functional groups shown in Table 1 may not be major adsorption sites on carbon surfaces. Dangling bonds are expected to be another adsorption site, because unpaired electrons commonly show strong affinity (21).

Figures 3(a) and (b) show ESR spectra of amorphous carbon and amorphous carbon with PFPE diol lubricants. In the figures, Δ indicates peaks of Mn^{2+} , that was used as the standard material. The peaks of approximately g of 2.0, shown by \blacktriangle , show ESR spectra of dangling bonds (22). Peak intensity of the dangling bond decreased after the PFPE diol lubricant was coated. This suggests that dangling bonds are major adsorption sites on carbon surfaces. A fifty percent reduction of dangling bond density is observed, and is shown in Table 2 after a lubricant coating is applied to the carbon surface. The ESR signal also involves dangling bonds in the bulk carbon, not only on the surface of carbon. If the lubricant adsorbs to the dangling bond on the carbon surface, the reduction rate for adsorbed dangling bond to the unad-

SAMPLE	g	SPIN DENSITY (g^{-1})
Amorphous Carbon	2.003	2.25×10^{19}
Lubricant Coated	2.004	1.09×10^{19}

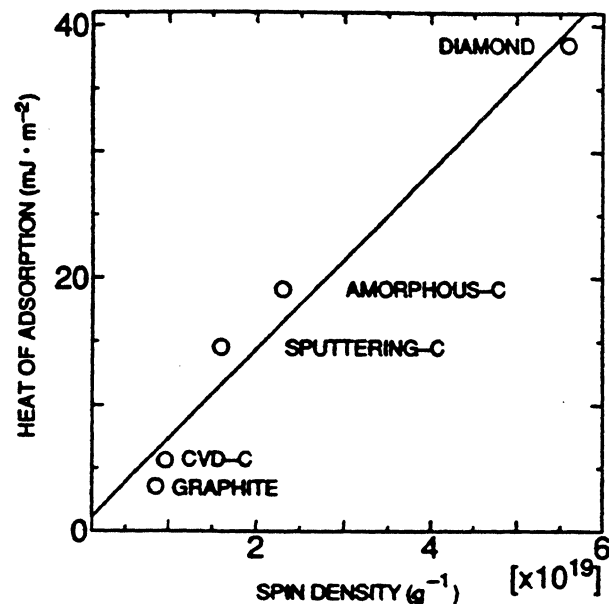


Fig. 4—Relation between heat of adsorption for PFPE diol and dangling bond density of carbon.

sorbed bond on the surface can be greater than the observed reduction rate in Fig. 3.

Relation between heat of adsorption, representing adsorption energy for PFPE diol, and spin density, representing amount of dangling bonds, is shown in Fig. 4. Heat of adsorption increases with increasing spin density. The correlation between the heat of adsorption and spin density shows that the graphite or the CVD carbon with sp^2 bond structure does not contribute to the adsorption of lubricants. Conversely, the sp^3 bond, involved in diamond, shows the heat of adsorption. When a bond dissociation occurs at the surface or in grain boundaries or dislocations, dangling bonds easily appear in sp^3 structures. However, the sp^2 structure does not create dangling bonds, because unsaturated bonds with π electrons are easy to rejoin after bond dissociations. Polycrystalline diamond, prepared in this study, can involve many dangling bonds on surface dislocations or in grain boundaries.

A question arises why dangling bonds are not saturated by hydrogen or contaminants. Some reports (23), (24) said that dangling bonds in carbon are relatively stable compared with silicon. Hydrogenated carbon film even contains dangling bonds (24), (25). Dangling bonds are not saturated by hydrogen because, different from the case of silicon, carbon shows an allotropic nature, i.e. the presence of unsaturated sp^3 bonding states, requiring incorporated hydrogen not only to passify the dangling bond but also to saturate the sp^2

graphite bonds (14). Even if the carbon is hydrogenated, the spin density of unpaired electrons in the hydrogenated carbon is found to decrease from 10^{16} to 10^{16} cm^{-3} by hydrogenation (25), but whole unpaired spins are not saturated by hydrogen. Further, there is no evidence that dangling bonds are satisfied by chemisorption. Carbon-hydrogen bonds are not observed on amorphous carbon by diffuse reflection FT-IR or $^1\text{H-NMR}$ within their resolution. The activity of dangling bonds remains even if water or other hydrogen-containing contaminants are adsorbed, because they are not chemically bonded, but physically adsorbed, i.e. covalent bonds between carbon and hydrogen are not formed.

In the case of diamond, Refs. (26)–(28) suggest that polished surfaces of single crystal diamond are hydrogenated (29), which could be formed by tribochemical reaction through polishing and following washing with hydrogen containing solvent, such as acetone (30) or olive oil (27). However, artificially synthesized diamond powder with a polycrystalline structure, used in the present report, has a history of neither mechanical polishing nor washing. Many dangling bonds can exist on polycrystalline diamond, because it can involve many defects or dislocations in grain boundaries. Further, there is no evidence of hydrogen-carbon bonding on diamond powder from NMR and diffuse reflection FT-IR within their resolution.

Intra-molecular Mobility of PFPE Molecule Adsorbed on Carbon Surfaces

Figure 5 shows $^1\text{H-NMR}$ spectra of PFPE diol liquid, amorphous carbon, and amorphous carbon with PFPE diol thin film as a function of PFPE diol thickness. The peaks, assigned to $\text{OCF}_2\text{CH}_2\text{OH}$ and $\text{OCF}_2\text{CH}_2\text{OH}^*$, are shifted to the lower magnetic field and are broadened with decreasing thickness. This may occur because an association between hydroxyl groups in diol molecules decreases and an interaction between hydroxyl groups and functional groups on carbon surfaces increases. A peak near 0.5 ppm in the spectrum for 0 nm is believed to be adsorbed water, because there is no proton on the carbon surface except water, according to diffuse reflection infrared (IR) spectroscopy, and the peak disappears by baking at 150°C . The rightward shift, i.e. toward the high magnetic field, of the water peak with increasing lubricant thickness saturating for a 0.7 nm thick diol film implies that the water interacts with lubricant molecules. The saturation at 0.7 nm may correspond to monolayer coverage, since the lubricant molecule is approximately 0.6 nm in size. Further, the rightward shift reveals that the bonding strength is weakened. For example, an inter-molecular interaction between water and adsorption site on the carbon surface can be weakened with adsorption of lubricant molecules. The proton in the weakly-bonded water molecule shows higher electron density than that of the strongly adsorbed water molecule, because electrons, used for the bonding, are concentrated around the proton nucleus. The bonding state is observed in NMR spectra because chemical shift is affected by electron density around the nucleus. High electron density requires high external magnetic field to interact with nuclear magnetic moment because the electron clouds shield the external magnetic field.

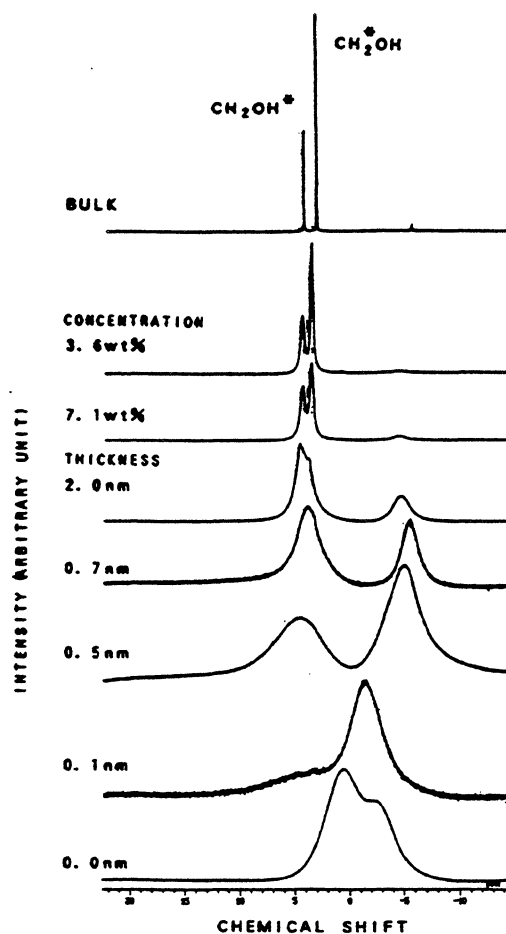


Fig. 5— $^1\text{H-NMR}$ spectra for PFPE diol liquid, amorphous carbon, and amorphous carbon with PFPE diol thin film, as a function of PFPE diol thickness.

Figure 6 shows $^{19}\text{F-NMR}$ spectra as a function of PFPE diol thickness. Three peaks, assigned to OCF_2 (-55.3 ppm, -53.6 ppm, and -52.0 ppm), $\text{OCF}_2\text{CH}_2\text{OH}$ (-83.2 ppm and -81.1 ppm), and OCF_2CF_2 (-90.6 ppm and -89.0 ppm), are slightly shifted to the lower magnetic field and are broadened with decreasing thickness. This indicates little interaction between ether groups and the carbon surface.

Peak width of NMR spectra increases with decreasing thickness of lubricant, because the mobility of lubricant molecules decreases. An error can be introduced when relaxation times are measured, because peak separation becomes difficult. In order to improve the peak separation, solid mode NMR was used. Different from liquid mode NMR, the solid mode NMR with CP-MAS (Cross-Polarization Magic Angle Spinning) technique shows a potential to obtain sharp NMR spectra of thin PFPE diol film on carbon surfaces, as shown in Fig. 7. The peaks of OH and CH_2 for PFPE diol film are clearly separated by the solid mode NMR (b), compared with the liquid mode (a).

Figure 8 shows the relation between the ratio of the film viscosity (ν_f) for the diol at the thickness of 0.5 nm, reduced from the relaxation time (T_1)_f to the bulk viscosity (ν_b) and the measurement temperature for the ^1H in the segments OH and CH_2 , and for the ^{19}F in the segments OCF_2 and

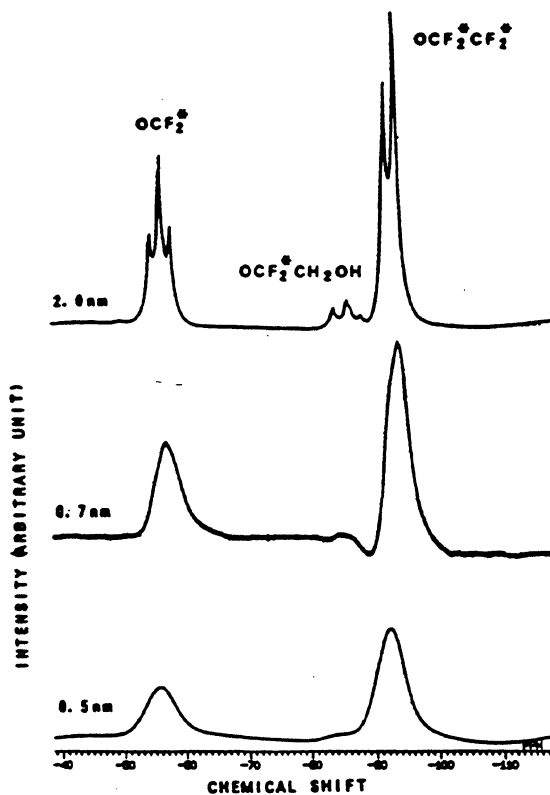


Fig. 6— ^{19}F -NMR spectra as a function of PFPE diol thickness.

OCF_2CF_2 . Thermal mobility of molecules usually increases with increasing temperature. A gradient of the molecular mobility for the temperature is affected by the magnitude of bonding, namely inter-molecular bonding between lubricant molecules or between lubricant molecules and functional groups on carbon surfaces. Since the molecular mobility of functional groups on solid surfaces is very small, the mobility of lubricant molecules which interact with carbon surfaces becomes small in comparison with that for liquid lubricant molecules. Therefore, the gradient of the ratio (v_f/v_b) for the temperature can show the relative magnitude of molecular mobility for bonded lubricant as a function of temperature. The ratio (v_f/v_b) for the proton segment increases with increasing temperature. This occurs because the molecular mobility for the bulk lubricant becomes thermally active because of the three dimensional degree of freedom, whereas adsorbed segments do not show active movement because of restriction to the carbon surface. Generally speaking, the v_f/v_b for the ^1H segment, OCF_2CF_2 , and OCF_2 increases in order. This order may stand for the magnitude of bondability of every segment to carbon surface. Specifically speaking, the molecular mobility becomes small when bonding strength is large. The large viscosity ratio (v_f/v_b) and the large gradient of the ratio for temperatures basically shows that lubricant molecules are bound to the carbon surface more tightly than the bonding among molecules. Since the OH group is the adsorption site itself, the maximum ratio and gradient are observed. The molecular mobility for the CH_2 segment is affected by that of the OH segment, because the proton in CH_2 locates in the neighbored position to OH.

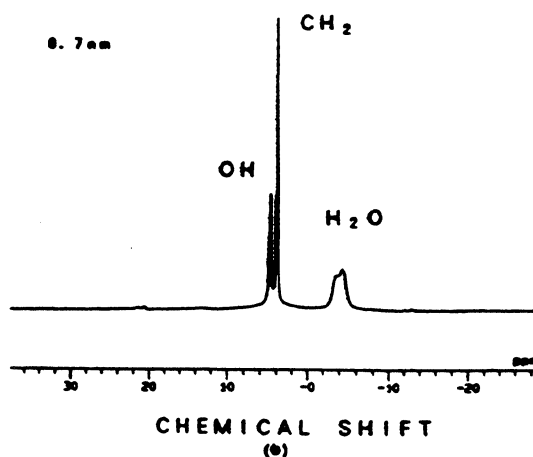
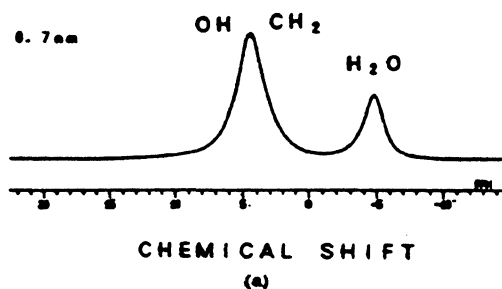


Fig. 7— ^1H -NMR spectra for PFPE diol film at thickness of 0.5 nm on amorphous carbon.

(a) liquid mode
(b) solid mode

Therefore, the viscosity ratio and gradient for the CH_2 segment are in second order. The viscosity ratio (v_f/v_b) for the segment OCF_2 and OCF_2CF_2 for thin diol film is almost the same as that for the bulk diol, because the fluorine atom in the OCF_2 segment is surrounded by the ether group ($-\text{O}-$) with large mobility. Exactly speaking, the ratio (v_f/v_b) for the ^{19}F segments seems to slightly decrease with increasing temperature. This may occur because the molecular mobility, particularly rotational motion, in main chain segments for the bulk lubricant, increases on the carbon surfaces. PFPE molecules in the main chain near 0.5 nm in thickness can be more mobile than bulk molecules when the PFPE film is too thin to form a homogeneous film on the carbon surface. This may be because molecules are isolated from other molecules; therefore, there is little interaction among them.

Figure 9 shows the diagram for the adsorbed diol molecule on the carbon surface at 20°C . The hydroxyl groups interact with functional groups on the carbon surface, where dangling bonds are effective adsorption sites. The attached number at the atoms shows the viscosity ratio, normalized by bulk viscosity. If the minimum mobility in the molecule determines the net viscosity, the film viscosity is 6.3 times greater than for bulk at 20°C . Therefore, the functional groups behave as an anchor. Conversely, segments in the main chain may behave as lubricants with low shearing stress. This ob-

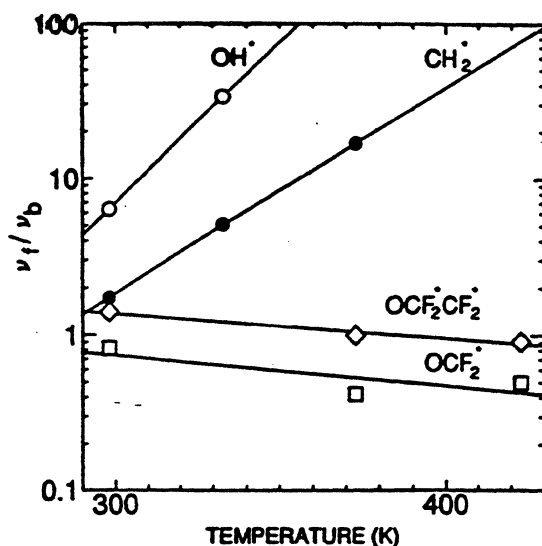


Fig. 8—Relation between the ratio of the film viscosity (ν_f) for the diol at thickness of 0.5 nm, reduced from the relaxation time (T_1), to the bulk viscosity (ν_b) vs. temperature for ^1H in the segments.

servation is important to consider in formulating a boundary lubrication mechanism for functional PFPE lubricants. This result agrees well with the observations of the molecular mobility, made by scanning tunneling microscopy (STM) (4).

Adsorption Energy Between PFPE Lubricants and Carbon Surfaces

The magnitude of interaction between various functional groups and various carbon surfaces is evaluated by heat of adsorption. Table 3 shows heats of adsorption for PFPE with no functional group, ester, piperonyl, and hydroxyl groups to graphite, CVD carbon, sputtered carbon, amorphous carbon, and diamond. The magnitude of heat of adsorption is in the order none < ester < piperonyl < hydroxyl. This order agrees with that of calculated inorganic character numbers, which are 60, 75, and 100 for ester, piperonyl, and hydroxyl, respectively. This suggests that hydrophilic groups adsorb well to dangling bonds. The order is general over five examined carbon materials. This suggests that dangling bonds are effective adsorption sites on carbon surfaces for PFPE derivatives.

It is remarkable that the piperonyl group seems to adsorb to carbons with either sp^2 and sp^3 structure. The first reason is that the heat of adsorption for the piperonyl group with one benzene ring and three ether groups is several times as much as that for the ester group or the nonfunctional group. Exactly speaking, PFPE with no functional group as the end group has ether groups in main chain. The large difference cannot be explained, if ether groups are effective functional group for the adsorption, because an ether group or an ester group shows small heat of adsorption. Therefore, the benzene ring in piperonyl group can be an effective functional group. The second reason is that the ratio of the heat of adsorption for the diamond with 100% sp^3 to that for the graphite with 100% sp^2 is 9.2, 5.8, or 10.8 for the ester group, the piperonyl group or the hydroxyl group, respectively. The ratio for piperonyl is smaller than that for ester and hydroxyl groups.

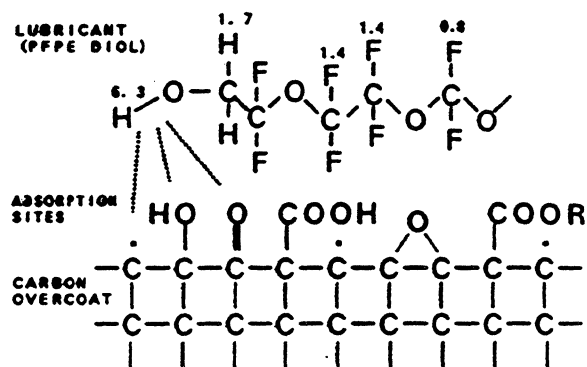
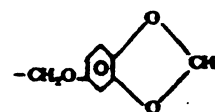


Fig. 9—Diagram for the diol molecules adsorbed on the carbon surface at 28°C.

TABLE 3—HEAT OF ADSORPTION FOR PFPEs WITH VARIOUS FUNCTIONAL GROUPS TO VARIOUS CARBON SURFACES

ADSORBENT (CARBON)	FUNCTIONAL GROUP (PFPE)	HEAT OF ADSORPTION (mj/m ²)
Graphite	No Functional	0.00
CVD Carbon	No Functional	0.01
Sputtered Carbon	No Functional	—
Amorphous Carbon	No Functional	0.05
Diamond	No Functional	0.07
Graphite	Ester	0.06
CVD Carbon	Ester	0.15
Sputtered Carbon	Ester	—
Amorphous Carbon	Ester	0.32
Diamond	Ester	0.55
Graphite	Piperonyl*	0.44
CVD Carbon	Piperonyl*	1.5
Sputtered Carbon	Piperonyl*	—
Amorphous Carbon	Piperonyl*	2.62
Diamond	Piperonyl*	2.57
Graphite	Hydroxyl	3.56
CVD Carbon	Hydroxyl	5.64
Sputtered Carbon	Hydroxyl	14.60
Amorphous Carbon	Hydroxyl	19.14
Diamond	Hydroxyl	38.47

*piperonyl



The ratios demonstrate that the contribution of piperonyl group to the adsorption for graphite with sp^2 is relatively large. As a result, the benzene ring in the piperonyl group shows an affinity to sp^2 carbon. However, its adsorption energy, equivalent to the heat of adsorption, is not so large compared with the hydroxyl group.

CONCLUSIONS

Interaction between various carbon surfaces and PFPE lubricants with various functional groups from a viewpoint of

adsorption sites, molecular conformation, intra-molecular mobility, and molecular adsorption energy. The following conclusions have been reached:

1. Many functional groups are detected on carbon surfaces as adsorption sites; however, the effective adsorption site appears to involve unpaired electrons, namely dangling bonds, because only small amounts of strong hydrophilic functional groups such as hydroxyl and carboxyl, were found on the surface. Secondly, the heat of adsorption was found to increase with increasing dangling bond density. Third, ESR indicated a decrease in dangling bond density with the adsorption of lubricant on the surface.
2. Intra-molecular mobility for PFPE diol molecules on amorphous carbon surface is investigated by NMR. Reduced viscosity near the hydroxyl group of PFPE diol shows 6.3 times greater than the bulk diol at 20°C. Conversely, main chains show almost same mobility as bulk liquid.
3. Adsorption energy between functional groups and carbons increases with increasing hydrophilic affinity of functional groups, namely inorganic character number.

ACKNOWLEDGMENTS

The author wishes to thank S. Esho and K. Tagami, Functional Devices Research Laboratories, for their encouraging support.

REFERENCES

- (1) Yanagisawa, M., "An Adsorption of Perfluoropolyethers on SiO₂ Surfaces for Thin Magnetic Disk Overcoats," in *Tribology and Mechanics of Magnetic Storage Systems*, Vol. 8, STLE, Park Ridge, IL, SP-35, pp 95-101, (1992).
- (2) Yanagisawa, M., "Molecular Dynamics of Thin Lubricant Films on Sol-Gel SiO₂ Surfaces for Thin Film Magnetic Disks," *Triol. Trans.*, **37**, 3, (1994).
- (3) Novotny, V. J., Humala, I., Turllet, J.-M. and Philpott, M. R., "Liquid Polymer Conformation on Solid Surfaces," *Jour. Chem. Phys.*, **90**, 10, pp 5861-5868, (1989).
- (4) Kaneko, R., Oguchi, S., Andoh, Y., Sugimoto, I. and Dekura, T., "Direct Observation of the Configuration, Adsorption, and Mobility of Lubricants by Scanning Tunneling Microscopy," in *Advances in Information Storage Systems*, Vol. 2, Bhushan, B., ed., ASME, New York, (1991), pp 23-34.
- (5) Merchant, K., Mee, P. and Smith, S., "Lubricant Bonding and Orientation on Carbon Coated Media," *IEEE Trans. on Mag.*, **26**, 5, pp 2688-2690, (1990).
- (6) Yanagisawa, M., "Observation of Thickness Profiles on Lubricants during Sliding Tests," *Japs. Jour. Appl. Phys.*, **27**, 9, pp 1609-1611, (1988).
- (7) Novotny, V. J. and Baldwinson, M. A., "Lubricant Dynamics in Sliding and Flying," *Jour. Appl. Phys.*, **70**, 10, pp 5647-5652, (1991).
- (8) Novotny, V. J., Karis, T. E. and Johnson, N. W., "Lubricant Removal, Degradation, and Recovery on Particulate Magnetic Recording Media," *ASME Jour. of Tribol.*, **114**, pp 61-67, (1992).
- (9) Yanagisawa, M., "Slip Effect for Thin Liquid Film on a Rotating Disk," *Jour. Appl. Phys.*, **61**, 3, pp 1034-1037, (1987).
- (10) Yanagisawa, M., "Depletion of Liquid Lubricants on Magnetic Recording Disks," in *Tribology and Mechanics of Magnetic Storage Systems*, Vol. 4, STLE, Park Ridge, IL, SP-22, (1987), pp 93-97.
- (11) Novotny, V. J., "Migration of Liquid Polymers on Solid Surfaces," *Jour. Chem. Phys.*, **92**, pp 3169-3196, (1990).
- (12) Yanagisawa, M., "Surface Migration and Lubrication Characteristics of Liquid Lubricants on Magnetic Thin Film Disks," in *Tribology and Mechanics of Magnetic Storage Systems*, Vol. 7, STLE, Park Ridge, IL, SP-29, (1990), pp 101-106.
- (13) Homola, A. M. and Nguyen, H. V., "Influence of Monomer Architecture on the Shear Properties of Molecularly Thin Polymer Melts," *Jour. Chem. Phys.*, **94**, 3, pp 2346-2351, (1991).
- (14) Tsui, H. and Bogy, D. B., "Critical Review, Characterization of Diamond-Like Carbon Films and Their Application as Overcoats on Thin-Film Media for Magnetic Recording," *Jour. Vac. Sci. Tech.*, **A5**, 6, pp 3287-3312, (1987).
- (15) Tsui, H. and Bogy, D. B., "Structure and Properties of Sputtered Carbon Overcoats on Rigid Magnetic Media Disks," *Jour. Vac. Sci. Tech.*, **A6**, 4, pp 2307-2315, (1988).
- (16) Silva, S. R. P., Amarantunga, A. J. and Constantinou, C. P., "Optical Properties of Amorphous C/Diamond Thin Films," *Jour. Appl. Phys.*, **72**, 3, pp 1149-1153, (1992).
- (17) Nagao, H., Hirai, H. and Yoshino, N., "A New Method of Quantitative Analysis for Estimation of Functional Groups on Carbon Fibers," *Kobunshi Ronbunshu*, **48**, 1, pp 75-77, (1992).
- (18) Barth, G., Corwin, R. D., and Tenley, A., "Characterizing the Surface Chemistry of Magnetic Disk Media through Surface Derivatization," *Solid State Tech.*, p 119, (1989).
- (19) Mehring, M., *High Resolution NMR in Solids*, Springer-Verlag, New York, (1981).
- (20) Fujita, A., "The Prediction of Organic Compounds by a Conceptual Diagram," *Pharm. Bull.*, **2**, 2, p 163, (1954).
- (21) Sanderson, R. T., *Chemical Bonds and Bond Energy*, Academic Press, New York, (1976).
- (22) Miller, D. J. and McKenzie, D. R., "Electron Spin Resonance Study of Amorphous Hydrogenated Carbon Films," *Thin Solid Films*, **108**, pp 257-264, (1983).
- (23) Wada, N., Gaczi, P. J. and Solin, S. A., "Diamond-Like Three-Fold Coordinated Amorphous Carbon," *Jour. Non-Cryst. Solids*, **35**, pp 543-548, (1980).
- (24) Miller, D. J. and McKenzie, D. R., "Electron Spin Resonance Study of Amorphous Hydrogenated Carbon Films," *Thin Solid Films*, **108**, pp 257-264, (1983).
- (25) Jansen, F., Machonkin, M., Kaplan, S. and Hark, S., "The Effects of Hydrogenation on the Properties of Ion Beam Sputter-Deposited Amorphous Carbon," *Jour. Vac. Sci. Tech.*, **A3**, pp 605-609, (1985).
- (26) Vidali, G. and Frankl, D. R., "He-Diamond Interaction Probed by Atom Beam," *Phys. Rev.*, **B27**, pp 2468-2467, (1983).
- (27) Pepper, S. V., "Transformation of the Diamond (110) Surface," *Jour. Vac. Sci. Tech.*, **20**, 2, pp 213-216, (1982).
- (28) Pace, B. B. and Spicer, W. E., "Electronic Structure of the Diamond (111) 1X1 Surface: Valence-Band Structure, Band Bending, and Band Gap States," *Jour. Vac. Sci. Tech.*, **17**, 5, pp 1087-1093, (1980).
- (29) Pace, B. B., Stefan, P. M., Binns, C., Jupiter, P. J., Shek, M. L., Lindau, I. and Spicer, W. E., "Formation of Surface States on the (111) Surface of Diamond," *Jour. Vac. Sci. Tech.*, **19**, 3, (1982).
- (30) Himpsel, F. J., Knapp, J. A., Van Vechten, J. A. and Eastman, D. E., "Quantum Photoyield of Diamond (111)—A Stable Negative-affinity Emitter," *Phys. Rev. B*, **20**, 2, pp 624-627, (1979).

Environmental Effects on Phosphazene Lubricated Thin-Film Disks

Min Yang and Frank E. Talke

Center for Magnetic Recording Research, University of California, San Diego, La Jolla, CA 92093

and

D. J. Perettie, T. A. Morgan and K. K. Kar

The Dow Chemical Company, Central Research and Development, Midland, MI 48674

Abstract—This paper examines the tribological performance of phosphazene lubricated disks under different environmental conditions. Three groups of disks with different lubricant thickness were evaluated. The disks with lubricant thickness of about 0.5 nm showed good tribological performance at ambient, high humidity and elevated temperature conditions.

I. INTRODUCTION

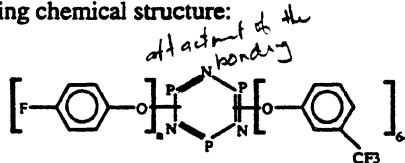
Phosphazene lubricants have recently been investigated as alternative lubricants for computer hard disks due to their extremely low vapor pressure, high thermal stability and good solubility in non-CFC or HFC solvents[1]. In ref. [2], the tribological performance of phosphazene lubricated disks was studied in terms of stiction and friction during contact start/stop (CSS) testing. It was found that the phosphazene lubricated disks performed well when the lubricant thickness was about 0.5 nm. This thickness is less than a monolayer since the molecules of X-1p lubricant are ellipsoids with diameters of 1.1 nm by 1.2 nm. In other words, the results in ref. [2] indicate that the disk surface is not covered completely with lubricant for conditions corresponding to best tribological behavior. Because of this incomplete coverage, concerns about phosphazene lubricant systems exist with respect to the effects of humidity and temperature. This paper investigates the effects of relative humidity and temperature on the tribological performance of phosphazene lubricated disks.

II. EXPERIMENTS

A custom-built environmental chamber was used to study the dependence of phosphazene lubricated disks on the environmental humidity and temperature. The chamber, made of stainless steel, accommodates a vacuum compatible disk, spindle and motor assembly, and allows variations in temperature, humidity and pressure. The test disk is

mounted on the spindle and a set of solid state strain gauges is attached on an I-beam slider holder to monitor friction during the test. Different gases may be introduced into the chamber, although for the current study air was used. The test gas passes through a dryer and a filter, after which it is separated into two lines, namely, the "wet line" and the "dry line". The gas in the wet line passes through a water bubbler and then mixes with the gas in the dry line before entering the chamber. The gas outlets inside the chamber are arranged toward the chamber wall to obtain uniformly distributed gas flow. By controlling the flow rates in the two lines, the humidity inside the chamber can be effectively controlled. To control the chamber temperature and ensure that there is no water condensation due to the fluctuation of temperature, the chamber is double walled with temperature controlled water inside the double walls. The gas lines in the humidifier have a spiral shape and are surrounded by a water jacket. A constant temperature circulator is used to pump water continuously into the chamber and the humidifier, thereby ensuring that the entire system is at the desired temperature during the tests.

Commercially available carbon overcoated disks of 65 mm diameter with a center line average R_a of approximately 5 nm were lubricated with a cyclic phosphazene lubricant, X-1p, by gravity drain coating using three drain rates. The solvent used is hexane and the concentration of X-1p is 0.1 wt%. The X-1p lubricant has the following chemical structure:



The lubricant thickness was measured by a Fisons S-probe X-ray Photoelectron Spectrometer with a spot size of approximately 200 μm x 400 μm . The lubricant thickness, D , is obtained using equation (1):

$$\left[1 - \frac{I}{I_0}\right] = \exp\left[-\frac{D}{\lambda_{\text{eff}}}\right] \quad (1)$$

where I and I_0 are XPS intensities for an element of the lubricant film on the hard disk and a "thick" lubricant film standard, respectively. The escape depth (λ) is sample dependent and relates to the photoelectron kinetic energy. For X-1p, the fluorine F(1s) signal was used to obtain the lubricant film thickness. The escape depth used for fluorine was 1.8 (± 0.5) nm. An estimation of the analysis accuracy from these data is about 20%. The measurements from the fluorine signal was cooperated with the measurements based on phosphorus. Eleven measurements were made from inner radius to outer radius on each analyzed disk. The average value of the lubricant thickness and the standard deviation were calculated for the disk.

Constant speed drag tests were then performed in the environmental chamber to examine the effects of humidity and temperature on the tribological behavior of the disks. Each group of disks lubricated by different drain rates was tested at (a) standard conditions (23 °C, 40% RH), (b) high humidity conditions (23 °C, 80% RH), and (c) elevated temperature conditions (60 °C, 40% RH). A new disk and a new slider were used for each test condition. The strain gauges were calibrated at different temperatures and the measurements were temperature-compensated to eliminate the effect of temperature on the strain gauges. The test velocity was 0.2 m/s and acceleration during start-up was 0.1m/s². Thin film sliders made of Al₂O₃-TiC (70% style with R_a of approximately 2.5 nm) were used in all tests with a preload of 68.6 mN. The head crown for all sliders was between zero and 50 nm, and the edge blend was less than 75 nm.

III. RESULTS

The lubricant thicknesses of the three groups of disks analyzed by XPS are shown in Table I. We note that the thicknesses are in the range of 0.3-0.8 nm, which is similar to the range in ref. [2], where the solvent used was Freon, rather than Hexane. In particular, the lubricant thickness of group A (0.46 nm) is close to the thickness that performed best during stiction and CSS tests reported in ref. [2].

TABLE I
LUBRICANT THICKNESS & DRAIN RATE

Group	Drain Rate (mm/min)	Lubricant thickness (nm)	Standard deviation (nm)
A	17.78	0.46	0.18
B	27.94	0.36	0.04
C	101.6	0.74	0.09

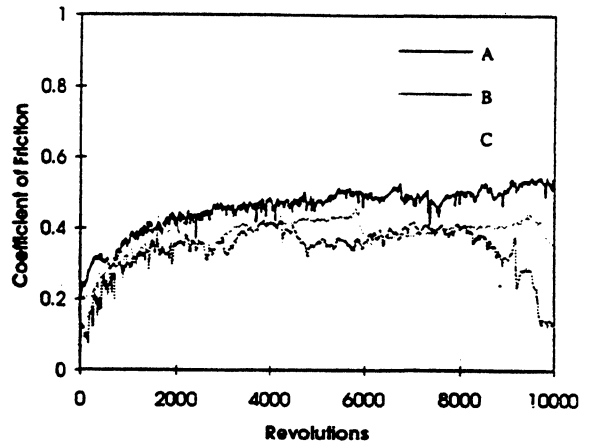


Fig. 1. Coefficient of friction versus revolution for 23 °C and 40% RH

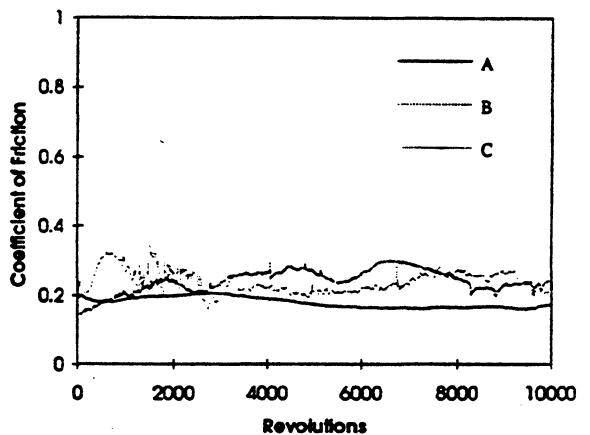


Fig. 2. Coefficient of friction versus revolution for 23 °C and 80% RH

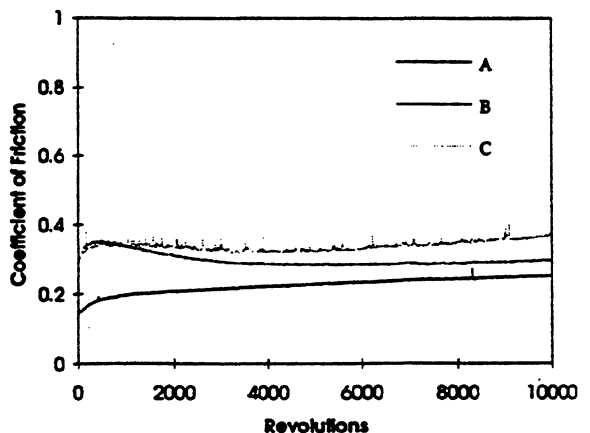


Fig. 3. Coefficient of friction versus revolution for 60 °C and 40% RH

Fig. 1 shows the variation of the coefficient of friction during drag testing at standard conditions. We observe that the coefficient of friction for group A is slightly higher than the other two groups. Although the coefficient of friction for group B is the lowest, it decreases after 8000 revolutions and a visible wear track was observed after testing. No visible wear tracks were observed on the other disks.

Fig. 2 shows the variation of the coefficient of friction as a function of the number of revolutions at high relative humidity. We observe that the coefficient of friction is lower at 80% RH than at 40% RH for all three groups of disks. Group A shows the lowest coefficient of friction at the high humidity conditions. The variation of the coefficient of friction for group A is smaller at 80% RH than at 40% RH. No visible wear track was observed for group A after testing, while wear tracks were observed on the disks of groups B and C after testing.

The variation of the coefficient of friction at elevated temperature is shown in Fig. 3. We observe that the coefficient of friction is lower at 60 °C than at 23 °C. Again, group A shows the lowest coefficient of friction among the disks. The coefficient of friction curves are fairly smooth except for the disk of group C. No visible wear track were observed on any disks after the tests.

IV. DISCUSSION

It is apparent that the disks of group A (0.46 nm lubricant thickness) performed best among the tested disks. This result is consistent with the results of stiction and CSS tests[2]. The lubricant thickness on the disks of group B seems to be too thin (0.3 nm) as the disks failed at both 40% and 80% RH. The lubricant on the disks of group C is strongly affected by high humidity and elevated temperature.

The observation that friction decreases with an increase of relative humidity from 40% to 80% seems to indicate that the X-1p lubricant interacts with water from the environment. However, X-1p is hydrophobic so the interaction between X-1p and water molecules could only be physical mixing. A possible explanation for the friction decrease in high humidity is that either the surface energy, or the viscosity of the lubricant, has decreased due to mixing.

The observation that friction decreases as environmental temperature increases from 23 °C to 60 °C seems to be related to viscosity. The viscosity of X-1p decreases from 1.401 Pas·s at 25 °C to 0.1 Pas·s at 60 °C (see Table II). Comparing Figs. 1 and 3, we observe that the disks performed better at elevated temperature. This seems to

TABLE II
VARIATION OF VISCOSITY WITH TEMPERATURE

Temperature (°C)	Viscosity (Pas·s, $\times 10^{-3}$)		
	X-1p	AM2001	Z-Dol
20	1401(25 °C)	75	87
40	312	32	35
60	100	14	16
80	35	6	8
100	15.6	1.5	3

suggest that a phosphazene type lubricant with lower viscosity may perform better from a tribological point of view. From Table II, we note that the viscosity of X-1p is much higher than that of AM2001 and Z-Dol at room temperature and that the viscosity of X-1p at 60 °C is close to the value of AM2001 and Z-Dol at 20 °C. To achieve a viscosity for the phosphazene lubricant systems corresponding to the viscosity of AM2001 and Z-Dol, it may be necessary to mix X-1p lubricant with some other low viscosity lubricant. Further studies is needed since the viscosity of a lubricant monolayer may be several times higher than that of the bulk material[3].

V. CONCLUSIONS

Phosphazenes are promising lubricants for hard disks. A typical phosphazene lubricant, X-1p, performs well at ambient, high humidity and elevated temperature conditions with a lubricant thickness of about 0.5 nm. It seems likely that a lower viscosity may improve the performance of the phosphazene lubricant system.

ACKNOWLEDGMENT

We would like to thank Prof. Lauer for helpful discussions during this project.

REFERENCES

- [1] B. S. Nader, K. K. Kar, T. A. Morgan, C. E. Pawloski, and W. L. Dilling, "Development and Tribological Properties of New Cyclotriphosphazene High Temperature Lubricants for Aircraft Gas Turbine Engines", *STLE Tribology Transactions, J. of Tribology*, Vol. 35, No. 1, 1992, pp. 37-44.
- [2] M. Yang, F. E. Talke, D. J. Peretti, T. A. Morgan, K. K. Kar, B. Dekoven and G. E. Potter, "Cyclotriphosphazenes as New Lubricants for Rigid Magnetic Recording Media", submitted for the *ASME/STLE Tribology Conference*, October 16-19, 1994 in Maui, Hawaii.
- [3] J. N. Israelachvili, P. M. McGuiggan and A. M. Homola, "Dynamic Properties of Molecularly Thin Liquid Films," *Science*, Vol. 240, 1988, pp.189-191.